Advanced Structured Materials

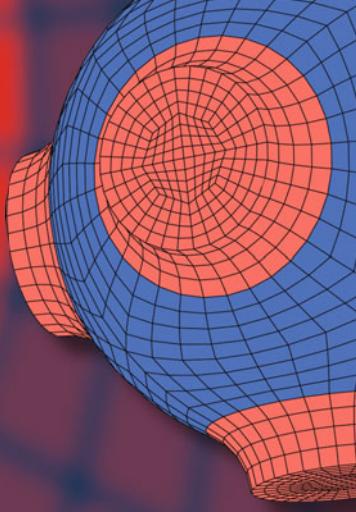

Holm Altenbach
Samuel Forest
Anton Krivtsov *Editors*

Generalized Continua as Models for Materials

With Multi-scale Effects or Under Multi-field Actions

Springer

Advanced Structured Materials

Volume 22

Series Editors

Andreas Öchsner
Lucas F. M. da Silva
Holm Altenbach

For further volumes:
http://www.springer.com/series/8611

Holm Altenbach · Samuel Forest
Anton Krivtsov
Editors

Generalized Continua as Models for Materials

With Multi-scale Effects or Under Multi-field Actions

Springer

Editors
Holm Altenbach
Lehrstuhl für Technische Mechanik
Otto-von-Guericke-Universität Magdeburg
Magdeburg
Germany

Samuel Forest
Centre des Materiaux CNRS UMR 7633
Mines ParisTech
Evry Cedex
France

Anton Krivtsov
Department of Theoretical Mechanics
St. Petersburg State Polytechnical University
St. Petersburg
Russia

ISSN 1869-8433 ISSN 1869-8441 (electronic)
ISBN 978-3-642-36393-1 ISBN 978-3-642-36394-8 (eBook)
DOI 10.1007/978-3-642-36394-8
Springer Heidelberg New York Dordrecht London

Library of Congress Control Number: 2013934985

Printed on acid-free paper

Springer is part of Springer Science+Business Media (www.springer.com)

Preface

The Mechanics of Generalized Continua is an established research topic since the end of the 1950s–early 1960s of the last century. The starting point of this development was the monograph of the Cosserat brothers, published in 1909[1] , and some previous works of such famous scientists like Lord Kelvin, Duhem, Helmholtz among others. All these contributions were focussed on the fact that in a continuum one has to define translations and rotations independently (or in other words, one has to establish force and moment actions independently as it was done by Jakob Bernoulli and Euler). At the same time the continuum was not modeled as an infinite number of continuously distributed points with properties like the mass, but as an infinite number of continuously distributed infinitesimal small bodies with properties like the mass.

The reason for the revival in the mid of 1950s of the last century was that some effects of the mechanical behavior of solids and fluids could not be explained by the available classical continuum models. Examples of this are the turbulence of a fluid or the behavior of solids with a significant and very complex microstructure. Since the suggested new models fulfill all requirements from *Continuum Thermomechanics* (the balance laws were formulated and the general representation of the constitutive equations were given) the scientific community was satisfied for a while. At the same time real applicative developments were missed.

Indeed, for practical applications the developed models were not useful. The reason for this was the gap between the formulated constitutive equations and the possibilities to identify the material parameters. As is often the case one had much more parameters compared to classical models, but no facilities to measure all properties. In addition, computational progress and available machines in these times were limited.

During the last ten years the situation has drastically changed. More and more researches emerged, being kindled by the partly forgotten models. Now one has available much more computational possibilities and very complex problems can be simulated numerically. In addition, with the increased attention paid to a large

[1] E. et F. Cosserat: Cosserat, F.: Théorie des Corps Déformables, Hermann Editeurs, Paris, 1909 (Reprint, Gabay, Paris, 2008).

number of materials with complex microstructure and a deeper understanding of the meaning of the material parameters (scale effects) the identification becomes much more well founded. Thus we have contributions describing the micro- and macro-behavior, new existence and uniqueness theorems, the formulation of multi-scale problems, etc., and now it is time to ponder again[2] the state of matter and to discuss new trends and applications.

The main focus in this book will be directed on the following items:

- Modeling and simulation of materials with significant microstructure;
- Generalized continua as a result of multi-scale models;
- Multi-field actions on materials resulting in generalized material models; and
- Comparison with discrete modeling approaches.

This book contains selected papers submitted to the Second Trilateral Seminar *Generalized Continua as Models for Materials With Multi-scale Effects or Under Multifield Actions*, which held at the *Leucorea* (Lutherstadt Wittenberg, Germany) from September 26 upto 30, 2012.[3] Special thanks to Andreas Kutschke who took all duties connected with realization of the Seminar. In addition, we kindly acknowledge Dr. Christoph Baumann and Benjamin Feuchter (Springer Publisher) for the support of the book project. Last but not least it should be mentioned that the Seminar was sponsored by grants of the French National Center for Scientific Research (CNRS), the German Research Foundation (DFG) AL341/41-1, and the Russian Foundation for Basic Research 12-01-91260RFG.

Magdeburg, December 2012 Holm Altenbach
Paris Samuel Forest
St. Petersburg Anton Krivtsov

[2] There were two proceedings within the last years which should be mentioned here: Gérard A. Maugin, Andrei V. Metrikine (Eds) Mechanics of Generalized Continua - One Hundred Years After the Cosserats, Springer, 2010 (Advances in Mechanics and Mathematics, Vol. 21) and Holm Altenbach, Gérard Maugin, Vladimir Erofeev (Eds) Mechanics of Generalized Continua, Springer, 2011 (Advanced Structured Materials, Vol. 7).

[3] The First Trilateral French–German–Russian Seminar held also in Lutherstadt Wittenberg (Germany) August 9–11, 2010.

Contents

Contributors

Eron L. Aero Institute of Problems in Mechanical Engineering, Bolshoy pr. 61, V.O., St. Petersburg, Russia 199178, e-mail: 16aero@mail.ru

Holm Altenbach Lehrstuhl für Technische Mechanik, Fakultät für Maschinenbau, Institut für Mechanik, Otto-von-Guericke-Universtät Magdeburg, Universitätsplatz 2, 39106 Magdeburg, Germany, e-mail: holm.altenbach@ovgu.de

Boris R. Andrievsky Institute of Problems in Mechanical Engineering, Bolshoy pr. 61, V.O., St. Petersburg, Russia 199178, e-mail: bandri@yandex.ru

Mohamed Assidi Centre de Recherche Public Henri Tudor, 29, Avenue John Kennedy, L-1885 Luxembourg, Luxembourg, e-mail: mohamed.assidi@tudor.lu

Nicolas Auffray Laboratoire Modélisation et Simulation MultiEchelle LMSME, Université Paris-Est, MSME UMR 8208 CNRS, 5 bd Descartes, 77454 Marne-la-Vallée, France, e-mail: Nicolas.auffray@univ-mlv.fr

Stéphane Berbenni Laboratoire d'Etudes des Microstructures et de Mécanique des Matériaux, LEM3, University of Lorraine, UMR CNRS 7239, 57045 Metz, France; Unité Mixte Internationale Georgia Tech Lorraine-CNRS, UMI CNRS 2958, 57070 Metz, France, e-mail: stephane.berbenni@univ-lorraine.fr

Laurent Capolungo Woodruff School of Mechanical Engineering, Georgia Institute of Technology/CNRS, 57070 Metz Cedex, France, e-mail: laurent.capolungo@me.gatech.edu

Mohammed Cherkaoui Unité Mixte Internationale Georgia Tech Lorraine-CNRS, UMI CNRS 2958, 57070 Metz, France; George W. Woodruff School of Mechanical Engineering, Georgia Institute of Technology, Atlanta, GA 30332-0405, USA, e-mail: mcherkaoui@me.gatech.edu

A. Das Laboratoire d'Etude des Microstructures et de Mécanique des Matériaux, Université de Lorraine/CNRS, Ile du Saulcy, 57045 Metz Cedex, France, e-mail: amitdas.cmu@gmail.com

Svyatoslav V. Derezin Faculty of Mathematics, Mechanics and Computer Science, Southern Federal University, Milchakova 8a, Rostov on Don, Russia 344090, e-mail: svd@hrz.tu-chemnitz.de

Stefan Diebels Chair of Applied Mechanics, Saarland University, Campus A4.2, D-66123 Saarbrücken, Germany, e-mail: s.diebels@mx.uni-saarland.de

Victor A. Eremeyev Lehrstuhl für Technische Mechanik, Fakultät für Maschinenbau, Institut für Mechanik, Otto-von-Guericke-Universtät Magdeburg, Universitätsplatz 2, 39106 Magdeburg, Germany; South Scientific Center of RASci and South Federal University, Milchakova St. 8a, Rostov on Don, Russia 344090, e-mail: eremeyev.victor@gmail.com; victor.eremeyev@ovgu.de

Vladimir I. Erofeev Nizhny Novgorod Mechanical Engineering, Research Institute of Russian Academy of Sciences, IMASH RAN, 85, Belinskogo st., Nizhny Novgorod, Russia 603024, e-mail: erf04@sinn.ru

Nachum Frage Department of Materials Engineering, Ben-Gurion University of the Negev, Beer-Sheva, Israel, e-mail: nfrage@bgu.ac.il

Claude Fressengeas Laboratoire d'Etude des Microstructures et de Mécanique des Matériaux, Université de Lorraine/CNRS, Ile du Saulcy, 57045 Metz Cedex, France, e-mail: claude.fressengeas@univ-lorraine.fr

Jean-François Ganghoffer LEMTA, Université de Lorraine, 2, Avenue de la Forêt de Haye, 54504 Vandoeuvrelès-Nancy Cedex, France, e-mail: jean-francois.ganghoffer@ensem.inpl-nancy.fr

Alexander Geringer Chair of Applied Mechanics, Saarland University, Campus A4.2, D-66123 Saarbrücken, Germany, e-mail: a.geringer@mx.uni-saarland.de

Ibrahim Goda LEMTA, Université de Lorraine, 2, Avenue de la Forêt de Haye, 54504 Vandoeuvrelès-Nancy Cedex, France, e-mail: ibrahim.goda@ensem.inpl-nancy.fr

Stefan Hartmann Institute of Applied Mechanics, Clausthal University of Technology, Adolph-Roemer-Str. 2a, 38678 Clausthal-Zellerfeld, Germany, e-mail: stefan.hartmann@tu-clausthal.de

Elena A. Ivanova St. Petersburg State Polytechnical University (SPbSPU), Politekhnicheskaya 29, St. Petersburg, Russia 195251; Institute for Problems in Mechanical Engineering, Russian Academy of Sciences, Bolshoy pr. V.O., 61, St. Petersburg, Russia 199178, e-mail: elenaivanova239@post.ru

Rasa Kazakevičiūtė-Makovska Mechanics-Continuum Mechanics, Ruhr University Bochum, Universitätsstr. 150, 44780 Bochum, Germany, e-mail: Rasa.Kazakeviciute-Makovska@rub.de

Vladimir V. Kazhaev Nizhny Novgorod Mechanical Engineering, Research Institute of Russian Academy of Sciences, IMASH RAN 85, Belinskogo st., Nizhny Novgorod, Russia 603024

Yaroslav E. Kolpakov Morion Inc., Kima ave. 13a, St. Petersburg, Russia 199155, e-mail: jaroslav@morion.com.ru

Anton Krivtsov Institute for Problems in Mechanical Engineering (IPME RAS), Bolshoy pr. V.O., 61, St. Petersburg, Russia 199178, ; St. Petersburg State Polytechnical University (SPbSPU), Politekhnicheskaya 29, St. Petersburg, Russia 195251, e-mail: akrivtsov@bk.ru

Arthur Lebée Laboratoire Navier (ENPC-IFSTTAR-CNRS), Ecole des Ponts Paris Tech, Université Paris-Est, 6-8 avenue Blaise Pascal, 77420 Champs-sur-Marne, France, e-mail: arthur.lebee@enpc.fr

Bernd Lenhof Chair of Applied Mechanics, Saarland University, Campus A4.2, D-66123 Saarbrücken, Germany, e-mail: b.lenhof@mx.uni-saarland.de

Christian Liebold Lehrstuhl für Kontinuumsmechanik und Materialtheorie, Institut für Mechanik, TU Berlin, Einsteinufer 5, 10587 Berlin, Germany, e-mail: christian.liebold@tu-berlin.de

Gérard A. Maugin Institut Jean le Rond d'Alembert, CNRS UMR 7190, Université Pierre et Marie Curie (Paris 6), 4 Place Jussieu, 75252 Paris Cedex 05, France, e-mail: gerard.maugin@upmc.fr

Thomas M. Michelitsch Institut Jean le Rond d'Alembert, CNRS UMR 7190, Université Pierre et Marie Curie (Paris 6), 4 Place Jussieu, 75252 Paris Cedex 05, France, e-mail: michel@lmm.jussieu.fr

Wolfgang H. Müller Lehrstuhl für Kontinuumsmechanik und Materialtheorie, Institut für Mechanik, TU Berlin, Einsteinufer 5, 10587 Berlin, Germany, e-mail: wolfgang.h.mueller@tu-berlin.de

Bhasker Paliwal Unité Mixte Internationale Georgia Tech Lorraine-CNRS, UMI CNRS 2958, 57070 Metz, France; George W. Woodruff School of Mechanical Engineering, Georgia Institute of Technology, Atlanta, GA 30332-0405, USA, e-mail: bpaliwal@gatech.edu

Igor S. Pavlov Nizhny Novgorod Mechanical Engineering, Research Institute of Russian Academy of Sciences, IMASH RAN, 85, Belinskogo st., Nizhny Novgorod, Russia 603024, e-mail: ispavl@mts-nn.ru

Wojciech Pietraszkiewicz Institute of Fluid-Flow Machinery, PASci, ul., Gen. J. Fiszera 14, 80-952 Gdańsk, Poland, e-mail: pietrasz@imp.gda.pl

Alexey V. Porubov Institute for Problems in Mechanical Engineering (IPME RAS), Bolshoy pr. V.O., 61, St. Petersburg, Russia 199178, e-mail: alexey.porubov@gmail.com

Steffen Rothe Institute of Applied Mechanics, Clausthal University of Technology, Clausthal-Zellerfeld, Germany, e-mail: steffen.rothe@tu-clausthal.de

Karam Sab Laboratoire Navier (ENPC-IFSTTAR-CNRS), Ecole des Ponts Paris Tech, Université Paris-Est, 6-8 avenue Blaise Pascal, 77420 Champs-sur-Marne, France, e-mail: karam.sab@enpc.fr

Denis Sheydakov South Scientific Center of Russian Academy of Sciences, Chekhova Ave. 41, Rostov on Don, Russia 344006, e-mail: sheidakov@mail.ru

Holger Steeb Mechanics-Continuum Mechanics, Ruhr University Bochum, Universitätsstr. 150, 44780 Bochum, Germany, e-mail: Holger.Steeb@rub.de

Vincent Taupin Laboratoire d'Etude des Microstructures et de Mécanique des Matériaux, Université de Lorraine/CNRS, Ile du Saulcy, 57045 Metz Cedex, France, e-mail: vincent.taupin@univ-lorraine.fr

Manas Upadhyay Woodruff School of Mechanical Engineering, Georgia Institute of Technology/CNRS, 57070 Metz Cedex, France, e-mail: manasvupadhyay@gmail.com

Elena Vilchevskaya Institute for Problems in Mechanical Engineering, Russian Academy of Sciences, Bolshoy pr. 61 V.O., St. Petersburg, Russia 199178, e-mail: vilchevska@gmail.com

Shells and Plates with Surface Effects

Holm Altenbach and Victor A. Eremeyev

Abstract The through-the-thickness integration procedure applied to a three-dimensional (3D) slender body leads to exact two-dimensional (2D) equations of plates and shells, see [36]. The procedure can be considered as a specific homogenization technique which results in a 2D generalized media—the non-linear theory of shells of Cosserat type. Within this theory the shell is described as a deformable surface each point of which has 3 translational and 3 rotational degrees of freedom similar to the 3D Cosserat continuum [15]. Below we discuss the through-the-thickness integration procedure applied to the non-classical problem of the theory of surface elasticity [21]. The theory can be applied to modeling of surface effects which are important in mechanics of nanostructured materials [11, 55]. Applying the through-the-thickness integration procedure we reduce 3D equations to 2D ones. The effective (apparent) stiffness properties of the shell are changed in comparison with the classical models of shells. Some examples of a plate bending are discussed taking into account surface effects.

H. Altenbach
Lehrstuhl für Technische Mechanik, Institut für Mechanik, Fakultät für Maschinenbau, Otto-von-Guericke-Universtät Magdeburg, Universitätsplatz 2, 39106 Magdeburg, Germany
e-mail: holm.altenbach@ovgu.de

V. A. Eremeyev (✉)
Faculty of Mechanical Engineering, Otto-von-Guericke University, 39106 Magdeburg, Germany
e-mail: eremeyev.victor@gmail.com

V. A. Eremeyev
South Scientific Center of RASci and South Federal University, Milchakova St. 8a, 344090 Rostov on Don, Russia
e-mail: victor.eremeyev@ovgu.de

H. Altenbach et al. (eds.), *Generalized Continua as Models for Materials*, Advanced Structured Materials 22, DOI: 10.1007/978-3-642-36394-8_1,

1 Introduction

Structures, which have a size of several μm and more, as usual are modeled within continuum mechanics taking into account only the properties of the bulk material. This statement is valid for any continuum theory—for the classical continuum mechanics in Cauchy's sense, Cosserat or micropolar theory and non-local theories among others. Special two-dimensional theories for plates and shells or one-dimensional theories for rods and beams can be introduced with the help of the through-the-thickness integration procedure or the through-the-cross-section integration procedure, respectively.

With respect to new technological developments an increasing miniaturization of devices and structural elements must be considered. Because of the changing surface-volume ratio in comparison with the classical sizes of the devices and structural elements the effects related to the surface phenomena have a significant influence on the mechanical behavior and should be taken into account. Here the possibilities to take into account these effects are demonstrated on plate- and shell-like structures.

1.1 Examples of Surface Phenomena

The influence of surface phenomena in deformable solid bodies is widely presented in the literature, see for example [6]. The main phenomena can be summarized as it follows:

- The development of nanotechnologies extends the field of application of the classical or non-classical theories of plates and shells towards the new thin-walled structures.
- In general, modern nanomaterials have physical properties which are different from the bulk material.
- The classical linear elasticity can be extended to the nanoscale by implementation of the theory of elasticity taking into account the surface stresses, cf. [11, 55].
- In particular, the surface stresses are responsible for the size-effect, that means the material properties of a specimen depend on its size. For example, Young's modulus of a cylindrical specimen increases significantly, when the cylinder diameter becomes very small [7, 9, 32, 39].
- The surface stresses are the generalization of the scalar surface tension which is a well-known phenomenon in the theory of capillarity.

The surface stresses which are the reason for the surface phenomena have influence on the following items:

- phase transitions (nucleation, crystal growth, etc.),
- fracture (Griffith criterion, effective surface energy density, line tension as a energy of a dislocation core),

- mechanics of porous media (nanoporous materials can be made stiffer than non-porous counterparts by surface modification) and
- other problems (surface diffusion, surface waves).

In various publications one reports on the changes of the mechanical properties in dependence on the size. Experimental results about the increasing Young's modulus with the decreasing size of nanowires made of ZnO are presented by Chen et al. [7]. Similar effects are described by Cuenot et al. [9] and Jing et al. [32] in the case of bending of nanobeams made of Ag and Pb. In [12] the behavior of nanoporous materials is discussed. In dependence on the size of the pores the material properties increase or decrease.

Taking into account only the elastic material behavior surface effects can be modeled within the classical theory of elasticity which was founded and influenced by French scientists in the $18^{\text{th}}/19^{\text{th}}$ century. The following contributions considering surface effects should be mentioned:

- First investigations of surface phenomena were initiated by Laplace [35], Young [58] and Gibbs [18].
- A modern treatise taking into account the surface stresses is given, for example, in the publications [21, 43, 44, 51]. Residual surface stresses are considered in [20, 24–26, 34, 53, 57].
- The treatment by the Finite Element Method or other numerical realizations is discussed in [27, 29–31].

For further reading about the history and the different approaches to modeling of the surface energy effects we recommend the reviews [11, 16, 41, 44, 47, 48, 55].

1.2 Basic Three-Dimensional Equations of Elasticity with Surface Effects

Let us summarize briefly the governing equations of the theory of elasticity with surface stresses in the sense of [21]. The reference configuration of the shell-like elastic body with surface stresses is shown in Fig. 1. The following equilibrium and boundary equations can be introduced

- Lagrangian equilibrium equation

$$\nabla_{\mathbf{X}} \cdot \mathbf{P} + \rho \mathbf{f} = \mathbf{0}, \tag{1}$$

- Equilibrium conditions on the upper and lower surfaces

$$(\mathbf{n} \cdot \mathbf{P} - \nabla_{\mathrm{S}} \cdot \mathbf{S})|_{\Omega_{\mathrm{S}}} = \mathbf{t}, \tag{2}$$

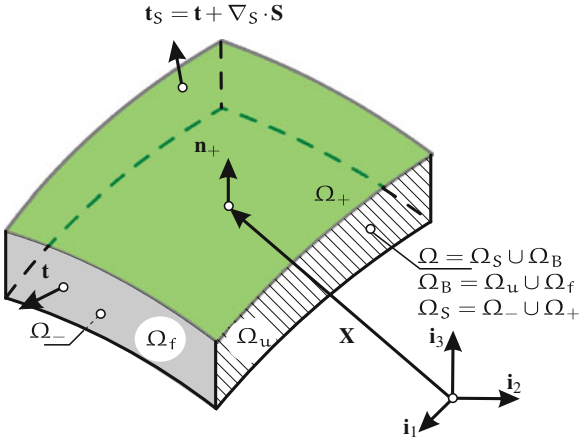

Fig. 1 Elastic body with surface effects

- Boundary conditions

$$\mathbf{u}|_{\Omega_u} = \mathbf{0}\,, \quad \mathbf{n} \cdot \mathbf{P}|_{\Omega_f} = \mathbf{t}\,. \tag{3}$$

Here $\mathbf{P}$ is the first Piola-Kirchhoff stress tensor, $\nabla_{\mathbf{X}}$ the 3D nabla operator, ∇_S the surface (2D) nabla operator, $\mathbf{S}$ the surface stress tensor of the first Piola-Kirchhoff type acting on the surfaces Ω_S, $\mathbf{u} = \mathbf{x} - \mathbf{X}$ the displacement vector, $\mathbf{x}$ and $\mathbf{X}$ are the position-vectors in the initial and actual configurations, respectively, $\mathbf{f}$ and $\mathbf{t}$ the body force and surface load vectors, respectively, and ρ the density. We assume that the part of the body surface Ω_u is fixed, while on Ω_f surface stresses $\mathbf{S}$ are absent. Equation (2) is the so-called generalized Young-Laplace equation describing the surface tension in solids.

The boundary-value problem (1)–(3) should be complemented by constitutive relations. For the bulk material we use the relation

$$\mathbf{P} = \frac{\partial W}{\partial \nabla_{\mathbf{X}} \mathbf{x}},$$

where W is the strain energy density. In the theory of Gurtin and Murdoch [21] the tensor $\mathbf{S}$ is similar to the membrane stress resultants defined as follows

$$\mathbf{S} = \frac{\partial \mathrm{U}}{\partial \mathbf{F}},$$

where U is the surface strain energy density and $\mathbf{F} = \nabla_S \mathbf{x}$ the surface deformation gradient.

In the case of residual stresses we assume that W and $\mathbf{P}$ possess the properties

$$W(\mathbf{I}) = 0, \quad \mathbf{P}(\mathbf{I}) = \mathbf{0},$$

while there exist residual (initial) surface energy and surface stresses that is

$$\mathsf{U}(\mathbf{A}) = \mathsf{U}_0 \neq 0, \quad \mathbf{S}(\mathbf{A}) = \mathbf{S}_0 \neq \mathbf{0},$$

where $\mathbf{I}$ and $\mathbf{A} \equiv \mathbf{I} - \mathbf{N} \otimes \mathbf{N}$ are the 3D and the surface unit tensors, respectively. In other words, we assume that the reference placement for the bulk material is natural one while for the attached on Ω_S membranes we assume the non-natural reference placement.

1.3 Linearized Relations

In the case of infinitesimal strains of an isotropic body we have the following constitutive equations:

- For the stresses in the bulk material the Hooke law is valid

$$\mathbf{P} = 2\mu\boldsymbol{\varepsilon} + \lambda\mathbf{I}\,\mathrm{tr}\boldsymbol{\varepsilon}, \tag{4}$$

  where λ and μ are the Lamé elastic moduli.
- For the surface stresses one can assume

$$\mathbf{S} = \mathbf{S_0} + \mathbf{C}_S : \mathbf{e} + \mathbf{S_0} \cdot \nabla_S \mathbf{u}, \tag{5}$$

  Here the first part is related to the residual stresses, the second is similar to Hooke's law with the elasticity tensor $\mathbf{C}_S$, the last part has the origin in the linearization of the surface Piola–Kirchhoff stress tensor.

In the case of initial uniform surface tension we have $\mathbf{S}_0 = \mathrm{p}\mathbf{A}$ and

$$\mathbf{S} = \mathrm{p}\mathbf{A} + 2\mu_S\mathbf{e} + \lambda_S\mathbf{A}\,\mathrm{tr}\mathbf{e} + \mathrm{p}\nabla_S\mathbf{u}, \tag{6}$$

where p is the initial surface tension, λ_S and μ_S are the surface elastic moduli called also the surface Lamé moduli.

The linearized strain-displacement relations are given as it follows

$$\boldsymbol{\varepsilon} = \frac{1}{2}\left[\nabla\mathbf{u} + (\nabla\mathbf{u})^{\mathrm{T}}\right], \quad \mathbf{e} = \frac{1}{2}\left[\nabla_S\mathbf{v}_S \cdot \mathbf{A} + \mathbf{A} \cdot (\nabla_S\mathbf{v}_S)^{\mathrm{T}}\right] \tag{7}$$

with

$$\mathbf{v}_S = \mathbf{u}\big|_{\Omega_S}.$$

The first Eq. (7) is valid for the bulk material, the second one for the surface contributions.

The number of material parameters is doubled in comparison with the classical isotropic case: instead of two we have now four. The requirement of the positive definiteness of the strain energy yields restrictions for λ, μ and λ_S, μ_S (see, for example, [2] and [28])

$$\mu > 0, \quad 3\lambda + 2\mu > 0; \quad \mu_S > 0, \quad \lambda_S + \mu_S > 0. \tag{8}$$

Note that $\mathbf{S}_0$ is an arbitrary second-order tensor, in general.

2 Two-Dimensional Theories of Nanosized Plates and Shells

The theory of elasticity with surface stresses was applied to the modifications of the two-dimensional theories of nano-sized plates and shells in [1, 3–5, 10, 14, 19, 22, 23, 37–39, 54, 57, 59], where various theories of plates and shells are formulated. The approaches can be classified, for example, by the starting point of the derivation. This can be the well-known three-dimensional continuum mechanics equations. In contrast, one can introduce à priory a two-dimensional deformable surface which is the basis for a more natural formulation of the two-dimensional governing equations. This so-called direct approach should be supplemented by the theoretical or experimental determination of the material parameters included in the constitutive equations.

Here we use the general theory of shells presented in [8, 15, 36] for the modification of the constitutive equations taking into account the surface stresses. We show that both the stress and the couple stress resultant tensors may be represented as a sum of two terms. The first term is the volume stress resultant while the second one determined by the surface stresses and the shell geometry. In the linear case this modification reduces to the add of new terms to the elastic stiffness parameters. The influence of these terms on the shell bending stiffness is discussed. We show that the surface elasticity makes the shell more stiffer in comparison with the shell without surface stresses.

2.1 Basic Equations of the 6-Parametric Elastic Shell Theory

The kinematics of the shell can be presented in the actual configuration by the position-vector $\mathbf{r}$ and a triad of three orthogonal vectors $\mathbf{d}_k$

$$\{\mathbf{r}(q^1,q^2,t);\, \mathbf{d}_k(q^1,q^2,t)\}; \qquad \mathbf{d}_k \cdot \mathbf{d}_m = \delta_{km}, \quad k,m = 1,2,3,$$

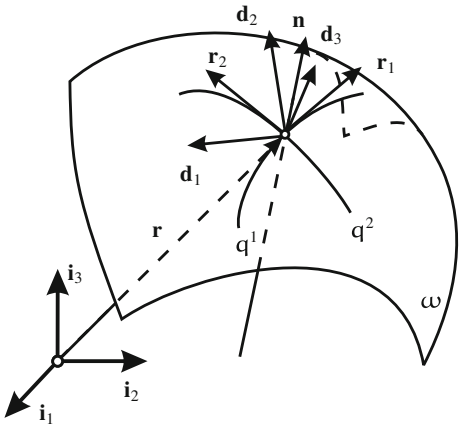

Fig. 2 Actual configuration of the shell

where δ_{km} is the Kronecker symbol, see Fig. 2. For the reference configuration one has the position-vector $\mathbf{R}$ and the triad $\mathbf{D}_k$

$$\{\mathbf{R}(q^1, q^2);\ \mathbf{D}_k(q^1, q^2)\};\quad \mathbf{D}_k \cdot \mathbf{D}_m = \delta_{km}.$$

Here q^1, q^2 are the Gaussian coordinates used for both configurations.

The quality of any continuum theory (three- or lower dimensional) depends significantly on the correct formulation of the corresponding constitutive equations that is in the case of elastic material the strain energy function. Let us assume

$$\mathcal{W} = \mathcal{W}(\mathbf{F}, \mathbf{Q}, \nabla_S \mathbf{Q}) \tag{9}$$

with

$$\mathbf{F} \stackrel{\triangle}{=} \nabla_S \mathbf{r},\quad \mathbf{Q} \stackrel{\triangle}{=} \mathbf{D}^k \otimes \mathbf{d}_k\,,$$

$$\nabla_S(\ldots) \stackrel{\triangle}{=} \mathbf{R}^\alpha \partial(\ldots)/\partial q^\alpha.$$

The base vectors are defined as

$$\mathbf{R}^\alpha \cdot \mathbf{R}_\beta = \delta^\alpha_\beta,\quad \mathbf{R}^\alpha \cdot \mathbf{N} = 0,\quad \mathbf{R}_\alpha = \partial \mathbf{R}/\partial q^\alpha,\quad \alpha,\beta = 1,2\,.$$

$\mathbf{Q}$ is an orthogonal tensor called the microrotation tensor, and $\mathbf{N}$ is the unit normal to the surface Ω in the reference configuration. After application of the principle of the frame indifference $\mathcal{W}$ takes the form

$$\mathcal{W} = \mathcal{W}(\mathbf{E},\mathbf{K}) \tag{10}$$

with the strain measures which are given by

$$\mathbf{E} \stackrel{\triangle}{=} \mathbf{F}\cdot\mathbf{Q}^{\mathrm{T}} - \mathbf{A}, \quad \mathbf{K} \stackrel{\triangle}{=} \frac{1}{2}\mathbf{R}^{\alpha} \otimes \left(\frac{\partial \mathbf{Q}}{\partial q^{\alpha}}\cdot\mathbf{Q}^{\mathrm{T}}\right)_{\times}. \tag{11}$$

Here $(\ldots)_{\times}$ denotes the vectorial invariant of the second-order tensor. In particular, for a diad it is given by

$$(\mathbf{a}\otimes\mathbf{b})_{\times} = \mathbf{a}\times\mathbf{b}.$$

The Lagrangian equilibrium equations are formulated as it follows

$$\nabla_S\cdot\mathbf{T} + \mathbf{q} = \mathbf{0}, \quad \nabla_S\cdot\mathbf{M} + \left[\mathbf{F}^{\mathrm{T}}\cdot\mathbf{T}\right]_{\times} + \mathbf{c} = \mathbf{0}. \tag{12}$$

The force and the moment tensors $\mathbf{T}$ and $\mathbf{M}$ can be computed from

$$\mathbf{T} \stackrel{\triangle}{=} \frac{\partial \mathcal{W}}{\partial \mathbf{E}}\cdot\mathbf{Q}, \quad \mathbf{M} \stackrel{\triangle}{=} \frac{\partial \mathcal{W}}{\partial \mathbf{K}}\cdot\mathbf{Q}. \tag{13}$$

They are the resultant tensors of the first Piola-Kirchhoff type on the deformable surface, while $\mathbf{q}$ and $\mathbf{c}$ are the external surface force and moment vectors, respectively. The equilibrium equations (12) are the exact consequence of three-dimensional equilibrium equations, see [8, 36]. Within the framework of the theory the approximation error is localized in the constitutive equation (10) only. The strain measures $\mathbf{E}$ and $\mathbf{K}$ are work-conjugate to the respective stress measures.

2.2 Plates and Shells with Surface Stresses

Applying the through-the-thickness integration technique described in [36] to shell-like bodies with surface stresses, we obtain the following 2D constitutive equations for nano-sized plates and shells, see [1]:

$$\mathbf{T}^{*} = \mathbf{T} + \mathbf{T}_S, \quad \mathbf{M}^{*} = \mathbf{M} + \mathbf{M}_S, \tag{14}$$

where

- $\mathbf{T}$,$\mathbf{M}$ are classical resultant tensors given by

$$\mathbf{T} = \int \mathbf{G}\cdot\mathbf{P}\,\mathrm{d}\zeta, \quad \mathbf{M} = -\int \mathbf{G}\cdot\mathbf{P}\times\mathbf{z}\,\mathrm{d}\zeta \tag{15}$$

  with

$$\int(\ldots)\,\mathrm{d}\zeta = \int_{h_-}^{h_+}(\ldots)\,\mathrm{d}\zeta$$

  and

- $\mathbf{T}_S$,$\mathbf{M}_S$ are the resultant tensors induced by surface stresses $\mathbf{S}_\pm$ acting on the shell faces $\Omega_\pm$

$$\begin{aligned} \mathbf{T}_S &= G_+\mathbf{S}_+ + G_-\mathbf{S}_-\,, \\ \mathbf{M}_S &= -\frac{h}{2}\left[G_+(\mathbf{S}_+)\times\mathbf{z}_+ - G_-(\mathbf{S}_-)\times\mathbf{z}_-\right]. \end{aligned} \tag{16}$$

Here $\mathbf{z}$ is the base reference deviation and $\mathbf{G} \equiv -\mathbf{N}\times(\mathbf{A}-\zeta\nabla_S\mathbf{N})\times\mathbf{N}$ is the geometrical tensor, $G \equiv \det(\mathbf{A}-\zeta\nabla_S\mathbf{N})$ is the geometric scale factor defined in [36], ζ is the coordinate along the unit normal $\mathbf{N}$ in the reference placement, $G_\pm = G\big|_{\zeta=\pm h/2}$, and h is the shell thickness, see Fig. 3.

3 Linear Theory of Plates with Surface Stresses

The theory can be significantly simplified for plates and infinitesimal strains. In this case the shell strain energy density is given by

$$\begin{aligned} 2\mathcal{W} = {}& \alpha_1 tr^2\mathbf{E}_\parallel + \alpha_3 tr\left(\mathbf{E}_\parallel\cdot\mathbf{E}_\parallel^T\right) + \alpha_4\mathbf{N}\cdot\mathbf{E}^T\cdot\mathbf{E}\cdot\mathbf{N} \\ & + \beta_1 tr^2\mathbf{K}_\parallel + \beta_3 tr\left(\mathbf{K}_\parallel\cdot\mathbf{K}_\parallel^T\right) + \beta_4\mathbf{N}\cdot\mathbf{K}^T\cdot\mathbf{K}\cdot\mathbf{N} \end{aligned} \tag{17}$$

with $\mathbf{E}_\parallel = \mathbf{E}\cdot\mathbf{A}$ and $\mathbf{K}_\parallel = \mathbf{K}\cdot\mathbf{A}$. α_i and β_i are elastic parameters

$$\begin{aligned} &\alpha_1 = C\nu,\ \alpha_3 = C(1-\nu),\ \alpha_4 = \alpha_s C(1-\nu)\,, \\ &\beta_1 = D\nu,\ \beta_3 = D(1-\nu),\ \beta_4 = \alpha_t D(1-\nu) \end{aligned} \tag{18}$$

with

$$C = \frac{Eh}{1-\nu^2},\quad D = \frac{Eh^3}{12(1-\nu^2)}\,.$$

E and ν are Young's modulus and Poisson's ratio of the bulk material, α_s and α_t are dimensionless coefficients, while h is the shell thickness. α_s is similar to the shear correction factor introduced by Reissner [45] ($\alpha_s = 5/6$) and Mindlin [40] ($\alpha_s = \pi^2/12$). The value $\alpha_t = 7/10$ was proposed in [42].

Considering the surface stress tensors $\mathbf{S}_\pm$ we assume $p = 0$ in (6). So we have

$$\begin{aligned} \mathbf{S}_\pm &= \lambda_S^\pm\mathbf{A}tr\mathbf{e}_\pm + 2\mu_S^\pm\mathbf{e}_\pm\,, \\ 2\mathbf{e}_\pm &= \nabla\mathbf{u}_\pm\cdot\mathbf{A} + \mathbf{A}\cdot(\nabla\mathbf{u}_\pm)^T\,, \end{aligned} \tag{19}$$

$\mathbf{u}_\pm = \mathbf{u}\big|_{\zeta=\pm h/2}$. For the sake of simplicity we consider the symmetric case with $\lambda_S^\pm = \lambda_S$ and $\mu_S^\pm = \mu_S$. Taking into account (19) we obtain the stiffness parameters

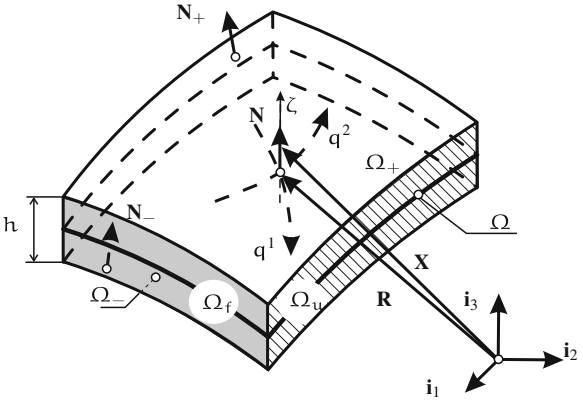

Fig. 3 Geometry (reference configuration) of the shell-like body

for the plate with surface stresses, see [4, 14]

$$\begin{aligned}
&\alpha_1 = C\nu + 2\lambda_S\,, \quad \alpha_3 = C(1-\nu) + 4\mu_S\,,\\
&\beta_1 = D\nu + h^2\lambda_S/2\,, \quad \beta_3 = D(1-\nu) + h^2\mu_S\,,\\
&C^* = C + 4\mu_S + 2\lambda_S,\\
&D^* = D + h^2\mu_S + h^2\lambda_S/2\,.
\end{aligned} \tag{20}$$

C^* and D^* are the effective in-plane and bending stiffness of the plate with surface stresses. $C^* > C$ and $D^* > D$, i.e. the plate with surface stresses is stiffer. α_4 and β_4 do not depend on λ_S and μ_S.

As an example let us consider a nanoplate made of aluminium. Using the data presented in [11] the dependence D^* versus the plate thickness h is shown in Fig. 4. Here $\mu = 34.7\,\text{GPa}$, $\nu = 0.3$, $\lambda_S = -3.48912\,\text{N/m}$, $\mu_S = 6.2178\,\text{N/m}$, where μ is the shear modulus. For these values of λ_S and μ_S the influence of the surface stresses is significant if $h \le 20\,\text{nm}$.

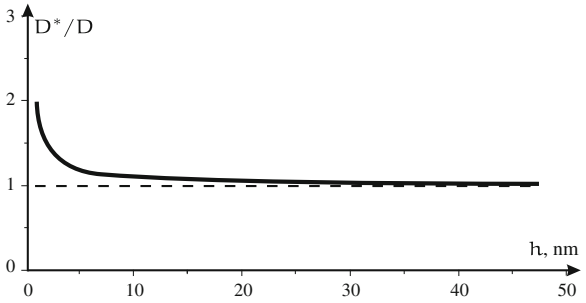

Fig. 4 Bending stiffness versus plate thickness

4 Viscoelastic Case

In most of contributions on the surface stresses the elastic medium is considered. On the other hand, dissipative processes in the vicinity of the surface are observed. These surface phenomena are related to the higher mobility of molecules near the surface, surface imperfections, absorbates, etc., see e.g. [50]. As a special case of inelastic behavior the surface viscoelasticity exists for both liquids and solids. The experimental methods of the surface viscoelasticity are different than in the case of bulk material, in general. One can use various types of microscopies, light scattering, etc., see e.g. [13, 17, 33, 49, 52, 56]. For the description of the surface dissipation of nanosized beams, Ru [46] proposed the one-dimensional constitutive law that is similar to the model of the standard viscoelastic solids. In [5] we extended Ru's model to the case of two-dimensional surface stresses.

The simplest case of analyzing viscoelastic material behavior is based on the correspondence principle. This principle states that if an elastic solution is known, the corresponding viscoelastic solution can be obtained by substituting the elastic quantities in the Laplace transforms of the unknown functions. In other words, one can use the solution of the boundary-value-problem (BVP) for the elastic material behavior as the solution of BVP for the viscoelastic material but given in terms of Laplace transforms. According to this principle we use the results of 3D to 2D reduction procedure for the elastic shell-like body [4].

Let us introduce the Laplace transform

$$\overline{f}(s) = \int_0^\infty f(t) e^{-st} dt.$$

Applying the Laplace transform to the viscoelastic constitutive equations at the surface we obtain the relation

$$\overline{\mathbf{S}} = 2s\overline{\mu}_S(s)\overline{\mathbf{e}} + s\overline{\lambda}_S(s)(\mathrm{tr}\,\overline{\mathbf{e}})\mathbf{A}, \tag{21}$$

which coincides formally with the surface Hooke law (6) but with two surface relaxation functions $\mu_S(t)$ and $\lambda_S(t)$. In addition, we establish the constitutive equations for the shell considering viscoelastic behavior in the form, see [5]

$$\mathbf{T} = \int_{-\infty}^{t} [C_1(t-\tau)\dot{\mathbf{e}}(\tau) + C_2(t-\tau)\mathbf{A}\mathrm{tr}\,\dot{\mathbf{e}}(\tau)]\, d\tau + \Gamma\boldsymbol{\gamma} \otimes \mathbf{N},$$

$$\mathbf{M} = -\int_{-\infty}^{t} [D_1(t-\tau)\dot{\boldsymbol{\kappa}}(\tau) + D_2(t-\tau)\mathbf{A}\mathrm{tr}\,\dot{\boldsymbol{\kappa}}(\tau)]\, d\tau \times \mathbf{N},$$

where $\boldsymbol{\epsilon}$, $\boldsymbol{\kappa}$, and $\boldsymbol{\gamma}$ are the surface strain measures expressed via the translation and rotation vectors $\mathbf{w}$ and $\boldsymbol{\vartheta}$ by

$$\begin{aligned}
\boldsymbol{\epsilon} &= \frac{1}{2}\left(\nabla_S \mathbf{w}\cdot\mathbf{A} + \mathbf{A}\cdot(\nabla_S \mathbf{w})^T\right),\\
\boldsymbol{\kappa} &= \frac{1}{2}\left(\nabla_S \boldsymbol{\vartheta}\cdot\mathbf{A} + \mathbf{A}\cdot(\nabla_S \boldsymbol{\vartheta})^T\right),\\
\boldsymbol{\gamma} &= \nabla_S(\mathbf{w}\cdot\mathbf{N}) - \boldsymbol{\vartheta}.
\end{aligned}$$

The relaxation functions are given by

$$\begin{aligned}
&C_1(t) = 2C_{22} + 4\mu_S(t), \quad C_2(t) = C_{11} - C_{22} + 2\lambda_S(t),\\
&D_1(t) = 2D_{22} + h^2\mu_S(t),\ D_2(t) = D_{33} - D_{22} + \frac{h^2}{2}\lambda_S(t),
\end{aligned}$$

$$\begin{aligned}
&C_{11} = \frac{Eh}{2(1-\nu)}, \quad C_{22} = \frac{Eh}{2(1+\nu)},\\
&D_{22} = \frac{Eh^3}{24(1+\nu)},\ D_{33} = \frac{Eh^3}{24(1-\nu)}, \quad \Gamma = k\mu h,\\
&E = 2\mu(1+\nu), \qquad \nu = \frac{\lambda}{2(\lambda+\mu)}.
\end{aligned}$$

E and ν are the Young modulus and Poisson ratio of the bulk material, Γ is the transverse shear stiffness, and k the transverse shear correction factor. The tangential and bending relaxation functions are given by

$$C = \frac{Eh}{1-\nu^2} + 4\mu_S(t) + 2\lambda_S(t), \qquad D = \frac{Eh^3}{12(1-\nu^2)} + \frac{h^2}{2}\left[2\mu_S(t) + \lambda_S(t)\right]. \quad (22)$$

Let us note that the surface stresses do not influence the transverse shear stiffness.

5 Conclusions

In this paper we discussed the two-dimensional equilibrium equations for plates and shells taking into account the surface stresses. We presented the expressions for effective stiffness parameters of plates and shells. In particular, the bending stiffness is bigger for the shells with surface stresses than for shells without surface elasticity. Elastic case is extended to viscoelastic behavior.

Acknowledgments The second author was supported by the DFG grant No. AL 341/33-1 and by the RFBR with the grant No. 12-01-00038.

References

1. Altenbach, H., Eremeyev, V.A.: On the shell theory on the nanoscale with surface stresses. Int. J. Eng. Sci. **49**(12), 1294–1301 (2011)
2. Altenbach, H., Eremeyev, V.A., Lebedev, L.P.: On the existence of solution in the linear elasticity with surface stresses. ZAMM **90**(7), 535–536 (2010)
3. Altenbach, H., Eremeyev, V.A., Morozov, N.F.: Linear theory of shells taking into account surface stresses. Dokl. Phys. **54**(12), 531–535 (2009)
4. Altenbach, H., Eremeyev, V.A., Morozov, N.F.: On equations of the linear theory of shells with surface stresses taken into account. Mech. Solid **45**(3), 331–342 (2010)
5. Altenbach, H., Eremeyev, V.A., Morozov, N.F.: Surface viscoelasticity and effective properties of thin-walled structures at the nanoscale. Int. J. Eng. Sci. **59**, 83–89 (2012)
6. Altenbach, H., Morozov, N.F. (eds.): Surface Effects in Solid Mechanics—Models, Simulations, and Applications. Springer, Berlin (2013)
7. Chen, C.Q., Shi, Y., Zhang, Y.S., Zhu, J., Yan, Y.J.: Size dependence of Young's modulus in ZnO nanowires. Phy. Rev. Lett. **96**(7), 075505–4 (2006)
8. Chróścielewski, J., Makowski, J., Pietraszkiewicz, W.: Statyka i dynamika powłok wielopłatowych. Nieliniowa teoria i metoda elementów skończonych. Wydawnictwo IPPT PAN, Warszawa (2004)
9. Cuenot, S., Frétigny, C., Demoustier-Champagne, S., Nysten, B.: Surface tension effect on the mechanical properties of nanomaterials measured by atomic force microscopy. Phys. Rev. B **69**(16), 165410–5 (2004)
10. Dahmen, K., Lehwald, S., Ibach, H.: Bending of crystalline plates under the influence of surface stress—a finite element analysis. Surf. Sci. **446**(1–2), 161–173 (2000)
11. Duan, H.L., Wang, J., Karihaloo, B.L.: Theory of elasticity at the nanoscale. In: Advances in Applied Mechanics, vol. 42, pp. 1–68. Elsevier, San Diego (2008)
12. Duan, H.L., Wang, J., Karihaloo, B.L., Huang, Z.P.: Nanoporous materials can be made stiffer than non-porous counterparts by surface modification. Acta Mater. **54**, 2983–2990 (2006)
13. Earnshaw, J.C., McGivern, R.C., McLaughlin, A.C., Winch, P.J.: Light-scattering-studies of surface viscoelasticity—direct data-analysis. Langmuir **6**(3), 649–660 (1990)
14. Eremeyev, V.A., Altenbach, H., Morozov, N.F.: The influence of surface tension on the effective stiffness of nanosize plates. Doklady Phys. **54**(2), 98–100 (2009)
15. Eremeyev, V.A., Lebedev, L.P., Altenbach, H.: Foundations of Micropolar Mechanics. Springer, Heidelberg (2012)
16. Finn, R.: Equilibrium Capillary Surfaces. Springer, New York (1986)
17. Garcia, R., Gómez, C.J., Martinez, N.F., Patil, S., Dietz, C., Magerle, R.: Identification of nanoscale dissipation processes by dynamic atomic force microscopy. Phys. Rev. Lett. **97**(1), 1–4 (2006). doi:10.1103/PhysRevLett.97.016103
18. Gibbs, J.W.: On the equilibrium of heterogeneous substances. In: Willard Gibbs, J. (ed.) The Collected Works, pp. 55–353. Longmans, Green & Co, New York (1928)
19. Guo, J.G., Zhao, Y.P.: The size-dependent elastic properties of nanofilms with surface effects. J. Appl. Phys. **98**(7), 074306–11 (2005)
20. Gurtin, M.E., Markenscoff, X., Thurston, R.N.: Effect of surface stress on natural frequency of thin crystalS. Appl. Phys. Lett. **29**(9), 529–530 (1976)
21. Gurtin, M.E., Murdoch, A.I.: A continuum theory of elastic material surfaces. Arch. Ration. Mech. Anal. **57**(4), 291–323 (1975)
22. He, L.H., Lim, C.W., Wu, B.S.: A continuum model for size-dependent deformation of elastic films of nano-scale thickness. Int. J. Solid Struct. **41**(3–4), 847–857 (2004)
23. Huang, D.W.: Size-dependent response of ultra-thin films with surface effects. Int. J. Solid Struct. **45**(2), 568–579 (2008)
24. Huang, Z., Sun, L.: Size-dependent effective properties of a heterogeneous material with interface energy effect: from finite deformation theory to infinitesimal strain analysis. Acta Mech. **190**, 151–163 (2007)

25. Huang, Z., Wang, J.: A theory of hyperelasticity of multi-phase media with surface/interface energy effect. Acta Mech. **182**, 195–210 (2006)
26. Huang, Z., Wang, J.: Micromechanics of nanocomposites with interface energy effect. In: Handbook on Micromechanics and Nanomechanics, p. 48 (in print). Pan Stanford Publishing (2012)
27. Javili, A., McBride, A., Steinmann, P.: Numerical modelling of thermomechanical solids with mechanically energetic (generalised) Kapitza interfaces. Comput. Mater. Sci. **65**, 542–551 (2012)
28. Javili, A., McBride, A., Steinmann, P., Reddy, B.D.: Relationships between the admissible range of surface material parameters and stability of linearly elastic bodies. Phil. Magazine **92**, 3540–3563 (2012)
29. Javili, A., Steinmann, P.: A finite element framework for continua with boundary energies. Part I: the two-dimensional case. Comput. Method Appl. Mech. Eng. **198**, 2198–2208 (2009)
30. Javili, A., Steinmann, P.: A finite element framework for continua with boundary energies. Part II: the three-dimensional case. Comput. Method Appl. Mech. Eng. **199**, 755–765 (2010)
31. Javili, A., Steinmann, P.: On thermomechanical solids with boundary structures. Comput. Method Appl. Mech. Eng. **47**, 3245–3253 (2010)
32. Jing, G.Y., Duan, H.L., Sun, X.M., Zhang, Z.S., Xu, J., Li, Y.D., Wang, J.X., Yu, D.P.: Surface effects on elastic properties of silver nanowires: contact atomic-force microscopy. Phys. Rev. B **73**(23), 235409–6 (2005)
33. Kajiyama, T., Tanaka, K., Ge, S.R., Takahara, A.: Morphology and mechanical properties of polymer surfaces via scanning force microscopy. Prog. Surf. Sci. **52**(1), 1–52 (1996)
34. Lagowski, J., Gatos, H.C., Sproles, E.S.: Surface stress and normal mode of vibration of thin crystals: GaAs. Appl. Phys. Lett. **26**(9), 493–495 (1975)
35. Laplace, P.S.: Supplément à la théorie de l'action capillaire. In: Traité de mécanique céleste, vol. X, pp. 1–68. Gauthier-Villars et fils, Paris (1805)
36. Libai, A., Simmonds, J.G.: The Nonlinear Theory of Elastic Shells, 2nd edn. Cambridge University Press, Cambridge (1998)
37. Lu, C.F., Lim, C.W., Chen, W.Q.: Size-dependent elastic behavior of FGM ultra-thin films based on generalized refined theory. Int. J. Solid Struct. **46**(5), 1176–1185 (2009)
38. Lu, P., He, L.H., Lee, H.P., Lu, C.: Thin plate theory including surface effects. Int. J. Solid Struct. **43**(16), 4631–4647 (2006)
39. Miller, R.E., Shenoy, V.B.: Size-dependent elastic properties of nanosized structural elements. Nanotechnology **11**(3), 139–147 (2000)
40. Mindlin, R.D.: Influence of rotatory inertia and shear on flexural motions of isotropic elastic plates. Transactions of ASME. J. Appl. Mech. **18**, 31–38 (1951)
41. Orowan, E.: Surface energy and surface tension in solids and fluids. Proc. Roy. Soc. London A **316**(1527), 473–491 (1970)
42. Pietraszkiewicz, W.: Finite Rotations and Langrangian Description in the Non-linear Theory of Shells. Polish Sci. Publ, Warszawa-Poznań (1979)
43. Podio-Guidugli, P., Caffarelli, G.V.: Surface interaction potentials in elasticity. Arch. Ration. Mech. Anal. **109**(4), 343–383 (1990)
44. Podstrigach, Y.S., Povstenko, Y.Z.: Introduction to Mechanics of Surface Phenomena in Deformable Solids (in Russian). Naukova Dumka, Kiev (1985)
45. Reissner, E.: On the theory of bending of elastic plates. J. Math. Phys. **23**, 184–194 (1944)
46. Ru, C.Q.: Size effect of dissipative surface stress on quality factor of microbeams. Appl. Phys. Lett. **94**, 051905–1-051905–3 (2009)
47. Rusanov, A.I.: Surface thermodynamics revisited. Surf. Sci. Rep. **58**(5–8), 111–239 (2005)
48. Rusanov, A.I.: Thermodynamics of solid surfaces. Surf. Sci. Rep. **23**(6–8), 173–247 (1996)
49. Sahoo, N., Thakur, S., Senthilkumar, M., Das, N.C.: Surface viscoelasticity studies of Gd_2O_3, SiO_2 optical thin films and multilayers using force modulation and force-distance scanning probe microscopy. Appl. Surf. Sci. **206**(1–4), 271–293 (2003)
50. Seoánez, C., Guinea, F., Castro Neto, A.H.: Surface dissipation in nanoelectromechanical systems: Unified description with the standard tunneling model and effects of metallic electrodes. Phys. Rev. B **77**(12), 195409 (2008)

51. Steigmann, D.J., Ogden, R.W.: Elastic surface-substrate interactions. Proc. Roy. Soc. London Ser. A Math. Phys. Eng. Sci. **455**(1982), 437–474 (1999)
52. Tranchida, D., Kiflie, Z., Acierno, S., Piccarolo, S.: Nanoscale mechanical characterization of polymers by atomic force microscopy (AFM) nanoindentations: viscoelastic characterization of a model material. Measur. Sci. Technol. **20**(9), 9 (2009)
53. Wang, G.F., Feng, X.Q.: Effects of surface elasticity and residual surface tension on the natural frequency of microbeams. Appl. Phys. Lett. **90**(23), 231,904 (2007)
54. Wang, J., Huang, Q.A., Yu, H.: Young's modulus of silicon nanoplates at finite temperature. Appl. Surf. Sci. **255**(5), 2449–2455 (2008)
55. Wang, J., Huang, Z., Duan, H., Yu, S., Feng, X., Wang, G., Zhang, W., Wang, T.: Surface stress effect in mechanics of nanostructured materials. Acta Mech. Solida Sin. **24**, 52–82 (2011)
56. Wang, X.P., Xiao, X.D., Tsui, O.K.C.: Surface viscoelasticity studies of ultrathin polymer films using atomic force microscopic adhesion measurements. Macromolecules **34**(12), 4180–4185 (2001)
57. Wang, Z.Q., Zhao, Y.P.: Self-instabilityand bending behaviors of nano plates. Acta Mech. Solida Sin. **22**(6), 630–643 (2009)
58. Young, T.: An essay on the cohesion of fluids. Philos. Trans. Roy. Soc. London **95**, 65–87 (1805)
59. Zhu, H.X., Wang, J.X., Karihaloo, B.L.: Effects of surface and initial stresses on the bending stiffness of trilayer plates and nanofilms. J. Mech. Mater. Struct. **4**(3), 589–604 (2009)

Geometrical Picture of Third-Order Tensors

Nicolas Auffray

Abstract Because of its strong physical meaning, the decomposition of a symmetric second-order tensor into a deviatoric and a spheric part is heavily used in continuum mechanics. When considering higher-order continua, third-order tensors naturally appear in the formulation of the problem. Therefore researchers had proposed numerous extensions of the decomposition to third-order tensors. But, considering the actual literature, the situation seems to be a bit messy: definitions vary according to authors, improper uses of denomination flourish, and, at the end, the understanding of the physics contained in third-order tensors remains fuzzy. The aim of this paper is to clarify the situation. Using few tools from group representation theory, we will provide an unambiguous and explicit answer to that problem.

1 Introduction

In classical continuum mechanics [28, 29], only the first displacement gradient is involved and all the higher-order displacement gradients are neglected in measuring the deformations of a body. This usual kinematical framework turns out not to be rich enough to describe a variety of important mechanical and physical phenomena. In particular, the size effects and non-local behaviors due to the discrete nature of matter at a sufficiently small scale, the presence of microstructural defects or the existence of internal constraints cannot be captured by classical continuum mechanics [2, 18, 24]. The early development of higher-order (or generalized) continuum theories of elasticity was undertaken in the 1960s and marked with the major contributions of [5, 19–21, 26]. For the last two decades, the development and application of high-order continuum theories have gained an impetus, owing to a growing interest in modeling

N. Auffray (✉)
Laboratoire Modélisation et Simulation Multi Echelle, LMSME, Université Paris-Est, MSME UMR 8208 CNRS, 5 bd Descartes, 77454 Marne-la-Vallée, France
e-mail: Nicolas.auffray@univ-mlv.fr

H. Altenbach et al. (eds.), *Generalized Continua as Models for Materials*, Advanced Structured Materials 22, DOI: 10.1007/978-3-642-36394-8_2,

and simulating size effects and non-local behaviors observed in a variety of materials, such as polycrystalline materials, geomaterials, biomaterials and nanostructured materials (see, e.g., [7, 17, 22]), and in small size structures. In order to take into account size-effects, the classical continuum mechanics has to be generalized. To construct such an extension there are, at least, two options:

- Higher-order continua:
  In this approach the set of degrees of freedom is extended; a classical example is the micromorphic theory [6, 11, 20];
- Higher-grade continua:
  In this approach the mechanical state is described using higher-order gradients of the displacement field; a classical example is the strain-gradient theory [19].

In the following section the linear formulation of micromorphic and strain-gradient theory we will be detailed. The aim is to anchor the analysis that will be made on third-order tensors into a physical necessity for the understanding of those models.

2 Some Generalized Continua

2.1 Micromorphic Elasticity

Let us begin with the micromorphic approach. In this theory the set of degrees of freedom (DOF) is extended in the following way

$$\text{DOF} = \{\underline{u}, \underset{\sim}{\chi}\} \quad ; \quad (\underline{u}, \underset{\sim}{\chi}) \in \mathbb{R}^3 \times \otimes^2 \mathbb{R}^3,$$

where $\otimes^k \mathbb{V}$ stands for the k-th order tensorial power of $\mathbb{V}$. In this formulation the second-order tensor $\underset{\sim}{\chi}$ is generally not symmetric. This micro-deformation tensor encodes the generally incompatibility deformation of the microstructure. As a consequence, the set of primary state variables (PSV) now becomes

$$\text{PSV} = \{\underline{u} \otimes \underline{\nabla}, \underset{\sim}{\chi} \otimes \underline{\nabla}\},$$

where $\underline{\nabla}$ is the classical nabla vector, i.e.

$$\underline{\nabla}^{\mathsf{T}} = \left(\frac{\partial}{\partial x} \; \frac{\partial}{\partial y} \; \frac{\partial}{\partial z} \right)$$

It can be observed that, despite being of higher-degree, the obtained model is still a 1st-grade continuum. The model is defined by the following set of strain measures:

- $\underset{\sim}{\varepsilon} = \varepsilon_{(ij)}$ is the strain tensor;

- $\underset{\sim}{e} = u \otimes \underline{\nabla} - \underset{\sim}{\chi}$ is the relative strain tensor;
- $\underset{\approx}{\kappa} = \underset{\sim}{\chi} \otimes \underline{\nabla}$ is the micro-strain gradient tensor;

where the notation $(..)$ indicates symmetry under in parentheses permutations. The first strain measure is the classical one and is, as usually, described by a symmetric second-order tensor. The relative strain tensor measures how the micro-deformation differs from the displacement gradient, this information is encoded into a non-symmetric second-order tensor. Finally, we have the third-order non-symmetric micro strain-gradient tensor. By duality the associated stress tensors can be defined:

- $\underset{\sim}{\sigma} = \sigma_{(ij)}$ is the Cauchy stress tensor;
- $\underset{\sim}{s} = s_{ij}$ is the relative stress tensor;
- $\underset{\approx}{S} = S_{ijk}$ is the double-stress tensor.

If we suppose that the relation between strain and stress tensors is linear, the following constitutive law is obtained:

$$\begin{cases} \underset{\sim}{\sigma} = \underset{\approx}{A} : \underset{\sim}{\varepsilon} + \underset{\approx}{B} : \underset{\sim}{e} + \underset{\cong}{C} \therefore \underset{\approx}{\kappa} \\ \underset{\sim}{s} = \underset{\approx}{B}^{T} : \underset{\sim}{\varepsilon} + \underset{\approx}{D} : \underset{\sim}{e} + \underset{\cong}{E} \therefore \underset{\approx}{\kappa} \\ \underset{\approx}{S} = \underset{\cong}{C}^{T} : \underset{\sim}{\varepsilon} + \underset{\cong}{E}^{T} : \underset{\sim}{e} + \underset{\sim}{\underset{\approx}{F}} \therefore \underset{\approx}{\kappa} \end{cases}$$

The behavior is therefore defined by

- three fourth-order tensors having the following index symmetries: $A_{\underline{(ij)}\,\underline{(lm)}}$; $B_{(ij)lm}$; $D_{\underline{ij}\,\underline{lm}}$;
- two fifth-order tensors having the following index symmetries: $C_{(ij)klm}$; E_{ijklm};
- one sixth-order tensor having the following index symmetries: $F_{\underline{ijk}\,\underline{lmn}}$,

where $\underline{..}$ indicates symmetry under block permutations.

2.2 Strain-Gradient Elasticity

In the strain-gradient elasticity the set of degrees of freedom is the usual one, but the primary state variables are extended to take the second gradient of $\underline{u}$ into account:

$$\text{PSV} = \{\underline{u} \otimes \underline{\nabla}, \underline{u} \otimes \underline{\nabla} \otimes \underline{\nabla}\}$$

We therefore obtain a second-grade continuum defined by the following set of strain measures:

- $\underset{\sim}{\varepsilon} = \varepsilon_{(ij)}$ is the strain tensor;
- $\underset{\approx}{\eta} = \underset{\sim}{\varepsilon} \otimes \underline{\nabla} = \eta_{(ij),k}$ is the strain-gradient tensor.

By duality, we obtain the related stress tensors:

- $\underset{\sim}{\sigma} = \sigma_{(ij)}$ is the Cauchy stress tensor;
- $\underset{\approx}{\tau} = \tau_{(ij)k}$ is the hyper-stress tensor.

Assuming a linear relation between these two sets we obtain:

$$\begin{cases} \underset{\sim}{\boldsymbol{\sigma}} = \underset{\approx}{\mathbf{A}} : \underset{\sim}{\varepsilon} + \underset{\approx}{\mathbf{C}} \therefore \underset{\simeq}{\eta} \\ \underset{\approx}{\boldsymbol{\tau}} = \underset{\approx}{\mathbf{C}}^{\mathrm{T}} : \underset{\sim}{\varepsilon} + \underset{\sim}{\mathbf{F}} \therefore \underset{\simeq}{\eta} \end{cases}$$

The strain-gradient and hyperstress tensors are symmetric under permutation of their two first indices. The constitutive tensors verify the following index permutation symmetry properties:

$$C_{\underline{(ij)}\,\underline{(lm)}} \quad ; \quad M_{(ij)(kl)m} \quad ; \quad A_{\underline{(ij)k}\,\underline{(lm)n}}$$

2.3 Synthesis

Those two models are distinct but under the kinematic constraint $\underset{\sim}{\chi} = \underline{u} \otimes \underline{\nabla}$ strain-gradient elasticity is obtained from the micromorphic model. In the first case, the micro strain-gradient is element of:

$$\mathbb{T}_{ijk} = \{\underset{\simeq}{T} | \underset{\simeq}{T} = \sum_{i,j,k=1}^{3} T_{ijk} \mathbf{e}_i \otimes \mathbf{e}_j \otimes \mathbf{e}_k\}$$

Assuming that we are in a 3D physical space, $\mathbb{T}_{ijk}$ is 27-dimensional and constructed as $\mathbb{T}_{ijk} = \otimes^3 \mathbb{R}^3$. For the strain-gradient theory, strain-gradient tensors belong to the following subspace of $\mathbb{T}_{ijk}$:

$$\mathbb{T}_{(ij)k} = \{\underset{\simeq}{T} | \underset{\simeq}{T} = \sum_{i,j,k=1}^{3} T_{ijk} \mathbf{e}_i \otimes \mathbf{e}_j \otimes \mathbf{e}_k, \;\; T_{ijk} = T_{jik}\}$$

which is 18-dimensional and constructed as[1] $\mathbb{T}_{(ij)k} = (\mathbb{R}^3 \otimes^S \mathbb{R}^3) \otimes \mathbb{R}^3$. Therefore, as it can be seen, the structure of the third-order tensors changes according to the considered theory.

Facing this kind of non-conventional model, a natural question is to ask what kind of information is encoded in these higher-order strain measures. In classical elasticity the physical content of symmetric second-order tensors is well-known through the

[1] The notation $\otimes^S$ indicates the symmetric tensor product.

physical meaning of its decomposition into a deviatoric (distorsion) and a spheric (dilatation) part. But the same result for third-order tensors is not so well-known, and its physical content has to be investigated. In the literature some results concerning the strain-gradient tensors can be found, but the situation seems to be fuzzy. In mechanics,[2] third-order tensor orthogonal decomposition was first investigated in the context of strain-gradient plasticity. According to the authors and the modeling assumptions the number of components varies from 2 to 4. In the appendices of [25] the authors introduced a first decomposition of the strain-gradient tensors under an incompressibility assumption, and expressed the decomposition into the sum of 3 mutually orthogonal parts. This decomposition was then used in [7, 8]. In [17] the situation is analyzed more in depth, and a decomposition into four parts is proposed. In some other works, it is said that strain-gradient can be divided into two parts. Therefore the following questions are raised:

- What is the right generalization of the decomposition of a tensor into deviatoric parts ?
- In how many orthogonal parts a third-order tensor can be split in a irreducible way ?
- Is this decomposition canonical ?

The aim of this paper is to answer these questions. These points will be investigated using the geometrical language of group action.

3 Harmonic Space Decomposition

To study the orthogonal decomposition of third-order tensors, and following the seemingly work of Georges Backus [3], an extensive use of harmonic tensors will be made. This section is thus devoted to formally introduce the concept of harmonic decomposition. After a theoretical introduction, the space of third-order tensors identified in the first section will be decomposed into a sum of harmonic tensor spaces. This $\mathrm{O}(3)$-irreducible[3] decomposition is the higher-order generalization of the well-known decomposition of $\mathbb{T}_{(\mathtt{ij})}$ into a deviatoric ($\mathbb{H}^2$) and spherical ($\mathbb{H}^0$) spaces.

3.1 The Basic Idea

Before studying decomposition of third-order tensors, let us get back for a while on the case of second-order symmetric ones. It is well known that any $\mathrm{T}_{(\mathtt{ij})} \in \mathbb{T}_{(\mathtt{ij})}$ admits the following decomposition:

[2] In field of condensed matter physics this decomposition is known since, at least, the 70' [15].

[3] $\mathrm{O}(3)$: the orthogonal group, i.e. the group of all isometries of $\mathbb{R}^3$ i.e. if $\mathrm{Q} \in \mathrm{O}(3)$ $\det(\mathrm{Q}) \pm 1$ and $\mathrm{Q}^{-1} = \mathrm{Q}^{\mathrm{T}}$.

$$T_{(ij)} = H^2_{(ij)} + \frac{1}{3}H^0\delta_{ij} = \phi(H^2_{(ij)}, H^0),$$

where $H^2 \in \mathbb{H}^2$ and $H^0 \in \mathbb{H}^0$ are, respectively, the 5-D deviatoric and 1-D spheric part of $T_{(ij)}$ and are defined by the following formula:

$$H^0 = T_{ii} \quad ; \quad H^2_{(ij)} = T_{(ij)} - \frac{1}{3}H^0\delta_{ij}$$

In fact ϕ, defined by the expression (3.1), is an isomorphism between $\mathbb{T}_{(ij)}$ and the direct sum of $\mathbb{H}^2$ and $\mathbb{H}^0$

$$\mathbb{T}_{(ij)} \cong \mathbb{H}^2 \oplus \mathbb{H}^0$$

The main property of this decomposition is to be $O(3)$-invariant, or expressed in another way the components $(H^0, \underset{\sim}{H}^2)$ are covariant with $\underset{\sim}{T}$ under $O(3)$-action, i.e.

$$\forall \underset{\sim}{Q} \in O(3),\ \forall \underset{\sim}{T} \in \mathbb{T}_{(ij)}, \quad \underset{\sim}{Q}\underset{\sim}{T}\underset{\sim}{Q}^T = \phi(\underset{\sim}{Q}\underset{\sim}{H}^2\underset{\sim}{Q}^T, H^0)$$

Irreducible tensors satisfying this property are called harmonic. By irreducible we mean that those tensors can not be split into other tensors satisfying this property. In a certain way harmonic tensors are the elementary gears of the complete tensor. Let now give a more precise and general definition of this decomposition.

3.2 Harmonic Decomposition

The $O(3)$-irreducible decomposition of a tensor is known as its harmonic decomposition. Such a decomposition is well-known in group representation theory. It allows to decompose any finite order tensor into a sum of irreducible ones [3, 14, 30]. Consider a n-th order tensor T belonging to $\mathbb{T}$ then its decomposition can be written [14]:

$$T = \sum_{k,\tau} H^{k,\tau},$$

where the tensors $H^{k,\tau}$ are components[4] of the irreducible decomposition, k denotes the order of the harmonic tensor embedded in H and τ separates the same order terms. This decomposition defines an isomorphism between $\mathbb{T}$ and a direct sum of harmonic tensor spaces $\mathbb{H}^k$ [10] as

[4] To be more precise, $H^{k,\tau}$ is the embedding of the τth irreducible component of order k into a n-th order tensor.

$$\mathbb{T} \cong \bigoplus_{k,\tau} \mathbb{H}^{k,\tau}$$

but, as explained in [12], this decomposition is not unique. Alternatively, the $O(3)$-isotypic decomposition, where same order spaces are grouped, is unique:

$$\mathbb{T} \cong \bigoplus_{k=0}^{n} \alpha_k \mathbb{H}^k,$$

where α_k is the multiplicity of $\mathbb{H}^k$ in the decomposition, i.e. the number of copies of the space $\mathbb{H}^k$ in the decomposition. Harmonic tensors are totally symmetric and traceless. In $\mathbb{R}^3$, the dimension of their vector space $\dim \mathbb{H}^k = 2k+1$. For $k = 0$ we obtain the space of scalars, $k = 1$ we obtain the space of vectors, $k = 2$ we obtain the space of deviators, and for $k > 2$ we obtain spaces of k-th order deviators. The family $\{\alpha_k\}$ is a function of the tensor space order and the index symmetries. Various methods exist to compute this family [1, 14, 30]. In $\mathbb{R}^3$ a very simple method based on the Clebsch-Gordan decomposition can be used.

In the next section this construction is introduced. It worths noting that we obtain the harmonic structure of the space under investigation modulo an unknown isomorphism. The construction of an isomorphism making this decomposition explicit is an ulterior step of the process. Furthermore, according to the nature of the sought information, the explicit knowledge of the isomorphism might by unnecessary. As an example, the determination of the set of symmetry classes of a constitutive tensor space does not require such a knowledge[5] [16, 23].

3.3 Computation of the Decomposition

The principle is based on the tensorial product of group representations. More details can be found in [1, 14]. The computation rule is simple. Consider two harmonic tensor spaces $\mathbb{H}^i$ and $\mathbb{H}^j$, whose product space is noted $\mathbb{G}^{i+k} := \mathbb{H}^i \otimes \mathbb{H}^j$. This space, which is $GL(3)$-invariant, admits the following $O(3)$-invariant decomposition:

$$\mathbb{G}^{i+j} = \bigoplus_{k=|i-j|}^{i+j} \mathbb{H}^k$$

For example, consider $\mathbb{H}^1_a$ and $\mathbb{H}^1_b$ two different first-order harmonic spaces. Elements of such spaces are vectors. According the above formula the $O(3)$-invariant decomposition of $\mathbb{G}^2$ is:

[5] Even if some authors explicitly construct this isomorphism [10, 13] this step is useless.

$$\mathbb{G}^2 = \mathbb{H}^1_{\mathtt{a}} \otimes \mathbb{H}^1_{\mathtt{b}} = \mathbb{H}^2 \oplus \mathbb{H}^{\sharp\,1} \oplus \mathbb{H}^0$$

In this decomposition, the space indicated with the $^\sharp$ superscript contains *pseudo-tensors*, also known as *axial*-tensors i.e. tensors which change sign if the space orientation is reversed. Other elements are true tensors, also known as *polar*, and transform according to the usual rules.

As an example, the tensorial product of two spaces of vectors generates a second-order tensor space. The resulting structure is composed of a scalar ($\mathbb{H}^0$), a vector ($\mathbb{H}^{\sharp 1}$) and a deviator ($\mathbb{H}^2$). The vector part corresponds to the pseudo-vector associated with the matrix antisymmetric part. This computation rule has to be completed by the following properties [14]:

Property 2.1. The decomposition of an even-order (resp. odd-order) completely symmetric tensor, i.e. invariant under any index permutation, only contains even-order (resp. odd-order) harmonic spaces.

Property 2.2. In the decomposition of an even-order (resp. odd-order) even-order (resp. odd-order) components are polar and odd-order axial (resp. even order).

3.4 Structure of Third-Order Strain Measures of Generalized Continua

These techniques can now be applied to the third-order tensors involved in the micromorphic and the strain-gradient elasticity model.

Micromorphic Elasticity

Let us begin with the space $\mathbb{T}_{\mathtt{ijk}}$ used in the micromorphic theory to model the micro-strain gradient $\underset{\sim}{\kappa}$. As $\mathbb{T}_{\mathtt{ijk}} \cong \otimes^3\mathbb{R}^3$, we have $\mathbb{T}_{\mathtt{ijk}} \cong \mathbb{H}^1 \otimes \mathbb{H}^1 \otimes \mathbb{H}^1$. Using the Clebsch-Gordan rule:

$$\begin{aligned}\mathbb{T}_{\mathtt{ijk}} &\cong \mathbb{H}^1 \otimes \mathbb{H}^1 \otimes \mathbb{H}^1 \\ &\cong (\mathbb{H}^2 \oplus \mathbb{H}^{\sharp 1} \oplus \mathbb{H}^0) \otimes \mathbb{H}^1 \\ &\cong \mathbb{H}^3 \oplus 2\mathbb{H}^{\sharp 2} \oplus 3\mathbb{H}^1 \oplus \mathbb{H}^{\sharp 0}\end{aligned}$$

Therefore $\mathbb{T}_{\mathtt{ijk}}$ decompose into:

Name	$\mathbb{H}^3$: 3rd-order deviator	$\mathbb{H}^{\sharp 2}$: Pseudo-deviator	$\mathbb{H}^1$: Vector	$\mathbb{H}^{\sharp 0}$: Pseudo-scalar
Dimension	7	5	3	1
Multiplicity	1	2	3	1
Total	7	10	9	1

And if we sum the dimension of all irreducible spaces the 27-D of $\mathbb{T}_{ijk}$ is retrieved.

Strain-Gradient Elasticity

Now consider the space $\mathbb{T}_{(ij)k}$ used in strain-gradient theory to model the strain-gradient η. As $\mathbb{T}_{(ij)k} \cong (\mathbb{R}^3 \otimes^S \mathbb{R}^3) \otimes \mathbb{R}^3$, we have $\mathbb{T}_{(ij)k} \cong (\mathbb{H}^{\sharp 2} \oplus \mathbb{H}^0) \otimes \mathbb{H}^1$. Using the $\cong$ Clebsch-Gordan rule:

$$\mathbb{T}_{(ij)k} \cong \mathbb{H}^3 \oplus \mathbb{H}^{\sharp 2} \oplus 2\mathbb{H}^1$$

Therefore $\mathbb{T}_{(ij)k}$ decompose into:

Name	$\mathbb{H}^3$: 3rd-order deviator	$\mathbb{H}^{\sharp 2}$: Pseudo-deviator	$\mathbb{H}^1$: Vector	$\mathbb{H}^{\sharp 0}$: Pseudo-scalar
Dimension	7	5	3	1
Multiplicity	1	1	2	0
Total	7	5	6	0

And if we sum the dimension of all irreducible spaces the 18-D of $\mathbb{T}_{(ij)k}$ is retrieved.

Analysis

Therefore, and despite what can be read in the literature, there is no spherical part in the decomposition of an element of $\mathbb{T}_{(ij)k}$. This worths being emphasized because in the micromorphic approach tensors do have such a component. Therefore, in order to avoid any misunderstanding, it is important to use the vocabulary in an appropriate way. Furthermore the use of a correct generalization of the harmonic decomposition to higher-order tensors provides useful information on the associated constitutive law. For example:

- the number of isotropic moduli associated to the isotropic related constitutive tensor (with great symmetry);
- the number and the dimension of eigenspaces of the related isotropic related constitutive tensor;
- the structure of anisotropy classes of the associated constitutive law [23];
- etc.

For the dimension of the isotropic symmetric constitutive law[6]

Theorem 2.1. *If* $\mathbb{T} \cong \bigoplus_{k=0}^{n} \alpha_k \mathbb{H}^k$ *then* $\dim\left(\mathrm{End}_S^{O(3)}(\mathbb{T})\right) = \sum_{k=0}^{n} \frac{\alpha_k(\alpha_k+1)}{2}$,

[6] The demonstration of theses theorems will be provided in a paper currently under redaction.

where $\mathrm{End}_S^{O(3)}(\mathbb{T})$ means the space of self-adjoint isotropic endomorphism of $\mathbb{T}$. For the next property we need to introduce the following definition.

Definition 2.1. Let L be a self-adjoint endomorphism of $\mathbb{T}$. The eigensignature of L, noted $\mathcal{ES}(L)$, is defined as the concatenation of the dimension of the eigenspaces of L.

For example, if we consider $\underset{\approx}{C}$ an isotropic elasticity tensor we have:

$$\mathcal{ES}(\underset{\approx}{C}) = \{51\}$$

as an isotropic elasticity tensor possesses two eigenspaces: one 5-dimensional and a unidimensional. The eigensignature of an operator contains both the number of its eigenspaces and theirs dimension.

Theorem 2.2. *If* $\mathbb{T} \cong \bigoplus_{k=0}^{n} \alpha_k \mathbb{H}^k$ *then for almost all* $L \in \mathrm{End}_S^{O(3)}(\mathbb{T})$ *;* $\mathcal{ES}(L) = \mathsf{C}_{k=0}^{n}\{\alpha_k \mathsf{C}\{2k+1\}\}$

in which C indicates the concatenation operator, and the notation $\alpha\mathsf{C}\{x\}$ indicates that α copies of x should be concatenated. The direct application of these results to our concern gives:

Theory	Third-order tensor decomposition	Number of isotropic moduli of the associated the sixth-order tensor	$\mathcal{ES}$
Micromorphic	$\mathbb{H}^3 \oplus 2\mathbb{H}^{\sharp 2} \oplus 3\mathbb{H}^1 \oplus \mathbb{H}^{\sharp 0}$	11	$\{75^2 3^3 1\}$
Strain-gradient	$\mathbb{H}^3 \oplus \mathbb{H}^{\sharp 2} \oplus 2\mathbb{H}^1$	5	$\{753^2\}$

Now the questions are (from a practical point of view):

1. How explicitly construct an associated isomorphism ?
2. Is this isomorphism canonical ?
3. Is there any mechanical meaning of that decomposition ?

In the following section, attention will restricted to the space of strain-gradient tensors.

4 Construction of the Isomorphism

As shown in the previous section:

$$\mathbb{T}_{(ij)k} \cong \mathbb{H}^3 \oplus \mathbb{H}^{\sharp 2} \oplus \mathbb{H}^{1,a} \oplus \mathbb{H}^{1,b}$$

It can be observed that any strain-gradient tensor contains 2 vectors in its decomposition. This fact is important since if the composition contains at least two harmonic components of the same order the isomorphism is not uniquely defined [12].

This indeterminacy will only concern the vector components since H^3 and $H^{\sharp 2}$ are uniquely defined. Therefore there is a degree of freedom in the definition of the vectors contained in the decomposition.

In fact, this situation also occurs in classical elasticity. The vector space of elasticity tensors can be decomposed as follows [3, 4, 10]

$$\mathbb{E}\mathrm{la} \cong \mathbb{H}^4 \oplus \mathbb{H}^2_{\mathrm{a}} \oplus \mathbb{H}^2_{\mathrm{b}} \oplus \mathbb{H}^0_{\mathrm{a}} \oplus \mathbb{H}^0_{\mathrm{b}}$$

In this decomposition the two scalar parts are the elastic isotropic coefficients and therefore the isotropic moduli are not uniquely defined. This results in multiple ways to choose those coefficients: Young modulus & Poisson's ratio, Lamé constants, shear modulus & bulk modulus, and so on. . ..

Therefore any construction is possible, but among them at least two are more natural since they give a physical meaning to the harmonic decomposition. The first one consists in splitting $\mathrm{T}_{(\mathrm{ij})\mathrm{k}}$ into a fully symmetric part and a remainder one before proceeding to the harmonic decomposition.

4.1 1st Decomposition: Stretch- and Rotation-Gradient

This approach is summed-up by the following diagram:

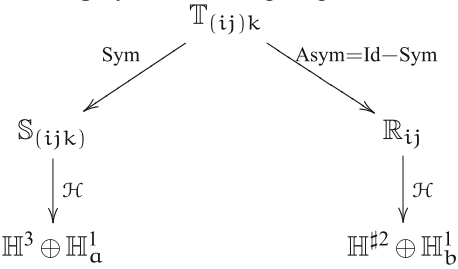

where Sym, Asym and $\mathcal{H}$ respectively stand for the symmetrization, anti-symmetrization and the harmonic decomposition processes. $\mathrm{T}_{(\mathrm{ij})\mathrm{k}}$ is first split into a full symmetric tensor and an asymmetric one:

$$\mathrm{T}_{(\mathrm{ij})\mathrm{k}} = \mathrm{S}_{\mathrm{ijk}} + \frac{1}{3}\left(\epsilon_{\mathrm{jkl}}\mathrm{R}_{\mathrm{li}} + \epsilon_{\mathrm{ikl}}\mathrm{R}_{\mathrm{lj}}\right)$$

The space of full symmetric third-order tensors is 10-dimensional meanwhile the space of asymmetric one is 8-dimensional, those spaces are in direct sum. In the strain-gradient literature [20] the complete symmetric part $\mathrm{S}_{(\mathrm{ijk})}$, defined:

$$\mathrm{S}_{(\mathrm{ijk})} = \frac{1}{3}(\mathrm{T}_{(\mathrm{ij})\mathrm{k}} + \mathrm{T}_{(\mathrm{ki})\mathrm{j}} + \mathrm{T}_{(\mathrm{jk})\mathrm{i}})$$

is the *stretch-gradient* part of $T_{(ij)k}$. Meanwhile the remaining traceless non-symmetric part R_{ij}:

$$R_{ij} = \epsilon_{ipq} T_{(jp)q}$$

is the *the rotation-gradient* part of $T_{(ij)k}$. In the couple-stress model, which is a reduced formulation of the strain-gradient model, only this tensor is taken into account in the mechanical formulation.

In terms of group action, it is important to note that this decomposition[7] is $GL(3)$-invariant,[8] and that each component is $GL(3)$-irreducible. In other terms, this decomposition of the strain-gradient into two "mechanisms" (stretch-gradient and rotation-gradient) is preserved under any invertible transformation. Under $O(3)$-action each part can further be decomposed in irreducible components by removing their different traces:

- $\mathbb{S}_{(ijk)}$ splits into a third-order deviator ($\dim \mathbb{H}^3 = 7$) and a vector ($\dim \mathbb{H}^1_a = 3$);
- $\mathbb{R}_{ij}$ splits into a pseudo-deviator ($\dim \mathbb{H}^{\sharp 2} = 5$) and a vector ($\dim \mathbb{H}^1_b = 3$).

Stretch-gradient tensors:
The space $\mathbb{S}_{(ijk)}$ is isomorphic to $\mathbb{H}^3 \oplus \mathbb{H}^1_{\nabla str}$. The structure of this decomposition shows that this isomorphism is unique. Doing some algebra we obtain

$$S_{(ijk)} = H_{(ijk)} + \frac{1}{5}\left(V^{\nabla str}_i \delta_{(jk)} + V^{\nabla str}_j \delta_{(ik)} + V^{\nabla str}_k \delta_{(ij)}\right)$$

with

$$V^{\nabla str}_i = S_{(pp)i} = \frac{1}{3}\left(T_{ppi} + 2T_{ipp}\right);$$
$$H_{(ijk)} = S_{(ijk)} - \frac{1}{5}\left(V^{\nabla str}_i \delta_{(jk)} + V^{\nabla str}_j \delta_{(ik)} + V^{\nabla str}_k \delta_{(ij)}\right)$$

In this formulation $V^{\nabla str}$ is the vector part of *the stretch gradient tensor*.
Rotation-gradient tensors:
The space $\mathbb{R}_{ij}$ is isomorphic to $\mathbb{H}^{\sharp 2} \oplus \mathbb{H}^1_{\nabla rot}$. The structure of this decomposition shows that this isomorphism is unique. Doing some algebra we obtain

$$R_{ij} = H_{(ij)} + \epsilon_{ijp} V^{\nabla rot}_p$$

with

$$V^{\nabla rot}_i = \frac{1}{2}\epsilon_{ipq}(R_{pq} - R_{qp}) = \frac{1}{2}\left(T_{ppi} - T_{ipp}\right);$$
$$H_{(ij)} = R_{ij} - \frac{1}{2}\epsilon_{ijp} V^{\nabla rot}_p = \frac{1}{2}(R_{pq} + R_{qp})$$

[7] This decomposition is sometimes known as the Schur decomposition.

[8] $GL(3)$ is the group of all the invertible transformations of $\mathbb{R}^3$, i.e. if $F \in GL(3)$ then $\det(F) \neq 0$.

In this formulation $V^{\nabla rot}$ is the vector part of *the rotation gradient tensor*, and is embedded in the third-order tensor in the following way:

$$T(\underline{V}^{\nabla rot})_{ijk} = \frac{1}{3}\left(-V_i^{\nabla rot}\delta_{(jk)} - V_j^{\nabla rot}\delta_{(ik)} + 2V_k^{\nabla str}\delta_{(ij)}\right)$$

Synthesis:
This decomposition can be summed-up in the following Matryoshka doll fashion[9]:

$$\mathbb{T}_{(ij)k} = \left(\mathbb{H}^3 \oplus \mathbb{H}^1_s\right)_{|GL(3)} \oplus \left(\mathbb{H}^{\sharp 2} \oplus \mathbb{H}^1_r\right)_{|GL(3)}$$

The decomposition into the in-parenthesis terms is preserved under any invertible transformation, and if this transformation is isometric the harmonic components are further more preserved. For a strain-gradient tensor this decomposition has the following meaning. Strain-gradient tensor encodes two orthogonal effects: stretch-gradient and rotation-gradient. These effects are canonically defined and preserved under invertible changes of variables. The harmonic decompositions of these elementary effects correspond to their decomposition in spherical harmonics. This construction has a meaning for any elements of $\mathbb{T}_{(ij)k}$.

4.2 2nd Decomposition: Distortion- and Dilatation-Gradient

Aside from this first construction, which was based on the algebra of third-order tensor, other constructions can be proposed. The following one is based on the derivation of the harmonic decomposition of a symmetric second-order tensor. As a consequence this construction has a physical meaning only for tensors constructed in this way.

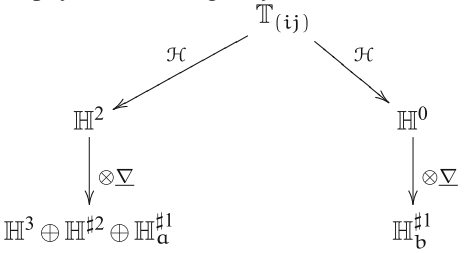

So the first step is to decompose a second-order symmetric tensor into its deviatoric and its spherical part:

$$T_{ij} = H^2_{ij} + \frac{1}{3}H^0\delta_{ij}$$

Such as

$$H^0 = T_{pp} \quad ; \quad H^2_{ij} = T_{ij} - \frac{1}{3}H^0\delta_{ij}$$

[9] Another layer can be introduced in this decomposition if one consider also in-plane isometries.

Using the Clebsch-Gordan rule in the following way

$$\mathbb{H}^n \otimes \nabla \cong \mathbb{H}^n \otimes \mathbb{H}^1 \cong \bigoplus_{k=|n-1|}^{n+1} \mathbb{H}^k$$

we obtain

$$\mathbb{H}^2 \otimes \underline{\nabla} = \mathbb{H}^3 \oplus \mathbb{H}^{\sharp 2} \oplus \mathbb{H}^1_{\nabla dev} \quad ; \quad \mathbb{H}^0 \otimes \underline{\nabla} = \mathbb{H}^1_{\nabla sph}$$

In a certain way we have

$$\mathbb{T}_{(ij)k} = \mathbb{T}_{(ij)} \otimes \underline{\nabla} = \left(\mathbb{H}^3 \oplus \mathbb{H}^{\sharp 2} \oplus \mathbb{H}^1_{\nabla dev}\right)_{|\mathbb{H}^2 \otimes \underline{\nabla}} \oplus \left(\mathbb{H}^1_{\nabla sph}\right)_{\mathbb{H}^0 \otimes \underline{\nabla}}$$

But conversely to the decomposition (4.1) the in-parenthesis terms are not GL(3)-invariant. The first in parenthesis block is the *distortion-gradient* part of the strain-gradient meanwhile the last one is the *dilatation-gradient*.

As H^3 and $H^{\sharp 2}$ are uniquely defined their expressions are the same as before. Therefore attention is focused on the vector parts, doing some algebra we obtain:

$$V_i^{\nabla sph} = T_{ppi} \quad ; \quad V_i^{\nabla dev} = \frac{2}{3}\left(T_{ipp} - \frac{1}{3}T_{ppi}\right)$$

For $V^{\nabla sph}$ the result is direct, for $V^{\nabla dev}$ we have:

$$\mathrm{Sym}\left(H_{ij,k}\right) = S_{ijk} - \frac{1}{9}\left(\delta_{ij}T_{ppk} + \delta_{ki}T_{ppj} + \delta_{jk}T_{ppi}\right)$$

Therefore,

$$\begin{aligned} V_k^{\nabla dev} &= \mathrm{Sym}(H_{ij,k})\delta_{ij} = S_{iik} - \frac{1}{9}\left(5T_{ppk}\right) = \frac{1}{3}\left(T_{ppk} + 2T_{kpp}\right) - \frac{5}{9}\left(T_{ppk}\right) \\ &= \frac{2}{3}\left(T_{kpp} - \frac{1}{3}T_{ppk}\right) \end{aligned}$$

Those vectors are embedded into the third-order tensor in the following way:

$$\begin{aligned} T(V^{\nabla sph})_{ijk} &= \frac{1}{3}V_k^{\nabla sph}\delta_{ij}; \\ T(V^{\nabla dev})_{ijk} &= \frac{1}{5}\left(V_i^{\nabla dev}\delta_{(jk)} + V_j^{\nabla dev}\delta_{(ik)} + V_k^{\nabla dev}\delta_{(ij)}\right) \end{aligned}$$

4.3 Synthesis

If elements of $\mathbb{T}_{(ij)k}$ are considered as gradient of a symmetric second-order tensors, their $O(3)$-irreducible decompositions, can be defined in, at least, two ways. The first construction is the more general one and is based on the algebra of $\mathbb{T}_{(ij)k}$, meanwhile the second is constructed from the algebra of $\mathbb{T}_{(ij)}$. Comparing the two decompositions, it appears that higher-order terms ($\mathbb{H}^3$ and $\mathbb{H}^{\sharp 2}$) are identical, whereas the vector parts are linear combination of each others. These results give an insight of the physical information encodes by H^3 and $H^{\sharp 2}$
H^3:

- Its is generated by a part of the distortion gradient;
- Its elements encode a part of the stretch-gradient effect.

H^2:

- Its is generated by a part of the distortion gradient;
- Its elements encode a part of the rotation-gradient effect.

On the other hand the non uniqueness of the definition of the vector components shows that (Stretch- and rotation-gradient) and (Distortion- and Dilatation-gradient) are entangled phenomena. As, for example, the dilatation-gradient generates both stretch- and rotation-gradient components. Using this approach some physical based simplified strain-gradient elasticity models can be proposed.

Theory	Harmonic decomposition $\mathbb{T}_{ijk}$	Dimension	Isotropic moduli
Strain gradient	$\mathbb{H}^3 \oplus \mathbb{H}^2 \oplus 2\mathbb{H}^1$	18	5
Distortion-gradient	$\mathbb{H}^3 \oplus \mathbb{H}^2 \oplus \mathbb{H}^1_{\nabla \mathrm{dev}}$	15	3
Stretch-gradient	$\mathbb{H}^3 \oplus \mathbb{H}^1_{\nabla \mathrm{str}}$	10	2
Rotation-gradient	$\mathbb{H}^2 \oplus \mathbb{H}^1_{\nabla \mathrm{rot}}$	8	2
Dilatation-gradient	$\mathbb{H}^1_{\nabla \mathrm{sph}}$	3	1

Therefore

$$\mathrm{V}^{\nabla \mathrm{str}} = \mathrm{V}^{\nabla \mathrm{dev}} + \frac{5}{9}\mathrm{V}^{\nabla \mathrm{sph}} \quad ; \quad \mathrm{V}^{\nabla \mathrm{rot}} = \frac{1}{3}\mathrm{V}^{\nabla \mathrm{sph}} - \frac{3}{4}\mathrm{V}^{\nabla \mathrm{dev}}$$

and conversely

$$\mathrm{V}^{\nabla \mathrm{sph}} = \frac{4}{3}\mathrm{V}^{\nabla \mathrm{rot}} + \mathrm{V}^{\nabla \mathrm{str}} \quad ; \quad \mathrm{V}^{\nabla \mathrm{dev}} = \frac{1}{9}(4\mathrm{V}^{\nabla \mathrm{str}} - \frac{20}{3}\mathrm{V}^{\nabla \mathrm{rot}})$$

The harmonic decomposition had been studied using two different but complementary constructions. In the context of strain-/stress-gradient [9] theories, these vector parts are related to differential operators acting on second-order symmetric tensors. To that aim, we consider $\underset{\sim}{\mathrm{T}} \in \mathbb{T}_{(ij)k}$ such that

$$\exists \underset{\sim}{D} \in \mathbb{T}_{(ij)} | \underline{\underline{T}} = \underset{\sim}{D} \otimes \underline{\nabla}$$

and we can define two vectors : $\nabla(\mathrm{tr}(\underset{\sim}{D}))$ and $\mathrm{div}(\underset{\sim}{D})$. The first vector is the same as $V^{\nabla sph}$ and second is:

$$V^{div} = \frac{3}{2} V^{\nabla dev} + \frac{1}{3} V^{\nabla sph} = \frac{1}{3} V^{\nabla str} - \frac{2}{3} V^{\nabla rot}$$

The irreducible vector parts of the harmonic can be expressed as a linear combination of these vectors. This is interesting because of their physical meaning. For strain-gradient elasticity, $\underline{V}^{\nabla sph}$ is the gradient of the infinitesimal volume variation δV, meanwhile $\underline{V}^{\nabla dev}$ is the strain divergence [27]. For the stress-gradient elasticity $\frac{1}{3}\underline{V}^{\nabla sph}$ represents the gradient of the isostatic pressure p, and $\underline{V}^{\nabla dev}$ is proportional to the volumic forces $\underline{f}$. Those vectors have, both for strain and stress gradient elasticity, a clear physical meaning.

	Strain-gradient	Stress-gradient
$\underline{V}^{\nabla sph}$	$\nabla \delta V$	$3\underline{\nabla p}$
$\underline{V}^{\nabla dev}$	$\frac{2}{3}\left(\mathrm{div}(\underset{\sim}{\varepsilon}) - \frac{1}{3}\nabla \delta V\right)$	$\frac{2}{3}\left(\underline{f} - \underline{\nabla p}\right)$
$\underline{V}^{\nabla str}$	$\frac{1}{3}\left(\nabla \delta V + 2\mathrm{div}(\underset{\sim}{\varepsilon})\right)$	$\underline{\nabla p} + \frac{2}{3}\underline{f}$
$\underline{V}^{\nabla rot}$	$\frac{1}{2}\left(\nabla \delta V - \mathrm{div}(\underset{\sim}{\varepsilon})\right)$	$\frac{1}{2}\left(3\underline{\nabla p} - \underline{f}\right)$

Appendix

In this appendix the explicit decompositions of $\underline{\underline{T}}$ are provided.

Affine Decomposition

Let be defined the following subspace of third-order tensors

$$\mathcal{S}^3 = \{\mathbb{T} | \mathbb{T} = \sum_{i,j,k=1}^{3} T_{ijk} \mathbf{e}_i \otimes \mathbf{e}_j \otimes \mathbf{e}_k, \ T_{ijk} = T_{jik}\} \tag{1}$$

which is an 18-dimensional vector space.

In order to express the strain gradient $\underline{\underline{T}}$ as a second-order tensor, we consider the tensor product of the orthonormal basis vectors of second-order symmetric tensors with the one of classical vector.

$$\hat{\underset{\sim}{T}} = \psi(\underset{\simeq}{T}) = \hat{T}_{\alpha k}\hat{\mathbf{e}}_\alpha \otimes \mathbf{e}_k,\ 1 \leqslant \alpha \leqslant 6, 1 \leqslant k \leqslant 3 \tag{2}$$

with

$$\hat{\mathbf{e}}_\alpha = \left(\frac{1-\delta_{ij}}{\sqrt{2}} + \frac{\delta_{ij}}{2}\right)(\mathbf{e}_i \otimes \mathbf{e}_j + \mathbf{e}_j \otimes \mathbf{e}_i) \quad 1 \leqslant \alpha \leqslant 6 \tag{3}$$

With the orthonormal basis (3), the relationship between the matrix components $\hat{T}_{\alpha k}$ and T_{ijk} is specified by

$$\hat{T}_{\alpha k} = \begin{cases} T_{ijk} \ \text{ if } \ i = j, \\ \sqrt{2}T_{ijk} \ \text{ if } \ i \neq j; \end{cases} \tag{4}$$

Therefore for $\underset{\simeq}{T}$ we obtain the following matrix representation:

$$[\underset{\simeq}{T}] = \begin{pmatrix} T_{111} & T_{112} & T_{113} \\ T_{221} & T_{222} & T_{223} \\ T_{331} & T_{332} & T_{333} \\ \sqrt{2}T_{121} & \sqrt{2}T_{122} & \sqrt{2}T_{123} \\ \sqrt{2}T_{131} & \sqrt{2}T_{132} & \sqrt{2}T_{133} \\ \sqrt{2}T_{231} & \sqrt{2}T_{232} & \sqrt{2}T_{233} \end{pmatrix}$$

We can now construct the explicit matrix decomposition of $\underset{\simeq}{T}$.

• *Stretch-gradient tensor:*

$$[\underset{\simeq}{T}(\underset{\simeq}{S})] = \begin{pmatrix} S_1 & S_4 & S_5 \\ S_7 & S_2 & S_6 \\ S_8 & S_9 & S_3 \\ \sqrt{2}S_4 & \sqrt{2}S_7 & \sqrt{2}S_{10} \\ \sqrt{2}S_5 & \sqrt{2}S_{10} & \sqrt{2}S_8 \\ \sqrt{2}S_{10} & \sqrt{2}S_6 & \sqrt{2}S_9 \end{pmatrix}$$

$$= \begin{pmatrix} T_{111} & \frac{1}{3}(T_{112}+2T_{121}) & \frac{1}{3}(T_{113}+2T_{131}) \\ \frac{1}{3}(T_{221}+2T_{122}) & T_{222} & \frac{1}{3}(T_{223}+2T_{232}) \\ \frac{1}{3}(T_{331}+2T_{133}) & \frac{1}{3}(T_{332}+2T_{233}) & T_{333} \\ \frac{\sqrt{2}}{3}(T_{112}+2T_{121}) & \frac{\sqrt{2}}{3}(T_{221}+2T_{122}) & \frac{\sqrt{2}}{3}(T_{123}+T_{321}+T_{213}) \\ \frac{\sqrt{2}}{3}(T_{113}+2T_{131}) & \frac{\sqrt{2}}{3}(T_{123}+T_{321}+T_{213}) & \frac{\sqrt{2}}{3}(T_{331}+2T_{133}) \\ \frac{\sqrt{2}}{3}(T_{123}+T_{321}+T_{213}) & \frac{\sqrt{2}}{3}(T_{223}+2T_{232}) & \frac{\sqrt{2}}{3}(T_{332}+2T_{233}) \end{pmatrix}$$

• *Rotation-gradient tensor:*

As a second-order tensor:

$$[\underset{\sim}{\mathrm{R}}] = \begin{pmatrix} \mathrm{T}_{123} - \mathrm{T}_{132} & \mathrm{T}_{223} - \mathrm{T}_{232} & \mathrm{T}_{233} - \mathrm{T}_{332} \\ \mathrm{T}_{131} - \mathrm{T}_{113} & \mathrm{T}_{231} - \mathrm{T}_{123} & \mathrm{T}_{331} - \mathrm{T}_{133} \\ \mathrm{T}_{112} - \mathrm{T}_{121} & \mathrm{T}_{122} - \mathrm{T}_{221} & \mathrm{T}_{132} - \mathrm{T}_{231} \end{pmatrix}$$

and embedded into $\underset{\simeq}{\mathrm{T}}$:

$$[\underset{\simeq}{\mathrm{T}}(\underset{\sim}{\mathrm{R}})] = \begin{pmatrix} 0 & -2\mathrm{R}_3 & -2\mathrm{R}_5 \\ -2\mathrm{R}_1 & 0 & -2\mathrm{R}_6 \\ -2\mathrm{R}_2 & -2\mathrm{R}_4 & 0 \\ \sqrt{2}\mathrm{R}_3 & \sqrt{2}\mathrm{R}_1 & \sqrt{2}\mathrm{R}_7 \\ \sqrt{2}\mathrm{R}_5 & -\sqrt{2}(\mathrm{R}_7 + \mathrm{R}_8) & \sqrt{2}\mathrm{R}_2 \\ \sqrt{2}\mathrm{R}_8 & \sqrt{2}\mathrm{R}_6 & \sqrt{2}\mathrm{R}_4 \end{pmatrix}$$

$$= \begin{pmatrix} 0 & -\frac{2}{3}(\mathrm{T}_{121} - \mathrm{T}_{112}) & -\frac{2}{3}(\mathrm{T}_{131} - \mathrm{T}_{113}) \\ -\frac{2}{3}(\mathrm{T}_{122} - \mathrm{T}_{221}) & 0 & -\frac{2}{3}(\mathrm{T}_{232} - \mathrm{T}_{223}) \\ -\frac{2}{3}(\mathrm{T}_{133} - \mathrm{T}_{331}) & -\frac{2}{3}(\mathrm{T}_{233} - \mathrm{T}_{332}) & 0 \\ \frac{\sqrt{2}}{3}(\mathrm{T}_{121} - \mathrm{T}_{112}) & \frac{\sqrt{2}}{3}(\mathrm{T}_{122} - \mathrm{T}_{221}) & \frac{\sqrt{2}}{3}(2\mathrm{T}_{123} - \mathrm{T}_{132} - \mathrm{T}_{231}) \\ \frac{\sqrt{2}}{3}(\mathrm{T}_{131} - \mathrm{T}_{113}) & \frac{\sqrt{2}}{3}(2\mathrm{T}_{132} - \mathrm{T}_{123} - \mathrm{T}_{231}) & \frac{\sqrt{2}}{3}(\mathrm{T}_{133} - \mathrm{T}_{331}) \\ \frac{\sqrt{2}}{3}(2\mathrm{T}_{231} - \mathrm{T}_{132} - \mathrm{T}_{123}) & \frac{\sqrt{2}}{3}(\mathrm{T}_{232} - \mathrm{T}_{223}) & \frac{\sqrt{2}}{3}(\mathrm{T}_{233} - \mathrm{T}_{332}) \end{pmatrix}$$

Harmonic Decomposition

• *Vector part of the stretch-gradient tensor:*

As a vector:

$$[\underline{\mathrm{V}}^{\nabla \mathrm{str}}] = \begin{pmatrix} \mathrm{V}_1^{\nabla \mathrm{str}} = \frac{1}{3}(3\mathrm{T}_{111} + (\mathrm{T}_{221} + 2\mathrm{T}_{122}) + (\mathrm{T}_{331} + 2\mathrm{T}_{133})) \\ \mathrm{V}_2^{\nabla \mathrm{str}} = \frac{1}{3}(3\mathrm{T}_{222} + (\mathrm{T}_{332} + 2\mathrm{T}_{233}) + (\mathrm{T}_{112} + 2\mathrm{T}_{121})) \\ \mathrm{V}_3^{\nabla \mathrm{str}} = \frac{1}{3}(3\mathrm{T}_{333} + (\mathrm{T}_{113} + 2\mathrm{T}_{131}) + (\mathrm{T}_{223} + 2\mathrm{T}_{232})) \end{pmatrix}$$

and embedded into $\underset{\simeq}{\mathrm{T}}$:

$$[\underset{\simeq}{\mathrm{T}}(\underline{V}^{\nabla \mathrm{str}})] = \begin{pmatrix} \frac{3}{5}V_1^{\nabla \mathrm{str}} & \frac{3}{15}V_2^{\nabla \mathrm{str}} & \frac{3}{15}V_3^{\nabla \mathrm{str}} \\ \frac{3}{15}V_1^{\nabla \mathrm{str}} & \frac{3}{5}V_2^{\nabla \mathrm{str}} & \frac{3}{15}V_3^{\nabla \mathrm{str}} \\ \frac{3}{15}V_1^{\nabla \mathrm{str}} & \frac{3}{15}V_2^{\nabla \mathrm{str}} & \frac{3}{5}V_3^{\nabla \mathrm{str}} \\ \frac{3\sqrt{2}}{15}V_2^{\nabla \mathrm{str}} & \frac{3\sqrt{2}}{15}V_1^{\nabla \mathrm{str}} & 0 \\ \frac{3\sqrt{2}}{15}V_3^{\nabla \mathrm{str}} & 0 & \frac{3\sqrt{2}}{15}V_1^{\nabla \mathrm{str}} \\ 0 & \frac{3\sqrt{2}}{15}V_3^{\nabla \mathrm{str}} & \frac{3\sqrt{2}}{15}V_2^{\nabla \mathrm{str}} \end{pmatrix}$$

• *Third-order deviator of any strain gradient tensor:*

We have the following relations:

$$\begin{cases} \mathrm{H}^3_{111} + \mathrm{H}^3_{122} + \mathrm{H}^3_{133} = 0 \\ \mathrm{H}^3_{222} + \mathrm{H}^3_{112} + \mathrm{H}^3_{233} = 0 \\ \mathrm{H}^3_{333} + \mathrm{H}^3_{223} + \mathrm{H}^3_{113} = 0 \end{cases}$$

Therefore

$$\begin{cases} \mathrm{H}^3_{133} = -\mathrm{H}^3_{111} - \mathrm{H}^3_{122} \\ \mathrm{H}^3_{112} = -\mathrm{H}^3_{222} - \mathrm{H}^3_{233} \\ \mathrm{H}^3_{223} = -\mathrm{H}^3_{333} - \mathrm{H}^3_{113} \end{cases}$$

Hence we got seven independent components $\mathrm{H}^3_{111}, \mathrm{H}^3_{122}, \mathrm{H}^3_{222}, \mathrm{H}^3_{233}, \mathrm{H}^3_{333}, \mathrm{H}^3_{113}$ and H^3_{123}, leading to the embedding

$$[\underset{\simeq}{\mathrm{T}}(\underset{\simeq}{\mathrm{H}}^3)] = \begin{pmatrix} \mathrm{H}^3_1 & -(\mathrm{H}^3_2 + \mathrm{H}^3_5) & \mathrm{H}^3_6 \\ \mathrm{H}^3_4 & \mathrm{H}^3_2 & -(\mathrm{H}^3_3 + \mathrm{H}^3_6) \\ -(\mathrm{H}^3_1 + \mathrm{H}^3_4) & \mathrm{H}^3_5 & \mathrm{H}^3_3 \\ -\sqrt{2}(\mathrm{H}^3_2 + \mathrm{H}^3_5) & \sqrt{2}\mathrm{H}^3_4 & \sqrt{2}\mathrm{H}^3_7 \\ \sqrt{2}\mathrm{H}^3_6 & \sqrt{2}\mathrm{H}^3_7 & -\sqrt{2}(\mathrm{H}^3_1 + \mathrm{H}^3_4) \\ \sqrt{2}\mathrm{H}^3_7 & -\sqrt{2}(\mathrm{H}^3_3 + \mathrm{H}^3_6) & \sqrt{2}\mathrm{H}^3_5 \end{pmatrix}$$

with

$$\mathrm{H}^3_1 = \mathrm{H}^3_{(111)} = \frac{1}{5}\left(2\mathrm{T}_{111} - (\mathrm{T}_{221} + 2\mathrm{T}_{122}) - (\mathrm{T}_{331} + 2\mathrm{T}_{133})\right)$$

$$\mathrm{H}^3_2 = \mathrm{H}^3_{(222)} = \frac{1}{5}\left(2\mathrm{T}_{222} - (\mathrm{T}_{332} + 2\mathrm{T}_{233}) - (\mathrm{T}_{112} + 2\mathrm{T}_{121})\right)$$

$$\mathrm{H}^3_3 = \mathrm{H}^3_{(333)} = \frac{1}{5}\left(2\mathrm{T}_{333} - (\mathrm{T}_{113} + 2\mathrm{T}_{131}) - (\mathrm{T}_{223} + 2\mathrm{T}_{232})\right)$$
$$\mathrm{H}^3_4 = \mathrm{H}^3_{(122)} = \frac{1}{15}\left(-3\mathrm{T}_{111} + 4(\mathrm{T}_{221} + 2\mathrm{T}_{122}) - (\mathrm{T}_{331} + 2\mathrm{T}_{133})\right)$$
$$\mathrm{H}^3_5 = \mathrm{H}^3_{(233)} = \frac{1}{15}\left(-3\mathrm{T}_{222} + 4(\mathrm{T}_{332} + 2\mathrm{T}_{233}) - (\mathrm{T}_{112} + 2\mathrm{T}_{121})\right)$$
$$\mathrm{H}^3_6 = \mathrm{H}^3_{(113)} = \frac{1}{15}\left(-3\mathrm{T}_{333} + 4(\mathrm{T}_{113} + 2\mathrm{T}_{311}) - (\mathrm{T}_{223} + 2\mathrm{T}_{322})\right)$$
$$\mathrm{H}^3_7 = \mathrm{H}^3_{(123)} = \frac{1}{3}\left(\mathrm{T}_{123} + \mathrm{T}_{321} + \mathrm{T}_{213}\right)$$

• *Vector part of the rotation-gradient tensor:*

As a vector:

$$[\underline{V}^{\nabla\mathrm{rot}}] = \begin{pmatrix} V_1^{\nabla\mathrm{rot}} = \frac{1}{2}((\mathrm{T}_{221} - \mathrm{T}_{122}) + (\mathrm{T}_{331} - \mathrm{T}_{133})) \\ V_2^{\nabla\mathrm{rot}} = \frac{1}{2}((\mathrm{T}_{332} - \mathrm{T}_{233}) + (\mathrm{T}_{112} - \mathrm{T}_{121})) \\ V_3^{\nabla\mathrm{rot}} = \frac{1}{2}((\mathrm{T}_{113} - \mathrm{T}_{311}) + (\mathrm{T}_{223} - \mathrm{T}_{322})) \end{pmatrix}$$

and embedded into $\underset{\simeq}{\mathrm{T}}$:

$$[\underset{\simeq}{\mathrm{T}}(\underline{V}^{\nabla\mathrm{rot}})] = \begin{pmatrix} 0 & \frac{2}{3}V_2^{\nabla\mathrm{rot}} & \frac{2}{3}V_3^{\nabla\mathrm{rot}} \\ \frac{2}{3}V_1^{\nabla\mathrm{rot}} & 0 & \frac{2}{3}V_3^{\nabla\mathrm{rot}} \\ \frac{2}{3}V_1^{\nabla\mathrm{rot}} & \frac{2}{3}V_2^{\nabla\mathrm{rot}} & 0 \\ -\frac{\sqrt{2}}{3}V_2^{\nabla\mathrm{rot}} & -\frac{\sqrt{2}}{3}V_1^{\nabla\mathrm{rot}} & 0 \\ -\frac{\sqrt{2}}{3}V_3^{\nabla\mathrm{rot}} & 0 & -\frac{\sqrt{2}}{3}V_1^{\nabla\mathrm{rot}} \\ 0 & -\frac{\sqrt{2}}{3}V_3^{\nabla\mathrm{rot}} & -\frac{\sqrt{2}}{3}V_2^{\nabla\mathrm{rot}} \end{pmatrix}$$

• *Second-order pseudo-deviator of any strain gradient tensor:*

As a second-order tensor:

$$[\underset{\sim}{H^2}] = \begin{pmatrix} \frac{1}{3}(2H_4^2 + H_5^2) & H_1^2 & H_2^2 \\ H_1^2 & \frac{1}{3}(H_5^2 + H_3^2) & H_3^2 \\ H_2^2 & H_3^2 & -\frac{1}{3}(H_4^2 + 2H_5^2) \end{pmatrix}$$

With

$$H_1^2 = \frac{1}{2}\left((T_{223} - T_{232}) + (T_{131} - T_{113})\right); H_2^2 = \frac{1}{2}\left((T_{233} - T_{332}) + (T_{112} - T_{121})\right)$$

$$H_3^2 = \frac{1}{2}\left((T_{331} - T_{313}) + (T_{122} - T_{221})\right); H_4^2 = \frac{1}{3}\left(2T_{123} - T_{132} - T_{231}\right)$$

$$H_5^2 = \frac{1}{3}\left(2T_{231} - T_{132} - T_{123}\right)$$

and embedded in $\underset{\simeq}{T}$:

$$[\underset{\simeq}{T}(\underset{\sim}{H^2})] = \begin{pmatrix} 0 & \frac{2}{3}H_2^2 & -\frac{2}{3}H_1^2 \\ -\frac{2}{3}H_3^2 & 0 & \frac{2}{3}H_1^2 \\ \frac{2}{3}H_3^2 & -\frac{2}{3}H_2^2 & 0 \\ -\frac{\sqrt{2}}{3}H_2^2 & \frac{\sqrt{2}}{3}H_3^2 & \sqrt{2}H_4^2 \\ \frac{\sqrt{2}}{3}H_1^2 & \sqrt{2}(H_4^2 + H_5^2) & -\frac{\sqrt{2}}{3}H_3^2 \\ -\sqrt{2}H_5^2 & -\frac{\sqrt{2}}{3}H_1^2 & \frac{\sqrt{2}}{3}H_2^2 \end{pmatrix}$$

Interpretation in Terms of Gradient

• *Dilatation-gradient vector:*

As a vector:

$$[\underline{V}^{\nabla sph}] = \begin{pmatrix} V_1^{\nabla sph} = T_{111} + T_{221} + T_{331} \\ V_2^{\nabla sph} = T_{112} + T_{222} + T_{332} \\ V_3^{\nabla sph} = T_{113} + T_{223} + T_{333} \end{pmatrix}$$

and embedded in $\underset{\simeq}{T}$:

$$[\underset{\simeq}{T}(\underline{V}^{\nabla \text{sph}})] = \begin{pmatrix} \frac{1}{3}V_1^{\nabla \text{sph}} & \frac{1}{3}V_2^{\nabla \text{sph}} & \frac{1}{3}V_3^{\nabla \text{sph}} \\ \frac{1}{3}V_1^{\nabla \text{sph}} & \frac{1}{3}V_2^{\nabla \text{sph}} & \frac{1}{3}V_3^{\nabla \text{sph}} \\ \frac{1}{3}V_1^{\nabla \text{sph}} & \frac{1}{3}V_2^{\nabla \text{sph}} & \frac{1}{3}V_3^{\nabla \text{sph}} \\ 0 & 0 & 0 \\ 0 & 0 & 0 \\ 0 & 0 & 0 \end{pmatrix}$$

$$= \begin{pmatrix} \frac{1}{3}(T_{111}+T_{221}+T_{331}) & \frac{1}{3}(T_{112}+T_{222}+T_{332}) & \frac{1}{3}(T_{113}+T_{223}+T_{333}) \\ \frac{1}{3}(T_{111}+T_{221}+T_{331}) & \frac{1}{3}(T_{112}+T_{222}+T_{332}) & \frac{1}{3}(T_{113}+T_{223}+T_{333}) \\ \frac{1}{3}(T_{111}+T_{221}+T_{331}) & \frac{1}{3}(T_{112}+T_{222}+T_{332}) & \frac{1}{3}(T_{113}+T_{223}+T_{333}) \\ 0 & 0 & 0 \\ 0 & 0 & 0 \\ 0 & 0 & 0 \end{pmatrix}$$

• *Distortion-gradient vector:*
As a vector:

$$[\underline{V}^{\nabla \text{dev}}] = \begin{pmatrix} V_1^{\nabla \text{dev}} = \frac{2}{9}(2T_{111} + (3T_{122} - T_{221}) + (3T_{133} - T_{331})) \\ V_2^{\nabla \text{dev}} = \frac{2}{9}(2T_{222} + (3T_{233} - T_{332}) + (3T_{121} - T_{112})) \\ V_3^{\nabla \text{dev}} = \frac{2}{9}(2T_{333} + (3T_{131} - T_{113}) + (3T_{232} - T_{223})) \end{pmatrix}$$

and embedded in $\underset{\simeq}{T}$:

$$[\underset{\simeq}{T}(\underline{V}^{\nabla \text{dev}})] = \begin{pmatrix} \frac{3}{5}V_1^{\nabla \text{dev}} & -\frac{3}{10}V_2^{\nabla \text{dev}} & -\frac{3}{10}V_3^{\nabla \text{dev}} \\ -\frac{3}{10}V_1^{\nabla \text{dev}} & \frac{3}{5}V_2^{\nabla \text{dev}} & -\frac{3}{10}V_3^{\nabla \text{dev}} \\ -\frac{3}{10}V_1^{\nabla \text{dev}} & -\frac{3}{10}V_2^{\nabla \text{dev}} & \frac{3}{5}V_3^{\nabla \text{dev}} \\ \frac{9\sqrt{2}}{20}V_2^{\nabla \text{dev}} & \frac{9\sqrt{2}}{20}V_1^{\nabla \text{dev}} & 0 \\ \frac{9\sqrt{2}}{20}V_3^{\nabla \text{dev}} & 0 & \frac{9\sqrt{2}}{20}V_1^{\nabla \text{dev}} \\ 0 & \frac{9\sqrt{2}}{20}V_3^{\nabla \text{dev}} & \frac{9\sqrt{2}}{20}V_2^{\nabla \text{dev}} \end{pmatrix}$$

References

1. Auffray, N.: Décomposition harmonique des tenseurs -Méthode spectrale-. Cr. Mecanique. **336**, 370–375 (2008)
2. Alibert, J., Seppecher, F., dell'Isola, F.: Truss modular beams with deformation energy depending on higher displacement gradients. Math. Mech. Solids **8**, 51–73 (2003)
3. Backus, G.: A geometrical picture of anisotropic elastic tensors. Rev. Geophys. **8**, 633–671 (1970)
4. Baerheim, R.: Harmonic decomposition of the anisotropic elasticity tensor. Q. J. Mech. Appl. Math **46**, 391–418 (1993)
5. Eringen, A.C.: Theory of micropolar elasticity. In: Leibowitz, H. (ed.) Fracture, vol. 2, pp. 621–629. Academic Press, New York (1968)
6. Eringen, A.C., Suhubi, E.S.: Nonlinear Theory of simple microelastic solids. Int. J. Eng. Sci. **2**, 189–203 (1964)
7. Fleck, N.A., Hutchinson, J.W.: Strain gradient plasticity. Adv. Appl. Mech. **33**, 295–361 (1997)
8. Fleck, N.A., Hutchinson, J.W.: An assessment of a class of strain gradient plasticity theories. J. Mech. Phys. Solids **49**, 2245–2272 (2001)
9. Forest, S., Sab, K.: Continuum stress gradient theory. Mech. Res. Commun. **40**, 16–25 (2012)
10. Forte, S., Vianello, M.: Symmetry classes for elasticity tensors. J. Elasticity **43**, 81–108 (1996)
11. Germain, P.: The method of virtual power in continuum mechanics. Part II: Application to continuum media with microstructure, SIAM. J. Appl Math. **25**, 556–755 (1973)
12. Golubitsky, M., Stewart, I., Schaeffer, D.G.: Singularities and Groups in Bifurcation Theory, vol. II, Springer, New York (1988)
13. Geymonat, P., Weller, T.: Symmetry classes of piezoelectric solids. CR Aacad. Sci. I **335**, 847–852 (2002)
14. Jerphagnon, J., Chemla, D., Bonneville, R.: The description of the physical properties of condensed matter using irreducible tensors. Adv. Phys. **27**, 609–650 (1978)
15. Jerphagnon, J.: Invariants of the third-rank Cartesian Tensor: optical nonlinear susceptibilities. Phys. Rev. B **2**, 1091–1098 (1970)
16. Le Quang, H., Auffray, N., He, Q.-C., Bonnet, G.: Symmetry groups and classes of sixth-order strain-gradient elastic tensors tensors. P. Roy. Soc. Lond. A. Mat. (submitted)
17. Lam, D.C.C., Yang, F., Chong, A.C.M., Wang, J., Tong, P.: Experiments and theory in strain gradient elasticity. J. Mech. Phys. Solids **51**, 1477–1508 (2003)
18. Marangantia, R., Sharma, P.: A novel atomistic approach to determine strain-gradient elasticity constants: tabulation and comparison for various metals, semiconductors, silica, polymers and the (Ir) relevance for nanotechnologies. J. Mech. Phys. Solids **55**, 1823–1852 (2007)
19. Mindlin, R.D., Eshel, N.N.: On first strain-gradient theories in linear elasticity. Int. J. Solids Struct. **4**, 109–124 (1968)
20. Mindlin, R.D.: Micro-structure in linear elasticity. Arch. Ration. Mech. Anal. **16**, 51–78 (1964)
21. Mindlin, R.D.: Second gradient of strain and surface-tension in linear elasticity. Int. J. Solids Struct. **1**, 417–438 (1965)
22. Nix, W.D., Gao, H.: Indentation size effects in crystalline materials: a law for strain gradient plasticity. J. Mech. Phys. Solids **46**, 411–425 (1998)
23. Olive, M., Auffray, N.: Symmetry classes for even-order tensors. Math. Mech. Compl. Sys. (Accepted) (2013)
24. Seppecher, P., Alibert, J.-J., dell'Isola, F.: Linear elastic trusses leading to continua with exotic mechanical interactions. J. Phys. Conf. Ser. **319**, 12018–12030 (2011)
25. Smyshlyaev, V.P., Fleck, N.A.: The role of strain gradients in the grain size effect for polycrystals. J. Mech. Phys. Solids **44**, 465–495 (1996)
26. Toupin, R.A.: Elastic materials with couple stresses. Arch. Ration. Mech. Anal. **11**, 385–414 (1962)
27. Tekoglu, C., Onck, P.R.: Size effects in two-dimensional Voronoi foams: a comparison between generalized continua and discrete models. J. Mech. Phys. Solids **56**, 3541–3564 (2008)

28. Truesdell, C., Toupin, R.: The Classical Field Theories, Encyclopedia of Physics (FlÃügge, ed.) vol. III/l, pp. 226–793. Springer, Berlin (1960)
29. Truesdell, C., Noll, W.: The Nonlinear Field Theories of Mechanics, Handbuch der Physik III/3. Springer, New York (1965)
30. Zou, W., Zheng, Q., Du, D., Rychlewski, J.: Orthogonal irreducible decompositions of tensors of high orders. Math. Mech. Solids **6**, 249–267 (2001)

Continuum Modelling of Shear-Coupled Grain Boundary Migration

Stéphane Berbenni, Bhasker Paliwal and Mohammed Cherkaoui

Abstract The deformation accommodation mechanisms associated to grain boundaries (GBs) significantly affect the mechanical behavior of nano-polycrystals. Among these mechanisms, stress-induced GB migration is now seen to compete or interplay with other intra-granular and GB mechanisms in a wide range of temperatures. A complete micromechanics-based model is here proposed using the concepts of continuum thermodynamics and kinematics to derive a new constitutive model able to describe stress-induced GB migration. Like non diffusive phase-transformations, stress-induced GB migration can be considered on the thermodynamics point of view of conservative nature (diffusionless but thermally activated) until high temperature with respect to melting point. Here, in the framework of continuum micro-mechanics which should be easily implemented in a polycrystalline model, we will first describe the micromechanical framework: the kinematics and the thermodynamics associated with additive mechanisms including plastic deformation in the bulk crystals, GB migration and GB sliding. For the sake of illustration of the present general theory, we will focus on planar bi-crystals and only perfect shear-coupling GB migration situations of [001] symmetric tilt GBs in Cu. Numerical examples and responses of

S. Berbenni (✉)
Laboratoire d'Etudes des Microstructures et de Mécanique des Matériaux, LEM3,
UMR CNRS 7239, University of Lorraine, 57045Metz, France
e-mail: stephane.berbenni@univ-lorraine.fr

S. Berbenni · B. Paliwal · M. Cherkaoui
Unité Mixte Internationale Georgia Tech Lorraine-CNRS, UMI CNRS 2958,
57070 Metz, France B. Paliwal
e-mail: bpaliwal@gatech.edu

M. Cherkaoui
e-mail: mcherkaoui@me.gatech.edu

B. Paliwal · M. Cherkaoui
George W. Woodruff School of Mechanical Engineering, Georgia Institute of Technology,
30332-0405Atlanta 22, GA, USA

H. Altenbach et al. (eds.), *Generalized Continua as Models for Materials*,
Advanced Structured Materials 22, DOI: 10.1007/978-3-642-36394-8_3,

the micromechanical model are given for these bi-crystals considering both isotropic and anisotropic elasticity. These ones are fed by computer-aided MD simulations for which deformation mechanisms are identified.

1 Introduction

"Shear-coupled" grain boundary (GB) migration is now seen to compete or interplay with other intra-granular GB mechanisms in a wide range of temperatures [1, 2]. In nanocrystalline (NC) metals, it now becomes challenging to understand stress-induced GB migration because this is thought to enhance grain growth at low temperatures, which is important for making stable structural materials for engineering applications. In these materials, the interplay of GB migration with other possible GB deformation mechanisms like GB sliding [3] becomes very complex due to the high GB volume fraction. The mechanism of stress-induced shear-coupled GB migration at room temperature is today well identified by a shear deformation accompanying GB migration for symmetric (coincident) tilt GB (here denoted STGB) but less for general non symmetric GB. This new deformation mechanism is different from strain-induced GB migration studied for recrystallization phenomena. The latter essentially comes from spatially heterogeneous intra-crystalline dislocation densities in the vicinity of GB.

Theoretical studies [4] as well as molecular dynamics (MD) simulations using the EAM potential for Cu bicrystals with STGB [1, 2, 5] show that stress-induced GB migration is characterized by a shear "coupling factor" (or shear deformation usually denoted β) which is defined by the ratio of the shear displacement parallel to the GB plane to the GB propagation normal to its plane. This coupling factor is purely geometric and depends on the tilt GB misorientation. "Shear-coupled" GB migration was recently analyzed by [1, 2] using the "Frank-Bilby" equation [6–8]. Due to the high resolved shear stresses required to move STGB [1, 2, 5, 9], it is expected that GB migration would play a key role in the understanding of inverse Hall-Petch effect in addition to GB sliding or GB dislocation nucleation-propagation-absorption.

Due to the complexity of atomistic mechanisms in the case of general GB, we will limit the present study to the constitutive behavior of Cu STGB undergoing shear-coupled migration. For Cu [001] STGB, two shear deformation modes associated to $<110>$ and $<100>$ crystallographic directions linked to two coupling factors (resp. negative and positive) were observed using MD simulations and confirmed experimentally by [10]. In particular, a dual temperature dependent behavior for certain misorientations (around 53°) may be observed at finite temperatures. According to [1], a transition exists above 800 K, where the shear-coupled GB migration may be interrupted by occasional sliding events. Between these sliding events, the GB plane continues to move accompanied by shear. This suggests that pure GB sliding occurs through atomistic mechanisms that preserve GB character. At medium and low temperatures, shear-coupled GB migration has a stick slip stress versus time characteristic response which can be retrieved by atomistic simulations [11, 12].

The objective of the present contribution is to provide a complete micromechanics-based constitutive model using the concepts of continuum mechanics to describe shear-coupled GB migration in bi-crystals. Kinematics and thermodynamics associated with different additive dissipative mechanisms will be introduced in Sect. 2. Here, shear-coupled GB migration will be considered as a shear process in the local coordinates associated to grain boundary plane that can be described in linearized kinematics by an *eigenstrain* (or plastic strain jump at the discontinuity GB surface) similarly to deformation twinning [13]. To illustrate the present theory, Sect. 3 will focus on bi-crystals with plane GB and pure shear-coupled GB migration situations without sliding in addition to intra-crystalline plastic deformation. It will be derived that the shear "coupling factor" β is related to plastic strain jump at the GB surface through an "orientation tensor" characterized by GB surface dislocation Burgers vector and slip plane. In Sect. 4, numerical examples and MD simulations will be restricted to the shear responses of three Cu STGB exhibiting shear-coupled GB migration with absence of bulk intra-crystalline plasticity (because crystal sizes are lower or equal to $10\,\mathrm{nm}$). In these situations, atomic scale deformation mechanisms are well identified using the concept of "displacement shift complete" (DSC) dislocations [14, 1] or "disconnections" [15]. These interfacial defects will be introduced in the constitutive framework and a discussion about the role of stress-induced GB migration coupled with anisotropic elasticity on stress-strain characteristics is provided in the light of the micromechanics-based model. Section 5 concludes and sketch some perspectives for the applicability of the present bi-crystal constitutive framework in mean field polycrystalline modeling involving NC materials and/or deformation twinning.

Throughout the paper, a "," indicates a spatial differentiation, a superposed dot a particle time derivative (or rate). "[A]" denotes the jump of a bulk field "A" at a discontinuity surface such that $[\mathrm{A}] = \mathrm{A}^{\mathrm{II}} - \mathrm{A}^{\mathrm{I}}$ to be consistent with Fig. 1, where I and II are both crystals forming a bicrystal (crystal II being the consumed crystal during interface motion). "$\langle \mathrm{A} \rangle$" denotes the average of a bulk field A across the interface defined by $\langle \mathrm{A} \rangle = \frac{1}{2}\left(\mathrm{A}^{\mathrm{II}} + \mathrm{A}^{\mathrm{I}}\right)$. The Einstein summation convention is also used throughout the paper.

2 Continuum Modeling

2.1 Kinematics

Following [16–18], the particle velocity vector jump at the internal discontinuity surface (GB) denoted hereafter S can be decomposed as follows (Fig. 1)

$$[v_i] = [v_i]^{(1)} + [v_i]^{(2)}, \tag{1}$$

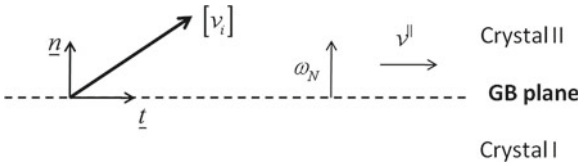

Fig. 1 Schematic representation of grain boundary (GB) migration and sliding (kinematics). $[v_i] = v_i^{II} - v_i^{I}$ denotes the jump of v_i at the interface (GB plane) oriented by unit normal vector n_i from crystal I to crystal II

where

$$[v_i]^{(1)} = -[u_{i,j}]\, n_j \omega_N \tag{2}$$

is the particle velocity jump due to normal GB propagation assuming linearized kinematics [19, 16] and $[v_i]^{(2)}$ is the part of particle velocity jump at the discontinuity surface due to tangential GB sliding.

In Eq. (2), $[u_{i,j}]$ represents the jump of displacement gradient or total distortion at the discontinuity surface S. ω_N is the GB normal velocity and n_i is the unit normal vector to the GB plane oriented from I towards II (Fig. 1). According to Fig. 1, the particle velocity jump contains a tangential part $v^{\parallel}$ and a normal one $v^{\perp}$ as follows

$$[v_i] = v^{\parallel} t_i + v^{\perp} n_i, \tag{3}$$

where $v^{\parallel}$ reads

$$v^{\parallel} = \beta \omega_N + v_s \tag{4}$$

In Eq. (4), $v_s = [v_i]^{(2)}\, t_i$ is the tangential velocity due to GB sliding. Furthermore, β is a purely geometric parameter that can be identified as the "coupling factor" following the terminology used by [4]. Using Eq. (2), β can be identified as a function of the interfacial jump of displacement gradient through the following expression

$$\beta = -[u_{i,j}]\, n_j t_i \tag{5}$$

It is noteworthy that Eq. (5) was postulated by [4] without any direct link to continuum-based kinematics like in the present contribution.

2.2 Thermodynamics

The mechanical dissipation D in the body V is defined as the difference between the power of the applied forces denoted P_{ext} and the rate of change of the stored energy $\dot{\Phi}$ (time derivative of the Helmholtz free energy), which corresponds under isothermal and quasi-static evolutions to the time derivative of the elastic energy [20, 21]

$$D = P_{ext} - \dot{\Phi} \tag{6}$$

Neglecting the excess interfacial energy effects at GB in Eq. (6), Φ is given by

$$\Phi = \int_V \frac{1}{2}\sigma_{ij}\varepsilon^e_{ij}\,dV, \tag{7}$$

where σ_{ij} and ε^e_{ij} are respectively the Cauchy stresses and the elastic strains.

The power of external forces is defined as

$$P_{ext} = \int_{\partial V} \sigma_{ij} n_j v_i\,dV, \tag{8}$$

where n_j is the unit outward normal vector at a point of the external boundary of V denoted ∂V and v_i is the material velocity at this point.

As described in the kinematics part (Sect. 2.1), the strains and stresses are discontinuous across the moving interface. Consequently, the elastic energy density $\varphi = \frac{1}{2}\sigma_{ij}\varepsilon^e_{ij}$ present in Eq. (7) is also discontinuous through the moving discontinuity surface S. Applying the transport theorem for growing discontinuity surface S to Eq. (7), $\dot{\Phi}$ is given by

$$\dot{\Phi} = \int_V \dot{\varphi}\,dV - \int_S [\varphi]\omega_N\,dS. \tag{9}$$

In Eq. (9), the first volume term containing $\dot{\varphi}$ can be easily computed using $\varepsilon_{ij} = \varepsilon^e_{ij} + \varepsilon^p_{ij}$ as follows

$$\int_V \dot{\varphi}\,dV = \int_V \sigma_{ij}\left(\dot{\varepsilon}_{ij} - \dot{\varepsilon}^p_{ij}\right)dV. \tag{10}$$

The second term of Eq. (9) which contains $[\varphi]$ is defined as

$$[\varphi] = \frac{1}{2}\left(\sigma^{II}_{ij}\left(\varepsilon^{II}_{ij} - \varepsilon^{pII}_{ij}\right) - \sigma^{I}_{ij}\left(\varepsilon^{I}_{ij} - \varepsilon^{pI}_{ij}\right)\right). \tag{11}$$

This expression is much simplified in the case of linear homogeneous elastic properties and using the usual symmetries of the homogeneous elastic stiffness tensor C_{ijkl} as follows

$$[\varphi] = \langle\sigma_{ij}\rangle\left[\varepsilon_{ij} - \varepsilon^p_{ij}\right]. \tag{12}$$

Thus, the expression for $\dot{\Phi}$ is obtained using Eqs. (9)–(11)

$$\dot{\Phi} = \int_V \sigma_{ij} \left(\dot{\varepsilon}_{ij} - \dot{\varepsilon}^p_{ij} \right) dV - \int_S [\varphi] \omega_N \, dS. \tag{13}$$

The expression of external power P_{ext} can be obtained after simplifications from Eq. (8)

$$P_{ext} = \int_V \sigma_{ij} \dot{\varepsilon}_{ij} \, dV - \int_S \langle \sigma_{ij} \rangle [\varepsilon_{ij}] \, \omega_N \, dS + \int_S \langle \sigma_{ij} n_j \rangle [v_i]^{(2)} \, dS. \tag{14}$$

By comparing Eqs. (13) and (14), the total dissipation D of the system is positive and reads according to Eq. (6)

$$D = \int_V \sigma_{ij} \dot{\varepsilon}^p_{ij} \, dV - \int_S \left(\langle \sigma_{ij} \rangle [\varepsilon_{ij}] - [\varphi] \right) \omega_N \, dS + \int_S \langle \sigma_{ij} n_j \rangle [v_i]^{(2)} \, dS. \tag{15}$$

For homogeneous elastic properties, Eq. (12) can be applied so that Eq. (15) simplifies into

$$D = \int_V \sigma_{ij} \dot{\varepsilon}^p_{ij} \, dV - \int_S \langle \sigma_{ij} \rangle \left[\varepsilon^p_{ij} \right] \omega_N \, dS + \int_S \langle \sigma_{ij} n_j \rangle [v_i]^{(2)} \, dS. \tag{16}$$

The first term in Eq. (15) is the classic bulk dissipation due to crystallographic slip evolution in crystals without surface of discontinuity. The second term in Eq. (15) is due to the propagation of surface discontinuities and can be related to shear-coupled GB migration. The associated driving force on the discontinuity surface S is given by $[\varphi] - \langle \sigma_{ij} \rangle [\varepsilon_{ij}]$ for heterogeneous elastic solids and simplifies into $-\langle \sigma_{ij} \rangle \left[\varepsilon^p_{ij} \right]$ for homogeneous elastic ones. This driving force can be related to the energy-momentum tensor $P_{lj} = \varphi \delta_{lj} - \sigma_{ij} u_{i,l}$ introduced by [22] through the jump relationship $[P_{lj}] n_j = \left([\varphi] - \langle \sigma_{ij} \rangle [\varepsilon_{ij}] \right) n_l$ for heterogeneous elastic solids. The last term in Eq. (15) or Eq. (16) is due to a possible incoherent interface authorizing tangential GB sliding (see Eq. (4).).

In the following, we first highlight the application of the continuum kinematics and thermodynamics frameworks to stress-induced shear-coupled GB migration. From the continuum mechanics viewpoint, GB is here considered as a continuously distributed dislocation (in the sense of collective continuum defects) for both LAGB and HAGB. In Sect. 16.3, the transport of GB dislocations is fully examined considering a bicrystal with planar GB and average mechanical fields in each crystal.

3 Shear-Coupled GB Migration with Infinite Plane Grain Boundaries

3.1 Dissipation and Transport Equations

In this part and in the rest of the paper, interfacial sliding will be disregarded, and we only focus on stress-induced motion of discontinuity surfaces like GB, assuming they are coherent interfaces. This means that only the first two terms of Eq. (15) are considered. This situation corresponds to "perfect shear-coupling" GB migration as defined in [4]. Thus, for planar bi-crystalline systems, such as the one represented in Fig. 2, Eq. (15) yields

$$\frac{D}{V} = f\sigma_{ij}^{I}\dot{\varepsilon}_{ij}^{pI} + (1-f)\sigma_{ij}^{II}\dot{\varepsilon}_{ij}^{pII} + \left([\varphi] - \langle\sigma_{ij}\rangle[\varepsilon_{ij}]\right)\dot{f}, \tag{17}$$

where f is the current volume fraction of crystal I. If crystal I moves into crystal II, $\dot{f}$ describes the rate of growth of the thickness of crystal I due to normal motion. In the particular case of homogeneous elasticity, $[\varphi] - \langle\sigma_{ij}\rangle[\varepsilon_{ij}]$ should be replaced by $-\langle\sigma_{ij}\rangle\left[\varepsilon_{ij}^{p}\right]$ in Eq. (17). Furthermore, the overall strain (resp. stress) evolution are given by the following transport equations (see also [23]) involving the strain (resp. stress) jump $\left[\varepsilon_{ij}\right]$ (resp. $\left[\sigma_{ij}\right]$) for the plane discontinuity surface S

$$\dot{E}_{ij} = \frac{1}{V}\int_{V}\dot{\varepsilon}_{ij}\,dV - \frac{1}{V}\int_{S}\left[\varepsilon_{ij}\right]\omega_N\,dS = f\dot{\varepsilon}_{ij}^{I} + (1-f)\dot{\varepsilon}_{ij}^{II} - \left[\varepsilon_{ij}\right]\dot{f}, \tag{18}$$

$$\dot{\Sigma}_{ij} = \frac{1}{V}\int_{V}\dot{\sigma}_{ij}\,dV - \frac{1}{V}\int_{S}\left[\sigma_{ij}\right]\omega_N\,dS = f\dot{\sigma}_{ij}^{I} + (1-f)\dot{\sigma}_{ij}^{II} - \left[\sigma_{ij}\right]\dot{f}. \tag{19}$$

From Eq. (18) and assuming homogeneous elasticity, the overall plastic strain rate reads

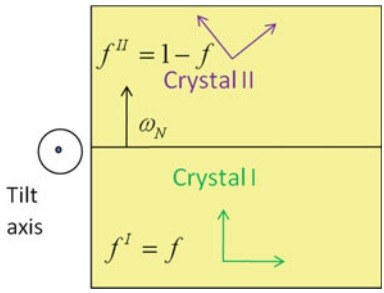

Fig. 2 Bicrystal configuration for shear-coupled GB migration with infinite planar interface (GB plane). Here, the consumed grain (crystal II) is chosen as the reference lattice

$$\dot{E}^{p}_{ij} = \frac{1}{V}\int_{V} \dot{\varepsilon}^{p}_{ij}\,dV - \frac{1}{V}\int_{S} \left[\varepsilon^{p}_{ij}\right]\omega_N\,dS = f\dot{\varepsilon}^{pI}_{ij} + (1-f)\dot{\varepsilon}^{pII}_{ij} - \left[\varepsilon^{p}_{ij}\right]\dot{f} \quad (20)$$

For an infinite plane discontinuity surface and considering heterogeneous elasticity, the strain concentration equations (given an applied overall strain for instance) are detailed in [24]. The calculations give the following general expressions for ε^{I}_{ij} and ε^{II}_{ij}

$$\begin{aligned} \varepsilon^{I}_{ij} &= A^{I}_{ijkl}E_{kl} - (1-f)\,G_{ijkl}\left[\sigma^{p}_{kl}\right], \\ \varepsilon^{II}_{ij} &= A^{II}_{ijkl}E_{kl} + fG_{ijkl}\left[\sigma^{p}_{kl}\right], \end{aligned} \quad (21)$$

where E_{ij} are the overall homogeneous strains, A^{I}_{ijkl}, A^{II}_{ijkl} are respectively the strain concentration tensors for crystals I and II, G_{ijkl} is a strain influence tensor which depends on the anisotropic elastic constants in crystals I and II. In Eq. (21), $\left[\sigma^{p}_{ij}\right]$ is defined by

$$\left[\sigma^{p}_{ij}\right] = C^{II}_{ijkl}\varepsilon^{pII}_{kl} - C^{I}_{ijkl}\varepsilon^{pI}_{kl}. \quad (22)$$

A^{I}_{ijkl}, A^{II}_{ijkl}, $\left[\sigma^{p}_{ij}\right]$ and G_{ijkl} are given in [24]. The strain jump $[\varepsilon_{ij}]$ can be easily derived from Eq. (21). In addition, the effective (overall) elastic moduli C^{eff}_{ijkl} of the bicrystal can be computed using Eq. (21) together with $\left[\sigma^{p}_{ij}\right] = 0$ and the static averaging rules. The complete expressions of the effective elastic moduli C^{eff}_{ijkl} are given elsewhere [24].

In Eq. (17), the term $\left([\varphi] - \langle\sigma_{ij}\rangle[\varepsilon_{ij}]\right)\dot{f}$ (general case) or $-\langle\sigma_{ij}\rangle\left[\varepsilon^{p}_{ij}\right]\dot{f}$ (for homogeneous elasticity) has to be expressed. These terms characterize the intrinsic dissipation per unit volume due the shear-coupled GB migration mechanism. In the following, the link between continuum-based GB dislocation density and the coupling factor β is recalled using the continuum dislocation density tensor introduced by [25] and [26].

3.2 GB Dislocation Densities and β Coupling Factor

In the continuum dislocation theory [25–27], the dislocation density tensor α_{hi} is defined as the *Curl* of the incompatible elastic distortion β^{e}_{ji} (i.e. the elastic incompatible part of the displacement gradient $u_{i,j} = \beta_{ji} = \beta^{e}_{ji} + \beta^{p}_{ji}$ in the linearized theory) as follows

$$\alpha_{hi} = \in_{hlj}\beta^{e}_{ji,l}, \quad (23)$$

where $\in_{hlj}$ is the permutation tensor. According to the Frank-Bilby theory of surface dislocations [6–8], the plastic distortion jump (or *eigendistortion*) due to the GB

dislocations (which is a continuum description of discrete GB defects present at the atomic scale and responsible for GB migration) can be obtained from the expression of surface dislocation densities [8, 28] defined as follows

$$\alpha^{S}_{hi} = \in_{hlj}\left[\beta^{e}_{ji}\right] n_l = \in_{hlj}\left(\beta^{eII}_{ji} - \beta^{eI}_{ji}\right) n_l. \tag{24}$$

Applying the 1st order Hadamard compatibility relation [19] at the discontinuity surface (i.e. $\in_{hlj}\left[\beta_{ji}\right] n_l = \in_{hlj}\left(\beta^{II}_{ji} - \beta^{I}_{ji}\right) n_l = 0$) , Eq. (24) yields

$$\alpha^{S}_{ij} = -\in_{jkl}\left[\beta^{p}_{li}\right] n_k. \tag{25}$$

Assuming t_l a given unit vector in the boundary plane (of unit normal n_m) in Fig. 3 and w_j a unit vector such as $w_j = \in_{jmn} n_m t_n$, then the resultant Burgers vector of dislocation lines cut by t_l is $B_i = \alpha^{S}_{ij} w_j$. Using Eq. (25), $\in_{jkl}\in_{jmn} = \delta_{km}\delta_{ln} - \delta_{kn}\delta_{lm}$ and $n_n t_n = 0$, it comes

$$B_i = -\left[\beta^{p}_{li}\right] t_l. \tag{26}$$

The plastic distortion jump $\left[\beta^{p}_{li}\right]$ results from plastic accommodation due the motion of gliding surface dislocation embodied by α^{S}_{ij}. This formalism was first applied to martensitic transformations by [8] and later by [2] for "shear-coupled" GB migration. If crystal II is consumed during the motion of crystal I into crystal II then crystal II will be considered as the reference lattice. This is similar to a parent phase in martensitic transformations as described in [8]. Thus,

$$\left[\beta^{p}_{li}\right] = -\beta l_i g_l, \tag{27}$$

where l_i and g_l are unit vectors defined with respect to the reference crystal (see Fig. 3) so that the interface dislocations can be considered for LAGB as discrete distributions of straight dislocations parallel to a unit vector. For HAGB, the interface dislocations are general surface dislocations. Eq. (27) characterizes a simple shear of magnitude β defined as the "coupling factor" by [4] during perfect shear-coupled GB migration (i.e. without sliding). This β factor was already identified in Sect. 2.1

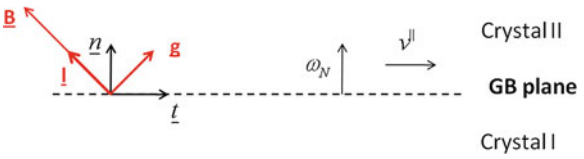

Fig. 3 Definition of surface dislocation Burgers vector B_i with respect to reference crystal II. l_i is a unit vector in the direction of the Burgers vector, and g_i represents the unit normal to the gliding plane of the surface dislocation

without making any reference to the surface dislocation concept like in the present section.

Here, l_i gives the direction of the Burgers vector content B_i such that $B_i = Bl_i$, where B is its magnitude, and g_i represents the unit normal to the gliding plane of the GB dislocations, such as Eqs. (26) and (27) give

$$B_i = \beta l_i g_l t_l = B l_i. \tag{28}$$

From the last equation, the relationship between B and β is found

$$\beta = \frac{B}{g_l t_l} \tag{29}$$

In the case of STGB with a tilt axis direction given by the unit vector

$$p_j = \epsilon_{jmn} l_m g_n = \epsilon_{jmn} t_m n_n,$$

simple geometric considerations using Fig. 3 gives the expression of the coupling factor

$$\beta = \frac{B}{l_l n_l}. \tag{30}$$

This relationship is consistent with [1]'s work through their *Eq. (21)*. In this section, the most important is the expression of $\left[\varepsilon^p_{ij}\right]$, the symmetric part of $\left[\beta^p_{ji}\right]$, which reads from Eq. (27)

$$\left[\varepsilon^p_{ij}\right] = -\widetilde{R_{ij}}\beta \tag{31}$$

with

$$\widetilde{R_{ij}} = \frac{1}{2}\left(l_i g_j + g_i l_j\right). \tag{32}$$

$\widetilde{R_{ij}}$ is defined as the "orientation tensor" associated to the shear deformation (or slip) of magnitude β coupled to GB migration. From the previous definitions of l_i and g_j in Fig. 3, $\widetilde{R_{ij}}$ and $\left[\varepsilon^p_{ij}\right]$ are traceless (i.e. $\widetilde{R_{kk}} = 0$) so that the induced plastic strain due to shear-coupled GB migration is incompressible.

3.3 Thermodynamic Driving Forces

From Eq. (17), the total dissipation per unit volume can be rewritten in the following general form

$$\frac{D}{V} = F_i\left(E_{kl}, \Sigma_{kl}, X_j\right)\dot{X}_i, \tag{33}$$

where F_i are the driving forces associated to internal variables X_i. These ones depend on the overall strains E_{ij} or stresses Σ_{ij} and on the three internal variables X_j (i.e. $\varepsilon_{ij}^{pI}, \varepsilon_{ij}^{pII}, f$). In this problem, the three driving forces $F_{\varepsilon^{pI}}, F_{\varepsilon^{pII}}, F_f$ associated respectively to $\varepsilon_{ij}^{pI}, \varepsilon_{ij}^{pII}, f$ (describing three independent inelastic processes) are listed below using Eq. (17)

$$\begin{aligned} F_{\varepsilon^{pI}} &= f\sigma_{ij}^{I}, \\ F_{\varepsilon^{pII}} &= (1-f)\,\sigma_{ij}^{II}, \\ F_f &= [\varphi] - \langle\sigma_{ij}\rangle\,[\varepsilon_{ij}], \end{aligned} \tag{34}$$

where $\sigma_{ij}^{I}, \sigma_{ij}^{II}, \langle\sigma_{ij}\rangle, [\varphi]$ and $[\varepsilon_{ij}]$ can be computed using Eq. (21). In the case of homogeneous elasticity without intra-crystalline slip, F_f simply becomes $F_f = -\langle\sigma_{ij}\rangle\left[\varepsilon_{ij}^{p}\right] = \langle\sigma_{ij}\rangle\widetilde{R_{ij}}\beta = \tilde{\tau}\beta$ following Sect. 3.2, where $\tilde{\tau}$ is the driving resolved shear stress on the surface dislocation gliding plane associated to $\left[\varepsilon_{ij}^{p}\right]$, $\widetilde{R_{ij}}$ is the orientation tensor previously defined in Sect. 3.2 and β is the shear coupling factor.

In the thermo-mechanics of plasticity [29, 21], the critical forces (corresponding to "threshold stresses" for the previous irreversible processes) are needed to complete the theory. The considered constitutive expressions for the critical forces and the kinetics law must be chosen with respect to a positive dissipation per unit volume in Eq. (33).

3.4 Critical Forces and Bi-Crystal's Overall Behavior

If the critical forces for intra-crystalline plastic deformation in both crystals ε_{ij}^{pI}, ε_{ij}^{pII}, f, here denoted $F_{\varepsilon^{pI}}^{C}, F_{\varepsilon^{pII}}^{C}$, are higher than their respective corresponding driving forces and only the critical force for shear-coupled GB migration denoted F_f^C is reached by F_f then

$$\begin{aligned} F_{\varepsilon^{pI}} &< F_{\varepsilon^{pI}}^{C}, \\ F_{\varepsilon^{pII}} &< F_{\varepsilon^{pII}}^{C}, \\ F_f &= F_f^C \end{aligned} \tag{35}$$

In the case of homogeneous elasticity, the last equation in Eq. (35) reduces to $\tilde{\tau} = \widetilde{\tau_C}$ for a given shear coupling factor β, where $\widetilde{\tau_C}$ is the critical shear stress resolved on the surface dislocation gliding plane. When F_f reaches F_f^C (or when $\tilde{\tau}$ reaches $\widetilde{\tau_C}$ in the case of homogeneous elasticity) in Eq. (35), the GB migration flux is given by the expression of $\dot{f}$ for an infinite GB plane as follows

$$\dot{f} = \frac{1}{V}\int_S \omega_N\,dS = \frac{\omega_N S}{V} = \frac{\omega_N}{L}, \tag{36}$$

where L is the total length of the deformed bicrystal in the normal direction to the GB.

The overall Hooke's law together with Eqs. (18), (19), (36) give the following constitutive relationship between the overall stress and strain rates

$$\dot{\Sigma}_{ij} = C^{eff}_{ijkl}\left(\dot{E}_{kl} + \frac{\omega_N}{L}\left([\varepsilon_{kl}] - S^{eff}_{klmn}[\sigma_{mn}]\right)\right), \tag{37}$$

where $[\sigma_{ij}]$ and $[\varepsilon_{ij}]$ are provided by Eq. (21) depending on homogeneous stress or strain conditions prescribed at the boundary of the bicrystal. Thus, for heterogeneous elastic bicrystals, Eq. (37) also writes

$$\dot{\Sigma}_{ij} = C^{eff}_{ijkl}\left(\dot{E}_{kl} - \dot{E}^{peff}_{kl}\right), \tag{38}$$

where $\dot{E}^{peff}_{ij}$ is the effective (overall) plastic strain rate due to shear-coupled GB migration defined as

$$\dot{E}^{peff}_{ij} = -\frac{\omega_N}{L}\left([\varepsilon_{ij}] - S^{eff}_{ijkl}[\sigma_{kl}]\right). \tag{39}$$

If homogeneous elasticity is assumed, the constitutive law simplifies into

$$\dot{\Sigma}_{ij} = C_{ijkl}\left(\dot{E}_{kl} + \left[\varepsilon^{p}_{kl}\right]\frac{\omega_N}{L}\right), \tag{40}$$

which gives, using Eq. (31) in the case, where crystal II is consumed,

$$\dot{\Sigma}_{ij} = C_{ijkl}\left(\dot{E}_{kl} - \widetilde{R_{kl}}\beta\frac{\omega_N}{L}\right). \tag{41}$$

Following recent experimental data [30], stress-driven shear-coupled GB migration exhibits a temperature dependence indicating that a thermally-activated process is at the origin of the shear-coupled GB migration. It is noteworthy that recent efforts were made to capture the kinetics law for the GB migration process at finite temperatures and strain rates by [11]. However, the accurate determination of the kinetics parameters for the three investigated Cu STGB will need specific simulation methods (parallel-replica dynamics, nudged elastic band methods) which are out of the scope of the present study.

Equation (38) shows that once GB migration is active for a given normal velocity ω_N (which also depends on the applied velocity to the bicrystal), the instantaneous stress decrease due to induced plastic strain is dependent on the effective elastic moduli C^{eff}_{ijkl} (or C_{ijkl} in the case of homogeneous elasticity), the GB character (through $\widetilde{R_{ij}}$ and β) and the bicrystal finite size L. The calculation of $\dot{f}$ (or equivalently the volume fraction increment dictated by the stepwise normal GB motion at each GB migration event) will be specified and discussed in Sect. 4 (for 0 and 500 K temperatures) with application to particular [001] Cu STGB (coincident GB). For

the latter, the atomistic mechanisms and collective steps when GB migrates are known following appropriate vectors of the "displacement shift complete" (DSC) lattice [1, 14].

4 Application to Cu [001] Symmetric Tilt Grain Boundaries (STGB)

4.1 Shear Modes

Following [1, 2, 11], we considered [001] STGB in cubic metals like Cu (f.c.c. metal). GB are generally characterized by five angles. Four angles are set up by choosing the tilt axis and the GB plane is a particular mirror plane of the bi-crystal containing the tilt axis. The misorientation angle θ is defined as the tilt angle between the [100] directions of both crystals in the counterclockwise direction, with $0 < \theta < \pi/2$ due to the four-fold symmetry around the tilt axis. Hence, the GB plane lies along the bisector between the [100] directions like in Fig. 4.

Following [2], two mappings for the Burgers circuit allows two possible B_i and two associated "coupling modes" to be defined. The first "coupling mode" called the <100> mode (or "mode I") is such that l_i is parallel to the cube direction [010] of the reference lattice (crystal II) and the Frank-Bilby dislocation slip planes are (100) [2]. The slip plane is represented to the left of the GB normal in Fig. 4. For small θ (LAGB), the expressions for B_i and the associated dislocation density can be resolved by a discrete distribution of single lattice dislocations of Burgers vectors $b_i = a_L$ [010], where a_L is the lattice parameter. For LAGB, the critical stress is proportional to the glide component of the Peach-Koehler force required to initiate the collective glide of the arrays of GB dislocations [10]. There are two kinds of LAGB: either for small θ or for θ close to π/2 (i.e. $\varphi = \pi/2 - \theta$ near 0). The latter corresponds to the GB "mode II" migration (<110> mode), where l_i is parallel to the direction $[1\ \bar{1}0]$

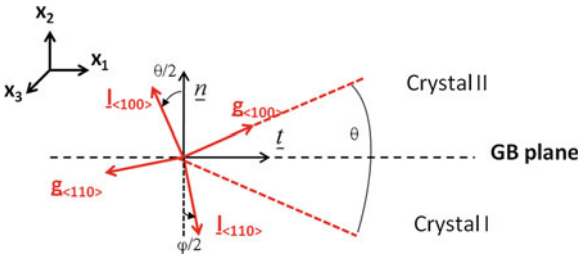

Fig. 4 Definition of the misorientation angle θ for [001]-type tilt boundaries. Two Burgers vectors B_i with directions given by unit vectors l_i are possible which correspond to two different mappings for Burgers circuit. The normal directions to the slip planes are given by unit vectors g_i. Angles θ and φ are linked each other by $\varphi = \pi/2 - \theta$

of the reference lattice (crystal I) and the associated resolved single dislocations are of type $B_i = a_L/2\left[1\bar{1}0\right]$. In this case, the Frank-Bilby surface dislocation glides along (110) planes, which is represented to the right of the GB normal in Fig. 4.

For HAGB, the discrete distributions of single dislocations can not be resolved anymore [31] and only the "Frank-Bilby equation" (Eq. (25)) is here used for these STGB. As established by [2], the Frank-Bilby equation (FBE) introduced in Sect. 3.2 provides two feasible solutions for [001] STGB and their continuous GB dislocation density.

These two solutions (as functions of θ) correspond to Burgers vectors either parallel to the [010] (denoted as B_i <100> for "mode I") or parallel to the $[1\bar{1}0]$ (denoted as B_i <110> for "mode II"). Here, [010] and $[1\bar{1}0]$ are crystallographic directions respectively defined in the crystal II and crystal I. For GB "mode I" migration, the consumed grain is crystal II (reference lattice) such as $\dot{f} \geqslant 0$, whereas for "mode II" migration, crystal I (reference lattice) is consumed with $\dot{f} \leqslant 0$. Under simple shear loading, these two coupling modes compete with each other, and the transition from one mode to the other occurs at a critical misorientation angle θ which depends on temperature (see Fig. 8 in [1]). Note that as the temperature drops, the θ range of "mode II" expands and it may be the only active coupling mode for all values of θ at $T = 0$ K. The invoked reason is that the activation of "mode I" requires the breaking of the mirror symmetry due to equivalent row translations by lattice vectors 1/2[001] and $1/2[00\bar{1}]$. This symmetry can only be broken at finite temperatures, where ledges and other defects may form easily. This issue was also checked using the gamma-surfaces associated to both modes at 0 K by [1].

Thus, due to the complexity of atomistic mechanisms in the case of general GB, we here limit atomistic investigations to study the constitutive behavior associated with the STGB shear-coupled migration. For this case, MD simulations are conducted for three Cu [001] STGB with misorientation angles $\theta = 77.32°, 53.13°, 28.07°$ which show the well-identified temperature dependent shear-coupling <100> and <110> modes linked to two characteristic coupling factors β (resp. positive and negative). According to [1], the coupling factor β depends on θ and on the "coupling modes" as follows

$$\begin{aligned} \beta_{<100>} &= 2\tan\left(\frac{\theta}{2}\right), \\ \beta_{<110>} &= -2\tan\left(\frac{\varphi}{2}\right), \end{aligned} \tag{42}$$

where $\varphi = \frac{\pi}{2} - \theta$. The atomistic MD simulations which are shown in Sect. 4.2 will first provide the shear stress response, the temperature dependent shear coupling mode as a function of the GB character, the critical shear stresses (or "peak stresses"), the stress accommodation due to shear (shear stress drop during GB migration) and the saw-tooth behavior (stick slip character). Second, the results of the developed micromechanics-based model regarding elastic slopes and shear stress drops will

be discussed in Sect. 4.3. The roles of GB character, bicrystal size and cubic elastic anisotropy will be studied in Sect. 4.3.

4.2 Molecular Dynamics (MD) Simulations

In this subsection, a few "flat" Cu [001] STGB, namely Σ41(540) ($\theta = 77.32°$), Σ5(210) ($\theta = 53.13°$), Σ17(410) ($\theta = 28.07°$), were studied at 0 K and at 500 K temperatures using the EAM interatomic potential provided by [32] for Cu. Note that in the work of [1], where MD simulations were performed under simple shear loading at 800 K, the first two STGB display "mode II" migration, and the last one displays the "mode I" (see Table 3.1 in [1]). However, all of them display the "mode II" (<110> mode) at 0 K as can be inferred from the plots in the Fig. 8 of [1]. Here, each bi-crystal with [001] STGB is created using the coincident site lattice (CSL) model by placing the first crystal on the top of the other using the following procedure (Fig. 5). The tilt axis (x3-axis) is along [001] direction. The horizontal plane (x1,x3) corresponds to the GB plane, and [100] directions for crystals I and II makes an angle θ. The gap between the two crystals is set to about 2 Angström before it is subjected to energy minimization. Several initial configurations are also tested by shifting the upper grain with respect to the lower along the (x1) direction so as to obtain the lowest energy state of a GB configuration after atomic relaxation. The energy minimization

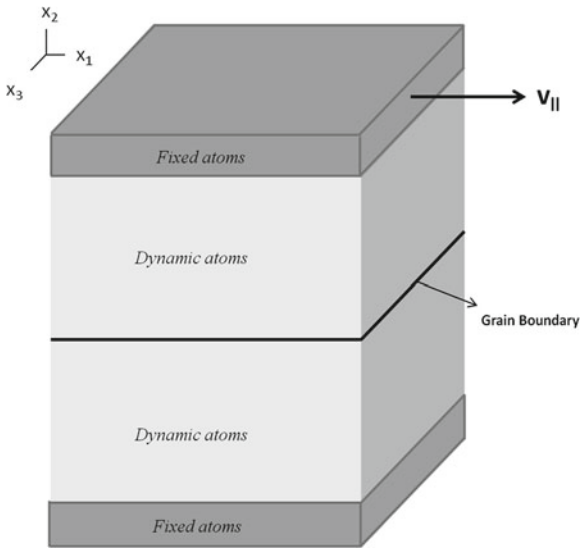

Fig. 5 Schematic figure of the computational atomistic unit cell box with coordinate axes and periodic boundary conditions. L is the total length in the normal direction (as defined in the text) to the GB plane for dynamic atoms subjected to shear

Table 1 Elastic shear moduli obtained by the MD results and by the present micromechanical model accounting for anisotropic elasticity for Σ41(540), Σ5(210), Σ17(410) [001] STGB

Effective elastic shear moduli (GPa)	Σ41(540)	Σ5(210)	Σ17(410)
Atomistic simulations	25.4	35.6	57.4
Present model (anisotropic)	25.7	39.5	61.8
Voigt-Reuss-Hill average (isotropic)	47.8	47.8	47.8

The isotropic Voigt-Reuss-Hill average is also given for comparisons

is performed with the LAMMPS simulator[1] using a conjugate gradient method. Each Cu crystal for simulations is approximately cubic shaped, and the simulation block for the bicrystal contains between 30000–45000 atoms with periodicity in the (x1) and the (x3) directions. After optimization, the relaxed structure is subjected to constant shear strain rate loading as follows. The simulation block (Fig. 5) is sandwiched between the top and the bottom layer (along the (x_2) axis) of thickness about 2 times the potential cut-off distance. These two layers do not participate in computing data from the simulations and serve only to impose simple shear loading. The bottom block is held fixed and the constant shear velocity $v_0 = v^{\parallel} = \dot{E}L$ is applied on the top part of the block in the (x_1) direction, where $\dot{E}$ is the constant shear strain rate ($\dot{E} = 10^8 s^{-1}$) and L is the simulation block length containing unconstrained atoms. Here, two different values were chosen to keep initial crystal characteristic sizes lower or equal to 10 nm to mimic nanocrystals, namely $L = 12.2$ nm and $L = 20$ nm. The time step is 1 fs. These simulations are conducted at 0.001 K and at 500 K, and the overall stress tensor was computed using the standard virial expression averaged over all dynamic atoms. The GB position was also tracked from the common neighborhood analysis (CNA) computation. The CNA value for atoms in f.c.c. lattice is 1 and for atoms forming GB structural units it is 5 [33, 34].

4.3 Discussion of the Continuum Model and Comparisons with MD Results

The micromechanics-based approach is applied to the three previously investigated Cu bi-crystals with [001] STGB. The motivation to study Cu bi-crystals lies in the fact that they exhibit a strongly anisotropic elastic behavior characterized by the following anisotropic coefficient $a = \dfrac{2C_{44}}{C_{11} - C_{12}} = 3.26$. The cubic elastic moduli for Cu are taken as $C_{11} = 170$ GPa, $C_{12} = 122.5$ GPa and $C_{44} = 76$ GPa. These elastic constants are given by [32] and were used by these authors to validate the EAM potential for Cu. In this paper, the application of the micromechanics-based theory is mainly focused on the effect of elastic anisotropy on the shear stress-strain curves before and at the first shear-coupled GB migration event (Fig. 6).

[1] LAMMPS Molecular Dynamics Simulator; http///lammps.sandia.gov/.

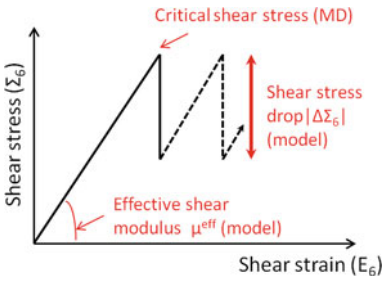

Fig. 6 Schematic representation of the shear stress versus shear strain curve and the quantitative values predicted by the micromechanical model: elastic slopes and shear stress drops. The critical shear stress (also called "peak stress") is obtained by MD simulations

For homogeneous isotropic elastic properties, the isotropic elastic coefficients for Cu are obtained using the classic "Voigt-Reuss-Hill average" model [35]. This model gives $\mu = 47.8$ GPa (isotropic elastic shear modulus) and $\nu = 0.345$ (Poisson ratio). The isotropic shear modulus is reported on Table 1 for comparisons with the effective elastic shear moduli μ^{eff} derived for general elastic anisotropy [24]. The numerical values for elastic moduli are computed in both crystals using the cubic symmetry for $\Sigma41(540)$ ($\theta = 77.32°$), $\Sigma5(210)$ ($\theta = 53.13°$), $\Sigma17(410)$ ($\theta = 28.07°$) that can be used to derive the effective elastic moduli for the three investigated bi-crystals. We find for $f = 1 - f$ (initial elastic slope) that the effective elastic shear moduli (Table 1) are in good agreement with the atomistic simulations at 0 K and at 500 K. In contrast, we remark that the classic isotropic assumption obtained from "Voigt-Reuss-Hill average" is sometimes far from the atomistic results for the studied Cu [001] STGB, which means that the simple elastic isotropic assumption is not realistic for the present application. The mechanical responses given by the micromechanical model can be enriched by the critical forces F_f^C or the critical resolved shear stresses on the GB slip plane $\widetilde{\tau_C}$ in Eq. (35) directly obtained from the peak stresses (or critical shear stresses τ_C) of the atomistic results (see Sect. 4.2). These peak stresses resulted from simple shear performed at an applied material velocity $v^{\parallel}$ parallel to the GB plane (Fig. 5).

Second, we focus on the analysis of shear stress drops in the light of the micromechanical approach after the first GB migration event, i.e. for $f = 1 - f$ in the constitutive model assuming isotropic elasticity or fully anisotropic elasticity in both crystals. Following MD results detailed in [24], we start by the analysis of first shear stress drops when the "mode II" (<110> mode) is activated at 0 K for the three GBs and at 500 K for $\Sigma41(540)$ and $\Sigma5(210)$. Then, the model is applied to the case when the "mode I" (<100> mode) is activated at 500 K for $\Sigma17(410)$. Lastly, the model is applied to understand the origin of bi-crystal size effects on stress drops at 0 K for the three STGBs.

As seen from atomistic simulations, "mode II" is a dominating shear mode especially at 0 K for the three GBs. According to Fig. 4, l_i and g_i are defined so that the <110> mode ("mode II") is characterized by

$$l_i n_i = g_i t_i = -\cos\left(\frac{\varphi}{2}\right) = -\cos\left(\frac{\pi}{4} - \frac{\theta}{2}\right)$$

which gives

$$l_i = \left(\sin\left(\frac{\pi}{4} - \frac{\theta}{2}\right), -\cos\left(\frac{\pi}{4} - \frac{\theta}{2}\right), 0\right)$$

and

$$g_i = \left(-\cos\left(\frac{\pi}{4} - \frac{\theta}{2}\right), -\sin\left(\frac{\pi}{4} - \frac{\theta}{2}\right), 0\right)$$

and $\widetilde{R_{ij}}$ from Eq. (32). Since crystal I is the parent grain, only crystal II undergoes plastic deformation, thus $\left[\varepsilon_{ij}^{p}\right] = \varepsilon_{ij}^{pII} = -\widetilde{R_{ij}}\beta$. When the critical shear stress is reached, shear-coupled GB migration is active. Then, time integration of Eq. (38) during the first shear-coupled GB migration event yields

$$\dot{\Sigma}_{ij}\delta t = C_{ijkl}^{eff}\dot{E}_{kl}\delta t + \frac{h_N}{L}\left(C_{ijkl}^{eff}\left[\varepsilon_{kl}\right] - \left[\sigma_{ij}\right]\right). \tag{43}$$

From atomistic results, the step time δt for each single shear-coupled GB migration event is a few *ps*. This time scale is out of the scope of continuum mechanics for which GB migration is seen as instantaneous. In Eq. (43), the strain and stress jumps (resp. $[\varepsilon_{ij}]$ and $[\sigma_{ij}]$) can be computed using Eq. (21) for homogeneous stress or strain boundary conditions. These jumps depend on the elastic properties of both crystals and depend on $\widetilde{R_{ij}}$ and β. In Eq. (43), h_N denotes the normal step height during stepwise GB motion (at the first GB migration event) which corresponds to the characteristic step height due to GB disconnection loop nucleation [15]. In the case of "mode II", the GB plane moves down (negative motion with respect to the (x_2) axis in Fig. 5) to a new position when τ_C is reached for which the activation energy for GB migration is overcome. At this point, the second term in Eq. (43), that contains the strain and stress jumps, h_N and the effective elastic moduli, is responsible for shear stress drop when migration is active. Without trying to determine the complete activation energy profile for the three studied STGB, the transition from an unstable state to a metastable state associated with the dissipative GB migration event is then described by a normal step height h_N. This characteristic distance h_N is also linked to the DSC lattice vector following for coincident (CSL) GB. The DSC ("displacement shift complete") lattice is the largest lattice including all the sites of the lattices of both crystals. According to [14, 1], the disconnection step height h_N is linked to the DSC lattice spacing. Thus, the expression of the disconnection step height h_N depends on the GB character (through θ) and on the lattice parameter a_L. For the $<110>$ mode, h_N is negative and is given by [1]

$$h_N{}^{<110>} = -\frac{a_L}{\sqrt{2}}\cos\left(\frac{\varphi}{2}\right), \tag{44}$$

Table 2 Normal step height h_N average values obtained by Eq. (44) (theory) compared to MD results for Cu Σ41(540), Σ5(210), Σ17(410) [001] STGB

h_N (nm) for <110> mode	Σ41(540)	Σ5(210)	Σ17(410)
Atomistic simulations (average values)	–0.255	–0.248	–0.220
Theory (for present model)	–0.254	–0.242	–0.219

where $a_L = 0.3615\,\text{nm}$ for Cu. The numerical values obtained for h_N from MD simulations are computed by averaging the different GB position steps. The comparisons between these values and the theoretical ones given by Eq. (44) are provided in Table 2 and show a very good agreement.

Here, the shear-coupled GB migration event is assumed instantaneous at the continuum mechanics time scale so that during the stepwise GB motion $\Delta E_{ij} = \dot{E}_{ij}\delta t = 0$ in Eq. (43), thus

$$\Delta\Sigma_{ij} = \frac{h_N}{L}\left(C^{\text{eff}}_{ijkl}\,[\varepsilon_{kl}] - [\sigma_{ij}]\right). \tag{45}$$

Assuming linear isotropic homogeneous elasticity, Eq. (45) simplifies into

$$\Delta\Sigma_{ij} = -2\mu\frac{h_N}{L}\beta\widetilde{R_{ij}} \tag{46}$$

since $\widetilde{R_{kk}} = 0$ (see Sect. 3.2).

In the following, the tensor to matrix convention is used. The pairs of subscripts ij and kl are converted to single subscripts as follows: $11\rightarrow 1$, $22\rightarrow 2$, $33\rightarrow 3$, 23 and $32\rightarrow 4$, 13 and $31\rightarrow 5$, 12 and $21\rightarrow 6$. For simple shear parallel to GB plane in the (x_1) direction as performed in the MD simulations (Fig. 5), the shear stress increment is obtained from Eq. (45) as follows

$$\Delta\Sigma_6 = \frac{h_N}{L}\left(C^{\text{eff}}_{62}\,[\varepsilon_2] + C^{\text{eff}}_{64}\,[\varepsilon_4] + C^{\text{eff}}_{66}\,[\varepsilon_6]\right) \tag{47}$$

since $[\sigma_6] = 0$. Thus, the strain concentration equations (Eq. (22)) are here applied. For isotropic elasticity, Eq. (46) simply yields

$$\Delta\Sigma_6 = -\mu\frac{h_N}{L}\beta\widetilde{R_6} \tag{48}$$

with $\widetilde{R_6} = l_1 g_2 + g_1 l_2 = \cos\left(\frac{\pi}{2} - \theta\right)$.

The present micromechanics-based model is able to describe the shear stress drop magnitude in the stick-slip behavior (Fig. 6). The shear stress drop magnitude can be defined as the absolute value of the shear stress increment $|\Delta\Sigma_6|$ obtained from Eq. (47) or Eq. (48). The stick-slip behavior is dependent on the grain boundary char-

Table 3 Shear stress drop magnitudes (in MPa) obtained by the MD results at 0 and 500 K and by the micromechanical model with anisotropic and isotropic elastic formulations for Cu Σ41(540), Σ5(210), Σ17(410) [001] STGB with $L = 12.2$ nm

$\lvert\Delta\Sigma_6\rvert$ (MPa) for $L = 12.2$ nm	Σ41(540) (0K,500K)	Σ5(210) (0K,500K)	Σ17(410) (0K)
Atomistic simulations	100	417	1080
Present model (anisotropic)	127	603	1024
Present model (isotropic)	216	506	485

acter (through θ), the effective elastic properties of the bicrystal, the lattice parameter (through h_N) and the bicrystal finite size L. The numerical values regarding shear stress drop magnitudes for Σ41(540) ($\theta = 77.32°$), Σ5(210) ($\theta = 53.13°$), Σ17(410) ($\theta = 28.07°$) are reported in Table 3 both from atomistic results and from the micromechanical approach (either Eq. (47) for anisotropic elasticity or Eq. (48) for isotropic elasticity). The $\beta_{<110>}$ coupling factors are respectively −0.222, −0.667, −1.200 for Σ41(540), Σ5(210), Σ17(410). The quantitative comparisons reported in Table 3 give reasonable agreement with the atomistic results in the case of anisotropic elasticity for the three investigated STGB. In this case, the relative errors with respect to MD results appear to be quite acceptable. Conversely, the isotropic elasticity assumption give unrealistic results which are far from the MD results especially for Σ41(540) STGB, where the relative error reaches ~120 %. The results show that the isotropic elastic assumption may only be relevant for the particular case of Σ5(210) STGB, where both fully anisotropic and isotropic elastic formulations give similar values.

Another example, where the micromechanical approach can be applied, is the specific Cu Σ13 (320) ($\theta = 67.4°$) STGB investigated by [11]. In this case, the shear stress drop magnitude obtained by the authors using atomistic simulations at 0 K with $L = 6$ nm was found to be ~450 MPa [11]. Taking into account anisotropic elasticity (Eq. (47)) and the fact that the "mode II" is active at 0 K (Eq. (44)), the present model gives $|\Delta\Sigma_6| = 573$ MPa, which represents a relative error of ~27 %.

For Cu Σ17 (410) STGB, "mode I" occurs at 500 K according to MD results [24]. In this <100> mode, B_i (or l_i) forms an angle $\theta/2$ counterclockwise with respect to n_i (Fig. 4) such that

$$l_i n_i = g_i t_i = \cos\left(\frac{\theta}{2}\right), \qquad l_i = \left(-\sin\left(\frac{\theta}{2}\right), \cos\left(\frac{\theta}{2}\right), 0\right),$$

$$g_i = \left(\cos\left(\frac{\theta}{2}\right), \sin\left(\frac{\theta}{2}\right), 0\right).$$

Here, crystal II is the parent grain and only crystal I undergoes plastic deformation, thus $\left[\varepsilon_{ij}^{p}\right] = -\varepsilon_{ij}^{pI} = -\widetilde{R_{ij}}\beta$, where $\widetilde{R_{ij}}$ is given by Eq. (32). In this case, the first shear stress drop obtaind by MD simulations is ~300 MPa. The micromechanical model can also be applied in the same way to the "mode I" observed at $T = 500$ K.

Table 4 Shear stress drop magnitudes (in MPa) obtained by the MD results and by the micromechanical model with anisotropic and isotropic elastic formulations for Cu Σ41(540), Σ5(210), Σ17(410) [001] STGB with $L = 20\,nm$ at 0 K

$\lvert\Delta\Sigma_6\rvert$ (MPa) for $L = 20\,nm$	Σ41(540)	Σ5(210)	Σ17(410)
Atomistic simulations (0 K)	60	244	641
Present model (anisotropic)	78	368	624
Present model (isotropic)	132	309	296

In this case, the theoretical h_N value is now positive and is given by [1]

$$h_N{}^{<100>} = \frac{a_L}{2}\cos\left(\frac{\theta}{2}\right). \tag{49}$$

Using Eq. (47) (elastic anisotropy), we obtain $|\Delta\Sigma_6| = 322$ MPa, which represents a relative error of ~7 %.

It looks clear that the large discrepancies sometimes observed between the atomistic results and the model with the isotropic elastic assumption are mainly due to a poor estimate of the effective elastic shear modulus and the strains in both crystals.

Bicrystal size effect is observed in atomistic results on shear stress drop magnitude for Σ41(540), Σ5(210), Σ17(410). The results of the micromechanical model for $L = 20$ nm are given in Table 4 (for both isotropic and anisotropic formulations). Overall, the bicrystal size effect is well reproduced for both STGB in the case, where anisotropic elasticity is accounted for, especially for Σ41(540) and Σ17(410). Even though the micromechanical approach supposes mean strain and stress fields in both crystals (no intracrystalline shear stress fluctuations along the normal axis (x_2) to the GB plane), it is found that the bicrystal size effect (characterized by the internal length scale L) on the shear stress drop magnitude scales with $\frac{h_N}{L}$.

Here, h_N is fixed for a given STGB because it is linked to the lattice parameter a_L in Eq. (44). Following Eq. (47) and the fact that the terms $C_{62}^{eff}[\varepsilon_2] + C_{64}^{eff}[\varepsilon_4] + C_{66}^{eff}[\varepsilon_6]$ are not length scale dependent, the stress drop magnitude ratio $\frac{|\Delta\Sigma_6|_{L=12.2nm}}{|\Delta\Sigma_6|_{L=20nm}} = \frac{20}{12.2} \sim 1.64$ is in good agreement with the one obtained by atomistic simulations for Σ41(540), Σ5(210) and Σ17(410) which are respectively 1.67, 1.71 and 1.68 from Tables 3 and 4.

5 Conclusions

A new micromechanics-based model was investigated to describe shear-coupled GB migration in bicrystals. Both MD simulations (at 0 and 500 K) and a micromechanical model assuming Frank-Bilby GB dislocations were applied to three Cu [001]

STGB: $\Sigma 41(540)$ ($\theta = 77.32°$), $\Sigma 5(210)$ ($\theta = 53.13°$), $\Sigma 17(410)$ ($\theta = 28.07°$). The critical shear stresses for shear-coupled GB migration can be obtained by MD simulations. The role of Cu elastic anisotropy on the stick-slip features of shear-coupled migration has been observed on the shear stress-strain curves. These ones have been analyzed in the light of the micromechanical model. In this paper, both formulations including heterogeneous and homogeneous elasticity have been developed. It has been shown that the elastic shear moduli obtained by MD simulations are captured by the micromechanics-based model when heterogeneous elasticity is accounted for. Furthermore, the trends regarding shear stress drops during first shear-coupling GB migration event at 0 K and 500 K are well described by the micromechanical approach especially when anisotropic elasticity is considered in the formulation. The model may also be extended to various strain rates and temperatures assuming the shear-coupling modes can be easily identified by atomistic simulations. Interestingly, for very low velocities up to 5 m/s, the shear stress drop is not very sensitive to shear rates [11]. Advanced atomistic methods dedicated to the kinetics of shear-coupled migration should be developed to improve the constitutive kinetics law at finite temperatures for shear-coupled GB migration. It could also be interesting to compare/predict the experimental results although overall stress/strain curves are seldom reported. As some perspective, the present constitutive and computational framework developed for bi-crystals with shear-coupled GB migration will be applied to study stress-induced twin boundary migration and will be incorporated in polycrystalline continuum models.

Acknowledgments The authors are grateful to the French "Agence Nationale de la Recherche" under contract agreement ANR-07-BLAN-0186 for financial support.

References

1. Cahn, J.W., Mishin, Y., Suzuki, A.: Coupling grain boundary motion to shear deformation. Acta Mater. **54**, 4953–4975 (2006)
2. Cahn, J.W., Mishin, Y.: Duality of dislocation content of grain boundaries. Philos. Mag. **86**, 1–11 (2006)
3. Bobylev, S.V., Mozorov, N.F., Ovid'ko, I.A.: Cooperative grain boundary sliding and migration process in nanocrystalline solids. Phys. Rev. Lett. 105, 055, 504 (2010)
4. Cahn, J.W., Taylor, J.E.: A unified approach to motion of grain boundaries, relative tangential translation along grain boundaries and grain rotation. Acta Mater. **52**, 4887–4898 (2004)
5. Zhang, H., Du, D., Srolovitz, D.J.: Effects of boundary inclination and boundary type on shear-driven grain boundary migration. Philos. Mag. **88**, 243–256 (2008)
6. Frank, F.C.: In: Symposium on the plastic deformation of crystalline solids, pp. 150–154. Carnegie Institute of Technology, Pittsburgh (1950)
7. Bilby, B.A.: In: Bristol Conference Report on Defects in Crystalline Solids, pp. 124–133. The Physical Society of London (1955)
8. Bullough, R., Bilby, B.A.: Continuous distributions of dislocations: surface dislocations and the crystallography of martensitic transformations. Proc. Phys. Soc. B **69**, 1276–1286 (1956)

9. Tucker, G.J., Zimmerman, J.A., McDowell, D.L.: Continuum metrics for deformation and microrotation from atomistic simulations: application to grain boundaries. Int. J. Eng. Sci. **49**, 1424–1434 (2011)
10. Molodov, D.A., Gorkaya, T., Gottstein, G.: Low angle tilt boundary migration coupled to shear deformation. Acta Mater. **55**, 1843–1848 (2007)
11. Mishin, Y., Suzuki, A., Uberuaga, B.P., Voter, A.F.: Stick-slip mechanism of grain boundaries studied by accelerated molecular dynamics. Phys. Rev. B 75, 224, 101 (2007)
12. Ivanov, V.A., Mishin, Y.: Dynamics of grain boundary motion coupled to shear deformation: an analytical model and its verification by molecular dynamics. Phys. Rev. B 78, 064, 106 (2008)
13. Fischer, F.D., Schaden, T., Appel, F., Clemens, H.: Mechanical twins, their development and growth. Eur. J. Mech. A. Solids **22**, 709–726 (2003)
14. Rae, C.M.F., Smith, D.A.: On the mechanisms of grain boundary migration. Philos. Mag. A **41**, 477–492 (1980)
15. Hirth, J.P., Pond, R.C.: Steps, dislocations and disconnections as interface defects relating to structure and phase transformations. Acta Mater. **44**, 4749–4763 (1996)
16. Abeyaratne, R., Knowles, J.K.: On the driving traction acting on a surface of strain discontinuity in a continuum. J. Mech. Phys. Solids **38**, 345–360 (1990)
17. Cermelli, P., Gurtin, M.E.: The dynamics of solid-solid phase transitions-2. Incoherent interfaces. Arch. Rational. Mech. Anal. **127**, 41–99 (1994)
18. Fischer, F.D., Simha, N.K., Svoboda, J.: Kinetics of diffusional transformation in multicomponent elastic-plastic materials. J. Engng. Mater. Tech. **125**, 266–276 (1998)
19. Hadamard, J.: Lecons sur la propagation des ondes et les equations de l'hydrodynamique. College de France, Paris (1903)
20. Coleman, B.D., Gurtin, M.E.: Thermodynamics with internal state variables. J. Chem. Phys. **47**, 597–613 (1967)
21. Maugin, G.A.: Configurational forces: Thermomechanics. Mathematics and Numerics. CRC Press, Taylor and Francis, New York (2011)
22. Eshelby, J.D.: Energy relations and energy-momentum tensor in continuum mechanics. In: Kanninen, M., et al. (eds.) Inelastic Behaviour of Solids, pp. 77–115. McGraw-Hill, New York (1970)
23. Petryk, H.: Macroscopic rate-variables in solids undergoing phase transformation. J. Mech. Phys. Solids **46**, 873–894 (1998)
24. Berbenni, S., Paliwal, B., Cherkaoui, M.: A micromechanics-based model for shear-coupled grain boundary migration in bicrystals. Int. J. Plasticity (2013),http://dx.doi.org/10.1016/j.ijplas.2012.11.011
25. Nye, J.F.: Some geometrical relations in dislocated crystals. Acta Metall. **1**, 153–162 (1953)
26. Kröner, E.: Kontinuumstheorie der Versetzungen und Eigenspannungen. In: Collatz, L., Loesch, F. (eds.) Ergebnisse der Angewewandte Mathematik 5. Springer Verlag, Berlin (1958)
27. Willis, J.R.: Second-order effects of dislocations in anisotropic crystals. Int. J. Eng. Sci. **5**, 171–190 (1967)
28. Mura, T.: Micromechanics of defects in solids. Kluwer Academic Publishers, Dordrecht, The Netherlands (1987)
29. Rice, J.R.: Continuum mechanics and thermodynamics plasticity in relation to microscale deformation mechanisms. In: Argon, A.S. (ed.) Constitutive Equations in Plasticity, pp. 23–75. MIT Press, Cambridge (1975)
30. Gorkaya, T., Molodov, D.A., Gottstein, G.: Stress-driven migration of symmetrical [100] tilt grain boundaries in Al bicrystals. Acta Mater. **57**, 5396–5405 (2009)
31. Li, J.C.M.: High-angle tilt boundary-a dislocation core model. J. Appl. Phys. **32**, 525–541 (1961)
32. Mishin, Y., Mehl, M.J., Papaconstantopoulos, D.A., Voter, A.F., Kress, J.D.: Structural stability and lattice defects in copper: Ab initio, tight-binding, and embedded-atom calculations. Phys. Rev. B 63, 224, 106 (2001)

33. Faken, D., Jonsson, H.: Systematic analysis of local atomic structure combined with 3D computer graphics. Comput. Mater. Sci. **2**, 279–286 (1994)
34. Tsuzuki, H., Branicio, P.S., Rino, J.P.: Structural characterization of deformed crystals by analysis of common atomic neighborhood. Comp. Phys. Comm. **177**, 518–523 (2007)
35. Hill, R.: The elastic behaviour of a crystalline aggregate. Proc. Phys. Soc. Lond. **65**, 349–354 (1952)

Buckling of Nonlinearly Elastic Plates with Microstructure

Svyatoslav Derezin

Abstract In the framework of the general nonlinear plate theory we consider a buckling problem for an elastic plate with incompatible plane strains generated by continuous distributions of edge dislocations and wedge disclinations as well as other sources of residual stress (non-elastic growth or plasticity). In contrast to the Föppl-von Kármán model the plane strains are not supposed to be small. To explore buckling transition of such kind of structures, the problem is reduced to a system of nonlinear partial differential equations with respect to the transverse deflection of the plate and the embedded metrics coefficients, which naturally leads to the non-trivial plate shapes that are seen even in the absence of any external forces. In the case of very thin plate (membrane) that doesn't resist bending we present several exact solutions for the axially-symmetric domains.

1 Introduction

The problem of plate buckling due to the presence of single dislocations of different types dates back to the work of Eshelby and Stroh [1]. Their study was continued in [2], with a single wedge disclination (removed or inserted sector in the terminology of [2]) being considered.

Later on Seung and Nelson [3] published a milestone paper on defects in crystalline membranes, where they generalized the continuum theory of dislocations to include buckling transition and solved exactly the disclination problem in the inextensional limit (Fig. 1). In order to do so, they used the Föppl-von Kármán plate model [4, 5] as was originally proposed in [1]. The work of Seung and Nelson is becoming more and more important in the contemporary graphene era.

S. Derezin (✉)
Southern Federal University, Milchakova 8a, Rostov-on-Don, Russia 344090
e-mail: svd@hrz.tu-chemnitz.de

H. Altenbach et al. (eds.), *Generalized Continua as Models for Materials*,
Advanced Structured Materials 22, DOI: 10.1007/978-3-642-36394-8_4,

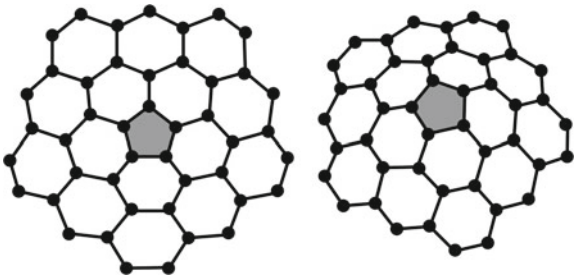

Fig. 1 Buckling of a *graphite membrane* with a single *positive* disclination

The question if it really makes sense to include torsional and couple-stress components in the equilibrium equations as in [6–9] is still open. In this chapter we deal only with the geometrical side of the problem, assuming that the equilibrium equations are satisfied identically, which means the complete relaxation of stresses (zero-stress in the classical setting or some special stress states in the framework of more advanced theory [6–9]).

A rigorous mathematical analysis of the Föppl-von Kármán plates containing incompatible strains was performed in [10]. An application of residual stresses in the Föppl-von Kármán plate to the problem of morphogenesis and biological growth was initiated in [11]. In [12] the Föppl-von Kármán model was applied to study fingerprint patterns as the result of a buckling instability in the basal cell layer of the fetal epidermis.

For modern applications of controllable buckling to thin-film electronics and residual stress measurement, see [13–16]. The strain-induced effects in the electronic structure of graphene are of great importance for the strain engineering. The buckling mechanism has been expected to be a new way to fabricate microscale devices or operate microstuctures.

The chapter is organized as follows. In Sect. 2 we present a planar nonlinear continuum theory of dislocations and disclinations following [17, 18]. In Sect. 3 we explain the buckling process in a nonlinear plate. In general, the problem can be reduced to a system of nonlinear partial differential equations with respect to the transverse deflection of the plate and the embedded metrics coefficients. In Sect. 4 we find explicitly the buckled form of nonlinear membrane with distributed edge dislocations using for this purpose the incompatibility conditions of the first order. In Sect. 5 we discuss in details the problem related to buckling of a membrane containing distributed wedge disclinations, which leads to the Monge-Ampère equation with a non-trivial right hand side. In Sect. 6 we draw some conclusions and give perspectives for the future work.

In the whole chapter we employ a version of tensor analysis used, for example, in [19, 20], where the first index always indicates differentiation, that allows to perform lengthy calculations.

2 Planar Nonlinear Continuum Theory of Dislocations and Disclinations

The mathematical theory of dislocations appeared for the first time in the work of Volterra [21]. He analyzed the behavior of linear elasticity solutions in multiply connected domains.

The continuum theory of translational dislocations was initiated mainly by the works of Kondo [22], Bilby et al. [23], and Kröner [24]. It is based on the notion of the elastic body as a differential-geometric manifold with definite properties. Modern expositions on continuum theory of dislocations in the framework of multiplicative elastoplasticity can be found in [25–27].

Later on [20, 28] there appeared the continuum theory of disclinations (rotational dislocations). Continuous distribution of disclinations in 3D is hampered by the fact of non-commutativity of finite rotations. In [29] continuum theory of disclinations was applied to model phase transformations.

Let ω be a 2D domain, $\mathbf{r}$ and $\mathbf{R}$ be the planar position vectors in the reference and actual configurations respectively, $\mathbf{F} = \nabla\mathbf{R} = \mathbf{r}^{\alpha}\mathbf{R}_{\alpha}$ be the planar deformation gradient (distortion tensor). $\nabla = \mathbf{r}^{\alpha}(\partial/\partial \mathrm{q}^{\alpha})$ is the two-dimensional gradient operator with respect to some curvilinear coordinates $\mathrm{q}^1, \mathrm{q}^2$ in the reference configuration. Here and below the Greek indices take the values $1, 2$. Consider the problem of determining the position $\mathbf{R}(\mathbf{r})$ by a given smooth and single valued field of $\mathbf{F}$. In a simply connected domain the solution may be written in terms of line integrals

$$\mathbf{R}(\mathcal{M}) = \int_{\mathcal{M}_0}^{\mathcal{M}} \mathrm{d}\mathbf{r} \cdot \mathbf{F} + \mathbf{R}(\mathcal{M}_0). \tag{1}$$

The integral in (1) does not depend on the path of integration connecting an initial point $\mathcal{M}_0$ with a final point $\mathcal{M}$ iff the following compatibility condition (of the first order) is fulfilled

$$\nabla \cdot (\mathbf{e} \cdot \mathbf{F}) = 0. \tag{2}$$

Here, $\mathbf{e} = e_{\alpha\beta}\mathbf{r}^{\alpha}\mathbf{r}^{\beta}$ is the 2D permutation tensor.

In the case of multiply connected domain (Fig. 2) the position vector in (1) is determined, in general, not uniquely, which means that dislocations of translational type can exist in the body, each of these is characterized by the Burgers vector

$$\mathbf{b}_{\mathrm{N}} = \oint_{\gamma_{\mathrm{N}}} \mathrm{d}\mathbf{r} \cdot \mathbf{F} \quad (\mathrm{N} = 1, 2, \ldots, \mathrm{N}_0). \tag{3}$$

Here, γ_{N} is a simple closed contour (the Burgers circuit) around the axis of the Nth dislocation. The total Burgers vector of a discrete set of N_0 dislocations is given by

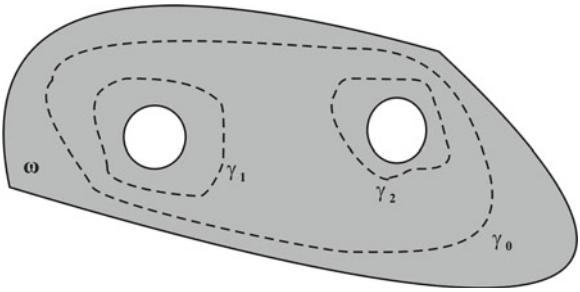

Fig. 2 Integration in a multiply connected *domain*

$$\mathbf{B} = \oint_{\gamma_0} \mathrm{d}\mathbf{r} \cdot \mathbf{F}, \tag{4}$$

where γ_0 is a contour enclosing the lines of all N_0 dislocations.

In the case of plane deformation, only edge dislocations are possible and their axes are orthogonal to the plane $q^1 q^2$.

The discrete set of dislocations can be replaced by a continuous one if we again consider the domain ω as simply connected and allow the space inside the dislocation hole shrink to zero along with multiplication the number of dislocations. Then, the integral in (4) may be transformed using the Green formula

$$\mathbf{B} = \iint_{\omega_0} \nabla \cdot (\mathbf{e} \cdot \mathbf{F})\, \mathrm{d}s. \tag{5}$$

Here, ω_0 is a planar domain bounded by the contour γ_0.

Relationship (5) makes it possible to introduce the density of continuously distributed edge dislocations $\boldsymbol{\alpha}$ (a vectorial quantity in 2D).

$$\mathbf{B} = \iint_{\omega_0} \boldsymbol{\alpha}\, \mathrm{d}s. \tag{6}$$

It means that the compatibility condition (2) is now replaced by

$$\nabla \cdot (\mathbf{e} \cdot \mathbf{F}) = \boldsymbol{\alpha}. \tag{7}$$

Equation (7) may be treated as the incompatibility condition of the first order. In Cartesian coordinates $q^1 = x_1$, $q^2 = x_2$ it has, for example, the following form

$$\frac{\partial F_{21}}{\partial x_1} - \frac{\partial F_{11}}{\partial x_2} = \alpha_1, \quad \frac{\partial F_{22}}{\partial x_1} - \frac{\partial F_{12}}{\partial x_2} = \alpha_2. \tag{8}$$

Let us now introduce the metric tensor of the deformed configuration $\mathbf{G}$ and the connection coefficients $\Gamma^{\nu}_{\alpha\beta}$ making use of the formulae

$$\mathbf{G} = \mathbf{F} \cdot \mathbf{F}^{\mathrm{T}} = G_{\alpha\beta}\mathbf{r}^{\alpha}\mathbf{r}^{\beta} = G^{\alpha\beta}\mathbf{r}_{\alpha}\mathbf{r}_{\beta}, \tag{9}$$

$$\frac{\partial \mathbf{R}_{\beta}}{\partial q^{\alpha}} = \Gamma^{\nu}_{\alpha\beta}\mathbf{R}_{\nu}, \quad \frac{\partial \mathbf{R}^{\beta}}{\partial q^{\alpha}} = -\Gamma^{\beta}_{\alpha\nu}\mathbf{R}^{\nu}. \tag{10}$$

From (9), (10) it follows that Ricci's lemma holds

$$\nabla_{\mu} G_{\alpha\beta} = \frac{\partial G_{\alpha\beta}}{\partial q^{\mu}} - \Gamma^{\nu}_{\mu\alpha} G_{\nu\beta} - \Gamma^{\nu}_{\mu\beta} G_{\alpha\nu} = 0. \tag{11}$$

Here, ∇_{μ} is the covariant derivative with respect to $\Gamma^{\nu}_{\alpha\beta}$.

The formulae (9)–(11) give us possibility to interprete the deformed configuration of an elastic body with dislocations as a metrically connected space $\mathcal{V}_2$ [30].

Incompatibilty equation (7) now reads as

$$S^{\cdot\cdot\nu}_{\alpha\beta} = \frac{1}{2} e_{\alpha\beta\alpha^{\nu}}, \tag{12}$$

where $S^{\cdot\cdot\nu}_{\alpha\beta}$ is the torsion tensor of É. Cartan [31]

$$S^{\cdot\cdot\nu}_{\alpha\beta} = \Gamma^{\nu}_{[\alpha\beta]} = \frac{1}{2}(\Gamma^{\nu}_{\alpha\beta} - \Gamma^{\nu}_{\beta\alpha}). \tag{13}$$

Let us consider the problem of specification the distortion $\mathbf{F}$ with the metric tensor $\mathbf{G}$ and the dislocation density vector $\boldsymbol{\alpha}$ being given. We use for this purpose the polar decomposition of $\mathbf{F}$

$$\mathbf{F} = \mathbf{U} \cdot \mathbf{A}, \quad \mathbf{U} = \mathbf{G}^{1/2}, \tag{14}$$

where $\mathbf{U}$ is the left stretch tensor (symmetric, positive-definite), $\mathbf{A}$ is the rotation tensor (properly orthogonal).

Under conditions of plane deformation $\mathbf{A}$ has the following representation

$$\mathbf{A} = (\mathbf{E} - \mathbf{i}_3\mathbf{i}_3)\cos\chi + \mathbf{e}\sin\chi + \mathbf{i}_3\mathbf{i}_3, \tag{15}$$

where $\mathbf{E}$ denotes the 3D identity tensor. Equation (15) means that the fibers rotate around the axis of $\mathbf{i}_3$, orthogonal to the plane q^1q^2, and χ is the angle of rotation. According to [17, 18] χ satisfies the following equation

$$\nabla\chi = \boldsymbol{\psi}, \quad \boldsymbol{\psi} = \mathrm{I}_2^{-1/2}\left[\mathbf{U}\cdot(\nabla\cdot\mathbf{e}\cdot\mathbf{U}) - \boldsymbol{\alpha}_0\cdot\mathbf{G}\right], \tag{16}$$

$$\mathrm{I}_2 = \det\mathbf{U} = \frac{1}{2}(\mathrm{tr}^2\mathbf{G} - \mathrm{tr}\mathbf{G}^2), \quad \boldsymbol{\alpha}_0 = \alpha^{\mu}\mathbf{r}_{\mu}.$$

Once again, the solution to (16) may be given in terms of line integrals

$$\chi(\mathcal{M}) = \int\limits_{\mathcal{M}_0}^{\mathcal{M}} \boldsymbol{\psi}\cdot\mathrm{d}\mathbf{r} + \chi(\mathcal{M}_0). \tag{17}$$

The integral in (17) does not depend on the path (in a simply connected domain) iff

$$\nabla\cdot\left[\mathrm{I}_2^{-1/2}\mathbf{e}\cdot\mathbf{U}\cdot(\nabla\cdot\mathbf{e}\cdot\mathbf{U})\right] - \nabla\cdot\left(\mathrm{I}_2^{-1/2}\mathbf{e}\cdot\mathbf{G}\cdot\boldsymbol{\alpha}_0\right) = 0. \tag{18}$$

Geometrically (18) is equivalent to the demand that the Gaussian curvature R of the Riemann-Cartan manifold $\mathcal{V}_2$ should vanish.

In a multiply connected domain (17) provides a single valued solution χ only up to a cyclic integral defined by

$$\theta_{\mathcal{M}} = \oint\limits_{\gamma_{\mathcal{M}}} \boldsymbol{\psi}\cdot\mathrm{d}\mathbf{r}. \tag{19}$$

The quantity $\theta_{\mathcal{M}}$ is called the Frank vector of $\mathcal{M}$th disclination. In the case of plane deformation only wedge disclinations are possible.

The total Frank vector of a set of $\mathcal{M}_0$ disclinations

$$\Theta = \sum_{\mathcal{M}=1}^{\mathcal{M}_0} \oint\limits_{\gamma_{\mathcal{M}}} \boldsymbol{\psi}\cdot\mathrm{d}\mathbf{r} = \oint\limits_{\gamma_0} \boldsymbol{\psi}\cdot\mathrm{d}\mathbf{r} \tag{20}$$

can be transformed into a surface integral in the case of continuous distribution of these

$$\Theta = \iint\limits_{\omega_0} \nabla\cdot(\mathbf{e}\cdot\boldsymbol{\psi})\,\mathrm{d}\sigma. \tag{21}$$

Formula (21) serves as a definition for the density of wedge disclinations β

$$\Theta = \iint\limits_{\omega_0} \beta\,\mathrm{d}\sigma. \tag{22}$$

The disclination density (a scalar quantity in 2D) satisfies the incompatibility condition of the second order

$$\nabla \cdot (\mathbf{e} \cdot \boldsymbol{\psi}) = \beta \tag{23}$$

or

$$\nabla \cdot \left[\mathrm{I}_2^{-1/2} \mathbf{e} \cdot \mathbf{U} \cdot (\nabla \cdot \mathbf{e} \cdot \mathbf{U}) \right] - \nabla \cdot \left(\mathrm{I}_2^{-1/2} \mathbf{e} \cdot \mathbf{G} \cdot \boldsymbol{\alpha}_0 \right) = \beta. \tag{24}$$

Geometrically (24) means that in the presence of distributed dislinations the Gaussian curvature R is proportional to the density of wedge disclinations

$$\mathrm{R} = \mathrm{I}_2^{-1/2} \beta. \tag{25}$$

In the linear elasticity this fact is known [20, 32] in the form

$$\mathbf{i}_3 \cdot \mathrm{Ink}\, \boldsymbol{\varepsilon} \cdot \mathbf{i}_3 = \nabla \cdot \mathbf{e} \cdot \boldsymbol{\alpha} + \beta \tag{26}$$

or in Cartesian coordinates

$$\frac{\partial^2 \varepsilon_{11}}{\partial x_2^2} + \frac{\partial^2 \varepsilon_{22}}{\partial x_1^2} - 2 \frac{\partial^2 \varepsilon_{12}}{\partial x_1 \partial x_2} = \frac{\partial \alpha_2}{\partial x_1} - \frac{\partial \alpha_1}{\partial x_2} + \beta. \tag{27}$$

Here, $\varepsilon_{\alpha\beta}$ are the components of the linear strain tensor $\boldsymbol{\varepsilon}$, $\mathrm{Ink}\, \boldsymbol{\varepsilon} = \nabla \times (\nabla \times \boldsymbol{\varepsilon})^{\mathrm{T}}$ is the incompatibility tensor.

3 Escape in the Third Dimension

The stresses due to distributed defects in the case of plane deformation of nonlinearly elastic material were found in [18]. The particular advantage of slender bodies makes it possible to consider relaxation of stresses by the escape in the third dimension (Fig. 3).

Here w is used to denote the transverse deflection of the plate. Then

$$\mathbf{R}^* = \mathbf{R} + w\mathbf{i}_3, \tag{28}$$

and

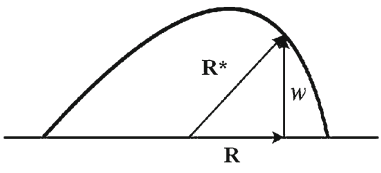

Fig. 3 Buckling of the *plate* due to the relaxation process

$$\mathbf{G}^* = \nabla\mathbf{R}^* \cdot \nabla\mathbf{R}^{*\mathsf{T}} = \nabla\mathbf{R} \cdot \nabla\mathbf{R}^{\mathsf{T}} + \nabla w \nabla w = \mathbf{G} + \nabla w \nabla w. \tag{29}$$

From (29) we have

$$\mathbf{G} = \mathbf{G}^* - \nabla w \nabla w. \tag{30}$$

Substituting now (30) into (24) written in terms of the embedded metric coefficients $G^*_{\alpha\beta}$ and the transverse deflection w we get a general form of geometrical equation that determine the bent form of the plate. It is quite lengthy and will not be presented here. In Sect. 5 a particular case of nonlinear membrane with distributed wedge disclinations will be studied in details.

4 Buckling of a Flat Membrane with Distributed Dislocations

The interesting fact about dislocations is that it is possible to solve problems directly appealing to the first order incompatibility condition (7). Mathematically it means that, when the disclination density vanishes, the incompatibility condition of the first order (7) may be considered in a way as a first integral for the incompatibility condition of the second order (24).

Let us introduce the polar coordinates r, φ and the corresponding vector basis $\mathbf{e}_r$, $\mathbf{e}_\varphi$ in the plane of a circular membrane of radius r_0 and assume that the edge dislocations are distributed with the density $\boldsymbol{\alpha}_0 = \alpha_\varphi(r)\mathbf{e}_\varphi$, which contains only the azimuthal component. The distortion tensor will be sought in the form that corresponds to the axisymmetric bending of the membrane [33]

$$\mathbf{F} = F_1(r)\mathbf{e}_r\mathbf{e}_r + F_2(r)\mathbf{e}_\varphi\mathbf{e}_\varphi + F_3(r)\mathbf{e}_r\mathbf{i}_3. \tag{31}$$

The incompatibility condition of the first order (7) reads then as

$$\frac{dF_2}{dr} + \frac{F_2 - F_1}{r} = \alpha_\varphi(r). \tag{32}$$

This equation has the following solution (under the condition $\mathbf{F} \cdot \mathbf{F}^{\mathsf{T}} = \mathbf{E}$)

$$F_1 = \cos\eta(r), \quad F_2 = 1, \quad F_3 = -\sin\eta(r), \tag{33}$$

where $\eta(r)$ satisfies

$$\cos\eta(r) = 1 - r\alpha_\varphi(r). \tag{34}$$

Solution (33) describes the membrane buckling which results in the release of residual stresses caused by dislocations. Although there is no displacement field with the distributed dislocations in the general case, in this special case, when $\boldsymbol{\alpha} \cdot \mathbf{i}_3 = 0$,

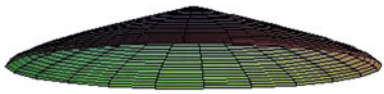

Fig. 4 Buckling of a *membrane* with distributed disclocations

it is possible to find the normal membrane deflection $w = \mathbf{R}^* \cdot \mathbf{i}_3$ from the relation $\mathbf{F}^* \cdot \mathbf{i}_3 = \nabla \mathbf{R}^* \cdot \mathbf{i}_3$. Using (33) and taking that $w(r_0) = 0$, we get

$$w(r) = \int_r^{r_0} \sqrt{2\rho\alpha_\varphi(\rho) - \rho^2\alpha_\varphi^2(\rho)}\,d\rho. \tag{35}$$

If $\alpha_\varphi(r) = \alpha$ is a constant function, then (35) gives the following exact solution

$$w(r) = \frac{1}{2\alpha}\Big[(1-\alpha r)\sqrt{2\alpha r - \alpha^2 r^2} - \arcsin(\alpha r - 1)\Big] + C, \tag{36}$$

where C corresponds to the boundary condition $w(r_0) = 0$. The buckled form of the membrane is presented in Fig. 4.

5 Buckling of a Flat Membrane with Distributed Disclinations

Substituting (30) into (24) and assuming $\boldsymbol{\alpha}_0 = 0$ we obtain the following equation in the membrane limit (when $\mathbf{G}$ equals the 2D identity tensor)

$$[w, w] = \Big[1 - (\nabla w)^2\Big]^{\frac{3}{2}}\beta, \tag{37}$$

$$[w, w] = (\Delta w)^2 - \mathrm{tr}(\nabla\nabla w \cdot \nabla\nabla w). \tag{38}$$

Here, $[w, w]$ is the Monge-Ampère operator. In Cartesian coordinates x_1, x_2 it has a usual representation

$$[w, w] = \frac{\partial^2 w}{\partial x_1^2}\frac{\partial^2 w}{\partial x_2^2} - \Big(\frac{\partial^2 w}{\partial x_1 \partial x_2}\Big)^2.$$

In the case of the Föppl-von Kármán theory [3, 34] we have in the membrane limit[1]

$$[w, w] = \beta. \tag{39}$$

[1] Seung and Nelson [3] deduced this equation in the *inextensional* limit.

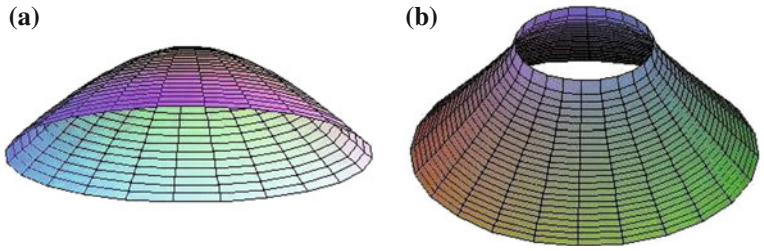

Fig. 5 **a** *Positive* disclinations; **b** *Negative* disclinations

This type of equation according to the general theory [35] gives no direct way of taking into account negative β.

Let the domain occupied by the plate, the distribution of wedge disclinations β and the transverse deflection w be axially-symmetric. Then Eq. (37) admits exact integration. We assume in addition the usual zero-slope condition in the center of the membrane: $w'(r)|_{r=0} = 0$.

Under such conditions for a constant positive β we obtain

$$w(r) = \frac{1}{\beta}\sqrt{\beta^2 r^2 + 4\beta} - \frac{1}{\sqrt{2\beta}} \log \left| \frac{\sqrt{2\beta} + \sqrt{\beta^2 r^2 + 4\beta}}{\sqrt{2\beta} - \sqrt{\beta^2 r^2 + 4\beta}} \right| - C, \tag{40}$$

whereas for a constant negative β

$$w(r) = \frac{1}{\beta}\sqrt{\beta^2 r^2 + 4\beta} + \frac{1}{\sqrt{-2\beta}} \arctan \frac{\sqrt{\beta^2 r^2 + 4\beta}}{\sqrt{-2\beta}} - C, \tag{41}$$

the constant C in both cases is furnished by vanishing $w(r)$ on the outer radius $r = r_0$ of the plate.

For negative β the solution exists only in some part of the circular disk, where $r \geqslant \sqrt{-4/\beta}$ (Fig. 5). The reason lies deeply in the topology of surfaces with negative Gaussian curvature. Being fixed on the outer radius the circular membrane can't be anymore a simply connected surface with everywhere negative Gaussian curvature (like a saddle point surface).

6 Conclusions

In the present chapter we gave some theoretical background and presented a few exact solutions for the buckling problem of a thin nonlinear plate containing continuously distributed fields of edge dislocations and wedge disclinations. As a particular application we have chosen the membrane model, because it allows to explore the geometrical side of the problem. The difficult challenge that still remains is to find

how non-axially-symmetric buckled regimes appear. The first attempt was done in [36] for the case of a single negative disclination. In the case of the Föppl-von Kármán plate model a rigorous stability analysis of the influence of distributed disclinations was performed numerically in [37].

It is interesting also to take into account couple-stress and strain gradient effects. For this purpose one can use, for example, a nonlinear model from [38], where a simple version of strain gradient elasticity, proposed in [39], was combined with the Föppl-von Kármán approach.

Acknowledgments The author thanks Prof. L.M. Zubov for fruitful discussions.

This work was supported by the Russian Foundation for Basic Research (via the grants 12-01-00038 and 12-01-91270) and the Federal target programme "Research and Pedagogical Cadre for Innovative Russia" for 2009–2013 years (state contract N P596).

References

1. Eshelby, J.D., Stroh, A.N.: Dislocations in thin plates. Phil. Mag. (Ser. 7) **42**, 1401–1405 (1951)
2. Mitchell, L.H., Head, A.K.: The buckling of a dislocated plate. J. Mech. Phys. Solids **9**, 131–139 (1961)
3. Seung, H.S., Nelson, D.R.: Defects in flexible membranes with crystalline order. Phys. Rev. A **38**(2), 1005–1018 (1988)
4. Föppl, A.: Vorlesungen über technische Mechanik. Bd. 5. Teubner, Leipzig (1907)
5. von Kármán, T.: Festigkeitsprobleme im Maschinenbau / Encyclopädie der Mathematischen Wissenschaften, vol. 4/4C. Teubner, Leipzig (1910)
6. Stojanovitch, R., Vujoshevitch, L.: Couple stress in non Euclidean continua. Publ. Inst. Math. (Beograd) (N.S.) **2**(16), 71–74 (1962)
7. Stojanovitch, R.: Equilibrium conditions for internal stresses in non-Euclidean continua and stress spaces. Int. J. Eng. Sci. **1**(3), 323–327 (1963)
8. Ben-Abraham, S.I.: Generalized stress and non-Riemannian geometry. In: Simmons, J.A., de Wit, R., Bullough, R. (eds.) Fundamental Aspects of Dislocation Theory, vol. 2, pp. 943–962. National Bureau of Standards Special Publication 317, Washington (1970)
9. Clayton, J.D.: On anholonomic deformation, geometry, and differentiation. Math. Mech. Solids **17**(7), 702–735 (2012)
10. Lewicka, M., Mahadevan, L., Pakzad, M.R.: The Föppl-von Kármán equations for plates with incompatible strains. Proc. R. Soc. A **467**, 402–426 (2011)
11. Dervaux, J., Ciarletta, P., Ben Amar, M.: Morphogenesis of thin hyperelastic plates: a constitutive theory of biological growth in the Föppl-von Karman limit. J. Mech. Phys. Solids **57**, 458–471 (2009)
12. Kücken, M., Newell, A.C.: A model for fingerprint formation. Europhys. Lett. **68**(1), 141–146 (2004)
13. Chen, S., Chrzan, D.C.: Continuum theory of dislocations and buckling in graphene. Phys. Rev. B **84**, 214103 (2011)
14. Kochetov, E.A., Osipov, V.A., Pincak, R.: Electronic properties of disclinated flexible membrane beyond the inextentional limit: application to graphene. J. Phys.: Condens. Matter **22**, 395502 (2010)
15. Li, K., Yan, S.P., Ni, Y., Liang, H.Y., He, L.H.: Controllable buckling of an elastic disc with actuation strain. Europhys. Lett. (EPL) **92**, 16003 (2010)
16. Qiao, D.-Y., Yuan, W.-Z., Yu, Y.-T., Liang, Q., Ma, Z.-B., Li, X.-Y.: The residual stress-induced buckling of annular thin plates and its application in residual stress measurement of thin films. Sens. Actuators A **143**, 409–414 (2008)

17. Derezin, S.V., Zubov, L.M.: Equations of a nonlinear elastic medium with continuously distributed dislocations and disclinations. Dokl. Phys. **44**(6), 391–394 (1999)
18. Derezin, S.V., Zubov, L.M.: Disclinations in nonlinear elasticity. Z. Angew. Math. Mech. **91**(6), 433–442 (2011)
19. Lurie, A.I.: Nonlinear Theory of Elasticity. North-Holland, Amsterdam (1990)
20. de Wit, R.: Linear theory of static disclinations. In: Simmons, J.A., de Wit, R., Bullough, R. (eds.) Fundamental Aspects of Dislocation Theory, vol. 1, pp. 651–673. National Bureau of Standards Special Publication 317, Washington (1970)
21. Volterra, V.: Sur l'équilibre des corps élastiques multiplement connexes. Ann. Ecole Norm. Super. (Ser. 3) **24**, 401–517 (1907)
22. Kondo, K.: Geometry of Elastic Deformation and Incompatibility: RAAG Memories, vol. 1, Division C. Gakujutsu Bunken Fukyu-kai, Tokyo (1955)
23. Bilby, B.A., Bullough, R., Smith, E.: Continuous distributions of dislocations: a new application of the methods of non-Riemannian geometry. Proc. R. Soc. London A **231**, 263–273 (1955)
24. Kröner, E.: Allgemeine Kontinuumstheorie der Versetzungen und Eigenspannungen. Arch. Rat. Mech. Anal. **4**, 273–334 (1960)
25. Le, K., Stumpf, H.: Nonlinear contimuum theory of dislocations. Int. J. Eng. Sci. **34**(3), 339–358 (1996)
26. Steinmann, P.: Views on multiplicative elastoplasticity and the continuum theory of dislocations. Int. J. Eng. Sci. **34**(15), 1717–1735 (1996)
27. Forest, S., Cailletaud, G., Sievert, S.: A Cosserat theory for elastoviscoplastic single crystals at finite deformation. Arch. Mech. **49**(4), 705–736 (1997)
28. Anthony, K.-H.: Die Theorie der Disklinationen. Arch. Rat. Mech. Anal. **39**, 43–88 (1970)
29. Acharya, A., Fressengeas, C.: Coupled phase transformations and plasticity as a field theory of deformation incompatibility. Int. J. Fract. **174**, 87–94 (2012)
30. Norden, A.P.: Affinely Connected Spaces. Nauka, Moscow (1976). (in Russian)
31. Cartan, E.: Sur les variétés à connexion affine et la théorie de la relativité généralisée. Ann. Sci. École Norm. Super. (Ser. 3) **40**, 325–412 (1923)
32. Mura, T.: Micromechanics of Defects in Solids. Kluwer Academic Publishers, Boston (1987)
33. Zubov, L.M.: Large deformation of elastic shells with distributed dislocations. Dokl. Phys. **57**(6), 254–257 (2012)
34. Zubov, L.M.: Von Kármán equations for an elastic plate with dislocations and disclinations. Dokl. Phys. **52**(1), 67–70 (2007)
35. Pogorelov, A.V.: Multidimensional Monge-Ampére Equation. Cambridge Scientific Publishers, Cambridge (2008)
36. Karyakin, M.I.: Equilibrium and stability of a nonlinear-elastic plate with a tapered disclination. Appl. Mech. Tech. Phys. **33**(3), 464–470 (1992)
37. Zubov, L.M., Pham, T.H.: Strong deflections of circular plate with continuously distributed disclinations (in Russian). Izv. VUZov, Sev.-Kav. Reg. Issue **4**, 28–33 (2010)
38. Lazopoulos, K.A.: On the gradient strain elasticity theory of plates. Euro. J. Mech. A. Solids **23**, 843–852 (2004)
39. Altan, B.S., Aifantis, E.C.: On the structure of the mode III crack-tip in gradient elasticity. Scr. Metall. **26**, 319–324 (1992)

Material Symmetry Group and Consistently Reduced Constitutive Equations of the Elastic Cosserat Continuum

Victor A. Eremeyev and Wojciech Pietraszkiewicz

Abstract We discuss the material symmetry group of the polar-elastic continuum and related consistently simplified constitutive equations. Following [1] we extent the definition of the group proposed by Eringen and Kafadar [2] by taking into account the microstructure curvature tensor as well as different transformation properties of polar and axial tensors. Our material symmetry group consists of ordered triples of tensors which make the strain energy density of the polar-elastic continuum invariant under change of the reference placement. Within the polar-elastic solids we discuss the isotropic, hemitropic, orthotropic, transversely isotropic and cubic-symmetric materials and give explicitly the consistently reduced representations of the strain energy density.

1 Introduction

Mechanics of Micropolar Continua (also called Cosserat Continua or Polar Continua) was first summarized in 1909 by the Cosserat brothers in their centurial book [3] but without consideration of the constitutive equations. In the books by Eringen [4, 5],

V. A. Eremeyev (✉)
Faculty of Mechanical Engineering, Otto-von-Guericke-University,
39106 Magdeburg, Germany
e-mail: eremeyev.victor@gmail.com; victor.eremeyev@ovgu.de

V. A. Eremeyev
South Scientific Center of RASci and South Federal University, Milchakova St. 8a,
Rostov on Don 344090, Russia

W. Pietraszkiewicz
Institute of Fluid-Flow Machinery, PASci, ul. Gen. J. Fiszera 14, 80-952 Gdańsk, Poland
e-mail: pietrasz@imp.gda.pl

H. Altenbach et al. (eds.), *Generalized Continua as Models for Materials*,
Advanced Structured Materials 22, DOI: 10.1007/978-3-642-36394-8_5,

Nowacki [6] and Eremeyev et al. [7] various constitutive equations of the micropolar elastic continuum were considered and widely discussed. The Cosserat continuum model is frequently used for description of complex media such as composites, foams, cellular solids, lattices, masonries, particle assemblies, magnetic rheological fluids, liquid crystals, etc. For characterizations of material behaviour of micropolar continua a great role plays the material symmetry group. The group for the non-linear micropolar continuum was first characterized by Eringen and Kafadar [2]. They discussed all density-preserving deformations and all microrotations of the reference placement of the micropolar continuum that cannot be experimentally detected. In terms of members of the group definitions of the simple micropolar solid and the simple micropolar fluid were given.

In [1] we extended the definition of the material symmetry group proposed by Eringen and Kafadar [2]. We considered the polar-elastic material characterized by the strain energy density W and introduced the following modifications:

1. At each material point the strain energy density W, satisfying the principle of material frame-indifference, depends explicitly not only on the natural Lagrangian stretch $\mathbf{E}$ and wryness $\boldsymbol{\Gamma}$ tensors, but additionally upon the microstructure curvature tensor $\mathbf{B}$ of the undeformed placement as the parametric tensor. The necessity of using these three fields in W was shown in [8]. The tensor $\mathbf{B}$ appears naturally during change of the reference placement. The case $\mathbf{B} \neq \mathbf{0}$ corresponds to non-uniform distribution of directors in the reference placement. In [2] the similar strain measures were used in W, but the referential mass density $\rho_{\varkappa}$ and the microinertia tensor $\mathbf{J}_{\varkappa}$ were introduced as the parametric quantities in W.
2. Considering invariance properties of W we take into account that $\mathbf{E}$ is the polar tensor, but $\boldsymbol{\Gamma}$ and $\mathbf{B}$ are the axial tensors which change their signs under inversion transformation (mirror reflection) of 3D space. Eringen and Kafadar [2] did not take into account that their $\boldsymbol{\Gamma}$ was the axial tensor. As a result, difference between the orthogonal tensors and the proper orthogonal tensors considered as members of our material symmetry group leads to additional essential reduction of W.
3. Our material symmetry group $\mathcal{G}_{\varkappa}$ consists of the ordered triple of tensors: the unimodular $\mathbf{P}$, the orthogonal $\mathbf{R}$, and the second-order $\mathbf{L}$ one. These tensors appear from transformation of $\mathbf{E}$, $\boldsymbol{\Gamma}$ and $\mathbf{B}$ under an arbitrary change of the reference placements of the micropolar body. The transformation properties of $\mathbf{B}$ are quite different from those of $\mathbf{J}_{\varkappa}$.

As a result of these modifications, the material symmetry group $\mathcal{G}_{\varkappa}$ in [1] does not coincide with the group introduced in [2].

In this paper we consider the consistently reduced constitutive equations of the non-linear anisotropic elastic micropolar solids. In addition to [1] we present the lists of additional joint invariants of W describing the orthotropic and transversely isotropic micropolar solids.

2 Basic Relations of the Cosserat Continuum

Let the micropolar body $\mathcal{B}$ deform in the three-dimensional (3D) Euclidean physical space $\mathcal{E}$ which translation vector space is E. The finite deformation of the polar-elastic body $\mathcal{B}$ can be described by the mapping from the reference (undeformed) placement $\varkappa(\mathcal{B}) = \mathsf{B}_\varkappa \subset \mathcal{E}$ to the actual (deformed) placement, $\gamma(\mathcal{B}) = \mathsf{B}_\gamma = \chi(\mathsf{B}_\varkappa) \in \mathcal{E}$.

In $\varkappa(\mathcal{B})$ the position $\mathsf{x} \in \mathcal{E}$ of the material particle $\mathsf{X} \in \mathcal{B}$ is given by the vector $\mathbf{x} \in \mathsf{E}$ relative to the origin $\mathsf{o} \in \mathcal{E}$ of an inertial frame $(\mathsf{o}, \mathbf{i}_\mathfrak{a})$, where $\mathbf{i}_\mathfrak{a} \in \mathsf{E}$, $\mathfrak{a} = 1, 2, 3$, is a right-handed triple of orthonormal vectors. Orientation of $\mathsf{X} \in \mathcal{B}$ in E is fixed by the right-handed triple of orthonormal directors $\mathbf{h}_\mathfrak{a} \in \mathsf{E}$.

In $\gamma(\mathcal{B})$, $\chi = \gamma \circ \varkappa^{-1}$, the position $\mathsf{y} \in \mathsf{B}_\varkappa$ of the same material particle $\mathsf{X} \in \mathcal{B}$ becomes defined by the vector $\mathbf{y} \in \mathsf{E}$ taken here relative to the same origin $\mathsf{o} \in \mathcal{E}$. The orientation of X becomes fixed by the right-handed triple of orthonormal directors $\mathbf{d}_\mathfrak{a} \in \mathsf{E}$.

As a result, the finite deformation of the polar-elastic body is described by the following two smooth mappings:

$$\mathbf{y} = \chi(\mathbf{x}) = \mathbf{x} + \mathbf{u}(\mathbf{x}), \qquad \mathbf{d}_\mathfrak{a} = \mathbf{Q}(\mathbf{x})\mathbf{h}_\mathfrak{a}, \tag{1}$$

where $\mathbf{u} \in \mathsf{E}$ is the translation vector and $\mathbf{Q} = \mathbf{d}_\mathfrak{a} \otimes \mathbf{h}_\mathfrak{a} \in \mathrm{Orth}^+$ is the proper orthogonal microrotation tensor, $\mathbf{Q}^{-1} = \mathbf{Q}^\mathsf{T}$, $\det \mathbf{Q} = +1$. Two independent fields $\mathbf{u}(\mathbf{x})$ and $\mathbf{Q}(\mathbf{x})$ describe translational and rotational degrees of freedom of the polar-elastic continuum.

The natural Lagrangian relative stretch and wryness (or change of the microstructure orientation) tensors $\mathbf{E}$ and $\boldsymbol{\Gamma}$ are defined according to [8] as

$$\mathbf{E} = \mathbf{Q}^\mathsf{T}\mathbf{F} - \mathbf{I}, \qquad \boldsymbol{\Gamma} = -\frac{1}{2}\mathsf{E} : (\mathbf{Q}^\mathsf{T}\mathrm{Grad}\,\mathbf{Q}). \tag{2}$$

Here $\mathbf{F} = \mathrm{Grad}\,\mathbf{y}$, $\det \mathbf{F} > 0$, is the classical deformation gradient tensor taken relative to $\mathsf{B}_\varkappa$, $\mathbf{I}$ is the identity (metric) tensor of the space E, $\mathsf{E} = -\mathbf{I} \times \mathbf{I}$ is the 3rd-order skew permutation tensor with $\times$ the vector product, while the double dot product : of two 3rd-order tensors A, B represented in the base $\mathbf{h}_\mathfrak{a}$ is defined as $\mathsf{A} : \mathsf{B} = A_{\mathfrak{a}\mathfrak{m}\mathfrak{n}} B_{\mathfrak{m}\mathfrak{n}\mathfrak{b}}\, \mathbf{h}_\mathfrak{a} \otimes \mathbf{h}_\mathfrak{b}$.

The wryness tensor $\boldsymbol{\Gamma}$ can also be expressed in the equivalent forms, see [8],

$$\boldsymbol{\Gamma} = -\frac{1}{2}\mathbf{h}_\mathfrak{a} \times (\mathbf{h}_\mathfrak{a}\, \mathbf{Q}^\mathsf{T}\mathrm{Grad}\,\mathbf{Q}) = \mathbf{Q}^\mathsf{T}\mathbf{C}\mathbf{F} - \mathbf{B}, \tag{3}$$

where $\mathbf{B}$ and $\mathbf{C}$ are the respective microstructure curvature tensors of the polar continuum in the reference and actual placements defined by

$$\mathbf{B} = \frac{1}{2}\mathbf{h}_\mathfrak{a} \times \mathrm{Grad}\,\mathbf{h}_\mathfrak{a}, \qquad \mathbf{C} = \frac{1}{2}\mathbf{d}_\mathfrak{a} \times \mathrm{grad}\,\mathbf{d}_\mathfrak{a}, \tag{4}$$

with the operator grad being taken in the deformed placement B_γ.

In what follows $\mathbf{B}$ and $\mathbf{C}$ play an important role because they characterize the non-uniform distribution of directors $\mathbf{h}_\alpha$ and $\mathbf{d}_\alpha$ in the reference and actual placements, respectively. In particular, if $\mathbf{h}_\alpha$ are constant in space then $\mathbf{B} = \mathbf{0}$. Tensors $\mathbf{B}$ and $\mathbf{C}$ can be used instead of $\mathbf{h}_\alpha$ and $\mathbf{d}_\alpha$ as primary quantities. Indeed, $\mathbf{h}_\alpha$ and $\mathbf{d}_\alpha$ can be found from $\mathbf{B}$ and $\mathbf{C}$, respectively, if some compatibility conditions in terms of $\mathbf{B}$ and $\mathbf{C}$ are fulfilled. The compatibility condition for $\mathbf{B}$ follows from

$$\mathbf{b}_{k,s} = \mathbf{b}_{s,k} + \mathbf{b}_s \times \mathbf{b}_k, \tag{5}$$

where $\mathbf{b}_k = \mathbf{B}\mathbf{i}_k$, and indices after comma denote differentiation with respect to Cartesian coordinates in the reference placement x_1, x_2, x_3, for example $\mathbf{b}_{s,k} = \dfrac{\partial \mathbf{b}_s}{\partial x_k}$. The compatibility condition for $\mathbf{C}$ follows from the relation similar to (5) but the vectors $\mathbf{c}_k = \mathbf{C}\mathbf{i}_k$ are differentiated with respect to Cartesian coordinates in the actual placement y_s.

The material behaviour of the micropolar (hyper)elastic continuum is described by the strain energy density $W_\varkappa$ per unit volume of the undeformed placement $\mathrm{B}_\varkappa$. The density $W_\varkappa$ satisfying the principle of material frame-indifference takes the reduced form

$$W_\varkappa = \widehat{W}_\varkappa(\mathbf{E}, \boldsymbol{\Gamma}; \mathbf{x}, \mathbf{B}). \tag{6}$$

We call the polar-elastic continuum homogeneous if there exists a reference placement $\mathrm{B}_\varkappa$ such that $W_\varkappa$ does not depend on $\mathbf{x}$ and materially uniform if $W_\varkappa$ does not depend on $\mathbf{B}$ or $\mathbf{B} \equiv \mathbf{0}$.

Definition of the material symmetry group is based on invariance of $W_\varkappa$ under change of the reference placement. Let us introduce another reference placement $\varkappa_*(\mathcal{B}) = \mathrm{B}_* \in \mathcal{E}$ of $\mathcal{B}$, in which the position $x_* \in \mathrm{B}_*$ of $X \in \mathcal{B}$ is given by the vector $\mathbf{x}_*$ relative to the same origin $o \in \mathcal{E}$ and its orientation is fixed by three orthonormal directors $\mathbf{h}_{*\alpha}$. Let $\mathbf{P} = \operatorname{Grad} \mathbf{x}_*$, $\det \mathbf{P} \neq 0$, be the deformation gradient tensor transforming $\mathrm{d}\mathbf{x}$ into $\mathrm{d}\mathbf{x}_*$, and $\mathbf{R} \in \mathrm{Orth}$ be the orthogonal tensor transforming $\mathbf{h}_\alpha$ into $\mathbf{h}_{*\alpha}$, so that

$$\mathrm{d}\mathbf{x}_* = \mathbf{P}\mathrm{d}\mathbf{x}, \quad \mathbf{h}_{*\alpha} = \mathbf{R}\mathbf{h}_\alpha. \tag{7}$$

In what follows all fields associated with deformation relative to the reference placement B_* will be marked by the lower index $*$. We obtain the following transformation relations, see [1] for details:

$$\mathbf{F} = \mathbf{F}_*\mathbf{P}, \quad \mathbf{Q} = \mathbf{Q}_*\mathbf{R}, \tag{8}$$

$$\begin{aligned} \mathbf{E}_* = \mathbf{Q}_*^{\mathrm{T}}\mathbf{F}_* - \mathbf{I} &= \mathbf{R}\mathbf{E}\mathbf{P}^{-1} + \mathbf{R}\mathbf{P}^{-1} - \mathbf{I} \\ &= \mathbf{R}(\mathbf{E} + \mathbf{I})\mathbf{P}^{-1} - \mathbf{I}, \end{aligned} \tag{9}$$

$$\mathbf{B}_* = (\det \mathbf{R})\mathbf{R}\mathbf{B}\mathbf{P}^{-1} - \mathbf{L}, \qquad \boldsymbol{\Gamma}_* = (\det \mathbf{R})\mathbf{R}\boldsymbol{\Gamma}\mathbf{P}^{-1} + \mathbf{L}, \tag{10}$$

where

$$\mathbf{L} = \mathbf{RZP}^{-1}, \quad \mathbf{Z} = -\frac{1}{2}\mathsf{E} : (\mathbf{R}\,\mathrm{Grad}\,\mathbf{R}^{\mathsf{T}}). \tag{11}$$

Let us note that the form of elastic strain energy density $W_{\varkappa}$ of the micropolar body at any particle $X \in \mathcal{B}$ depends upon the choice of the reference placement, in general. Particularly important are sets of reference placements which leave unchanged the form of the energy density. Transformations of the reference placement under which the energy density remains unchanged we call here invariant transformations. Knowledge of all such invariant transformations allows one to precisely define the fluid, the solid, the liquid crystal or the subfluid as well as to introduce notions of isotropic or anisotropic hyper-elastic continua. Similar approach is used in classical continuum mechanics and in non-linear elasticity in [9, 10].

The elastic strain energy density W_* relative to the changed reference placement B_* depends in each point $\mathrm{x}_* \in \mathrm{B}_\star$ on the stretch tensor $\mathbf{E}_*$, the wryness tensor $\mathbf{\Gamma}_*$, and also upon the structure curvature tensor $\mathbf{B}_*$. This dependence may, in general, be different than that of $W_{\varkappa}(\mathbf{E}, \mathbf{\Gamma}; \mathbf{x}, \mathbf{B})$. However, the strain energy of any part of the polar-elastic continuum should be conserved, so that

$$\int_{\mathrm{P}_{\varkappa}} W_{\varkappa}\, \mathrm{d}v_{\varkappa} = \int_{\mathrm{P}_*} W_*\, \mathrm{d}v_* \tag{12}$$

for any part of the micropolar body $\mathrm{P}_{\varkappa} \subset \mathrm{B}_{\varkappa}$ corresponding to $\mathrm{P}_* \subset \mathrm{B}_*$, because the functions $W_{\varkappa}$ and W_* describe the strain energy density of the same deformed state of $\mathrm{P}_\gamma \subset \mathrm{B}_\gamma = \chi(\mathrm{P}_{\varkappa}) = \chi_*(\mathrm{P}_*)$, where χ_* is the deformation function from B_* to B_γ.

Changing variables $\mathbf{x}_* \to \mathbf{x}$ in the right-hand side integral of (12) we obtain

$$\int_{\mathrm{P}_*} W_*[\mathbf{E}_*(\mathbf{x}_*), \mathbf{\Gamma}_*(\mathbf{x}_*); \mathbf{x}_*, \mathbf{B}_*(\mathbf{x}_*)]\, \mathrm{d}v_* = \int_{\mathrm{P}_{\varkappa}} |\det \mathbf{P}|\, W_*[\mathbf{E}_*(\mathbf{x}), \mathbf{\Gamma}_*(\mathbf{x}); \mathbf{x}, \mathbf{B}_*(\mathbf{x})]\, \mathrm{d}v_{\varkappa}.$$

Thus, from (12) it follows that W_* and $W_{\varkappa}$ are related by

$$|\det \mathbf{P}|\, W_*(\mathbf{E}_*, \mathbf{\Gamma}_*; \mathbf{x}, \mathbf{B}_*) = W_{\varkappa}(\mathbf{E}, \mathbf{\Gamma}; \mathbf{x}, \mathbf{B}).$$

Here $\mathbf{E}_*$, $\mathbf{\Gamma}_*$, and $\mathbf{B}_*$ are expressed as in (9) and (10).

From physical reasons invariant transformations of the reference placement should preserve the elementary volume of $\mathrm{B}_{\varkappa}$. Hence, the tensor $\mathbf{P}$ should belong to the unimodular group for which $|\det \mathbf{P}| = 1$.

The assumption that the constitutive relation is insensitive to the change of the reference placement means that the explicit forms of the strain energy densities $W_{\varkappa}$ and W_* should coincide, that is

$$W_{\varkappa}(\mathbf{E},\boldsymbol{\Gamma};\mathbf{x},\mathbf{B}) = W_{\varkappa}(\mathbf{E}_*,\boldsymbol{\Gamma}_*;\mathbf{x},\mathbf{B}_*).$$

In other words, this means that one may use the same function for the strain energy density independently on the choice of $\mathrm{B}_{\varkappa}$ or B_*, but with different expressions for stretch and wryness tensors as well as for the microstructure curvature tensor. In what follows we not always explicitly indicate that all the functions depend also on the position vector $\mathbf{x}$ and W is taken relative to the undeformed placement $\mathrm{B}_{\varkappa}$.

Using (9) and (10) we obtain the following invariance requirement for W under change of the reference placement:

$$W(\mathbf{E},\boldsymbol{\Gamma};\mathbf{B}) = W[\mathbf{R}\mathbf{E}\mathbf{P}^{-1} + \mathbf{R}\mathbf{P}^{-1} - \mathbf{I},\ (\det\mathbf{R})\mathbf{R}\boldsymbol{\Gamma}\mathbf{P}^{-1} + \mathbf{L};\ (\det\mathbf{R})\mathbf{R}\mathbf{B}\mathbf{P}^{-1} - \mathbf{L}]. \tag{13}$$

The relation (13) holds locally, i.e. it should be satisfied at any x and $\mathbf{B}$, and the tensors $\mathbf{P}$, $\mathbf{R}$, $\mathbf{L}$ are treated as independent here. As a result, the local invariance of W under change of the reference placement is described by the triple of tensors $(\mathbf{P},\mathbf{R},\mathbf{L})$.

In what follows we use the following nomenclature:

$\mathtt{Orth} = \{\mathbf{O} : \mathbf{O}^{-1} = \mathbf{O}^{\mathsf{T}},\ \det\mathbf{O} = \pm 1\}$—the group of orthogonal tensors;

$\mathtt{Orth}^{+} = \{\mathbf{O} : \mathbf{O} \in \mathtt{Orth},\ \det\mathbf{O} = 1\}$—the group of rotation tensors;

$\mathtt{Unim} = \{\mathbf{P} : \mathbf{P} \in \mathsf{E}\otimes\mathsf{E},\ \det\mathbf{P} = \pm 1\}$—the unimodular group;

$\mathtt{Lin} = \{\mathbf{L} \in \mathsf{E}\otimes\mathsf{E}\}$—the linear group.

Here $\mathtt{Orth}$ and $\mathtt{Unim}$ are groups with regard to multiplication, and $\mathtt{Lin}$ is the group with regard to addition.

3 Definition of the Material Symmetry Group

Following [1] and using (13) we give the following definition:

Definition 5.1. *By the material symmetry group $\mathcal{G}_{\varkappa}$ at x and $\mathbf{B}$ of the polar-elastic continuum we call all sets of ordered triples of tensors*

$$\mathbb{X} = (\mathbf{P} \in \mathtt{Unim}, \mathbf{R} \in \mathtt{Orth}, \mathbf{L} \in \mathtt{Lin}), \tag{14}$$

satisfying the relation

$$W(\mathbf{E},\boldsymbol{\Gamma};\mathbf{B}) = W\Big[\mathbf{R}\mathbf{E}\mathbf{P}^{-1} + \mathbf{R}\mathbf{P}^{-1} - \mathbf{I},\ (\det\mathbf{R})\mathbf{R}\boldsymbol{\Gamma}\mathbf{P}^{-1} + \mathbf{L};\ (\det\mathbf{R})\mathbf{R}\mathbf{B}\mathbf{P}^{-1} - \mathbf{L}\Big] \tag{15}$$

for any tensors $\mathbf{E}$, $\boldsymbol{\Gamma}$, $\mathbf{B}$ in domain of definition of the function W.

The set $\mathcal{G}_{\varkappa}$ is the group relative to the group operation $\circ$ defined by

$$(\mathbf{P}_1,\mathbf{R}_1,\mathbf{L}_1)\circ(\mathbf{P}_2,\mathbf{R}_2,\mathbf{L}_2) = \Big[\mathbf{P}_1\mathbf{P}_2,\ \mathbf{R}_1\mathbf{R}_2,\ \mathbf{L}_1 + (\det\mathbf{R}_1)\mathbf{R}_1\mathbf{L}_2\mathbf{P}_1^{-1}\Big].$$

In terms of members of $\mathcal{G}_{\mathcal{K}}$ the polar-elastic fluids, solids, liquid crystals, and subfluids can be conveniently defined, see [1] for details.

In what follows we restrict ourselves to the polar-elastic solids which are defined as follows:

Definition 5.2. *The micropolar elastic continuum is called the polar-elastic solid at* x *and* $\mathbf{B}$ *if there exists a reference placement* $\mathrm{B}_{\mathcal{K}}$*, called undistorted, such that the material symmetry group relative to* $\mathrm{B}_{\mathcal{K}}$ *is given by*

$$\mathcal{G}_{\mathcal{K}} = \mathcal{R}_{\mathcal{K}} \equiv \{(\mathbf{P} = \mathbf{O}, \mathbf{O}, \mathbf{0}) : \quad \mathbf{O} \in \mathcal{O}_{\mathcal{K}} \subset \mathrm{Orth}\}. \tag{16}$$

The group $\mathcal{R}_{\mathcal{K}}$ is fully described by a subgroup $\mathcal{O}_{\mathcal{K}}$ of orthogonal group Orth. Invariance requirement of W leads here to finding the subgroup $\mathcal{O}_{\mathcal{K}}$ such that

$$W(\mathbf{E}, \boldsymbol{\Gamma}; \mathbf{B}) = W\left[\mathbf{O}\mathbf{E}\mathbf{O}^{\mathrm{T}}, (\det \mathbf{O})\mathbf{O}\boldsymbol{\Gamma}\mathbf{O}^{\mathrm{T}}; (\det \mathbf{O})\mathbf{O}\mathbf{B}\mathbf{O}^{\mathrm{T}}\right], \quad \forall \mathbf{O} \in \mathcal{O}_{\mathcal{K}}. \tag{17}$$

4 Consistently Simplified Forms of the Strain Energy Density

Let us discuss consistently simplified forms of W corresponding to some particular cases of anisotropic micropolar solids. We begin from the isotropic material.

Definition 5.3. Isotropic material. *The polar-elastic solid is called isotropic at* x *and* $\mathbf{B}$ *if there exists a reference placement* $\mathrm{B}_{\mathcal{K}}$*, called undistorted, such that the material symmetry group relative to* $\mathrm{B}_{\mathcal{K}}$ *takes the form*

$$\mathcal{G}_{\mathcal{K}} = \mathcal{S}_{\mathcal{K}} \equiv \{(\mathbf{P} = \mathbf{O}, \mathbf{O}, \mathbf{0}) : \quad \mathbf{O} \in \mathrm{Orth}\}. \tag{18}$$

This definition means that the strain energy density of the polar-elastic isotropic solid satisfies the relation

$$W(\mathbf{E}, \boldsymbol{\Gamma}; \mathbf{B}) = W\left[\mathbf{O}\mathbf{E}\mathbf{O}^{\mathrm{T}}, (\det \mathbf{O})\mathbf{O}\boldsymbol{\Gamma}\mathbf{O}^{\mathrm{T}}; (\det \mathbf{O})\mathbf{O}\mathbf{B}\mathbf{O}^{\mathrm{T}}\right], \quad \forall \mathbf{O} \in \mathrm{Orth}.$$

Scalar-valued isotropic functions of a few 2nd-order tensors can be expressed by the so-called representation theorems in terms of joint invariants of the tensorial arguments, called also the integrity basis, see [11, 12]. Decomposing the non-symmetric tensors $\mathbf{E}$, $\boldsymbol{\Gamma}$ and $\mathbf{B}$ into their symmetric and skew parts,

$$\mathbf{E} = \mathbf{E}_S + \mathbf{E}_A, \quad \mathbf{E}_S = \frac{1}{2}(\mathbf{E} + \mathbf{E}^T), \quad \mathbf{E}_A = \frac{1}{2}(\mathbf{E} - \mathbf{E}^T),$$
$$\boldsymbol{\Gamma} = \boldsymbol{\Gamma}_S + \boldsymbol{\Gamma}_A, \quad \boldsymbol{\Gamma}_S = \frac{1}{2}(\boldsymbol{\Gamma} + \boldsymbol{\Gamma}^T), \quad \boldsymbol{\Gamma}_A = \frac{1}{2}(\boldsymbol{\Gamma} - \boldsymbol{\Gamma}^T),$$
$$\mathbf{B} = \mathbf{B}_S + \mathbf{B}_A, \quad \mathbf{B}_S = \frac{1}{2}(\mathbf{B} + \mathbf{B}^T), \quad \mathbf{B}_A = \frac{1}{2}(\mathbf{B} - \mathbf{B}^T),$$

we represent the strain energy density as the function of three symmetric and three skew tensors,

$$W = W(\mathbf{E}_S, \mathbf{E}_A, \boldsymbol{\Gamma}_S, \boldsymbol{\Gamma}_A; \mathbf{B}_S, \mathbf{B}_A). \tag{19}$$

The integrity basis for the proper orthogonal group is given by Spencer, see Table 1 in [11] or Table II in [12]. For the proper orthogonal group there is no difference in transformations of the axial and polar tensors. It is not the case if one considers transformations using the full orthogonal group. Since $\boldsymbol{\Gamma}_S, \boldsymbol{\Gamma}_A, \mathbf{B}_S, \mathbf{B}_A$ are the axial tensors, not all invariants listed in [11, 12] are absolute invariants under orthogonal transformations, because some of them change sign under non-proper orthogonal transformations. Such invariants are called relative invariants [12]. Examples of relative invariants are $\operatorname{tr} \boldsymbol{\Gamma}_S$, $\operatorname{tr} \boldsymbol{\Gamma}_S^3$, $\operatorname{tr} \mathbf{E}_S\boldsymbol{\Gamma}_S$, $\operatorname{tr} \mathbf{E}_S\mathbf{B}_S$, etc. This gives us the following property of W:

$$W(\mathbf{E}_S, \mathbf{E}_A, \boldsymbol{\Gamma}_S, \boldsymbol{\Gamma}_A; \mathbf{B}_S, \mathbf{B}_A) = W(\mathbf{E}_S, \mathbf{E}_A, -\boldsymbol{\Gamma}_S, -\boldsymbol{\Gamma}_A; -\mathbf{B}_S, -\mathbf{B}_A). \tag{20}$$

Using the representations given by Zheng [13], we present the lists of absolute and relative polynomial invariants for the polar-elastic isotropic solid in Table 1. In this case there are 119 invariants. They constitute the so-called irreducible integrity basis. The strain energy density of the polar-elastic isotropic solid is given by any scalar-valued function of these invariants satisfying (20).

Further simplifications are possible if we neglect the explicit dependence of W on $\mathbf{B}$, that is if we assume that $W = W(\mathbf{E}, \boldsymbol{\Gamma})$. The integrity basis of two non-symmentric tensors under the orthogonal group contains 39 members, see Ramezani et al. [14], where these invariants are listed and the corresponding constitutive equations are proposed. Kafadar and Eringen [15] constructed the list of independent invariants. Table 1 contains the invariants of [14] and of [15] as well as additional joint invariants of $\mathbf{E}$, $\boldsymbol{\Gamma}$ and $\mathbf{B}$. According to [15], the isotropic scalar-valued function $W = W(\mathbf{E}, \boldsymbol{\Gamma})$ is expressible in terms of 15 invariants

$$W = W(\mathrm{I}_1, \mathrm{I}_2, \ldots, \mathrm{I}_{15}), \tag{21}$$

where I_k are given by

$$\begin{aligned}
&\mathrm{I}_1 = \operatorname{tr} \mathbf{E}, \quad \mathrm{I}_2 = \operatorname{tr} \mathbf{E}^2, \quad \mathrm{I}_3 = \operatorname{tr} \mathbf{E}^3,\\
&\mathrm{I}_4 = \operatorname{tr} \mathbf{E}\mathbf{E}^T, \ \mathrm{I}_5 = \operatorname{tr} \mathbf{E}^2\mathbf{E}^T, \ \mathrm{I}_6 = \operatorname{tr} \mathbf{E}^2\mathbf{E}^{T2},\\
&\mathrm{I}_7 = \operatorname{tr} \mathbf{E}\boldsymbol{\Gamma}, \quad \mathrm{I}_8 = \operatorname{tr} \mathbf{E}^2\boldsymbol{\Gamma}, \quad \mathrm{I}_9 = \operatorname{tr} \mathbf{E}\boldsymbol{\Gamma}^2,
\end{aligned}$$

Table 1 119 invariants in W in the case of polar-elastic isotropic solid

Agencies	Invariants			
$\mathbf{E}_S$	$\operatorname{tr}\mathbf{E}_S$	$\operatorname{tr}\mathbf{E}_S^2$	$\operatorname{tr}\mathbf{E}_S^3$	
$\mathbf{E}_A$	$\operatorname{tr}\mathbf{E}_A^2$			
$\mathbf{E}_S, \mathbf{E}_A$	$\operatorname{tr}\mathbf{E}_S\mathbf{E}_A^2$	$\operatorname{tr}\mathbf{E}_S^2\mathbf{E}_A^2$	$\operatorname{tr}\mathbf{E}_S^2\mathbf{E}_A^2\mathbf{E}_S\mathbf{E}_A$	
$\boldsymbol{\Gamma}_S$	$\operatorname{tr}\boldsymbol{\Gamma}_S$	$\operatorname{tr}\boldsymbol{\Gamma}_S^2$	$\operatorname{tr}\boldsymbol{\Gamma}_S^3$	
$\boldsymbol{\Gamma}_A$	$\operatorname{tr}\boldsymbol{\Gamma}_A^2$			
$\boldsymbol{\Gamma}_S, \boldsymbol{\Gamma}_A$	$\operatorname{tr}\boldsymbol{\Gamma}_S\boldsymbol{\Gamma}_A^2$	$\operatorname{tr}\boldsymbol{\Gamma}_S^2\boldsymbol{\Gamma}_A^2$	$\operatorname{tr}\boldsymbol{\Gamma}_S^2\boldsymbol{\Gamma}_A^2\boldsymbol{\Gamma}_S\boldsymbol{\Gamma}_A$	
$\mathbf{B}_S$	$\operatorname{tr}\mathbf{B}_S$	$\operatorname{tr}\mathbf{B}_S^2$	$\operatorname{tr}\mathbf{B}_S^3$	
$\mathbf{B}_A$	$\operatorname{tr}\mathbf{B}_A^2$			
$\mathbf{B}_S$,$\mathbf{B}_A$	$\operatorname{tr}\mathbf{B}_S\mathbf{B}_A^2$	$\operatorname{tr}\mathbf{B}_S^2\mathbf{B}_A^2$	$\operatorname{tr}\mathbf{B}_S^2\mathbf{B}_A^2\mathbf{B}_S\mathbf{B}_A$	
$\mathbf{E}_S$,$\boldsymbol{\Gamma}_S$	$\operatorname{tr}\mathbf{E}_S\boldsymbol{\Gamma}_S$	$\operatorname{tr}\mathbf{E}_S^2\boldsymbol{\Gamma}_S$	$\operatorname{tr}\mathbf{E}_S\boldsymbol{\Gamma}_S^2$	$\operatorname{tr}\mathbf{E}_S^2\boldsymbol{\Gamma}_S^2$
$\mathbf{E}_S, \mathbf{B}_S$	$\operatorname{tr}\mathbf{E}_S\mathbf{B}_S$	$\operatorname{tr}\mathbf{E}_S^2\mathbf{B}_S$	$\operatorname{tr}\mathbf{E}_S\mathbf{B}_S^2$	$\operatorname{tr}\mathbf{E}_S^2\mathbf{B}_S^2$
$\boldsymbol{\Gamma}_S, \mathbf{B}_S$	$\operatorname{tr}\boldsymbol{\Gamma}_S\mathbf{B}_S$	$\operatorname{tr}\boldsymbol{\Gamma}_S^2\mathbf{B}_S$	$\operatorname{tr}\boldsymbol{\Gamma}_S\mathbf{B}_S^2$	$\operatorname{tr}\boldsymbol{\Gamma}_S^2\mathbf{B}_S^2$
$\mathbf{E}_S, \boldsymbol{\Gamma}_S, \mathbf{B}_S$	$\operatorname{tr}\mathbf{E}_S\boldsymbol{\Gamma}_S\mathbf{B}_S$			
$\mathbf{E}_A, \boldsymbol{\Gamma}_A$	$\operatorname{tr}\mathbf{E}_A\boldsymbol{\Gamma}_A$			
$\mathbf{E}_A, \mathbf{B}_A$	$\operatorname{tr}\mathbf{E}_A\mathbf{B}_A$			
$\boldsymbol{\Gamma}_A, \mathbf{B}_A$	$\operatorname{tr}\boldsymbol{\Gamma}_A\mathbf{B}_A$			
$\mathbf{E}_A$,$\boldsymbol{\Gamma}_A, \mathbf{B}_A$	$\operatorname{tr}\mathbf{E}_A\boldsymbol{\Gamma}_A\mathbf{B}_A$			
$\mathbf{E}_S, \boldsymbol{\Gamma}_A$	$\operatorname{tr}\mathbf{E}_S\boldsymbol{\Gamma}_A^2$	$\operatorname{tr}\mathbf{E}_S^2\boldsymbol{\Gamma}_A^2$	$\operatorname{tr}\mathbf{E}_S^2\boldsymbol{\Gamma}_A^2\mathbf{E}_S\boldsymbol{\Gamma}_A$	
$\mathbf{E}_S, \mathbf{B}_A$	$\operatorname{tr}\mathbf{E}_S\mathbf{B}_A^2$	$\operatorname{tr}\mathbf{E}_S^2\mathbf{B}_A^2$	$\operatorname{tr}\mathbf{E}_S^2\mathbf{B}_A^2\mathbf{E}_S\mathbf{B}_A$	
$\boldsymbol{\Gamma}_S, \mathbf{E}_A$	$\operatorname{tr}\boldsymbol{\Gamma}_S\mathbf{E}_A^2$	$\operatorname{tr}\boldsymbol{\Gamma}_S^2\mathbf{E}_A^2$	$\operatorname{tr}\boldsymbol{\Gamma}_S^2\mathbf{E}_A^2\boldsymbol{\Gamma}_S\mathbf{E}_A$	
$\boldsymbol{\Gamma}_S, \mathbf{B}_A$	$\operatorname{tr}\boldsymbol{\Gamma}_S\mathbf{B}_A^2$	$\operatorname{tr}\boldsymbol{\Gamma}_S^2\mathbf{B}_A^2$	$\operatorname{tr}\boldsymbol{\Gamma}_S^2\mathbf{B}_A^2\boldsymbol{\Gamma}_S\mathbf{B}_A$	
$\mathbf{B}_S, \boldsymbol{\Gamma}_A$	$\operatorname{tr}\mathbf{B}_S\boldsymbol{\Gamma}_A^2$	$\operatorname{tr}\mathbf{B}_S^2\boldsymbol{\Gamma}_A^2$	$\operatorname{tr}\mathbf{E}_S^2\boldsymbol{\Gamma}_A^2\mathbf{B}_S\boldsymbol{\Gamma}_A$	
$\mathbf{B}_S, \mathbf{E}_A$	$\operatorname{tr}\mathbf{B}_S\mathbf{E}_A^2$	$\operatorname{tr}\mathbf{B}_S^2\mathbf{E}_A^2$	$\operatorname{tr}\mathbf{B}_S^2\mathbf{E}_A^2\mathbf{B}_S\mathbf{E}_A$	
$\mathbf{E}_S, \boldsymbol{\Gamma}_S, \mathbf{E}_A$	$\operatorname{tr}\mathbf{E}_S\boldsymbol{\Gamma}_S\mathbf{E}_A$	$\operatorname{tr}\mathbf{E}_S^2\boldsymbol{\Gamma}_S\mathbf{E}_A$	$\operatorname{tr}\mathbf{E}_S\boldsymbol{\Gamma}_S^2\mathbf{E}_A$	$\operatorname{tr}\mathbf{E}_S\mathbf{E}_A^2\boldsymbol{\Gamma}_S\mathbf{E}_A$
$\mathbf{E}_S, \boldsymbol{\Gamma}_S, \boldsymbol{\Gamma}_A$	$\operatorname{tr}\mathbf{E}_S\boldsymbol{\Gamma}_S\boldsymbol{\Gamma}_A$	$\operatorname{tr}\mathbf{E}_S^2\boldsymbol{\Gamma}_S\boldsymbol{\Gamma}_A$	$\operatorname{tr}\mathbf{E}_S\boldsymbol{\Gamma}_S^2\boldsymbol{\Gamma}_A$	$\operatorname{tr}\mathbf{E}_S\boldsymbol{\Gamma}_A^2\boldsymbol{\Gamma}_S\boldsymbol{\Gamma}_A$
$\mathbf{E}_S, \boldsymbol{\Gamma}_S, \mathbf{B}_A$	$\operatorname{tr}\mathbf{E}_S\boldsymbol{\Gamma}_S\mathbf{B}_A$	$\operatorname{tr}\mathbf{E}_S^2\boldsymbol{\Gamma}_S\mathbf{B}_A$	$\operatorname{tr}\mathbf{E}_S\boldsymbol{\Gamma}_S^2\mathbf{B}_A$	$\operatorname{tr}\mathbf{E}_S\mathbf{B}_A^2\boldsymbol{\Gamma}_S\mathbf{B}_A$
$\mathbf{E}_S, \mathbf{B}_S, \mathbf{E}_A$	$\operatorname{tr}\mathbf{E}_S\mathbf{B}_S\mathbf{E}_A$	$\operatorname{tr}\mathbf{E}_S^2\mathbf{B}_S\mathbf{E}_A$	$\operatorname{tr}\mathbf{E}_S\mathbf{B}_S^2\mathbf{E}_A$	$\operatorname{tr}\mathbf{E}_S\mathbf{E}_A^2\mathbf{B}_S\mathbf{E}_A$
$\mathbf{E}_S, \mathbf{B}_S, \boldsymbol{\Gamma}_A$	$\operatorname{tr}\mathbf{E}_S\mathbf{B}_S\boldsymbol{\Gamma}_A$	$\operatorname{tr}\mathbf{E}_S^2\mathbf{B}_S\boldsymbol{\Gamma}_A$	$\operatorname{tr}\mathbf{E}_S\mathbf{B}_S^2\boldsymbol{\Gamma}_A$	$\operatorname{tr}\mathbf{E}_S\boldsymbol{\Gamma}_A^2\mathbf{B}_S\boldsymbol{\Gamma}_A$
$\mathbf{E}_S, \mathbf{B}_S, \mathbf{B}_A$	$\operatorname{tr}\mathbf{E}_S\mathbf{B}_S\mathbf{B}_A$	$\operatorname{tr}\mathbf{E}_S^2\mathbf{B}_S\mathbf{B}_A$	$\operatorname{tr}\mathbf{E}_S\mathbf{B}_S^2\mathbf{B}_A$	$\operatorname{tr}\mathbf{E}_S\mathbf{B}_A^2\mathbf{B}_S\mathbf{B}_A$
$\boldsymbol{\Gamma}_S, \mathbf{B}_S, \mathbf{E}_A$	$\operatorname{tr}\boldsymbol{\Gamma}_S\mathbf{B}_S\mathbf{E}_A$	$\operatorname{tr}\boldsymbol{\Gamma}_S^2\mathbf{B}_S\mathbf{E}_A$	$\operatorname{tr}\boldsymbol{\Gamma}_S\mathbf{B}_S^2\mathbf{E}_A$	$\operatorname{tr}\boldsymbol{\Gamma}_S\mathbf{E}_A^2\mathbf{B}_S\mathbf{E}_A$
$\boldsymbol{\Gamma}_S, \mathbf{B}_S, \boldsymbol{\Gamma}_A$	$\operatorname{tr}\boldsymbol{\Gamma}_S\mathbf{B}_S\boldsymbol{\Gamma}_A$	$\operatorname{tr}\boldsymbol{\Gamma}_S^2\mathbf{B}_S\boldsymbol{\Gamma}_A$	$\operatorname{tr}\boldsymbol{\Gamma}_S\mathbf{B}_S^2\boldsymbol{\Gamma}_A$	$\operatorname{tr}\boldsymbol{\Gamma}_S\boldsymbol{\Gamma}_A^2\mathbf{B}_S\boldsymbol{\Gamma}_A$
$\boldsymbol{\Gamma}_S, \mathbf{B}_S, \mathbf{B}_A$	$\operatorname{tr}\boldsymbol{\Gamma}_S\mathbf{B}_S\mathbf{B}_A$	$\operatorname{tr}\boldsymbol{\Gamma}_S^2\mathbf{B}_S\mathbf{B}_A$	$\operatorname{tr}\boldsymbol{\Gamma}_S\mathbf{B}_S^2\mathbf{B}_A$	$\operatorname{tr}\boldsymbol{\Gamma}_S\mathbf{B}_A^2\mathbf{B}_S\mathbf{B}_A$
$\mathbf{E}_S, \mathbf{E}_A, \boldsymbol{\Gamma}_A$	$\operatorname{tr}\mathbf{E}_S\mathbf{E}_A\boldsymbol{\Gamma}_A$	$\operatorname{tr}\mathbf{E}_S\mathbf{E}_A^2\boldsymbol{\Gamma}_A$	$\operatorname{tr}\mathbf{E}_S\mathbf{E}_A\boldsymbol{\Gamma}_A^2$	
$\mathbf{E}_S, \mathbf{E}_A, \mathbf{B}_A$	$\operatorname{tr}\mathbf{E}_S\mathbf{E}_A\mathbf{B}_A$	$\operatorname{tr}\mathbf{E}_S\mathbf{E}_A^2\mathbf{B}_A$	$\operatorname{tr}\mathbf{E}_S\mathbf{E}_A\mathbf{B}_A^2$	
$\mathbf{E}_S, \boldsymbol{\Gamma}_A, \mathbf{B}_A$	$\operatorname{tr}\mathbf{E}_S\boldsymbol{\Gamma}_A\mathbf{B}_A$	$\operatorname{tr}\mathbf{E}_S\boldsymbol{\Gamma}_A^2\mathbf{B}_A$	$\operatorname{tr}\mathbf{E}_S\boldsymbol{\Gamma}_A\mathbf{B}_A^2$	
$\boldsymbol{\Gamma}_S, \mathbf{E}_A, \boldsymbol{\Gamma}_A$	$\operatorname{tr}\boldsymbol{\Gamma}_S\mathbf{E}_A\boldsymbol{\Gamma}_A$	$\operatorname{tr}\boldsymbol{\Gamma}_S\mathbf{E}_A^2\boldsymbol{\Gamma}_A$	$\operatorname{tr}\boldsymbol{\Gamma}_S\mathbf{E}_A\boldsymbol{\Gamma}_A^2$	
$\boldsymbol{\Gamma}_S, \mathbf{E}_A, \mathbf{B}_A$	$\operatorname{tr}\boldsymbol{\Gamma}_S\mathbf{E}_A\mathbf{B}_A$	$\operatorname{tr}\boldsymbol{\Gamma}_S\mathbf{E}_A^2\mathbf{B}_A$	$\operatorname{tr}\boldsymbol{\Gamma}_S\mathbf{E}_A\mathbf{B}_A^2$	
$\boldsymbol{\Gamma}_S, \boldsymbol{\Gamma}_A, \mathbf{B}_A$	$\operatorname{tr}\boldsymbol{\Gamma}_S\boldsymbol{\Gamma}_A\mathbf{B}_A$	$\operatorname{tr}\boldsymbol{\Gamma}_S\boldsymbol{\Gamma}_A^2\mathbf{B}_A$	$\operatorname{tr}\boldsymbol{\Gamma}_S\boldsymbol{\Gamma}_A\mathbf{B}_A^2$	
$\mathbf{B}_S, \mathbf{E}_A, \boldsymbol{\Gamma}_A$	$\operatorname{tr}\mathbf{B}_S\mathbf{E}_A\boldsymbol{\Gamma}_A$	$\operatorname{tr}\mathbf{B}_S\mathbf{E}_A^2\boldsymbol{\Gamma}_A$	$\operatorname{tr}\mathbf{B}_S\mathbf{E}_A\boldsymbol{\Gamma}_A^2$	
$\mathbf{B}_S, \mathbf{E}_A, \mathbf{B}_A$	$\operatorname{tr}\mathbf{B}_S\mathbf{E}_A\mathbf{B}_A$	$\operatorname{tr}\mathbf{B}_S\mathbf{E}_A^2\mathbf{B}_A$	$\operatorname{tr}\mathbf{B}_S\mathbf{E}_A\mathbf{B}_A^2$	
$\mathbf{B}_S, \boldsymbol{\Gamma}_A, \mathbf{B}_A$	$\operatorname{tr}\mathbf{B}_S\boldsymbol{\Gamma}_A\mathbf{B}_A$	$\operatorname{tr}\mathbf{B}_S\boldsymbol{\Gamma}_A^2\mathbf{B}_A$	$\operatorname{tr}\mathbf{B}_S\boldsymbol{\Gamma}_A\mathbf{B}_A^2$	

$$\mathrm{I}_{10} = \operatorname{tr}\boldsymbol{\Gamma}, \quad \mathrm{I}_{11} = \operatorname{tr}\boldsymbol{\Gamma}^2, \quad \mathrm{I}_{12} = \operatorname{tr}\boldsymbol{\Gamma}^3,$$
$$\mathrm{I}_{13} = \operatorname{tr}\boldsymbol{\Gamma}\boldsymbol{\Gamma}^{\mathrm{T}}, \ \mathrm{I}_{14} = \operatorname{tr}\boldsymbol{\Gamma}^2\boldsymbol{\Gamma}^{\mathrm{T}}, \ \mathrm{I}_{15} = \operatorname{tr}\boldsymbol{\Gamma}^2\boldsymbol{\Gamma}^{\mathrm{T}2}.$$

Taking into account that $W = W(\mathbf{E}, \boldsymbol{\Gamma})$ is an even function with respect to $\boldsymbol{\Gamma}$, because in our case the group $\mathcal{S}_{\varkappa}$ contains the reflection $-\mathbb{I}$, W becomes also the even function with respect to some invariants,

$$W(\mathrm{I}_1, \mathrm{I}_2, \mathrm{I}_3, \mathrm{I}_4, \mathrm{I}_5, \mathrm{I}_6, \mathrm{I}_7, \mathrm{I}_8, \mathrm{I}_9, \mathrm{I}_{10}, \mathrm{I}_{11}, \mathrm{I}_{12}, \mathrm{I}_{13}, \mathrm{I}_{14}, \mathrm{I}_{15})$$
$$= W(\mathrm{I}_1, \mathrm{I}_2, \mathrm{I}_3, \mathrm{I}_4, \mathrm{I}_5, \mathrm{I}_6, -\mathrm{I}_7, -\mathrm{I}_8, \mathrm{I}_9, -\mathrm{I}_{10}, \mathrm{I}_{11}, -\mathrm{I}_{12}, \mathrm{I}_{13}, -\mathrm{I}_{14}, \mathrm{I}_{15}). \tag{22}$$

Expanding W into the Taylor series relative to $\mathbf{E}$ and $\boldsymbol{\Gamma}$, and keeping up to quadratic terms, we obtain the approximate polynomial representation of (22),

$$W = w_0 + \mathrm{a}_1\mathrm{I}_1 + \mathrm{b}_1\mathrm{I}_1^2 + \mathrm{b}_3\mathrm{I}_{10}^2 + \mathrm{b}_4\mathrm{I}_4 + \mathrm{b}_5\mathrm{I}_2 + \mathrm{b}_7\mathrm{I}_{11} + \mathrm{b}_8\mathrm{I}_{13}$$
$$+ \mathrm{O}(\max(\|\mathbf{E}\|^3, \|\boldsymbol{\Gamma}\|^3)), \tag{23}$$

where w_0, a_1, $\mathrm{b}_1, \ldots, \mathrm{b}_8$ are material constants.

We may also consider the representation of W which takes the form of sum of two scalar functions each depending on one strain measure,

$$W = W_1(\mathbf{E}) + W_2(\boldsymbol{\Gamma}). \tag{24}$$

The form (24) was used for example in [14] in order to generalize the classical neo-Hookean and Moony-Rivlin models to the polar-elastic solids. Using [16] we obtain the following representation of W:

$$W = \widetilde{W}_1(\mathrm{I}_1, \ldots, \mathrm{I}_6) + \widetilde{W}_2(\mathrm{I}_{10}, \ldots, \mathrm{I}_{15}), \tag{25}$$

where $\widetilde{W}_2$ has the property

$$\widetilde{W}_2(\mathrm{I}_{10}, \mathrm{I}_{11}, \mathrm{I}_{12}, \mathrm{I}_{13}, \mathrm{I}_{14}, \mathrm{I}_{15}) = \widetilde{W}_2(-\mathrm{I}_{10}, \mathrm{I}_{11}, -\mathrm{I}_{12}, \mathrm{I}_{13}, -\mathrm{I}_{14}, \mathrm{I}_{15}). \tag{26}$$

Expanding (25) with (26) into the Taylor series and keeping up to quadratic terms in $\mathbf{E}$ and $\boldsymbol{\Gamma}$, W takes the form (24) with

$$W_1 = w_0 + \mathrm{a}_1\mathrm{I}_1 + \mathrm{b}_1\mathrm{I}_1^2 + \mathrm{b}_4\mathrm{I}_4 + \mathrm{b}_5\mathrm{I}_2, \quad W_2 = \mathrm{b}_3\mathrm{I}_{10}^2 + \mathrm{b}_7\mathrm{I}_{11} + \mathrm{b}_8\mathrm{I}_{13}.$$

If in the definition (18) we use only the proper orthogonal tensors then the resulting constitutive equations correspond to the hemitropic polar-elastic continuum.

Definition 5.4. Hemitropic material. *The polar-elastic solid is called hemitropic at* x *and* $\mathbf{B}$ *if there exists a reference placement* $\mathrm{B}_{\varkappa}$*, called undistorted, such that the material symmetry group relative to* $\mathrm{B}_{\varkappa}$ *takes the form*

$$\mathcal{G}_{\varkappa} = \mathcal{S}^{+}_{\varkappa} \equiv \left\{(\mathbf{P} = \mathbf{O}, \mathbf{O}, \mathbf{0}) : \quad \mathbf{O} \in \mathsf{Orth}^{+}\right\}. \tag{27}$$

The strain energy density of the hemitropic polar-elastic solid satisfies the relation

$$W(\mathbf{E}, \boldsymbol{\Gamma}; \mathbf{B}) = W\left(\mathbf{O}\mathbf{E}\mathbf{O}^{\mathsf{T}}, \mathbf{O}\boldsymbol{\Gamma}\mathbf{O}^{\mathsf{T}}; \mathbf{O}\mathbf{B}\mathbf{O}^{\mathsf{T}}\right), \quad \forall\, \mathbf{O} \in \mathsf{Orth}^{+}. \tag{28}$$

The hemitropic polar-elastic solid is insensitive to the change of orientation of the space. In the case of reduced strain energy density $W = W(\mathbf{E}, \boldsymbol{\Gamma})$ the representation of W is given by (21), but the property (22) does not hold, in general. Obviously, the polar-elastic isotropic solid is also hemitropic.

Definitions (18) and (28) are somewhat similar to the corresponding definition of the isotropic polar-elastic solid proposed by Eringen and Kafadar [2]. However, the properties (22) or (26) do not follow from the definition used in [2].

Definition 5.5. Orthotropic material. *The polar-elastic solid is called orthotropic at* x *and* $\mathbf{B}$ *if the material symmetry group for some reference placement* $\mathrm{B}_{\varkappa}$ *takes the form*

$$\mathcal{G}_{\varkappa} = \{(\mathbf{P} = \mathbf{O}, \mathbf{O}, \mathbf{0})\} : \mathbf{O} = \{\mathbf{I},\ -\mathbf{I},\ 2\mathbf{e}_1 \otimes \mathbf{e}_1 - \mathbf{I},\ 2\mathbf{e}_2 \otimes \mathbf{e}_2 - \mathbf{I},\ 2\mathbf{e}_3 \otimes \mathbf{e}_3 - \mathbf{I}\}, \tag{29}$$

where $\mathbf{O}$ *are orthogonal tensors performing the mirror reflections and rotations of* 180° *about three orthonormal vectors* $\mathbf{e}_{\mathrm{k}}$.

Obviously, the polar-elastic isotropic solid is also orthotropic. Thus, the invariants given in Tables 1 enter the representation of the strain energy density of the polar-elastic orthotropic solid. The additional list of 60 absolute and relative invariants for the polar-elastic orthotropic solid, which are responsible for the orthotropic properties, is presented in Table 2. Therefore, the full list of Tables 1 and 2 contains 179 invariants.

Definition 5.6. Transversely isotropic solid. *The polar-elastic solid is called transversely isotropic at* x *and* $\mathbf{B}$ *with respect to a direction described by* $\mathbf{e}$ *if the material symmetry group for some reference placement* $\mathrm{B}_{\varkappa}$ *takes the form*

$$\mathcal{G}_{\varkappa} = \{(\mathbf{P} = \mathbf{O}, \mathbf{O}, \mathbf{0})\} : \qquad \mathbf{O} = \{\mathbf{I},\ -\mathbf{I},\ \mathbf{O}(\varphi\mathbf{e}), \quad \forall\ \varphi\}, \tag{30}$$

where $\mathbf{O}(\varphi\mathbf{e}) = (\mathbf{I} - \mathbf{e} \otimes \mathbf{e}) \cos\varphi + \mathbf{e} \otimes \mathbf{e} + \mathbf{e} \times \mathbf{I} \sin\varphi$ *is the rotation tensor with the rotation angle* φ *about the unit vector* $\mathbf{e}$.

167 invariants for the polar-elastic transversely isotropic solid are presented in Tables 1 and 3.

Definition 5.7. Cubic symmetry. *The polar-elastic solid is called cubic-symmetric at* x *and* $\mathbf{B}$ *if the material symmetry group for some reference placement* $\mathrm{B}_{\varkappa}$ *takes the form*

Table 2 Additional 60 invariants in W in the case of polar-elastic orthotropic solid

Agencies		Invariants		
$\mathbf{E}_S$	$\operatorname{tr} \mathcal{V}\mathbf{E}_S$	$\operatorname{tr} \mathcal{V}^2\mathbf{E}_S$	$\operatorname{tr} \mathcal{V}\mathbf{E}_S^2$	$\operatorname{tr} \mathcal{V}^2\mathbf{E}_S^2$
$\mathbf{E}_A$	$\operatorname{tr} \mathcal{V}\mathbf{E}_A^2$	$\operatorname{tr} \mathcal{V}^2\mathbf{E}_A^2$	$\operatorname{tr} \mathcal{V}^2\mathbf{E}_A^2\,\mathcal{V}\mathbf{E}_A$	
$\mathbf{E}_S$, $\mathbf{E}_A$	$\operatorname{tr} \mathcal{V}\mathbf{E}_S\,\mathbf{E}_A$	$\operatorname{tr} \mathcal{V}^2\mathbf{E}_S\,\mathbf{E}_A$	$\operatorname{tr} \mathcal{V}\mathbf{E}_S^2\,\mathbf{E}_A$	
$\boldsymbol{\Gamma}_S$	$\operatorname{tr} \mathcal{V}\boldsymbol{\Gamma}_S$	$\operatorname{tr} \mathcal{V}^2\boldsymbol{\Gamma}_S$	$\operatorname{tr} \mathcal{V}\boldsymbol{\Gamma}_S^2$	$\operatorname{tr} \mathcal{V}^2\boldsymbol{\Gamma}_S^2$
$\boldsymbol{\Gamma}_A$	$\operatorname{tr} \mathcal{V}\boldsymbol{\Gamma}_A^2$	$\operatorname{tr} \mathcal{V}^2\boldsymbol{\Gamma}_A^2$	$\operatorname{tr} \mathcal{V}^2\boldsymbol{\Gamma}_A^2\,\mathcal{V}\boldsymbol{\Gamma}_A$	
$\boldsymbol{\Gamma}_S$, $\boldsymbol{\Gamma}_A$	$\operatorname{tr} \mathcal{V}\boldsymbol{\Gamma}_S\,\boldsymbol{\Gamma}_A$	$\operatorname{tr} \mathcal{V}^2\boldsymbol{\Gamma}_S\,\boldsymbol{\Gamma}_A$	$\operatorname{tr} \mathcal{V}\boldsymbol{\Gamma}_S^2\,\boldsymbol{\Gamma}_A$	
$\mathbf{B}_S$	$\operatorname{tr} \mathcal{V}\mathbf{B}_S$	$\operatorname{tr} \mathcal{V}^2\mathbf{B}_S$	$\operatorname{tr} \mathcal{V}\mathbf{B}_S^2$	$\operatorname{tr} \mathcal{V}^2\boldsymbol{\Gamma}_S^2$
$\mathbf{B}_A$	$\operatorname{tr} \mathcal{V}\mathbf{B}_A^2$	$\operatorname{tr} \mathcal{V}^2\mathbf{B}_A^2$	$\operatorname{tr} \mathcal{V}^2\mathbf{B}_A^2\,\mathcal{V}\mathbf{B}_A$	
$\mathbf{B}_S$, $\mathbf{B}_A$	$\operatorname{tr} \mathcal{V}\mathbf{B}_S\,\mathbf{B}_A$	$\operatorname{tr} \mathcal{V}^2\mathbf{B}_S\,\mathbf{B}_A$	$\operatorname{tr} \mathcal{V}\mathbf{B}_S^2\,\mathbf{B}_A$	
$\mathbf{E}_S$, $\boldsymbol{\Gamma}_S$	$\operatorname{tr} \mathcal{V}\mathbf{E}_S\,\boldsymbol{\Gamma}_S$			
$\mathbf{E}_S$, $\mathbf{B}_S$	$\operatorname{tr} \mathcal{V}\mathbf{E}_S\,\mathbf{B}_S$			
$\boldsymbol{\Gamma}_S$, $\mathbf{B}_S$	$\operatorname{tr} \mathcal{V}\boldsymbol{\Gamma}_S\,\mathbf{B}_S$			
$\mathbf{E}_A$, $\boldsymbol{\Gamma}_A$	$\operatorname{tr} \mathcal{V}\mathbf{E}_A\,\boldsymbol{\Gamma}_A$	$\operatorname{tr} \mathcal{V}\mathbf{E}_A^2\,\boldsymbol{\Gamma}_A$	$\operatorname{tr} \mathcal{V}\mathbf{E}_A\,\boldsymbol{\Gamma}_A^2$	
$\mathbf{E}_A$, $\mathbf{B}_A$	$\operatorname{tr} \mathcal{V}\mathbf{E}_A\,\mathbf{B}_A$	$\operatorname{tr} \mathcal{V}\mathbf{E}_A^2\,\mathbf{B}_A$	$\operatorname{tr} \mathcal{V}\mathbf{E}_A\,\mathbf{B}_A^2$	
$\boldsymbol{\Gamma}_A$, $\mathbf{B}_A$	$\operatorname{tr} \mathcal{V}\boldsymbol{\Gamma}_A\,\mathbf{B}_A$	$\operatorname{tr} \mathcal{V}\boldsymbol{\Gamma}_A^2\,\mathbf{B}_A$	$\operatorname{tr} \mathcal{V}\boldsymbol{\Gamma}_A\,\mathbf{B}_A^2$	
$\mathbf{E}_S$, $\boldsymbol{\Gamma}_A$	$\operatorname{tr} \mathcal{V}\mathbf{E}_S\,\boldsymbol{\Gamma}_A$	$\operatorname{tr} \mathcal{V}^2\mathbf{E}_S\,\boldsymbol{\Gamma}_A$	$\operatorname{tr} \mathcal{V}\mathbf{E}_S^2\,\boldsymbol{\Gamma}_A$	
$\mathbf{E}_S$, $\mathbf{B}_A$	$\operatorname{tr} \mathcal{V}\mathbf{E}_S\,\mathbf{B}_A$	$\operatorname{tr} \mathcal{V}^2\mathbf{E}_S\,\mathbf{B}_A$	$\operatorname{tr} \mathcal{V}\mathbf{E}_S^2\,\mathbf{B}_A$	
$\boldsymbol{\Gamma}_S$, $\mathbf{E}_A$	$\operatorname{tr} \mathcal{V}\boldsymbol{\Gamma}_S\,\mathbf{E}_A$	$\operatorname{tr} \mathcal{V}^2\boldsymbol{\Gamma}_S\,\mathbf{E}_A$	$\operatorname{tr} \mathcal{V}\boldsymbol{\Gamma}_S^2\,\mathbf{B}_A$	
$\boldsymbol{\Gamma}_S$, $\mathbf{B}_A$	$\operatorname{tr} \mathcal{V}\boldsymbol{\Gamma}_S\,\mathbf{B}_A$	$\operatorname{tr} \mathcal{V}^2\boldsymbol{\Gamma}_S\,\mathbf{B}_A$	$\operatorname{tr} \mathcal{V}\boldsymbol{\Gamma}_S^2\,\mathbf{B}_A$	
$\mathbf{B}_S$, $\boldsymbol{\Gamma}_A$	$\operatorname{tr} \mathcal{V}\mathbf{B}_S\,\boldsymbol{\Gamma}_A$	$\operatorname{tr} \mathcal{V}^2\mathbf{B}_S\,\boldsymbol{\Gamma}_A$	$\operatorname{tr} \mathcal{V}\mathbf{B}_S^2\,\boldsymbol{\Gamma}_A$	
$\mathbf{B}_S$, $\mathbf{E}_A$	$\operatorname{tr} \mathcal{V}\mathbf{B}_S\,\mathbf{E}_A$	$\operatorname{tr} \mathcal{V}^2\mathbf{B}_S\,\mathbf{E}_A$	$\operatorname{tr} \mathcal{V}\mathbf{B}_S^2\,\mathbf{E}_A$	

Table 3 Additional 48 invariants in W in the case of polar-elastic transverse isotropic solid

Agencies		Invariants	
$\mathbf{E}_S$	$e\cdot\mathbf{E}_S\,e$	$e\cdot\mathbf{E}_S^2\,e$	
$\mathbf{E}_A$	$e\cdot\mathbf{E}_A^2\,e$		
$\mathbf{E}_S$, $\mathbf{E}_A$	$e\cdot\mathbf{E}_S\,\mathbf{E}_A\,e$	$e\cdot\mathbf{E}_S^2\,\mathbf{E}_A\,e$	$e\cdot\mathbf{E}_A\,\mathbf{E}_S\,\mathbf{E}_A^2\,e$
$\boldsymbol{\Gamma}_S$	$e\cdot\boldsymbol{\Gamma}_S\,e$	$e\cdot\boldsymbol{\Gamma}_S^2\,e$	
$\boldsymbol{\Gamma}_A$	$e\cdot\boldsymbol{\Gamma}_A^2\,e$		
$\boldsymbol{\Gamma}_S$, $\boldsymbol{\Gamma}_A$	$e\cdot\boldsymbol{\Gamma}_S\,\boldsymbol{\Gamma}_A\,e$	$e\cdot\boldsymbol{\Gamma}_S^2\,\boldsymbol{\Gamma}_A\,e$	$e\cdot\boldsymbol{\Gamma}_A\,\boldsymbol{\Gamma}_S\,\boldsymbol{\Gamma}_A^2\,e$
$\mathbf{B}_S$	$e\cdot\mathbf{B}_S\,e$	$e\cdot\mathbf{B}_S^2\,e$	
$\mathbf{B}_A$	$e\cdot\mathbf{B}_A^2\,e$		
$\mathbf{B}_S$, $\mathbf{B}_A$	$e\cdot\mathbf{B}_S\,\mathbf{B}_A\,e$	$e\cdot\mathbf{B}_S^2\,\mathbf{B}_A\,e$	$e\cdot\mathbf{B}_A\,\mathbf{B}_S\,\mathbf{B}_A^2\,e$
$\mathbf{E}_S$,$\boldsymbol{\Gamma}_S$	$e\cdot\mathbf{E}_S\,\boldsymbol{\Gamma}_S\,e$		
$\mathbf{E}_S$, $\mathbf{B}_S$	$e\cdot\mathbf{E}_S\,\mathbf{B}_S\,e$		
$\boldsymbol{\Gamma}_S$, $\mathbf{B}_S$	$e\cdot\boldsymbol{\Gamma}_S\,\mathbf{B}_S\,e$		
$\mathbf{E}_A$, $\boldsymbol{\Gamma}_A$	$e\cdot\mathbf{E}_A\,\boldsymbol{\Gamma}_A\,e$	$e\cdot\mathbf{E}_A^2\,\boldsymbol{\Gamma}_A\,e$	$e\cdot\mathbf{E}_A\,\boldsymbol{\Gamma}_A^2\,e$
$\mathbf{E}_A$, $\mathbf{B}_A$	$e\cdot\mathbf{E}_A\,\mathbf{B}_A\,e$	$e\cdot\mathbf{E}_A^2\,\mathbf{B}_A\,e$	$e\cdot\mathbf{E}_A\,\mathbf{B}_A^2\,e$
$\boldsymbol{\Gamma}_A$, $\mathbf{B}_A$	$e\cdot\boldsymbol{\Gamma}_A\,\mathbf{B}_A\,e$	$e\cdot\boldsymbol{\Gamma}_A^2\,\mathbf{B}_A\,e$	$e\cdot\boldsymbol{\Gamma}_A\,\mathbf{B}_A^2\,e$
$\mathbf{E}_S$,$\boldsymbol{\Gamma}_A$	$e\cdot\mathbf{E}_S\,\boldsymbol{\Gamma}_A\,e$	$e\cdot\mathbf{E}_S^2\,\boldsymbol{\Gamma}_A\,e$	$e\cdot\boldsymbol{\Gamma}_A\,\mathbf{E}_S\,\boldsymbol{\Gamma}_A^2\,e$
$\mathbf{E}_S$, $\mathbf{B}_A$	$e\cdot\mathbf{E}_S\,\mathbf{B}_A\,e$	$e\cdot\mathbf{E}_S^2\,\mathbf{B}_A\,e$	$e\cdot\mathbf{B}_A\,\mathbf{E}_S\,\mathbf{B}_A^2\,e$,
$\boldsymbol{\Gamma}_S$, $\mathbf{E}_A$	$e\cdot\boldsymbol{\Gamma}_S\,\mathbf{E}_A\,e$	$e\cdot\boldsymbol{\Gamma}_S^2\,\mathbf{E}_A\,e$	$e\cdot\mathbf{E}_A\,\boldsymbol{\Gamma}_S\,\mathbf{E}_A^2\,e$
$\boldsymbol{\Gamma}_S$, $\mathbf{B}_A$	$e\cdot\boldsymbol{\Gamma}_S\,\mathbf{B}_A\,e$	$e\cdot\boldsymbol{\Gamma}_S^2\,\mathbf{B}_A\,e$	$e\cdot\mathbf{B}_A\,\boldsymbol{\Gamma}_S\,\mathbf{B}_A^2\,e$
$\mathbf{B}_S$, $\boldsymbol{\Gamma}_A$	$e\cdot\mathbf{B}_S\,\boldsymbol{\Gamma}_A\,e$	$e\cdot\mathbf{B}_S^2\,\boldsymbol{\Gamma}_A\,e$	$e\cdot\boldsymbol{\Gamma}_A\,\mathbf{B}_S\,\boldsymbol{\Gamma}_A^2\,e$
$\mathbf{B}_S$, $\mathbf{E}_A$	$e\cdot\mathbf{E}_S\,\mathbf{E}_A\,e$	$e\cdot\mathbf{E}_S^2\,\mathbf{E}_A\,e$	$e\cdot\mathbf{E}_A\,\mathbf{E}_S\,\mathbf{E}_A^2\,e$

$$\mathcal{G}_{\varkappa} = \{(\mathbf{P} = \mathbf{O}, \mathbf{O}, \mathbf{0})\} : \qquad (31)$$
$$\mathbf{O} = \{\mathbf{I},\ -\mathbf{I},\ \mathbf{e}_1 \otimes \mathbf{e}_1 \mp \mathbf{e}_1 \times \mathbf{I},\ \mathbf{e}_2 \otimes \mathbf{e}_2 \mp \mathbf{e}_2 \times \mathbf{I},\ \mathbf{e}_3 \otimes \mathbf{e}_3 \mp \mathbf{e}_3 \times \mathbf{I}\},$$

where $\mathbf{O}$ *are orthogonal tensors performing the mirror reflections and rotations of* 90° *about three orthonormal vectors* $\mathbf{e}_k$.

Here we have discussed the structure of the strain energy density of micropolar elastic solids under finite deformations. Within the linear micropolar elasticity the explicit structure of stiffness tensors was presented is [17] for 14 symmetry groups, see [4].

5 Conclusions

We have discussed here the new definition of the material symmetry group $\mathcal{G}_{\varkappa}$ of the non-linear polar elastic continuum. The group $\mathcal{G}_{\varkappa}$ consists of an ordered triple of tensors which make the strain energy density invariant under change of the reference placement. Reduced forms of the constitutive equations for the polar-elastic solids are given for several particular cases of material symmetry groups.

Acknowledgments The first author was supported by the DFG grant No. AL 341/33-1 and by the RFBR with the grant No. 12-01-00038.

References

1. Eremeyev, V.A., Pietraszkiewicz, W.: Material symmetry group of the non-linear polar-elastic continuum. Int. J. Solids Struct. **49**(14), 1993–2005 (2012)
2. Eringen, A.C., Kafadar, C.B.: Polar field theories. In: Eringen, A.C. (ed.) Continuum Physics, vol. IV, pp. 1–75. Academic Press, New York (1976)
3. Cosserat, E., Cosserat, F.: Théorie des corps déformables. Herman et Fils, Paris (1909)
4. Eringen, A.C.: Microcontinuum Field Theory I. Foundations and Solids. Springer, New York (1999)
5. Eringen, A.C.: Microcontinuum Field Theory II. Fluent Media. Springer, New York (2001)
6. Nowacki, W.: Theory of Asymmetric Elasticity. Pergamon-Press, Oxford (1986)
7. Eremeyev, V.A., Lebedev, L.P., Altenbach, H.: Foundations of Micropolar Mechanics. Springer, Heidelberg (2012)
8. Pietraszkiewicz, W., Eremeyev, V.A.: On natural strain measures of the non-linear micropolar continuum. Int. J. Solids Struct. **46**(3–4), 774–787 (2009)
9. Truesdell, C., Noll, W.: The nonlinear field theories of mechanics. In: Flügge, S. (ed.) Handbuch der Physik, Vol III/3, pp 1–602. Springer, Berlin (1965)
10. Wang, C.C., Truesdell, C.: Introduction to Rational Elasticity. Noordhoof Int. Publishing, Leyden (1973)
11. Spencer, A.J.M.: Isotropic integrity bases for vectors and second-order tensors. Part II. Arch. Ration. Mech. Anal. **18**(1), 51–82 (1965)
12. Spencer, A.J.M.: Theory of invariants. In: Eringen, A.C. (ed.) Continuum Physics, vol. 1, pp. 239–353. Academic Press, New York (1971)

13. Zheng, Q.S.: Theory of representations for tensor functions–a unified invariant approach to constitutive equations. Appl. Mech. Rev. **47**(11), 545–587 (1994)
14. Ramezani, S., Naghdabadi, R., Sohrabpour, S.: Constitutive equations for micropolar hyperelastic materials. Int. J. Solids Struct. **46**(14–15), 2765–2773 (2009)
15. Kafadar, C.B., Eringen, A.C.: Micropolar media–I. The classical theory. Int. J. Eng. Sci. **9**, 271–305 (1971)
16. Smith, M.M., Smith, R.F.: Irreducable expressions for isotropic functions of two tensors. Int. J. Eng. Sci. **19**(6), 811–817 (1971)
17. Zheng, Q.S., Spencer, A.J.M.: On the canonical representations for Kronecker powers of orthogonal tensors with application to material symmetry problems. Int. J. Eng. Sci. **31**(4), 617–635 (1993)

Nonlinear Localized Strain Waves in a 2D Medium with Microstructure

Vladimir I. Erofeev, Vladimir V. Kazhaev and Igor S. Pavlov

Abstract A two-dimensional model of the crystalline (granular) medium is considered that represents a square lattice consisting of elastically interacting particles, which possess translational and rotational degrees of freedom. In the long-wavelength approximation the partial derivatives equations have been derived that describe propagation of longitudinal, transverse and rotational waves in such a medium. In the field of low frequencies, when the rotational degree of freedom of particles can be neglected, the obtained nonlinear three-mode system degenerates into a two-mode system. Analytical dependencies of the velocities of elastic waves and the nonlinearity coefficients on the sizes of particles and the parameters of interactions between them have been found for both nonlinear models. Due to these dependencies, numerical estimations of the nonlinearity coefficients are performed. The two-mode system is shown to be reduced by the multi-scale method to Kadomtsev–Petviashvili evolutionary equation for transverse deformation, which has a soliton solution. For some crystals with a cubic symmetry it is found out, whether soliton is steady and what kind of polarity it has.

1 Introduction

As a rule, adequate description of wave processes in a structurally-heterogeneous material necessitates consideration of some scale levels, which interact with each other on account of internal connections [1]. The following scales are usually

V. I. Erofeev (✉) · V. V. Kazhaev · I. S. Pavlov
Nizhny Novgorod Mechanical Engineering Research Institute of Russian Academy of Sciences, IMASH RAN 85, Belinskogo st., Nizhny Novgorod, Russia 603024
e-mail: erf04@sinn.ru

I. S. Pavlov
e-mail: ispavl@mts-nn.ru

H. Altenbach et al. (eds.), *Generalized Continua as Models for Materials*, Advanced Structured Materials 22, DOI: 10.1007/978-3-642-36394-8_6,

distinguished: atomic or *microlevel* (characteristic sizes are angstroms and nanometers), *mesolevel* (from 10^{-8}–10^{-6} m), and *macrolevel* (larger than 10^{-6} m).

Mental breaking of a material into parts is restricted by some limit consisting in a qualitative change of physical properties on a given scale level, i.e. in this case a size effect [2, 3] arises. There are materials, where qualitative changes occur gradually, but in crystal solids this limit is expressed rather accurately and takes place in the field of nanometers. During studying of wave processes in materials, the size effects start to be shown, when the characteristic spatial scale of effect (for example, length of an elastic or electromagnetic wave) becomes comparable with the characteristic spatial scale of a material—the size of grain, the lattice period, etc. In process of accumulation of knowledge about microstructure of a material there arises a transition to new level of knowledge—a theory is created that enables one to explain mechanical behavior of a material from new positions. It is necessary to emphasize that in this case real values of "microscales" of a medium can lie in the field of both microns and nanometers or angstroms. However, with the viewpoint of methodology of theoretical research, smallness of some scales in comparison with other ones is more important than their absolute values.

In the mathematical simulation of microstructured media, two approaches can be distinguished. The first approach consists in the passage from atomic-level models to mesoscale models and is based on the laws of quantum theory. In this case, the medium is considered as a discrete system of particles coupled by the interaction forces determined from the first principles [4]. This approach allows one to understand the nature of physical laws and to explain the origin of some properties having no substantiation in the classical theory.

The second approach means passing from description of a medium on a macrolevel to mesoscale models. The continuum-phenomenological method of modeling of microstructured media is related to this approach. This method lies at the boundary of mechanics and physics of solid-state. It consists in improvement of the classical models of media by including qualitatively new characteristics inherent in actual discrete structures [1, 5, 6]. At present, structurally-heterogeneous materials are frequently simulated by the generalized micropolar theories of the Cosserat continuum type [7–9]. These theories involve a large number of material constants, which have to be determined experimentally. The relationships between these quantities and the material structure are not always clear. Besides, there is an alternative—the method of structural modeling, according to which a certain minimum volume is separated in the bulk material—a representative structural element that is capable of reflecting the main features of the macroscopic behavior of the given material [1, 10–12]. In this method, a nanocrystalline material is represented by a regular or quasi-regular lattice, with small-size bodies possessing internal degrees of freedom (rather than material points) occupying the lattice sites. The role of these bodies can be played by domains, grains, fullerenes, nanotubes, or clusters consisting of nanoparticles. Advantages of the structural modeling consist in a clear relationship between the structure of a medium and its macroparameters, as well as in possibility of purposeful design of materials with the given properties, and shortcomings are absence of

universality of modeling procedure and complexity of the accounting of nonlinear and nonlocal effects of interparticle interactions.

Construction of mechanical and mathematical models is a base of research of the dynamic (wave) phenomena [13] in both natural and artificial materials possessing unique properties. It should be noted that an adequate description of this or that wave process in the certain structured material necessitates a corresponding mathematical model. For example, in [14] it was shown that in the field of high frequencies the accounting of rotation motions of particles is necessary, in a low-frequency range it is enough to use the equations of the classical theory of elasticity, which considers particles as material points and does not take into account rotation of particles, and, at last, in the intermediate area, the equations of the second-order gradient theory of elasticity should be used, which do not contain rotations of particles in an explicit form, but the sizes of particles influence on factors of these equations.

In this work, the nonlinear differential equations describing propagation of longitudinal, transverse and rotational waves in the two-dimensional crystal (granular) medium are derived by the method of structural modeling. After that, in the field of low frequencies, when the rotational wave does not propagate, the received three-mode set of equations degenerates into the two-mode model corresponding to the continuum "with the restricted rotation of particles" [5]. Due to application of the method of structural modeling, analytical dependencies of the linear and nonlinear macroparameters of the medium on sizes of the particles and on parameters of interactions between them have been established, and numerical estimates of the nonlinearity parameters have been performed both for the complete (three-mode) system and for the reduced (two-mode) model. Using the multi-scale method, the two-mode system is reduced to Kadomtsev–Petviashvili evolutionary equation with respect to transverse deformation. This equation has a soliton-type solution. Different variants of behavior of a plane solitary wave are analyzed, depending on initial conditions of Kadomtsev–Petviashvili equation and its factors that depend on the microstructure parameters of the considered medium.

2 Discrete Model

We consider a square lattice (Fig. 1), the sites of which are occupied by homogeneous round particles (granules) having mass M and diameter d. In the initial state, the centers of mass of the particles are located in lattice sites, and the distance between them is a. The lattice sites N are enumerated using the subscripts (i, j). Each particle has three degrees of freedom: displacements $u_{ij}(t)$ and $w_{ij}(t)$ of the center of mass along axes x and y, respectively, and the angle of rotation $\varphi_{ij}(t)$ with respect to an axis passing through the center of mass of a particle (Fig. 2). The kinetic energy of the cell is as follows:

$$T_{i,j} = \frac{M}{2}\left(\dot{u}_{i,j}^2 + \dot{w}_{i,j}^2\right) + \frac{J}{2}\dot{\varphi}_{i,j}^2, \tag{1}$$

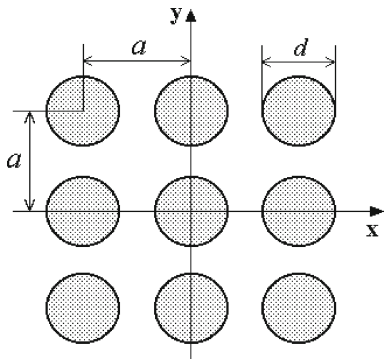

Fig. 1 A square lattice consisting of round particles

where $J = Md^2/8 = MR^2$ is the moment of inertia about the axis passing through its mass center and $R = d\Big/\sqrt{8}$ is the radius of gyration of the particle. The dots denote derivatives with respect to time.

Since we consider only small deviations of particles from equilibrium positions, their force and moment interactions can be described by a power potential. In the harmonic approximation, the interaction potential is a quadratic form of the variables of the system state. The potential energy per cell is equal to the potential energy of a particle located at site N and interacting with its neighbors and can be described by the following expression:

$$
\begin{aligned}
U_N\left(\Delta_{nr}q^k, \varphi, \Delta_{nr}\varphi\right) = &\sum_{k,s=1}^{2}\sum_{n,r,l,m}\frac{\partial^2 U}{\partial\left(\Delta_{nr}q^k\right)\partial\left(\Delta_{lm}q^s\right)}\Delta_{nr}q^k\Delta_{lm}q^s \\
&+\sum_{n,r,l,m}\frac{\partial^2 U}{\partial\left(\Delta_{nr}\varphi\right)\,\partial\left(\Delta_{lm}\varphi\right)}\,\Delta_{nr}\varphi\,\Delta_{lm}\varphi \\
&+\sum_{k=1}^{2}\sum_{n,r,l,m}\frac{\partial^2 U}{\partial\left(\Delta_{nr}q^k\right)\partial\left(\Delta_{lm}\varphi\right)}\Delta_{nr}q^k\,\Delta_{lm}\varphi \\
&+\sum_{k=1}^{2}\sum_{n,r}\frac{\partial^2 U}{\partial\left(\Delta_{nr}q^k\right)\,\partial\varphi}\Delta_{nr}q^k\varphi+\frac{\partial^2 U}{(\partial\varphi)^2}\varphi^2.
\end{aligned}
$$

Here $\left\{q_{ij}^k\right\} = \left\{q_{ij}^1, q_{ij}^2\right\} = \{u_{ij}, w_{ij}\}$ are the components of the displacement vector of the center of mass for a particle located at the site with subscripts (*i, j*), $\Delta_{nr}q^k = \left(q_{i+n\,j+r}^k - q_{ij}^k\right)\Big/a$ is the relative variation of interparticle distances, $\Delta_{nr}\varphi = \left(\varphi_{i+n\,j+r} - \varphi_{ij}\right)\Big/a$ is the relative variation of the particle orientation angles, and $n = \pm 1$, $r = \pm 1$ are the subscripts determining the spatial positions of the neighboring particles. The second-order derivatives of the potential energy are

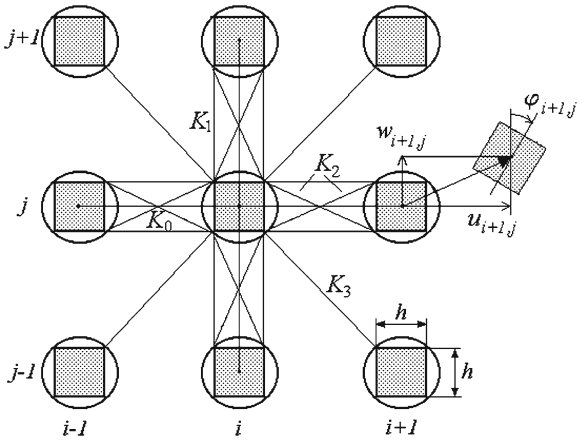

Fig. 2 Schematic for force interactions between the particles and kinematics

the constants of quasi-elastic interactions of the particles and represent the elements of force matrices of the crystalline structure [15]. In phenomenological theories, the material constants are assumed to be known from experiments. Their relation to the geometric structure and interaction parameters in the crystal lattice is generally unclear. From the general energy considerations and the symmetry conditions, only certain restrictions on their values [5] can be derived. The proposed structural approach makes it possible to find explicit relationships between the force matrix elements and lattice parameters.

For structural modeling of crystalline media, an equivalent force scheme is introduced as a system of rods or springs that incorporates the transmission of forces and moments between the structural elements [10–12] instead of a field description of the interaction of the particles. For convenience, the round particles are replaced by inscribed polygons, the shape of which repeats that of the cell. The springs simulating the interactions between particles are considered anchored at the vertices of polygons.

In the present paper, a spring model is used for modeling. Displacements of the granules are assumed to be small compared to the size of the elementary cell of the lattice. The particle N is supposed to interact directly with eight nearest neighbors in the lattice. The mass centers of four of them are on horizontal and vertical lines (these particles are called *particles of the first coordination sphere*), while the mass centers of the other four neighboring particles lie along diagonals (*particles of the second coordination sphere*). The potential energy per cell of the square lattice produced by its interaction with eight neighbors is described by

$$\mathrm{U_N} = \frac{1}{2}\left(\sum_{n=1}^{4}\frac{\mathrm{K_0}}{2}\mathrm{D_{0n}^2} + \sum_{n=1}^{8}\frac{\mathrm{K_1}}{2}\mathrm{D_{1n}^2} + \sum_{n=1}^{8}\frac{\mathrm{K_2}}{2}\mathrm{D_{2n}^2} + \sum_{n=1}^{4}\frac{\mathrm{K_3}}{2}\mathrm{D_{3n}^2}\right), \quad (2)$$

where D_{ln} ($l = 0, 1, 2, 3$) are extensions of arbitrary enumerated springs of four types, which connect a particle with its neighbors. The central springs having rigidity K_0, together with the non-central springs with rigidity K_1 define interaction forces of extension/compression of the material, whereas the springs with K_1 transmit also moments to particle rotation. The diagonal springs with rigidity K_2 characterize force interactions of the granules of shear deformations in the material. The springs possessing rigidity K_3 model interactions with the particles of the second coordination sphere. For convenience of further calculations, we shall assume that points of connection of springs K_0 are located in the centers of the particles, whereas ones of the springs K_1, K_2 and K_3 lie in the vertices of a square that is entered in a circumference and has a side $h = d/\sqrt{2}$ (Fig. 2). Equation (2) contains additional factor 0.5 because the potential energy of the spring is equal to the sum of the potential energies of two particles, which are connected by this spring.

We shall calculate expressions for extensions of the springs, D_{ln}, supposing that quantities $\Delta u_i \sim \Delta w_i \sim \Delta u_j \sim \Delta w_j \sim a\varepsilon$, $\Delta\varphi_i \sim \Delta\varphi_j \sim \varepsilon^{3/2}$, and $\Phi_i \sim \sqrt{\varepsilon}$ are small, where $\Delta u_i = u_{i,j} - u_{i-1,j}$, $\Delta u_j = u_{i,j} - u_{i,j-1}$, $\Phi_i = (\varphi_{i-1,j} + \varphi_{i,j})/2 \ll \pi/2$, and $\varepsilon \ll 1$ is a measure of cell deformation. After substitution of these expressions into (2) we shall make up Lagrange function $L = T_{i,j} - U_{i,j}$ for the particle with number (i, j) to an accuracy of terms of order $\varepsilon^{5/2}$. Thus, only geometrical nonlinearity is taken into account in this model. Then, using Lagrange equations of the second kind it is possible to obtain differential-different equations describing dynamics of the considered lattice. However, the continuum approximation of the proposed model will be considered in this chapter.

3 Continuum Approximation

For a comparison of the structural model of the medium with the well-known models of a deformable solid, it is expedient to pass from the discrete description to a continuous description. In the case of the long wavelength perturbations, for which $a/\Lambda \ll 1$ (Λ is the characteristic spatial deformation scale), the discrete variables i and j can be replaced by the continuous variables $x = ia$ and $y = ja$, and the functions $u_{ij}(t)$, $w_{ij}(t)$, $\varphi_{ij}(t)$ can be interpolated by the fields of displacements $u(x, y, t)$, $w(x, y, t)$ and microrotations $\varphi(x,y,t)$, respectively.

Depending on the order of approximation, it is possible to consider various continuous models. In the first approximation the following Lagrangian of the considered medium with microstructure yields:

$$L = \frac{M}{2}\left(u_t^2 + w_t^2 + R^2\varphi_t^2\right) - \frac{M}{2}[c_1^2(u_x^2 + w_y^2) + c_2^2(w_x^2 + u_y^2) + R^2c_3^2(\varphi_x^2 + \varphi_y^2) + s^2(u_x w_y + u_y w_x) + 2\beta^2(w_x - u_y)\varphi + 2\beta^2\varphi^2$$

$$
\begin{aligned}
&+\alpha_1(u_x^3+w_y^3)+\alpha_2(u_y^3+w_x^3+u_x^2u_y+u_xu_y^2+w_x^2w_y+w_xw_y^2\\
&-u_x^2w_x-u_y^2w_x-u_x^2w_y-u_yw_y^2-u_yw_x^2-u_xw_y^2)\\
&-2\alpha_2(u_xu_y(w_x+w_y)+w_xw_y(u_x+u_y))+\alpha_3(u_xw_x^2+u_y^2w_y)\\
&+\alpha_4(w_xw_y\varphi-u_xu_y\varphi+\frac{1}{2}(w_x^2-u_x^2+w_y^2-u_y^2)\varphi)\\
&+\alpha_5(u_y\varphi^2+w_x\varphi^2)+\alpha_6(u_x\varphi^2+w_y\varphi^2)+\alpha_7(u_xw_x\varphi+u_yw_y\varphi)].
\end{aligned}
\tag{3}
$$

Using Lagrangian (3), a set of nonlinear differential equations describing the dynamic processes in a 2D crystalline medium with non-dense packing of the particles is derived in agreement with Hamilton's variational principle:

$$
\begin{aligned}
u_{tt}&=c_1^2u_{xx}+c_2^2u_{yy}+s^2w_{xy}-\beta^2\varphi_y+\frac{1}{2}\frac{\partial F_1}{\partial x}+\frac{1}{2}\frac{\partial F_2}{\partial y},\\
w_{tt}&=c_2^2w_{xx}+c_1^2w_{yy}+s^2u_{xy}+\beta^2\varphi_x+\frac{1}{2}\frac{\partial F_3}{\partial x}+\frac{1}{2}\frac{\partial F_4}{\partial y},\\
R^2\varphi_{tt}&=R^2c_3^2(\varphi_{xx}+\varphi_{yy})+\beta^2(u_y-w_x)-2\beta^2\varphi-F_5.
\end{aligned}
\tag{4}
$$

Here, the following notation has been introduced: c_i $(i=1,2,3)$ are the velocities of propagation of longitudinal, transverse, and rotational waves, respectively, s is the coefficient of linear coupling between the longitudinal and transverse deformations in a material, β is the dispersion parameter. Dependencies of the coefficients of equations (4) on the force constants K_0, K_1, K_2, and K_3, the lattice period a and grain size $h=d/\sqrt{2}$ (d is a diameter of the particle) have the following form [14]:

$$
\begin{aligned}
c_1^2&=\frac{a^2}{M}\left(K_0+2K_1+\frac{2(a-h)^2}{(a-h)^2+h^2}K_2+K_3\right),\\
c_2^2&=\frac{a^2}{M}\left(\frac{2h^2}{(a-h)^2+h^2}K_2+K_3\right),\\
c_3^2&=\frac{a^2h^2}{2MR^2}\left(K_1+\frac{a^2}{(a-h)^2+h^2}K_2\right),\\
s^2&=\frac{2a^2}{M}K_3,\quad \beta^2=\frac{2a^2}{M}\left(\frac{h^2}{(a-h)^2+h^2}K_2\right).
\end{aligned}
\tag{5}
$$

Moreover, the nonlinearity functions contain in the right-hand sides of Eqs. (4):

$$
\begin{aligned}
F_1&=3\alpha_1u_x^2+\alpha_2(2u_xu_y+u_y^2-2u_xw_x-u_xw_y-w_y^2)+\alpha_3w_x^2\\
&\quad-2\alpha_2(u_yw_x+u_yw_y+w_xw_y)-\alpha_4(u_y\varphi+u_x\varphi)+\alpha_6\varphi^2+\alpha_7w_x\varphi,\\
F_2&=\alpha_2(3u_y^2+u_x^2+2u_xu_y-2u_yw_x-w_y^2-w_x^2)+2\alpha_3u_yw_y
\end{aligned}
$$

$$
\begin{aligned}
&- 2\alpha_2(u_x w_x + u_x w_y + w_x w_y) - \alpha_4(u_x \varphi + u_y \varphi) + \alpha_5 \varphi^2 + \alpha_7 w_y \varphi,\\
F_3 = {}& \alpha_2(3w_x^2 + 2w_x w_y + w_y^2 - u_x^2 - u_y^2 - 2u_y w_x\\
&- 2u_x u_y + u_x w_y) + 2\alpha_3 u_x w_x + \alpha_4(w_y \varphi + w_x \varphi) + \alpha_5 \varphi^2 + \alpha_7 u_x \varphi,\\
F_4 = {}& 3\alpha_1 w_y^2 + \alpha_2(w_x^2 + 2w_x w_y - u_x^2 - 2u_y w_y - 2u_x w_y) + \alpha_3 u_y^2 \qquad (6)\\
&- 2\alpha_2(u_x u_y + u_x w_x + u_y w_x) + \alpha_4(w_x \varphi + w_y \varphi) + \alpha_6 \varphi^2 + \alpha_7 u_y \varphi,\\
F_5 = {}& \alpha_4 \left(w_x w_y - u_x u_y + \frac{1}{2}(w_x^2 - u_x^2 + w_y^2 - u_y^2) \right)\\
&+ 2\alpha_5(u_y \varphi + w_x \varphi) + 2\alpha_6(u_x \varphi + w_y \varphi) + \alpha_7(u_x w_x + u_y w_y),
\end{aligned}
$$

where α_i ($i = 1,...,7$) are the nonlinearity coefficients depending on the microstructure parameters:

$$
\begin{aligned}
M\alpha_1 &= \frac{K_2}{r^4} a^3 (a-h) h^2 + \frac{K_3}{4(a-h)} a^3, \quad M\alpha_2 = \frac{K_3}{4(a-h)} a^3,\\
M\alpha_3 &= K_0 a^2 + K_1 \frac{a^3}{a-h} + \frac{K_2}{r^4} a^3 (a-h)(a^2 - 2ah - h^2) - \frac{K_3 a^3}{4(a-h)},\\
M\alpha_4 &= \frac{2a^2 h K_3}{a-h}, \quad M\alpha_5 = \frac{K_3}{(a-h)^2} a^2 h^2, \qquad (7)\\
M\alpha_6 &= K_1 \frac{ah^2}{a-h} + K_2 \frac{ah^2}{r^4} (2h-a)(5ah - 2h^2 - a^2) + \frac{K_3}{(a-h)^2} a^2 h^2,\\
M\alpha_7 &= K_1 \frac{2a^2 h}{a-h} + \frac{2a^3 h}{r^4} K_2 \left(5h^2 - 5ah + a^2 \right).
\end{aligned}
$$

Here $r = \sqrt{(a-h)^2 + h^2}$ is the initial length of the springs with rigidity K_2 (Fig. 2).

Equations (4) describe the dynamics of a crystalline (granular) medium accounting for local interactions of the grain, and coincide with the dynamic equations of the 2D anisotropic Cosserat continuum consisting of centrally-symmetric particles [5]. Such equations differ from the equations of the classical theory of elasticity by the additional equation for the microrotation wave. In the continuous approach, this equation follows from the conservation law of moment of momentum (or angular momentum), if the internal moments of the particles of the medium are introduced into the consideration.

4 Approximation of the Second-Order Gradient Theory of Elasticity

Theoretical estimates [14] and experimental data [16] show that rotational waves in solids exist in the high-frequency range ($>10^9$–10^{11} Hz), where it is quite difficult, with a technical point of view, to carry out acoustic experiments. Nevertheless,

information about microstructure of the medium can be received even by means of acoustic measurements on rather low frequencies (10^6–10^7 Hz), when the rotational waves do not propagate in a medium. Therefore we will consider low-frequency approximation of Eqs. (4), in which the microrotations of the particles of the medium are not independent and are determined by a displacement field. The inter-relationship between the microrotations φ_j and displacements u and w can be found from the third Eq. (4) by the method of stepwise approximations. In the first approximation

$$\varphi(x,t) \approx \frac{1}{2}(u_y - w_x). \tag{8}$$

This relationship between the rotations of the particles of the medium and a vorticity of a displacement field, is a characteristic feature of the *Cosserat pseudo-continuum* model (continuum with the restricted rotation of the particles) [5]. Taking account of Eq. (8) leads to the "freezing" of the rotational degree of freedom. Thus, excitations, which are caused by the microrotations, do not propagate in the medium, but they influence on propagation of the longitudinal and transverse waves. In this case, the Lagrange function L takes on the simpler form:

$$\begin{aligned} L = {} & \frac{M}{2}\left(u_t^2 + w_t^2 + \frac{R^2}{4}(u_{yt} - w_{xt})^2\right) \\ & - \frac{M}{2}\Bigg[c_1^2(u_x^2 + w_y^2) + c_2^2(w_x^2 + u_y^2) + \frac{R^2}{4}c_3^2((u_{xy} - w_{xx})^2 \\ & + (u_{yy} - w_{xy})^2) + s^2(u_x w_y + u_y w_x) - \frac{\beta^2}{2}(w_x - u_y)^2 \\ & + \alpha_1(u_x^3 + w_y^3) - \alpha_2(u_x^2 w_y + u_x w_y^2 + 2u_x u_y w_y + 2u_x w_x w_y) \\ & + \gamma_1(u_y^3 + w_x^3 - u_y w_x^2 - u_y^2 w_x) + \gamma_2(u_x u_y^2 + w_x^2 w_y) \\ & + \gamma_3 u_x w_x^2 + \gamma_4 u_y^2 w_y + \gamma_5(u_x^2 u_y + w_x w_y^2 - u_x^2 w_x - u_y w_y^2) \\ & - (2\gamma_5 + \gamma_6)u_x u_y w_x - (2\gamma_5 + \gamma_7)u_y w_x w_y\Bigg]. \end{aligned} \tag{9}$$

Here

$$\gamma_1 = \alpha_2 + \frac{\alpha_5 - \alpha_4}{4}, \quad \gamma_2 = \alpha_2 + \frac{\alpha_6}{4} - \frac{\alpha_4}{2}, \quad \gamma_3 = \alpha_3 + \frac{\alpha_6}{4} - \frac{\alpha_7}{2}, \tag{10}$$

$$\gamma_4 = \alpha_3 + \frac{\alpha_6}{4} + \frac{\alpha_7}{2}, \quad \gamma_5 = \alpha_2 - \frac{\alpha_4}{4}, \quad \gamma_6 = \frac{1}{2}(\alpha_6 - \alpha_7), \quad \gamma_7 = \frac{1}{2}(\alpha_6 + \alpha_7).$$

In contrast to the classical case, in Lagrangian (9), there are terms containing second-order derivatives from the field of displacements. The terms u_{yt} and w_{xt} take into account the contribution of the rotational motions to the kinetic energy, and the terms with spatial derivatives u_{xy}, w_{xx}, etc. describe the contribution to the

potential energy of the stresses provided by bending of the lattice. The nonlinear differential equations describing the propagation and interaction of the longitudinal and transverse waves in the nanocrystalline medium in the low-frequency approximation have the form:

$$
\begin{aligned}
&u_{tt} - c_1^2 u_{xx} - \left(c_2^2 - \frac{\beta^2}{2}\right) u_{yy} - \left(s^2 + \frac{\beta^2}{2}\right) w_{xy} \\
&\quad = \frac{R^2}{4}\frac{\partial}{\partial y}\left[\frac{\partial^2}{\partial t^2}(u_y - w_x) - c_3^2 \Delta (u_y - w_x)\right] + \frac{1}{2}\frac{\partial H_1}{\partial x} + \frac{1}{2}\frac{\partial H_2}{\partial y}, \qquad (11) \\
&w_{tt} - \left(c_2^2 - \frac{\beta^2}{2}\right) w_{xx} - c_1^2 w_{yy} - \left(s^2 + \frac{\beta^2}{2}\right) u_{xy} \\
&\quad = -\frac{R^2}{4}\frac{\partial}{\partial x}\left[\frac{\partial^2}{\partial t^2}(u_y - w_x) - c_3^2 \Delta (u_y - w_x)\right] + \frac{1}{2}\frac{\partial H_3}{\partial x} + \frac{1}{2}\frac{\partial H_4}{\partial y}.
\end{aligned}
$$

Here, the symbol Δ means the 2D Laplacian $\Delta = \partial^2/\partial x^2 + \partial^2/\partial y^2$, $H_{1,2,3,4}$ are the nonlinearity functions:

$$
\begin{aligned}
H_1 &= 3\alpha_1 u_x^2 - 2\alpha_2 \left(u_x w_y + \frac{1}{2} w_y^2 + u_y w_y + w_x w_y\right) \\
&\quad + \gamma_2 u_y^2 + \gamma_3 w_x^2 + 2\gamma_5 (u_x u_y - u_x w_x) - (2\gamma_5 + \gamma_6) u_y w_x, \\
H_2 &= -2\alpha_2 u_x w_y + \gamma_1 (3u_y^2 - w_x^2 - 2u_y w_x) + 2\gamma_2 u_x u_y + 2\gamma_4 u_y w_y \\
&\quad + \gamma_5 (u_x^2 - w_y^2) - (2\gamma_5 + \gamma_6) u_x w_x - (2\gamma_5 + \gamma_7) w_x w_y, \\
H_3 &= -2\alpha_2 u_x w_y + \gamma_1 (3w_x^2 - u_y^2 - 2u_y w_x) + 2\gamma_2 w_x w_y + 2\gamma_3 u_x w_x \\
&\quad + \gamma_5 (w_y^2 - u_x^2) - (2\gamma_5 + \gamma_6) u_x u_y - (2\gamma_5 + \gamma_7) u_y w_y, \\
H_4 &= 3\alpha_1 w_y^2 - 2\alpha_2 \left(u_x w_y + \frac{1}{2} u_x^2 + u_x u_y + u_x w_x\right) \\
&\quad + \gamma_2 w_x^2 + \gamma_4 u_y^2 + 2\gamma_5 (w_x w_y - u_y w_y) - (2\gamma_5 + \gamma_7) u_y w_x.
\end{aligned}
$$

Equations such as Eqs. (11) are usually called *equations of the second-order gradient theory of elasticity* [17], as the terms with spatial fourth-order derivatives take into account the coupled stresses arising at the translational displacements of the particles. It should be noted that, in spite of absence of microrotations in Eqs. (11), the coefficients of these equations changed because of influence of microstructure—in the considered low-frequency approximation, the transverse wave velocity is diminished by quantity $\beta^2/2$, and the parameter s^2 increases by the same quantity.

5 The Problem of Parametric Identification

The real-world problem of identification of the Cosserat continuum (see Eqs. (4)) is still actual for a lot of heterogeneous materials that are suitable for application of this model [18]. However, even in the simplest case of the elastic isotropic Cosserat continuum, there are rather few reliable results, confirmed by different researchers, concerning determination of model parameters. The further proposed procedure of estimating of macroparameters of the medium, which is based on the method of structural modeling, is intended for solving this problem.

Among velocities of propagation of translational waves in a square lattice consisting of round particles there are three independent quantities—in accordance with number of elasticity constants of the second order (C_{11}, C_{12} and C_{44}) in Lame equations of the classical theory of elasticity for media with cubic symmetry [19]:

$$\rho u_{tt} = C_{11}u_{xx} + C_{44}u_{yy} + (C_{12} + C_{44})\, w_{xy},$$
$$\rho w_{tt} = C_{44}w_{xx} + C_{11}w_{yy} + (C_{12} + C_{44})\, u_{xy}.$$

From comparison of these equations with Eqs. (11), which factors depend on the sizes of the particles, it is possible to receive the following relationships:

$$c_1^2 = \frac{C_{11}}{\rho}, \quad c_2^2 = \frac{2C_{44} - C_{12}}{\rho}, \quad s^2 = \frac{2C_{12}}{\rho}, \quad \beta^2 = \frac{2(C_{44} - C_{12})}{\rho}. \tag{12}$$

It should be noted that the equality $c_2^2 = \beta^2 + s^2/2$ follows both from (12) and from (5). Taking into account that $C_{11} - C_{12} = 2\rho v^2$ [19], where ρ is the density of the medium, v is the transverse wave velocity in the crystallographic direction $\langle 110 \rangle$

$$v^2 = (2c_1^2 - s^2)/4, \tag{13}$$

Equations (12) will be rewritten in the form [20]:

$$C_{11} = \rho c_1^2, \quad C_{12} = \rho(c_1^2 - 2v^2), \quad C_{44} = \rho(c_1^2 + c_2^2 - 2v^2)/2. \tag{14}$$

Formulas (14) show, how to determine effective moduli of elasticity of the nanocrystalline medium using acoustic measurements. Due to equations (12)–(14), it is possible to use freely any set of basis quantities: (c_1, c_2, s), (c_1, c_2, v) or (C_{11}, C_{12}, C_{44}). In particular, starting from known constants of elasticity of the second order, we come to the following expressions of parameters of interparticle interactions:

$$\frac{K_1}{a} = \frac{1}{2+K}\left[C_{11} - C_{12} - 2\,(C_{44} - C_{12})\left(\frac{1}{p} - 1\right)^2\right], \qquad (15)$$
$$\frac{K_2}{a} = (C_{44} - C_{12})\left(1 + \left(\frac{1}{p} - 1\right)^2\right), \quad \frac{K_3}{a} = C_{12},$$

where $K = K_0/K_1$ is the relation between the central and noncentral interactions, $p = h/a = d/a\sqrt{2}$ is the relative size of the particle.

Relations (5) depending on the values of microstructure parameters were analyzed in details in [14] and chap. 3 of monograph [1]. As a result of the analysis, using known experimental data ρ, C_{11}, C_{12} and C_{44} (at normal temperature) [21], the wave velocities c_1,c_2,c_3, parameters β and s, and also modeling parameters of power interactions between particles are calculated for some cubic crystals. The calculations were carried out for $K = 10$ (the central interactions dominate) and $d/a = 0.9$. In this work by means of equalities (15) we will estimate factors of nonlinearities (7) (see Table 1) which dependencies on microstructure parameters K and p, and the elasticity constants of the second order have the following appearance:

$$\begin{aligned}
\rho\alpha_1 &= \frac{1-p}{(1-p)^2+p^2}\,(C_{44} - C_{12}), \quad \rho\alpha_2 = \frac{C_{12}}{4(1-p)},\\
\rho\alpha_3 &= \frac{K(1-p)+1}{(2+K)(1-p)}\left[C_{11} - C_{12} - 2\,(C_{44} - C_{12})\,\frac{(1-p)^2}{p^2}\right]\\
&\quad + (C_{44} - C_{12})\,\frac{(1-p)(1-2p-p^2)}{((1-p)^2+p^2)p^2},\\
\rho\alpha_4 &= \frac{2pC_{12}}{1-p}, \quad \rho\alpha_5 = \frac{p^2C_{12}}{(1-p)^2}, \qquad (16)\\
\rho\alpha_6 &= \frac{1}{2+K}\left[(C_{11} - C_{12})\frac{p^2}{1-p} - 2\,(C_{44} - C_{12})\,(1-p)\right]\\
&\quad + (C_{44} - C_{12})\,\frac{(2p-1)(5p-2p^2-1)}{(1-p)^2+p^2},\\
\rho\alpha_7 &= \frac{2}{2+K}\left[(C_{11} - C_{12})\frac{p}{1-p} - 2\,(C_{44} - C_{12})\,\frac{1-p}{p}\right]\\
&\quad +2\,(C_{44} - C_{12})\,\frac{(5p^2-5p+1)}{p((1-p)^2+p^2)}
\end{aligned}$$

From (16) it follows that, if $p \to 0$, as shown in work [11], the Cauchy relation $C_{12} = C_{44}$ is valid and, as a result

$$\alpha_2 \to \frac{C_{12}}{4\rho}, \quad \alpha_3 \to \frac{K+1}{(2+K)\rho}(C_{11} - C_{12}),$$

Table 1 Structural parameters for crystals with cubic symmetry

Structural parameters		Crystals		
		LiF	NaF	NaBr
Density (kg/m^3)	ρ	2600	2800	3200
Elasticity constants ($10^9\,N/m^2$)	C_{11}	113.00	97.00	32.55
	C_{12}	48.00	25.60	13.14
	C_{44}	63.00	28.00	13.26
Wave velocities (m/s)	c_1	6593	5890	3190
	c_2	5477	3295	2045
	v	3536	3571	1741
	c_3	5659	2896	1092
Coefficient of linear coupling between the longitudinal and transverse deformations (m/s)	s	6076	4276	2866
Dispersion parameter (m/s)	β	3396	1309	274
Parameters of force interactions between the particles ($10^9\,N/m^2$)	K_0/a	46.01	58.19	16.11
	K_1/a	4.601	5.819	1.611
	K_2/a	19.897	3.183	0.159
	K_3/a	48.00	25.60	13.14
Nonlinearity coefficients in the original model ($10^6\,m^2/s^2$)	α_1	16.60	6.87	2.85
	α_2	12.69	6.29	2.82
	α_3	–34.75	0.38	–4.91
	α_4	64.63	32.00	14.37
	α_5	56.65	28.01	12.58
	α_6	62.55	30.92	13.17
	α_7	0.90	6.49	1.73
Nonlinearity coefficients in the two-mode model ($10^6\,m^2/s^2$)	γ_1	10.68	5.29	2.37
	γ_2	–3.98	–1.99	–1.07
	γ_3	–19.56	4.87	–2.49
	γ_4	–18.66	11.36	–0.76
	γ_5	–3.46	–1.71	–0.77
	γ_6	30.83	12.22	5.72
	γ_7	31.72	18.70	7.45

and all the other nonlinearity factors tend to zero. For $p = 1/2$ the Cauchy relation is not valid and

$$\alpha_1 = (C_{44} - C_{12})/\rho, \quad \alpha_2 = C_{12}/2\rho, \quad \alpha_3 = (C_{11} + 2C_{12} - 3C_{44})/\rho,$$
$$\alpha_4 = 2C_{12}/\rho, \quad \alpha_5 = C_{12}/\rho,$$
$$\alpha_6 = \frac{C_{11} + C_{12} - 2C_{44}}{2(2+K)\rho}, \quad \alpha_7 = \frac{C_{11} + 3C_{12} - 4C_{44}}{2(2+K)\rho}.$$

Here α_3 does not depend on the parameter of interparticle interactions $K = K_0/K_1$, and any of nonlinearity coefficients does not tend to zero.

Numerical estimates of the nonlinearity factors presented in Table 1 show that only parameters γ_2 and γ_5 are negative for all considered crystals, whereas factors α_3, γ_3 and γ_4 can be both positive and negative. In the three-mode model, parameter α_4 is the greatest for all considered materials, and parameter γ_7 has maximal values in the two-mode one. For the certain material γ_7 exceeds the smallest absolute value of a factor γ_i up to 11 times, and for parameters α_i this ratio is greater—up to 72 times. Besides, some α_i can even surpass a square of the longitudinal wave velocity, c_1^2, that proves importance of the accounting of the nonlinear terms.

6 Kadomtsev–Petviashvili Evolutionary Equation for the Two-Mode Model

We shall consider propagation of localized strain waves in a medium, depending on parameters of its microstructure. For this purpose, we introduce new coordinates and time $\xi = x - vt$, $\eta = \sqrt{\varepsilon}y$, $\tau = \varepsilon t$; $u = \sqrt{\varepsilon}u$, $w = w$ in Eqs. (11). So, these equations take on the form:

$$\begin{aligned}
&\sqrt{\varepsilon}v^2\frac{\partial^2 u}{\partial\xi^2} - 2\varepsilon\sqrt{\varepsilon}v\frac{\partial^2 u}{\partial\xi\,\partial\tau} - \sqrt{\varepsilon}c_1^2\frac{\partial^2 u}{\partial\xi^2} - (c_2^2 - \frac{\beta^2}{2})\varepsilon\sqrt{\varepsilon}\frac{\partial^2 u}{\partial\eta^2} - (s^2 + \frac{\beta^2}{2})\frac{\partial^2 w}{\partial\xi\,\partial\eta}\sqrt{\varepsilon} \\
&\quad = \frac{R^2}{4}\sqrt{\varepsilon}\frac{\partial}{\partial\eta}\left[v^2\frac{\partial^2}{\partial\xi^2}\left(\varepsilon\frac{\partial u}{\partial\eta} - \frac{\partial w}{\partial\xi}\right) - 2\varepsilon v\frac{\partial^2}{\partial\xi\,\partial\tau}\left(\varepsilon\frac{\partial u}{\partial\eta} - \frac{\partial w}{\partial\xi}\right)\right. \\
&\qquad \left. - c_3^2\left(\frac{\partial^2}{\partial\xi^2} + \varepsilon\frac{\partial^2}{\partial\eta^2}\right)\left(\sqrt{\varepsilon}\frac{\partial u}{\partial\eta} - \frac{\partial w}{\partial\xi}\right)\right] + \frac{1}{2}\frac{\partial H_1}{\partial\xi} + \frac{1}{2}\frac{\partial H_2}{\partial\eta}, \qquad (17) \\
&v^2\frac{\partial^2 w}{\partial\xi^2} - 2\varepsilon v\frac{\partial^2 w}{\partial\xi\,\partial\tau} - \left(c_2^2 - \frac{\beta^2}{2}\right)\frac{\partial^2 w}{\partial\xi^2} - \varepsilon c_1^2\frac{\partial^2 w}{\partial\eta^2} - \left(s^2 + \frac{\beta^2}{2}\right)\varepsilon\frac{\partial^2 u}{\partial\xi\,\partial\eta} \\
&\quad = -\frac{R^2}{4}\frac{\partial}{\partial\xi}\left[v^2\frac{\partial^2}{\partial\xi^2}\left(\varepsilon\frac{\partial u}{\partial\eta} - \frac{\partial w}{\partial\xi}\right) - 2\varepsilon v\left(\varepsilon\frac{\partial u}{\partial\eta} - \frac{\partial w}{\partial\xi}\right)\right. \\
&\qquad \left. - c_3^2\left(\frac{\partial^2}{\partial\xi^2} + \varepsilon\frac{\partial^2}{\partial\eta^2}\right)\left(\sqrt{\varepsilon}\frac{\partial u}{\partial\eta} - \frac{\partial w}{\partial\xi}\right)\right] + \frac{1}{2}\frac{\partial H_3}{\partial\xi} + \frac{1}{2}\frac{\partial H_4}{\partial\eta}.
\end{aligned}$$

As various terms of Eqs. (17) have different orders of smallness, we shall consider some approximations step-by-step.

Approximation of ε^0-order has the form: $\left(v^2 - \left(c_2^2 - \frac{\beta^2}{2}\right)\right)\frac{\partial^2 w}{\partial\xi^2} = 0$, hence,

$$v^2 = c_2^2 - \frac{\beta^2}{2}. \qquad (18)$$

Approximation of $\sqrt{\varepsilon}$-order: $(v^2 - c_1^2)\dfrac{\partial^2 u}{\partial \xi^2} - \left(s^2 + \dfrac{\beta^2}{2}\right)\dfrac{\partial^2 w}{\partial \xi\, \partial \eta} = 0$, therefore,

$$\frac{\partial u}{\partial \xi} = \frac{s^2 + \beta^2/2}{v^2 - c_1^2}\frac{\partial w}{\partial \eta}. \tag{19}$$

Approximation of ε-order:

$$\begin{aligned} &-2\varepsilon v\frac{\partial^2 w}{\partial \xi\, \partial \tau} - \varepsilon c_1^2\frac{\partial^2 w}{\partial \eta^2} - \left(s^2 + \frac{\beta^2}{2}\right)\varepsilon\frac{\partial^2 u}{\partial \xi\, \partial \eta} \\ &= -\frac{R^2}{4}\frac{\partial}{\partial \xi}\left[v^2\frac{\partial^2}{\partial \xi^2}\left(\varepsilon\frac{\partial u}{\partial \eta}\right) - 2\varepsilon v\left(-\frac{\partial w}{\partial \xi}\right)\right. \\ &\left. - c_3^2\left(\varepsilon\frac{\partial^2}{\partial \eta^2}\right)\left(-\frac{\partial w}{\partial \xi}\right)\right] + 3\gamma_1\frac{\partial w}{\partial \xi}\frac{\partial^2 w}{\partial \xi^2}. \end{aligned} \tag{20}$$

After entering the designation $\dfrac{\partial w}{\partial \xi} = U$ in Eq. (20) and taking into account expressions (18) and (19), Eq. (20) is reduced to the following equation:

$$2vU_{\xi\tau} + q_1(U^2)_{\xi\xi} + \frac{R^2}{4}q_2U_{\xi\xi\xi\xi} + q_3U_{\eta\eta} = 0, \tag{21}$$

where

$$\frac{3\gamma_1}{2\varepsilon} = q_1,\ \frac{2c_2^2 - 2c_3^2 - \beta^2}{2\varepsilon} = q_2,\ c_1^2 + \frac{(2s^2 + \beta^2)^2}{4(c_2^2 - c_1^2) - 2\beta^2} = q_3. \tag{22}$$

We will introduce designations: $U/U_0 = W$, $\xi/\xi_0 = X$, $\tau/\tau_0 = T$, $\eta/\eta_0 = Y$. If to put $U_0 = 1$ and $\eta_0 = \xi_0$, then $W = U$ and, in terms of new variables, Eq. (22) yields:

$$2\frac{\partial^2 U}{\partial X\, \partial T} + \frac{q_1}{v}\frac{\tau_0}{\xi_0}\frac{\partial^2 (U^2)}{\partial X^2} + \frac{R^2}{4v}q_2\frac{\tau_0}{\xi_0^3}\frac{\partial^4 U}{\partial X^4} + q_3\frac{\tau_0}{v\xi_0}\frac{\partial^2 U}{\partial Y^2} = 0. \tag{23}$$

We choose scales ξ_0 and τ_0 so, that the last coefficient in Eq. (23) would be equal to 1:

$$\frac{\tau_0}{\xi_0} = \frac{v}{q_3}.$$

If to take in this relation $\xi_0 = R/2$, then Eq. (23) is transformed into well-known Kadomtsev–Petviashvili equation

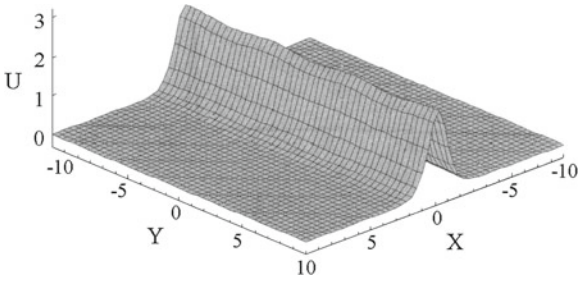

Fig. 3 The plane localized strain wave [22]

$$2\frac{\partial^2 U}{\partial X\,\partial T}+\frac{q_1}{q_3}\frac{\partial^2(U^2)}{\partial X^2}+\frac{q_2}{q_3}\frac{\partial^4 U}{\partial X^4}+\frac{\partial^2 U}{\partial Y^2}=0. \tag{24}$$

This equation has a solution in the form of a plane solitary strain wave (soliton) (Fig. 3):

$$U(\theta)=A_s\,\mathrm{ch}^{-2}(\theta/\Delta), \tag{25}$$

where $\theta = X - kY - VT$ is the wave phase. The amplitude of soliton, A_s, and its width Δ are determined by relations:

$$A_s=\left|\frac{3q_3(k^2-2V)}{2q_1}\right|, \tag{26}$$

$$\Delta=2\sqrt{\left|\frac{q_2}{q_3(k^2-2V)}\right|}.$$

It should be noted that product

$$A_s\Delta^2=\left|\frac{6q_2}{q_1}\right|=\left|\frac{2c_2^2-2c_3^2-\beta^2}{\gamma_1}\right|$$

is the constant for each material.

The plane solitary wave (25) is known to be stable, if $q_2/q_3 > 0$, and it is unstable with respect to transverse perturbations, when $q_2/q_3 < 0$ [22]. In this case, Kadomtsev–Petviashvili equation has an other precise solution [23]:

$$U(X,Y,T)=\frac{6q_2}{q_1}\frac{\partial^2}{\partial X^2}\ln\left[1+\exp(2q\theta)+\exp(2p(\theta+\psi)\right. \\ \left.+\,A\exp((q+p)\theta+p\psi)\cos kY\right]. \tag{27}$$

Here p and q are integration constants,

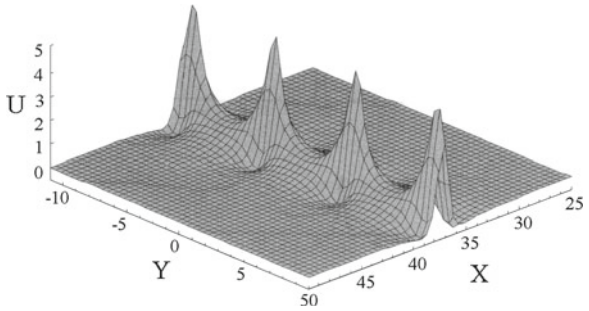

Fig. 4 The plane wave modulated in the transverse direction [22]

$$\theta = X - (1 + \frac{2q_2}{q_3}q^2)T, \quad \psi = -4p\frac{q_2}{q_3}(p^2 - q^2)T,$$
$$A = \frac{4\sqrt{pq}}{p+q}, \quad k = (q^2 - p^2)\sqrt{\frac{-3q_2}{q_3}}.$$

Formula (27) describes a periodic chain of two-dimensional solitary strain waves (Fig. 4). If $q_2/q_3 < 0$, i.e. the condition of soliton instability with respect to transverse perturbations takes place, the plane solitary wave (25) plotted in Fig. 3 will be transformed into Eq. (27). Polarity of solitons (25) and (27) depends on sign of expression q_1/q_2. The solitons have a positive polarity (this case is represented in Figs. 3 and 4), when $q_1/q_2 > 0$, and their polarity is negative, if $q_1/q_2 < 0$.

Let us analyze obtained from (27) dependencies of coefficients q_1/q_2 and q_2/q_3 on the macroparameters of the medium:

$$\frac{q_1}{q_2} = \frac{3\gamma_1}{2c_2^2 - 2c_3^2 - \beta^2}, \tag{28}$$

$$\frac{q_2}{q_3} = \frac{(2c_2^2 - 2c_3^2 - \beta^2)(2c_2^2 - 2c_1^2 - \beta^2)}{\varepsilon(2c_1^2(2c_2^2 - \beta^2) - 4c_1^4 + (2s^2 + \beta^2)^2)}. \tag{29}$$

From (10) and (7) follows that

$$\gamma_1 = \alpha_2 + \frac{\alpha_5 - \alpha_4}{4} = \frac{K_3}{M}\left(\frac{a^3}{4(a-h)} + \frac{a^2h^2}{4(a-h)^2} - \frac{a^2h}{2(a-h)}\right)$$
$$= \frac{K_3a^2(a^2 - 3ah + 3h^2)}{4M(a-h)^2} > 0.$$

Thus, $q_1/q_2 > 0$ for $c_2^2 > c_3^2 + \beta^2/2$, and $q_1/q_2 < 0$ for $c_2^2 < c_3^2 + \beta^2/2$.

Table 2 Existence of stable plane solitons of deformations and their polarity in some cubic crystals

Crystal	LiF	NaF	NaBr
Sign of q_2/q_3	+	+	−
Sign of q_1/q_2	−	+	+
Stable solitons of plane deformation and their polarity			no

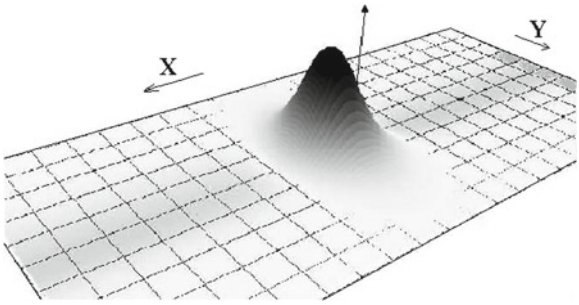

Fig. 5 A 2D soliton without plane front ($T = 0$)

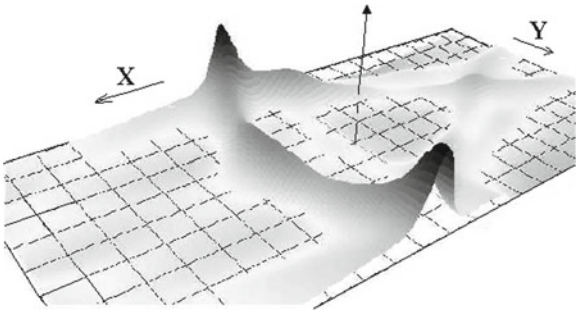

Fig. 6 Spreading of the 2D soliton ($T = 5$)

According to the data presented in Table 1, we will determine signs of expressions q_1/q_2 and q_2/q_3. Existence and polarity of steady plane solitons of deformations for the media with such parameters as for cubic crystals of LiF, NaF, and NaBr depend on signs of these expressions and are presented in Table 2.

If to take as an initial condition for Kadomtsev–Petviashvili equation a 2D soliton without plane front (Fig. 5), i.e. perturbation in the form

$$U_0(X, Y) = 12\mathrm{sech}^2\left(\frac{X - 32}{4}\right)\mathrm{sech}(Y - 8), \tag{30}$$

and to carry out numerical simulation by means of the semi-implicit pseudo-spectral scheme [24] with parameters: 256×64 is dimension of a grid, $\Delta X = 0.25$ is a length of a step along X-axis, $\Delta Y = 0.25$ is a length of a step along Y-axis, $\Delta T = 0.003$ is a length of a step along T-axis, then an other behavior of the solitary wave will

be observed. In fact, the peak of excitations (30) moves forward (along X-axis) and simultaneously spreads along Y-axis. Eventually, the amplitude of excitation grows till a certain value ($A = 7.1$) near the boundaries, spreading aside and moving forward, that leads to appearance of the crosswise structures (Fig. 6).

7 Conclusions

The nonlinear mathematical model of the two-dimensional crystalline (granular) medium with a non-dense packing of the particles possessing two translational and one rotational degrees of freedom, has been elaborated in this work. In the field of low frequencies the obtained set of equations is reduced to the two-mode set, linear parts of which equations coincide with a two-dimensional analog of the classical Lame equations for media with cubic symmetry. But even in this case, the effect of the medium microstructure is still left in the form of the relationship between the macroscopic characteristic parameters of the medium and the micromodel parameters.

Analytical dependencies of the elastic and rotational wave velocities and the nonlinearity factors on the sizes of particles and the parameters of interactions between them have been found. The velocities of elastic waves along the various crystallographic directions can be measured experimentally without any difficulties, but it is rather complicated or even, sometimes, impossible to determine from experiments the rotational wave velocity, the threshold frequency of this wave and the factors of nonlinear interactions between the waves of various types. For this reason, the estimates of these quantities can be very useful that are obtained by the following way. First, due to obtained expressions (5) for the experimentally measured velocities of elastic waves depending on the microstructure parameters of the material, inverse relationships (15) are derived, and then they are used for calculation of other macroparameters of the medium. In this work, by such a way the factors of nonlinear interactions of complete three-mode set (7) and two-mode model of the medium with the restricted rotation of particles (10) are calculated. Some of these factors are shown to be negative, whereas the other ones can exceed a square of the longitudinal wave velocity.

In its turn, the two-mode system is reduced by the multi-scale method to Kadomtsev–Petviashvili evolutionary equation with respect to shear deformation, which has a solution in the form of plane soliton. Due to the method of structural modeling used in this work, it is shown that in the crystal medium with parameters as for NaBr, the plane soliton is unstable with respect to two-dimensional perturbations, in NaF-crystal the soliton has a positive polarity, and in LiF-crystal it has a negative polarity.

Acknowledgments The research was carried out under the financial support of the RFBR (grants Nr. 12-08-90032-Bel-a, 10-08-01108-a).

References

1. Potapov, A.I. (ed.): Introduction to Micro- and Nanomechanics: Mathematical Models and Methods. Nizhny Novgorod Technical State University (2010) (in Russian)
2. Miller, R.E., Shenoy, V.B.: Size-dependent elastic properties of nanosized structural elements. Nanotechnology **11**(3), 139–147 (2000)
3. Lauke, B.: On the effect of particle size on fracture toughness of polymer composites. Compos. Sci. Technol. **68**, 3365–3372 (2008)
4. Maksimov, E.G., Zinenko, V.I., Zamkova, N.G.: Ab initio calculations of the physical properties of ionic crystals. Phys. Usp. **47**, 1075–1099 (2004)
5. Eringen, A.C.: Microcontinuum Field Theories-1: Foundation and Solids. Springer, New York (1999)
6. Lisina, S.A., Potapov, A.I.: Generalized continuum models in nanomechanics. Doklady Phys. **53**(5), 275–277 (2008)
7. Cosserat, E., Cosserat, F.: Theorie des Corps Deformables. Librairie Scientifique A, Hermann et Fils, Paris (1909, Reprint, 2009)
8. Maugin, G.A., Metrikine, A.V. (eds.): Mechanics of Generalized Continua: One Hundred Years After the Cosserats. Springer, New York (2010)
9. Altenbach, H., Maugin, G.A., Erofeev, V.I. (eds.): Mechanics of Generalized Continua. Springer, Berlin, Heidelberg (2011)
10. Li, C., Chou, T.-W.: A structural mechanics approach for the analysis of carbon nanotubes. Int. J. Solids Struct. **40**, 2487–2499 (2003)
11. Pavlov, I.S., Potapov, A.I., Maugin, G.A.: A 2D granular medium with rotating particles. Int. J. Solids Struct. **43**(20), 6194–6207 (2006)
12. Pavlov, I.S., Potapov, A.I.: Structural models in mechanics of nanocrystalline media. Doklady Phys. **53**(7), 408–412 (2008)
13. Erofeyev, V.I.: Wave Processes in Solids with Microstructure. World Scientific Publishing, New Jersey (2003)
14. Potapov, A.I., Pavlov, I.S., Lisina, S.A.: Acoustic identification of nanocrystalline media. J. Sound Vib. **322**(3), 564–580 (2009)
15. Born, M., Kun, H.: Dynamical Theory of Crystal Lattices. Clarendon Press, Oxford (1954)
16. Gross, E., Korshunov, A.: Rotational oscillations of molecules in a crystal lattice of organic substances and scattering spectra. J. Exp. Theor. Phys. **16**(1), 53–59 (1946) (in Russian)
17. Vardoulakis, I., Sulem, J.: Bifurcation Analysis in Geomechanics. Blackie Academic and Professional, London (1995)
18. Pelevin, A., Lauke, B., Heinrich, G., Svistkov, A., Adamov, A.A.: Algorithm of constant definition for a visco-elastic rubber model based cyclic experiments, stress relaxation and creep data. In: Heinrich, G., Kaliske, M., Lion, A., Reese, S. (eds.) Constitutive Models for Rubber, vol. 1. CRC Press, Boca Raton (2009)
19. Tucker, J.W., Rampton, V.W.: Microwave Ultrasonics in Solid State Physics. North-Holland Publishing Company, Amsterdam (1972)
20. Pavlov, I.S.: Acoustic identification of the anisotropic nanocrystalline medium with non-dense packing of particles. Acoust. Phys. **56**(6), 924–934 (2010)
21. Frantsevich, I.N., Voronov, F.F., Bakuta, S.A.: Elastic Constants and Elasticity Moduli of Metals and Nonmetals. Reference Book Frantsevich, I.N. (ed.) Naukova Dumka, Kiev (1982) (in Russian)
22. Porubov, A.V.: Amplification of Nonlinear Strain Waves in Solids. World Scientific, Singapore (2003)
23. Pelinovsky, D.E., Stepanyants, YuA: Self-focusing instability of plane solitons and chains of two-dimensional solitons in positive-dispersion media. J. Exp. Theor. Phys. **77**(4), 602–609 (1993)
24. Press, W.H., Teukolsky, S.L., Vetterling, W.T., Flannery, B.P.: Numerical Recipes in C. The Art of Scientific Computing. Cambridge University Press, Cambridge (1992)

Cosserat Anisotropic Models of Trabecular Bone from the Homogenization of the Trabecular Structure: 2D and 3D Frameworks

Ibrahim Goda, Mohamed Assidi and Jean-Francois Ganghoffer

Abstract Cosserat models of trabecular bone are constructed in 2D and 3D situations, based on micromechanical approaches to investigate microstructure-related scale effects on the macroscopic properties of bone. The effective mechanical properties of cancellous bones considered as cellular solids are obtained thanks to the discrete homogenization technique. The cell walls of the bone microstructure are modeled as Timoshenko thick beams. An anisotropic micropolar equivalent continuum model is constructed, the effective mechanical properties of which are identified. Closed form expressions of the equivalent properties are obtained versus the geometrical and mechanical microparameters, accounting for the effects of bending, axial, and transverse shear deformations; torsion is additionally considered for a 3D geometry. The classical and micropolar effective moduli and the internal flexural and torsional lengths are identified versus the micropolar material constants. The stress distribution in a cracked bone sample is computed based on the effective micropolar model, highlighting the regularizing effect of the Cosserat continuum in comparison to a classical elasticity continuum model.

I. Goda · J. Ganghoffer (✉)
LEMTA, Université de Lorraine. 2, Avenue de la Forêt de Haye,
54504 Vandœuvre-lès-Nancy Cedex, France
e-mail: jean-francois.Ganghoffer@univ-lorraine.fr

I. Goda
e-mail: ibrahim.goda@ensem.inpl-nancy.fr

M. Assidi
Center de Recherche Public Henri Tudor. 29, Avenue John F. Kennedy,
L-1885Luxembourg-Kirchberg, Luxembourg
e-mail: mohamed.assidi@tudor.lu

H. Altenbach et al. (eds.), *Generalized Continua as Models for Materials*,
Advanced Structured Materials 22, DOI: 10.1007/978-3-642-36394-8_7,

1 Introduction

There are two major forms of bone tissue at the macroscopic level, *compact* or *cortical* bone, and *cancellous* or *trabecular* bone. The location of these bone types in the femur is illustrated in Fig. 1; cortical or compact bone is a dense material with a specific gravity of almost two in humans and sligthly over two in cattle; it forms most of the outer shell of a whole bone, a shell of variable thickness.
In mechanical terms, bone is a complex hierarchical material in which different geometrical features occur over several length scales that can be classified as follows: a) The nanoscale represents a single fiber and crystals, b) the microscale represents the random network of trabecular bone composed of random struts or plates), and c) the macroscale represents the whole bone, which includes both trabecular (porous) and cortical (solid) bone types. These structural levels are illustrated on Fig. 2.
Cancellous bone generally exists only within the confines of the cortical bone coverings; it is also called trabecular bone because it is composed of short struts of bone material called trabeculae. The connected trabeculae give cancellous bone a spongy

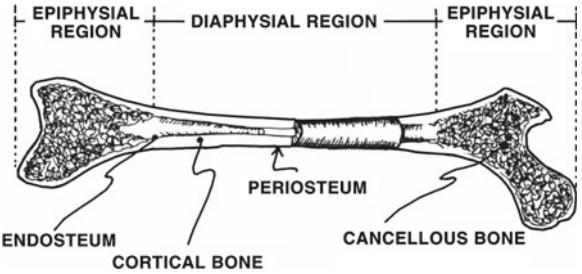

Fig. 1 Longitudinal section of the femur illustrating cancellous and cortical bone types [7]

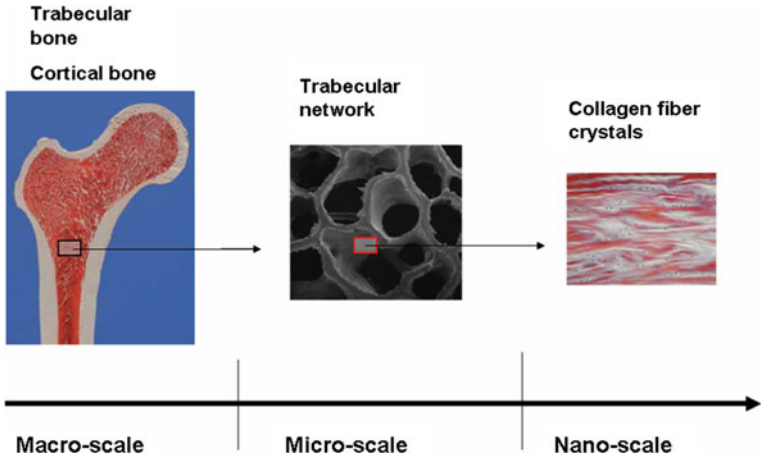

Fig. 2 Multi-scale aspects of bone structure [14]

appearance, and it is consequently often called spongy bone. Trabecular bone is very complex due to its randomness and spatial heterogeneity. In order to simplify the forthcoming analysis, one can choose to represent bone as having an idealized periodic microstructure: in this contribution, we model bone as having a periodic prismatic structure in a two dimensional context. This work addresses the modeling of trabecular bone as hexagonal periodic structures, considering successively 2D and 3D geometries.

Bone is a strongly heterogeneous material with microstructural features, requiring generalized continuum mechanics theories when the macroscopic length scale (identified as the smallest length scale of the deformation pattern) becomes comparable or smaller than the typical microstructural length scale, such as the size of trabeculae in cancellous bone. Especially, the classical assumption inherent to classical elasticity is no more valid under such conditions, which occur in zones of high stress and strain gradients, for instance in the vicinity of cracks or within a bone prosthesis region. Although there have been many continuum models of bone developed over the last two decades on the basis of classical elasticity [3, 44], those models ignore microstructure-related scale effects on the macroscopic mechanical properties. Consequently, they do not provide a complete description of the mechanical behavior when the microstructural size of bone approaches the macroscopic length scale. Such microstructural effects are most pronounced near bone–implant interfaces and in areas of high strain gradients. This issue is presently investigated by studying generalized continuum mechanics theories which account for the influence of microstructure-related scale effects on the macroscopic properties of bone.

In the class of micropolar models developed in this contribution, independent rotational degrees of freedom are considered in addition to the translational degrees of freedom (the displacement vector), in the form of a microrotation vector field. This entails that the material can transmit couple stresses in addition to tractions; those couple stresses develop internal work in the variation of microcurvatures, defined as the spatial gradients of the microrotation, a second order tensor. From a historical perspective, the Cosserat Brothers, who introduced the concept bearing their name [6], developed the theory of non-symmetric elasticity, and further developments emerged in the sixties [11, 31, 32]. Based on the generalized continuum theory established by the Cosserat brothers about 100 years ago, a general theory of Cosserat continuum coined the micropolar theory was formulated in [10–13], adequate for materials possessing microstructures, such as bones, but also for granular composites, amorphous metals/ceramics, polymers. This theory can well explain the discrepancies between experiments and the classical theory of elasticity in cases when the effects of material microstructures are known to contribute significantly to the body's overall deformation, for example, in materials with a granular microstructure such as human bones [24, 26, 40]. A special case of Cosserat theory is the *couple-stress* theory, in which the microrotation and macrorotation coincide, [23]. Micropolar theory assumes that the interaction between continuum particles through a surface element $\mathbf{dA}$occurs not only through a force vector ($\mathbf{F}_i\mathbf{dA}$) but also through a moment vector ($\mathbf{M}_i\mathbf{dA}$). This establishes the "force-stress" tensor expressed as force per unit area, $\boldsymbol{\sigma}_{ij}$, and the "couple-stress" tensor expressed as moment per unit area, $\mathbf{m}_{ij}$, from the

Euler- Cauchy equilibrium principle. In terms of kinematics, material particles have additional rotational degrees of freedom φ_i allowing to better capture the behavior of heterogeneous materials like bone, which have microstructural dimensions comparable to the size of specimen.

The existence of couple stress has been first evidenced by Yang and Lakes (1981), who measured the effect of the size of a bone specimen on the apparent stiffness of cortical bone in quasi-static torsion; they further obtained the characteristic length scales for torsion and bending for cortical bone in the context of couple stress theory. As an example, bone trabeculae are modelled as isotropic micropolar materials in [25]. Lakes and co-workers conducted a series of experiments on bone and other cellular materials, in which they observed a stiffening effect in such materials in bending and in torsion [36](Lakes, 1987) and a tougher notched bone [24] than expected from classical Cauchy-type elasticity. Those last authors found that Cosserat elasticity provides better predictions of the response of bone than classical elasticity theory. [43] represented the trabeculae as beam elements in a lattice structure in which the lattice elements are rigidly interconnected to each other, for the purpose of bone remodeling. The microstructure was then embedded in the continuum in the context of the couple stress theory. The issue of application of higher-order continuum theories to mechanical analysis of bone (both cortical and cancellous) has further been addressed by [15], who analysed a simplified two-dimensional bone-prosthesis configuration using a micropolar-based FE formulation. The stress and strain intensities they calculated at the bone-prosthesis interface are different from those predicted by classical elasticity. In addition, [16] identified the micropolar elastic constants of cancellous bone in the context of micromechanical analyses. In this approach, it is assumed that at the microscopic level the bone tissue is an isotropic, Cauchy-type elastic material, whereas cancellous bone behaves as a homogeneous, anisotropic micropolar-type continuum at the macroscopic level. The effective elastic constants for the micropolar continuum were determined from the response of a bone specimen, whose microstructure was obtained from micro-CT scans.

This work focuses on the modeling of the micropolar elastic response of trabecular bone using 2D and 3D geometric models successivly.

2 Two-Dimensional Anisotropic Cosserat Bone Model from Lattice Homogenization

We adopt the viewpoint of trabecular bone as a cellular solid consisting of a quasi periodical lattice of cells having an hexagonal topology, the cell walls being modeled as thick beams. The characteristics of many periodic cellular structures are discussed in detail in the well-known contribution of [20], wherein the equivalent mechanical properties of honeycomb lattices are derived by analyzing strain and stress states in unit cells through the application (in most cases) of beam theory. Taking bending as the sole deformation mechanism, [19] derived the in-plane elastic constants for regular honeycombs with cell walls of uniform thickness; their normalized results

are consequently independent of the honeycomb relative density. Taking bending and stretching as the main deformation mechanisms, [46] also developed a model to study the in-plane elastic properties of honeycombs. Considering the transverse shear as an additional deformation mechanism, [41, 49] obtained the closed form in-plane elastic constants of regular honeycombs. Taking bending, stretching and hinging the deformation mechanisms, [28] theoretically analyzed the in-plane elastic constants of honeycombs. The normalized in-plane elastic constants of honeycombs generally depend on the honeycomb relative density [41, 49, 50], because the axial stretching/compression and transverse shear play an important role in the deformation.
A two-dimensional micropolar continuum model equivalent to the initial lattice is next constructed relying on discrete homogenization, and its mechanical properties are identified versus the microbeams geometry and mechanical behavior.

2.1 Discrete Homogenization of Bone Microstructure

The adopted beam model includes transverse shear, which is necessary for thick beams. In a local coordinate systems attached to each beam element, the normal (tension) force adopts the expression

$$N^b = \frac{AE_s}{L}\left(\mathbf{e}^b.\left(\mathbf{u}_E - \mathbf{u}_O\right)\right) \tag{1}$$

The transverse force is given by

$$T_t^b = \frac{12E_sI_z}{L^3(1+\Phi_y)}\left(\mathbf{e}^{b\perp}.\left(\mathbf{u}_E - \mathbf{u}_O\right) - \frac{L}{2}\left(\phi_O + \phi_E\right)\right) \tag{2}$$

The moments at both extremities of the beam are expressed as:

$$\begin{aligned} M^{O(b)} &= \frac{6E_sI_z}{L^2(1+\Phi_y)}\left(-\mathbf{e}^{b\perp}.\left(\mathbf{u}_\mathrm{E} - \mathbf{u}_\mathrm{O}\right)\right) \\ &\quad + \frac{E_sI_z}{L(1+\Phi_y)}\left((4+\Phi_y)\phi_O + (2-\Phi_y)\phi_E\right) \\ M^{E(b)} &= \frac{6E_sI_z}{L^2(1+\Phi_y)}\left(-\mathbf{e}^{b\perp}.\left(\mathbf{u}_\mathrm{E} - \mathbf{u}_\mathrm{O}\right)\right) \\ &\quad + \frac{E_sI_z}{L(1+\Phi_y)}\left((2-\Phi_y)\phi_O + (4+\Phi_y)\phi_E\right) \end{aligned} \tag{3}$$

with the non-dimensional factor $\Phi_y = 12E_sI_z/G_s\kappa_sL^2$ vanishing when transverse shear is neglected, $\mathbf{e}^b$ the unit director for each beam, and $\mathbf{e}^{b\perp}$ the transverse unit vector.
The coefficients E_s, G_s are respectively the young's modulus and shear modulus of the beam material, A, L are respectively, the cross-sectional area and the length of

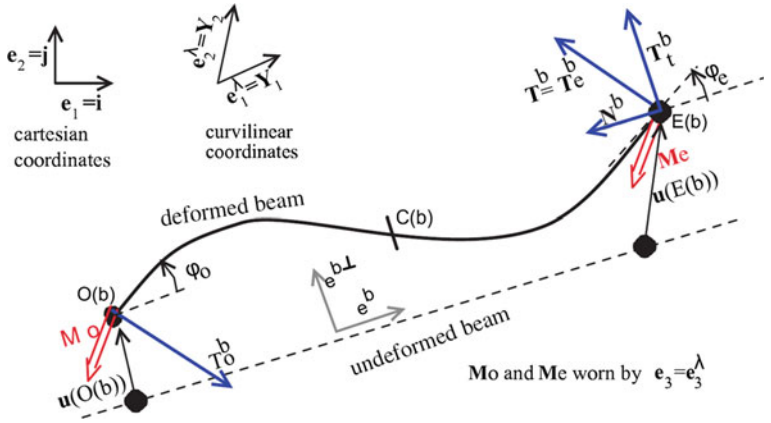

Fig. 3 Kinematic and static parameters of a beam element

the beam, I_z is the second moment of area of the beam cross-section, and κ_s is the shear correction factor.

Those expressions of the resultant forces and moments are next involved in the homogenization of the initially discrete lattice towards an equivalent continuum.

The discrete homogenization method is a mathematical technique to derive the equivalent continuous medium behaviour of repetitive discrete structures. This technique is inspired from the homogenization of periodic media developed thirties years ago by [1, 35, 39] and more recently applied by Warren and Byskhov (2002) and [33]. It has also been combined with the energy method by [38] and applied to discrete homogenization. Note that Cosserat models and micropolar type theories have been obtained from discrete particle models, for instance by [5, 34, 42].

The kinematic and static variables for any beam in the lattice are represented in the local coordinate system associated to the Timoshenko beam element in Fig. 3.

The discrete homogenization method consists in assuming asymptotic series expansions of both the node displacements, tension, moments and external forces versus a small parameter labelled ε, defined as the ratio of a characteristic length of the basic cell to a characteristic length of the lattice structure. Those expansions are then inserted into the equilibrium equation, conveniently expressed in weak form. The balance equation of the nodes, forces-displacement relations and the moment-rotation relations of the beams are developed by inserting those series expansions and by using Taylor's expansion of finite differences. The discrete sums are finally converted in the limit of a continuous density of beams into Riemann integrals, thereby highlighting continuous stress and strain measures. The calculations may be done for a quite general truss and closed form expressions of the effective (homogenized) properties are obtained from the effective compliance of rigidity matrix. The method has given rise to implementation into dedicated software. It has been recently applied to calculate the equivalent mechanical properties of auxetic lattices giving rise to negative Poisson's ratio [9].

The displacement difference $\Delta \mathrm{U}^{\mathrm{b}\varepsilon}$ between the extremity and origin node of each beam is expressed by a Taylor series development as

$$\begin{aligned}\Delta \mathrm{U}^{\mathrm{b}\varepsilon} = \mathrm{u}^{\varepsilon}(E(b)) - \mathrm{u}^{\varepsilon}(O(b)) &= \varepsilon\left(\mathrm{u}_1^{E_{R(b)}}\left(\lambda^{\varepsilon}\right) - \mathrm{u}_1^{O_{R(b)}}\left(\lambda^{\varepsilon}\right) + \frac{\partial \mathrm{u}_0\left(\lambda^{\varepsilon}\right)}{\partial \lambda^i}\delta^{ib}\right) \\ &\quad + \varepsilon^2\left(\mathrm{u}_2^{E_{R(b)}}\left(\lambda^{\varepsilon}\right) - \mathrm{u}_2^{O_{R(b)}}\left(\lambda^{\varepsilon}\right)\right) \\ &= \varepsilon \Delta \mathrm{U}_1^{\mathrm{b}} + \varepsilon^2 \Delta \mathrm{U}_2^{\mathrm{b}} \end{aligned} \tag{4}$$

with δ^i the shift factor for nodes belonging to a neighboring cell and λ the curvilinear coordinate of the points within the lattice.
The asymptotic expansion of nodal microrotation $\phi^{\varepsilon n}$ is limited to the first order in ε; it is defined successively at the origin and extremity of each beam as

$$\phi^{O(b)\varepsilon} = \phi_0^{O_{R(b)}} + \varepsilon \phi_1^{O_{R(b)}}; \qquad \phi^{E(b)\varepsilon} = \phi_0^{E_{R(b)}} + \varepsilon\left(\frac{\partial \phi_0}{\partial \lambda^i}\delta^{ib} + \phi_1^{E_{R(b)}}\right) \tag{5}$$

The expressions of the asymptotic expansions of the normal and transverse efforts, and the moment at the beam extremities based on a Timoshenko beam model versus the kinematic nodal variables are successively written as

$$N^{b\varepsilon} = E_s \eta\left(\mathbf{e}^b.\left(\varepsilon \Delta \mathrm{U}_1^{\mathrm{b}} + \varepsilon^2 \Delta \mathrm{U}_2^{\mathrm{b}}\right)\right) = \varepsilon N_1^b + \varepsilon^2 N_2^b \tag{6}$$

with the first and second order relative displacement given in (7.4).
The transverse force is expressed similarly as

$$\begin{aligned} T_t^{b\varepsilon} &= \frac{E_s \eta^3}{\left(1 + \frac{E_s \eta^2}{(G_s \kappa_s)}\right)}\left(\mathbf{e}^{b\perp}.\left(\varepsilon \Delta \mathrm{U}_1^{\mathrm{b}} + \varepsilon^2 \Delta \mathrm{U}_2^{\mathrm{b}}\right)\right. \\ &\quad \left. - \varepsilon \frac{L^b}{2}\left(\phi_0^{O_{R(b)}} + \phi_0^{E_{R(b)}} + \varepsilon\left(\phi_1^{O_{R(b)}} + \phi_1^{E_{R(b)}} + \frac{\partial \phi_0}{\partial \lambda^i}\delta^{ib}\right)\right)\right) \\ &= \varepsilon T_{t1}^b + \varepsilon^2 T_{t2}^b \end{aligned} \tag{7}$$

and the moments are expressed at both ends on two orders versus ε as:

$$\mathbf{M}^{O(b)\varepsilon} = \varepsilon^2 M_1^{O(b)} + \varepsilon^3 M_2^{O(b)}; \quad \mathbf{M}^{E(b)\varepsilon} = \varepsilon^2 M_1^{E(b)} + \varepsilon^3 M_2^{E(b)} \tag{8}$$

with

$$\begin{aligned} M_1^{O(b)} &= \frac{E_s \eta^3 L^b}{2\left(1 + \frac{E_s \eta^2}{(G_s \kappa_s)}\right)}\left(-\mathbf{e}^{b\perp}.\Delta \mathrm{U}_1^{\mathrm{b}}\right) + \frac{E_s \eta^3 \left(L^b\right)^2}{12\left(1 + \frac{E_s \eta^2}{(G_s \kappa_s)}\right)} \\ &\quad \left(\left(4 + \frac{E_s \eta^2}{(G_s \kappa_s)}\right)\phi_0^{O_{R(b)}} + \left(2 - \frac{E_s \eta^2}{(G_s \kappa_s)}\right)\phi_0^{E_{R(b)}}\right) \end{aligned}$$

$$M_2^{O(b)} = \frac{E_s\eta^3 L^b}{2\left(1+\frac{E_s\eta^2}{(G_s\kappa_s)}\right)}\left(-\mathbf{e}^{b\perp}.\Delta \mathrm{U}_2^{\mathrm{b}}\right)+\frac{E_s\eta^3\left(L^b\right)^2}{12\left(1+\frac{E_s\eta^2}{(G_s\kappa_s)}\right)}\left(\left(4+\frac{E_s\eta^2}{(G_s\kappa_s)}\right)\phi_1^{O_{R(b)}}\right.$$
$$\left.+\left(2-\frac{E_s\eta^2}{(G_s\kappa_s)}\right)\phi_1^{E_{R(b)}}+\left(2-\frac{E_s\eta^2}{(G_s\kappa_s)}\right)\frac{\partial\phi_0}{\partial\lambda^i}\delta^{ib}\right) \tag{9}$$

$$M_1^{E(b)} = \frac{E_s\eta^3 L^b}{2\left(1+\frac{E_s\eta^2}{(G_s\kappa_s)}\right)}\left(-\mathbf{e}^{b\perp}.\Delta \mathrm{U}_1^{\mathrm{b}}\right)+\frac{E_s\eta^3\left(L^b\right)^2}{12\left(1+\frac{E_s\eta^2}{(G_s\kappa_s)}\right)}$$
$$\left(\left(2-\frac{E_s\eta^2}{(G_s\kappa_s)}\right)\phi_0^{O_{R(b)}}+\left(4+\frac{E_s\eta^2}{(G_s\kappa_s)}\right)\phi_0^{E_{R(b)}}\right)$$

$$M_2^{E(b)} = \frac{E_s\eta^3 L^b}{2\left(1+\frac{E_s\eta^2}{(G_s\kappa_s)}\right)}\left(-\mathbf{e}^{b\perp}.\Delta \mathrm{U}_2^{\mathrm{b}}\right)+\frac{E_s\eta^3\left(L^b\right)^2}{12\left(1+\frac{E_s\eta^2}{(G_s\kappa_s)}\right)}\left(\left(2-\frac{E_s\eta^2}{(G_s\kappa_s)}\right)\phi_1^{O_{R(b)}}\right.$$
$$\left.+\left(4+\frac{E_s\eta^2}{(G_s\kappa_s)}\right)\phi_1^{E_{R(b)}}+\left(4+\frac{E_s\eta^2}{(G_s\kappa_s)}\right)\frac{\partial\phi_0}{\partial\lambda^i}\delta^{ib}\right)$$

The constitutive behavior of the equivalent anisotropic micropolar continuum is obtained in the present 2D context in matrix format as

$$\begin{Bmatrix}\sigma_x\\ \sigma_y\\ \sigma_{xy}\\ \sigma_{yx}\\ m_{xz}\\ m_{yz}\end{Bmatrix} = \begin{bmatrix}[\mathbf{A}] & [\mathbf{B}]\\ [\mathbf{C}] & [\mathbf{D}]\end{bmatrix}\begin{Bmatrix}\epsilon_x\\ \epsilon_y\\ \epsilon_{xy}\\ \epsilon_{yx}\\ \kappa_{xz}\\ \kappa_{yz}\end{Bmatrix} \tag{10}$$

This constitutive law can further be simplified basing on symmetry properties of the studied lattices: it has indeed been shown that for centro-symmetrical lattices, the pseudo-tensors [**B**] and [**C**] vanish [9]. Focusing herewith on such lattices, the previous constitutive equation then implies that the vectors μ_1^{i} and $\mathrm{S}_2^{\mathrm{i}}$ should vanish; this leads to an important simplification of the stress and couple stress vectors

$$\mathrm{S}^{\mathrm{i}} = \mathrm{S}_1^i = \sum_{b\in B_R}\left(\left(\mathrm{E}_s\eta\left(\mathbf{e}^b.\Delta \mathrm{U}_1^{\mathrm{b}}\right)\mathbf{e}^b+\left(\frac{E_s\eta^3}{\left(1+\frac{E_s\eta^2}{(G_s\kappa_s)}\right)}\left(\mathbf{e}^{\perp b}.\Delta \mathrm{U}_1^{\mathrm{b}}-\frac{L^b}{2}\right.\right.\right.\right.$$
$$\left.\left.\left.\left.\left(\phi_0^{O_{R(b)}}+\phi_0^{E_{R(b)}}\right)\right)\right)\mathbf{e}^{b\perp}\right)\right)\delta^{ib} = \sum_{b\in B_R}\left(N_1^b\mathbf{e}^b+T_{t1}^b\mathbf{e}^{b\perp}\right)\delta^{ib} \tag{11}$$

$$\mu^{\mathrm{i}} = \mu_2^{\mathrm{i}} = \sum_{b\in B_R}\left(\mathrm{E}_s\eta^3\frac{\left(L^b\right)^2}{12}\left(\phi_1^{E_{R(b)}}-\phi_1^{O_{R(b)}}+\frac{\partial\phi_0}{\partial\lambda^i}\delta^{ib}\right)\right)\delta^{ib}$$

$$= \sum_{b \in B_R} \left(\frac{1}{2} \left(M_2^{E(b)} - M_2^{O(b)} \right) \right) \delta^{ib}$$

with N_1^b, T_{t1}^b, and, M_2^n, respectively, the first order normal and transverse effort and the second order moment. Those expressions still involve the unknown displacements $u_1^n, u_2^n$and rotations ϕ_0^n, ϕ_1^n(this defines the so called localization problem over the representative cell), which are determined for all nodes and as a last step by solving the equilibrium equations in translation and rotation.

2.2 *Effective Micropolar Properties of Bone Modeled as a Hexagonal Lattice*

The general anisotropic hexagonal unit cell of two-dimensional honeycomb under consideration is pictured in Fig. 4; it consists of three beams, a vertical beam of length h and two inclined beams of length l. The vertical beams have elastic and shear moduli E_{s1} and G_{s1}, respectively, while the two inclined beams have elastic and shear moduli E_s and G_s, respectively. The dimensionless parameters θ and $\alpha = h/l$ are descriptors of the cell shape, as well as the aspect ratio of the cell walls $\eta = t/l$, a parameter determining the relative density or area fraction of the solid phase. The lattice is called re-entrant when the angle θ between the two inclined beams relative to the horizontal is negative (see Fig. 5b). When this angle takes the value 30°, the classical hexagonal lattice is obtained. When $\theta < 0$, $\left(\theta \in \left[-\frac{\pi}{2} \frac{\pi}{2}\right]\right)$, an auxetic lattice [9, 21] having a negative Poisson's ratio is obtained. Regular unit cells correspond to the specific geometrical parameters α=1 and $\theta = 30°$ and anisotropic unit cells correspond to all other values.

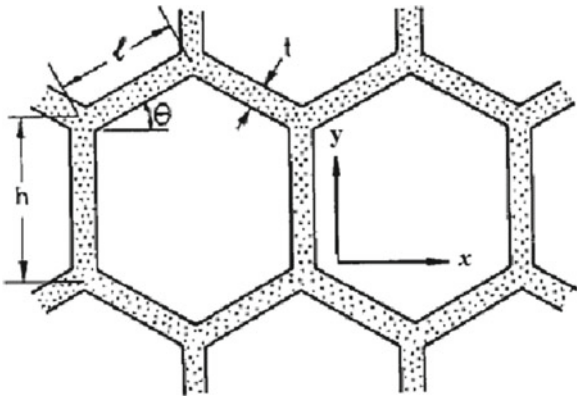

Fig. 4 General anisotropic unit cell for two dimensional honeycomb models. The geometrical descriptors are the cell angle (θ), the vertical cell length (h), the inclined cell length (l), and the wall thickness (t)

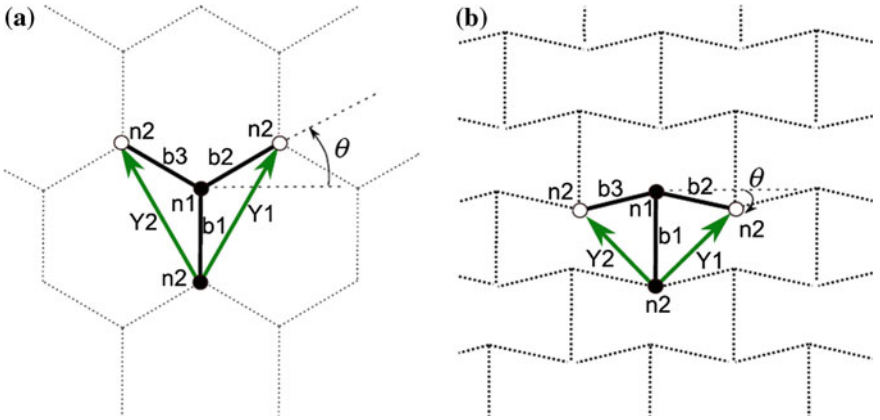

Fig. 5 Representative unit cell of the investigated lattices: (**a**) hexagonal lattice, (**b**) re-entrant lattice ($\theta < 0$)

Table 1 connectivity array for the 2D hexagonal lattice

Beam	1	2	3
O(b)	2	1	1
E(b)	1	2	2
δ_1	0	1	0
δ_2	0	0	1

The representative unit cell is easily identified for the hexagonal lattice (Fig. 5).
The periodicity vectors (norm of $\mathbf{Y}_1$ and $\mathbf{Y}_2$ in the Cartesian basis) share a common length given by $L_1 = L_2 = \sqrt{(l\cos\theta)^2 + (h + l\sin\theta)^2}$; the other features of the lattice are collected in the connectivity Table 1.
The homogenization scheme provides the effective mechanical properties (classical and micropolar moduli) versus the geometrical and micromechanical parameters of the considered bone microstructure. The reader is referred to [9] for a detailed exposition of the method. In the general anisotropic case, the relative density is computed in terms of η, α and θ by

$$\frac{\rho^*}{\rho_s} = \frac{1}{2}\frac{\eta\,(\alpha + 2)}{\cos\theta\,(\alpha + \sin\theta)} \tag{12}$$

For negative cell angles, the geometrical constraint $h \geq 2l\sin\theta$ is required in order to maintain a hexagonal geometry.
After calculations, we extract the effective homogenized moduli of the hexagonal lattice from the equivalent stiffness matrix, expressed versus the dimensionless parameters $\eta, \alpha, \theta, \kappa_s$, and κ_{s1} and the elastic and shear moduli of the solid cell walls E_s, E_{s1}, G_{s1}, and G_s as follows:

$$
\begin{aligned}
E_1^* &= -\frac{E_s\eta^3 C_t}{\left(-1+C_t^2-C_t^2\eta^2+\frac{C_t^2E_s\eta^2}{G_s\kappa_s}-\frac{E_s\eta^2}{G_s\kappa_s}\right)(S_t+\alpha)},\\
E_2^* &= \frac{(S_t+\alpha)\,E_sE_{s1}\eta^3}{\left(C_t^2E_{s1}+\frac{C_t^2E_sE_{s1}\eta^2}{G_s\kappa_s}+E_{s1}\eta^2+2E_s\eta^2\alpha-C_t^2E_{s1}\eta^2\right)C_t},\\
G_{12}^* &= \frac{(S_t+\alpha)\,E_sE_{s1}\eta^3C_t}{\left(\frac{E_s\eta^2\alpha^2C_t^2E_{s1}}{G_s\kappa_s}+\alpha^2E_{s1}C_t^2+\frac{2E_sE_{s1}\eta^2\alpha C_t^2}{G_{s1}\kappa_{s1}}+2\alpha^3C_t^2E_s\right.}\\
&\qquad \left.+\,2E_{s1}\eta^2\alpha S_t+E_{s1}\eta^2+\alpha^2E_{s1}\eta^2-E_{s1}\eta^2\alpha^2C_t^2\right)},\\
\nu_{12}^* &= -\frac{\left(\frac{E_s\eta^2}{G_s\kappa_s}-\eta^2+1\right)S_tC_t^2}{\left(\frac{C_t^2E_s\eta^2}{G_s\kappa_s}-C_t^2\eta^2+C_t^2-\frac{E_s\eta^2}{G_s\kappa_s}-1\right)(S_t+\alpha)},\\
\nu_{21}^* &= \frac{\left(\frac{E_s\eta^2}{G_s\kappa_s}-\eta^2+1\right)S_t\,(S_t+\alpha)\,E_{s1}}{\left(\frac{C_t^2E_sE_{s1}\eta^2}{G_s\kappa_s}+E_{s1}C_t^2+E_{s1}\eta^2+2E_s\eta^2\alpha-C_t^2E_{s1}\eta^2\right)},\\
D_{11} &= \frac{1}{12}\frac{E_s\eta^3l^2C_t}{\alpha+S_t},\, D_{22}=\frac{1}{12}\frac{l^2E_s\eta^3E_{s1}\,(\alpha+S_t)}{(2E_s\alpha+E_{s1})\,C_t}.
\end{aligned}
\tag{13}
$$

with the trigonometric functions $C_t = \cos\theta$ and $S_t = \sin\theta$ therein.
Because of the variation in trabecular architecture even at constant density, two geometries of trabecular bone corresponding to $\theta = 30°$ and $60°$ are considered, with the geometrical parameter $\alpha = 0.5$. The scaling behaviour of the equivalent elastic moduli versus the relative densities from 0.01 to 0.4 for both trabecular geometries is calculated, as pictured in Fig. 6 (properties of both vertical and inclined members are the same; $E_s = E_{s1}, G_s = G_{s1}$, and$\kappa_s = \kappa_{s1}$). Here and in the sequel, the ratio of the effective properties to the bulk value is recorded; considering $G_s = 0.5 * E_s/(1+\nu_s)$, with Poisson's ratio $\nu_s = 0.3$. The results show that the Young's and shear moduli of trabecular bone strongly depend on the relative density; they both express as a power law function of the relative density, with exponents approximately equal to 2.9 for the tensile effective moduli and about 2.8 for the effective shear modulus.

3 Numerical Determination of the Effective Micropolar Rigidities

In a 2D plane stress situation, the stress tensor has four independent components σ_x, σ_y, σ_{xy}, σ_{yx} and the couple stress tensor (or moment per unit area) has two components m_{xz}, m_{yz}. The deformation and micro-curvature components express versus the displacement gradients and micro-rotations as

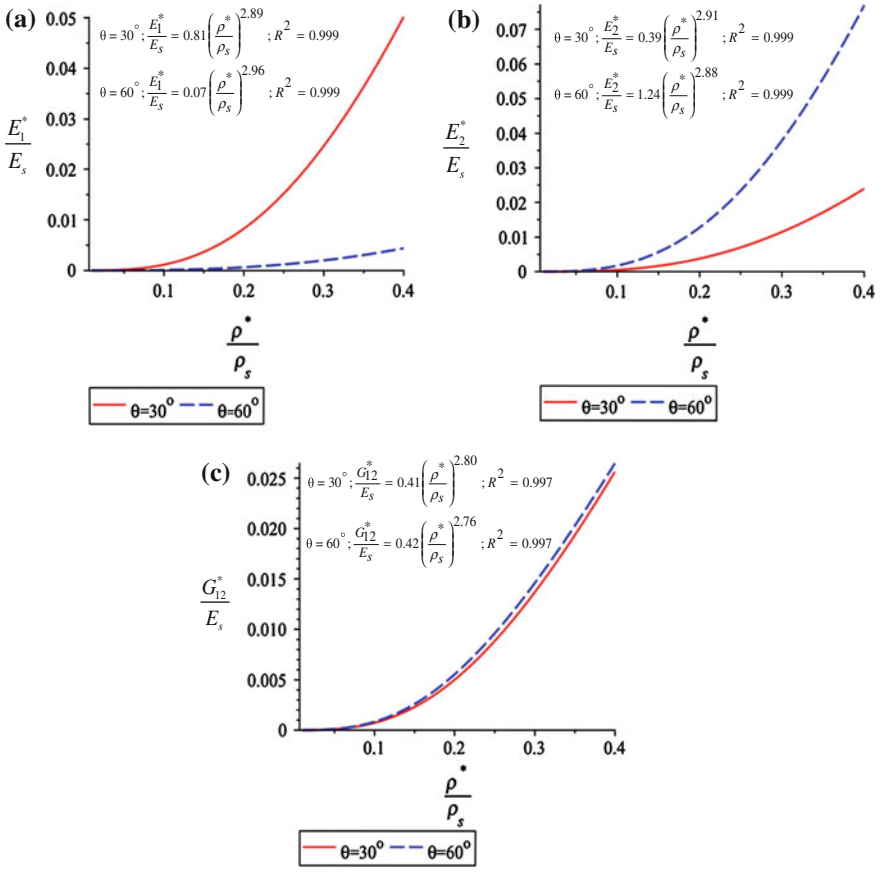

Fig. 6 Variation of the elastic and shear moduli of trabecular bone versus the relative density. $\alpha = 0.5$.

$$\epsilon_x = \partial u/\partial x, \quad \epsilon_y = \partial v/\partial y, \quad \epsilon_{xy} = \partial v/\partial x - \phi, \epsilon_{yx} = \partial u/\partial y + \phi$$
$$\kappa_{xz} = \partial \phi/\partial x, \quad \kappa_{yz} = \partial \phi/\partial y \tag{14}$$

In the Cosserat theory, the rotation ϕ is an independent field, whereas in the couple-stress theory it is related to displacement gradients as in classical elasticity (it is equal to the local rigid rotation), $\phi = (\partial v/\partial x - \partial u/\partial y)/2$. As a result, in the couple-stress theory, the strain tensor ϵ_{ij} is symmetrical with components defined as $\epsilon_{xy} = \epsilon_{yx} = (\partial v/\partial x + \partial u/\partial y)/2$.
The equilibrium in translation and rotation, ignoring body forces and body moments, writes as the set of equations

$$\partial \sigma_x/\partial x + \partial \sigma_{yx}/\partial y = 0, \quad \partial \sigma_{xy}/\partial x + \partial \sigma_y/\partial y = 0,$$
$$\partial m_{xz}/\partial x + \partial m_{yz}/\partial y + \sigma_{xy} - \sigma_{yx} = 0. \tag{15}$$

The last Eq. (15), implies that the shear stress σ_{xy} differs from σ_{yx}; [30] suggested then resolving σ_{xy} and σ_{yx} into a symmetric part σ_S and an anti-symmetric part σ_A.

$$\sigma_S = \left(\sigma_{xy} + \sigma_{yx}\right)/2, \quad \sigma_A = \left(\sigma_{xy} - \sigma_{yx}\right)/2. \tag{16}$$

The symmetric part of the shear stress produces the usual shear strain ϵ_{xy}, while the anti-symmetric part tends to produce a local rigid rotation. Thus, the constitutive equation can be expressed in the following uncoupled form (for a centrally symmetric unit cell structure) as

$$\begin{Bmatrix} \sigma_x \\ \sigma_y \\ \sigma_S \\ m_{xz} \\ m_{yz} \end{Bmatrix} = \begin{bmatrix} \mathbf{A} & 0 \\ 0 & \mathbf{D} \end{bmatrix} \begin{Bmatrix} \epsilon_x \\ \epsilon_y \\ \epsilon_{xy} \\ \kappa_{xz} \\ \kappa_{yz} \end{Bmatrix} \tag{17}$$

with

$$\mathbf{A} = \begin{bmatrix} A_{11} & A_{12} & 0 \\ A_{12} & A_{22} & 0 \\ 0 & 0 & A_{66} \end{bmatrix}, \mathbf{D} = \begin{bmatrix} D_{11} & 0 \\ 0 & D_{22} \end{bmatrix}. \tag{18}$$

Matrix **A** contains the classical moduli, while matrix **D** contains the micropolar moduli relating the two couple stress components to the corresponding curvatures.
The numerical homogenization technique consists in determining the overall effective mechanical properties (couple-stress moduli and characteristic lengths) over a representative unit cell of trabecular bone, relying on a finite element discretization of the unit cell geometry. Each cell wall is modeled with a three-node beam element (element type B22 in ABAQUS), endowed with bending, stretching and shearing deformation mechanisms. An earlier study by [45] showed that using such a beam element to model each cell wall is sufficient for convergence.
We consider here a unit cell of trabecular bone with geometrical parameters given from [18] as: $\alpha = h/l = 0.5; \eta = t/l = 0.25; l = 1\ mm; \theta = 60°$ (Fig. 7). The bulk mechanical properties of the unit cells wall representative of the behavior of human femur [20] are taken as $E_s = 12000$ MPa; $\nu_s = 0.3$.
Since the trabecular bone unit cell is cut out of an infinite structure, it that can be regarded as periodic, thus spatially periodic boundary conditions should be applied to ensure that the predicted properties of the unit cell are representative of those of the macroscopic structure. The boundary surfaces of the unit cell must always appear in parallel pairs; the displacements on a pair of parallel opposite boundary surfaces can be written as

$$\begin{aligned} u_i^{k+} &= \tilde{\epsilon}_{ij} x_j^{k+} + u_i^* \\ u_i^{k-} &= \tilde{\epsilon}_{ij} x_j^{k-} + u_i^* \end{aligned} \tag{19}$$

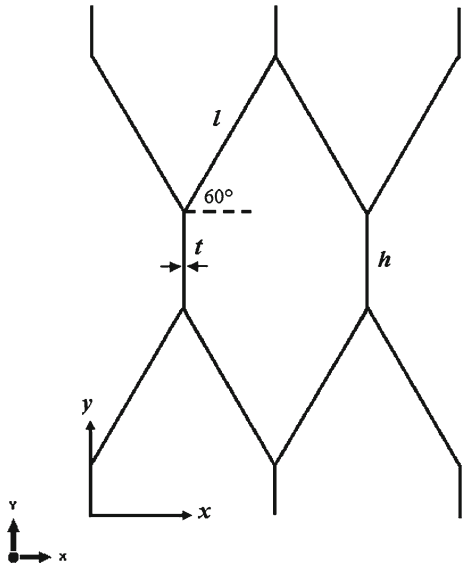

Fig. 7 Geometrical model of an elementary cell of trabecular bone

where indices "k^+" and "k^-" identify the kth pair of two opposite parallel boundary surfaces of a repeated unit cell. Note that u_i^* is the same at the two parallel boundaries (periodicity), thus the difference between the above two equations gives

$$u_i^{k+} - u_i^{k-} = \tilde{\epsilon}_{ij}(x_j^{k+} - x_j^{k-}) = \tilde{\epsilon}_{ij}\Delta x_j^k \tag{20}$$

with $\tilde{\epsilon}_{ij}$ the macroscopic (average) strains of the unit cell. Since the quantities Δx_j^k are constants for each pair of the parallel boundary surfaces, with specified $\tilde{\epsilon}_{ij}$, the right-hand side in Eq. (20) becomes constant. The constraint equations are applied as nodal displacement constraint equations, instead of giving Eq. (19) directly as boundary conditions.

The main purpose of this section is to determine the effective constitutive constants of the couple-stress continuum from the unit cell response of trabecular structure. We design different boundary conditions for the determination of the independent components of the constitutive (rigidity) constants over a unit cell domain Ω (Fig. 7) with boundary $\partial\Omega$. Without loss of generality, the thickness in z-direction is set to unity. In each case, we force the unit cell to bear the designed specific deformation $\{\epsilon_x \quad \epsilon_y \quad \epsilon_{xy}\kappa_{xz} \quad \kappa_{yz}\}^T$ and compute numerically the total elastic strain energy $U_{discrete}$ stored in the unit cell under the corresponding boundary conditions. The numerical procedure used here is similar to [2]: the total strain energy stored in the unit cell is equated with the energy of an equivalent homogeneous couple-stress continuum, thus

$$U_{discrete} = U_{continuum} = \frac{V}{2}\left[\epsilon_{ij}A_{ijkl}\epsilon_{kl} + \kappa_{ij}D_{ijkl}\kappa_{kl}\right] \tag{21}$$

where $V = |\Omega|$ is the volume of the unit cell. The strain energy $U_{continuum}$ stored in the effective homogeneous couple-stress continuum can be obtained by the prescribed strain/stress fields.
In order to evaluate the components of the couple-stress stiffness tensors **A** and **D** for the unit cell, we conduct the following six elementary tests:
The first four tests are constructed to determine the stiffness matrix **A**.
Test 1- Horizontal uniaxial extension test for A_{11}: We apply the following unit strain to the unit cell

$$\epsilon_x = 1,\ \epsilon_y = \epsilon_{xy} = 0,\ \kappa_{xz} = \kappa_{yz} = 0, \quad \text{in } \Omega \tag{22}$$

The corresponding boundary conditions are

$$u = x,\ v = 0, \text{ on } \quad \partial\Omega \tag{23}$$

It gives $A_{11} = 2U_{discrete}/V$
Test 2- Vertical uniaxial extension test for A_{22}: Applying the unit strain to the unit cell

$$\epsilon_x = \epsilon_{xy} = 0,\ \epsilon_y = 1,\ \kappa_{xz} = \kappa_{yz} = 0, \text{ in } \Omega \tag{24}$$

The corresponding boundary conditions are

$$u = 0, v = y, \quad \text{on } \partial\Omega \tag{25}$$

It gives $A_{22} = 2U_{discrete}/V$
Test 3- Biaxial extension test for A_{12}: one applies the unit strain to the unit cell

$$\epsilon_x = \epsilon_y = 1,\ \epsilon_{xy} = 0,\ \kappa_{xz} = \kappa_{yz} = 0, \text{ in } \Omega \tag{26}$$

The corresponding boundary conditions are

$$u = x,\ v = y, \text{ on } \partial\Omega \tag{27}$$

It yields $A_{12} = (2U_{discrete}/V - A_{11} - A_{22})/2$
Test 4- Shear test for A_{66}: the following unit strain is applied to the unit cell

$$\epsilon_x = \epsilon_y = 0,\ \epsilon_{xy} = 1,\ \kappa_{xz} = \kappa_{yz} = 0, \text{ in } \Omega \tag{28}$$

The corresponding kinematic boundary conditions are

$$u = y/2,\ v = x/2, \text{ on } \partial\Omega \tag{29}$$

It yields $A_{66} = 2U_{discrete}/V$
The displacement and stress distributions within the trabecular bone unit cell for the above four tests under the corresponding displacement boundary conditions are shown in Figs. 8, 9, 10 and 11.

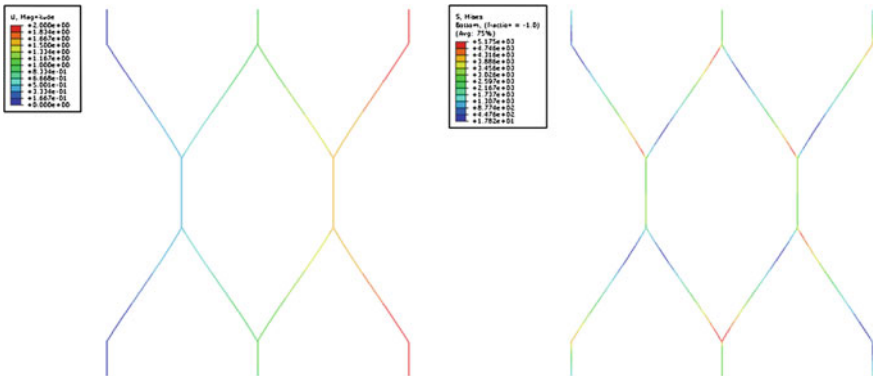

Fig. 8 Displacement and stress distributions due to horizontal uniaxial extension

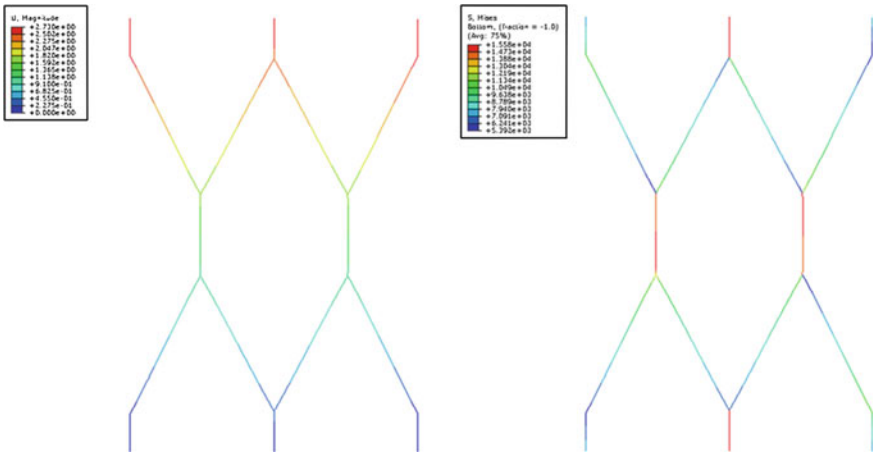

Fig. 9 Displacement and stress distributions due to vertical uniaxial extension

The values of $A_{11}, A_{12}, A_{22}, A_{66}$ computed through the above numerical analyses (from elastic strain energy) are summarized in Table 2, showing a good agreement is obtained with those calculated by discrete homogenization.

In order to evaluate the components of the stiffness matrix **D**, the following two bending tests are performed:

Test 5- Bending test for D_{11}: for an enforced uniform curvature κ_{xz} applied to the boundary, the corresponding kinematic boundary conditions write

$$u\,|_{\partial\Omega} = -xy, v\,|_{y=0} = x^2/2 \tag{30}$$

which gives $D_{11} = 2U_{\text{discrete}}/V - E_1^* y^2$, when $\kappa_{xz} = 1$.

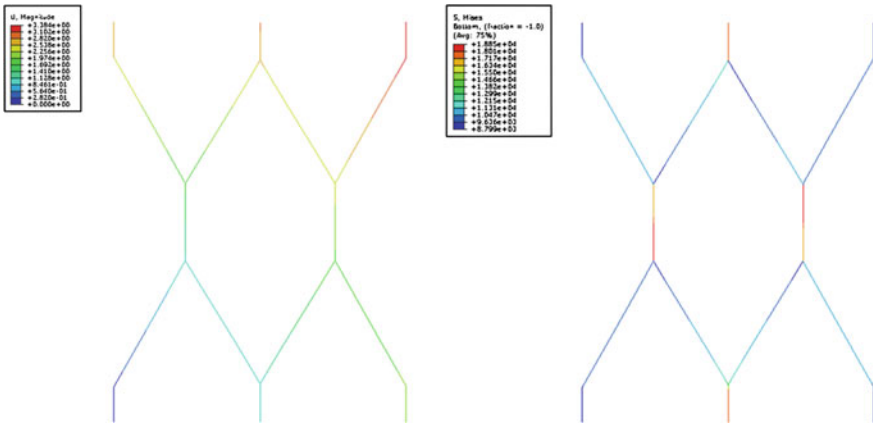

Fig. 10 Displacement and stress distributions due to biaxial extension

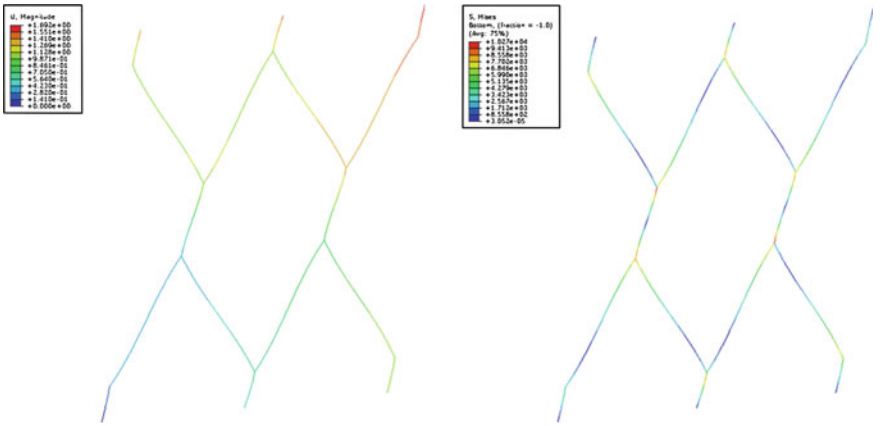

Fig. 11 Displacement and stress distributions due to shearing

with

$$E_1^* = A_{11}\left(1 - \nu_{12}^*\nu_{21}^*\right),\ \nu_{12}^* = A_{12}/A_{22},\ \nu_{21}^* = A_{12}/A_{11} \tag{31}$$

Test 6- Bending test for D_{22}: for an imposed uniform curvature κ_{yz}applied to the boundary, the corresponding kinematic boundary conditions write

$$u\,|_{x=0} = -y^2/2,\ v\,|_{\partial\Omega} = xy \tag{32}$$

which gives $D_{22} = 2U_{discrete}/V - E_2^* x^2$, when $\kappa_{yz} = 1$.
with

$$E_2^* = A_{22}\left(1 - \nu_{12}^*\nu_{21}^*\right) \tag{33}$$

Table 2 The couple-stress elastic constants and characteristics lengths of trabecular bone unit cell

	Discrete homogenization	Finite element simulation
A_{11} (MPa)	212.7	215.0
A_{12} (MPa)	698.3	745.0
A_{22} (MPa)	3547.4	3743.2
A_{66} (MPa)	407.5	427.8
D_{11}(N)	5.7	4.7
D_{22}(N)	21.3	17.5
E_1^*(MPa)	75.2	66.5
E_2^*(MPa)	1255.0	1161.5
ν_{12}^*	0.197	0.199
ν_{21}^*	3.28	3.47
l_{Gx} (μm)	59.0	52.5
l_{Gy} (μm)	114.0	101.0
l_{Ex} (μm)	402.7	397.4
l_{Ey} (μm)	100.8	95.0

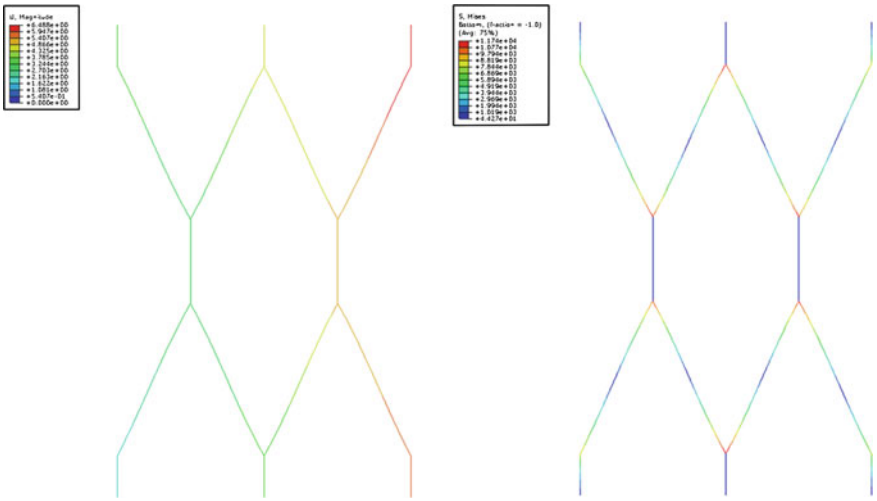

Fig. 12 Displacement and stress distributions due to bending (κ_{xz})

The displacement and stress distributions of the trabecular bone unit cell for the last two bending tests under the corresponding displacement boundary conditions are shown in Figs. 12 and 13.

For the planar orthotropic couple-stress model considered in this work, there are four characteristics lengths which are defined by the following expressions in terms of the engineering constants [2, 37]

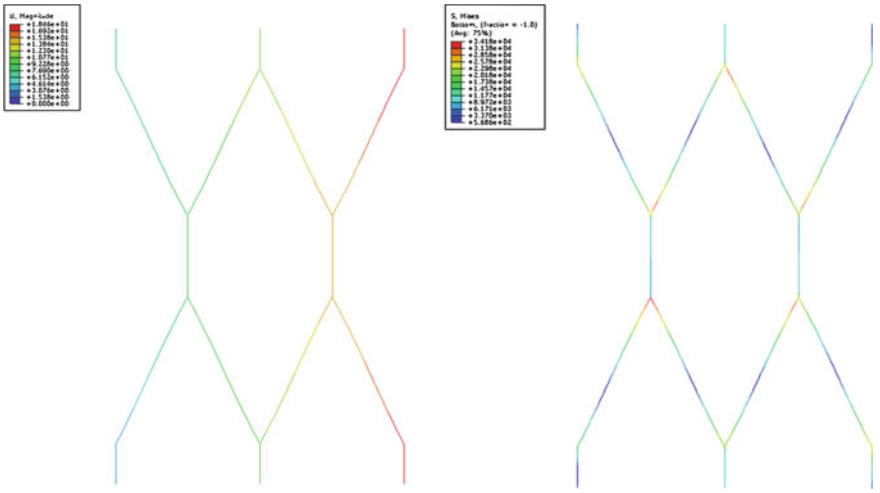

Fig. 13 Displacement and stress distributions due to bending (κ_{yz})

$$l_{Gx} = \sqrt{\frac{D_{11}}{4A_{66}}}, \quad l_{Gy} = \sqrt{\frac{D_{22}}{4A_{66}}}$$
$$l_{Ex} = \sqrt{\frac{(1+\nu_{21}^{*})D_{11}}{2E_1^{*}}}, \quad l_{Ey} = \sqrt{\frac{(1+\nu_{12}^{*})D_{22}}{2E_2^{*}}} \tag{34}$$

The components of the effective couple-stiffness tensors and micropolar elastic constants of trabecular bone evaluated by discrete homogenization and FE simulation are compared in Table 2.
It is shown that the homogenized properties are representative of the bone architecture overall behavior, since they approximate the simulated values with a good accuracy (the relative variation is at most 15%).

4 Applications to Bone Fracture

Simulations of a square bone sample including a crack are performed, using the previously obtained homogenized anisotropic micropolar model (Fig. 14). The results are compared to those obtained by a classical four node finite element called CPS4 within the Abaqus environment. The principal directions of orthotropy are supposed to be aligned with the fiber directions within the selected bone sample, which by definition coincide with the X and Y directions of the representative volume element (the unit cell). The geometrical and mechanical parameters of the unit cells of trabecular bone are taken as in Sect. 3.

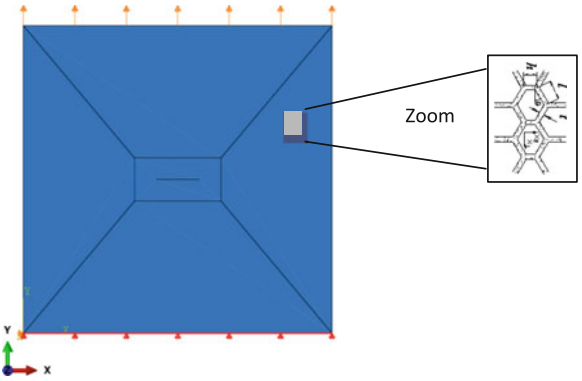

Fig. 14 Applied loading and boundary conditions of the 2D bone specimen with bone fracture (*left*). Zoom of the material specimen on two hexagonal unit cells (*right*)

The specimen dimensions correspond to 1mm width and 1 mm height. The effective material properties calculated by the discrete homogenization technique are summarized in the following matrix:

$$[K] = \begin{bmatrix} 212.7 & 698.3 & 0 & 0 & 0 & 0 \\ 698.3 & 3547.4 & 0 & 0 & 0 & 0 \\ 0 & 0 & 436.2 & 378.8 & 0 & 0 \\ 0 & 0 & 271.6 & 543.4 & 0 & 0 \\ 0 & 0 & 0 & 0 & 5.7 & 0 \\ 0 & 0 & 0 & 0 & 0 & 21.3 \end{bmatrix} \tag{35}$$

A horizontal crack representing 14% of the total specimen width is introduced to represent longitudinal fracture (Fig. 14). The bottom edge of the specimen ($1 \times 1\ \text{mm}^2$) is simply supported in Y-direction (the corner node at the origin is fixed), and the top edge is submitted to a uniaxial displacement magnitude equal to 0.25 mm in the vertical direction. This corresponds to an induced vertical traction of magnitude 420 MPa.

A stress concentration occurs for both models close to the crack tip, a well-known fact in the field of fracture mechanics [4]. However, the amplitude of the peak stress is significantly reduced when the Cosserat continuum model is employed; the percentage of reduction is evaluated for each stress component (and each mesh size) in Table 3. It reaches up to 50% for the fine mesh, a value in agreement with the amount of reduction of the stress concentration factor obtained for sharp cracks using a linear isotropic Cosserat behavior in [24].

We observe from the isovalues of the two in-plane displacement components, U1 and U2 (Fig. 15) a more diffuse displacement field when Cosserat model is employed, in comparison to Cauchy continuum, for which steep stress gradients are obtained. This confirms the regularizing effect of the Cosserat continuum model.

Table 3 Comparison of peak stress values for the two models (Cauchy and micropolar)

	Cosserat finite element			CPS4 finite element (Abaqus)			% of stress reduction $\frac{S_{Cauchy}-S_{Cosserat}}{S_{Cauchy}} \times 100$		
	S11	S12	S22	S11	S12	S22	S11	S12	S22
Coarse	28	63	752	41	133	752	31.7	52.6	0
Medium	81	148	902	156	206	1096	48.1	28.2	17.7
Fine	112	213	1038	227	350	1396	50.7	39.2	25.6

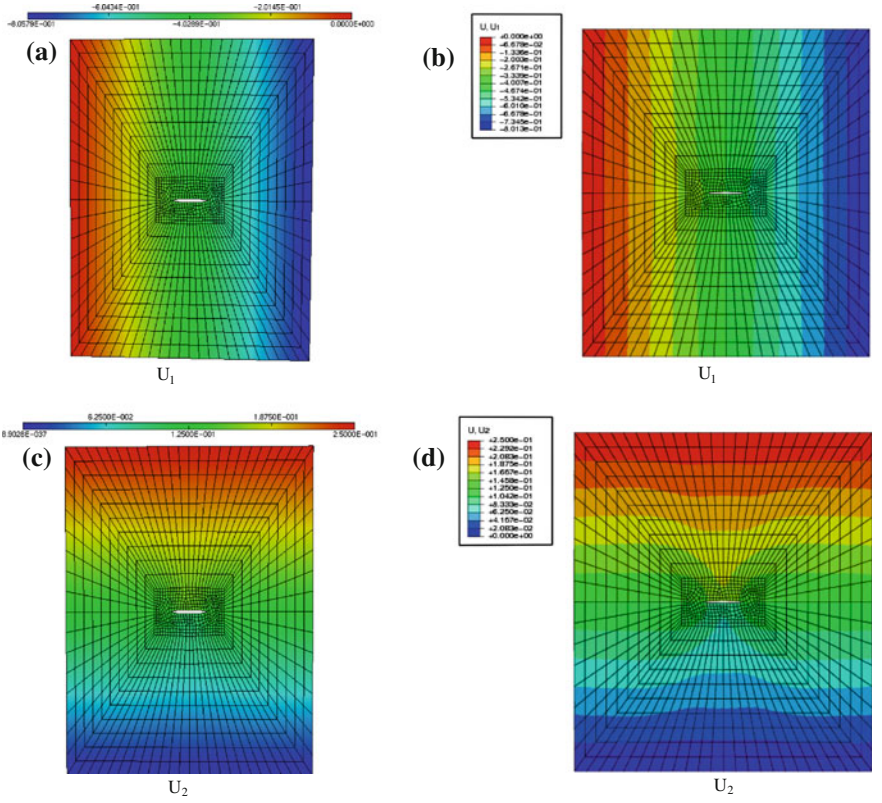

Fig. 15 Displacement distribution. (**a**), (**c**) correspond to Cosserat finite element results and (**b**), (**d**) correspond to the classical four node finite element. Fine mesh (1188 elements)

In the next section a 3D micropolar effective continuum model of trabecular bone is constructed using asymptotic homogenization of 3D discrete media considering axial, shear, flexural and torsional deformations of the cell struts. The overall mechanical behavior of trabecular bone in a 3D geometry is analyzed in the consequence.

5 Three-Dimensional Anisotropic Effective Behavior of Cancellous Bone

A general 3-D anisotropic hexagonal lattice with horizontal struts of lengths L and h (lengths of in-plane struts) and vertical struts of length L_v (out-of-plane), both endowed with circular cross-section of diameter d, is considered (Fig. 16). This geometry is representative of the unit cell of vertebral bone, as advocated in [22]. The whole lattice is generated from the repetition of the unit cell shown in Fig. 16 thanks to three periodicity vectors defined in the Cartesian basis. The considered hexagonal unit cell is composed of five beams; three horizontal beams b_1, b_2, and b_3 and the vertical beams b_4 and b_5. The horizontal beams b_2 and b_3 have the same length L and are inclined by the angle θ with the horizontal direction, while b_1 has length h. The two vertical beams b_4 and b_5 have the same length L_v. The connectivity Table 4 gives the numbering of beams and nodes within the chosen representative unit cell.

The relative density of the general 3D anisotropic hexagonal is computed in terms of the geometrical parameters L, h, L_v, r and θ as

$$\frac{\rho^*}{\rho_s} = \frac{1}{2} \frac{\pi r^2 \left(h + 2L + 2L_v\right)}{L L_v \cos\theta \left(h + L \sin\theta\right)} \tag{36}$$

Since each beam is in self-equilibrium, we choose to define the efforts at node E (efforts at node O are opposite), which is considered as the end node. Using the local

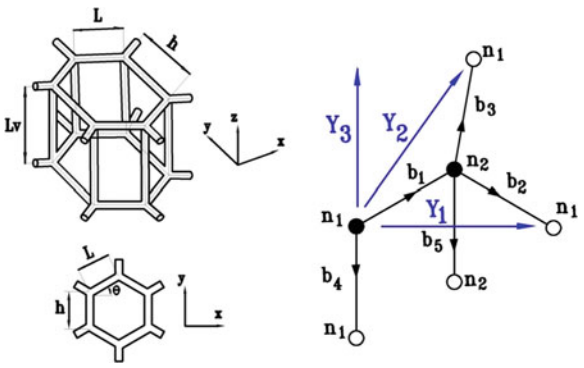

Fig. 16 General anisotropic unit cell for 3D hexagonal models. The geometric parameters include the cell angle θ, the in-plane strut lengths (L, h), and the vertical length L_v. Right picture: topology of the 3D hexagonal unit cell with the periodicity vector

Table 4 Connectivity array for the 3D hexagonal lattice

Beam	1	2	3	4	5
O(b)	1	2	2	1	2
E(b)	2	1	1	1	2
δ_1	0	1	0	0	0
δ_2	0	0	1	0	0
δ_3	0	0	0	−1	−1

coordinate systems for each member element, the normal (tension) force receives the expression

$$F_{x2_p} = \frac{AE_s}{L}\left(\mathbf{e}_x.\left(\mathbf{u}_E - \mathbf{u}_O\right)\right) \tag{37}$$

The transverse force F_{y2_p} is given by

$$F_{y2_p} = \frac{12E_sI_z}{L^3(1+\Phi_y)}\left(\mathbf{e}_y.\left(\mathbf{u}_E - \mathbf{u}_O\right) - \frac{L}{2}\left(\mathbf{e}_z.\left(\phi_O + \phi_E\right)\right)\right) \tag{38}$$

Similarly, the transverse force F_{z2_p} is given by

$$F_{z2_p} = \frac{12E_sI_y}{L^3(1+\Phi_z)}\left(\mathbf{e}_z.\left(\mathbf{u}_E - \mathbf{u}_O\right) + \frac{L}{2}\left(\mathbf{e}_y.\left(\phi_O + \phi_E\right)\right)\right) \tag{39}$$

The moments express at both extremities of the member express as follows: for the moments about the x'-axis (twist in y'-z' plane), the load-displacement relationship is very similar to axial loading, viz

$$M_{x1_p} = \frac{G_sJ}{L}(\mathbf{e}_x.(\varphi_O - \varphi_E)); M_{x2_p} = \frac{G_sJ}{L}(\mathbf{e}_x.(\varphi_E - \varphi_O)) \tag{40}$$

The bending moments about the y'-axis write

$$\begin{aligned} M_{y1_p} &= \frac{6E_sI_y}{L^2(1+\Phi_z)}\left(\mathbf{e}_z.\left(\mathbf{u}_E - \mathbf{u}_O\right)\right) \\ &\quad + \frac{E_sI_y}{L(1+\Phi_z)}\left(\mathbf{e}_y.\left((4+\Phi_z)\phi_O + (2-\Phi_z)\phi_E\right)\right) \\ M_{y2_p} &= \frac{6E_sI_y}{L^2(1+\Phi_z)}\left(\mathbf{e}_z.\left(\mathbf{u}_E - \mathbf{u}_O\right)\right) \\ &\quad + \frac{E_sI_y}{L(1+\Phi_z)}\left(\mathbf{e}_y.\left((2-\Phi_z)\phi_O + (4+\Phi_z)\phi_E\right)\right) \end{aligned} \tag{41}$$

The bending moments about the z'-axis express as

$$\begin{aligned} M_{z1_p} &= \frac{6E_sI_z}{L^2(1+\Phi_y)}\left(-\mathbf{e}_y.\left(\mathbf{u}_E - \mathbf{u}_O\right)\right) \\ &\quad + \frac{E_sI_z}{L(1+\Phi_y)}\left(\mathbf{e}_z.\left((4+\Phi_y)\phi_O + (2-\Phi_y)\phi_E\right)\right) \\ M_{z2_p} &= \frac{6E_sI_z}{L^2(1+\Phi_y)}\left(-\mathbf{e}_y.\left(\mathbf{u}_E - \mathbf{u}_O\right)\right) \\ &\quad + \frac{E_sI_z}{L(1+\Phi_y)}\left(\mathbf{e}_z.\left((2-\Phi_y)\phi_O + (4+\Phi_y)\phi_E\right)\right) \end{aligned} \tag{42}$$

with the non-dimensional factors $\Phi_y = 12E_sI_z/G_sAk_{ys}L^2$ and $\Phi_z = 12E_sI_y/G_sAk_{zs}L^2$, vanishing when transverse shear can be neglected (hence a Bernoulli beam model is recovered), I_y and I_z are the second moments of area of the member cross-section, k_{ys} and k_{zs} are the transverse shear correction factors, and J is the torsional modulus, which is identical to the polar moment of inertia of the circular cross-sectional area.

The asymptotic expansions of the previous expressions of normal, transverse efforts, and moments at the beam extremities in the framework of 3D Timoshenko beams versus the kinematic nodal variables are performed and they are next involved in the homogenization of the initially discrete lattice towards an equivalent 3D micropolar continuum.

The constitutive equations for the equivalent anisotropic micropolar continuum are obtained in 3D matrix format as

$$\begin{Bmatrix} \sigma_{xx} \\ \sigma_{yy} \\ \sigma_{zz} \\ \sigma_{xy} \\ \sigma_{yx} \\ \sigma_{yz} \\ \sigma_{zy} \\ \sigma_{zx} \\ \sigma_{xz} \end{Bmatrix} = [\mathbf{A}] \begin{Bmatrix} \dfrac{\partial u_x}{\partial x} \\ \dfrac{\partial u_y}{\partial y} \\ \dfrac{\partial u_z}{\partial z} \\ \dfrac{\partial u_y}{\partial x} - \phi_z \\ \dfrac{\partial u_x}{\partial y} + \phi_z \\ \dfrac{\partial u_z}{\partial y} - \phi_x \\ \dfrac{\partial u_y}{\partial z} + \phi_x \\ \dfrac{\partial u_x}{\partial z} - \phi_y \\ \dfrac{\partial u_z}{\partial x} + \phi_y \end{Bmatrix}; \begin{Bmatrix} m_{xx} \\ m_{yy} \\ m_{zz} \\ m_{xy} \\ m_{yx} \\ m_{yz} \\ m_{zy} \\ m_{zx} \\ m_{xz} \end{Bmatrix} = [\mathbf{D}] \begin{Bmatrix} \dfrac{\partial \phi_x}{\partial x} \\ \dfrac{\partial \phi_y}{\partial y} \\ \dfrac{\partial \phi_z}{\partial z} \\ \dfrac{\partial \phi_y}{\partial x} \\ \dfrac{\partial \phi_x}{\partial y} \\ \dfrac{\partial \phi_z}{\partial y} \\ \dfrac{\partial \phi_y}{\partial z} \\ \dfrac{\partial \phi_x}{\partial z} \\ \dfrac{\partial \phi_z}{\partial x} \end{Bmatrix} \tag{43}$$

where, according to the orthotropic nature of the problem, the matrix representation of [**A**] is

$$[\mathbf{A}] = \begin{bmatrix} A_{11} & A_{12} & A_{13} & 0 & 0 & 0 & 0 & 0 & 0 \\ A_{21} & A_{22} & A_{23} & 0 & 0 & 0 & 0 & 0 & 0 \\ A_{31} & A_{32} & A_{33} & 0 & 0 & 0 & 0 & 0 & 0 \\ 0 & 0 & 0 & A_{44} & A_{45} & 0 & 0 & 0 & 0 \\ 0 & 0 & 0 & A_{54} & A_{55} & 0 & 0 & 0 & 0 \\ 0 & 0 & 0 & 0 & 0 & A_{66} & A_{67} & 0 & 0 \\ 0 & 0 & 0 & 0 & 0 & A_{76} & A_{77} & 0 & 0 \\ 0 & 0 & 0 & 0 & 0 & 0 & 0 & A_{88} & A_{89} \\ 0 & 0 & 0 & 0 & 0 & 0 & 0 & A_{98} & A_{99} \end{bmatrix} \tag{44}$$

The curvature tensor [**D**] in (43) has the same structure.

The present 3D micropolar model substantiates both the classical and micropolar material constants. The micropolar shear constant κ couples the rotation of particles to shear stresses; if $\kappa = 0$ (coupling number $(N) = 0$) the Cauchy stress does not depend on the rotational degree of freedom. The limit $\kappa \to \infty$ is a condition energetically admissible, similar to "incompressibility" in classical elasticity, and corresponds to $N = 1$ (upper bound) which is called "couple stress theory". The modulus γ sets the intensity of couple stresses and is proportional to the characteristic lengths for bending and torsion, quantities l_b and l_t respectively. In Cauchy solids, the internal characteristic length is of the order of the atomic distance and moments of forces and consequently does not produce any macroscopic effect. However, in microstructured solids such as hard biological tissues having a cellular structure where an intrinsic internal length at least of the order of microns may be detected, couple stresses may influence the macroscopic behavior. In the limit situation $\gamma = 0$, Cauchy elasticity is recovered. The characteristic lengths for bending and torsion are next identified from the homogenized stiffness matrix [**A**] relating stresses to strains and curvature tensor [**D**] relating couple stresses to curvatures as

$$
\begin{aligned}
&l_{b_{12}}^2 = \frac{D_{99}}{2\,(A_{45}+A_{44})};\; l_{b_{21}}^2 = \frac{D_{66}}{2\,(A_{54}+A_{55})};\; l_{b_{23}}^2 = \frac{D_{55}}{2\,(A_{67}+A_{66})};\\
&l_{b_{32}}^2 = \frac{D_{88}}{2\,(A_{76}+A_{77})};\; l_{b_{31}}^2 = \frac{D_{77}}{2\,(A_{89}+A_{88})};\; l_{b_{13}}^2 = \frac{D_{44}}{2\,(A_{98}+A_{99})};\\
&l_{t_{12}}^2 = \frac{D_{99}+D_{98}}{A_{44}+A_{45}};\; l_{t_{21}}^2 = \frac{D_{66}+D_{67}}{A_{54}+A_{55}};\; l_{t_{23}}^2 = \frac{D_{55}+D_{54}}{A_{66}+A_{67}};\\
&l_{t_{32}}^2 = \frac{D_{88}+D_{89}}{A_{76}+A_{77}};\; l_{t_{31}}^2 = \frac{D_{77}+D_{76}}{A_{88}+A_{89}};\; l_{t_{13}}^2 = \frac{D_{44}+D_{45}}{A_{98}+A_{99}}.
\end{aligned}
\tag{45}
$$

One additional micropolar constant, the coupling number *N*, determines the strength of the micropolar behavior; it is calculated for the three planes x-y, y-z and x-z as

$$
\begin{aligned}
&N_{12}^2 = \frac{A_{44}-A_{45}}{2A_{44}};\; N_{21}^2 = \frac{A_{55}-A_{54}}{2A_{55}};\; N_{23}^2 = \frac{A_{66}-A_{67}}{2A_{66}};\; N_{32}^2 = \frac{A_{77}-A_{76}}{2A_{77}};\\
&N_{31}^2 = \frac{A_{88}-A_{89}}{2A_{88}};\; N_{13}^2 = \frac{A_{99}-A_{98}}{2A_{99}}.
\end{aligned}
\tag{46}
$$

We choose $h/L = 0.5$, a value for trabecular bone given by [17]. Hence, a combination of $h/L = 0.5$and $L_v/L = 1$ is used to simulate the anisotropic trabecular bone. We consider all struts (trabeculae) with identical cross-section geometry of diameter $d = 0.25$ mm and strut lengths $L = 1$mm (Miller and Fuchs, 2005). The mechanical parameters of the trabeculae building structure are: $G_s = 0.5 * E_s/(1+\nu_s)$, with Poisson's ratio $\nu_s = 0.3$ [48]. The shear correction coefficient is $k_{ys} = k_{zs} = 9/10$. We plot the calculated homogenized effective elastic properties obtained for trabecular bone versus the geometrical parameter θ (Figs. 17, 18 and 19) with a range of

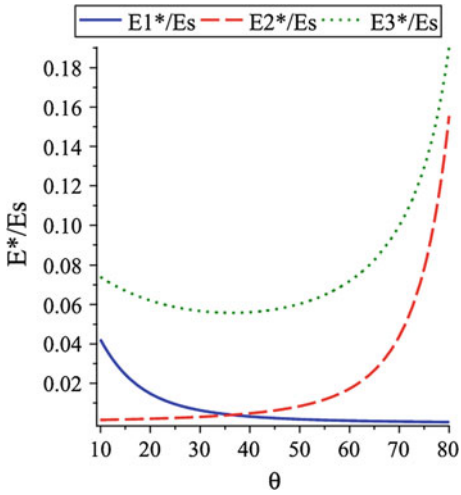

Fig. 17 Effective elastic moduli E_1^*, E_2^*, and E_3^* of trabecular bone plotted versus the geometrical parameter θ

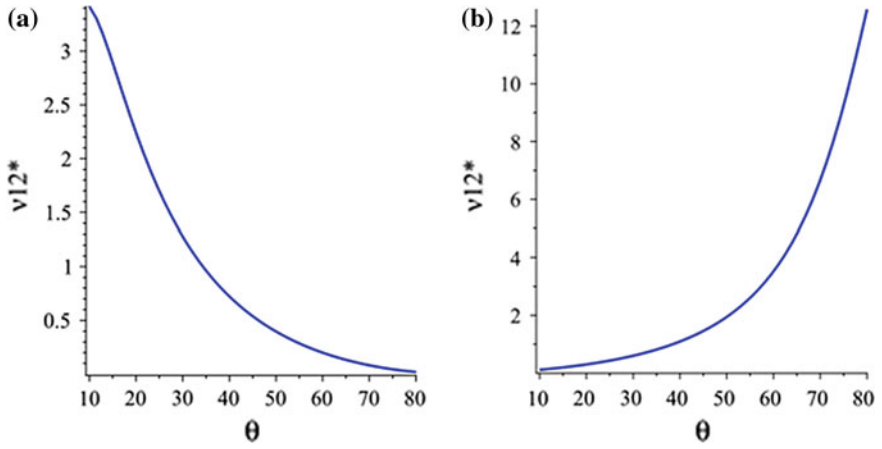

Fig. 18 Effective in-plane Poisson's ratios of trabecular bone plotted versus angle θ

variation chosen in the interval [10°, 80°], supported by [27], who scanned specimens of vertebral trabecular bone using microcomputed tomography.

The elastic (E_1^*andE_2^*) and shear moduli (G_{12}^*, G_{23}^*, and G_{13}^*) exhibit a power law dependency on the relative density (Fig. 20), and transverse shear has a clear impact on those scaling laws.

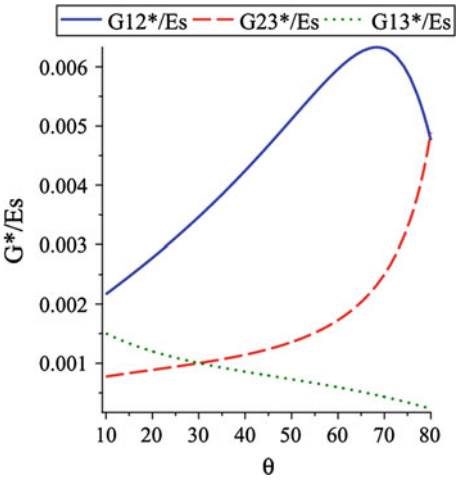

Fig. 19 Effective shear moduli G^*_{12}, G^*_{23}, and G^*_{13} of trabecular bone plotted versus angle θ

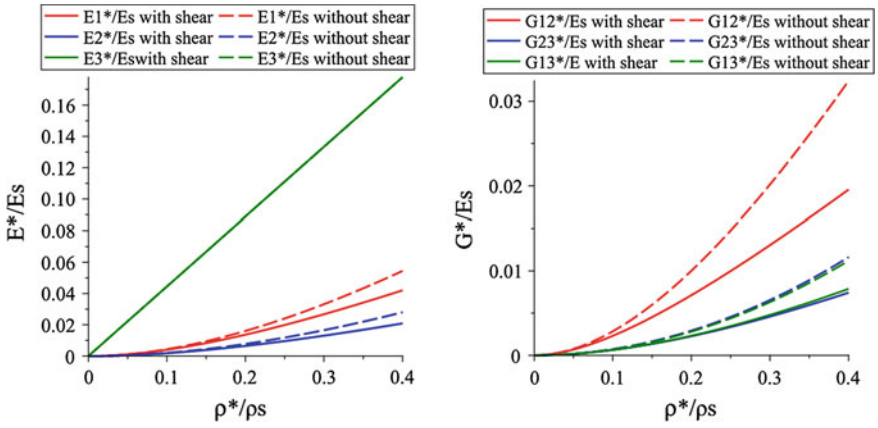

Fig. 20 Effective elastic and shear moduli of trabecular bone versus the relative density ρ^*/ρ_s. $\theta = 30°$

The coupling number and the ratio of the characteristic internal micropolar lengths for bending and torsion, quantities l_b and l_t, to the characteristic unit cell size $2L\cos(\theta)$ are plotted to assess the strength of the micropolar effect (Figs. 21 a–d).
It appears that those ratio reach values close to unity and higher than unity for l_{b31}, l_{t31}, clearly indicating that micropolar effects indeed impact the continuum behavior.

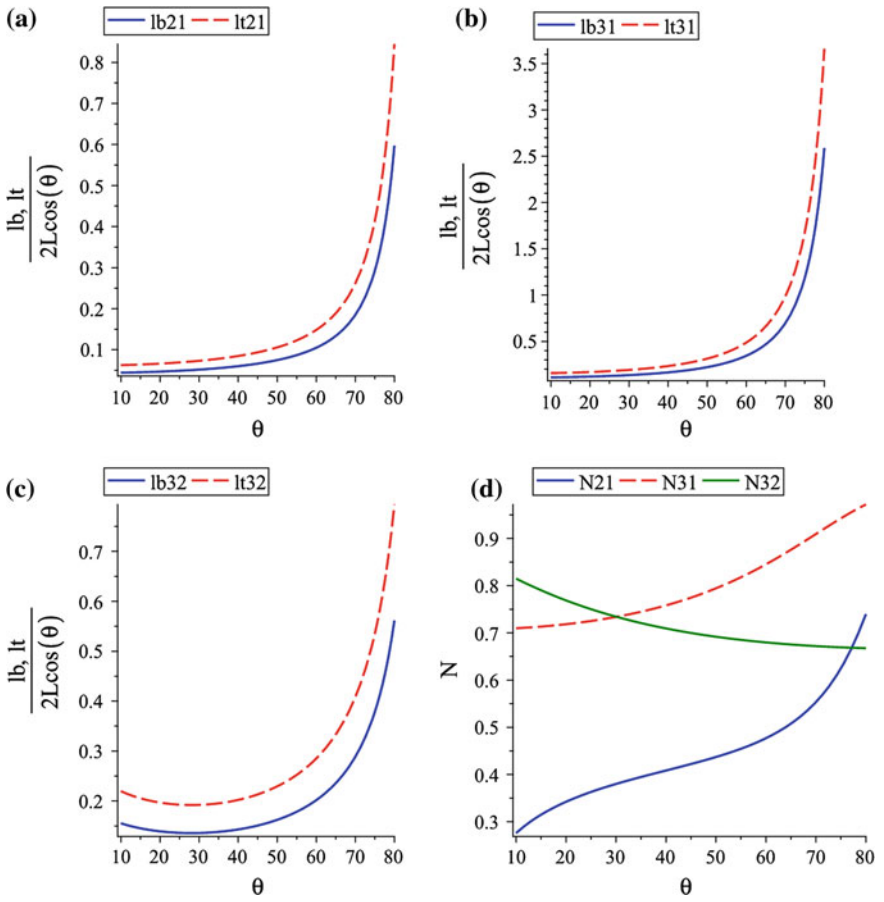

Fig. 21 (**a**), (**b**), (**c**) Ratio of the characteristic micropolar lengths in bending and torsion to the unit cell size of trabecular bone and (**d**) Micropolar coupling number plotted versus the angle θ

6 Conclusion

A micromechanical approach of microstructural effects of trabecular bone has been developed. As a main novelty, a Cosserat anisotropic continuum model has been developed from the discrete homogenization of a quasi periodical lattice model of the cancellous bone microstructure, whereby the effective mechanical properties of bone are directly related to the lattice micro-geometry and micromechanical elastic properties. The cell walls of this cellular material are modeled as linear elastic Timoshenko beams, accounting for the transverse shear occurring in thick beams in the regime of high bone density. The first stiffness tensor and the second couple stress stiffness tensor have been evaluated, allowing in turn the identification of the micropolar (non classical) constants of cancellous bone (in addition to the classical moduli),

including internal flexural lengths. The equivalent moduli have been recorded versus the geometrical descriptors of the unit cell. A planar linear Cosserat finite element model of a cracked bone sample has been developed on the basis of the constructed effective Cosserat continuum, in order to illustrate the microstructural effects on the macroscopic response of cancellous bone. The FE analysis of the cracked configuration evidence an important reduction of the stress concentration in the vicinity of the crack; this feature reflects the trabecular architecture of cancellous bone and the regularizing effect of the employed Cosserat elasticity model. The effective micropolar properties obtained from discrete homogenization are in good agreement with corresponding rigidities provided by FE simulations over a unit cell.
Such micromechanically based enhanced continuum models developed at the mesoscopic scale pave the way towards realistic simulations of the mechanical response of complete bone structures submitted to complex loadings.

References

1. Bakhvalov, N., Panasenko, G.: Homogenisation: averaging processes in periodic media. Kluwer Academic Pub, Dordrecht (1984)
2. Bouyge, F., Jasiuk, I., Boccara, S., Ostoja-Starzewski, M.: A micromechanically based couple-stress model of an elastic orthotropic two-phase composite. Eur. J. Mech. A. Solids. **21**, 465–481 (2002)
3. Bowman, S.M., et al.: Creep contributes to the fatigue behavior of bovine trabecular bone'. J. Biomech. Eng. **120**, 647–654 (1998)
4. Broek, D.: Elementary fracture mechanics. Noordhoff, Leyden (1974).
5. Chang, C.S., Kuhn, M.R.: Mechanics of Solids and Structures: Hierarchical Modeling and the Finite Element Solution. On virtual work and stress in granular media. Int. J. Solids. Struct. **42**(13), 3773–3793 (2005)
6. Cosserat, E., Cosserat, F.: Théorie Des Corps Déformables. A. Hermann et Fils, Paris (1909)
7. Cowin, S.C., Doty, S.B.: Tissue Mechanics. Springer, New York (2007)
8. Dos Reis, F.: Homogenization automatique de milieux discrets périodiques. Applications aux mousses polymères et aux milieux auxétique. Ph.D. Thesis, Institut National Polytechnique de Lorraine (2010)
9. Dos Reis, F., Ganghoffer, J.F.: Equivalent mechanical properties of auxetic lattices from discrete homogenization. Comput. Mater. Sci. **51**, 314–321 (2012)
10. Eringen, A.C.: Linear theory of micropolar elasticity. J. Math. Mech. **15**, 909–923 (1966)
11. Eringen, A.C.: Theory of Micropolar Elasticity. In: Liebowitz, H. (ed.) Fracture, vol. II, pp. 621–729. Academic Press, New York (1968)
12. Eringen, A.C.: Continuum Physics - Non-local Field Theories. Academic Press, New York (1976)
13. Eringen, A.C.: Microcontinuum field theories: i foundations and solids. Springer Verlag, New York (1999)
14. Fang, Z.: Image-guided modeling, fabrication and micromechanical analysis of bone and heterogeneous structure. PhD thesis Drexel University, Philadelphia (2005)
15. Fatemi, J., van Keulen, F., Onck, P.R.: Generalized continuum theories: application to stress analysis in bone. Meccanica. **37**, 385–396 (2002)
16. Fatemi, J., Onck, P.R., Poort, G., Van Keulen, F.: Cosserat moduli of anisotropic cancellous bone: a micromechanical analysis. J. Phys. IV France. **105**, 273–280 (2003)
17. Ford, C.M., Keaveny, T.M.: The dependence of shear failure properties of trabecular bone on apparent density and trabecular orientation. J Biomech **29**, 1309 (1996)

18. Ford, C.M., Gibson, L.J.: Uniaxial strength asymmetry in cellular materials: an analytical model Int. J. Mech. Sci. **40**(521), 531 (1998)
19. Gibson, L.J., Ashby, M.F., Schajer, G.S., Robertson, C.I.: The mechanics of two-dimensional cellular materials. Proc. Roy. Soc. Lond. A **382**, 25–42 (1982)
20. Gibson, L.J., Ashby, M.F.: Cellular Solids: Structures and Properties. Cambridge University Press, Cambridge (1997)
21. Gonella, S., Ruzzene, M.: Homogenization and equivalent in-plane properties of two dimensional periodic lattices. Int. J. Solids. Struct. **45**, 2897–2915 (2008)
22. Kim, H.S., Al-Hassani, S.T.S.: A morphological model of vertebral trabecular bone. J. Biomech. **35**, 1101–1114 (2002)
23. Koiter, W.T.: Couple stress in the theory of elasticity. Proc. Koninklijke Nederland Akademie van Wettenschappen B **67**, 17–44 (1964)
24. Lakes, R., Nakamura, S., Behiri, J., Bonfield, W.: Fracture mechanics of bone with short cracks. J. Biomech. **23**, 967–975 (1990)
25. Lakes, R.: Materials with structural hierarchy. Nature **361**, 511–515 (1993)
26. Lakes, R.: Experimental methods for study of Cosserat elastic solids and other generalized elastic continua. In: Muhlhaus, H.-B. (ed.) Continuum Models for Materials with Microstructure, pp. 1–22. Wiley, New York (1995)
27. Liu, S.X., Zhang, H.X., Guo, E.X.: Contributions of trabecular rods of various orientations in determining the elastic properties of human vertebral trabecular bone. Bone **45**, 158–163 (2009)
28. Masters, I.G., Evans, K.E.: Models for the elastic deformation of honeycombs. Compos. Struct. **35**, 403–422 (1996)
29. Miller, Z., Fuchs, M.B.: Effect of trabecular curvature on the stiffness of trabecular bone. J. Biomech. **38**, 1855–1864 (2005)
30. Mindlin, R.D.: Influence of couple-stresses on stress concentrations. Exp. Mech. **3**, 1–7 (1963)
31. Mindlin, R.D.: Micro-structure in linear elasticity. Arch. Rational Mech. Anal. **16**, 51–78 (1964)
32. Mindlin, R.D., Tiersten, H.F.: Effects of couple stresses in linear elasticity. Arch. Rational Mech. Anal. **11**, 415–448 (1962)
33. Mourad, A., Caillerie, D.A., Raoult, A.: A nonlinearly elastic homogenized constitutive law for the myocardium, pp. 1779–1781. Computational Fluid and Solid Mechanics, Cambridge (2003)
34. Muhlhaus, H.B., Oka, F.: Dispersion and wave propagation in discrete and continuous models for granular materials. Int. J. Solids Struct. **33**, 2841–2858 (1996)
35. Panasenko, G.P.: Averaging of processes in frame constructions with random properties. Zh. Vychisl. Mat. Mat. Fiz. **23**, 1098–1109 (1983)
36. Park, H.C., Lakes, R.S.: Torsion of a micropolar elastic prism of square cross section. Int. J. Solids. Struct. **23**, 485–503 (1987)
37. Rovati, M., Veber, D.: Optimal topologies for micropolar solids. Struct. Multidisc. Optim. **33**, 47–59 (2007)
38. Sab, K., Pradel, F.: Homogenisation of periodic Cosserat media. Int. J. Comput. Appl. Technol. **34**, 60–71 (2009)
39. Sanchez-Palencia, E.: Non-homogeneous media and vibration theory, Lecture notes in Physics, 127. Springer-Verlag, Berlin (1980)
40. Shmoylova, E., Potapenko, S., Rothenburg, L.: Stress distribution around a crack in plane micropolar elasticity. J. Elast. **86**, 19–39 (2007)
41. Silva, M.J., Hayes, W.C., Gibson, L.J.: The effects of non-periodic microstructure on the elastic properties of two-dimensional cellular solids. Int. J. Mech. Sci. **37**, 1161–1177 (1995)
42. Suiker, A.S.J., de Borst, R., Chang, C.S.: Micro-mechanical modelling of granular material. Part 1: derivation of a secondgradient micro-polar constitutive theory. Acta. Mech. **149**, 161–180 (2001)
43. Tanaka, M., Adachi, T.: Lattice continuum model for bone remodeling considering microstructural optimality of trabecular architecture. In: Pedersen, P., Bendsoe, M.P. (eds.) IUTAM Symposium on Synthesis in Bio Solid Mechanics, pp. 43–54. Kluwer Academic Publishers, The Netherlands (1999)

44. Taylor, M., Cotton, J., Zioupos, P.: Finite element simulation of the fatigue behaviour of cancellous bone. Meccanica. **37**, 419–429 (2002)
45. Warren, W.E., Byskov, E.: Three-fold symmetry restrictions on two-dimensional micropolar materials. Eur. J. Mech. A. Solids. **21**, 779–792 (2002)
46. Warren, W.E., Kraynik, A.M.: Foam mechanics: the linear elastic response of two dimensional spatially periodic cellular materials. Mech. Mater. **6**, 27–37 (1987)
47. Yang, J.F.C., Lakes, R.S.: Transient study of couple stress effects in compact bone: Torsion. J. Biomech. Engng. **103**, 275–279 (1981)
48. Yoo, A., Jasiuk, I.: Couple-stress moduli of a trabecular bone idealized as a 3D periodic cellular network. J. Biomech. **39**, 2241–2252 (2006)
49. Zhu, H.X.: Size-dependent elastic properties of micro- and nanohoneycombs. J. Mech. Phys. Solids. **58**, 679–696 (2010)
50. Zhu, H.X., Hobdell, J.R., Windle, A.H.: Effects of cell irregularity on the elastic properties of 2D Voronoi honeycombs. J. Mech. Phys. Solids. **49**, 857–870 (2001)

Electro-Thermo-Elastic Simulation of Graphite Tools Used in SPS Processes

Stefan Hartmann, Steffen Rothe and Nachum Frage

Abstract In the range of field-assisted sintering technology or spark plasma sintering all materials in the testing machine undergo very large temperature changes. The powder material, which has to be sintered, is filled into a graphite die and mechanically loaded by a graphite punch. The heat is produced by electrical induction and the cooling process is performed by conduction and radiation. Both the heating and the cooling process are very fast. In order to understand the process of the highly loaded graphite parts, experiments, modeling and computations have to be carried out. On the thermal side the temperature-dependent material properties such as heat capacity and heat conductivity have to be modeled. Since the heat capacity is not independent of the Helmholtz free-energy a particular consideration of the free-energy is carried out. On the other hand, the temperature changes of the electrical resistivity and the material properties of the graphite tool must be taken into considerations. Accordingly, the material properties of "Ohm's law" must be modeled as well. The fully coupled system comprising the electrical, thermal and mechanical field are solved numerically by a monolithic finite element approach. After the spatial discretization using finite elements one arrives at a system of differential-algebraic equations which is solved by means of diagonally implicit Runge-Kutta methods. Issues and open questions in the numerics are addressed and problems in modeling a real application are discussed.

S. Hartmann (✉) · S. Rothe
Institute of Applied Mechanics, Clausthal University of Technology,
Clausthal-Zellerfeld, Germany
e-mail: stefan.hartmann@tu-clausthal.de

S. Rothe
e-mail: steffen.rothe@tu-clausthal.de

N. Frage
Department of Materials Engineering, Ben-Gurion University of the Negev,
Beer-Sheva, Israel
e-mail: nfrage@bgu.ac.il

H. Altenbach et al. (eds.), *Generalized Continua as Models for Materials*,
Advanced Structured Materials 22, DOI: 10.1007/978-3-642-36394-8_8,

1 Introduction

The numerical treatment of powder compaction processes requires the experimental basis, appropriate constitutive models and sophisticated algorithms both for the powder and the tools itself. In field-assisted sintering technology (FAST) the mechanical and thermal loads are applied more or less in parallel. An overview of the technical development of FAST-processes can be found in [1–4]. In the literature there exists only few attempts to model the whole thermo-electro-mechanical problem. In the work of [5] the SPS-process (spark plasma sintering) is modeled without powder to study the thermal and the electrical field together with a small strain thermoelasticity relation for the tooling system. Wang et al. [6] investigated the electrical, temperature and stress fields in order to evaluate stress gradients in the fully densed sample (copper and alumina). In this study the electrical current is treated as a constant. Differently, [7] modelled the time dependence of the electrical current by the use of experimental recorded current for a specific experiment. In [8] a PID control for the closed loop control of the current is added to achieve a prescribed temperature path. In this investigation temperature and stress gradients for a fully densed alumina and copper sample are analyzed. Wang et al. [9] studied the effect of different die sizes, heating rates and pressures on the temperature and stress distribution inside a alumina sample, the tooling system and on the resulting microstructure. Maizza et al. [10] investigated the influence of moving punch on the temperature. He emphasizes the reliability of the model predictions highly depend on the correct modeling of the contact resistances. Cincotti et al. [5] compared simulation results to measured temperature, voltage and displacement data including electric and thermal resistance as a function of temperature and applied mechanically load. Recently two articles also dealing with the densification process are published, [11, 12]. Since the temperature in the powder, and, accordingly the final material properties of the sintering process, is essentially influenced by the graphite tools (given by the die, where the powder is encapsulated, and the punches treating the mechanical loads to compress the powder), the investigation of the die/punch system in view of the temperature and stress distribution is of principle interest. Moreover, the heat is applied using electrical induction so that the temperature and stress distribution during the processes are coupled. Since the applied temperatures vary within a large range, most of the material parameters depend on the temperature itself so that the final initial boundary-value problem is a coupled system represented by the equilibrium conditions, heat equation and the electrical field equation. In view of the investigations in [13] inertia effects are not considered because the investigated temperature-rates are not as fast enough to take resulting phenomena into account. Moreover, the investigated temperature are below the phase transition effects in the graphite tools and the powder material (copper or alumina).

In this article we assume in the first instance thermo-elasticity for small strains and a instationary non-linear heat equation. Particularly, small strain thermo-elasticity is seemingly well understood, see for example, [13, 14]. However, frequently some terms are neglected by intuition or by the assumption of small rates or small

temperature changes. These assumptions are not always applicable, particularly not in FAST-processes. In this case the graphite tools have temperature-dependent properties, such as a temperature-dependent heat-capacity, directly influencing the form of the free-energy and the thermo-mechanical coupling term. Moreover, the well-known effect of a temperature-dependent electrical resistivity influences the evolution of the electrical potential. In this article, we propose some experiments determining the temperature-dependent material properties first. These experiments are given by purely thermal agencies to determine the heat expansion, the heat capacity, the heat conductivity and the electrical resistivity. All these quantities are more or less temperature-dependent. Particularly, the heat capacity influences directly the representation of the free-energy. Thus, aspects of the modeling are touched as well. On the basis of these properties phenomenological models are developed and calibrated to the experimental data.

Since the entire problem is coupled, all practical applications have to be computed numerically. Here, use is made of the finite element method. In [15] coupled problems are discussed within the method of vertical lines. This procedure, well-known as a solution technique for partial differential equations, makes use of two subsequent steps, namely the spatial and the temporal discretization. In our case the spatial discretization using finite elements yields a system of differential-algebraic equations, or, shortly, a DAE-system. In other words, ordinary differential equations are coupled with algebraic equations. In this context, the differential part of the DAE-system results from the discretized instationary non-linear heat equation and the algebraic parts stem from the discretized equilibrium equations and the stationary charge equation, see for general remarks [16]. These systems are frequently solved using a Backward-Euler scheme or a trapezoidal rule (Crank-Nicholson procedure) for the differential part resulting from the fact that the numerical solution of DAEs are commonly not known in the finite element literature. In this article, high-order stiffly accurate diagonally-implicit Runge-Kutta methods (SDIRK-methods), see, for example, [17, 18], are applied having the side-product of an efficient step-size control technique. The reason for this stems from the application of embedded SDIRK methods.

The notation in use is defined in the following manner: geometrical vectors are symbolized by lower case bold-faced letters $\mathbf{a}$ and second order tensors $\mathbf{A}$ by bold-faced Roman letters. Furthermore, we introduce matrices at global level of the finite element procedure symbolized by bold-faced italic letters $\boldsymbol{A}$.

2 Constitutive Modeling and Initial Boundary-Value Problem

Before developing a constitutive model for the graphite material, the mechanical, thermal and electrical properties are discussed. The elasticity parameters are determined using ultrasound measurements, [19, 20], leading to the Young's modulus $\mathrm{E} = 11500\ \mathrm{N/mm^2}$ and the Poisson-ratio $\nu = 0.2$. The temperature-dependence of the elasticity parameters cannot be provided. Moreover, any viscous effects or

remaining deformations are, currently, not known, i.e. measured. Thus, a model of linear thermo-elasticity is assumed. Moreover, any viscous effects or remaining deformations are not taken into considerations. Thus, a model of thermo-elasticity is assumed. The heat expansion is measured to be nearly temperature-independent within the measured range of temperature, see Fig. 1a. According to the assumption that the thermal strains are purely volumetrical,

$$\mathbf{E}_\Theta = \varphi(\Theta(\mathbf{x}, t))\mathbf{I} \tag{1}$$

(pure volumetric heat expansion), Fig. 1a suggest the linear function

$$\varphi(\Theta) = \alpha_\Theta \vartheta = \alpha_\Theta(\Theta - \Theta_0), \tag{2}$$

where α_Θ is the heat expansion coefficient, $\vartheta(\mathbf{x}, t) = \Theta(\mathbf{x}, t) - \Theta_0$ the temperature difference, Θ_0 the reference temperature, and Θ the absolute temperature. The heat expansion coefficient is given by $\alpha_\Theta = 4.55 \times 10^{-6}$ 1/K (here, use is made of a Unitherm 1252 ultra high temperature dilatometer). Further measurements are carried out using a Netzsch Laserflash-device LFA 457 to determine the temperature-dependent heat conductivity, see Fig. 2a. The heat capacity at constant pressure is provided by the manufacturer of the material and the mathematical representation is shown in Fig. 2b.

In order to obtain a more or less reasonable curvature, even outside the range of experimental data, the functions

$$\kappa_\Theta(\Theta) = b_1 e^{-b_2\Theta} + b_3 e^{-b_4\Theta} \tag{3}$$

$$c_\Theta(\Theta) = d_1 + d_2\Theta + d_3 \tanh(d_4\Theta - d_5) \tag{4}$$

are chosen. The parameters are identified with

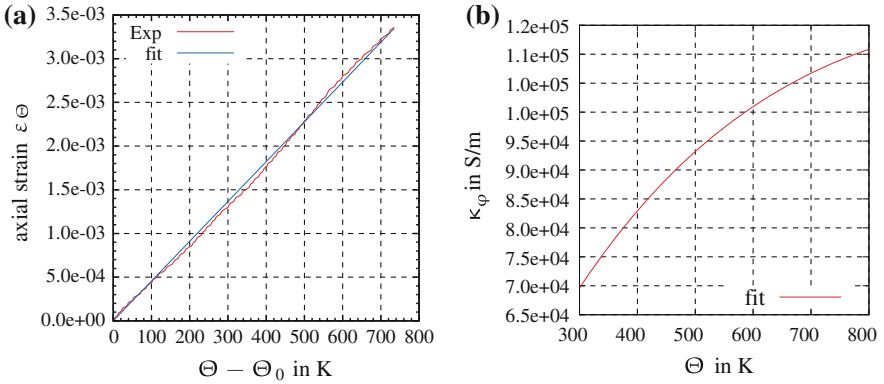

Fig. 1 Heat expansion and electrical conductivity in dependence of the temperature of graphite. (**a**) Heat expansion, (**b**) Electrical conductivity

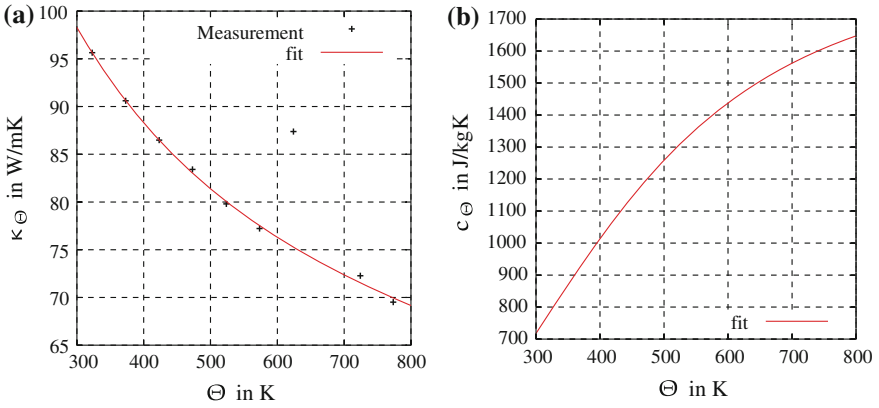

Fig. 2 Heat conductivity and heat capacity in dependence of the temperature. (**a**) Heat conductivity, (**b**) Heat capacity

$$b_1 = 85.7\ \frac{W}{mK}, b_2 = 5.124 \times 10^{-3}\ \frac{1}{K}, b_3 = 88.1\ \frac{W}{mK}, b_4 = 3.292 \times 10^{-4}\ \frac{1}{K},$$
$$d_1 = 586.5\ \frac{J}{kgK}, d_2 = 0.3507\ \frac{J}{kgK^2}, d_3 = 839.4\ \frac{J}{kgK}, d_4 = 3.247 \times 10^{-3}\ \frac{1}{K},$$

and $d_5 = 0.9431$.

In Fig. 1b the model response of the data for the electrical conductivity in dependence of the temperature provided by the manufacturer is shown as well, which is modeled by

$$\kappa_\varphi(\Theta) = c_1 e^{-c_2\Theta} - c_3 e^{-c_4\Theta} \tag{5}$$

with

$$c_1 = 1.69 \times 10^5\ \frac{S}{m}, c_2 = 2.168 \times 10^{-4}\ \frac{1}{K}, c_3 = 1.661 \times 10^5\ \frac{S}{m}, c_4 = 2.089 \times 10^{-3}\ \frac{1}{K}.$$

The mechanical constitutive equations are applied as follows. First of all, a dependence of the mechanical material parameters on the electrical current and the temperature is not assumed. These properties have not been available so far. For a first instance thermo-elasticity is assumed. There, it is common to prescribe a specific free-energy function and calculate the heat capacity, or to define the heat capacity constant (commonly contradicting the choice of the specific free-energy), or to make use of the experimentally determined heat capacity and to integrate those equations to obtain the specific free-energy. Here, use is made of the latter concept. Thus, the case of thermo-elasticity has to be recapped. Since we assume small strains, the linearized strain tensor $\mathbf{E}(\mathbf{x}, t) = (\text{grad}\ \mathbf{u}(\mathbf{x}, t) + \text{grad}^{\,T}\mathbf{u}(\mathbf{x}, t))/2$ is introduced. $\mathbf{u}(\mathbf{x}, t)$ defines the displacement field, where $\mathbf{x}$ symbolizes the spatial coordinate and t defines the time. As it is common, the strain tensor is decomposed into a mechanical $\mathbf{E}_M$ and a

thermal part $\mathbf{E}_\Theta$,

$$\mathbf{E} = \mathbf{E}_M + \mathbf{E}_\Theta, \tag{6}$$

with $\mathbf{E}_\Theta$ given in Eq. (1). In view of the subsequent development the strain-rates are required, i.e. the mechanical strain-rate reads

$$\dot{\mathbf{E}}_M = \dot{\mathbf{E}} - \dot{\mathbf{E}}_\Theta = \dot{\mathbf{E}} - \alpha_\Theta \dot{\Theta}\mathbf{I} \quad \text{with} \quad \dot{\mathbf{E}}_\Theta = \alpha_\Theta \dot{\Theta}\mathbf{I}. \tag{7}$$

In the following, it is assumed that the free-energy $\psi(\mathbf{E}_M, \Theta)$ can be decomposed into one part $\psi_M(\mathbf{E}_M)$ depending only on the mechanical-based deformation, and another part $\psi_\Theta(\Theta)$ resulting from the temperature effects

$$\psi(\mathbf{E}_M, \Theta) = \psi_M(\mathbf{E}_M) + \psi_\Theta(\Theta). \tag{8}$$

In the case of linear thermo-elasticity

$$\rho\psi_M(\mathbf{E}_M) = \frac{K}{2}(\operatorname{tr}\mathbf{E}_M)^2 + G\mathbf{E}_M^D \cdot \mathbf{E}_M^D \tag{9}$$

defining the mechanical part of the specific free-energy (isotropic linear elasticity relation), where K symbolizes the bulk modulus, G the shear modulus, and $\rho(\mathbf{x})$ the mass density. For the given Young's modulus E and the Poisson-ratio ν the bulk and shear moduli are

$$K = \frac{E}{3(1-2\nu)} = 6389\text{N/mm}^2, \quad G = \frac{E/}{2(1+\nu)} = 4792\text{N/mm}^2,$$

respectively.

Remark 8.1. The elastic constants might be depend on the temperature. However, the experimental results for the underlying material are still an open issue. Accordingly, as a first attempt temperature-independent bulk and shear moduli are assumed. This also addresses the form of the classically simple form of the specific free-energy function. □

$\operatorname{tr}\mathbf{A} = a_k^k$ defines the trace and $\mathbf{A}^D = \mathbf{A} - 1/3(\operatorname{tr}\mathbf{A})\mathbf{I}$ denotes the deviator operator of a second order tensor $\mathbf{A}$. $\operatorname{tr}\mathbf{E}_M$ is interpreted as the volumetric mechanical strains resulting from the interpretation that for the isothermal, small strain theory $\varepsilon_V := \operatorname{tr}\mathbf{E} = \operatorname{tr}(\operatorname{grad}\mathbf{u}) = \operatorname{div}\mathbf{u}$ holds, where ϵ_V represents the volumetric strain. The thermal part of the free-energy is unknown so far and is related to the heat capacity.

The Clausius-Duhem inequality (CDI) is assumed to guarantee thermo-mechanical consistence, which reads

$$-\dot{e} + \Theta\dot{s} + \frac{1}{\rho}\mathbf{T} \cdot \dot{\mathbf{E}} - \frac{1}{\Theta}\mathbf{q} \cdot \mathbf{g} \geqslant 0. \tag{10}$$

$e(\mathbf{x},t)$ is the specific internal energy, $s(\mathbf{x},t)$ the specific entropy, $\mathbf{q}(\mathbf{x},t)$ the heat flux vector, and $\mathbf{g}(\mathbf{x},t) = \operatorname{grad}\Theta(\mathbf{x},t)$ the temperature gradient, see [21]. Additionally, it is assumed that there exists a relation between the specific internal energy e and the free-energy ψ, the total temperature Θ and the specific entropy s by

$$e = \psi + \Theta s \tag{11}$$

implying

$$\dot{e} = \dot{\psi} + \dot{\Theta}s + \Theta\dot{s}. \tag{12}$$

Inserting this relation and the time-derivative of the free-energy

$$\dot{\psi} = \frac{\partial\psi}{\partial\mathbf{E}_M}\cdot\dot{\mathbf{E}}_M + \frac{\partial\psi}{\partial\Theta}\dot{\Theta} = \frac{d\psi_M}{d\mathbf{E}_M}\cdot\dot{\mathbf{E}}_M + \frac{d\psi_\Theta}{d\Theta}\dot{\Theta} \tag{13}$$

into the CDI (10) yields the inequality

$$-\dot{\psi} - \dot{\Theta}s + \frac{1}{\rho}\mathbf{T}\cdot\dot{\mathbf{E}} - \frac{1}{\Theta}\mathbf{q}\cdot\mathbf{g} \geqslant 0 \tag{14}$$

i.e.

$$\begin{aligned} &-\frac{d\psi_M}{d\mathbf{E}_M}\cdot\dot{\mathbf{E}}_M - \frac{d\psi_\Theta}{d\Theta}\dot{\Theta} - s\dot{\Theta} + \frac{1}{\rho}\mathbf{T}\cdot(\dot{\mathbf{E}}_M + \dot{\mathbf{E}}_\Theta) - \frac{1}{\Theta}\mathbf{q}\cdot\mathbf{g} = \\ &= \left(\frac{1}{\rho}\mathbf{T} - \frac{d\psi_M}{d\mathbf{E}_M}\right)\cdot\dot{\mathbf{E}}_M - \left(s + \frac{d\psi_\Theta}{d\Theta} - \frac{\alpha_\Theta}{\rho}\mathbf{T}\cdot\mathbf{I}\right)\cdot\dot{\Theta} - \frac{1}{\Theta}\mathbf{q}\cdot\mathbf{g} \geqslant 0, \end{aligned} \tag{15}$$

where in addition to Eq. $(7)_2$ the decomposition $(7)_1$ is taken into consideration. Using $\operatorname{tr}\mathbf{T} = \mathbf{T}\cdot\mathbf{I}$, the strain-energies (9) and $\psi_\Theta(\Theta)$ yield for arbitrary processes the classical potential relations for the assumption of a small strain thermo-elastic material

$$\mathbf{T} = \rho\frac{d\psi_M}{d\mathbf{E}_M} = K(\operatorname{tr}\mathbf{E}_M)\mathbf{I} + 2G\mathbf{E}_M^D = K(\operatorname{tr}\mathbf{E} - 3\alpha_\Theta\vartheta)\mathbf{I} + 2G\mathbf{E}^D \tag{16}$$

$$s = -\frac{d\psi_\Theta}{d\Theta} + \frac{\alpha_\Theta}{\rho}(\operatorname{tr}\mathbf{T}) = -\frac{d\psi_\Theta}{d\Theta} + \frac{3\alpha_\Theta K}{\rho}(\operatorname{tr}\mathbf{E} - 3\alpha_\Theta\vartheta) \tag{17}$$

Furthermore, $(1/\Theta)\mathbf{q}\cdot\mathbf{g} \leqslant 0$ has to be satisfied, which, frequently, is modeled by Fourier's model

$$\mathbf{q} = -\kappa_\Theta(\Theta)\mathbf{g} = -\kappa_\Theta(\Theta)\operatorname{grad}\Theta, \tag{18}$$

where $\kappa_\Theta(\Theta) \geqslant 0$ represents the temperature-dependent heat conductivity. Thus, all constitutive assumptions are explained, only the thermal part of the specific free-

energy function, $\psi_\Theta(\Theta)$, is unknown so far and has to be determined by the heat capacity c_Θ.

In the following, the coupled partial differential equations required for computing boundary-value problems must be derived. First of all, the elasticity relation (16) has to be inserted into the balance of linear momentum (here the inertia terms are neglected)

$$\operatorname{div} \mathbf{T} + \rho \mathbf{k} = \mathbf{0}, \tag{19}$$

where $\rho\mathbf{k}$ is the specific volume force ($\mathbf{k}$ represents the acceleration of gravity). Second, the balance of energy must be considered

$$\dot{e} = -\frac{1}{\rho} \operatorname{div} \mathbf{q} + r_\varphi + p. \tag{20}$$

p defines the stress power describing the coupling term

$$p = \frac{1}{\rho} \mathbf{T} \cdot \dot{\mathbf{E}} = \frac{d\psi_M}{d\mathbf{E}_M} \cdot \dot{\mathbf{E}} = (K(\operatorname{tr} \mathbf{E} - 3\alpha_\Theta \vartheta)\mathbf{I} + 2G\mathbf{E}^D) \cdot \dot{\mathbf{E}}, \tag{21}$$

i.e. it represents a heat source for the heat equation resulting from the mechanical behavior. r_φ symbolizes a volumetrically distributed heat source caused by the electrical current, see Eq. (30).

It is common, to exchange the internal energy e in the instationary non-linear heat equation (20) by the rate of the specific internal energy (12). Using Eqs. (7), (13), (16) and (17) leads to

$$\begin{aligned} \rho\dot{\psi} &= \rho \frac{d\psi_M}{d\mathbf{E}_M} \cdot (\dot{\mathbf{E}} - \alpha_\Theta \dot{\Theta} \mathbf{I}) + \rho \frac{d\psi_\Theta}{d\Theta} \dot{\Theta} = \mathbf{T} \cdot \dot{\mathbf{E}} - \rho \left(\alpha_\Theta (\operatorname{tr} \mathbf{T}) - \frac{d\psi_\Theta}{d\Theta} \right) \dot{\Theta} \\ &= \mathbf{T} \cdot \dot{\mathbf{E}} - \rho s \dot{\Theta}. \end{aligned} \tag{22}$$

It follows that the instationary non-linear heat equation, see Eqs. (20) and (12), reads

$$\rho\Theta\dot{s} = -\operatorname{div} \mathbf{q} + \rho r_\varphi. \tag{23}$$

The time-derivative of the specific entropy s in Eq. (17),

$$\dot{s} = \left(\frac{9K\alpha_\Theta^2}{\rho} + \frac{d^2\psi_\Theta}{d\Theta^2} \right) \dot{\Theta} + \frac{3\alpha_\Theta K}{\rho} (\operatorname{tr} \dot{\mathbf{E}}), \tag{24}$$

can be inserted now,

$$\rho \left(-\frac{d^2\psi_\Theta}{d\Theta^2} - \frac{9K\alpha_\Theta^2}{\rho} \right) \Theta\dot{\Theta} = \operatorname{div} (\kappa_\Theta(\Theta) \operatorname{grad} \Theta) + \rho r_\varphi - 3\alpha_\Theta K (\operatorname{tr} \dot{\mathbf{E}}) \Theta. \tag{25}$$

This is the analytically exact form of the instationary heat equation in thermo-elasticity without any further assumptions to reduce its complexity. The mathematical structure is as follows

$$\rho c_\Theta(\Theta)\dot{\Theta} = \operatorname{div}\left(\kappa_\Theta(\Theta)\,\operatorname{grad}\Theta\right) + \rho r_\varphi - \gamma(\dot{\mathbf{E}}, \Theta) \tag{26}$$

which is coupled with the local balance equation (19) and the elasticity relation (16). Obviously, the typical assumption of a constant specific heat capacity

$$c_\Theta(\Theta) = -\left(\frac{d^2\psi_\Theta}{d\Theta^2} - \frac{9K\alpha_\Theta^2}{\rho}\right)\Theta \tag{27}$$

is not valid anymore, see Fig. 2b, and it occurs a thermo-elastic coupling (production) term

$$\gamma(\dot{\mathbf{E}}, \Theta) = 3\alpha_\Theta K\Theta(\operatorname{tr}\dot{\mathbf{E}}), \tag{28}$$

which is commonly not considered due to the fact that it is very small. In view of the heat capacity (4) the thermal part of the specific free-energy in Eq. (27) one obtains

$$\frac{d^2\psi_\Theta}{d\Theta^2} = -\frac{1}{\Theta}d_1 - d_2 - \frac{d_3}{\Theta}\tanh(d_4\Theta - d_5) + \frac{9K\alpha_\Theta^2}{\rho}. \tag{29}$$

However, the second term is analytically non-integrable. Of course, it is possible to generate a power series around Θ_0, but this is not the scope of the article and is not necessary within the whole approach. It must be remarked that for a temperature-dependent heat expansion or more sophisticated constitutive models it is hard to obtain a consistent relation between the specific free-energy and the heat capacity. Another possibility is to assume a free energy $\psi_\Theta(\Theta)$ reflecting the experimental data. The advantage is that one has only to carry out two differentiation steps. However, one has to know a priorily the course of the curve of the second derivative $\psi''_\Theta(\Theta)$, which does not simplify the problem. In the case of small strain thermo-elasticity the proposed approach has no influence although there is no analytical expression. However, for models of internal variables or in the case of large strains there is a discrepancy, which commonly is overcomed by assuming $\psi_\Theta(\Theta)$ and letting c_Θ constant being a rough approximation. In the case of large temperature changes, however, this is a very rough assumption. The remaining coupling term results from the heat generation by the electrical current, which is described by the volumetrical heat source r_φ, called Joule-heating, in Eq. (26),

$$r_\varphi = \frac{1}{\rho}\mathbf{e}\cdot\mathbf{j} = \frac{1}{\rho}\kappa_\varphi(\Theta)\operatorname{grad}\varphi(\mathbf{x},t)\cdot\operatorname{grad}\varphi(\mathbf{x},t), \tag{30}$$

where the electrical field $\mathbf{e}(\mathbf{x},t) = -\operatorname{grad}\varphi(\mathbf{x},t)$ is related to the electrical potential $\varphi(\mathbf{x},t)$ and the electrical current $\mathbf{j}(\mathbf{x},t) = \kappa_\varphi(\Theta)\mathbf{e}(\mathbf{x},t)$ reflects Ohm's law.

$\kappa_\varphi(\Theta)$, see Eq. (5), defines the electrical conductivity. In other words, there is a coupling between the electrical potential $\varphi(\mathbf{x}, t)$ in electrostatics and the conservation of charge

$$\operatorname{div} \mathbf{j}(\mathbf{x}, t) = 0, \quad \text{i.e.} \quad \operatorname{div} (\kappa_\varphi(\Theta) \operatorname{grad} \varphi) = 0, \tag{31}$$

(assumption of a stationary electrical current, see [16, 22, 23] for further reading as well). In conclusion, there is a coupling of the three partial differential equations (19), (26) and (31). The non-linearities result from the temperature-dependence of the material parameters and the boundary-conditions such as convection and radiation.

3 Time-Adaptive Monolithic Finite Element Approach

In the following, the coupled equations mentioned above, i.e. the equilibrium conditions (19), with the thermo-elasticity relation (16), the instationary non-linear heat equation (25), i.e. (26), using the abbreviations (27), (28) and (30), and the stationary current equation (31), are treated within finite elements. Here, use is made of the method of vertical lines, where in the first step the spatial discretization is carried out using the finite element discretization, see [15]. In the second step the temporal discretization is performed applying stiffly accurate diagonally implicit Runge-Kutta methods.

The weak formulation of Eq. (19) is derived by multiplying the partial differential equation with virtual displacements, integrating over the volume and applying the divergence theorem

$$\int_V \mathbf{T} \cdot \delta\mathbf{E} \, dV - \int_A \mathbf{t} \cdot \delta\mathbf{u} \, dA - \int_V \rho\mathbf{k} \cdot \delta\mathbf{u} \, dV = 0, \tag{32}$$

where $\delta\mathbf{E}(\mathbf{x}) = (\operatorname{grad} \delta\mathbf{u}(\mathbf{x}) + \operatorname{grad}^{\mathsf{T}} \delta\mathbf{u}(\mathbf{x}))/2$ defines the virtual strain tensor, i.e. the symmetric part of the gradient of the virtual displacements $\delta\mathbf{u}(\mathbf{x})$. In this context it has to hold $\delta\mathbf{u}(\mathbf{x}) = \mathbf{0}$ on the boundary A^u of the material body, where the displacements are prescribed, $A = A^\sigma \cup A^u$, $\mathbf{u}(\mathbf{x}, t) = \mathbf{q}u(t)$ on A^u (Dirichlet boundary conditions). $\mathbf{t}(\mathbf{x}, t) = \mathbf{T}(\mathbf{x}, t)\mathbf{n}(\mathbf{x}, t)$ defines the stress vector on the surface A^σ, where $\mathbf{n}$ represents the surface normal. $\mathbf{t}(\mathbf{x}, t) = \mathbf{q}t(\mathbf{x}, t)$ on A^σ define the Neumann boundary conditions. V stands for the volume of the material body.

In the case of the instationary non-linear heat equation (26) the derivation is similar. First, the heat equation is multiplied with the virtual temperatures $\delta\Theta(\mathbf{x})$, integrated over the volume, and the divergence theorem is applied,

$$\int_V \rho c_\Theta(\Theta)\dot{\Theta}\delta\Theta \, dV = \int_A q \, \delta\Theta \, dA - \int_V \kappa_\Theta(\Theta) \operatorname{grad} \Theta \cdot \operatorname{grad} \delta\Theta \, dV + \int_V (\rho r_\varphi - \gamma(\dot{\mathbf{E}}, \Theta))\delta\Theta \, dV, \tag{33}$$

see [24–26]. Analogously to the mechanical field problem, the virtual temperature has the property $\delta\Theta = 0$ on A^{Θ}, i.e. the surface where the temperatures are known, $\Theta(\mathbf{x}, t) = \overline{\Theta}(\mathbf{x}, t)$ on A^{Θ} (Dirichlet boundary conditions). Furthermore, on the boundary A^{q} the heat transport $q = -\mathbf{q} \cdot \mathbf{n}$ is prescribed, $q(\mathbf{x}, t) = \overline{q}(\mathbf{x}, t)$ on A^{q}, $A = A^{\Theta} \cup A^{q}$. In the case of convection the linear model $q(\Theta) = h(\Theta - \Theta_{\text{ref}})$ and for radiation the non-linear boundary condition $q(\Theta) = \sigma\varepsilon(\Theta^4 - \Theta_{\infty}^4)$ are considered, where σ symbolizes the Stefan Boltzmann constant and ε the emissivity.

The equation of electrostatics (31) can be treated similar to the heat equation because it has the same mathematical structure. In this context one obtains

$$\int_V \kappa_{\varphi}(\Theta)\,\text{grad}\,\varphi \cdot \text{grad}\,\delta\varphi \; dV = \int_A j\,\delta\varphi \; dA \tag{34}$$

where $\delta\varphi$ represents the virtual electrical potential and j the electrical current density. Analogously, $\delta\varphi = 0$ on A^{φ}, i.e. the surface where the electrical potential is prescribed, $\varphi(\mathbf{x}, t) = \overline{\varphi}(\mathbf{x}, t)$ on A^{φ} (Dirichlet boundary conditions). Furthermore, on the boundary A^{j} the electrical current density $j = -\mathbf{j} \cdot \mathbf{n}$ is prescribed, $j(\mathbf{x}, t) = \overline{j}(\mathbf{x}, t)$ on A^{j}, $A = A^{\varphi} \cup A^{j}$.

The equation of electrostatics to compute thermoelectric coupling effects can be found in several publications. In Seifert et al. [27] a one dimensional model is solved by Mathematica to compute the thermoelectric behavior of Peltier coolers. In the work of Pérez-Aparicio et al. [28] a three-dimensional, non-linear fully coupled thermoelectric finite element simulation is carried out in order to simulate Peltier coolers. They included the Seebeck, Peltier, Thompson, and Joule effect in their analysis. The finite element method is combined with a Monte Carlo simulation for a material sensitivity analysis. Palma et al. [29] used a modified Fourier law yielding a hyperbolic heat equation for the simulation of micro-devices under rapid transient effects. They simulated thermoelectric material with a non-linear dynamic finite element formulation. Munir et al. [30] simulated the current and temperature distributions to find out temperature and current gradients in axial and radial direction for a SPS-process. In the underlying article, however, the field is coupled to mechanical and thermal influences.

The spatial discretization makes use of shape functions for the displacements, the temperature and the electrical potential. This leads to the linear system of equations (in two unknowns)

$$\boldsymbol{K}_{u}\boldsymbol{u}(t) + \boldsymbol{K}_{u\Theta}\boldsymbol{\Theta}(t) = \boldsymbol{r}_{u}(t), \tag{35}$$

where $\boldsymbol{u}(t) \in \mathbb{R}^{n_u}$ are the unknown nodal displacements and $\boldsymbol{\Theta}(t) \in \mathbb{R}^{n_\Theta}$ the unknown nodal temperatures. $\boldsymbol{K}_{u}$ symbolizes the mechanical stiffness matrix of linear elasticity and $\boldsymbol{K}_{u\Theta}$ the stiffness matrix resulting from the heat expansion. The right-hand side contains the prescribed Dirichlet- and Neumann boundary conditions and a term coming from the reference temperature Θ_0. The weak form of the heat equation (33) can be treated in a similar manner, see, for example, [25], yielding the system of ordinary differential equations

Table 1 Material parameters of the materials in a FAST-process

Material	c_Θ $mm^2/(s^2K)$	κ_Θ $tmm/(s^3K)$	κ_φ $10^{-3}A/(Vmm)$	α_Θ 1/K	ρ t/mm^3	E MPa	ν –
Copper	$c_{\Theta,Cu}(\Theta)$	$\kappa_{\Theta,Cu}(\Theta)$	$\kappa_{\varphi,Cu}(\Theta)$	1.6×10^{-5}	8.92×10^{-9}	120 000	0.3
Alumina (Al_2O_3)	$c_{\Theta,Al}(\Theta)$	$\kappa_{\Theta,Al}(\Theta)$	1×10^{-8}	8.5×10^{-6}	3.7×10^{-9}	350 000	0.22
Graphite	$c_\Theta(\Theta)$	$\kappa_\Theta(\Theta)$	$\kappa_\varphi(\Theta)$	4.55×10^{-6}	1.85×10^{-9}	11500	0.2

The material functions $\kappa_\Theta(\Theta)$, $\kappa_\varphi(\Theta)$, and $c_\Theta(\Theta)$ are given in Eqs. (3), (4) and (5)

$$\boldsymbol{C}_\Theta(t, \boldsymbol{\Theta})\dot{\boldsymbol{\Theta}}(t) = \boldsymbol{r}_\Theta(t, \dot{\boldsymbol{u}}, \boldsymbol{\Theta}, \boldsymbol{\Phi}). \tag{36}$$

$\boldsymbol{C}_\Theta \in \mathbb{R}^{n_\Theta \times n_\Theta}$ represents the temperature-dependent heat capacity matrix and $\boldsymbol{r}_\Theta \in \mathbb{R}^{n_\Theta}$ contains the right-hand side of Eq. (33), i.e. the heat conduction and the terms resulting from the boundary conditions and the heat source of the electrical potential. The coupling results from Joule heating, i.e. it depends on the nodal values of the electrical potential $\boldsymbol{\Phi}(t)$. Analogously, the charge equation (34) leads in its discretized form to

$$\boldsymbol{K}_\varphi(t, \boldsymbol{\Theta})\boldsymbol{\Phi}(t) = \boldsymbol{r}_\varphi(t, \boldsymbol{\Theta}), \tag{37}$$

where the "stiffness matrix" $\boldsymbol{K}_\varphi \in \mathbb{R}^{n_\varphi \times n_\varphi}$ is temperature-dependent caused by the electrical conductivity. $\boldsymbol{\Phi}(t) \in \mathbb{R}^{n_\varphi}$ are the unknown nodal values of the electrical potential. Equations (35), (36) and (37) represent a DAE-system, where the algebraic part results from the mechanical equilibrium conditions (35) and the equation of electrostatics (37) and the differential part stems from the instationary heat equation (36). According to a number of publications use is made of stiffly accurate diagonally implicit Runge-Kutta methods (SDIRK-methods) having the advantage to be of higher order and to have time-adaptivity for free by a local error estimation using embedded schemes, see for their basic ideas [17, 18, 31], in the context of constitutive modeling with evolutionary-type [32–35] and for further problems [25, 36, 37]. The application of SDIRK-methods yields in each stage (points in time in the interval t_n to t_{n+1}) a coupled system of non-linear equations, which can be solved by any kind of non-linear equation solver. In the examples below the Newton-Raphson and the Newton-Raphson-Chord method are applied, see [38, 39].

4 Simulations

In the following the application of SDIRK-methods is investigated. Here, a real process occurring in field assisted sintering is studied and the problems concerned are worked out. For these computations the material parameters are compiled in Table 1. The material functions for copper and alumina are listed in the appendix.

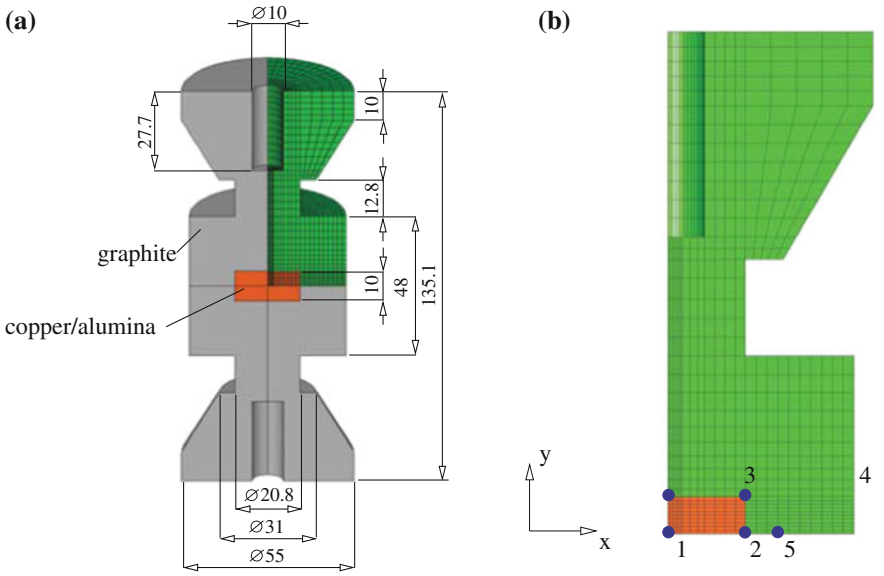

Fig. 3 Mesh (linear hexahedral elements with $n_u = 27722$, $n_\Theta = 9907$, and $n_\varphi = 9588$ unknowns) and geometry. **a** Geometry in mm, **b** Mesh and evaluation points in xy-plane

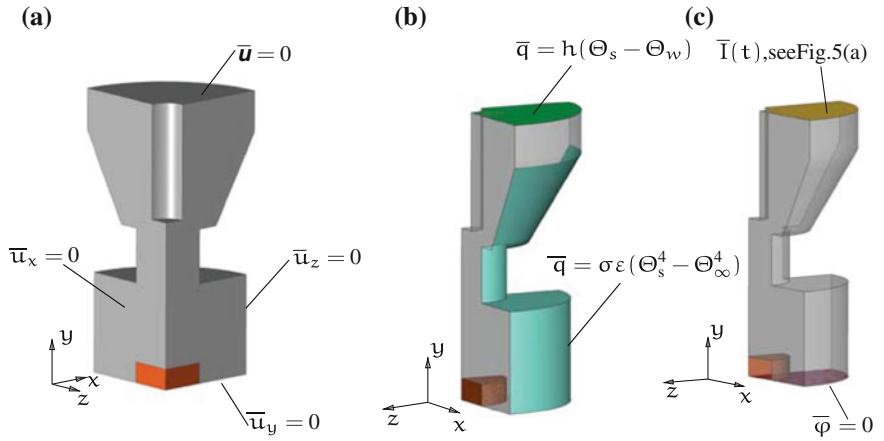

Fig. 4 Boundary conditions. **a** Mechanical field, **b** Thermal field, **c** Electrical field

In Fig. 3 the geometry of a die/punch system is shown, where the rectangular region close to the center contains the compacted powder material. In this context it has to be mentioned that not the compaction process itself is treated, but "only" the temperature evolution in the die/punch/powder system is studied. The boundary conditions are shown in Fig. 4 for the displacements/forces, temperatures/heat fluxes, and electrical potential/electrical current at the surfaces. Θ_s is the surface temperature

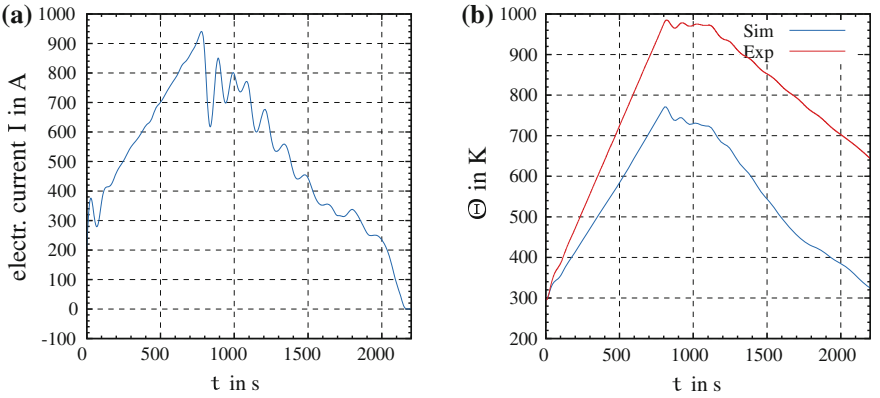

Fig. 5 Measured electrical current taken from the FAST-machine used as boundary condition. **a** Prescribed electrical current ($I = \int_A \mathbf{j} \cdot \mathbf{n}\, dA$), **b** Measured and simulated temperature evolution in point 5 ($\Theta_0 = 273$ K)

of the graphite tools, Θ_w the water temperature and h the heat transfer coefficient ($h = 0.88$ t/(s^{3}K),$\Theta_w = 295.15$K). This represents a very rough modeling of the cooling channels in the steel parts adjacent to the upper graphite surface. In view of radiation the classical model is chosen having the Boltzmann constant $\sigma = 5.6704 \times 10^{-12}$t/(s^{3}K^4) and the emissivity of $\varepsilon = 0.8$. The temperature of the chamber wall is supposed to be $\Theta_\infty = 303.15$ K. Since the chamber is under vacuum, convection on the lateral surfaces is not taken into consideration.

From the testing machine one obtains the data of the electrical current prescribed at the upper surface, see Fig. 5a for the smoothed response. In Fig. 5b the temperature response for copper powder is depicted, see for the chosen material [40], showing that the temperature at point 5 is underestimated, see Fig. 3. The heating rate in the experiment is $\dot{\Theta} = 50$ K/min. The reason of this can be seen for the absence of heat reflection in the machine's chamber, which leads to a larger surface temperature, and the inaccurate modeling of the convection at the upper surface, where the adjacent steel parts with the water cooling channels are located. However, more pronounced seems to be the influence of the electrical contact conditions between steel and graphite, graphite-graphite and graphite-powder, as reported in [10, 41, 42], which is not modeled. Particularly, an imperfect contact changes the resistivity and, accordingly, the heat generation. First attempts using a commercial finite element program confirms this behavior, which is not shown here.

The comparison of electrically conducting and non-conducting material (copper powder and a ceramic powder (alumina)) yields the fact that the electrically insulating powder increases the heat in the graphite tool, see Fig. 6a, which is obvious since the electrically conducting cross-section is smaller for ceramic powder than for metal powder. However, the temperature inside the die is homogenously distributed as indicated in Fig. 6b.

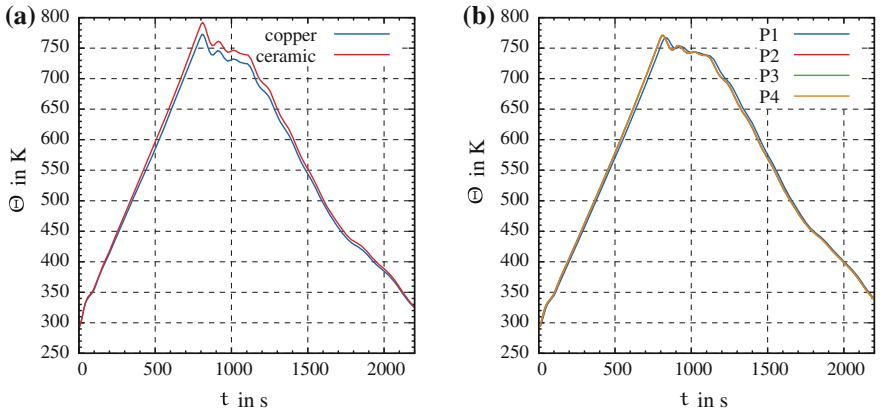

Fig. 6 Comparison of electrical conducting and non-conducting copper and ceramic powder. **a** Comparison between copper and ceramic powder in point 1, **b** Temperature for ceramic powder at the four corners 1–4, see numbering in Fig. 3b

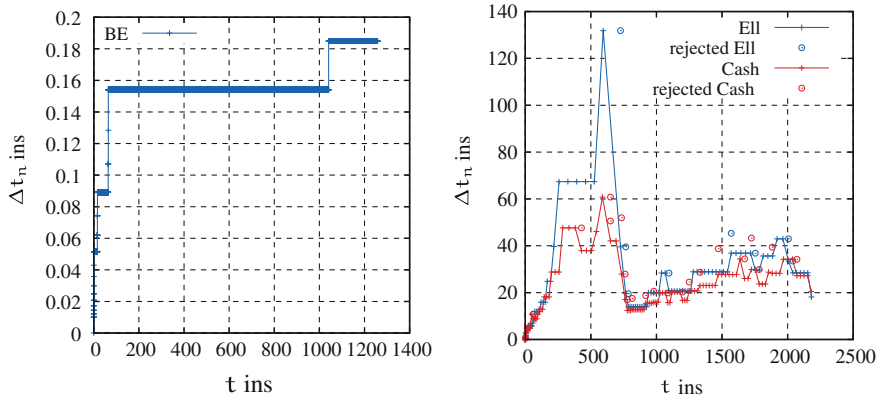

Fig. 7 Step-size behavior using various time-integrator. **a** Backward-Euler method with step-size control using the number of iterations, **b** Method of Ellsiepen (2nd order) and Cash (3rd order) using embedded methods

In view of the numerical treatment using time-adaptive SDIRK-methods, the classical Backward-Euler scheme is chosen as a first choice. Using this procedure a common adaptive scheme makes use of the number of Newton-Raphson iterations to estimate the step-size. If the number of iterations is less than 5, the step-size is increased. However, if one looks at the step-size behavior in Fig. 7a, an appropriate computational time cannot be obtained (we terminated the computation due to an excessive computational amount). Thus, a time-adaptive second-order and third-order SDIRK-method of Ellsiepen, see [32, 43], and [44], are applied leading to much larger time increments. Accordingly, reasonable computational costs are obtained. However, there are a number of step-size rejections resulting from

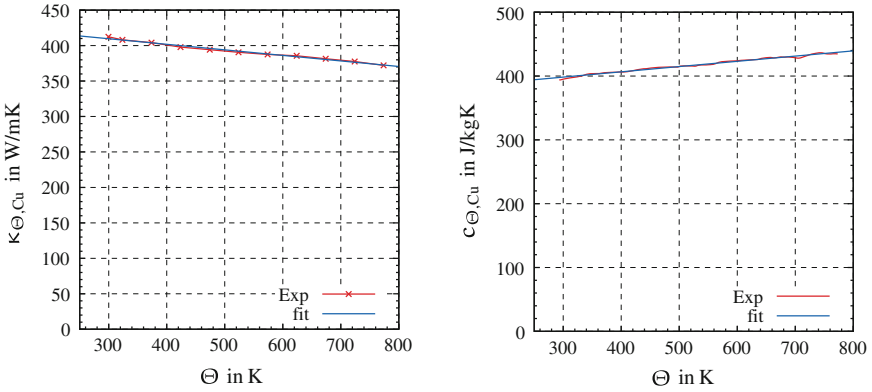

Fig. 8 Heat conductivity and heat capacity of copper in dependence of the temperature. **a** Thermal conductivity, **b** Heat capacity

the non-smoothness of the prescribed electrical current function. It seems that the second-order method of Ellsiepen is better than the third order method of Cash. Furthermore, it turns out that a Newton-Raphson-Chord method, see [38, 39], is much more efficient (approximately 10–15 % of the computational time) than using a Newton-Raphson method. However, an starting vector estimation for the Newton-Raphson method is always required, see in this context [38].

5 Conclusions

The modeling of electro-thermo-mechanical structures is done on the basis of all possible experimental data, i.e. the temperature-dependent heat capacity, heat conductivity and electrical conductivity as well as the elasticity parameters are obtained and modeled. It turns out that the boundary conditions and the contact conditions between the tools have a significant influence on the accuracy of the prediction, which have to be taken into consideration in future applications. The numerical treatment of the resulting coupled system of differential-algebraic equations is carried out using high-order and time-adaptive schemes. The application of second-order time-integration method using embedded SDIRK-methods yields a sufficient fast computation, particularly, if time-adaptivity is chosen, a starting vector estimation is applied and the Newton-Raphson-Chord method is considered. In this case fast computations are possible even for highly non-linear input data.

Acknowledgments First of all, we would like to thank the German Research Foundation (DFG) for supporting this work under the grant no. HA2024/7-1. Furthermore, the authors would like

to thank PD Dr.-Ing. habil. Bernd Weidenfeller for measuring the heat capacity and the thermal conductivity of copper.

Appendix

In the numerical studies the copper is used in the die system. For this the temperature-dependent heat capacity and conductivity are measured, see Fig. 8. The heat capacity at constant pressure of copper is measured with a Netzsch DSC 204 F1 Phoenix apparatus, which uses the Differential Scanning Calorimetry, see Fig. 8b. The thermal diffusivity $a(\Theta)$ of copper is measured with a Netzsch Laserflash LFA 457 and subsequently the thermal conductivity is computed by $\kappa_\Theta(\Theta) = a(\Theta)\rho c_\Theta(\Theta)$, see Fig. 8a. For both quantities a linear temperature dependence is assumed,

$$\kappa_{\Theta,\mathrm{Cu}}(\Theta) = -78.3347 \times 10^{-3}\ \mathrm{W/(mK^2)}\Theta + 433.173\mathrm{W/(mK)} \tag{38}$$

$$c_{\Theta,\mathrm{Cu}}(\Theta) = 82.2141 \times 10^{-3}\ \mathrm{J/(kgK^2)}\Theta + 373.728\mathrm{J/(kgK^2)} \tag{39}$$

which fit very well with experimental data. The properties of alumina and the electrical conductivity of copper are taken from the literature, see [30]. The investigated temperature range in this publication is between 300 K and 1300 K.

$$\kappa_{\Theta,\mathrm{Al}}(\Theta) = \frac{65181330.4 + \Theta}{-669628.8 + 8175.85\Theta} \quad \text{in} \quad \mathrm{W/(mK)}, \tag{40}$$

$$c_{\Theta,\mathrm{Al}}(\Theta) = \frac{7770.25\Theta}{249.4 + \Theta} + \frac{790.15}{249 + \Theta} + 0.008\Theta \quad \text{in} \quad \mathrm{J/(kgK)}, \tag{41}$$

$$\kappa_{\varphi,\mathrm{Al}} = 10^{-8}\mathrm{A/(Vm)} \tag{42}$$

$$\kappa_{\varphi,\mathrm{Cu}}(\Theta) = (5.5 + 0.038\Theta) \times 10^{9} \quad \text{in} \quad \mathrm{A/(Vm)} \tag{43}$$

References

1. Garay, J.: Current-activated, pressure-assisted densification of materials. Annu. Rev. Mater. Res. **40**(1), 445–468 (2010)
2. Grasso, S., Sakka, Y., Maizza, G.: Electric current activated/assisted sintering (ECAS): a review of patents 1906–2008. Sci. Tech. Adv. Mater. **10**(5), 053001 (2009)
3. Munir, Z.A., Anselmi-Tamburini, U., Ohyanagi, M.: The effect of electric field and pressure on the synthesis and consolidation of materials: a review of the spark plasma sintering method. J. Mater. Sci. **41**(3), 763–777 (2006)
4. Munir, Z.A., Quach, D.V.: Electric current activation of sintering: a review of the pulsed electric current sintering process. J. Am. Ceram. Soc. **94**, 1–19 (2010)
5. Cincotti, A., Locci, A.M., Orru, R., Cao, G.: Modeling of SPS apparatus: temperature, current and strain distribution with no powders. AIChE J. **53**(3), 703–719 (2007)

6. Wang, X., Casolco, S.R., Xu, G., Garay, J.E.: Finite element modeling of electric current-activated sintering: the effect of coupled electrical potential, temperature and stress. Acta Mater. **55**, 3611–3622 (2007)
7. Antou, G., Mathieu, G., Trolliard, G., Maitre, A.: Spark plasma sintering of zirconium carbide and oxycarbide: finite lement modeling of current density, temperature, and stress distributions. J. Mater. Res. **24**, 404–412 (2009)
8. Muñoz, S., Anselmi-Tamburini, U.: Parametric investigation of temperature distribution in field activated sintering apparatus. Int. J. Adv. Manuf, Technol (2012)
9. Wang, C., Cheng, L., Zhao, Z.: FEM analysis of the temperature and stress distribution in spark plasma sintering: modelling and experimental validation. Comput. Mater. Sci. **49**(2), 351–362 (2010)
10. Maizza, G., Grasso, S., Sakka, Y., Noda, T., Ohashi, O.: Relation between microstructure, properties and spark plasma sintering (SPS) parameters of pure ultrafine WC powder. Sci. Tech. Adv. Mater. **8**(7–8), 644–654 (2007)
11. Olevsky, E.A., Garcia-Cardona, C., Bradbury, W.L., Haines, C.D., Martin, D.G., Kapoor, D.: Fundamental aspects of spark plasma sintering: II. Finite element analysis of scalability. J. Am. Ceram. Soc. **95**(8), 2414–2422 (2012)
12. Song, Y., Li, Y., Zhou, Z., Lai, Y., Ye, Y.: A multi-field coupled FEM model for one-step-forming process of spark plasma sintering considering local densification of powder material. J. Mater. Sci. **46**, 5645–5656 (2011)
13. Boley, B.A., Weiner, J.H.: Theory of Thermal Stresses. Dover Publications, Mineola, USA (1997)
14. Nowacki, W.: Thermoelasticity. Addison-Wesley Publishing Co., Reading (1962)
15. Hartmann, S., Rothe, S.: A rigorous application of the method of vertical lines to coupled systems in finite element analysis. In: Ansorge, R., Bijl, H., Meister, A., Sonar, T. (eds.) Recent Developments in the Numerics of Nonlinear Hyperbolic Conservation, Notes on Numerical Fluid Mechanics and Multidisciplinary Design, pp. 161–175. Springer, Berlin (2012)
16. Eringen, A.C., Maugin, G.A.: Electrodynamics of Continua I. Springer, New York (1990)
17. Hairer, E., Wanner, G.: Solving Ordinary Differential Equations II, 2nd revised edn. Springer, Berlin (1996)
18. Strehmel, K., Weiner, R.: Numerik gewöhnlicher Differentialgleichungen. Teubner Verlag, Stuttgart (1995)
19. Krautkrämer, J., Krautkrämer, H.: Ultrasonic Testing of Materials. Springer, Verlag (1990)
20. Workman, G., Kishoni, D., Moore, P.: Ultrasonic testing. Nondestructive testing handbook. American Society for Nondestructive Testing, Nondestructive Testing Handbook (2007)
21. Haupt, P.: Continuum Mechanics and Theory of Materials, 2nd edn. Springer, Berlin (2002)
22. Griffiths, D.J.: Elektrodynamik, 3rd edn. Pearson Education, München (2011)
23. Landau, L.D., Lifshitz, E.M., Pitaevskii, L.P.: Electrodynamics of continuous media, 2nd edn. Elsevier, Amsterdam (2008)
24. Lewis, R.W., Morgan, K., Thomas, H.R., Seetharamu, K.N.: The Finite Element Method in Heat Transfer Analysis. Wiley, Chichester (1996)
25. Quint, K.J., Hartmann, S., Rothe, S., Saba, N., Steinhoff, K.: Experimental validation of high-order time-integration for non-linear heat transfer problems. Comput. Mech. **48**, 81–96 (2011)
26. Reddy, J.N., Gartling, D.K.: The Finite Element Method in Heat Transfer and Fluid Dynamics. CRC Press, Boca Raton, FL (2000)
27. Seifert, W., Ueltzen, M., Müller, E.: One-dimensional modelling of thermoelectric cooling. Phys. Status Solidi **194**(1), 277–290 (2002)
28. Pérez-Aparicio, J.L., Palma, R., Taylor, R.L.: Finite element analysis and material sensitivity of Peltier thermoelectric cells coolers. Int. J. Heat Mass Transf. **55**, 1363–1374 (2012)
29. Palma, R., Pérez-Aparicio, J.L., Taylor, R.L.: Non-linear finite element formulation applied to thermoelectric materials under hyperbolic heat conduction model. Comput. Methods Appl. Mech. Eng. **213–216**, 93–103 (2012)
30. Anselmi-Tamburini, U., Gennari, S., Garay, J.E., Munir, Z.A.: Fundamental investigations on the spark plasma sintering/synthesis process II. Modeling of current and temperature distributions. Mater. Sci. Eng. A **394**, 139–148 (2005)

31. Hairer, E., Norsett, S.P., Wanner, G.: Solving Ordinary Differential Equations I, 2nd revised edn. Springer, Berlin (1993)
32. Ellsiepen, P., Hartmann, S.: Remarks on the interpretation of current non-linear finite-element-analyses as differential-algebraic equations. Int. J. Numer. Methods Eng. **51**, 679–707 (2001)
33. Hartmann, S.: Computation in finite strain viscoelasticity: finite elements based on the interpretation as differential-algebraic equations. Comput. Methods Appl. Mech. Eng. **191**(13–14), 1439–1470 (2002)
34. Hartmann, S., Bier, W.: High-order time integration applied to metal powder plasticity. Int. J. Plast. **24**(1), 17–54 (2008)
35. Hartmann, S., Quint, K.J., Arnold, M.: On plastic incompressibility within time-adaptive finite elements combined with projection techniques. Comput. Methods Appl. Mech. Eng. **198**, 178–193 (2008)
36. Birken, P., Quint, K.J., Hartmann, S., Meister, A.: A time-adaptive fluid-structure interaction method for thermal coupling. Comput. Vis. Sci. **13**, 331–340 (2010)
37. Hamkar, A.-W., Hartmann, S.: Theoretical and numerical aspects in weak-compressible finite strain thermo-elasticity. J. Theoret. Appl. Mech. **50**, 3–22 (2012)
38. Hartmann, S., Duintjer Tebbens, J., Quint, K.J., Meister, A.: Iterative solvers within sequences of large linear systems in non-linear structural mechanics. J. Appl. Math. Mech. (ZAMM) 89(9), 711–728 (2009)
39. Kelley, C.T.: Solving Nonlinear Equations with Newton's Method. SIAM Society for Industrial and Applied Mathematics, Philadelphia (2003)
40. Bier, W., Dariel, M.P., Frage, N., Hartmann, S., Michailov, O.: Die compaction of copper powder designed for material parameter identification. Int. J. Mech. Sci. **49**, 766–777 (2007)
41. Vanmeensel, K., Laptev, A., Hennicke, J., Vleugels, J., der Biest, O.: Modelling of the temperature distribution during field assisted sintering. Acta Mater. **53**, 4379–4388 (2005)
42. Zavaliangos, A., Zhang, J., Krammer, M., Groza, J.R.: Temperature evolution during field activated sintering. Mater. Sci. Eng. **379**, 218–228 (2004)
43. Ellsiepen, P.: Zeit- und ortsadaptive Verfahren angewandt auf Mehrphasenprobleme poröser Medien. Doctoral thesis, Institute of Mechanics II, University of Stuttgart. Report No. II-3 (1999)
44. Cash, J.R.: Diagonally implicit Runge-Kutta formulae with error estimates. J. Inst. Math. Appl. **24**, 293–301 (1979)

The Use of Moment Theory to Describe the Piezoelectric Effect in Polar and Non-Polar Materials

Elena A. Ivanova and Yaroslav E. Kolpakov

Abstract It is well known that the properties of polar and non-polar piezoelectric materials are different. For example, the polar piezoelectric materials (ferroelectrics) possess spontaneous polarization, while for non-polar materials such behavior cannot be observed. However, in the classical linear theory of piezoelectricity there is no qualitative difference between polar and non-polar materials. According to the classical theory the only difference between them consists in the fact that the piezoelectric moduli of polar materials are much greater than those of non-polar materials. The objective of our investigation is to describe piezoelectricity taking into account the qualitative peculiarities of polar and non-polar materials. Starting from the consideration of microstructure of piezoelectric materials we propose two theories of piezoelectricity based on the equations of micro-polar continuum. The first theory describes the piezoelectric effect in polar materials. This theory is based on the model of complex particle possessing a non-zero dipole moment and having seven degrees of freedom. The second theory describes the piezoelectric effect in non-polar materials. This theory is based on the model of an unit cell which has a non-zero quadrupole moment and zero dipole moment. Under certain simplifying assumptions both theories can be reduced to the classical theory of piezoelectricity.

E. A. Ivanova (✉)
St. Petersburg State Polytechnical University (SPbSPU), Politekhnicheskaya 29,
St. Petersburg, Russia 195251
e-mail: elenaivanova239@post.ru

E. A. Ivanova
Institute for Problems in Mechanical Engineering, Russian Academy of Sciences,
Bolshoy pr. V. O., 61, St. Petersburg, Russia 199178

Y. E. Kolpakov
Morion Inc., Kima ave. 13a, St. Petersburg, Russia 199155
e-mail: jaroslav@morion.com.ru

H. Altenbach et al. (eds.), *Generalized Continua as Models for Materials*,
Advanced Structured Materials 22, DOI: 10.1007/978-3-642-36394-8_9,

1 Introduction

There exist many crystals having piezoelectric properties. The piezoelectric properties reveal themselves as a result of the influence of electromagnetic fields on matter. Piezoelectric materials can be divided into two classes: polar and non-polar piezoelectrics. For example, $LiGaO_2$, Li_2GeO_3, $CdTe$, $BaTiO_3$, PZT, $Pb_5Ge_3O_3$ are polar piezoelectrics, and $\alpha - HIO_3$, KH_2PO_4, TeO_2, $Bi_{12}GeO_{20}$, $Bi_{12}SiO_{20}$, $\beta - ZnS$, $\alpha - SiO_2$ are non-polar piezoelectrics. The qualitative difference of properties of polar and non-polar piezoelectric materials consists in the fact that in contrast to non-polar piezoelectrics the polar piezoelectric materials (ferroelectrics) have non-zero dipole moment unit volume, i. e. they possess spontaneous polarization. However, in the classical theory of piezoelectricity [1, 2] based on the equations of electrostatics and symmetric theory of elasticity, as well as in the improved theory of piezoelectricity [3] based on the equations of electrostatics and non-symmetric (moment) theory of elasticity, there is no qualitative difference between polar and non-polar materials. According to the classical theory the only difference between polar and non-polar materials is that the piezoelectric moduli of polar materials are much greater than those of non-polar materials. The most known approaches which allow us to take into account the electric microstructure and permanent electric polarization are developed in [4–6]. We consider the method of description of piezoelectricity which allows us to take into account the qualitative peculiarities of polar and non-polar materials. This method was proposed by P. A. Zhilin (see [7, 8]). The main ideas of the method are to consider the microstructure of piezoelectric materials and use the equations of micro-polar continuum. By another method, but also taking into account the microstructure of materials, the theories of polar piezoelectrics are constructed in [9–12]. The theory of micromorphic thermoelastic continua taking into account electromagnetic effects is considered in [13]. On the basis of this theory the different aspects of theories of micromorphic piezoelectricity, micromorphic thermopiezoelectricity and magneto-electro-elasticity are discussed in [14–17]. In the case of non-polar materials the microstructure approach to description of piezoelectric effects is also of interest because it allows us to take into account electric quadrupoles [18]. We propose two theories of piezoelectricity. The first theory describes the piezoelectric effect in polar materials, and the second one describes the piezoelectric effect in non-polar materials. We show that under certain simplifying assumptions both theories are reduced to the classical theory of piezoelectricity.

2 Polar Piezoelectric Materials

2.1 Model of the Dipole Particle

We consider the medium with particles that are neutral dipoles. The neutral dipole is a pair of charges $q^+ = q$ and $q^- = -q$ separated by a distance. The dipole can

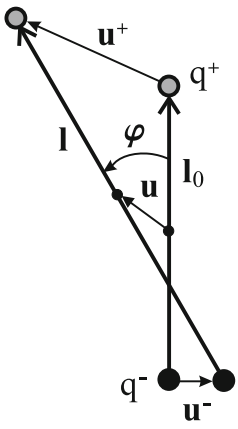

Fig. 1 The electric dipole

move and rotate in space, and also change its value, i. e. it can stretch and compress. The reference position of the dipole (see Fig. 1) is characterized by the following quantities. Radius-vectors $\mathbf{R}_0^+$ and $\mathbf{R}_0^-$ determine the positions of charges q^+ and q^- correspondingly, vector $\mathbf{l}_0$ determines the relative position of the dipole charges, and radius-vector $\mathbf{r}_0$ determines the position of dipole center. When passing to the actual position the charges q^+ and q^- move to the points determined by radius-vectors $\mathbf{R}^+$ and $\mathbf{R}^-$ correspondingly, the dipole center moves to the point determined by radius-vector $\mathbf{r}$. Vector $\mathbf{l}$ determining the relative position of the charges of dipole in the actual configuration is equal to $\mathbf{R}^+ - \mathbf{R}^-$. The quantities characterizing the displacements of the dipole center and dipole charges are determined as

$$\mathbf{u} = \mathbf{r} - \mathbf{r}_0, \qquad \mathbf{u}^+ = \mathbf{R}^+ - \mathbf{R}_0^+, \qquad \mathbf{u}^- = \mathbf{R}^- - \mathbf{R}_0^-. \tag{1}$$

Let us introduce the dipole moments in the reference and actual positions and denote them by $\mathbf{d}_0$ and $\mathbf{d}$, correspondingly:

$$\mathbf{d}_0 = q\mathbf{l}_0 = q(\mathbf{R}_0^+ - \mathbf{R}_0^-), \qquad \mathbf{d} = q\mathbf{l} = q(\mathbf{R}^+ - \mathbf{R}^-). \tag{2}$$

In addition, let us introduce the polarization vector $\mathbf{p}$ equal to change in dipole moment and the scalar quantity ξ being the relative change in absolute value of dipole moment:

$$\mathbf{p} = \mathbf{d} - \mathbf{d}_0, \qquad |\mathbf{d}| = |\mathbf{d}_0|(1 + \xi). \tag{3}$$

After simple transformations we obtain the following formula for $\mathbf{p}$:

$$\mathbf{p} = \mathbf{p}_1 + \mathbf{p}_2, \qquad \mathbf{p}_1 = \xi\mathbf{d}_0, \qquad \mathbf{p}_2 = \boldsymbol{\varphi} \times \mathbf{d}_0, \tag{4}$$

where $\boldsymbol{\varphi}$ is the rotation vector of the dipole. Equation (4) is obtained under the assumption of smallness of rotation and extension of the dipole. This assumption is justified because we consider the linear theory.

Now we write the expression for the rate of energy change due to the influence of electric field on the dipole:

$$\dot{e} = \mathbf{F}^+ \cdot \mathbf{v}^+ + \mathbf{F}^- \cdot \mathbf{v}^- . \tag{5}$$

Here $\mathbf{F}^+$ and $\mathbf{F}^-$ are forces acting on the positive charge and negative charge, correspondingly; $\mathbf{v}^+$, $\mathbf{v}^-$ are the velocities of these charges. Using the known formula for force acting on a charged particle we have $\mathbf{F} = q\mathbf{E}$, where $\mathbf{E}$ is the electric field vector. Let us perform the following transformations:

$$\begin{aligned}
\dot{e} &= q^+ \mathbf{E}(\mathbf{R}^+) \cdot \dot{\mathbf{u}}^+ + q^- \mathbf{E}(\mathbf{R}^-) \cdot \dot{\mathbf{u}}^- \\
&= q\big(\mathbf{E}(\mathbf{R}^+) - \mathbf{E}(\mathbf{R}^-)\big) \cdot \dot{\mathbf{u}} + q\mathbf{E}(\mathbf{R}^+) \cdot \frac{1}{2q}\dot{\mathbf{p}} + q\mathbf{E}(\mathbf{R}^-) \cdot \frac{1}{2q}\dot{\mathbf{p}} \\
&= \mathbf{d}_0 \cdot (\nabla \mathbf{E}) \cdot \dot{\mathbf{u}} + \mathbf{E} \cdot \dot{\mathbf{p}}.
\end{aligned}$$

Using Eq. (4) we calculate the time derivative of the polarization vector

$$\dot{\mathbf{p}} = \dot{\xi}\mathbf{d}_0 + \dot{\boldsymbol{\varphi}} \times \mathbf{d}_0. \tag{6}$$

Thus, the rate of energy change has the form

$$\dot{e} = \mathbf{d}_0 \cdot (\nabla \mathbf{E}) \cdot \dot{\mathbf{u}} + (\mathbf{d}_0 \times \mathbf{E}) \cdot \dot{\boldsymbol{\varphi}} + (\mathbf{d}_0 \cdot \mathbf{E})\, \dot{\xi}. \tag{7}$$

2.2 *Spontaneous and Piezoelectric Polarization of the Medium*

Now we introduce the density of the spontaneous polarization $\mathcal{P}^s$ of a continuous medium

$$\mathcal{P}^s = \lim_{\Delta V \to 0} \frac{\sum_{k \in \Delta V} \mathbf{d}_{0k}}{\Delta V}. \tag{8}$$

We define the density of the piezoelectric polarization $\mathcal{P}^p$ as a limit of the ratio

$$\mathcal{P}^p = \lim_{\Delta V \to 0} \frac{\sum_{k \in \Delta V} \mathbf{p}_k}{\Delta V} = \mathcal{P}^p_1 + \mathcal{P}^p_2, \tag{9}$$

where

$$\mathcal{P}^p_1 = \xi \mathcal{P}^s, \qquad \mathcal{P}^p_2 = \boldsymbol{\varphi} \times \mathcal{P}^s. \tag{10}$$

Thus, vector $\mathcal{P}^{\mathrm{p}}$ is a sum of the piezoelectric polarizations of different nature. Vector $\mathcal{P}_1^{\mathrm{p}}$ is concerned with the change in absolute value of dipole moment, and vector $\mathcal{P}_2^{\mathrm{p}}$ is concerned with the rotation of dipole moment. These vectors are mutually orthogonal.

Using Eqs. (9), (10) we write the analogue of Eq. (7) for continuous medium

$$\dot{\mathcal{E}} = \mathcal{P}^{\mathrm{s}} \cdot (\nabla \mathbf{E}) \cdot \dot{\mathbf{u}} + (\mathcal{P}^{\mathrm{s}} \times \mathbf{E}) \cdot \dot{\boldsymbol{\varphi}} + (\mathcal{P}^{\mathrm{s}} \cdot \mathbf{E})\, \dot{\xi}. \tag{11}$$

We suppose the effect of electric field to be an external action. There are two ways to calculate the power of this external action. On the one hand, the power of external actions per unit volume of continuous medium is equal to $\rho\mathbf{F} \cdot \dot{\mathbf{u}} + \rho\mathbf{L} \cdot \dot{\boldsymbol{\varphi}}$, where $\rho\mathbf{F}$ is the body force, $\rho\mathbf{L}$ is the body moment. On the other hand, the power of external actions is equal to that part of the rate of energy change $\dot{\mathcal{E}}$ which depends on the velocities $\dot{\mathbf{u}}$ and $\dot{\boldsymbol{\varphi}}$. Thus, we obtain

$$\rho\mathbf{F} \cdot \dot{\mathbf{u}} + \rho\mathbf{L} \cdot \dot{\boldsymbol{\varphi}} = \mathcal{P}^{\mathrm{s}} \cdot (\nabla \mathbf{E}) \cdot \dot{\mathbf{u}} + (\mathcal{P}^{\mathrm{s}} \times \mathbf{E}) \cdot \dot{\boldsymbol{\varphi}}. \tag{12}$$

Comparing the left-hand and the right-hand sides of Eq. (12) we conclude that the coefficient of $\dot{\mathbf{u}}$ on the right-hand side of the equation can be associated with a body force and the coefficient of $\dot{\boldsymbol{\varphi}}$ on the right-hand side of the equation can be associated with a body moment:

$$\rho\mathbf{F} = \mathcal{P}^{\mathrm{s}} \cdot \nabla \mathbf{E}, \qquad \rho\mathbf{L} = \mathcal{P}^{\mathrm{s}} \times \mathbf{E}. \tag{13}$$

Thus, the physical meaning of the first two terms on the right-hand side of Eq. (11) has been determined. The last term can be associated with the quantity $\mathcal{Q}$ characterizing the energy supply from an external source:

$$\mathcal{Q} = (\mathcal{P}^{\mathrm{s}} \cdot \mathbf{E})\dot{\xi}. \tag{14}$$

2.3 Equations of Polar Piezoelectric Medium

In view of expressions (13) for the body force and moment, the equations of motion of the polar piezoelectric medium in the linear approximation are written as

$$\nabla \cdot \boldsymbol{\tau} - \frac{1}{2}\nabla \times \mathbf{q} + \mathcal{P}^{\mathrm{s}} \cdot \nabla \mathbf{E} = \rho\ddot{\mathbf{u}}, \tag{15}$$

$$\nabla \times \mathbf{m} + \mathbf{q} + \mathcal{P}^{\mathrm{s}} \times \mathbf{E} = \rho\mathbf{J} \cdot \ddot{\boldsymbol{\varphi}}. \tag{16}$$

Here $\boldsymbol{\tau}$ is the symmetric part of stress tensor, $\mathbf{q}$ is the vector characterizing the antisymmetric part of stress tensor, $\mathbf{m}$ is the vector characterizing the antisymmetric

part of moment stress tensor, ρ is the mass density in the reference configuration and $\mathbf{J}$ is the inertia tensor per unit mass.

We introduce the electric induction vector $\mathbf{D}$ by the relation

$$\mathbf{D} = \varepsilon_0 \mathbf{E} + \mathcal{P}^{\mathrm{p}}, \tag{17}$$

where ε_0 is the permittivity of free space. Using Eqs. (9), (10) we rewrite Eq. (17) in the form

$$\mathbf{D} = \varepsilon_0 \mathbf{E} + \xi \mathcal{P}^{\mathrm{s}} + \boldsymbol{\varphi} \times \mathcal{P}^{\mathrm{s}}. \tag{18}$$

In view of Eq. (18) the equation of electrostatics

$$\nabla \cdot \mathbf{D} = 0 \tag{19}$$

takes the form

$$\nabla \cdot \left[\varepsilon_0 \mathbf{E} + \xi \mathcal{P}^{\mathrm{s}} + \boldsymbol{\varphi} \times \mathcal{P}^{\mathrm{s}} \right] = 0. \tag{20}$$

According to Eq. (20) the Cauchy–Green relation between $\mathbf{D}$ and $\mathbf{E}$ adopted in the classical theory of piezoelectricity is unnecessary in the theory under consideration and it should be replaced by the Cauchy–Green relation between ξ and the projection of $\mathbf{E}$ on $\mathcal{P}^{\mathrm{s}}$. This is one of the essential differences between the micro-polar theory of piezoelectric medium and the classical theory of piezoelectricity.

Now we formulate the energy balance equation

$$\rho \dot{\mathscr{U}} = \boldsymbol{\tau} \cdot\cdot \dot{\mathbf{g}} - \mathbf{q} \cdot \dot{\theta} - \mathbf{m} \cdot \dot{\boldsymbol{\gamma}} + \nabla \cdot \mathbf{h} + \mathscr{Q}, \tag{21}$$

where $\mathbf{h}$ is the heat flow vector, $\mathscr{Q}$ is the rate of energy supply from an external source, $\mathbf{g}$ is the strain tensor, θ and $\boldsymbol{\gamma}$ are the strain vectors connected with the rotational degrees of freedom:

$$\mathbf{g} = \frac{1}{2} \left(\nabla \mathbf{u} + \nabla \mathbf{u}^{\mathsf{T}} \right), \qquad \theta = \boldsymbol{\varphi} - \frac{1}{2} \nabla \times \mathbf{u}, \qquad \boldsymbol{\gamma} = \nabla \times \boldsymbol{\varphi}. \tag{22}$$

In order to obtain the Cauchy–Green relations we use the method developed by P. A. Zhilin [7, 8]. We represent $\boldsymbol{\tau}$, $\mathbf{q}$ and $\mathbf{m}$ in the form

$$\boldsymbol{\tau} = \boldsymbol{\tau}_e + \boldsymbol{\tau}_{\mathrm{f}}, \qquad \mathbf{q} = \mathbf{q}_e + \mathbf{q}_{\mathrm{f}}, \qquad \mathbf{m} = \mathbf{m}_e + \mathbf{m}_{\mathrm{f}}, \tag{23}$$

where $\boldsymbol{\tau}_e$, $\mathbf{q}_e$, $\mathbf{m}_e$ are the elastic (independent of strain rate) parts of the force and moment stresses, and $\boldsymbol{\tau}_{\mathrm{f}}$, $\mathbf{q}_{\mathrm{f}}$ and $\mathbf{m}_{\mathrm{f}}$ are the dissipative parts of these stresses. In view of Eq. (23) and the expression for the rate of energy supply (14) the energy balance equation (21) can be rewritten in the form

$$\rho\dot{\mathscr{U}} = \boldsymbol{\tau}_e \cdot\cdot\, \dot{\mathbf{g}} - \mathbf{q}_e \cdot \dot{\boldsymbol{\theta}} - \mathbf{m}_e \cdot \dot{\boldsymbol{\gamma}} + (\mathbf{E} \cdot \mathcal{P}^s)\, \dot{\xi} + \nabla \cdot \mathbf{h} + \boldsymbol{\tau}_f \cdot\cdot\, \dot{\mathbf{g}} - \mathbf{q}_f \cdot \dot{\boldsymbol{\theta}} - \mathbf{m}_f \cdot \dot{\boldsymbol{\gamma}}. \tag{24}$$

Let us introduce two scalar quantities ϑ and $\mathscr{H}$ satisfying the equation

$$\vartheta\dot{\mathscr{H}} = \nabla \cdot \mathbf{h} + \boldsymbol{\tau}_f \cdot\cdot\, \dot{\mathbf{g}} - \mathbf{q}_f \cdot \dot{\boldsymbol{\theta}} - \mathbf{m}_f \cdot \dot{\boldsymbol{\gamma}}, \tag{25}$$

and call them the temperature and entropy, correspondingly. The following constitutive equation can be used for the heat flow vector $\mathbf{h}$:

$$\mathbf{h} = k\nabla\vartheta, \tag{26}$$

where k is the heat-conduction coefficient of the medium. Substituting Eq. (26) into Eq. (25) we obtain the heat conduction equation

$$k\Delta\vartheta - \vartheta\dot{\mathscr{H}} = -\boldsymbol{\tau}_f \cdot\cdot\, \dot{\mathbf{g}} + \mathbf{q}_f \cdot \dot{\boldsymbol{\theta}} + \mathbf{m}_f \cdot \dot{\boldsymbol{\gamma}}. \tag{27}$$

The terms on the right-hand side of Eq. (27) characterize the heat production connected with the dissipative processes.

Using Eq. (25) we rewrite the energy balance equation (21) in the form

$$\rho\dot{\mathscr{U}} = \boldsymbol{\tau}_e \cdot\cdot\, \dot{\mathbf{g}} - \mathbf{q}_e \cdot \dot{\boldsymbol{\theta}} - \mathbf{m}_e \cdot \dot{\boldsymbol{\gamma}} + (\mathbf{E} \cdot \mathcal{P}^s)\, \dot{\xi} + \vartheta\dot{\mathscr{H}}. \tag{28}$$

Hence $\mathscr{U} = \mathscr{U}(\mathbf{g}, \boldsymbol{\theta}, \boldsymbol{\gamma}, \mathcal{P}, \xi, \mathscr{H})$, from Eq. (28) we obtain the Cauchy–Green relations

$$\boldsymbol{\tau}_e = \frac{\partial\rho\mathscr{U}}{\partial\mathbf{g}}, \quad \mathbf{q}_e = -\frac{\partial\rho\mathscr{U}}{\partial\boldsymbol{\theta}}, \quad \mathbf{m}_e = -\frac{\partial\rho\mathscr{U}}{\partial\boldsymbol{\gamma}}, \quad \mathbf{E} \cdot \mathcal{P}^s = \frac{\partial\rho\mathscr{U}}{\partial\xi}, \quad \vartheta = \frac{\partial\rho\mathscr{U}}{\partial\mathscr{H}}. \tag{29}$$

Let us represent the internal energy as the positive defined quadratic form

$$\begin{aligned}\rho\mathscr{U} = {} & \frac{1}{2}\mathbf{g} \cdot\cdot\, \mathbf{C}^{(g)} \cdot\cdot\, \mathbf{g} + \frac{1}{2}\boldsymbol{\theta} \cdot \mathbf{C}^{(\theta)} \cdot \boldsymbol{\theta} + \frac{1}{2}\boldsymbol{\gamma} \cdot \mathbf{C}^{(\gamma)} \cdot \boldsymbol{\gamma} + \frac{1}{2}C^{(\xi)}\xi^2 \\ & + \frac{1}{2}C^{(\mathscr{H})}\mathscr{H}^2 + \boldsymbol{\theta} \cdot \mathbf{C}^{(\theta g)} \cdot\cdot\, \mathbf{g} + \boldsymbol{\gamma} \cdot \mathbf{C}^{(\gamma g)} \cdot\cdot\, \mathbf{g} + \xi\mathbf{C}^{(\xi g)} \cdot\cdot\, \mathbf{g} \\ & + \mathscr{H}\mathbf{C}^{(\mathscr{H} g)} \cdot\cdot\, \mathbf{g} + \boldsymbol{\gamma} \cdot \mathbf{C}^{(\gamma\theta)} \cdot \boldsymbol{\theta} + \xi\mathbf{C}^{(\xi\theta)} \cdot \boldsymbol{\theta} + \mathscr{H}\mathbf{C}^{(\mathscr{H}\theta)} \cdot \boldsymbol{\theta} \\ & + \xi\mathbf{C}^{(\xi\gamma)} \cdot \boldsymbol{\gamma} + \mathscr{H}\mathbf{C}^{(\mathscr{H}\gamma)} \cdot \boldsymbol{\gamma} + C^{(\xi,\mathscr{H})}\xi\mathscr{H}.\end{aligned} \tag{30}$$

Substituting Eq. (30) into the Cauchy–Green relations (29) we get the constitutive equations

$$\begin{aligned}
\boldsymbol{\tau}_e &= \mathbf{C}^{(\mathrm{g})} \cdot\cdot\, \mathbf{g} + \boldsymbol{\theta} \cdot \mathbf{C}^{(\boldsymbol{\theta}\mathrm{g})} + \boldsymbol{\gamma} \cdot \mathbf{C}^{(\boldsymbol{\gamma}\mathrm{g})} + \mathbf{C}^{(\xi\mathrm{g})}\xi + \mathbf{C}^{(\mathscr{H}\mathrm{g})}\mathscr{H}, \\
-\mathbf{q}_e &= \mathbf{C}^{(\boldsymbol{\theta}\mathrm{g})} \cdot\cdot\, \mathbf{g} + \mathbf{C}^{(\boldsymbol{\theta})} \cdot \boldsymbol{\theta} + \boldsymbol{\gamma} \cdot \mathbf{C}^{(\boldsymbol{\gamma}\boldsymbol{\theta})} + \mathbf{C}^{(\xi\boldsymbol{\theta})}\xi + \mathbf{C}^{(\mathscr{H}\boldsymbol{\theta})}\mathscr{H}, \\
-\mathbf{m}_e &= \mathbf{C}^{(\boldsymbol{\gamma}\mathrm{g})} \cdot\cdot\, \mathbf{g} + \mathbf{C}^{(\boldsymbol{\gamma}\boldsymbol{\theta})} \cdot \boldsymbol{\theta} + \mathbf{C}^{(\boldsymbol{\gamma})} \cdot \boldsymbol{\gamma} + \mathbf{C}^{(\xi\boldsymbol{\gamma})}\xi + \mathbf{C}^{(\mathscr{H}\boldsymbol{\gamma})}\mathscr{H}, \\
\mathbf{E} \cdot \mathcal{P}^{\mathrm{s}} &= \mathbf{C}^{(\xi\mathrm{g})} \cdot\cdot\, \mathbf{g} + \mathbf{C}^{(\xi\boldsymbol{\theta})} \cdot \boldsymbol{\theta} + \mathbf{C}^{(\xi\boldsymbol{\gamma})} \cdot \boldsymbol{\gamma} + \mathrm{C}^{(\xi)}\xi + \mathrm{C}^{(\xi\mathscr{H})}\mathscr{H}, \\
\vartheta &= \mathbf{C}^{(\mathscr{H}\mathrm{g})} \cdot\cdot\, \mathbf{g} + \mathbf{C}^{(\mathscr{H}\boldsymbol{\theta})} \cdot \boldsymbol{\theta} + \mathbf{C}^{(\mathscr{H}\boldsymbol{\gamma})} \cdot \boldsymbol{\gamma} + \mathrm{C}^{(\xi\mathscr{H})}\xi + \mathrm{C}^{(\mathscr{H})}\mathscr{H}.
\end{aligned} \tag{31}$$

In order to close the set of equations (15), (16), (20), (22), (23), (27), (31) the constitutive equations for the dissipative parts of force and moment stresses $\boldsymbol{\tau}_{\mathrm{f}}$, $\mathbf{q}_{\mathrm{f}}$, $\mathbf{m}_{\mathrm{f}}$ should be formulated.

2.4 The Simplest Theory of Polar Medium

Now we neglect the inertia of rotation and the moment interactions, i. e. we suppose that $\mathbf{J} = \mathbf{0}$ and $\mathbf{m} = \mathbf{0}$. Then the equation of the angular momentum balance (16) takes the form

$$\mathbf{q} = -\mathcal{P}^{\mathrm{s}} \times \mathbf{E}. \tag{32}$$

Substituting Eq. (32) into the equation of momentum balance (15) we obtain

$$\nabla \cdot \boldsymbol{\tau} + \frac{1}{2}\nabla \times (\mathcal{P}^{\mathrm{s}} \times \mathbf{E}) + \mathcal{P}^{\mathrm{s}} \cdot \nabla \mathbf{E} = \rho \ddot{\mathbf{u}}. \tag{33}$$

Let us neglect the dissipative and thermal effects. Then in view of Eq. (32) the constitutive equations (31) take the form

$$\begin{aligned}
\boldsymbol{\tau} &= \mathbf{C}^{(\mathrm{g})} \cdot\cdot\, \mathbf{g} + \boldsymbol{\theta} \cdot \mathbf{C}^{(\boldsymbol{\theta}\mathrm{g})} + \mathbf{C}^{(\xi\mathrm{g})}\xi, \\
\mathcal{P}^{\mathrm{s}} \times \mathbf{E} &= \mathbf{C}^{(\boldsymbol{\theta}\mathrm{g})} \cdot\cdot\, \mathbf{g} + \mathbf{C}^{(\boldsymbol{\theta})} \cdot \boldsymbol{\theta} + \mathbf{C}^{(\xi\boldsymbol{\theta})}\xi, \\
\mathbf{E} \cdot \mathcal{P}^{\mathrm{s}} &= \mathbf{C}^{(\xi\mathrm{g})} \cdot\cdot\, \mathbf{g} + \mathbf{C}^{(\xi\boldsymbol{\theta})} \cdot \boldsymbol{\theta} + \mathrm{C}^{(\xi)}\xi,
\end{aligned} \tag{34}$$

where index e of tensor $\boldsymbol{\tau}$ is left out since the dissipative part of this tensor is equal to zero. In view of the relation between angles $\boldsymbol{\varphi}$ and $\boldsymbol{\theta}$ the expression (18) takes the form

$$\mathbf{D} = \varepsilon_0 \mathbf{E} + \xi \mathcal{P}^{\mathrm{s}} + \boldsymbol{\theta} \times \mathcal{P}^{\mathrm{s}} + \frac{1}{2}(\nabla \times \mathbf{u}) \times \mathcal{P}^{\mathrm{s}} \tag{35}$$

and the equation of electrostatics (20) is written as

$$\nabla \cdot \left[\varepsilon_0 \mathbf{E} + \xi \mathcal{P}^{\mathrm{s}} + \boldsymbol{\theta} \times \mathcal{P}^{\mathrm{s}} + \frac{1}{2}(\nabla \times \mathbf{u}) \times \mathcal{P}^{\mathrm{s}} \right] = 0. \tag{36}$$

Thus, the set of equations (33)–(36) represents the formulation of the simplest theory of polar piezoelectric medium. Here the basic variables are the displacement vector $\mathbf{u}$, the shear vector θ and the quantity ξ, characterizing the dipole deformation.

2.5 Comparison with the Classical Theory

To compare Eqs. (33)–(36) with the equations of classical theory of piezoelectricity we should obtain the relations between $\boldsymbol{\tau}$, $\mathbf{D}$ and $\mathbf{g}$, $\mathbf{E}$. In order to do this we solve the system of second and third equations in (34) with respect to θ and ξ. Then we substitute the obtained expressions into the first equation in Eqs. (34) and into Eq. (35). As a result we get

$$\boldsymbol{\tau} = \mathbf{C} \cdot\cdot\, \mathbf{g} - \mathbf{E} \cdot \mathcal{M}, \qquad \mathbf{D} = \mathcal{M} \cdot\cdot\, \mathbf{g} + \boldsymbol{\epsilon} \cdot \mathbf{E} - \frac{1}{2} \mathcal{P}^{s} \times (\nabla \times \mathbf{u}), \tag{37}$$

where $\mathbf{C}$ is the stiffness tensor; $\mathcal{M}$ is the tensor of piezoelectric moduli; $\boldsymbol{\epsilon}$ is the permittivity tensor. Tensors $\mathbf{C}, \mathcal{M}, \boldsymbol{\epsilon}$ can be expressed in terms of the material tensors introduced above by the sufficiently complicated formulas.

Comparison of the constitutive equations (37) and the corresponding constitutive equations of the classical theory [1, 2]

$$\boldsymbol{\tau} = \mathbf{C} \cdot\cdot\, \mathbf{g} - \mathbf{E} \cdot \mathcal{M}, \qquad \mathbf{D} = \mathcal{M} \cdot\cdot\, \mathbf{g} + \boldsymbol{\epsilon} \cdot \mathbf{E} \tag{38}$$

reveals that the constitutive equations for $\boldsymbol{\tau}$ are the same and the constitutive equations for $\mathbf{D}$ differ by the additional term which depends on the curl of displacement vector in the case of the micro-polar theory.

The equation of motion (33) differs from the classical equation of motion

$$\nabla \cdot \boldsymbol{\tau} + \rho \mathbf{F} = \rho \ddot{\mathbf{u}}, \qquad \boldsymbol{\tau} = \boldsymbol{\tau}^{\mathrm{T}} \tag{39}$$

by the presence of two terms modelling the effect of the electric field. The equation of electrostatics has the same form (19) in both theories.

3 Non-Polar Piezoelectric Materials

3.1 Model of the Unit Cell of Crystal Lattice

We consider the crystal lattice with unit cells consisting of N ions which have charges q_i (see Fig. 2). In the reference configuration the position of mass center of the cell is determined by the radius-vector $\mathbf{r}$, the positions of ions are determined by the

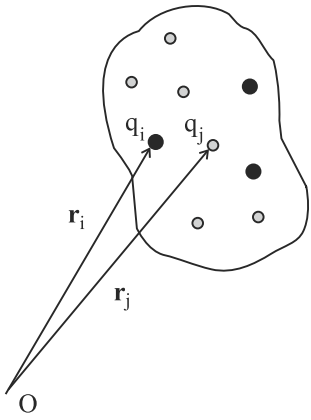

Fig. 2 Arbitrary unit cell of *crystal lattice*

radius-vectors $\mathbf{r}_i = \mathbf{r} + \mathbf{b}_i$, where the radius-vectors $\mathbf{b}_i$ determine the positions of ions relative to the mass center of the cell.

Let us introduce the electrical characteristics of the unit cell: the total charge q, the dipole moment $\mathbf{d}$ and the quadrupole moment $\mathbf{Q}$, which are calculated by the formulas

$$q = \sum_i q_i, \qquad \mathbf{d} = \sum_i q_i \mathbf{b}_i, \qquad \mathbf{q} = \frac{1}{2} \sum_i q_i \mathbf{b}_i \mathbf{b}_i. \tag{40}$$

Note that the definition of the quadrupole moment (40) is not standard. Usually another definition of quadrupole moment is introduced, namely

$$\mathbf{Q}_* = \sum_i q_i (3\mathbf{b}_i \mathbf{b}_i - \mathbf{b}_i^2 \mathbf{I}), \tag{41}$$

where $\mathbf{I}$ is the unit tensor. In crystals the total charge of the unit cell is equal to zero whereas the dipole moment $\mathbf{d}$ and the quadrupole moment $\mathbf{Q}$ can be zero or non-zero depending on the type of material. It is known that if the total charge and the dipole moment are equal to zero then the quadrupole moment does not depend on the point with respect to which it is calculated. This is true for both definitions of quadrupole moment.

To describe the kinematics of the unit sell we introduce the displacement vectors of ions $\mathbf{u}_i$. Further all displacements are supposed to be small and the following representation for $\mathbf{u}_i$ is used:

$$\mathbf{u}_i = \mathbf{u} + \boldsymbol{\varphi} \times \mathbf{b}_i + \boldsymbol{\xi}_i. \tag{42}$$

Here $\mathbf{u}$ is the displacement vector of the center of the unit cell, $\boldsymbol{\varphi}$ is the vector of small rotation of the unit cell as a rigid body, $\boldsymbol{\xi}_i$ are variables characterizing the

deformation of the unit cell. We suppose the ion displacements associated with the deformation of the unit cell to be much less than the ion displacements connected with the movement of the cell as a rigid body. In other words, we assume that $|\boldsymbol{\xi}_i| \ll |\mathbf{u}|$ and $|\boldsymbol{\xi}_i| \ll |\boldsymbol{\varphi} \times \mathbf{b}_i|$. Let us introduce the polarization vector $\mathbf{p}$:

$$\mathbf{p} = \sum_i q_i(\boldsymbol{\varphi} \times \mathbf{b}_i + \boldsymbol{\xi}_i). \tag{43}$$

In view of Eq. (40) the formula (43) can be reduced to the form

$$\mathbf{p} = \mathbf{p}_r + \mathbf{p}_d, \qquad \mathbf{p}_r = \boldsymbol{\varphi} \times \mathbf{d}, \qquad \mathbf{p}_d = \sum_i q_i \boldsymbol{\xi}_i. \tag{44}$$

Here $\mathbf{p}_r$ is the polarization due to the rotation of the unit cell, and $\mathbf{p}_d$ is the polarization due to the deformation of the unit cell.

Now we write the expression for the rate of the energy change due to the work of the electric field on the ions of unit cell:

$$\dot{e} = \sum_i q_i \mathbf{E}(\mathbf{r}_i) \cdot \mathbf{v}_i, \tag{45}$$

where $\mathbf{v}_i = \dot{\mathbf{u}}_i$ is the velocity vector of the ion with the number i. Assuming that the electric field slowly varies over distances comparable with the characteristic dimensions of the unit cell we use the expansion of vector $\mathbf{E}$ in a Taylor series. Keeping the first three terms in the Taylor series we have

$$\mathbf{E}(\mathbf{r}_i) \approx \mathbf{E}(\mathbf{r}) + \mathbf{b}_i \cdot \nabla\mathbf{E} + \frac{1}{2}\mathbf{b}_i\mathbf{b}_i \cdot\cdot \nabla\nabla\mathbf{E}. \tag{46}$$

Using Eqs. (42), (46) we reduce the expression for the rate of energy change (45) to the form

$$\dot{e} \approx (\mathbf{d} \cdot \nabla\mathbf{E} + \mathbf{Q} \cdot\cdot \nabla\nabla\mathbf{E}) \cdot \dot{\mathbf{u}} + \left(\mathbf{d} \times \mathbf{E} + 2\mathbf{Q} \cdot \times \nabla\mathbf{E}\right) \cdot \dot{\boldsymbol{\varphi}} + \mathbf{E} \cdot \dot{\mathbf{p}}_d. \tag{47}$$

The formula (47) is derived in view of the fact that the total charge of the unit cell is equal to zero, and also $|\boldsymbol{\xi}_i| \ll |\mathbf{u}|$ and $|\boldsymbol{\xi}_i| \ll |\boldsymbol{\varphi} \times \mathbf{b}_i|$.

3.2 Polarization of Continuous Medium

Now we write the analogue of Eq. (47) for the continuous medium. In order to pass from the discrete model to the corresponding continuum model we use standard line

of reasoning based on symmetry properties of the crystal lattice and the long-wave approximation. The description of the method can be found in [19]. Application of this method in the case when the rotational motion and moment interaction are taken into account is discussed in [20]. Thus, the continuous analogue of Eq. (47) is

$$\dot{\mathcal{E}} \approx (\boldsymbol{\mathcal{P}}^{\mathrm{s}} \cdot \boldsymbol{\nabla}\mathbf{E} + \boldsymbol{\mathcal{Q}} \cdot\cdot \boldsymbol{\nabla}\boldsymbol{\nabla}\mathbf{E}) \cdot \dot{\mathbf{u}} + \left(\boldsymbol{\mathcal{P}}^{\mathrm{s}} \times \mathbf{E} + 2\boldsymbol{\mathcal{Q}} \cdot \times \boldsymbol{\nabla}\mathbf{E}\right) \cdot \dot{\boldsymbol{\varphi}} + \mathbf{E} \cdot \dot{\boldsymbol{\mathcal{P}}}^{\mathrm{p}}. \quad (48)$$

Here the parameters of the medium $\boldsymbol{\mathcal{P}}^{\mathrm{s}}$ (volume density of spontaneous polarization) and $\boldsymbol{\mathcal{Q}}$ (volume density of the quadrupole moments) are

$$\boldsymbol{\mathcal{P}}^{\mathrm{s}} = \lim_{\Delta V \to 0} \frac{\sum_{\mathrm{k} \in \Delta V} \mathbf{d}_{\mathrm{k}}}{\Delta V}, \qquad \boldsymbol{\mathcal{Q}} = \lim_{\Delta V \to 0} \frac{\sum_{\mathrm{k} \in \Delta V} \mathbf{q}_{\mathrm{k}}}{\Delta V}, \quad (49)$$

and the volume density of piezoelectric polarization $\boldsymbol{\mathcal{P}}^{\mathrm{p}}$ being one of the basic variables is introduced by the formula

$$\boldsymbol{\mathcal{P}}^{\mathrm{p}} = \lim_{\Delta V \to 0} \frac{\sum_{\mathrm{k} \in \Delta V} \mathbf{p}_{\mathrm{dk}}}{\Delta V}. \quad (50)$$

We suppose the electric field to be an external factor. The power of external actions per unit volume is equal to $\rho\mathbf{F} \cdot \dot{\mathbf{u}} + \rho\mathbf{L} \cdot \dot{\boldsymbol{\varphi}}$. The corresponding power of the electric field action is equal to that part of the rate of energy change $\dot{\mathcal{E}}$ which depends on the translational velocity $\dot{\mathbf{u}}$ and the angular velocity $\dot{\boldsymbol{\varphi}}$. Thus, we obtain

$$\rho\mathbf{F} \cdot \dot{\mathbf{u}} + \rho\mathbf{L} \cdot \dot{\boldsymbol{\varphi}} = (\boldsymbol{\mathcal{P}}^{\mathrm{s}} \cdot \boldsymbol{\nabla}\mathbf{E} + \boldsymbol{\mathcal{Q}} \cdot\cdot \boldsymbol{\nabla}\boldsymbol{\nabla}\mathbf{E}) \cdot \dot{\mathbf{u}} + \left(\boldsymbol{\mathcal{P}}^{\mathrm{s}} \times \mathbf{E} + 2\boldsymbol{\mathcal{Q}} \cdot \times \boldsymbol{\nabla}\mathbf{E}\right) \cdot \dot{\boldsymbol{\varphi}}. \quad (51)$$

Comparing the left-hand and the right-hand sides of Eq. (51) we conclude that the coefficient of $\dot{\mathbf{u}}$ on the right-hand side of the equation can be associated with a body force and the coefficient of $\dot{\boldsymbol{\varphi}}$ on the right-hand side of the equation can be associated with a body moment:

$$\rho\mathbf{F} = \boldsymbol{\mathcal{P}}^{\mathrm{s}} \cdot \boldsymbol{\nabla}\mathbf{E} + \boldsymbol{\mathcal{Q}} \cdot\cdot \boldsymbol{\nabla}\boldsymbol{\nabla}\mathbf{E}, \qquad \rho\mathbf{L} = \boldsymbol{\mathcal{P}}^{\mathrm{s}} \times \mathbf{E} + 2\boldsymbol{\mathcal{Q}} \cdot \times \boldsymbol{\nabla}\mathbf{E}. \quad (52)$$

In the case of non-polar piezoelectrics $\boldsymbol{\mathcal{P}}^{\mathrm{s}} = \mathbf{0}$ and the expressions (52) take the simpler form

$$\rho\mathbf{F} = \boldsymbol{\mathcal{Q}} \cdot\cdot \boldsymbol{\nabla}\boldsymbol{\nabla}\mathbf{E}, \qquad \rho\mathbf{L} = 2\boldsymbol{\mathcal{Q}} \cdot \times \boldsymbol{\nabla}\mathbf{E}. \quad (53)$$

The last term in Eq. (51) can be associated with the quantity $\mathscr{Q}$ characterizing the energy supply from an external source that cannot be expressed in terms of the power of external forces and moments:

$$\mathscr{Q} = \mathbf{E} \cdot \dot{\boldsymbol{\mathcal{P}}}^{\mathrm{p}}. \quad (54)$$

3.3 Equations of Non-Polar Piezoelectric Medium

In view of the expressions for external force and moment (53) the equations of motion of the non-polar piezoelectric medium in the linear approximation take the form

$$\nabla \cdot \boldsymbol{\tau} - \frac{1}{2}\nabla \times \mathbf{q} + \Omega \cdot\cdot \nabla\nabla \mathbf{E} = \rho \ddot{\mathbf{u}}, \tag{55}$$

$$\nabla \times \mathbf{m} + \mathbf{q} + 2\Omega \cdot \times \nabla \mathbf{E} = \rho \mathbf{J} \cdot \ddot{\boldsymbol{\varphi}}. \tag{56}$$

Introducing electric induction vector $\mathbf{D}$ by means of Eq. (17) we write the equation of electrostatics (19) as

$$\nabla \cdot \left[\varepsilon_0 \mathbf{E} + \mathcal{P}^{\mathrm{p}}\right] = 0. \tag{57}$$

Starting from the energy balance equation in the form of Eq. (21) and using the line of reasoning similar to those which were held in the case of polar medium we obtain the heat conduction Eq. (27) and the reduced energy balance equation

$$\rho \dot{\mathscr{U}} = \boldsymbol{\tau}_{\mathrm{e}} \cdot\cdot \dot{\mathbf{g}} - \mathbf{q}_{\mathrm{e}} \cdot \dot{\boldsymbol{\theta}} - \mathbf{m}_{\mathrm{e}} \cdot \dot{\boldsymbol{\gamma}} + \mathbf{E} \cdot \dot{\mathcal{P}}^{\mathrm{p}} + \vartheta \dot{\mathscr{H}}. \tag{58}$$

Note that Eq. (58) is derived in view of the expression (54) for the rate of energy supply from an external source. The Cauchy–Green relations which follow from Eq. (58) are

$$\boldsymbol{\tau}_{\mathrm{e}} = \frac{\partial \rho \mathscr{U}}{\partial \mathbf{g}}, \quad \mathbf{q}_{\mathrm{e}} = -\frac{\partial \rho \mathscr{U}}{\partial \boldsymbol{\theta}}, \quad \mathbf{m}_{\mathrm{e}} = -\frac{\partial \rho \mathscr{U}}{\partial \boldsymbol{\gamma}}, \quad \mathbf{E} = \frac{\partial \rho \mathscr{U}}{\partial \mathcal{P}^{\mathrm{p}}}, \quad \vartheta = \frac{\partial \rho \mathscr{U}}{\partial \mathscr{H}}. \tag{59}$$

The internal energy is assumed to be the positive defined quadratic form

$$\begin{aligned}
\rho \mathscr{U} = {} & \frac{1}{2}\mathbf{g} \cdot\cdot \mathbf{C}^{(\mathrm{g})} \cdot\cdot \mathbf{g} + \frac{1}{2}\boldsymbol{\theta} \cdot \mathbf{C}^{(\theta)} \cdot \boldsymbol{\theta} + \frac{1}{2}\boldsymbol{\gamma} \cdot \mathbf{C}^{(\gamma)} \cdot \boldsymbol{\gamma} \\
& + \frac{1}{2}\mathcal{P}^{\mathrm{p}} \cdot \mathbf{C}^{(\mathcal{P})} \cdot \mathcal{P}^{\mathrm{p}} + \frac{1}{2}C^{(\mathscr{H})}\mathscr{H}^2 + \boldsymbol{\theta} \cdot \mathbf{C}^{(\theta \mathrm{g})} \cdot\cdot \mathbf{g} + \boldsymbol{\gamma} \cdot \mathbf{C}^{(\gamma \mathrm{g})} \cdot\cdot \mathbf{g} \\
& + \mathcal{P}^{\mathrm{p}} \cdot \mathbf{C}^{(\mathcal{P}\mathrm{g})} \cdot\cdot \mathbf{g} + \mathscr{H}\mathbf{C}^{(\mathscr{H}\mathrm{g})} \cdot\cdot \mathbf{g} + \boldsymbol{\gamma} \cdot \mathbf{C}^{(\gamma\theta)} \cdot \boldsymbol{\theta} + \boldsymbol{\theta} \cdot \mathbf{C}^{(\theta\mathcal{P})} \cdot \mathcal{P}^{\mathrm{p}} \\
& + \mathscr{H}\mathbf{C}^{(\mathscr{H}\theta)} \cdot \boldsymbol{\theta} + \mathcal{P}^{\mathrm{p}} \cdot \mathbf{C}^{(\mathcal{P}\gamma)} \cdot \boldsymbol{\gamma} + \mathscr{H}\mathbf{C}^{(\mathscr{H}\gamma)} \cdot \boldsymbol{\gamma} + \mathscr{H}\mathbf{C}^{(\mathscr{H}\mathcal{P})} \cdot \mathcal{P}^{\mathrm{p}}.
\end{aligned} \tag{60}$$

Substituting Eq. (60) into the Cauchy–Green relations (59) we get

$$\begin{aligned}
\boldsymbol{\tau}_{\mathrm{e}} &= \mathbf{C}^{(\mathrm{g})} \cdot\cdot \mathbf{g} + \boldsymbol{\theta} \cdot \mathbf{C}^{(\theta \mathrm{g})} + \boldsymbol{\gamma} \cdot \mathbf{C}^{(\gamma \mathrm{g})} + \mathcal{P}^{\mathrm{p}} \cdot \mathbf{C}^{(\mathcal{P}\mathrm{g})} + \mathbf{C}^{(\mathscr{H}\mathrm{g})}\mathscr{H}, \\
-\mathbf{q}_{\mathrm{e}} &= \mathbf{C}^{(\theta \mathrm{g})} \cdot\cdot \mathbf{g} + \mathbf{C}^{(\theta)} \cdot \boldsymbol{\theta} + \boldsymbol{\gamma} \cdot \mathbf{C}^{(\gamma\theta)} + \mathbf{C}^{(\theta\mathcal{P})} \cdot \mathcal{P}^{\mathrm{p}} + \mathbf{C}^{(\mathscr{H}\theta)}\mathscr{H}, \\
-\mathbf{m}_{\mathrm{e}} &= \mathbf{C}^{(\gamma \mathrm{g})} \cdot\cdot \mathbf{g} + \mathbf{C}^{(\gamma\theta)} \cdot \boldsymbol{\theta} + \mathbf{C}^{(\gamma)} \cdot \boldsymbol{\gamma} + \mathcal{P}^{\mathrm{p}} \cdot \mathbf{C}^{(\mathcal{P}\gamma)} + \mathbf{C}^{(\mathscr{H}\gamma)}\mathscr{H},
\end{aligned} \tag{61}$$

$$\mathbf{E} = \mathbf{C}^{(\mathcal{P}\mathrm{g})} \cdot\cdot\, \mathbf{g} + \boldsymbol{\theta} \cdot \mathbf{C}^{(\theta\mathcal{P})} + \mathbf{C}^{(\mathcal{P}\gamma)} \cdot \boldsymbol{\gamma} + \mathbf{C}^{(\mathcal{P})} \cdot \boldsymbol{\mathcal{P}}^{\mathrm{p}} + \mathbf{C}^{(\mathscr{H}\mathcal{P})} \mathscr{H},$$
$$\vartheta = \mathbf{C}^{(\mathscr{H}\mathrm{g})} \cdot\cdot\, \mathbf{g} + \mathbf{C}^{(\mathscr{H}\theta)} \cdot \boldsymbol{\theta} + \mathbf{C}^{(\mathscr{H}\gamma)} \cdot \boldsymbol{\gamma} + \mathbf{C}^{(\mathscr{H}\mathcal{P})} \cdot \boldsymbol{\mathcal{P}}^{\mathrm{p}} + \mathrm{C}^{(\mathscr{H})} \mathscr{H}.$$

In order to close the set of equations (22), (23), (27), (55)–(57), (61) the constitutive equations for the dissipative parts of force and moment stresses $\boldsymbol{\tau}_{\mathrm{f}}$, $\mathbf{q}_{\mathrm{f}}$, $\mathbf{m}_{\mathrm{f}}$ should be formulated.

3.4 Comparison with the Classical Theory

To compare the theory stated above with the classical theory of piezoelectricity we leave out the thermal effects and moment interactions and neglect the inertia of rotation. Since $\boldsymbol{\mu} = \mathbf{0}$, $\mathbf{J} = \mathbf{0}$ the angular momentum balance equation (56) takes the form

$$\mathbf{q} = -2\boldsymbol{\mathcal{Q}} \cdot \times \boldsymbol{\nabla}\mathbf{E}. \tag{62}$$

In view of Eq. (62) the momentum balance equation (55) is reduced to the form

$$\boldsymbol{\nabla} \cdot \boldsymbol{\tau} + \boldsymbol{\mathcal{Q}} \cdot \boldsymbol{\nabla}\boldsymbol{\nabla} \cdot \mathbf{E} = \rho\ddot{\mathbf{u}}. \tag{63}$$

In view of the foregoing assumptions the constitutive equations (61) can be rewritten as

$$\begin{aligned} \boldsymbol{\tau} &= \mathbf{C}^{(\mathrm{g})} \cdot\cdot\, \mathbf{g} + \boldsymbol{\theta} \cdot \mathbf{C}^{(\theta\mathrm{g})} + \boldsymbol{\mathcal{P}}^{\mathrm{p}} \cdot \mathbf{C}^{(\mathrm{P}\mathrm{g})}, \\ -\mathbf{q} &= \mathbf{C}^{(\theta\mathrm{g})} \cdot\cdot\, \mathbf{g} + \mathbf{C}^{(\theta)} \cdot \boldsymbol{\theta} + \mathbf{C}^{(\theta\mathrm{P})} \cdot \boldsymbol{\mathcal{P}}^{\mathrm{p}}, \\ \mathbf{E} &= \mathbf{C}^{(\mathrm{P})} \cdot \boldsymbol{\mathcal{P}}^{\mathrm{p}} + \mathbf{C}^{(\mathrm{P}\mathrm{g})} \cdot\cdot\, \mathbf{g} + \boldsymbol{\theta} \cdot \mathbf{C}^{(\theta\mathrm{P})}, \end{aligned} \tag{64}$$

where indices e of tensor $\boldsymbol{\tau}$ and vector $\mathbf{q}$ are left out because the dissipative part of these tensors are equal to zero. Further two versions of the simplified theory are considered.

Variant 1. We suppose that the shear strain $\boldsymbol{\theta}$ is equal to zero, but the corresponding part of the stress tensor determined by vector $\mathbf{q}$ is a finite quantity. Then the constitutive equations (64) take the simpler form. In view of Eq. (17) the obtained constitutive equations can be reduced to Eq. (38) where tensors $\mathbf{C}$, $\boldsymbol{\mathcal{M}}$, $\boldsymbol{\epsilon}$ are expressed in terms of the material tensors introduced above. Thus the first variant of the simplified theory is the set of equations of piezoelectricity (19), (38), (63) which differs from the classical one only by the term $\boldsymbol{\mathcal{Q}} \cdot \boldsymbol{\nabla}\boldsymbol{\nabla} \cdot \mathbf{E}$ in the equation of motion (63). Substituting the first equation in Eq. (38) into Eq. (63) we obtain

$$\boldsymbol{\nabla} \cdot (\mathbf{C} \cdot\cdot\, \mathbf{g}) - \boldsymbol{\nabla}\mathbf{E} \cdot\cdot\, \boldsymbol{\mathcal{M}} + \boldsymbol{\mathcal{Q}} \cdot \boldsymbol{\nabla}\boldsymbol{\nabla} \cdot \mathbf{E} = \rho\ddot{\mathbf{u}}. \tag{65}$$

In the case of long-wave processes the contribution of the term $\mathfrak{Q} \cdot \nabla\nabla \cdot \mathbf{E}$ is small compared to the contribution of the term $\nabla\mathbf{E} \cdot\cdot \mathfrak{M}$. However, in the case of short-wave processes the contribution of the term $\mathfrak{Q} \cdot \nabla\nabla \cdot \mathbf{E}$ can be significant.

Variant 2. The case when $\theta \neq \mathbf{0}$ is considered. By the simple transformations in view of Eqs. (17), (62) the constitutive equations (64) are reduced to the form

$$\boldsymbol{\tau} = \mathbf{C} \cdot\cdot \mathbf{g} - \mathbf{E} \cdot \mathfrak{M} + \mathfrak{N} \cdot\cdot \nabla\mathbf{E}, \qquad \mathbf{D} = \mathfrak{M} \cdot\cdot \mathbf{g} + \boldsymbol{\epsilon} \cdot \mathbf{E} - \boldsymbol{\varepsilon} \cdot\cdot \nabla\mathbf{E}. \tag{66}$$

Here tensors $\mathbf{C}$, $\mathfrak{M}$, $\mathfrak{N}$, $\boldsymbol{\epsilon}$, $\boldsymbol{\varepsilon}$ can be expressed in terms of the material tensors introduced above by the complicated formulas. It is easy to see that the constitutive equations (66) differ from the classical ones by the terms containing $\nabla\mathbf{E}$. Now it is impossible to quantify the contribution of these terms since to determine the tensors $\mathfrak{N}$ and $\boldsymbol{\varepsilon}$ the physical experiments should be carried out. However, it is clear that in the case of short-wave processes the relative contribution of the terms containing $\nabla\mathbf{E}$ is greater than in the case of long-wave processes.

4 Conclusion

Above two micro-polar theories of piezoelectricity based on the continuum with internal degrees of freedom are considered. One of these theories describes the polar piezoelectric materials, and the other describes the non-polar materials. In contrast to the classical theory where the constitutive equations establish the relations between the electric field vector $\mathbf{E}$ and the electric induction vector $\mathbf{D}$, in the proposed micro-polar theories the constitutive equations relate the electric field vector $\mathbf{E}$ and the polarization vector $\mathcal{P}^{\mathrm{p}}$. It is proved that under certain simplifying assumptions the proposed theories of piezoelectricity pass into the quasi-classical ones. The quasi-classical theories differ from the classical theory of piezoelectricity by the presence of additional terms of piezoelectric nature in the equations of motion and the constitutive equations.

Acknowledgments The work was supported by the grant of RFBR N 12-01-00815-a.

References

1. Cady, W.G.: Piezoelectricity: An Introduction to the Theory and Applications of Electro-mechanical Phenomena in Crystals. Dover Publications, New York (1964)
2. Tiersten, H.F.: Linear Piezoelectric Plate Vibrations. Plenum Press, New York (1969)
3. Kolpakov, J.E., Zhilin, P.A.: Generalized continuum and linear theory of piezoelectric materials. In: Proceedings of XXIX Summer School-Conference "Advanced Problems in Mechanics", pp. 364–375. St. Petersburg (2002)
4. Eringen, A.C., Maugin, G.A.: Electrodynamics of Continua, vol. 1. Springer, New York (1990)

5. Maugin, G.A.: Continuum Mechanics of Electromagnetic Solids. North-Holland, Amsterdam (1988)
6. Nelson, D.F.: Electric, Optic and Acoustic Interactions in Dielectrics. Wiley-Interscience, New York (1979)
7. Zhilin, P.A.: Advanced Problems in Mechanics, vol. 2. IPME RAS, St. Petersburg (2006)
8. Zhilin, P.A.: Rational Continuum Mechanics. Politechnic University Publishing House, St. Petersburg (2012). (In Russian)
9. Treugolov, I.G.: Moment theory of electromagnetic effects in anisotropic solids. Appl. Math. Mech. **53**(6), 992–997 (1989). (In Russian)
10. Dixon, R.C., Eringen, A.C.: A dynamical theory of polar elastic dielectrics-I. Int. J. Eng. Sci. **3**, 359–377 (1965)
11. Demiray, H., Eringen, A.C.: On constitutive relations of polar elastic dielectrics. Lett. Appl. Eng. Sci. **1**, 517–527 (1973)
12. Demiray, H., Dost, S.: Diatomics elestic dielectrics with polarization gradient. Int. J. Eng. Sci. **27**, 1275–1284 (1989)
13. Eringen, A.C.: Continuum theory of micromorphic electromagnetic thermoelastic solids. Int. J. Eng. Sci. **41**, 653–665 (2003)
14. Gales, C., Ghiba, I.D., Ignyatescu, I.: Asymptotic partition of energy in micromorphic thermopiezoelectricity. J. Therm. Stresses **34**, 1241–1249 (2011)
15. Gales, C.: Spatial behavior in the electromagnetic theory of microstretch elasticity. Int. J. Solids Struct. **48**, 2755–2763 (2011)
16. Gales, C.: Some results in micromorphic piezoelectricity. Eur. J. Mech. A. Solids **31**, 37–46 (2011)
17. Gales, C.: Spatial behavior and continuous dependence results in the linear dynamic theory of magnetoelectroelasticity. J. Elast. **108**, 209–223 (2012)
18. Prechtl, A.: Defirmable bodies with electric and magnetic quadrupoles. Int. J. Eng. Sci. **18**, 665–680 (1980)
19. Born, M., Huang, K.: Dynamics Theory of Crystal Lattices. Clarendon Press, Oxford (1954)
20. Ivanova, E.A., Kirvtsov, A.M., Morozov, N.F.: Derivation of macroscopic relations of the elasticity of complex crystal lattices taking into account the moment interactions at the microlevel. Appl. Math. Mech. **71**(4), 543–561 (2007)

Description of Thermal and Micro-Structural Processes in Generalized Continua: Zhilin's Method and its Modifications

Elena Ivanova and Elena Vilchevskaya

Abstract The method of description of thermal and micro-structural processes, developed by P.A.Zhilin is discussed. The main idea of the method consists of transformation of the energy balance equation to a special form called the reduced equation of energy balance. This form is obtained by separation of the stress tensors into elastic and dissipative components and introduction of quantities characterizing the physical processes associated with neglected degrees of freedom. As a result the energy balance equation is divided into two or more parts, one of them is the reduced equation of energy balance, and the rest have a sense of heat conduction equation, diffusion equation, equation of structural transformations, etc. We discuss the applicability of this method to generalized continua, in particular, to media with rotational degrees of freedom and media with microstructure. Comparative analysis of various modifications of Zhilin's method, differed in the way of temperature, entropy and chemical potential introduction, is carried out.

1 Introduction

The idea of generalized continua goes back to the work of the Cosserat brothers [6]. The main idea of generalized continua is to consider extra degrees of freedom for material points in order to be able to better model materials with microstructure in the framework of continuum mechanics. Many developments have been reported since

E. Ivanova (✉)
Saint-Petersburg State Polytechnical University (SPbSPU), Politekhnicheskaja 29, Saint-Petersburg 195251, Russia
e-mail: elenaivanova239@post.ru

E. Vilchevskaya
Institute for Problems in Mechanical Engineering, Russian Academy of Sciences, V.O., Bolshoy pr. 61, Saint-Petersburg 199178, Russia
e-mail: vilchevska@gmail.com

H. Altenbach et al. (eds.), *Generalized Continua as Models for Materials*, Advanced Structured Materials 22, DOI: 10.1007/978-3-642-36394-8_10,

the seminal work of the Cosserat brothers (see [8, 13, 18, 25, 26] and references therein). One of the most fundamental references on the theory of polar media is the paper written by Kafadar and Eringen [9, 14], where the nonlinear Cosserat medium of a general type is considered. The more recent developments can be seen in [4, 7, 10, 21, 24] and references therein. Due to the effort of Eringen and his contemporaries Cosserat's theory appreciably evolved, however, after a time the interest in studying of the Cosserat 3D-continuum began to wane. One of the reasons was that the attempts to determine the additional elastic moduli experimentally were not successful. At the same time the effect of these constants is so small that in fact the Cosserat theory of elasticity does not provide any improvement in comparison with the classical theory of elasticity.

At the beginning of XXI century a new method of describing of various inelastic processes in solids and multicomponent mixtures by means of the Cosserat continuum was proposed by P. A. Zhilin (see original papers [1, 30–33] and books [34, 35] based on these papers). One of the key ideas of the method consists in the separation of force and moment stresses into elastic and inelastic (dissipative) components. To describe the inelastic processes associated with phase transitions and structural transformations, plastic flow, dynamics of bulk solids, dynamics of granular media, fragmentation and defragmentation of materials, particle diffusion, chemical reactions, etc. it is important to introduce the additional state variables such as temperature, entropy, chemical potential and particle distribution density. In fact, the introduction of these quantities in continuum mechanics should be considered as an attempt to take into account the microstructural processes at the macro level by means of some integral characteristics. Zhilin's method tolerates various modifications of the definitions of entropy and chemical potential as well as other state variables being quantities that cannot be measured. In this paper we consider different ways of introduction of such quantities and carry out their comparative analysis.

The paper is organized as follows. In Sect. 2, in order to describe structure modifications, we introduce the density of particle distribution as an independent characteristic and recall the basic balance equations for the spatial distribution. Following Zhilin [32, 34] in Sect. 3 we rewrite the energy balance equation in a special form called the reduced equation of energy balance. This form is obtained by separation of the stress tensors into elastic and dissipative components and introduction of quantities characterizing the physical processes associated with neglected degrees of freedom. As a result the energy balance equation is divided into two or more parts, one of them is the reduced equation of energy balance, and the rest have a sense of heat conduction equation, equation of structural transformations, etc. Section 4 aims at comparison of Truesdell's and Zhilin's methods of constitutive equations derivation and provides some constitutive equations for the dissipative part of stress tensors. In Sect. 5 we discuss in details the different ways of the entropy and chemical potential introduction and compare these approaches in Sect. 6.

2 Balance Equations for Cosserat Continuum with Microstructure

The majority of the researches were focused on the fact that in a continuum one has to define translations and rotations independently (or in other words, one has to establish force and moment actions as it was done by Euler). Therefore one symmetric stress tensor is not enough to represent the response of the continuum on the external loading. As a result two independent laws of motion appear: the balance of momentum and the balance of angular momentum. Another internal degree of freedom which can be considered explicitly is the distribution of the particle density. Considering this quantity independently of mass density allows to take into account media microstructure changes due to its fragmentation or particle diffusion. Further we formulate the balance equations for a continuum with angular degrees of freedom and microstructure.

Let us choose an inertial reference system and observe the volume V (control volume) fixed in the reference system and containing some amount of body-points. It is assumed that a body-point occupies zero volume and has both translational and angular degrees of freedom. To derive dynamical equations of the continuum we apply the spatial description. Let vector $\mathbf{r}$ determine a position of some point of space. We denote a mass density of the material medium in the point of space by $\rho(\mathbf{r}, t)$, a velocity field by $\mathbf{v}(\mathbf{r}, t)$, fields of rotation tensor and angular velocity vector of the body-point by $\mathbf{Q}(\mathbf{r}, t)$ and $\boldsymbol{\omega}(\mathbf{r}, t)$.

The local form of the mass conservation law can be written as:

$$\frac{\delta\rho}{\delta t} + \rho\ \nabla \cdot \mathbf{v} = 0. \tag{1}$$

Here $\delta/\delta t$ is the material derivative, ∇ denotes the nabla operator.

In addition to the mass density we introduce a particle density $n(\mathbf{r}, t)$ as an independent variable. Such differentiation is important, for example, when the material tends to fragmentation, as in this case the mass is preserved, but the number of particles changes. In other words considering the particle density as an independent characteristic corresponds to introducing an additional degree of freedom which accounts for structural changes. As a result an additional balance equation for the new variable has to be formulated. This equation can be written by analogy to Eq. (1) with a source term. Thus, the particle balance equations takes the form [1, 35]

$$\frac{\delta n}{\delta t} + n\nabla \cdot \mathbf{v} = \chi. \tag{2}$$

Here χ is the rate of particle production per unit volume.

From combination of Eqs. (1) and (2) it follows that

$$\frac{\delta z}{\delta t} = -\frac{\chi(\mathbf{r}, t)}{n(\mathbf{r}, t)}, \qquad z \equiv \ln\left(\frac{\rho(\mathbf{r}, t) n_0(\mathbf{r})}{\rho_0(\mathbf{r}) n(\mathbf{r}, t)}\right), \tag{3}$$

where $n_0(\mathbf{r})$ and $\rho_0(\mathbf{r})$ are reference distributions of densities of particles and mass.

To formulate the rest of the balance equations we assume that the kinetic energy of the substance K in the control volume V is an additive function of mass, and thus can be written in terms of a kinetic energy mass density κ

$$K = \int_V \rho\,\kappa\,dV.$$

Then, following [32, 35], we postulate that κ is a quadratic form of translational and angular velocities of the body-point

$$\kappa = \frac{1}{2}\mathbf{v}\cdot\mathbf{v} + \mathbf{v}\cdot\mathbf{B}\cdot\boldsymbol{\omega} + \frac{1}{2}\boldsymbol{\omega}\cdot\mathbf{C}\cdot\boldsymbol{\omega}, \tag{4}$$

where $\mathbf{B} = \mathbf{Q}\cdot\mathbf{B}_0\cdot\mathbf{Q}^T$ and $\mathbf{C} = \mathbf{Q}\cdot\mathbf{C}_0\cdot\mathbf{Q}^T$ are the mass densities of the inertia tensors of the body-point. $\mathbf{B}_0$ and $\mathbf{C}_0$ are the inertia tensors in the reference state per unit mass. $\mathbf{Q}$ is a rotation tensor. It relates to $\boldsymbol{\omega}$ by the equation:

$$\frac{d\mathbf{Q}(\mathbf{r},\,t)}{dt} = \boldsymbol{\omega}(\mathbf{r},\,t)\times\mathbf{Q}(\mathbf{r},\,t)$$

Then the linear momentum is defined by expression

$$\mathbf{K}_1 = \int_V \rho\,\mathcal{K}_1\,dV, \qquad \mathcal{K}_1 = \frac{\partial\kappa}{\partial\mathbf{v}} = \mathbf{v} + \mathbf{B}\cdot\boldsymbol{\omega}, \tag{5}$$

where $\mathcal{K}_1$ is the mass density of momentum.

The angular momentum calculated relative to the origin is defined as:

$$\mathbf{K}_2 = \int_V \rho\,\mathcal{K}_2\,dV, \qquad \mathcal{K}_2 = \mathbf{r}\times\mathcal{K}_1 + \mathcal{L}, \tag{6}$$

where

$$\mathcal{L} \equiv \frac{\partial\kappa}{\partial\boldsymbol{\omega}} = \mathbf{v}\cdot\mathbf{B} + \mathbf{C}\cdot\boldsymbol{\omega} \tag{7}$$

is the mass density of the dynamic spin.

Euler's first dynamical law momentum balance equation for the control volume V bounded by smooth surface Σ within the spatial description may be written

$$\frac{d}{dt}\int_V \rho\,\mathcal{K}_1\,dV = \int_V \rho\,\mathbf{F}\,dV + \int_\Sigma (\mathbf{T}_n - \rho\,\mathbf{n}\cdot\mathbf{v}\mathcal{K}_1)\,d\Sigma, \tag{8}$$

where d/dt is the total time derivative, $\mathbf{F}$ is an external force per unit mass, $\mathbf{T}_n$ is a stress vector acting upon an elementary surface, $\mathbf{n}$ is normal to this surface.

The local form of Euler's first dynamical law is:

$$\rho \frac{\delta}{\delta t}\mathcal{K}_1 = \nabla \cdot \mathbf{T} + \rho \mathbf{F}, \tag{9}$$

where $\mathbf{T}$ is the Cauchy stress tensor ($\mathbf{T}_n = \mathbf{n} \cdot \mathbf{T}$).

Euler's second dynamical law (the equation for balance of the angular momentum) within spatial description is as follows:

$$\frac{\mathrm{d}}{\mathrm{dt}} \int\limits_V \rho \mathcal{K}_2 \, \mathrm{dV} = \int\limits_V \rho \left(\mathbf{r} \times \mathbf{F} + \mathbf{L}\right) \, \mathrm{dV} + \int\limits_\Sigma \left(\mathbf{r} \times \mathbf{T}_n + \mathbf{M}_n - \rho \mathbf{n} \cdot \mathbf{v}\mathcal{K}_2\right) \, \mathrm{d}\Sigma, \tag{10}$$

where $\mathbf{L}$ is an external moment per unit mass, $\mathbf{M}_n$ is a moment acting upon a surface with the normal $\mathbf{n}$.

Using Euler's first dynamical law one can obtain the local form for Euler's second dynamical law for a generalized continuum

$$\rho \frac{\delta}{\delta t}\mathcal{K}_2 = \nabla \cdot \mathbf{M} + \mathbf{T}_\times + \rho \mathbf{L}, \tag{11}$$

where $\mathbf{M}$ is a couple tensor introduced in analogy to the stress tensor, $\mathbf{T}_\times$ is a vector invariant of a second rank tensor. For the dyad $\mathbf{ab}$ it is defined by $(\mathbf{ab})_\times = \mathbf{a} \times \mathbf{b}$. The material derivative of the angular momentum has the form:

$$\frac{\delta}{\delta t}\mathcal{K}_2 = \mathbf{v} \times \mathcal{K}_1 + \frac{\delta}{\delta t}\mathcal{L} = \mathbf{v} \times \mathbf{B} \cdot \boldsymbol{\omega} + \frac{\delta}{\delta t}\mathcal{L} \tag{12}$$

The first law of thermodynamics (the energy balance equation) states that there is a function of state U (called internal energy) satisfying the equation

$$\frac{\mathrm{d}}{\mathrm{dt}}(\mathsf{K} + \mathsf{U}) = \mathsf{N}^{\mathrm{e}} + \mathsf{Q}, \tag{13}$$

where N^{e} is the power of external forces, Q is the energy supply from external sources per unit time.

The definition of internal energy is less formal than that of the kinetic energy. As a matter of fact, the internal energy is the energy of motion on degrees of freedom which are ignored in the model under consideration. Indeed, the momentum balance equation and the angular momentum balance equation are obtained by choosing the kinetic energy as a quadratic form of translational and angular velocities corresponding to the translational and rotational degrees of freedom. Other degrees of freedom that are ignored in the kinetic energy are taken into account by means of the internal energy. As a rule the sense of the internal energy depends on the mathematical model

used for description of the system. For example, in classical equilibrium thermodynamics the internal energy of the ideal gas is an additive function of the number of particles and proportional to the temperature [19, 23]. In statistical thermodynamics the internal energy is determined by the elastic interactions of the particles, and for the ideal gas it is equal to zero [16]. The difference between the approaches can not give the cause for doubts about their correctness. The fact is that the internal energy is a quantity that cannot be measured, and so there are no physical experiments which let us know what the internal energy of the system under consideration is.

Usually in many continuum mechanics applications the internal energy is an additive function of the mass [20, 27, 29]. Here we intend to take into account the structure changes in the media caused by a change of the number of particles in the medium. Therefore we suppose that the internal energy is an additive function of the number of particles [32], and we will study the consequences of our supposition. Thus we accept

$$U = \int_V n u \, dV,$$

where u is the specific internal energy.

The power of external forces and coupled forces can be represented in the following form:

$$N^e = \int_V \rho \left(\mathbf{F} \cdot \mathbf{v} + \mathbf{L} \cdot \boldsymbol{\omega} \right) dV + \int_\Sigma \left(\mathbf{T}_n \cdot \mathbf{v} + \mathbf{M}_n \cdot \boldsymbol{\omega} \right) d\Sigma \tag{14}$$

The energy supply per unit time is determined by the adding (moving away) of new particles to the control volume and by the heat supply per unit time Q which is the sum of the heat supply per unit time directly in the volume V and through the boundary of volume Σ

$$Q = \int_V n q \, dV - \int_\Sigma \mathbf{n} \cdot \mathbf{h} \, d\Sigma - \int_\Sigma \mathbf{n} \cdot \mathbf{v} (\rho \kappa + n u) d\Sigma,$$

where q is the energy supply per unit time into the particles of the medium, $\mathbf{h}$ is the heat flow.

Taking into account Gauss' theorem and balance laws (1), (2), (9) and (11) one can obtain the local form of energy balance equation[1]

$$n \frac{\delta u}{\delta t} = n u \frac{\delta z}{\delta t} + \mathbf{T}^{\mathsf{T}} \cdot\cdot (\nabla \mathbf{v} + \mathbf{I} \times \boldsymbol{\omega}) + \mathbf{M}^{\mathsf{T}} \cdot\cdot \nabla \boldsymbol{\omega} - \nabla \cdot \mathbf{h} + n q, \tag{15}$$

where $\mathbf{I}$ is a unit tensor. However such a form of the energy balance equation is not that good since it is not clear on which arguments the internal energy depends. In

[1] Details are presented in E.N. Vilchevskaya. Appendix: Formula calculus in [35].

the following section we will transform (15) to obtain the so-called reduced energy balance equation.

3 Transformation of the Energy Balance Equation

Let us consider Eq. (15). The right-hand side of this equation contains the power of forces and moments. A part of this power leads to the change of the internal energy. The remaining part of the power is partly conserved within the body as heat and is partly emanated into external medium. In order to separate these parts let us introduce the following decomposition

$$\mathbf{T} = -(p_e + p_f)\mathbf{I} + \boldsymbol{\tau}_e + \boldsymbol{\tau}_f, \qquad \mathbf{M} = \mathbf{M}_e + \mathbf{M}_f, \qquad \operatorname{tr}\boldsymbol{\tau}_e = \operatorname{tr}\boldsymbol{\tau}_f = 0, \tag{16}$$

where the quantities with the index "e" are independent of velocities. These quantities always affect the internal energy. The quantities with the index "f" account for an internal friction. These quantities may have an influence on the internal energy but only by means of additional parameters like entropy or chemical potential. Taking (16) into account we rewrite the energy balance equation in the form:

$$\begin{aligned} n\frac{\delta u}{\delta t} = nu\frac{\delta z}{\delta t} - p_e\nabla\cdot\mathbf{v} + \boldsymbol{\tau}_e^{\mathsf{T}}\cdot\cdot(\nabla\mathbf{v} + \mathbf{I}\times\boldsymbol{\omega}) + \mathbf{M}_e^{\mathsf{T}}\cdot\cdot\nabla\boldsymbol{\omega} \\ -\nabla\cdot\mathbf{h} + nq - p_f\nabla\cdot\mathbf{v} + \boldsymbol{\tau}_f^{\mathsf{T}}\cdot\cdot(\nabla\mathbf{v} + \mathbf{I}\times\boldsymbol{\omega}) + \mathbf{M}_f^{\mathsf{T}}\cdot\cdot\nabla\boldsymbol{\omega} \end{aligned} \tag{17}$$

The part of the power of forces and moments that does not depend on velocities can be represented as:

$$\begin{aligned} \boldsymbol{\tau}_e^{\mathsf{T}}\cdot\cdot(\nabla\mathbf{v} + \mathbf{I}\times\boldsymbol{\omega}) + \mathbf{M}_e^{\mathsf{T}}\cdot\cdot\nabla\boldsymbol{\omega} = \mathbf{f}_1^{\mathsf{T}}\cdot\cdot\frac{\delta\mathbf{E}}{\delta t} + \mathbf{M}_e^{\mathsf{T}}\cdot\cdot\frac{\delta\mathbf{F}}{\delta t} + \frac{1}{2}\mathbf{f}_2^{\mathsf{T}}\cdot\cdot\frac{\delta\mathbf{Q}}{\delta t} \\ \mathbf{f}_1^{\mathsf{T}} = -\left(\boldsymbol{\tau}_e + \mathbf{M}_e\cdot\mathbf{F}^{\mathsf{T}}\right)\cdot\mathbf{E}^{-\mathsf{T}}, \qquad \mathbf{f}_2^{\mathsf{T}} = \left(\mathbf{M}_e^{\mathsf{T}}\cdot\mathbf{F} - \boldsymbol{\tau}_e\right)_\times\times\mathbf{Q}, \end{aligned} \tag{18}$$

where the strain measure $\mathbf{F}$ and the deformation gradient $\mathbf{E}$ are determined by:

$$\nabla\mathbf{Q} = \mathbf{F}\times\mathbf{Q}, \qquad \mathbf{E} = \mathbf{I} - \nabla\mathbf{u} \tag{19}$$

$\mathbf{u}$ is a displacement field. From the mass balance it follows that

$$\nabla\cdot\mathbf{v} = \frac{\rho}{\rho_0}\frac{\delta\sigma}{\delta t}, \qquad \sigma = \frac{\rho_0}{\rho} \tag{20}$$

and as a result the energy balance equation takes the form:

$$\begin{aligned} n\frac{\delta u}{\delta t} &= nu\frac{\delta z}{\delta t} - p_e\frac{\rho}{\rho_0}\frac{\delta \sigma}{\delta t} + \mathbf{f}_1^{\mathsf{T}}\cdot\cdot\frac{\delta \mathbf{E}}{\delta t} + \mathbf{M}_e^{\mathsf{T}}\cdot\cdot\frac{\delta \mathbf{F}}{\delta t} + \frac{1}{2}\mathbf{f}_2^{\mathsf{T}}\cdot\cdot\frac{\delta \mathbf{Q}}{\delta t} \\ &\underline{-\nabla\cdot\mathbf{h} + nq - p_f\nabla\cdot\mathbf{v} + \boldsymbol{\tau}_f^{\mathsf{T}}\cdot\cdot(\nabla\mathbf{v} + \mathbf{I}\times\boldsymbol{\omega}) + \mathbf{M}_f^{\mathsf{T}}\cdot\cdot\nabla\boldsymbol{\omega}} \end{aligned} \tag{21}$$

A transformation of the underlined terms is not as formal as the above ones. In order to state the full form of the reduced equation of the energy balance we need to define the concepts of temperature, entropy and chemical potential that will be discussed later.

4 Constitutive Equations

There are several methods of the constitutive equations derivation in continuum mechanics. We start with comparing Zhilin's method with one of the best known and widely used methods—the method of Truesdell.

Truesdell's method [29] is based on the combined use of the first and second laws of thermodynamics. The essence of this method is as follows. The second law of thermodynamics is written in the form of the Clausius–Duhem inequality. Then some thermal terms, namely the rate of heat supply per unit volume and divergence of the heat flow, are excluded from the inequality by means of the energy balance equation. As a result the so-called reduced dissipation inequality is obtained. It must be satisfied for all processes occurring in the medium. Since neither the external mechanical actions nor the heat supply from external sources are included in the reduced dissipation inequality this inequality imposes restrictions to the constitutive equations. In the case of an elastic medium the reduced dissipation inequality allows us to obtain the Cauchy–Green relations for the stress tensor, moment stress tensor and temperature, and imposes restrictions to the choice of the constitutive equation for heat flow vector. After substituting the Cauchy–Green relations into the energy balance equation and performing some mathematical transformations the heat conduction equation is obtained. This equation relates the temperature and entropy, divergence of the heat flow vector and the terms characterizing the rate of heat supply per unit volume. The heat conduction equation closes the system of equations of coupled problem of thermoelasticity. If a medium possesses inelastic properties then the reduced dissipation inequality does not allow us to obtain the constitutive equations in the formal way and only makes it possible to eliminate those constitutive equations which contradict the second law of thermodynamics in the form of the Clausius–Duhem inequality. Thus other methods of the constitutive equations obtaining should be used, for example, the method of rheological models or the method of theory of media with fading memory. At the same time the statement of the heat conduction equation in the form that is obtained in the problem of thermoelasticity is an open question.

The basic idea of Zhilin's method is to transform the energy balance equation into a special form. During this transformation the stresses are represented as a sum of elastic and dissipative components, the temperature and entropy are introduced, and

the energy balance equation is divided into two equations. One of them is the reduced energy balance equation which contains the internal energy, the elastic components of stress tensor and moment stress tensor, and also temperature and entropy. Another equation is the heat conduction equation which contains temperature and entropy, the dissipative components of stress tensor and moment stress tensor, the divergence of the heat flow vector, and the terms characterizing the rate of heat supply per unit volume. In contrast to the reduced dissipation inequality, the reduced energy balance equation used in Zhilin's method allows us to obtain the Cauchy–Green relations for the temperature and the elastic component of the stress tensor in the case of an inelastic medium. Note that by Zhilin's method the Cauchy–Green relations are obtained without use of the second law of thermodynamics, which is used only for the formulation of the constitutive equations for the dissipative components of stress tensors and heat flow vector. In addition, Zhilin's formulation of the second law of thermodynamics differs from the Clausius–Duhem inequality and represents the set of two inequalities [32, 35].

$$\mathbf{h} \cdot \nabla\vartheta \leqslant 0, \qquad \delta = -\mathrm{p}_\mathrm{f} \nabla \cdot \mathbf{v} + \boldsymbol{\tau}_\mathrm{f}^\mathsf{T} \cdot\cdot (\nabla \mathbf{v} + \mathbf{I} \times \boldsymbol{\omega}) + \mathbf{M}_\mathrm{f}^\mathsf{T} \cdot\cdot \nabla \boldsymbol{\omega} \geqslant 0, \tag{22}$$

where ϑ is the temperature measured by a thermometer. This formulation is more restrictive than the Clausius–Duhem inequality [28], which follows from Zhilin's formulation.

The first inequality expresses the intuitive condition that heat flows in the direction of the negative gradient of temperature and imposes restriction of the constitutive equation for heat flow vector. The second one can be associated with the statement that the dissipative forces and moments can not perform a positive work and imposes restriction of the constitutive equations for the dissipative components of stress tensors. According to Zhilin [1, 30–35] the components of stress tensors connected with inelastic behavior and internal dissipation can be related with antisymmetric tensors. Bellow we give some examples of constitutive equations for the dissipative components of stress tensors.

To describe the inelastic behavior of solids, for example, plasticity and dynamics of granular media Zhilin proposed [30–35] the following constitutive equations

$$\mathrm{p}_\mathrm{f} = 0, \qquad \boldsymbol{\tau}_\mathrm{f} = \mathbf{I} \times \mathbf{t}, \qquad \mathbf{M}_\mathrm{f} = \mathbf{0}, \tag{23}$$

where vector $\mathbf{t}$ is determined by analogy with the Coulomb dry friction and takes the form

$$\mathbf{t} = \mathrm{k} \, |\mathbf{n} \cdot \boldsymbol{\tau}_e \cdot \mathbf{n}| \, \sigma(\mathbf{n} \cdot \boldsymbol{\tau}_e \cdot \mathbf{n}) \, \frac{2\boldsymbol{\omega} - \nabla \times \mathbf{v}}{|2\boldsymbol{\omega} - \nabla \times \mathbf{v}|}, \qquad \boldsymbol{\omega} \neq \frac{1}{2} \nabla \times \mathbf{v}. \tag{24}$$

Here $\mathrm{k} > 0$ is the parameter of friction, and the function $\sigma(\mathbf{n} \cdot \boldsymbol{\tau}_e \cdot \mathbf{n})$ is determined as follows

$$\sigma(\mathbf{n} \cdot \boldsymbol{\tau}_e \cdot \mathbf{n}) = \begin{cases} 1, \, \mathbf{n} \cdot \boldsymbol{\tau}_e \cdot \mathbf{n} < 0, \\ 0, \, \mathbf{n} \cdot \boldsymbol{\tau}_e \cdot \mathbf{n} \geqslant 0. \end{cases} \tag{25}$$

The unit vector $\mathbf{n}$ in Eq. (24) is found by tensor $\boldsymbol{\tau}_e$ as a solution of the problem

$$\mathbf{n} \cdot \boldsymbol{\tau}_e \cdot \mathbf{m} = \max, \qquad \forall\, \mathbf{n}, \mathbf{m}: \quad |\mathbf{n}| = |\mathbf{m}| = 1, \quad \mathbf{n} \cdot \mathbf{m} = 0. \tag{26}$$

The solution of problem (26) is unique. This fact is proved in [30, 35]. It is easy to see that the constitutive equations (23), (24) satisfy the second law of thermodynamics in the form of Eq. (22). Indeed,

$$\boldsymbol{\tau}_f^{\mathsf{T}} \cdot\cdot\, (\nabla \mathbf{v} + \mathbf{I} \times \boldsymbol{\omega}) \equiv 2\mathbf{t} \cdot \left(\boldsymbol{\omega} - \frac{1}{2} \nabla \times \mathbf{v} \right). \tag{27}$$

Hence, in view of Eqs. (24), (25) and the fact that $\mathrm{k} > 0$ we have

$$\boldsymbol{\tau}_f^{\mathsf{T}} \cdot\cdot\, (\nabla \mathbf{v} + \mathbf{I} \times \boldsymbol{\omega}) = \mathrm{k}\, |\mathbf{n} \cdot \boldsymbol{\tau}_e \cdot \mathbf{n}|\, \sigma(\mathbf{n} \cdot \boldsymbol{\tau}_e \cdot \mathbf{n})\, |2\boldsymbol{\omega} - \nabla \times \mathbf{v}| \geqslant 0. \tag{28}$$

All aforesaid relates to the case of sliding. If there is no sliding, i.e. the condition $2\boldsymbol{\omega} = \nabla \times \mathbf{v}$ is satisfied, then vector $\mathbf{t}$ is found from the equations of motion. To be exact, by using the equation of the angular momentum balance vector $\mathbf{t}$ can be excluded from the equation of the momentum balance. Note that if there is no sliding, the friction force is conservative and there is no energy dissipation. In this case the constitutive equations (23) also satisfy the second law of thermodynamics in the form of Eq. (22).

In [32, 35] Zhilin noted that in many cases Coulomb dry friction can be replaced by viscous friction, i.e. instead of Eq. (24) we can use the constitutive equation

$$\mathbf{t} = \mathrm{k} \left(\boldsymbol{\omega} - \frac{1}{2} \nabla \times \mathbf{v} \right), \tag{29}$$

where $\mathrm{k} > 0$ is the coefficient of viscous friction.

To describe the behavior of a two-component micropolar medium Zhilin proposed [1, 34, 35] the constitutive equations for inelastic components of stress tensors which contain both symmetric and antisymmetric parts. The first component of this medium is a viscous fluid and the second one is a solid-liquid component consisting of fibres.

The constitutive equations for the fluid component are

$$\mathrm{p}'_f = 0, \qquad \boldsymbol{\tau}'_f = 2\boldsymbol{\mu} \cdot\cdot\, \mathbf{D} + \mathbf{t}' \times \mathbf{I}, \qquad \mathbf{M}'_f = \mathbf{0}, \tag{30}$$

where

$$\mathbf{D} = \frac{1}{2} \left(\nabla \mathbf{v}_1 + \nabla \mathbf{v}_1^{\mathsf{T}} - \frac{2}{3} (\nabla \cdot \mathbf{v}_1) \mathbf{I} \right). \tag{31}$$

Vector $\mathbf{t}'$ is a vector of viscous friction which depends on the particle distribution density of the solid-liquid component:

$$\mathbf{t}' = \eta_2 \, \boldsymbol{\mu}_1 \cdot \left(\boldsymbol{\omega} - \frac{1}{2} \nabla \times \mathbf{v}_1 \right). \tag{32}$$

The first term in Eq. $(30)_2$ is a standard term for a viscous fluid. The second term in Eq. $(30)_2$ characterizes friction due to the presence of a solid-liquid component.

The constitutive equations for the solid-liquid component are

$$\mathrm{p}''_{\mathrm{f}} = 0, \qquad \boldsymbol{\tau}''_{\mathrm{f}} = \mathbf{t}'' \times \mathbf{I}, \qquad \mathbf{M}''_{\mathrm{f}} = \mathbf{m}'' \times \mathbf{I}, \tag{33}$$

where vectors $\mathbf{t}''$ and $\mathbf{m}''$ are

$$\mathbf{t}'' = \eta_2 \, \boldsymbol{\mu}_2 \cdot \left(\boldsymbol{\omega} - \frac{1}{2} \nabla \times \mathbf{v}_2 \right), \qquad \mathbf{m} = - \, \eta_2 \, \mu_3 \, (\nabla \times \boldsymbol{\omega}) \, . \tag{34}$$

The tensors of viscous friction coefficients must satisfy the relations

$$\begin{gathered} \forall \, \mathbf{a}, \mathbf{b}, \mathbf{c} \ \text{ with } \ \mathbf{c} = -\mathbf{c}^{\mathsf{T}} : \qquad \mathbf{a} \cdot \cdot \boldsymbol{\mu} \cdot \cdot \mathbf{a} \geqslant 0, \qquad \mathbf{b} \cdot \boldsymbol{\mu}_1 \cdot \mathbf{b} \geqslant 0, \qquad \mu_3 \geqslant 0, \\ \mathbf{a} \cdot \cdot \boldsymbol{\mu} = \boldsymbol{\mu} \cdot \cdot \mathbf{a}, \qquad \mathbf{c} \cdot \cdot \boldsymbol{\mu} = \mathbf{0}, \qquad \mathbf{I} \cdot \cdot \boldsymbol{\mu} = \mathbf{0}, \qquad \mathbf{b} \cdot \boldsymbol{\mu}_1 = \boldsymbol{\mu}_1 \cdot \mathbf{b}. \end{gathered} \tag{35}$$

The inelastic components of stress tensors are responsible for the conversion of mechanical energy into heat. In accordance with Zhilin's constitutive equations the transfer of energy into heat is associated with the motion by rotational degrees of freedom, i. e. by those degrees of freedom for which there are no elastic interactions. Note that the classical model of viscous fluid is constructed similarly: the pressure is assumed to be elastic and depends on the mass density (or volume strain, that is the same) whereas the viscous stresses are determined by the deviatoric part of the stress tensor and depend on the deviatoric part of the strain tensor. Thus, in this model of fluid the dissipation of mechanical energy occurs by degrees of freedom without elastic interactions. It is not possible within the framework of classical continuum to implement this principle in relation to the solid where elastic interactions are described by a symmetric stress tensor. The use of a generalized continuum allows us to associate mechanical energy dissipation with the degrees of freedom for which there is no elastic interactions, namely the rotational degrees of freedom which correspond to the moment stress tensor and the antisymmetric parts of the stress tensor.

5 Different Ways of Entropy and Chemical Potential Introduction

Usually the concepts of temperature, entropy, internal energy and chemical potential are supposed to be well-known. However, in fact there are no satisfactory definitions for them in continuum mechanics. The problem is that it is impossible to prove

that the temperature as it is introduced in thermodynamics or in statistical physics coincides with the temperature definition as it is used in continuum mechanics. A situation with the definition of variables that cannot be measured such as the entropy, internal energy or chemical potential is even more complicated. Such quantities are characteristics of a mathematical model and they are necessary for obtaining some relations connecting measurable quantities. Consequently, the preference of this or that definition is determined by specific features of problems under consideration.

In fact, the entropy is introduced as an attempt to take into account a dependence of the internal energy on the velocities of the ignored degrees of freedom. There are different ways of entropy introduction (see [3, 5, 17, 22] for example) and it is difficult to say unambiguously which of them is more preferable. A new thermodynamical quantity—chemical potential is introduced to describe a change of density of particles. As usual in thermodynamics the chemical potential is defined as the derivative of the internal energy with respect to the number of particles [12, 23]. However there exist other definitions of the chemical potential. For example, Baierlein [2] proposed to introduce the chemical potential by describing its properties instead of explaining the chemical potential by relating it to an energy change. These ideas have a further development in [11]. Zhilin [32] suggested a new concept of the chemical potential as a conjugate variable to the number of particles. Its definition is given by means of pure mechanical arguments, which are based on using a special form of the energy balance equation.

Further different ways of the entropy and chemical potential introduction based on the method developed by Zhilin [34, 35] are considered.

5.1 Variant 1

Let us introduce the temperature $\vartheta(\mathbf{r}, t)$ and entropy $\eta(\mathbf{r}, t)$ by the following equation:

$$n q - \nabla \cdot \mathbf{h} - p_f \nabla \cdot \mathbf{v} + \boldsymbol{\tau}_f^T \cdot\cdot (\nabla \mathbf{v} + \mathbf{I} \times \boldsymbol{\omega}) + \mathbf{M}_f^T \cdot\cdot \nabla \boldsymbol{\omega} = n \vartheta \frac{\delta \eta}{\delta t} \qquad (36)$$

The above given definition brings about a few remarks. First, the temperature ϑ is considered to be some characteristic of the medium that is measured by a thermometer, and the entropy η related to one particle is introduced as a quantity conjugate with the temperature. Second, since we suppose that the internal energy is an additive function of the number of particles then it is assumed that the entropy is also an additive function of the number of particles. Note that this definition of entropy is different from the definition used, for example, in classical thermodynamics or physics, where an inequality is introduced. In particular, the proposed definition does not coincide with the concept of an equilibrium process. The Eq. (36) is the heat conduction equation, i.e. equation describing a non-equilibrium process.

Accounting for (36) one may rewrite the Eq. (21) in the form:

$$n\frac{\delta u}{\delta t} = nu\,\frac{\delta z}{\delta t} - p_e\frac{\rho}{\rho_0}\frac{\delta \sigma}{\delta t} + \mathbf{f}_1^{\mathsf{T}}\cdot\cdot\frac{\delta \mathbf{E}}{\delta t} + \mathbf{M}_e^{\mathsf{T}}\cdot\cdot\frac{\delta \mathbf{F}}{\delta t} + \frac{1}{2}\mathbf{f}_2^{\mathsf{T}}\cdot\cdot\frac{\delta \mathbf{Q}}{\delta t} + n\vartheta\frac{\delta \eta}{\delta t} \tag{37}$$

It is seen that the internal energy is a function of the following arguments

$$u = u(z, \sigma, \eta, \mathbf{E}, \mathbf{F}, \mathbf{Q}) \tag{38}$$

Note that from (38) and (47) it follows that

$$u = \frac{\partial u}{\partial z} \tag{39}$$

In thermodynamics the derivative of the internal energy with respect to the number of particles is usually called chemical potential [12, 23]. Introduction of the temperature and entropy by (36) means that a role of the chemical potential can be played by the internal energy.

Let us show that the variable z can be excluded from the arguments of the internal energy. Indeed from (39) it follows that

$$u = u_*(\sigma, \eta, \mathbf{E}, \mathbf{F}, \mathbf{Q})\,\frac{\rho_0}{n_0}\exp z \quad \Rightarrow \quad u = \frac{\rho}{n}u_*, \tag{40}$$

where u_* is a mass density of the internal energy. It should be noted that the last equation is only valid, if there are no massless particles in the system.

Insertion of (39) into (37) gives

$$\begin{aligned}\rho\,\frac{\delta u_*}{\delta t} = &-\frac{p_e}{\sigma}\frac{\delta \sigma}{\delta t} + n\vartheta\,\frac{\delta \eta}{\delta t} + \left(\mathbf{E}^{-1}\cdot\boldsymbol{\tau}_e^{\mathsf{T}} + \mathbf{E}^{-1}\cdot\mathbf{F}\cdot\mathbf{M}_e^{\mathsf{T}}\right)\cdot\cdot\frac{\delta \mathbf{E}}{\delta t}\\ &+ \mathbf{M}_e^{\mathsf{T}}\cdot\cdot\frac{\delta \mathbf{F}}{\delta t} + \frac{1}{2}\left((\mathbf{M}_e^{\mathsf{T}}\cdot\mathbf{F} - \boldsymbol{\tau}_e)_\times \times \mathbf{Q}\right)^{\mathsf{T}}\cdot\cdot\frac{\delta \mathbf{Q}}{\delta t}\end{aligned} \tag{41}$$

From the reduced energy balance equation one can derive the Cauchy-Green relations

$$p_e = -\frac{\partial\,\rho_0\,u_*}{\partial\,\sigma}, \qquad \vartheta = \frac{1}{\sigma n}\frac{\partial\,\rho_0\,u_*}{\partial \eta}, \qquad \sigma\,\mathbf{M}_e = \frac{\rho_0\,\partial u_*}{\partial \mathbf{F}}, \tag{42}$$

$$\sigma\,\boldsymbol{\tau}_e = -\frac{\rho_0\,\partial u_*}{\partial \mathbf{E}}\cdot\mathbf{E}^{\mathsf{T}} - \frac{\rho_0\,\partial u_*}{\partial \mathbf{F}}\cdot\mathbf{F}^{\mathsf{T}}$$

and constrains which the internal energy has to satisfy

$$\begin{aligned}\left(\frac{\partial u_*}{\partial \mathbf{E}}\right)^{\mathsf{T}}\cdot\cdot\mathbf{E} + \left(\frac{\partial u_*}{\partial \mathbf{F}}\right)^{\mathsf{T}}\cdot\cdot\mathbf{F} = 0,\\ \left(\frac{\partial u_*}{\partial \mathbf{E}}\right)^{\mathsf{T}}\cdot\cdot(\mathbf{A}\cdot\mathbf{E}) + \left(\frac{\partial u_*}{\partial \mathbf{Q}}\right)^{\mathsf{T}}\cdot\cdot(\mathbf{A}\cdot\mathbf{Q}) + \left(\frac{\partial u_*}{\partial \mathbf{F}}\right)^{\mathsf{T}}\cdot\cdot(\mathbf{A}\cdot\mathbf{F} - \mathbf{F}\cdot\mathbf{A}) = 0,\end{aligned} \tag{43}$$

where $\mathbf{A}$ is an arbitrary antisymmetric tensor.

Note that the function $\rho_0 u_*$ is independent of z. It means that only the constitutive equation for the temperature depends on the distribution density of the particles. The heat conduction equation depends on n only by means of $n\vartheta\frac{\delta \eta}{\delta t}$, and the chemical potential does not appear in any equation.

Considering function $\rho_0 u_*$ implies that we assume that the internal energy is an additive function of mass. In this case it is natural to assume that the entropy is also additive by mass. Thus instead of (36) we can introduce the temperature and entropy η_* by means of

$$\rho q_* - \nabla \cdot \mathbf{h} - p_f \nabla \cdot \mathbf{v} + \boldsymbol{\tau}_f^T \cdot\cdot (\nabla \mathbf{v} + \mathbf{I} \times \boldsymbol{\omega}) + \mathbf{M}_f^T \cdot\cdot \nabla \boldsymbol{\omega} = \rho \vartheta \frac{\delta \eta_*}{\delta t} \tag{44}$$

Then the reduced equation of the energy balance has the form

$$\rho \frac{\delta u_*}{\delta t} = -\frac{p_e}{\sigma}\frac{\delta \sigma}{\delta t} + \rho \vartheta \frac{\delta \eta_*}{\delta t} + \left(\mathbf{E}^{-1} \cdot \boldsymbol{\tau}_e^T + \mathbf{E}^{-1} \cdot \mathbf{F} \cdot \mathbf{M}_e^T\right) \cdot\cdot \frac{\delta \mathbf{E}}{\delta t} \tag{45}$$

$$+ \mathbf{M}_e^T \cdot\cdot \frac{\delta \mathbf{F}}{\delta t} + \frac{1}{2}\left((\mathbf{M}_e^T \cdot \mathbf{F} - \boldsymbol{\tau}_e)_\times \times \mathbf{Q}\right)^T \cdot\cdot \frac{\delta \mathbf{Q}}{\delta t}$$

All Cauchy-Green relations (42) are still valid except the one for the temperature, which now has the form

$$\vartheta = \frac{\partial u_*}{\partial \eta_*} \tag{46}$$

It is seen that the heat conduction equation (44) as well as the constitutive equations (42) do not depend on the particle density. Thus the influence of the mechanical and thermal processes on the change of the particle distribution can be taken into account only by means of the source term in the particle balance equation (2). So the stress-strain state and the temperature conditions can affect the changes of particle distribution density since the source term in the particle balance equation can depend on all these factors. Hence, this method of temperature and entropy introduction can be used to describe the structure transformations and phase transitions which occur without the release or absorption of heat and are not accompanied by significant changes in the mechanical and thermodynamical characteristics but only leads to changes in other physical characteristics such as, for example, electrical or magnetic properties.

5.2 Variant 2

An alternative form of the reduced energy balance equation makes use of the particle balance equation. We insert (3) into (21) and obtain

$$\begin{aligned} n\frac{\delta u}{\delta t} &= -p_e\frac{\rho}{\rho_0}\frac{\delta\sigma}{\delta t} + \mathbf{f}_1^{\mathsf{T}}\cdot\cdot\frac{\delta\mathbf{E}}{\delta t} + \mathbf{M}_e^{\mathsf{T}}\cdot\cdot\frac{\delta\mathbf{F}}{\delta t} + \frac{1}{2}\mathbf{f}_2^{\mathsf{T}}\cdot\cdot\frac{\delta\mathbf{Q}}{\delta t} \\ &\quad -\chi u - \nabla\cdot\mathbf{h} + nq - p_f\nabla\cdot\mathbf{v} + \boldsymbol{\tau}_f^{\mathsf{T}}\cdot\cdot(\nabla\mathbf{v} + \mathbf{I}\times\boldsymbol{\omega}) + \mathbf{M}_f^{\mathsf{T}}\cdot\cdot\nabla\boldsymbol{\omega} \end{aligned} \tag{47}$$

and as a result the source term in the particle balance equation χ appears in the energy balance equation.

Now let us define the temperature and entropy by the equation

$$-\chi u - \nabla\cdot\mathbf{h} + nq - p_f\nabla\cdot\mathbf{v} + \boldsymbol{\tau}_f^{\mathsf{T}}\cdot\cdot(\nabla\mathbf{v} + \mathbf{I}\times\boldsymbol{\omega}) + \mathbf{M}_f^{\mathsf{T}}\cdot\cdot\nabla\boldsymbol{\omega} = n\vartheta\frac{\delta\eta}{\delta t} \tag{48}$$

and investigate the consequences. This equation differs from (36) only due to the term χu standing for the energy supply per unit time caused by the structural transitions of the medium. Then the reduced energy balance equation takes the form

$$\begin{aligned} n\frac{\delta u}{\delta t} &= -\frac{p_e}{\sigma}\frac{\delta\sigma}{\delta t} + \left(\mathbf{E}^{-1}\cdot\boldsymbol{\tau}_e^{\mathsf{T}} + \mathbf{E}^{-1}\cdot\mathbf{F}\cdot\mathbf{M}_e^{\mathsf{T}}\right)\cdot\cdot\frac{\delta\mathbf{E}}{\delta t} \\ &\quad + \mathbf{M}_e^{\mathsf{T}}\cdot\cdot\frac{\delta\mathbf{F}}{\delta t} + \frac{1}{2}\left((\mathbf{M}_e^{\mathsf{T}}\cdot\mathbf{F} - \boldsymbol{\tau}_e)_\times\times\mathbf{Q}\right)^{\mathsf{T}}\cdot\cdot\frac{\delta\mathbf{Q}}{\delta t} + n\vartheta\frac{\delta\eta}{\delta t} \end{aligned} \tag{49}$$

Thus the internal energy is a function of the following independent arguments

$$u = u(\sigma, \eta, \mathbf{E}, \mathbf{F}, \mathbf{Q}) \tag{50}$$

and the Cauchy-Green relations are

$$\begin{aligned} &p_e = -n\sigma\frac{\partial u}{\partial\sigma}, \qquad \vartheta = \frac{\partial u}{\partial\eta}, \qquad \sigma\mathbf{M}_e = n\frac{\partial u}{\partial\mathbf{F}}, \\ &\boldsymbol{\tau}_e = -n\frac{\partial u}{\partial\mathbf{E}}\cdot\mathbf{E}^{\mathsf{T}} - n\frac{\partial u}{\partial\mathbf{F}}\cdot\mathbf{F}^{\mathsf{T}} \end{aligned} \tag{51}$$

The constraints for the internal energy u are the same as they were in Variant 1 for u_*.

Note that now the internal energy does not play role of the chemical potential as it was in Variant 1. At the same time the heat conduction equation (48) has a term connected with particle distribution changes and this term depends on the internal energy. Thus, this method of introduction of temperature can be used to describe the structure transformations and phase transitions accompanied by the release or absorption of heat. Note that the first and second variants of derivation of the constitutive equations and the heat conduction equation are correct both in the case when the mass density and the particle distribution density are independent quantities and in the case when they are linearly related (i.e. when the source term in the particle balance equation is equal to zero).

5.3 Variant 3

Let us assume that some part of the underlined terms in (21) is responsible for the change in the number of particles. Therefore, instead of Eq. (36) we will use a more general equation containing an additional term that accounts for structural transitions. We denote

$$n q - \nabla \cdot \mathbf{h} - p_f \nabla \cdot \mathbf{v} + \boldsymbol{\tau}_f^{\mathsf{T}} \cdot\cdot (\nabla \mathbf{v} + \mathbf{I} \times \boldsymbol{\omega}) + \mathbf{M}_f^{\mathsf{T}} \cdot\cdot \nabla \boldsymbol{\omega} = n\vartheta \frac{\delta \eta}{\delta t} + \psi \frac{\delta n}{\delta t} \tag{52}$$

Analogous to the temperature and entropy, n and ψ appear in Eq. (52) as the conjugate variables. Equation (52) is the combined equation of structural transitions (e.g., fragmentation) and heat conduction.

Substituting Eq. (52) into (21) after some transformation we obtain the reduced energy balance equation in the form

$$\frac{\delta(n u)}{\delta t} = \frac{p_e + n u}{\rho} \frac{\delta \rho}{\delta t} + \mathbf{f}_1^{\mathsf{T}} \cdot\cdot \frac{\delta \mathbf{E}}{\delta t} + \mathbf{M}_e^{\mathsf{T}} \cdot\cdot \frac{\delta \mathbf{F}}{\delta t} + \frac{1}{2} \mathbf{f}_2^{\mathsf{T}} \cdot\cdot \frac{\delta \mathbf{Q}}{\delta t} + n\vartheta \frac{\delta \eta}{\delta t} + \psi \frac{\delta n}{\delta t} \tag{53}$$

It is significant that such a form of the reduced energy balance equation is valid only if the mass density and the density of particle distribution are independent variables.

From Eq. (53) there follow the Cauchy-Green relations

$$p_e = \rho^2 \frac{\partial}{\partial \rho} \left(\frac{n u}{\rho} \right), \qquad \vartheta = \frac{1}{n} \frac{\partial (n u)}{\partial \eta}, \qquad \psi = \frac{\partial (n u)}{\partial n}, \tag{54}$$

$$\mathbf{M}_e = \frac{\partial (n u)}{\partial \mathbf{F}}, \qquad \boldsymbol{\tau}_e = -\frac{\partial (n u)}{\partial \mathbf{E}} \cdot \mathbf{E}^{\mathsf{T}} - \frac{\partial (n u)}{\partial \mathbf{F}} \cdot \mathbf{F}^{\mathsf{T}}$$

From Eq. $(54)_3$ it is seen that ψ is a chemical potential. Similar expressions to $(54)_3$ are given in the classical textbooks [15, 19, 20, 23].

Note that Eq. (52) characterizes only overall influence of the entropy and chemical potential on the internal energy. To clarify their roles in the considered processes it is necessary to split Eq. (52) into two equations: the heat conduction equation and the equation of structural transitions.

$$n\vartheta \frac{\delta \eta}{\delta t} + Q = n q_1 - \nabla \cdot \mathbf{h}_1 - p_1 \nabla \cdot \mathbf{v} + \boldsymbol{\tau}_f^{\mathsf{T}} \cdot\cdot (\nabla \mathbf{v} + \mathbf{I} \times \boldsymbol{\omega}) + \mathbf{M}_f^{\mathsf{T}} \cdot\cdot \nabla \boldsymbol{\omega}, \tag{55}$$

$$\psi \frac{\delta n}{\delta t} - Q = n q_2 - \nabla \cdot \mathbf{h}_2 - p_2 \nabla \cdot \mathbf{v} \tag{56}$$

Where the following decompositions are used

$$\mathbf{h} = \mathbf{h}_1 + \mathbf{h}_2, \qquad q = q_1 + q_2, \qquad p_f = p_1 + p_2 \tag{57}$$

The equivalence of Eqs. (52) and (55) is determined by the presence of the undefined quantity Q characterizing the rate of energy exchange in the processes of the heat conductivity and the structural transitions.

The definition (55) given above brings about a necessity to formulate constitutive equations for all new quantities: $\mathbf{h}_i$, q_i, p_i $(i = 1, 2)$ and Q. The following circumstances have to be taken into account. First, suppose that the expression for the internal energy u and the source term χ are given. Then we have two equations for n and ψ—the particle balance equation, and Cauchy-Green relation relating these quantities. It means that the term $\psi \dfrac{\delta n}{\delta t}$ in the equation of structural transformations is determined. Therefore the constitutive equations for $\mathbf{h}_2, q_2, p_2$ and Q can not be independent. Second, arbitrarily given constitutive equations for $\mathbf{h}_2, q_2, p_2$ and Q together with the equation of structural transitions and corresponding Cauchy-Green relation determines the quantities n and ψ. Then the particle balance equation allows us to determine the source term χ. Finally a third variant exists. We can arbitrarily choose the constitutive equations for $\mathbf{h}_2, q_2, p_2, Q$ and χ, but in this case there is no freedom in choosing internal energy.

Introduction of the chemical potential as an independent variable is necessary to describe the diffusion processes and chemical reactions as well as the structure transformations and phase transitions which are accompanied by the release or absorption of heat and occur at a constant temperature.

6 Discussion

The investigation carried out shows that the mass density and particle density can be considered as independent variables without the chemical potential introduction. In some cases the role of the chemical potential can be played by the internal energy or the source term in the particle balance equation. Of course there is no reason to say that there is no necessity for the chemical potential introduction in general. The preference of this or that approach is determined by specific features of the problems under consideration. For example, if experimental data allow us to formulate the constitutive equation for the quantity Q characterizing the rate of energy exchange in the processes of the heat conductivity and the structural transitions, then the third variant of unmeasurable parameters introduction looks more preferable. In the opposite case an approach based on smaller amount of the constitutive equations should be chosen. The first and the second approaches require only the source term χ specification and do not impose any constraints on the internal energy definition. Thus they are easier in this sense, but of course a number of problems stays beyond the consideration.

Also it is important to lay stress on the fact that the equations of structural transitions and heat conduction (44), (48) and (52) define not only the entropy and chemical

potential but also the internal energy. Thus all these quantities should be introduced simultaneously.

References

1. Altenbach, H., Naumenko, K., Zhilin, P.: A micro-polar theory for binary media with application to phase-transitional flow of fiber suspensions. Continuum Mech. Thermodyn. **15**(6), 539–570 (2003)
2. Baierlein, R.: The elusive chemical potential. Am. J. Phys. **69**(4), 423–434 (2001)
3. Boltzmann, L.: Zur Theorie der elastischen Nachwirkung. Kaiserl. Akad. Wiss. Wien. Math. Naturw. Kl. **70**(II), 275–306 (1874)
4. Capriz, G.: Continua with Microstructure. Springer, Berlin (1989)
5. Clausius, R.: On the motive power of heat and on the laws which can be deducted from it for the theory of heat (translated from German by Magie, W.F.). Dover, New York (1960)
6. Cosserat, E., Cosserat F.: Théorie des corps déformables. Hermann, Paris (1909)
7. Epstein, M., de Leon, M.: Geometrical theory of uniform Cosserat media. J. Geom. Phys. **26**, 127–170 (1998)
8. Ericksen, J.L., Truesdell, C.: Exact theory of stress and strain in rods and shells. Arch. Ration. Mech. Anal. **1**, 295–323 (1957)
9. Eringen, A.C.: Theory of Micropolar Elastisity. Academic Press, New York (1968)
10. Eringen, A.C.: Microcontinuum Field Theories. Springer, New York (1999)
11. Job, G., Herrmann, F.: Chemical potential—a quantity in search of recognition. Eur. J. Phys. **27**, 353–371 (2006)
12. Gibbs, J.W.: On the equilibrium of heterogeneous substances. Trans. Conn. Acad. Sci. **III**, 108–248 (1875)
13. Green, A.E., Rivlin, R.S.: Multipolar continuum mechanics. Arch. Ration. Mech. Anal. **17**, 113–147 (1964)
14. Kafadar, C.B., Eringen, A.C.: Micropolar media-I: the classical theory. Int. J. Eng. Sci. **9**, 271–305 (1971)
15. Kondepudi, D., Prigogine, I.: Modern thermodynamics. From Heat Engines to Dissipative Structures. Wiley, New York (1998)
16. Laurendeau, N.M.: Statistical Thermodynamics—Fundamentals and Applications. Cambridge University Press, New York (2005)
17. Maugin, G.A.: Thermomechanics of Nonlinear Irreversible Behaviors: An Introduction. World Scientific, Singapore, New York (1999)
18. Mindlin, R.D.: Micro-structure in linear elasticity. Arch. Ration. Mech. Anal. **16**, 51–78 (1964)
19. Müller, I.: A History of Thermodynamics: The Doctrine of Energy and Entropy. Springer, Berlin (2007)
20. Müller, I., Müller, W.H.: Fundamentals of thermodynamics and applications: with historical annotations and many citations from Avogadro to Zermelo. Springer, Berlin (2009)
21. Muschik, W., Papenfuss, C., Ehrentraut, H.: A sketch of continuum thermodynamics. J. Non-newton. Fluid Mech. **96**, 255–290 (2001)
22. Nowacki, W.: Dynamic Problems of Thermoelasticity. Polish Scientific Publisher, Warszawa (1975)
23. Prigogine, I.: Introduction to Thermodynamics of Irreversible Processes. Charles C. Thomas Publishers, Springfield (1955)
24. Slawianowski, J.J.: Classical and quantized affine models of structured media. Meccanica **40**, 365–387 (2005)
25. Toupin, R.A.: Elastic materials with couple-stresses. Arch. Ration. Mech. Anal. **11**, 385–414 (1962)

26. Toupin, R.A.: Theories of elasticity with couple stresses. Arch. Rational Mech. Anal. **17**, 85–112 (1964)
27. Truesdell, C., Toupin, R.A.: The classical field theories. In: Flügge, S. (ed.) Encyclopedia of Phycics, vol. III/1. Springer, Heidelberg (1960)
28. Truesdell, C.: Rational Thermodynamics. Springer, New York (1984)
29. Truesdell, C.: The Elements of Continuum Mechanics. Springer, New York (1965)
30. Zhilin, P.A.: Basic equations of the theory of non-elastic media. Proc. of the XXVIII Summer School "Actual Problems in Mechanics". St. Petersburg, pp 14–58 (in Russ.) (2001)
31. Zhilin, P.A.: Phase Transitions and General Theory of Elasto-Plastic Bodies. Proc. of XXIX Summer School - Conference "Advanced Problems in Mechanics". St. Petersburg, pp 36–48 (2002)
32. Zhilin, P.A.: Mathematical theory of non-elastic media. Uspechi mechaniki (Advances in Mechanics) **2**(4), 3–36 (in Russ.) (2003)
33. Zhilin, P.A.: On the general theory of non-elastic media. Mechanics of materials and strength of constructions. Proc. of St. Petersburg State Polytechnical University, vol. 489, pp 8–27 (in Russ.) (2004)
34. Zhilin, P.A.: Advanced Problems in Mechanics, vol. 2, St. Petersburg (2006)
35. Zhilin, P.A.: Racional'naya mekhanika sploshnykh sred (Rational Continuum Mecanics, in Russ.). Politechnic university publishing house, St. Petersburg (2012)

Hierarchical Architecture and Modeling of Bio-Inspired Mechanically Adaptive Polymer Nanocomposites

Rasa Kazakevičiūtė-Makovska and Holger Steeb

Abstract This work is concerned with a new class of polymer nanocomposites with tailored mechanical properties. Such materials can reversibly switch their mechanical stiffness by up to three orders of magnitude in response to biomedically relevant chemical stimuli. The architecture of the new synthetic polymer nanocomposites was inspired by the dermis of sea cucumbers and their mechanically adaptivity and exceptional high reinforcement property are potentially suitable for use in biomedicine. According to the current literature, the mechanical morphing of these polymer nanocomposites is a result of changing nanoparticle interactions and it is described in the framework of two mechanical models, viz. the percolation model applies to a stiff (unstimulated) state and the Halpin-Kardos model describes a soft (stimulated) state. In this work, a new model is proposed to describe the reinforcement and adaptivity effects in such nanocomposites within a single theory. The change from the stiff to soft states and back is modulated by a single scalar parameter that describes the extent of stimulus. The essence of the new model lies in physically based modifications of the classical percolation theory applied to the evolution of the network formed by cellulose whisker nanoparticles, which are responsible for the stress-transfer in this class of polymer nanocomposites.

1 Introduction

Typical engineered materials are passive, i.e., they are unable to adapt their mechanical properties in response to chemically or biologically relevant stimuli. A new generation of synthetic materials that would possess such properties could be useful for many

R. Kazakevičiūtė-Makovska (✉) · H. Steeb
Mechanics-Continuum Mechanics, Ruhr University Bochum,
Universitätsstr. 150, 44780 Bochum, Germany
e-mail: Rasa.Kazakeviciute-Makovska@rub.de

H. Steeb
e-mail: Holger.Steeb@rub.de

H. Altenbach et al. (eds.), *Generalized Continua as Models for Materials*,
Advanced Structured Materials 22, DOI: 10.1007/978-3-642-36394-8_11,

applications ranging from biomedicine to space engineering, and nature offers many exciting ways to create such adaptive materials [1].

In recent studies, attention has been drawn to amazing self-defending skin of many echinoderms like sea cucumbers [2–6]. Their inner dermis is composed of rigid collagen nanofibres embedded in a viscoelastic matrix of fibrillin microfibres. In the face of danger, the sea cucumber secretes certain macromolecular chemicals that activate transient interactions between the nanofibres and this facilitates a change of the dermal stiffness.

Drawing inspiration from the sea cucumber's self-defense mechanism, novel polymer nanocomposites have been designed that can adapt their mechanical properties in response to chemical stimuli in a similar fashion [7]. The first such nanocomposites have been developed using cellulose nanofibres that were embedded in a matrix formed from either an ethyleneoxide-epichlorohydrin (EO-EPI) copolymer or from polyvinyl acetate (PVAc) [7] and the degree of interaction between the nanofibres was modulated by a water-based solvent. In the following years, next generations of polymer nanocomposites having this property have been designed and studied experimentally [8–12].

All polymer nanocomposites of this new class of stimuli-responsive materials can reversibly switch their mechanical stiffness by up to three orders of magnitude in response to the relevant stimuli [7, 8, 12]. According to the current literature, the mechanical morphing of these nanocomposites is a result of changing nanoparticle interactions and it is described in the framework of two mechanical models, viz. the percolation model applies to a stiff (unstimulated) state and the Halpin-Kardos model that applies to a soft (stimulated) state [7–12].

In this work, a new model is proposed to describe the reinforcement and adaptivity effects of these polymer nanocomposites within a single theory. The change from stiff to soft states and back is modulated by a single scalar parameter, which describes the extent of stimulus. The essence of the proposed model lies in a physically based modification of the classical percolation theory applied to the evolution of the network formed by the cellulose whisker nanoparticles that are responsible for the stress-transfer in this class of polymer nanocomposites. The applicability of the proposed approach is illustrated by a comparison of the experimentally determined storage modulus with model predictions for different polymer nanocomposites with varying filler extent. It is shown that the basic concept of the new model may naturally be extended to the analysis of rheological and thermal properties of the examined nanocomposites. Finally, an attempt is made to adopt the proposed approach to description of the mechanically adaptive materials in the non-linear domain.

2 Native and Synthetic Stiffness-Changing Nanocomposites

Holothuroids, also known as sea cucumbers, are marine animals living in all oceans of the world [3, 5, 6]. They have the unique and fascinating self-defending skin. Recent studies [3–6] have proved that the major constituent of the dermis of Cucumaria

frendosa and other sea cucumber species is a network of 10–14 nm microfibrils that surrounds and penetrates bundles of collagen fibrils. This network is immersed in a viscoelastic matrix of fibrillin microfibers. At the sign of danger, sea cucumber secretes certain soluble macromolecule chemicals that trigger the formation of transient interactions between the nanofibres [2, 4]. This facilitates, in a matter of seconds, the rapid and reversible change of the stiffness of inner dermis by regulating the interactions among collagen fibrils with a change in tensile modulus by a factor of 10 (5–40 MPa). Although the mechanism for the ability to alter the stiffness of dermis is not well understood, there are currently several competing models for this biomaterial (for a review, see [5, 6]).

The hierarchical architecture and the nanocomposite structure of the dermis of sea cucumbers (sketched in Fig. 1) have been an inspiration for the development of synthetic nanocomposites that can adapt their mechanical properties in response to chemical stimuli. Although such possibility was discussed in 2000 by Trotter et al. [3], only in 2008, Capadona and his colleagues [7] did a significant work in engineering the biological model, i.e. the sea cucumber dermis. These authors developed two synthetic nanocomposites in that interactions between the rigid fillers can be switched "on" and "off" in response to a chemical stimulus. To mimic the sea cucumber dermis structure, they used the low-modulus 1:1 ethyleneoxide/epichlorohydrin copolymer (EO-EPI) in place of a viscoelastic matrix of fibrillin microfibrils found in the native material. Instead of collagen fibrils, cellulose nanofibers were used as rigid filler. The interactions among these nanofibers are controlled by hydrogen bonding between surface hydroxyl groups and hence these interactions may be controlled by chemical stimuli. The second developed nanocomposite [7] was based on the poly(vinyl acetate) (PVAc) as a soft polymer matrix with cellulose nanofibers as rigid filler. It should be noted that unlike in the biological material, where the soft state is the "relaxed" natural state, in this men-made model the "unstimulated" state is the stiff state (see Fig. 1).

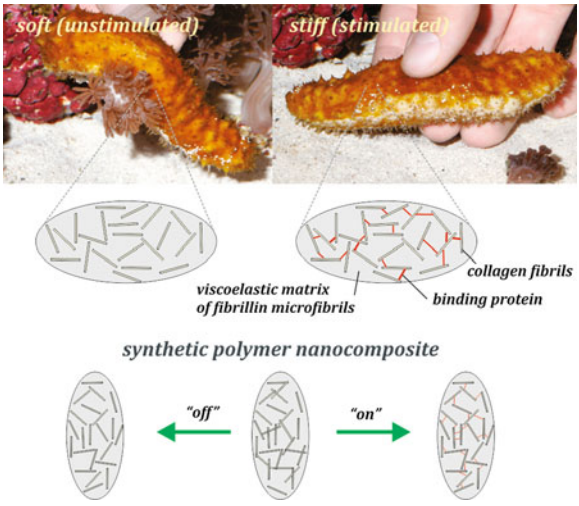

Fig. 1 Picture of sea cucumber in the stiff and soft states and schematic representation of the architecture of its dermis in the two states (adopted from Shanmuganathan [7, 8, 10])

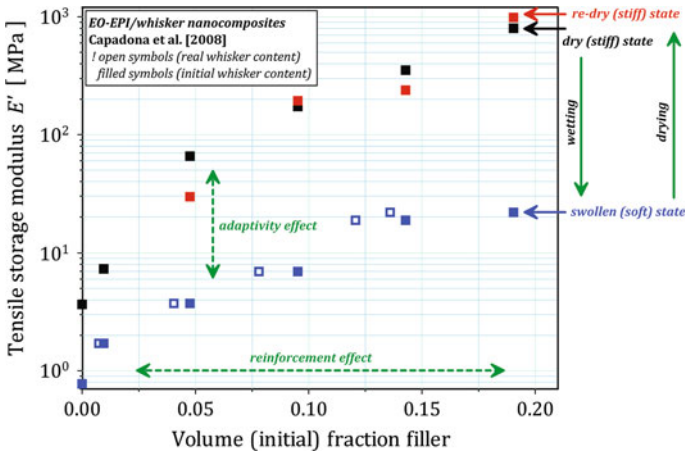

Fig. 2 Reinforcement and adaptivity effects in polymer nanocomposites at small strains

To illustrate the stiffness-changing property of the developed synthetic materials, Capadona et al. [7] compared experimentally determined values for the tensile storage modulus of the EO-EPI/whisker nanocomposites with varying amount of filler. Their results show that these nanocomposites are stiff in the dry state due to whisker-whisker interactions resulting in a percolated network of fillers. Water used as a chemical stimulus disrupts the hydrogen bonding between the cellulose whiskers within the polymer matrix and dissociates the fillers from each other. In effect, the nanocomposites soften and the tensile storage modulus decreases by a few order. The switching effect was also found to be reversible with the re-dried samples showing modulus close to the original value in dry state. For illustration of this mechanisms, their main experimental results are summarized in Fig. 2.

Following Capadona et al. [7], new stiffness-changing polymer nanocomposites have been developed using different polymer matrices, filler sources, and combination of one or more stimuli [8–12]. This new class of polymer nanocomposites is currently referred to as mechanically adaptive material [8]. In comparison to more familiar polymer nanocomposites such as carbon black or silica filled elastomers [13–16], they are characterized by the exceptionally high reinforcement property and the adaptivity effect. These two effects need to be modeled with a view to gain insights into the structure-property relationships in these materials.

3 Models of Nanofiber Composites and Reinforcement Effect

Mechanically adaptive polymers considered in Sect. 2 belong to the very large class of materials known as nanocomposites [17–20]. The macroscopic properties of a composite material reinforced with nanofillers are determined by various factors, such as [21–23]

- the composition and characteristics of each component,
- the geometry of filler and the filler dispersion,
- the filler-filler and filler-matrix interactions and possibly
- the modification of characteristics of the matrix itself.

These parameters have the important influence on final properties of the polymer nanocomposite and they are strongly interconnected. Therefore, it is problematic to draw conclusions on relative influences of the individual parameters.

A wide array of theoretical and modeling strategies including effective medium approaches, percolation theory, scaling, and micromechanical analyses has been applied toward achieving predictive and microscopic understanding of nanocomposite properties (see reviews [15, 16, 21]). Many of these models have been successfully applied in analysis of the reinforcement effect in carbon black or silica filled elastomers. However, their hierarchical architecture and reinforcement mechanisms are very different from that observed in the nanocomposites discussed in Sect. 2.

Two models of composite materials have been used in analysis of mechanically adaptive polymer nanocomposites [7–12]. The first one takes into account the reinforcement effect due to the presence of rigid inclusions (fibres) in a soft polymeric matrix without considering either filler-filler or filler-matrix interactions. This mean field approximation forms the basis of the Halpin-Kardos model that correctly predicts the composite behavior containing randomly oriented fibers [15, 16, 23]. Within this model, the polymer composite is assumed to be equivalent to many layers of unidirectional plies oriented at various angles to give a quasi-isotropic composite. The mechanical properties of each ply are derived from the micromechanical equations of Halpin-Tsai [15, 23].

The second model used in analysis of polymer nanocomposites is based on the consideration of filler-filler interactions and the percolation concept [24] well adapted to describe a percolating network of cellulose whiskers. In this approach, the whiskers are assumed to be linked by strong hydrogen bonds. The interactions between cellulose nanofibers induce the mechanical percolation of the fibers, and mechanical properties of the polymer nanocomposite can be predicted following the method of Ouali et al. [25]. In effect, the tensile elastic modulus E of the composite is given by the following empirical mixture rule

$$E = \frac{(1 - 2\xi + \xi\upsilon)E_m E_r + (1 - \upsilon)\xi E_r^2}{(\upsilon - \xi)E_m + (1 - \upsilon)E_r} . \tag{1}$$

The subscripts m and r refer to the soft (matrix) and rigid (filler) phase, respectively, and υ corresponds to the volume fraction of filler (rigid phase). The adjustable parameter ξ involved in this model corresponds to the volume fraction of the percolating rigid phase, i.e., the volume fraction of filler that participates in load (stress) transfer. With υ_c being the critical volume fraction of the rigid phase at the percolation threshold and β the corresponding critical exponent, ξ is given by the following rule [7, 8]

$$\xi = \upsilon \left(\frac{\upsilon - \upsilon_c}{1 - \upsilon_c} \right)^{\beta}, \quad \upsilon_c \leqslant \upsilon < 1 \,, \tag{2}$$

and $\xi = 0$ for $0 \leqslant \upsilon < \upsilon_c$. In general, $\beta = 0.4$ and for a 3D network the critical volume fraction υ_c depends on the aspect ratio L/d of the nanofiber as [7, 8]

$$\upsilon_c = A r^{-1}, \quad r \equiv L/d \,. \tag{3}$$

In application to the cellulose whisker based polymer nanocomposites, the coefficient A is set to 0.7 and the aspect ratio r depends on the source of whiskers [17, 19, 20].

It has been shown in [7, 8] that the reinforcement in the unstimulated (dry) state of the mechanically adaptive nanocomposites follows the percolation model as described by relations (1)–(3). It was concluded that the stress-transfer process is dominated by the formation of a continuous network of cellulose whiskers and strong interactions (hydrogen bonding) between them. It has been further observed that the behavior of the same nanocomposites in the stimulated (wet) state is correctly predicted by the Halpin-Kardos model based on a mean field approach, which does not account for the interactions between filler nanoparticles. This is well illustrated by the results shown in Fig. 3.

It follows that the mechanical morphing of this class of nanocomposites is a result of changing nanoparticle interactions and it is described in the framework of two different composite models. This situation, however, is not satisfactory from the theoretical point of view because two different constitutive models are needed to describe two states or phases of the same polymer nanocomposite, i.e. for the modeling the adaptivity effect. A more direct approach to this problem is proposed in Sect. 4.

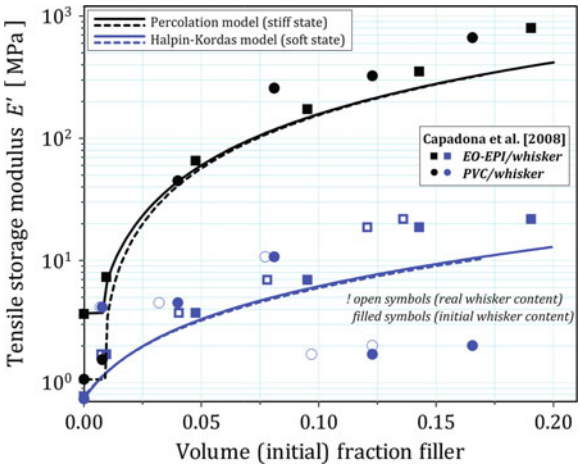

Fig. 3 Comparison of data with predictions according to two different models

4 Evolution of Percolating Network and Adaptivity Effect

According to the percolation type theory, the tensile elastic modulus E of a polymer nanocomposite may be expressed in the following general form

$$E = E\,(E_m, E_r, \upsilon, \xi) \tag{4}$$

with percolation parameter ξ being a function of the volume fraction of rigid phase υ and it depends in parametric form on the critical volume fraction υ_c, that is $\xi = \xi\,(\upsilon; \upsilon_c)$.

According to the micromechanical analysis [7–9], the stiffness-changing property or adaptivity effect in whisker-based polymer nanocomposites is mainly due to the percolation network formed by whisker nanoparticles. This network is entirely responsible for the stress transfer in the dry or unstimulated state of the nanocomposite. In the wet or stimulated state of the nanocomposite, the interactions between the nanoparticles in the network are partially or entirely broken by water or an alternative stimulating fluid. This physical micromechanism may be built into the macroscopic model by a single order parameter z with $z = 0$ corresponding to unstimulated state and $z = 1$ in the fully stimulated state. The scalar variable z is a measure of the stimulus extent and it enters the macroscopic theory only through the law for the percolation parameter ξ, which now takes the following general form

$$\xi = \xi\,(\upsilon, z; \upsilon_c)\,, \quad 0 \leqslant z \leqslant 1\,. \tag{5}$$

The parameter ξ represents at macroscopic level the stress-transfer in the percolation network of whisker nanoparticles with the value given by formula (2) in the unstimulated state and $\xi = 0$ in the fully stimulated state. This suggests the simple special form of the general law (5), namely,

$$\begin{aligned} &\xi = \xi\,(\upsilon, z; \upsilon_c) = (1 - z)\xi_A(\upsilon; \upsilon_c), \\ &\xi_A(\upsilon; \upsilon_c) \equiv \upsilon \left(\frac{\upsilon - \upsilon_c}{1 - \upsilon_c}\right)^{\beta}, 0 \leqslant z \leqslant 1\,, \end{aligned} \tag{6}$$

and $\xi = 0$ for $0 \leqslant \upsilon < \upsilon_c$. Moreover, the law for the tensile modulus may be assumed in the Takayanagi-Ouali form (1).

The applicability of these simple modifications of the classical percolation-type theory to describe the adaptivity effect in the considered class of polymer nanocomposites is illustrated in Fig. 4. The theoretical results shown in this figure have been obtained using the classical expression (1) for the elastic modulus of nanocomposite and the proposed modification (6) of expression (2) for the percolation parameter. The Takayanagi series-parallel model for the elastic modulus as given by (1) consists in a mixing rule between the two limits of the classical series and parallel models, better known as Reuss and Voigt models [15, 16]. Accordingly, it may be considered as a special case of the general mixture rule [21], which may be used to derive

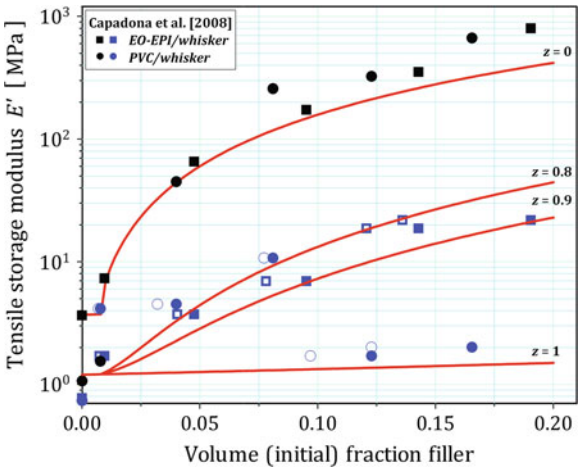

Fig. 4 Comparison of data with predictions according to proposed model of the adaptivity effect

the more accurate expression of form (4) for the nanocomposite modulus. However, these possibilities are not considered in this work due to lack of experimental data.

5 Dynamic Moduli of Nanocomposites

In order to obtain a better correlation of the hierarchical architecture and the macroscopically observed behavior of mechanically adaptive nanocomposites, it is necessary to experimentally characterize and theoretically model their viscoelastic properties. In the linear range, Dynamic Mechanical Analysis (DMA) is the most universal technique used for the rheological characterization of polymer nanocomposites [13, 14]. From the measured complex modulus E^*, not only the storage and loss moduli, E' and E'', are determined but also the creep compliance and relaxation moduli may be derived through the use of equivalence principles.

The development of linear viscoelastic models for the mechanically adaptive polymers may be based on the three-phase material concept presented in Sect. 4 for the analysis of the elastic modulus of polymer/whisker nanocomposites. The basic idea is very simple: one has only to replace the elastic moduli E_m and E_r in the general expression (4) by the corresponding complex moduli E^*_m and E^*_r for the polymer matrix and the reinforcing filler. In effect, the complex modulus E^* of the nanocomposite is obtained in the form

$$\mathrm{E}^* = \mathrm{E}' + \mathrm{i}\mathrm{E}'' \equiv \mathrm{E}\left(\mathrm{E}^*_\mathrm{m}, \mathrm{E}^*_\mathrm{r}, \upsilon, \xi\right) \ . \tag{7}$$

In the special case, when the complex modulus (7) is assumed in the Takayanagi-Ouali form (1), the storage modulus E' and the loss modulus E'' of the polymer

nanocomposite deduced from (7) are given by

$$E' = \frac{(AC + BD)\,E_r' - (BC - AD)\,E_r''}{C^2 + D^2},$$
$$E'' = \frac{(BC - AD)\,E_r' - (AC + BD)\,E_r''}{C^2 + D^2}, \tag{8}$$

where

$$A = (1 - 2\xi + \upsilon\xi)\,E_m' + (1 - \xi)\,\xi E_r',$$
$$B = (1 - 2\xi + \upsilon\xi)\,E_m'' + (1 - \xi)\,\xi E_r'',$$
$$C = (\upsilon - \xi)\,E_r' + (1 - \xi)\,\xi E_r',$$
$$D = (\upsilon - \xi)\,E_r'' + (1 - \xi)\,\xi E_r''. \tag{9}$$

These expressions follow directly from the separation of the real and imaginary parts of the complex modulus (7). They appear to take quite complex form and their calculations require the knowledge of the storage and loss moduli for both a polymer matrix and rigid filler particles.

In the relevant literature [7, 8], a more direct approach is generally adopted, i.e., the formula (1) for the elastic modulus of the nanocomposite is simply used for the calculation of the storage modulus of the same material. It is now clear that the two possible approaches are not equivalent for the mechanically adaptive nanocomposites with notable rheological properties, but they coincide for the purely elastic behavior. The differences between the two possibilities in modeling the rheological properties of the mechanically adaptive nanocomposites may be illustrated with simple examples. Figure 5 shows the comparison of the storage modulus calculated from expression (8) with the values obtained from expression (1) for the elastic modulus. It is seen that the computed values are close to each other implying that these particular polymer nanocomposites are nearly perfectly elastic in the wide range of temperature and filler content.

6 Temperature Dependent Moduli of Nanocomposites

The next step in characterizing and modeling the mechanically adaptive nanocomposites must necessarily be concerned with thermal effects. From an experimental point of view, DMA temperature sweep tests provide the best thermal characterization of this and other classes of polymeric materials. The representative results taken from the literature are reproduced in Fig. 6a and 7a. They show the storage modulus and the loss factor for dry polymer/whisker nanocomposites as a function of temperature for different whisker content.

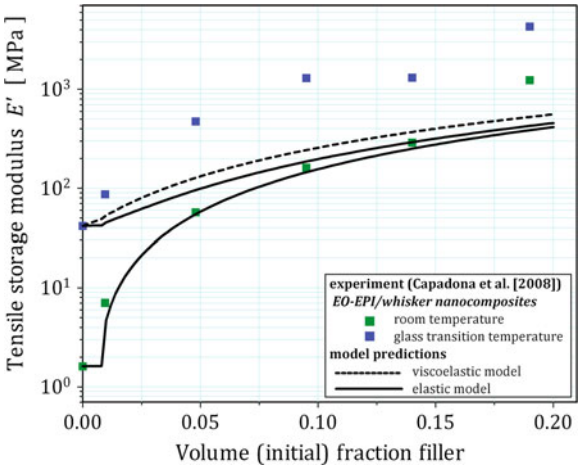

Fig. 5 Comparison of data with predictions according to viscoelastic model

The simplest approach to model thermal effects in the mechanically adaptive nanocomposites may again be based on the three-phase model with the modification that the respective moduli of polymer matrix and whisker nanoparticles depend in known or experimentally determined way on temperature. In Sect. 4, all quantities and relations are defined at the reference temperature, usually the room temperature. Assuming that these relations are valid at any temperature θ, the elastic modulus of polymer composite is obtained as

$$\mathrm{E}(\theta) = \mathrm{E}\left(\mathrm{E}_{\mathrm{m}}(\theta), \mathrm{E}_{\mathrm{r}}(\theta), \upsilon, \xi\right) \tag{10}$$

with percolation parameter ξ given by the general rule (5). Here $\mathrm{E}_{\mathrm{m}}(\theta)$ and $\mathrm{E}_{\mathrm{r}}(\theta)$ are the temperature dependent elastic moduli of the polymer matrix and whisker nanoparticles, respectively. In the particular case of the Takayanagi-Ouali model, this general assumption yields

$$\mathrm{E}(\theta) = \frac{(1-2\xi+\xi\upsilon)\,\mathrm{E}_{\mathrm{m}}(\theta)\,\mathrm{E}_{\mathrm{r}}(\theta) + (1-\upsilon)\,\xi\,(\mathrm{E}_{\mathrm{r}}(\theta))^2}{(1-\upsilon)\,\mathrm{E}_{\mathrm{r}}(\theta) + (1-\upsilon)\,\mathrm{E}_{\mathrm{m}}(\theta)} \tag{11}$$

with (6) as the associated, temperature independent law governing the evolution of the percolation parameter.

The same approach may be used for the temperature dependent complex modulus $\mathrm{E}^*(\theta)$ of polymer composite from which the storage and loss moduli, $\mathrm{E}'(\theta)$ and $\mathrm{E}''(\theta)$, may be deduced as in Sect. 5.

Figures 6b and 7b show the storage modulus and the loss factor computed by this approach for the polymer nanocomposite for which the measured data are shown in Fig. 6a and 7a. There are a few possible reasons of observed differences between data and computed values. First of all, no temperature dependent data are available for

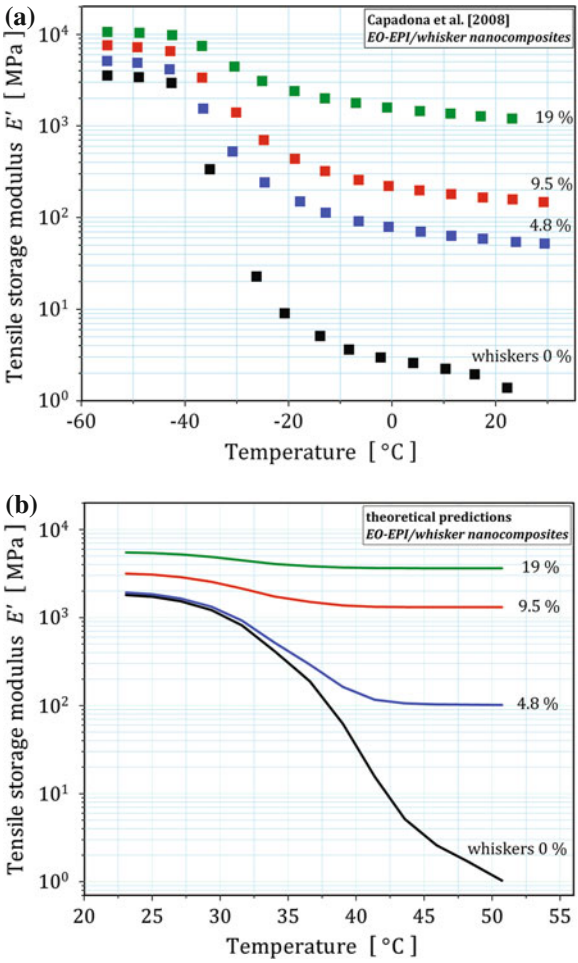

Fig. 6 DMTA temperature sweep tests: Comparison of data (**a**) with model predictions (**b**)

the cellulose whisker used as filler in this nanocomposite. Accordingly, the constant value given in [7, 8] was assumed for the calculation, but obviously this is a very rough approximation. Moreover, these discrepancies may indicate limitations of the adopted approach.

The problem with verification of this theoretical concept lies in lack of the required data. For the mechanically adaptive nanocomposites, DMA temperature sweeps data have been published but not separately for the polymer matrix and whisker nanoparticles. Moreover, to model the temperature dependency of the adaptivity property of these materials, such data are required for both dray and swollen states.

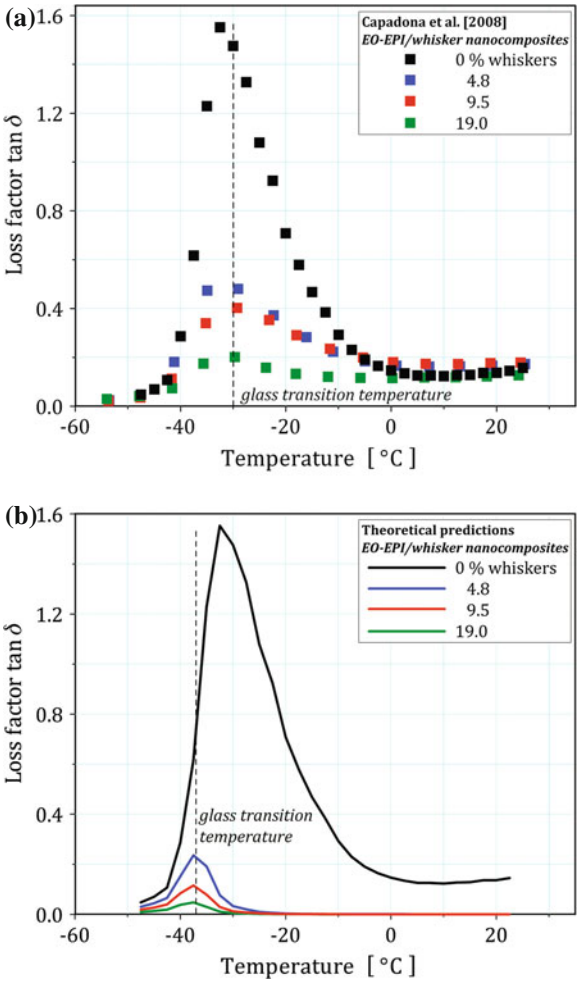

Fig. 7 DMTA temperature sweep tests: Comparison of data (**a**) with model predictions (**b**)

7 Non-Linear Effects

The behavior of mechanically adaptive polymer nanocomposites in the nonlinear domain is obviously highly complex, and the constitutive modeling of this behavior is challenging because there are no experimental data available so far. An adequate constitutive model for this class of materials must account for (1) the evolution of reinforcement effect with strains for every specified kind and amount of filler, (2) the coupling between the extent of stimulus and the strain level, and (3) possible variations in the architectural structure of percolating network at different deformation levels.

The first step in the formulation of non-linear constitutive model may be based on the transformation of a nonlinear problem into a sequence of linear ones by

using an approximation of the linear correspondence between the tangent modulus of composite (estimated by the tangent slope of stress-strain curve along the load path) and the tangent modulus of matrix and fillers. In the non-linear domain, elastic or not, the stress-strain relation for the neat (pure) polymer and the rigid phase (filler) may be written in the rate form as

$$\dot{\sigma} = \mathrm{D}_{\mathrm{m}}(\epsilon, \ldots)\,\dot{\epsilon}, \quad \dot{\sigma} = \mathrm{D}_{\mathrm{r}}(\epsilon, \ldots)\,\dot{\epsilon}\,, \tag{12}$$

respectively. Here $\mathrm{D}_{\mathrm{m}}(\epsilon, \ldots)$ and $\mathrm{D}_{\mathrm{r}}(\epsilon, \ldots)$ are the corresponding tangential moduli along the loading path and the superimposed dot stands for time derivative. The basic idea of incrementally linear models is to write the stress-strain relation for a nanocomposite in the same rate form

$$\dot{\sigma} = \mathrm{D}(\epsilon, \ldots)\,\dot{\epsilon} \tag{13}$$

with the tangential modulus $\mathrm{D}(\epsilon, \ldots)$ assumed to be given by relations of the same form as for the linear theory. That is, the tangential modulus of the nanocomposite is obtained from (1) by replacing the elastic moduli by the corresponding tangential moduli

$$\mathrm{D}(\epsilon, \ldots) = \mathrm{D}\left[\mathrm{D}_{\mathrm{m}}(\epsilon, \ldots), \mathrm{D}_{\mathrm{r}}(\epsilon, \ldots), \vartheta, \xi\right]\,. \tag{14}$$

In the first approximation, the percolation parameter ξ may also be assumed in the same form as in the linear theory, that is, in the form (2). The relations (12)–(14) determine the incrementally linear constitutive model for the polymer nanocomposite from the know tangential moduli for the soft (matrix) and rigid (filler) phases. If the rigid phase may be assumed to be linearly elastic, then its tangential modulus is simply equal the value of the elastic modulus $\mathrm{D}_{\mathrm{r}}(\epsilon, \ldots) = \mathrm{E}_{\mathrm{r}}$ and it is independent of the strain.

A particular form of the non-linear constitutive law (12) for the neat polymer may be derived from the experimentally determined stress-strain curve using the methodology presented in [26] for another class of materials. Such a law is needed in the derivation of the tangential modulus as given by formula (14). However, for the analysis of data, we do not need to assume any theory of neat polymers because the tangential modulus may be estimated from the slope of measured stress-strain curve along the loading path such as shown in Fig. 8a. The calculations based on the simple model described above may then be compared with the data for nanocomposites filled with different amount and type of fillers. The representative results of such analysis are shown in Fig. 8b. The comparison of theoretical results based on the same concept with data for the dry and swollen nanocomposite is shown in the Fig. 9.

It is not surprising that there are observed certain differences between theoretical results and data for both the reinforcement and adaptivity effects. Actually, this analysis provides a experimental verification of the applicability in the non-linear domain of micromechanical assumptions adopted in the linear theories. In particular, it still remains to experimentally determine the dependency of both effects on the extent of deformation.

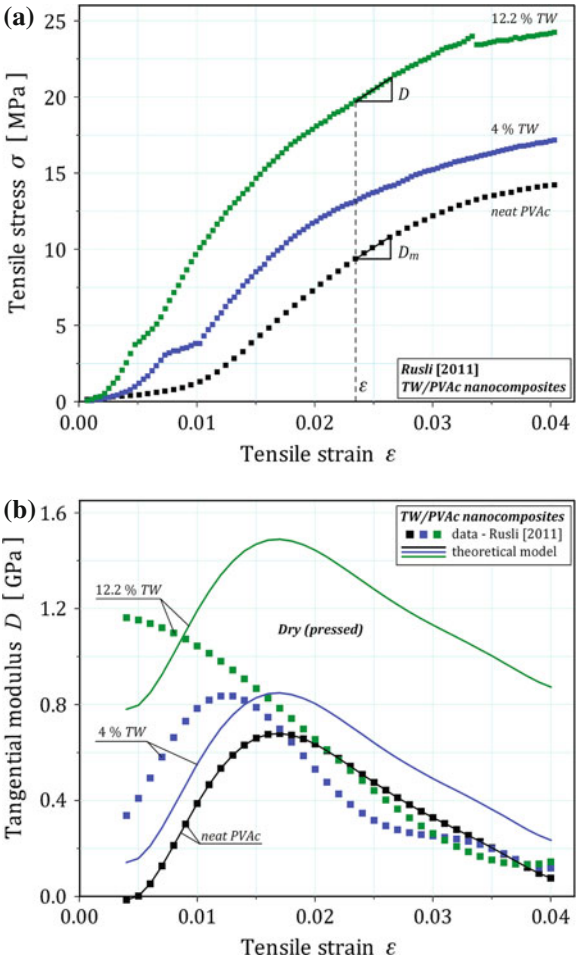

Fig. 8 Non-linear behavior of neat and filled polymer nanocomposites in dry (unstimulated) state: Measured stress-strain curves (**a**) and comparison of experimental and computed tangential moduli (**b**)

8 Discussion

The theoretical approach presented in this work is entirely based on the currently accepted micromechanisms of the reinforcement and adaptivity effects of cellulose based polymer nanocomposites. According to the literature [7–9], the dynamic mechanical behavior of these materials is achieved through a nanocomposite architecture in which rigid, high-aspect-ratio cellulose whisker nanoparticles are randomly dispersed in a soft, viscoelastic polymer matrix. The stiffness of such nanocomposites is regulated by controlling nanoparticle interactions that form the percolation network responsible for the stress transfer in the composite. Through chemical stimuli, reinforcing cellulose network can be disrupted resulting in a dramatic stiffness

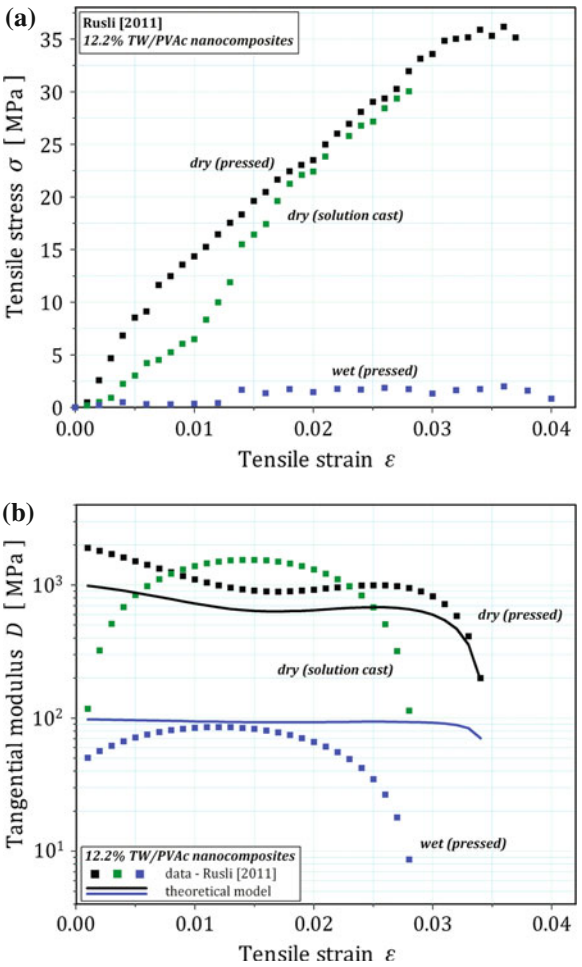

Fig. 9 Non-linear behavior of filled polymer nanocomposites in dry (unstimulated) and wet (stimulated) states: Measured stress-strain curves (**a**) and comparison of experimental and computed tangential moduli (**b**)

reduction even in the polymer nanocomposite comprising small amount of whiskers. Moreover, the original stiffness is restored when the composites are dried.

In the proposed model, the described micromechanism is represented by the evolution law for the parameter representing the volume fraction of percolating network. This law depends in a parametric way on the extent of stimulus that regulates the level of the stress-transfer in the mechanically adaptive polymer nanocomposite and hence its stiffness. The illustrative calculations based on this concept and the comparison with experimental data from literature support the conclusion that the stiffness change in the considered polymer nanocomposites is due to the mechanism of altered

whisker–whisker interactions rather than other effects that govern the reinforcement in elastomeric materials [15, 16, 21] and shape memory polymer nanocomposites [27]. However, no direct physical evidence for these mechanisms has yet been reported in the literature (see the discussion in [9]). Recent studies using Raman spectroscopy [9, 12] has attempted to clarify this issue but with limited success.

Finally, one has to note that even less is known on the physical mechanisms governing the adaptivity property of native materials such as sea cucumbers' skin. In fact, there are two different ideas suggested in the literature regarding the mechanism of skin's stiffening [3, 4], but no model has been proposed so far. It may be concluded that the new class of native and synthetic materials discussed in this paper has been already extensively studied from biological, chemical, and physical point of view. But there remains much to be done in the theoretical modeling of these materials.

References

1. Rowan, S.J.: Polymers with bio-inspired strength. Nat. Chem. **1**, 347–348 (2009)
2. Szulgit, G.K., Shadwick, R.E.: Dynamic mechanical characterization of a mutable collagenous tissue: response of sea cucumber dermis to cell lysis and dermal extracts. J. Exp. Biol. **203**, 1539–1550 (2000)
3. Trotter, J.A., Tipper, J., Lyons-Levy, G., et al.: Towards a fibrous composite with dynamically controlled stiffness: lessons from echinoderms. Biochem. Soc. Trans. **28**, 357–362 (2000)
4. Motokawa, T., Tsuchi, A.: Dynamic mechanical properties of body-wall dermis in various mechanical states and their implications for the behavior of sea cucumbers. Biol. Bull. **205**, 261–275 (2003)
5. Wilkie, I.C.: Mutable collagenous tissue: overview and biotechnological perspective. Echinodermata Prog. Mol. Subcell Biol. **39**, 221–250 (2005)
6. Barbaglio, A., Tricarico, S., Ribeiro, A., et al.: The mechanically adaptive connective tissue of echinoderms: its potential for bio-innovation in applied technology and ecology. Mar. Environ. Res. **76**, 108–113 (2012)
7. Capadona, J.R., Shanmuganathan, K., Tyler, D.J., et al.: Stimuli-responsive polymer nanocomposites inspired by the sea cucumber dermis. Science **319**, 1370–1374 (2008)
8. Shanmuganathan, K.: Bio-inspired stimuli-responsive mechanically dynamic nanocomposites. Ph.D. thesis, Case Western Reserve University (2010)
9. Rusli, R., Shanmuganathan, K., Rowan, S.J., et al.: Stress-transfer in anisotropic and environmentally adaptive cellulose whisker nanocomposites. Biomacromolecules **11**, 762–768 (2010)
10. Shanmuganathan, K., Capadona, J.R., Rowan, S.J., et al.: Biomimetic mechanically adaptive nano-composites. Prog. Polym. Sci. **35**, 212–222 (2010)
11. Rusli, R.: Interfacial micromechanics of natural cellulose whisker polymer nanocomposites using Raman spectroscopy. Ph.D. thesis, University of Manchester (2011)
12. Harris, J.P.: The glia-neuronal response to cortical electrodes: interactions with substrate stiffness and electrophysiology. Ph.D. thesis, Case Western Reserve University (2012)
13. Jordan, J., Jacob, K.I., Tannenbaum, R., et al.: Experimental trends in polymer nanocomposites—a review. Mater Sci. Eng. A **393**, 1–11 (2005)
14. Tjong, S.C.: Structural and mechanical properties of polymer nanocomposites. Mater. Sci. Eng. R **53**, 73–197 (2006)
15. Valavala, P.K., Odegard, G.M.: Modeling techniques for determination of mechanical properties of polymer nanocomposites. Rev. Adv. Mater. Sci. **9**, 34–44 (2005)
16. Ahmed, S., Jones, F.R.: A review of particulate reinforcement theories for polymer composites. J. Mater. Sci. **25**, 4933–4942 (1990)

17. Favier, V., Cavaille, J.Y., Canova, G.R., et al.: Mechanical percolation in cellulose whisker nanocomposites. Polym. Eng. Sci. **37**, 1732–1739 (1997)
18. Capadona, J.R., van den Berg, O., Capadona, L.A., et al.: A versatile approach for the processing of polymer nanocomposites with self-assembled nanofibre templates. Nat. Nanotechnol. **2**, 765–769 (2007)
19. Ljungberg, N., Bonini, C., Bortolussi, F., et al.: New nanocomposite materials reinforced with cellulose whiskers in atactic po-lypropylene: effect of surface and dispersion characteristics. Biomacromolecules **6**, 2732–2739 (2005)
20. Moon, R.J., Martini, A., Nairn, J., et al.: Cellulose nanomaterials review: structure, properties and nanocomposites. Chem. Soc. Rev. **40**, 3941–3994 (2011)
21. Kumar, P., Sandeep, K.P., Alavi, S., et al.: A review of experimental and modeling techniques to determine properties of biopolymer-based nanocomposites. J. Food Sci. **76**, E2–E14 (2011)
22. Fornes, T.D., Paul, D.R.: Modeling properties of nylon 6/clay nanocomposites using composite theories. Polymer **44**, 4993–5013 (2003)
23. Tucker, C.L., Liang, E.: Stiffness predictions for unidirectional short-fiber composites: review and evaluation. Compos. Sci. Technol. **59**, 655–671 (1999)
24. Takayanagi, M., Imada, K., Kajiyama, T.: Mechanical properties and fine structure of drawn polymers. J. Polym. Sci. A **15**, 263–281 (1966)
25. Ouali, N., Cavaillé, J.Y., Perez, J.: Elastic, viscoelastic and plastic behavior of multiphase polymer blends. Plast. Rubber Compos. Process. Appl. **16**, 55–60 (1991)
26. Kazakevičiūtė-Makovska, R., Steeb, H.: Superelasticity and self-healing of proteinaceous biomaterials. Procedia Eng. **10**, 2597–2602 (2011)
27. Kazakevičiūtė-Makovska, R., Steeb, H.: On recoverable strain and stress relationships for shape memory polymer nanocomposites. KGK-Kaut Gummi Kunst **64**, 24–28 (2011)

Justification of the Bending-Gradient Theory Through Asymptotic Expansions

Arthur Lebée and Karam Sab

Abstract In a recent work, a new plate theory for thick plates was suggested where the static unknowns are those of the Kirchhoff-Love theory, to which six components are added representing the gradient of the bending moment [1]. This theory, called the Bending-Gradient theory, is the extension to multilayered plates of the Reissner-Mindlin theory which appears as a special case when the plate is homogeneous. This theory was derived following the ideas from Reissner [2] without assuming a homogeneous plate. However, it is also possible to give a justification through asymptotic expansions. In the present paper, the latter are applied one order higher than the leading order to a laminated plate following monoclinic symmetry. Using variational arguments, it is possible to derive the Bending-Gradient theory. This could explain the convergence when the thickness is small of the Bending-Gradient theory to the exact solution illustrated in [3]. However, the question of the edge-effects and boundary conditions remains open.

1 Introduction

The classical theory of plates, known also as Kirchhoff-Love plate theory is based on the assumption that the normal to the mid-plane of the plate remains normal after transformation. This theory is also the first order of the asymptotic expansion with respect to the thickness [4]. Thus, it presents a good theoretical justification and was soundly extended to the case of periodic plates [5, 6]. It enables to have a first-order estimate of the macroscopic deflection as well as local stress fields.

A. Lebée (✉) · K. Sab
Laboratoire Navier (ENPC–IFSTTAR–CNRS), École des Ponts ParisTech, Université Paris-Est, 6 et 8 avenue Blaise Pascal, 77455 Marne-la-Vallée, France
e-mail: arthur.lebee@enpc.fr

K. Sab
e-mail: karam.sab@enpc.fr

H. Altenbach et al. (eds.), *Generalized Continua as Models for Materials*, Advanced Structured Materials 22, DOI: 10.1007/978-3-642-36394-8_12,

In most applications the first-order deflection is accurate enough. However, this theory does not capture the local effect of shear forces on the microstructure because shear forces are one higher-order derivative of the bending moment in equilibrium equations ($Q_\alpha = M_{\alpha\beta,\beta}$).

Because shear forces are part of the macroscopic equilibrium of the plate, their effect is also of great interest for engineers when designing structures. However, modeling properly the action of shear forces is still a controversial issue. Reissner [2] suggested a model for homogeneous plates based on a parabolic distribution of transverse shear stress through the thickness (Reissner-Mindlin theory). This model performs well for homogeneous plates and gives more natural boundary conditions than those of Kirchhoff-Love theory. Thus, it is appreciated by engineers and broadly used in applied mechanics. However, the direct extension of this model to laminated plates raised many difficulties.

Two main path were followed for deriving models suitable for laminated plates: axiomatic approaches and asymptotic approaches.

In asymptotic approaches, a plate model is derived directly from the full 3D formulation of the problem, assuming the thickness of the plate goes to zero. In these approaches, the asymptotic expansion method plays a central role. As already mentioned, the leading order leads to Kirchhoff-Love plate theory [4–6]. Hence one needs to seek higher orders for bringing out the effect of shear forces. However, in the cases of laminated plates, this procedure does not lead to Reissner-Mindlin plate theory [7, 8].

In axiomatic approaches, 3D fields are assumed *a priori* and a plate theory is derived using integration through the thickness and variational tools. The reader can refer to the following reviews [9–12]. Most suggestions leading to Reissner-Mindlin-like theories show discontinuous transverse shear stress through the thickness or are limited to some geometric configurations (orthotropy or cylindrical bending for instance). In this field, these limitations even led to the suggestion of "layer-wise" models which give more satisfying results but are much more numerically intense than Reissner-Mindlin theory [12, 13]. Finally, let us point out that the theory suggested by Reissner [2] is usually considered as an axiomatic approach since the parabolic transverse shear stress distribution of the stress was derived without asymptotic arguments. Consequently, some work took literally this distribution and applied it to laminated plates. Like in many unsuccessful axiomatic approaches this led to discontinuous displacement fields and raised an unjustified suspicion over the original work.

Revisiting the approach from Reissner [2] directly with laminated plates, Lebée and Sab [1, 3] showed that the transverse shear static variables which come out when the plate is heterogeneous are not shear forces Q_α but the full gradient of the bending moment $R_{\alpha\beta\gamma} = M_{\alpha\beta,\gamma}$. Using conventional variational tools, they derived a new plate theory—called Bending-Gradient theory—which is actually turned into Reissner-Mindlin theory when the plate is homogeneous. This new plate theory is seen by the authors as an extension of Reissner's theory to heterogeneous plates which preserves most of its simplicity. It was applied to the cylindrical bending of carbon fibers laminated plates and compared to exact solutions in [3]. Very good

agreement for the transverse shear distribution as well as in-plane displacement was pointed out and convergence with the slenderness was observed.

Originally designed for laminated plates, the Bending-Gradient theory was also extended to in-plane periodic plates using averaging considerations such as Hill-Mandel principle and successfully applied to sandwich panels [14, 15] as well as space frames [16].

Because the derivation of the Bending-Gradient theory followed the ideas from Reissner [2], one can argue that it is basically an axiomatic approach. However, it is the intention of the present paper to demonstrate that there is a close link between the derivation of the Bending-Gradient theory and the asymptotic expansion method. Since the Bending-Gradient is turned into the Reissner-Mindlin theory when the plate is homogeneous, this link will be also demonstrated for the original work from Reissner [2].

In order to derive the Bending-Gradient theory through asymptotic expansions, we first set in Sect. 2 the 3D problem, its symmetries and the asymptotic expansions framework. For the sake of simplicity we choose the constitutive material and the loadings of the plate such that the bending moment is fully uncoupled with the membrane stress. Then in Sect. 3 we perform the standard resolution of the auxiliary problems and conclude that bringing out transverse shear effects through this approach is not satisfying. Then in Sect. 4 we derive the Bending-Gradient theory using variational considerations.

2 The Asymptotic Expansion Framework

In this section, the asymptotic expansion framework is set in the special case of a laminated plate. This procedure was established by Sanchez-Palencia [17] for linear dynamics of 3D continuum. It starts with the definition of the 3D problem of the laminated plate which is under consideration. Then this problem is scaled in order to separate the in-plane and the out-of-plane variables and we assume that the fields follow an expansion depending on a small parameter: the inverse of the plate slenderness. Finally, the equations are gathered for each order of this parameter.

2.1 Notations

Vectors and higher-order tensors, up to sixth order, are used in the following. When using short notation, several underlining styles are used: vectors are straight underlined, $\underline{u}$. Second order tensors are underlined with a tilde: $\underset{\sim}{M}$ and $\underset{\sim}{K}$. Third order tensors are underlined with a parenthesis: $\underset{\frown}{R}$ and $\underset{\frown}{\Gamma}$. Fourth order tensors are doubly underlined with a tilde: $\underset{\approx}{D}$ and $\underset{\approx}{s}$. Sixth order tensors are doubly underlined with a parenthesis: $\underset{\frown}{\underset{\frown}{h}}$ and $\underset{\frown}{\underset{\frown}{I}}$. The full notation with indices is also used. Then

we follow Einstein's notation on repeated indices. Furthermore, Greek indices $\alpha, \beta, \delta, \gamma = 1, 2$ denotes in-plane dimensions and Latin indices $i, j, k, l = 1, 2, 3$, all three dimensions. The transpose operation ${}^{T}\bullet$ is applied to any order tensors as follows: $\left({}^{T}a\right)_{\alpha\beta\ldots\psi\omega} = a_{\omega\psi\ldots\beta\alpha}$. Three contraction products are defined, the usual dot product ($\underline{a} \cdot \underline{b} = a_i b_i$), the double contraction product ($\underset{\sim}{a} : \underset{\sim}{b} = a_{ij} b_{ji}$) and a triple contraction product ($\underset{\approx}{a} \vdots \underset{\approx}{a} = a_{\alpha\beta\gamma} a_{\gamma\beta\alpha}$). The derivation operator $\underline{\nabla}$ is also formally represented as a vector: $\underset{\sim}{a} \cdot \underline{\nabla} = a_{ij} \nabla_j = a_{ij,j}$ is the divergence and $\underset{\sim}{a} \otimes \underline{\nabla} = a_{ij} \nabla_k = a_{ij,k}$ is the gradient. Here $\otimes$ is the dyadic product.

2.2 The 3D Problem

The laminated plate occupies a domain $\Omega^t = \omega^L \times]-\frac{t}{2}, \frac{t}{2}[$ where ω^L is the middle surface of the plate (its typical size is L) and t its thickness. The boundary of the plate, $\partial\Omega^t$, is decomposed into three parts:

$$\partial\Omega^t = \partial\Omega_{lat} \cup \partial\Omega_3^+ \cup \partial\Omega_3^-$$
$$\text{with} \quad \partial\Omega_{lat} = \partial\omega^L \times]-\frac{t}{2}, \frac{t}{2}[\quad \text{and} \quad \partial\Omega_3^{\pm} = \omega^L \times \left\{\pm\frac{t}{2}\right\}. \tag{1}$$

The plate is fully clamped on its lateral boundary, $\partial\Omega_{lat}$, and is submitted to the same distributed and purely transverse force $\underline{f} = f_3(x_1, x_2)\underline{e}_3$ both on its upper and lower boundaries $\partial\Omega_3^+$ and $\partial\Omega_3^-$.

The fourth-order stiffness tensor $\underset{\approx}{C}^t(x_3)$ characterizing the elastic properties of the constituent material at every point $\underline{x} = (x_1, x_2, x_3)$ of Ω^t is introduced. We assume the following monoclinic symmetry: $C^t_{3\alpha\beta\gamma} = C^t_{\alpha 333} = 0$. In addition, $\underset{\approx}{C}^t$ does not depend on (x_1, x_2) and is an even function of x_3 to ensure full uncoupling between in-plane and out-of-plane problems. Thus, the constitutive equation writes as:

$$\underset{\sim}{\sigma}^t\left(\underline{x}\right) = \underset{\approx}{C}^t(x_3) : \underset{\sim}{\varepsilon}^t\left(\underline{x}\right) \tag{2}$$

where $\underset{\sim}{\sigma}^t = \left(\sigma^t_{ij}\left(\underline{x}\right)\right)$ is the stress tensor and $\underset{\sim}{\varepsilon}^t = \left(\varepsilon^t_{ij}\left(\underline{x}\right)\right)$ is the strain tensor at point $\underline{x}$. The tensor $\underset{\approx}{C}^t$ follows the classical symmetries of linear elasticity and is positive definite.

The full 3D elastic problem, $\mathcal{P}^{3D}$, is to find in Ω^t a displacement vector field $\underline{u}^t$, a strain tensor field $\underset{\sim}{\varepsilon}^t$ and a stress tensor field $\underset{\sim}{\sigma}^t$ such that the static conditions ($SC^{3D,t}$):

$$SC^{3D,t}: \begin{cases} \underset{\sim}{\sigma}^t \cdot \underline{\nabla} = 0 \text{ on } \Omega^t & \text{(3a)} \\ \underset{\sim}{\sigma}^t \cdot \left(\pm\underline{e}_3\right) = \underline{f} \text{ on } \partial\Omega_3^{\pm}, & \text{(3b)} \end{cases}$$

the kinematic conditions ($KC^{3D,t}$):

$$KC^{3D,t}: \begin{cases} \underset{\sim}{\varepsilon}^t = \underline{u}^t \otimes^s \underline{\nabla} \text{ on } \Omega^t & (4a) \\ \underline{u}^t = 0 \text{ on } \partial\Omega_{lat} & (4b) \end{cases}$$

and the constitutive law (2) are satisfied. Here, $(\underline{e}_1, \underline{e}_2, \underline{e}_3)$ is the orthonormal basis associated with coordinates (x_1, x_2, x_3) and $\bullet \otimes^s \underline{\nabla}$ denotes the symmetric part of the gradient operator.

2.2.1 Variational Formulation of the 3D Problem

The strain and stress energy density w^{3D} and w^{*3D} are respectively given by:

$$w^{3D}(\underset{\sim}{\varepsilon}) = \frac{1}{2}\,\underset{\sim}{\varepsilon} : \underset{\approx}{C}^t : \underset{\sim}{\varepsilon}, \qquad w^{*3D}(\underset{\sim}{\sigma}) = \frac{1}{2}\,\underset{\sim}{\sigma} : \underset{\approx}{S}^t : \underset{\sim}{\sigma} \tag{5}$$

They are related by the following Legendre-Fenchel transform:

$$w^{*3D}(\underset{\sim}{\sigma}) = \sup_{\underset{\sim}{\varepsilon}} \left\{ \underset{\sim}{\sigma} : \underset{\sim}{\varepsilon} - w^{3D}(\underset{\sim}{\varepsilon}) \right\} \tag{6}$$

The kinematic variational approach states that the strain solution $\underset{\sim}{\varepsilon}^t$ of $\mathcal{P}^{3D}$ is the one that minimizes P^{3D} among all kinematically compatible strain fields:

$$P^{3D}(\underset{\sim}{\varepsilon}^t) = \min_{\underset{\sim}{\varepsilon} \in KC^{3D,t}} \left\{ P^{3D}(\underset{\sim}{\varepsilon}) \right\} \tag{7}$$

where P^{3D} is the potential energy given by:

$$P^{3D}(\underset{\sim}{\varepsilon}) = \int_{\Omega^t} w^{3D}(\underset{\sim}{\varepsilon})\, d\Omega^t - \int_{\omega^L} \left(\underline{f} \cdot \underline{u}^+ + \underline{f} \cdot \underline{u}^- \right) d\omega^L \tag{8}$$

and $\underline{u}^{\pm} = \underline{u}(x_1, x_2, \pm t/2)$ are the 3D displacement fields on the upper and lower faces of the plate.

The static variational approach states that the stress solution $\underset{\sim}{\sigma}^t$ of $\mathcal{P}^{3D}$ is the one that minimizes P^{*3D} among all statically compatible stress fields:

$$P^{*3D}(\underset{\sim}{\sigma}^t) = \min_{\underset{\sim}{\sigma} \in SC^{3D,t}} \left\{ P^{*3D}(\underset{\sim}{\sigma}) \right\} \tag{9}$$

where P^{*3D} is the complementary potential energy given by:

$$P^{*3D}\left(\underset{\sim}{\sigma}\right) = \int_{\Omega^t} w^{*3D}\left(\underset{\sim}{\sigma}\right) d\Omega^t \tag{10}$$

2.2.2 Effect of Symmetries

For the sake of simplicity, we chose the 3D plate problem such that only flexural part is involved and no membranal part.

The 3D problem $\mathcal{P}^{3D}$ is skew-symmetric through a planar symmetry with respect to the mid-plane of the plate (known also as "mirror symmetry" in laminates engineering) because $\underset{\approx}{C}^t$ is an even function of only x_3. This means that, when applying the transformation $x_3 \to -x_3$ the problem remains unchanged but the boundary condition (3b) changes its sign. Consequently the in-plane displacement $u^t_\alpha(x_1, x_2, x_3)$ is an odd function of x_3 and the out-of-plane displacement $u^t_3(x_1, x_2, x_3)$ is an even function of x_3. Similarly, the in-plane stress $\sigma^t_{\alpha\beta}(x_1, x_2, x_3)$ and transverse compression $\sigma^t_{33}(x_1, x_2, x_3)$ are odd functions of x_3 and the transverse shear stress $\sigma^t_{\alpha 3}(x_1, x_2, x_3)$ is an even function of x_3.

In terms of resultants and averaged displacements, the integration through the thickness of u^t_α and $\sigma^t_{\alpha\beta}$ vanish and then the plate problem will be purely flexural. Of course, this result affects also the asymptotic expansion procedure and enables many simplifications.

2.3 Scaling

Once the 3D problem is set, we scale it for clearly separating the in-plane variables (which are related to macroscopic problems) and the out-of-plane variable (which is related to microscopic perturbations). Hence, L is the typical scale of the in-plane variables (e.g. the span and also the wavelength of the loadings). We introduce the following change of variable $Y_\alpha = L^{-1}x_\alpha$ for the in-plane variable where $Y_\alpha \in \omega$. The domain ω is the scaled mid-plane of the plate. Moreover we define $z = t^{-1}x_3$ for the out-of-plane variable, $z \in]-\frac{1}{2}, \frac{1}{2}[$. Consequently, we define the small parameter as: $\eta = t/L$.

Based on this change of variables, the fourth-order elasticity tensor can be rewritten as:

$$\underset{\approx}{C}^t(x_3) = \underset{\approx}{\mathbb{C}}\left(t^{-1}x_3\right) = \underset{\approx}{\mathbb{C}}(z) \tag{11}$$

where $\underset{\approx}{\mathbb{C}}$ is a function of z. In the following, double-stroke fonts denote fields which are only function of the local variable z (i.e. localization fields).

The distributed forces are classically scaled the following way (see [4, 5, 18]):

$$\underline{f}(x_1, x_2) = \eta^2 \frac{F_3(Y_1, Y_2)}{2} \underline{e}_3 \tag{12}$$

Similarly, in the following, fields with capital letters are only function of (Y_1, Y_2) (i.e. macroscopic fields).

Furthermore, from the fields of the 3D problem $(\underline{u}^t, \underline{\underline{\varepsilon}}^t, \underline{\underline{\sigma}}^t)$ we define the non-dimensional fields $(\underline{u}, \underline{\underline{\varepsilon}}, \underline{\underline{\sigma}})$ as follows:

$$\begin{cases} \underline{u}^t\ (x_1, x_2, x_3) = L\,\underline{u}\ (x_1/L, x_2/L, x_3/t) = L\,\underline{u}\ (Y_1, Y_2, z) \\ \underline{\underline{\varepsilon}}^t\ (x_1, x_2, x_3) = \quad \underline{\underline{\varepsilon}}\ (x_1/L, x_2/L, x_3/t) = \quad \underline{\underline{\varepsilon}}\ (Y_1, Y_2, z) \\ \underline{\underline{\sigma}}^t\ (x_1, x_2, x_3) = \quad \underline{\underline{\sigma}}\ (x_1/L, x_2/L, x_3/t) = \quad \underline{\underline{\sigma}}\ (Y_1, Y_2, z) \end{cases} \tag{13}$$

The derivation rule for those functions is:

$$\begin{aligned} \underline{\nabla} &= \left(\frac{d}{dx_1}, \frac{d}{dx_2}, \frac{d}{dx_3}\right) \\ &= L^{-1}\left(\frac{\partial}{\partial Y_1}, \frac{\partial}{\partial Y_2}, 0\right) + t^{-1}\left(0, 0, \frac{\partial}{\partial z}\right) = L^{-1}\underline{\nabla}_Y + t^{-1}\underline{\nabla}_z. \end{aligned} \tag{14}$$

We will also use the variational formulation of the 3D problem. Hence we provide here the scaled variational formulation. The set of statically compatible fields can be rewritten as:

$$SC^{3D}: \begin{cases} \underline{\underline{\sigma}} \cdot \underline{\nabla}_{(Y,z)} = 0 \text{ on } \Omega, & \text{(15a)} \\ \underline{\underline{\sigma}} \cdot (\pm \underline{e}_3) = \dfrac{\eta^2}{2} F_3 \underline{e}_3 \quad \text{on } \partial\Omega_3^{\pm}, & \text{(15b)} \end{cases}$$

where $\underline{\nabla}_{(Y,z)} = \underline{\nabla}_Y + \dfrac{1}{\eta}\underline{\nabla}_z$. The kinematically compatible fields becomes (KC^{3D}):

$$KC^{3D}: \begin{cases} \underline{\underline{\varepsilon}} = \underline{u} \otimes^s \underline{\nabla}_{(Y,z)} \text{ on } \Omega, & \text{(16a)} \\ \underline{u} = 0 \quad \text{on } \partial\omega \times]-\dfrac{1}{2}, +\dfrac{1}{2}[& \text{(16b)} \end{cases}$$

Then the potential energy is rewritten as:

$$P^{3D}\left(\underline{\underline{\varepsilon}}\right) = tL^2 \int_\omega \left(\left\langle w^{3D}\left(\underline{\underline{\varepsilon}}\right)\right\rangle - \eta \frac{u_3^+ + u_3^-}{2} F_3 \right) d\omega \tag{17}$$

where $\langle \bullet \rangle$ is the integration through the thickness: $\langle \bullet \rangle = \displaystyle\int_{-\frac{1}{2}}^{\frac{1}{2}} \bullet \, dz$. The complementary energy becomes also:

$$P^{*3D}\left(\underline{\underline{\sigma}}\right) = tL^2 \int_\omega \left\langle w^{*3D}\left(\underline{\underline{\sigma}}\right)\right\rangle d\omega \tag{18}$$

Now, $\underset{\approx}{\mathbb{C}}$, ω and F_3 being fixed, the homogenization problem is to find a consistent approximation of the solution of the 3D problem $\mathcal{P}^{3D}$ (2–4) assuming η is small.

2.4 Expansion

The asymptotic expansion method [17, 19] will be used to provide a formal justification of the Bending-Gradient theory. The starting point of the method is to assume that the solution to (2–4) can be written as a series in power of η in the following form:

$$\begin{cases} \underline{u} = \eta^{-1}\underline{u}^{-1} + \eta^0\underline{u}^0 + \eta^1\underline{u}^1 + \cdots \\ \underset{\sim}{\varepsilon} = \eta^0\underset{\sim}{\varepsilon}^0 + \eta^1\underset{\sim}{\varepsilon}^1 + \cdots \\ \underset{\sim}{\sigma} = \eta^0\underset{\sim}{\sigma}^0 + \eta^1\underset{\sim}{\sigma}^1 + \cdots \end{cases} \tag{19}$$

where $p = -1, 0, 1, 2 \ldots$ and $\underline{u}^p$, $\underset{\sim}{\varepsilon}^p$ and $\underset{\sim}{\sigma}^p$ are functions of (Y_1, Y_2, z) which follow the same parity as the 3D solution (Sect. 2.2.2). The series are started from the order η^0 for $\underset{\sim}{\sigma}$ and $\underset{\sim}{\varepsilon}$, and from the order η^{-1} for $\underline{u}$. Then, the expansion (19)—taking into account the change of variable—must be inserted in the equations (2–4) and all the terms of the same order η^p must be identified.

2.4.1 Statically Admissible Fields

The 3D equilibrium equation, $\underset{\sim}{\sigma}^t \cdot \underline{\nabla} = 0$ on Ω^t, becomes:

$$L\left(\underset{\sim}{\sigma}^t \cdot \underline{\nabla}\right) = \eta^{-1}\left(\underset{\sim}{\sigma}^0 \cdot \underline{\nabla}_z\right) + \eta^0\left(\underset{\sim}{\sigma}^0 \cdot \underline{\nabla}_Y + \underset{\sim}{\sigma}^1 \cdot \underline{\nabla}_z\right) + \cdots = 0.$$

Identifying all the terms of the above series to be zero, it is found:

$$\sigma^0_{i3,3} = 0 \tag{20}$$

for the order η^{-1},

$$\sigma^p_{i\alpha,\alpha} + \sigma^{p+1}_{i3,3} = 0 \tag{21}$$

for the order η^p with $p \geqslant 0$. The derivation $\bullet_{,i}$ is performed without ambiguity with respect to (Y_1, Y_2, z). The boundary condition, $\underset{\sim}{\sigma}^t \cdot \underline{e}_3 = \pm\underline{f}$ on $\partial\Omega_3^{\pm}$, gives the following equations:

$$\sigma^p_{i3}\left(Y_1, Y_2, \pm\frac{1}{2}\right) = 0 \tag{22}$$

for the order $p \geqslant 0$ and $p \neq 2$. When $p = 2$ we have:

$$\sigma^2_{\alpha 3}\left(Y_1, Y_2, \pm\frac{1}{2}\right) = 0 \quad \text{and} \quad \sigma^2_{33}\left(Y_1, Y_2, \pm\frac{1}{2}\right) = \pm\frac{1}{2} F_3\left(Y_1, Y_2\right) \tag{23}$$

2.4.2 Kinematically Compatible Fields

From the compatibility equation, it is found that the strain rate field can be written as:

$$\underset{\sim}{\varepsilon}^t = L\,\underline{u} \otimes^s \underline{\nabla} = \eta^{-2}\underset{\sim}{\varepsilon}^{-2} + \eta^{-1}\underset{\sim}{\varepsilon}^{-1} + \eta^0\underset{\sim}{\varepsilon}^0 + \cdots \tag{24}$$

with:

$$\varepsilon^{-2}_{\alpha\beta} = 0, \quad \varepsilon^{-2}_{\alpha 3} = \frac{1}{2}u^{-1}_{\alpha,3} \quad \text{and} \quad \varepsilon^{-2}_{33} = u^{-1}_{3,3} \tag{25}$$

and for all $p \geqslant -1$:

$$\varepsilon^p_{\alpha\beta} = \frac{1}{2}\left(u^p_{\alpha,\beta} + u^p_{\beta,\alpha}\right), \quad \varepsilon^p_{\alpha 3} = \frac{1}{2}\left(u^{p+1}_{\alpha,3} + u^p_{3,\alpha}\right) \quad \text{and} \quad \varepsilon^p_{33} = u^{p+1}_{3,3} \tag{26}$$

The boundary condition over $\partial\Omega_{\text{lat}}$ leads to:

$$\forall p \geqslant -1 \quad \text{and} \quad \forall\left(Y_1, Y_2\right) \in \partial\omega, \quad \underline{u}^p = 0. \tag{27}$$

3 Explicit or Cascade Resolution

Now that the asymptotic expansion framework is set, we detail the explicit resolution which is classically performed (see [5, 7] for instance). Basically it starts with the derivation of low order displacements which do not generate local strain but are related to purely macroscopic displacement fields. Then the zeroth-order equations are gathered. They enable the definition of the first auxiliary problem and the construction of the well-known Kirchhoff-Love macroscopic plate model. Then the first-order is solved the same way. Of course it would be possible to carry on the process any order higher.

3.1 Low Order Displacement Fields

The assumption (19) provides the following equations:

$$\underset{\sim}{\varepsilon}^{-2} = 0, \tag{28}$$

and

$$\underset{\sim}{\varepsilon}^{-1} = 0, \tag{29}$$

From (28) it is deduced that $\underline{u}^{-1}$ is a rigid-body velocity field in z. Moreover, the in-plane displacement has zero average because of the symmetry condition (Sect. 2.2.2). Hence:

$$\underline{u}^{-1} = U_3^{-1}(Y_1, Y_2)\,\underline{e}_3. \tag{30}$$

Using (29) and the boundary conditions (27) it can be found that $\underline{u}^0$ has the following form:

$$\underline{u}^0 = \begin{pmatrix} -zU_{3,1}^{-1} \\ -zU_{3,2}^{-1} \\ U_3^0 \end{pmatrix}, \tag{31}$$

with the boundary conditions:

$$\forall (Y_1, Y_2) \in \partial\omega,\ U_3^{-1} = U_{3,\alpha}^{-1} n_\alpha = U_3^0 = 0. \tag{32}$$

where $\underline{n}$ is the outer normal to $\partial\omega$. Note that, since U_3^{-1} is null over $\partial\omega$, its tangential derivative will be also null over $\partial\omega$, hence only the normal gradient $U_{3,\alpha}^{-1} n_\alpha$ is required to be explicitly set to zero in this boundary condition.

3.2 Zeroth-Order Plate Model (Kirchhoff-Love)

3.2.1 Zeroth-Order Auxiliary Problem

Gathering equilibrium equation for order -1, compatibility equation, boundary conditions and constitutive equations of order 0 we get the zeroth-order auxiliary problem for $z \in [-\frac{1}{2}, \frac{1}{2}]$:

$$\begin{cases} \sigma_{i3,3}^0 = 0 & \text{(33a)} \\ \sigma_{ij}^0 = \mathbb{C}_{ijkl}\varepsilon_{kl}^0 & \text{(33b)} \\ \varepsilon_{\alpha\beta}^0 = zK_{\alpha\beta}^{-1}, \quad \varepsilon_{\alpha 3}^0 = \frac{1}{2}\left(u_{\alpha,3}^1 + U_{3,\alpha}^0\right) \quad \text{and} \quad \varepsilon_{33}^0 = u_{3,3}^1 & \text{(33c)} \\ \sigma_{i3}^0\left(z = \pm\frac{1}{2}\right) = 0 & \text{(33d)} \end{cases}$$

where we define the lowest-order curvature as:

$$K_{\alpha\beta}^{-1} = -U_{3,\alpha\beta}^{-1} \tag{34}$$

Solving this problem does not raise difficulty. Using short notation, the displacement field writes as:

$$\underset{\sim}{\mathfrak{u}}^1 = \underset{\approx}{\mathfrak{u}}^{\mathsf{K}} : \underset{\sim}{\mathsf{K}}^{-1} - z\mathfrak{U}_3^0 \otimes \underset{\sim}{\nabla}_\gamma + \mathfrak{U}_3^1 \underset{\sim}{e}_3 \tag{35}$$

More precisely, the localization related to the curvature is:

$$\mathfrak{u}_{3\alpha\beta}^{\mathsf{K}} = -\left[\int_{-\frac{1}{2}}^{z} y \frac{\mathbb{C}_{33\alpha\beta}}{\mathbb{C}_{3333}} dy\right]^* \quad \text{and} \quad \mathfrak{u}_{\alpha\beta\gamma}^{\mathsf{K}} = 0 \tag{36}$$

where $[\bullet]^*$ denotes the averaged-out distribution: $[\bullet]^* = \bullet - \langle \bullet \rangle$. Finally $\mathfrak{U}_3^1$ is an integration constant which will load the next auxiliary problem. (There are no in-plane integration constants because of the symmetry already invoked with lower orders.) The stress localization writes as:

$$\underset{\sim}{\mathfrak{o}}^0 = \underset{\approx}{\mathfrak{s}}^{\mathsf{K}} : \underset{\sim}{\mathsf{K}}^{-1} \tag{37}$$

where the fourth-order stress localization tensor is:

$$\mathfrak{s}_{\alpha\beta\gamma\delta}^{\mathsf{K}} = z\mathbb{C}_{\alpha\beta\gamma\delta}^{\sigma} \quad \text{and} \quad \mathfrak{s}_{i3\gamma\delta}^{\mathsf{K}} = 0 \tag{38}$$

and $\mathbb{C}^{\sigma}{}_{\alpha\beta\gamma\delta} = \mathbb{C}_{\alpha\beta\gamma\delta} - \mathbb{C}_{\alpha\beta33}\mathbb{C}_{33\gamma\delta}/\mathbb{C}_{3333}$ denotes the plane-stress elasticity tensor. Hence the plate is under pure plane-*stress* at this order.

The strain is derived using the local constitutive equation:

$$\varepsilon_{\alpha\beta}^0 = z\mathsf{K}_{\alpha\beta}^{-1}, \quad \varepsilon_{\alpha 3}^0 = 0 \quad \text{and} \quad \varepsilon_{33}^0 = -\frac{z\mathbb{C}_{33\alpha\beta}}{\mathbb{C}_{3333}}\mathsf{K}_{\alpha\beta}^{-1} \tag{39}$$

This confirms Kirchhoff's assumption regarding the in-plane strain. The reader's attention is drawn to the fact that the out-of-plane strain is not zero, as already mentioned in several works [4, 5] in contrast to the original assumption from Kirchhoff.

Hence, for given macroscopic fields $\mathfrak{U}_3^{-1}$ and its derivatives, the microscopic strain and stress are fully determined at this order. However, we also need $\mathfrak{U}_3^0$ and $\mathfrak{U}_3^1$ for estimating the displacement field. This requires solving higher-order problems.

At this order, there remains to derive the macroscopic problem which enables the derivation of $\mathfrak{U}_3^{-1}$.

3.2.2 Macroscopic Problem

The Macroscopic equilibrium is derived integrating the first two components of $z \times$ (21) for $p = 0$. This gives after integrating by parts over z:

$$\mathsf{M}_{\alpha\beta,\beta}^0 - \mathsf{Q}_\alpha^1 = 0 \tag{40}$$

where the zeroth-order bending moment is defined as:

$$M^0_{\alpha\beta}(Y_1, Y_2) = \left\langle z\, \sigma^0_{\alpha\beta} \right\rangle, \tag{41}$$

and the first-order shear force is:

$$Q^1_\alpha(Y_1, Y_2) = \left\langle \sigma^1_{3\alpha} \right\rangle. \tag{42}$$

It can be easily established that $\left\langle \sigma^0_{3\alpha} \right\rangle = 0$ because of the equilibrium (20) and the boundary condition (22). Therefore, averaging the third component of Eq. (21) for $p = 0$ leads to a trivial equation. Using the second order boundary condition (23, $p = 2$) and averaging the third component of the first-order equilibrium equation (21), for $p = 1$ gives:

$$Q^1_{\alpha,\alpha} + F_3 = 0. \tag{43}$$

We obtain also the constitutive equation by plugging the local stress derived in Eq. (37) into the definition of $\underset{\sim}{M}^0$. This leads to the well-known Kirchhoff-Love constitutive equation:

$$\underset{\sim}{M}^0 = \underset{\approx}{D} : \underset{\sim}{K}^{-1} \quad \text{where}: \quad \underset{\approx}{D} = \left\langle z^2\, \underset{\approx}{\mathbb{C}}^\sigma \right\rangle \tag{44}$$

Gathering the preceding results leads to the definition of the Kirchhoff-Love plate problem:

$$\begin{cases} \underset{\sim}{M}^0 : \left(\underline{\nabla}_Y \otimes \underline{\nabla}_Y\right) + F_3 = 0, \quad \text{on} \quad \omega & \text{(45a)} \\ \underset{\sim}{M}^0 = \underset{\approx}{D} : \underset{\sim}{K}^{-1}, \quad \text{on} \quad \omega & \text{(45b)} \\ \underset{\sim}{K}^{-1} = U_3^{-1} \underline{\nabla}_Y \otimes \underline{\nabla}_Y, \quad \text{on} \quad \omega & \text{(45c)} \\ U_3^{-1} = 0 \quad \text{and} \quad \left(U_3^{-1} \otimes \underline{\nabla}_Y\right) \cdot \underline{n} = 0 \quad \text{on} \quad \partial\omega & \text{(45d)} \end{cases}$$

Finally, solving this macroscopic problem enables the derivation of the macroscopic displacement fields U_3^{-1}. However U_3^0 and U_3^1 remain unknown.

The well-known limitation of Kirchhoff-Love plate model is that it does not incorporate the effect of shear forces. In order to bring out the contribution of transverse shear, we need to go further in the expansion.

3.3 First-Order Plate Model

3.3.1 First-Order Auxiliary Problem

Gathering equilibrium equation for order 0, compatibility equation, boundary conditions and constitutive equations of order 1 we get the first-order auxiliary problem

for $z \in [-\frac{1}{2}, \frac{1}{2}]$:

$$\begin{cases} \sigma^0_{i\alpha,\alpha} + \sigma^1_{i3,3} = 0 & \text{(46a)} \\ \sigma^1_{ij} = \mathbb{C}_{ijkl}\varepsilon^1_{kl} & \text{(46b)} \\ \varepsilon^1_{\alpha\beta} = \frac{1}{2}\left(u^1_{\alpha,\beta} + u^1_{\beta,\alpha}\right), \quad \varepsilon^1_{\alpha 3} = \frac{1}{2}\left(u^2_{\alpha,3} + u^1_{3,\alpha}\right) \\ \quad \text{and} \quad \varepsilon^1_{33} = u^2_{3,3} & \text{(46c)} \\ \sigma^1_{i3}\left(z = \pm\frac{1}{2}\right) = 0 & \text{(46d)} \end{cases}$$

In this auxiliary problem, the zeroth-order displacement field $\underset{\sim}{u}^1$ (Eq. (35)) and stress field $\underset{\sim}{\sigma}^0$ (Eq. (37)) are local fields which depend linearly on $\underset{\sim}{K}^{-1}$, $U^0_{3,\alpha}$ and U^1_3. Hence, the first-order solution $\underset{\sim}{u}^2$ (as well as $\underset{\sim}{\varepsilon}^1$ and $\underset{\sim}{\sigma}^1$) will be a linear superposition of localization fields which depend on the gradient of those macroscopic fields.

The displacement field solution of this problem writes as:

$$\underset{\sim}{u}^2 = \underset{\approx}{\mathfrak{u}}^{K\nabla} \vdots \left(\underset{\sim}{K}^{-1} \otimes \underline{\nabla}_Y\right) + \underset{\approx}{\mathfrak{u}}^{K} : \underset{\sim}{K}^0 - zU^1_3 \otimes \underline{\nabla}_Y + U^2_3 \underline{e}_3 \tag{47}$$

where the displacement localization tensor related to the curvature gradient writes as:

$$\mathfrak{u}^{K\nabla}_{\alpha\beta\gamma\delta} = -\left[\int_{-\frac{1}{2}}^{z}\left(4\mathfrak{S}_{\alpha 3\eta 3}\int_{-\frac{1}{2}}^{y} \nu\, \mathbb{C}^{\sigma}_{\eta\beta\gamma\delta}\, d\nu + \delta_{\alpha\beta}\mathfrak{u}^{K}_{3\gamma\delta}\right) dy\right]^{*}$$
$$\text{and} \quad \mathfrak{u}^{K\nabla}_{3\beta\gamma\delta} = 0 \tag{48}$$

The first order stress writes as:

$$\underset{\sim}{\sigma}^1 = \underset{\approx}{\mathfrak{s}}^{K\nabla} \vdots \left(\underset{\sim}{K}^{-1} \otimes \underline{\nabla}_Y\right) + \underset{\approx}{\mathfrak{s}}^{K} : \underset{\sim}{K}^0 \tag{49}$$

where we defined the fifth-order localization tensor as:

$$\mathfrak{s}^{K\nabla}_{\alpha\beta\gamma\delta\eta} = 0, \quad \mathfrak{s}^{K\nabla}_{\alpha 3\beta\gamma\delta} = -\int_{\frac{1}{2}}^{z} y\, \mathbb{C}^{\sigma}_{\alpha\beta\gamma\delta}\, dy \quad \text{and} \quad \mathfrak{s}^{K\nabla}_{33\beta\gamma\delta} = 0 \tag{50}$$

Hence, this order involves only transverse shear effects.

3.3.2 Higher-Order Macroscopic Problem

Exactly as for the zeroth-order, it is possible to derive the macroscopic equilibrium equation as:

$$M^1_{\alpha\beta,\beta\alpha} = 0 \tag{51}$$

which holds also for higher orders ($p \geqslant 1$). For the constitutive equation, we have again:

$$\underset{\sim}{M}^1 = \left\langle\left\langle z\, \sigma^1_{\alpha\beta}\right\rangle\right\rangle = \underset{\approx}{D} : \underset{\sim}{K}^0 \tag{52}$$

Finally, U_3^0 is solution of the same Kirchhoff-Love problem as with the zeroth-order case (Eq. (45)), without external loads. Thus the solution is trivially zero everywhere. This is due to the monoclinic symmetry of the local constitutive equation. It is the analogue of the centro-symmetric assumption in the case of asymptotic expansion of a 3D medium (see [20] for instance). Thus, if we want to capture transverse shear effects following the asymptotic expansion procedure, we have to go one order higher. At this order, the macroscopic problem will not be trivial. However, it will require the derivation of the second gradient of the curvature $\underset{\sim}{K}^{-1}$ and consequently the fourth derivative of the deflection. This raises an issue in terms of physical meaning of this variable as well as of numerical implementation.

In contrast, it is remarkable that transverse shear effects are included in the localization field already at this order. Hence we suggest to stop at this order the asymptotic expansion and switch to variational arguments for deriving the Bending-Gradient theory.

3.4 Additional Remarks on the Asymptotic Expansion Approach

Before going further in the derivation of the Bending-Gradient theory, let us point out some useful remarks regarding the asymptotic expansion procedure.

In the present paper, we performed the asymptotic expansion up to the very next order after the classical homogenization procedure. However, this formalism has already been studied up to "infinite order" in other elasticity problems (see [21] for instance) and convergence results were derived [22]. Those works show that the fully reconstructed field $\underline{u}$ is actually a double sum: a sum over orders, as expected because of the expansion, but also over degrees of derivative of the macroscopic displacement field. This is also the case in the present plate problem. If we gather all the fields derived in the cascade resolution we get the following:

$$\begin{aligned}\underline{u} = &\left(\frac{U_3^{-1}}{\eta} + U_3^0 + \eta U_3^1 + \eta^2 U_3^2 + \cdots\right)\underline{e}_3 \\ &- z\left(U_3^{-1} + \eta U_3^0 + \eta^2 U_3^1 + \cdots\right)\otimes\underline{\nabla}_Y \\ &+ \eta\left(\underset{\approx}{\mathfrak{u}}^K : \left(\underset{\sim}{K}^{-1} + \eta\underset{\sim}{K}^0 + \cdots\right)\right) + \eta^2\left(\underset{\approx}{\mathfrak{u}}^{K\nabla} \vdots \left(\underset{\sim}{K}^{-1}\otimes\underline{\nabla}_Y + \cdots\right)\right) + \cdots\end{aligned} \tag{53}$$

Assuming that this double sum converges, it is legitimate to define:

$$U_3 = \sum_{p=-1}^{\infty} \eta^{p+1} U_3^p \tag{54}$$

and rewrite the total displacement field as:

$$\underline{u} = \frac{U_3}{\eta}\underline{e}_3 - zU_3 \otimes \underline{\nabla}_Y + \eta\, \underline{\underline{u}}^K : \underset{\sim}{K} + \eta^2\, \underline{\underline{\underline{u}}}^{K\nabla} \vdots \underset{\sim}{K} \otimes \underline{\nabla}_Y + \cdots \tag{55}$$

where $\underset{\sim}{K} = U_3 \underline{\nabla}_Y \otimes \underline{\nabla}_Y$. This was suggested by Boutin [23] and further justified in [21]. We have also for the stress field:

$$\underset{\sim}{\sigma} = \underline{\underline{s}}^K : \underset{\sim}{K} + \eta\, \underline{\underline{\underline{s}}}^{K\nabla} \vdots \underset{\sim}{K} \otimes \underline{\nabla}_Y + \cdots \tag{56}$$

Finally, this reasoning holds also true for the equilibrium equation and we formally get:

$$\underset{\sim}{M} : \left(\underline{\nabla}_Y \otimes \underline{\nabla}_Y\right) + F_3 = 0 \tag{57}$$

where $M_{\alpha\beta} = \langle z\, \sigma_{\alpha\beta} \rangle$. Hence, it seems that going higher-order in the asymptotic expansion only involves higher gradients of the displacement inside the constitutive equation. However, as already pointed out in these papers, the problem remains ill-posed as it stands here. Some caution must be taken when considering the constitutive equation as well as the boundary conditions if one wants to derive a mathematically sound problem.

First, in order to derive the constitutive equation it seems straightforward to take directly the elastic energy of the infinite order stress or strain (Eq. (56)) and to truncate this energy up to a given order *afterward*. However, this will lead to a non-positive quadratic form and makes the higher-order problem unstable. Hence, as pointed out by [21] it is critical to truncate the expansion of the stress or strain *before* taking the related energy to ensure positivity.

Second, whereas the boundary conditions are set at each order in the cascade resolution of the asymptotic expansion (here Eq. (45d) at each order), in the format presented here, it is not possible to make distinction between orders and then the problem is not well-posed anymore. Now, variational tools will enable the derivation of consistent boundary conditions with the choice of macroscopic degrees of freedom.

4 The Bending-Gradient Theory

Keeping in mind the difficulties mentioned regarding the asymptotic expansion, the Bending-Gradient theory is derived as follows. First, instead of keeping the first gradient of the curvature as higher-order unknown, we introduce the gradient of the

bending moment. This will relax the compatibility condition between $\underset{\sim}{\mathrm{K}}$ and $\underset{\sim}{\mathrm{K}} \otimes \underline{\nabla}_Y$. After this change of variable, we define the stress localization as the truncation of the infinite order stress. Then we introduce the set of statically compatible macroscopic fields. Finally, using variational arguments, the kinematics as well as the boundary conditions of the plate model are derived. Once the plate model is solved, we are able to reconstruct an approximation of the 3D displacement field.

We select first the bending moment and its gradient instead of the curvature and its gradient for carrying the energy. Hence we define the bending gradient as:

$$\underset{\sim\sim}{\mathrm{R}} = \underset{\sim}{\mathrm{M}} \otimes \underline{\nabla}_Y \tag{58}$$

Using Kirchhoff-Love constitutive equation and the following change of variable,

$$\underset{\sim\sim}{\mathrm{R}} = \underset{\approx}{\mathrm{D}} : \underset{\sim}{\mathrm{K}} \otimes \underline{\nabla}_Y \tag{59}$$

it is possible to rewrite the strain and stress localization fields derived with the asymptotic expansion (Eq. (3)) only in terms of $\underset{\sim}{\mathrm{M}}$ and $\underset{\sim\sim}{\mathrm{R}}$:

$$\underset{\sim}{\sigma}^{\mathrm{BG}} = \underset{\approx}{\mathbb{S}}^{\mathrm{M}} : \underset{\sim}{\mathrm{M}} + \eta \underset{\approx}{\mathbb{S}}^{\mathrm{R}} \vdots \underset{\sim\sim}{\mathrm{R}} \tag{60}$$

where:

$$\underset{\approx}{\mathbb{S}}^{\mathrm{M}} = \underset{\approx}{\mathbb{S}}^{\mathrm{K}} : \underset{\approx}{\mathrm{d}}, \quad \underset{\approx}{\mathbb{S}}^{\mathrm{R}} = \underset{\approx}{\mathbb{S}}^{\mathrm{K}\nabla} : \underset{\approx}{\mathrm{d}} \quad \text{and} \quad \underset{\approx}{\mathrm{d}} = \underset{\approx}{\mathrm{D}}^{-1} \tag{61}$$

It is easy to check that this stress field satisfies the 3D equilibrium equation (15), as well as the $z = \pm 1/2$ face boundary conditions, up to the order η^1. Hence, even if it does not define properly a restriction of SC^{3D}, it remains a good approximation in the sense of the asymptotic expansion.

Now, based on the macroscopic equilibrium equations derived through the asymptotic expansion and the definition of $\underset{\sim\sim}{\mathrm{R}}$, we suggest the following set of statically compatible fields for the Bending-Gradient theory:

$$SC^{\mathrm{BG}} : \begin{cases} \underset{\sim\sim}{\mathrm{R}} = \underset{\sim}{\mathrm{M}} \otimes \underline{\nabla}_Y & \text{(62a)} \\ \left(\underset{\approx}{\mathrm{i}} \vdots \underset{\sim\sim}{\mathrm{R}} \right) \cdot \underline{\nabla}_Y + \mathrm{F}_3 = 0 & \text{(62b)} \end{cases}$$

where the shear forces were substituted and we used the following relation:

$$\underset{\approx}{\mathrm{i}} \vdots \underset{\sim\sim}{\mathrm{R}} = \underset{\sim}{\mathrm{M}} \cdot \underline{\nabla}_Y \tag{63}$$

where $\mathrm{i}_{\alpha\beta\gamma\delta} = \frac{1}{2}\left(\delta_{\alpha\gamma}\delta_{\beta\delta} + \delta_{\alpha\delta}\delta_{\beta\gamma}\right)$ is the identity for in-plane fourth-order tensors following the symmetries of linear elasticity.

Plugging $\underset{\sim}{\sigma}^{\mathrm{BG}}$ into the complementary energy of the full 3D problem leads to the following functional:

$$P^{*BG}\left(\underset{\sim}{M},\underset{\frown}{R}\right)=\int_{\omega} w^{*KL}\left(\underset{\sim}{M}\right)+\eta^2 w^{*BG}\left(\underset{\frown}{R}\right)d\omega \tag{64}$$

where the stress elastic energies are defined as:

$$w^{*KL}\left(\underset{\sim}{M}\right)=\frac{1}{2}\underset{\sim}{M}:\underset{\approx}{d}:\underset{\sim}{M} \quad \text{and} \quad w^{*BG}\left(\underset{\frown}{R}\right)=\frac{1}{2}{}^{T}\underset{\frown}{R}\vdots\underset{\approx\approx}{h}\vdots\underset{\frown}{R} \tag{65}$$

with:

$$\underset{\approx\approx}{h}=\left\langle {}^{T}\underset{\approx}{\$}^{R}:\underset{\approx}{\$}:\underset{\approx}{\$}^{R}\right\rangle \tag{66}$$

This sixth-order tensor is the compliance related to the transverse shear of the plate. It is strictly identical to the one derived in [1]. Let us recall here that it is positive, symmetric, but not definite. More details about $\underset{\approx\approx}{h}$ properties were discussed in [1].

NB: There is no uncoupling in the complementary energy (64) between $\underset{\sim}{M}$ and $\underset{\frown}{R}$ because of the monoclinic symmetry of the local constitutive equation. In the auxiliary problems, this symmetry enforces the localization related to $\underset{\sim}{M}$ to be purely in-plane and the one related to $\underset{\frown}{R}$ to be pure transverse shear. Hence the cross terms in the 3D elastic energy vanish.

Now we define the generalized strains as:

$$\underset{\sim}{\chi}=\frac{\partial w^{*KL}}{\partial \underset{\sim}{M}} \quad \text{and} \quad \underset{\frown}{\Gamma}=\frac{\partial w^{*BG}}{\partial \underset{\frown}{R}} \tag{67}$$

which leads to the following constitutive equations:

$$\begin{cases} \underset{\sim}{\chi}=\underset{\approx}{d}:\underset{\sim}{M} & \text{(68a)} \\ \underset{\frown}{\Gamma}=\underset{\approx\approx}{h}\vdots\underset{\frown}{R} & \text{(68b)} \end{cases}$$

Introducing respectively $\Phi_{\alpha\beta\gamma}$, U_3 as Lagrange multipliers of Eqs. (62a) and (62b) and taking the variations with respect to the static variables leads to the following definition for the strains:

$$KC^{BG}:\begin{cases} \underset{\sim}{\chi}=\underset{\frown}{\Phi}\cdot\underset{\sim}{\nabla}_Y & \text{(69a)} \\ \eta^2\underset{\frown}{\Gamma}=\underset{\frown}{\Phi}+\underset{\approx}{i}\cdot\underset{\sim}{\nabla}_Y U_3 & \text{(69b)} \end{cases}$$

where both $\underset{\frown}{\Phi}$ and $\underset{\frown}{\Gamma}$ are third-order tensors which follows the same index symmetry as $\underset{\frown}{R}$. Setting $\eta^2=0$ in those definitions leads exactly to Kirchhoff-Love strains. Hence, the Bending-Gradient curvature is slightly different from the one of the asymptotic expansion and Eq. (69a) rewrites:

$$\underset{\sim}{\chi}=\underset{\sim}{K}+\eta^2\underset{\frown}{\Gamma}\cdot\underset{\sim}{\nabla}_Y \tag{70}$$

Namely it is the sum of the conventional curvature and a small correction term which relaxes this compatibility relation.

Considering the variations of the Lagrangian on the edges leads also to the following clamped boundary conditions:

$$\mathrm{U}_3 = 0 \quad \text{and} \quad \underset{\frown}{\Phi} \cdot \underline{n} = 0 \text{ on } \partial\omega \tag{71}$$

Finally we have a well-posed plate theory.

Once the exact solution of the macroscopic problem is derived, it is possible to reconstruct the local displacement field. We suggest the following 3D displacement field where U_3, $\underset{\frown}{\Phi}$ are the fields solution of the plate problem:

$$\underline{u}^{BG} = \frac{\mathrm{U}_3}{\eta}\underline{e}_3 - z\mathrm{U}_3 \otimes \underline{\nabla}_Y + \eta\, \underline{\underset{\sim}{u}}^{K} : \underset{\sim}{\chi} + \eta^2\, \underline{\underset{\frown}{u}}^{K\nabla} \vdots \left(\underset{\sim}{\chi} \otimes \underline{\nabla}_Y\right) \tag{72}$$

Defining the strain as $\underset{\sim}{\varepsilon}^{BG} = \underset{\sim}{\mathbb{S}} : \underset{\sim}{\sigma}^{BG}$ it is possible to check that:

$$\varepsilon\left(\underline{u}^{BG}\right)_{(Y,z)} - \underset{\sim}{\varepsilon}^{BG} = \eta^2\left(\left(\underset{\sim}{\delta} \otimes^s \underline{\underset{\frown}{u}}^{K\nabla}\right) :: \left(\underset{\sim}{\chi} \otimes \underline{\nabla}_Y^2\right) + z\underset{\frown}{\Gamma} \cdot \underline{\nabla}_Y\right) \tag{73}$$

which shows that the compatibility equation between the reconstructed displacement field $\underline{u}^{BG}$ and strain localization $\underset{\sim}{\varepsilon}^{BG}$ is satisfied up to the η^2 order.

5 Conclusion

Finally, we derived a plate model which enables the full description of local 3D fields ($\underline{u}^{BG}$, $\underset{\sim}{\varepsilon}^{BG}$ and $\underset{\sim}{\sigma}^{BG}$) including the effects of transverse shear. Compared to the classical theory from Reissner [2], we just add four macroscopic variables included into the generalized rotation $\underset{\frown}{\Phi}$ and which are related to transverse shear warping. Contrary to the asymptotic expansions approach or the approach suggested in [21], our theory does not require the derivation of the first or even the second gradient of the curvature. Actually, when looking at the definition of strains in Eq. (69), only the first derivatives of U_3 and $\underset{\frown}{\Phi}$ are involved. Having low-order interpolation is a serious advantage compared to "strain-gradient-like" approaches given in [7, 21].

Now, let us recall that the derivation of the Bending-Gradient theory through asymptotic expansions was purely formal. The small parameter η was essentially used for discriminating between orders. More precisely, the 3D local fields chosen for the Bending-Gradient theory satisfy the 3D compatibility equation and the 3D equilibrium equation one order higher than the Kirchhoff-Love fields. However, this is not a proof of convergence even if the good results in [3] are clearly encouraging. Especially, it is broadly acknowledged that the boundary have a critical role on that matter when going in higher orders. This question raises already with asymptotic

expansions: it was demonstrated that the approximation which is derived in the bulk is not compatible with the actual 3D boundary condition and can only be fulfilled weakly (see [24, 25] for a clear illustration in the case of beams and also [26]). In the case of the Bending-Gradient theory the boundary conditions are different from the asymptotic expansions and requires further analysis which is out of the scope of this paper.

References

1. Lebée, A., Sab, K.: A Bending-Gradient model for thick plates. Part I: Theory. Int. J. Solids Struct. **48**(20), 2878–2888 (2011)
2. Reissner, E.: The effect of transverse shear deformation on the bending of elastic plates. J. Appl. Mech. **12**(2), 69–77 (1945)
3. Lebée, A., Sab, K.: A Bending-Gradient model for thick plates. Part II: Closed-form solutions for cylindrical bending of laminates. Int. J. Solids Struct. **48**(20), 2889–2901 (2011)
4. Ciarlet, P.G., Destuynder, P.: Justification of the 2-dimensional linear plate model. J. Mecan. **18**(2), 315–344 (1979)
5. Caillerie, D.: Thin elastic and periodic plates. Math. Methods Appl. Sci. **6**(1), 159–191 (1984)
6. Kohn, R.V., Vogelius, M.: A new model for thin plates with rapidly varying thickness. Int. J. Solids Struct. **20**(4), 333–350 (1984)
7. Lewiński, T.: Effective models of composite periodic plates: I. Asymptotic solution. Int. J. Solids Struct. **27**(9), 1155–1172 (1991)
8. Sutyrin, V.G., Hodges, D.H.: On asymptotically correct linear laminated plate theory. Int. J. Solids Struct. **33**(25), 3649–3671 (1996)
9. Reddy, J.N.: On refined computational models of composite laminates. Int. J. Numer. Methods Eng. **27**(2), 361–382 (1989)
10. Altenbach, H.: Theories for laminated and sandwich plates. Mech. Comp. Mater. **34**(3), 243–252 (1998)
11. Noor, A.K., Malik, M.: An assessment of five modeling approaches for thermo-mechanical stress analysis of laminated composite panels. Comput. Mech. **25**(1), 43–58 (2000)
12. Carrera, E.: Theories and finite elements for multilayered, anisotropic, composite plates and shells. Arch. Comput. Methods Eng. **9**(2), 87–140 (2002)
13. Diaz Diaz, A.: Un modèle de stratifiés. C. R. Acad. Sci. Ser. IIB Mech. **329**(12), 873–879 (2001)
14. Lebée, A., Sab, K.: Homogenization of thick periodic plates: application of the Bending-Gradient plate theory to a folded core sandwich panel. Int. J. Solids Struct. **49**(19–20), 2778–2792 (2012)
15. Lebée, A., Sab, K.: Homogenization of cellular sandwich panels. C. R. Mécan. **340**(4–5), 320–337 (2012)
16. Lebée, A., Sab, K.: Homogenization of a space frame as a thick plate: application of the Bending-Gradient theory to a beam lattice. Comput. Struct. (accepted). doi:10.1016/j.compstruc.2013.01.011
17. Sanchez-Palencia, E.: Non-Homogeneous Media and Vibration Theory, Lecture Notes in Physics, vol. 127. Springer, Berlin (1980)
18. Dallot, J., Sab, K.: Limit analysis of multi-layered plates. Part I: The homogenized Love-Kirchhoff model. J. Mech. Phys. Solids **56**(2), 561–580 (2008)
19. Sanchez Hubert, J., Sanchez-Palencia, E.: Introduction aux méthodes asymptotiques et à l'homogénéisation: application à la mécanique des milieux continus, Masson, Paris (1992)
20. Triantafyllidis, N., Bardenhagen, S.: The influence of scale size on the stability of periodic solids and the role of associated higher order gradient continuum models. J. Mech. Phys. Solids **44**(11), 1891–1928 (1996)

21. Smyshlyaev, V.P., Cherednichenko, K.D.: On rigorous derivation of strain gradient effects in the overall behaviour of periodic heterogeneous media. J. Mech. Phys. Solids **48**(6–7), 1325–1357 (2000)
22. Bakhvalov, N., Panasenko, G.: Homogenisation: averaging processes in periodic media. Kluwer Academic Publishers, Dordrecht (1989)
23. Boutin, C.: Microstructural effects in elastic composites. Int. J. Solids Struct. **33**(7), 1023–1051 (1996)
24. Buannic, N., Cartraud, P.: Higher-order effective modeling of periodic heterogeneous beams. I. Asymptotic expansion method. Int. J. Solids Struct. **38**(40–41), 7139–7161 (2001)
25. Buannic, N., Cartraud, P.: Higher-order effective modeling of periodic heterogeneous beams. II. Derivation of the proper boundary conditions for the interior asymptotic solution. Int. J. Solids Struct. **38**(40–41), 7163–7180 (2001)
26. Berdichevsky, V.L.: Variational-asymptotic method of constructing a theory of shells. J. Appl. Math. Mech. **43**(4), 711–736 (1979)

Macroscopic Modeling of Size Effects in Foams Using an Order-Parameter Approach

Bernd Lenhof, Alexander Geringer and Stefan Diebels

Abstract Foams show size effects under mechanical loading. Typically a stiffening effect in shear experiments is observed if the specimen is reduced in size (smaller is stiffer). It is documented in several publications that a micro-polar model is able to describe this effect which is microscopically motivated by the bending stiffness of the cell walls. In the present contribution a microscopic model of an open-cell foam is used to generate virtual experimental data. Stiff boundary layer effects are found under shear loading while tension shows a weakening effect due to the reduced connectivity of the beams on the free boundary. Using a parameter identification procedure allows for the determination of the parameters of the micro-polar model if the focus is laid on the stiffening size effect. Weakening size effects cannot be predicted by the micro-polar model if a physical interpretation of the rotational degrees of freedom is preserved. Therefore, an order-parameter approach is chosen as an alternative on the macro-scale. It is shown in the contribution, that this different type of macroscopic model allows to describe both types of size effects.

1 Introduction

Open-cell foams are well established engineering materials. Nevertheless, their mechanical properties are more complex and less understood compared to the mechanical properties of classical engineering materials like steel.

B. Lenhof (✉) · A. Geringer · S. Diebels
Chair of Applied Mechanics, Saarland University, Saarbrücken, Germany
e-mail: b.lenhof@mx.uni-saarland.de

A. Geringer
e-mail: a.geringer@mx.uni-saarland.de

S. Diebels
e-mail: s.diebels@mx.uni-saarland.de

H. Altenbach et al. (eds.), *Generalized Continua as Models for Materials*,
Advanced Structured Materials 22, DOI: 10.1007/978-3-642-36394-8_13,

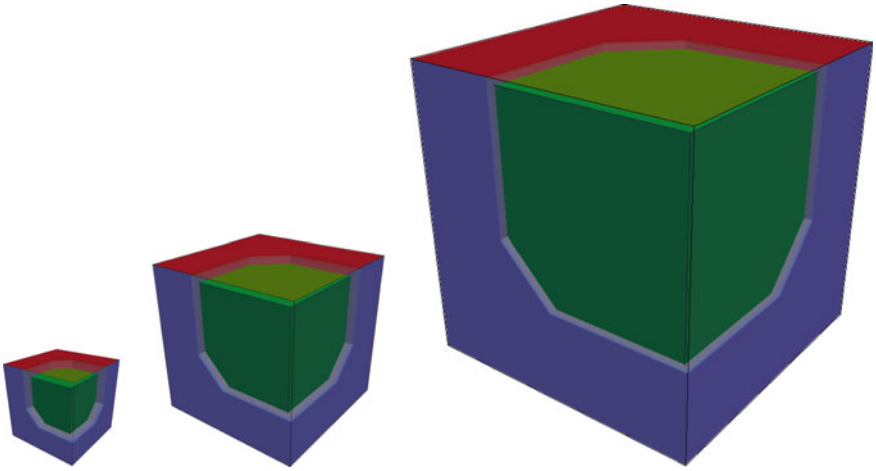

Fig. 1 The cubes represent the same continuum model of a foam but for different sizes (height ratios between the species from *left* to *right* 1:2:4). The *green* area shows the surface of the sub-cube, inside which certain value is constant, e.g. shear modulus. Outside the sub-cube, the value is influenced by the boundary. As can be seen in the picture, the depth of boundary influence does not scale with the cube dimensions

One major difference to classical materials is a size effect that foams show (cf. Andrews et al. [1, 2], Diebels and Steeb [7], Lakes [12], Onck et al. [14], Tekoğlu [19], Tekoğlu and Onck [21]). Depending on the size of the specimen, there is a change in stiffness. A rule of thumb is 'the smaller the specimen, the larger the change in stiffness (cf. Fig. 1). Whether the specimen reacts stiffer or weaker depends on the load case, i.e. small foam specimen show a weakening in tensile tests and a stiffening in simple shear tests.

Standard Boltzmann continua are not able to reproduce these size effects. Hence, the continuum theory has to be extended properly. One such well-known extension is the micro-polar model (also known as Cosserat model [6]). The micro-polar model is able to reproduce the stiffening behavior in simple shear tests. Unfortunately, it fails in modeling the weakening in tensile tests (cf. Tekoğlu and Onck [20]). Here, we introduce an order-parameter model to overcome the drawback of the micro-polar model, while keeping the number of additional fields small. This model approach has been successfully used by Steeb and Diebels [16], Diebels et al. [8] and Diebels and Geringer [9] to model boundary effects in polymers. In difference to the micro-polar approach, the order-parameter model does not try to capture micro-mechanical details in terms of additional kinematic degrees of freedom but to model macroscopically measurable inhomogeneities. It will be shown, that the proposed order-parameter model is in fact able to model both size effects and is, hence, an alternative to the micro-polar model.

The contribution consists of 4 sections. In Sect. 2, the equations of the order-parameter model is thermodynamically consistent derived and compared to

the micro-polar model. In Sect. 3, the strong form is further developed into the weak form to obtain, afterwards, the pertinent finite element formulation. Moreover, parameter studies and parameter identification for a simple shear test and a tension test have been carried out which show the viability of the approach. Finally, conclusions are drawn in Sect. 4.

2 Modeling

Here, the basic equations of the order-parameter model are established. The derivation follows the line of argumentation of Steeb and Diebels [17]. Their reasoning is founded on the work of Capriz [5] and Svendsen [18]. Additionally, the pertinent equations for the micro-polar model are stated. Those equations are not derived, the interested reader is referred to the work of the Cosserat brothers [6] or Eringen [10]. However, there is a short comparison of the order-parameter model and the micro-polar model at the end of this section.

2.1 The Order-Parameter Model

To derive the order-parameter model used in this work, the work by Capriz [5] and Steeb and Diebels [17] are utilized. As a starting point, the following equations are stated

$$\dot{\rho} + \rho \operatorname{div}\dot{\mathbf{x}} = 0, \tag{1}$$

$$\rho\ddot{\mathbf{x}} - \operatorname{div}\mathbf{T} - \rho\mathbf{b} = \mathbf{0}, \tag{2}$$

$$\rho k\ddot{\xi} - \operatorname{div}\mathbf{S} - \rho g = 0, \tag{3}$$

where (1) is the continuity equation on macro-level, (2) is the balance of momentum on macro-level and (3) is a constitutive equation for the order-parameter which has the structure of a balance equation. Here, ρ denotes the density of the material, $\mathbf{T}$ is the Cauchy stress tensor, $\mathbf{b}$ labels the macroscopic body force, $\mathbf{x}$ is a material point in the actual placement and $\frac{\mathrm{d}}{\mathrm{d}t} = (\dot{})$ indicates the material time derivative. As to the balance equation for the order-parameter, k is a model function, $\mathbf{S}$ is a flux vector, ρg is a supply term and, finally, ξ represents the order-parameter. As a side note, the order-parameter is not an additional kinematic quantity, hence, the function k is not an inertia term.

Going on in the usual way of doing, the local balance equation for the internal energy density is given in its most general form as (cf. e.g. Hutter and Jöhnk [11])

$$\dot{\Gamma} = \Sigma - \operatorname{div}\mathbf{\Phi}, \tag{4}$$

where Γ is the energy density, Σ denotes the energy supply terms and $\mathbf{\Phi}$ contains the energy flux terms. The energy density is, given as

$$\Gamma = \frac{1}{2}\rho\dot{\mathbf{x}}\cdot\dot{\mathbf{x}} + \rho\epsilon + \frac{1}{2}\rho k\dot{\xi}^2, \tag{5}$$

consists of a kinetic part, the internal energy and an additional part due to the order-parameter. Since the order-parameter is not a kinematic quantity, there is at a first glance no need to define the related energy density in a kinetic fashion. However, the term $\frac{1}{2}\rho\dot{\xi}^2$ turns out to be consistent to Eq. (3) (cf. Capriz [5]). The energy supply,

$$\Sigma = \rho\mathbf{b}\cdot\dot{\mathbf{x}} + \rho r + \rho g\dot{\xi}, \tag{6}$$

contains the mechanical power from the body forces, a supply from heat radiation r and an additional part from the supply of order-parameter. Finally, the energy flux,

$$\mathbf{\Phi} = -\mathbf{T}\cdot\dot{\mathbf{x}} + \mathbf{q} - \mathbf{S}\dot{\xi}, \tag{7}$$

consists of the mechanical power due to stresses, a heat flux term and the flux term of the order-parameter. Insertion of the Eqs. (5)–(7) into (4) leads to

$$\begin{aligned}\frac{\partial}{\partial t}(\rho\varepsilon + \frac{1}{2}\rho\dot{\mathbf{x}}\cdot\dot{\mathbf{x}} + \frac{1}{2}\rho k\dot{\xi}^2) + (\rho\varepsilon + \frac{1}{2}\rho\dot{\mathbf{x}}\cdot\dot{\mathbf{x}} + \frac{1}{2}\rho k\dot{\xi}^2)\,\mathrm{div}\dot{\mathbf{x}}\\ = \mathrm{div}(\mathbf{T}\cdot\dot{\mathbf{x}}) + \mathrm{div}\mathbf{S}\dot{\xi} - \mathrm{div}\mathbf{q} + \rho\mathbf{b}\cdot\dot{\mathbf{x}} + \rho g\dot{\xi} + \rho r.\end{aligned} \tag{8}$$

The repeated use of the balance Eqs. (1)–(3) reduces Eq. (8) to

$$\rho\dot{\epsilon} + \frac{1}{2}\rho\dot{k}\dot{\xi}^2 = \mathbf{T}\colon \mathrm{grad}\dot{\mathbf{x}} + \mathbf{S}\cdot\mathrm{grad}\dot{\xi} - \mathrm{div}\mathbf{q} + \rho g\dot{\xi} + \rho r. \tag{9}$$

In anticipation of the use of the energy balance in the entropy inequality, the internal energy is replaced in a standard fashion via Legendre transformation with the Helmholtz free energy. By use of

$$\Psi = \varepsilon - \eta\theta, \tag{10}$$

$$\dot{\varepsilon} = \dot{\Psi} + \dot{\eta}\theta + \eta\dot{\theta}, \tag{11}$$

where Ψ denotes the Helmholtz free energy, η the entropy and θ the temperature, we obtain from (9)

$$\rho\dot{\eta}\theta + \mathrm{div}\mathbf{q} - \rho r = \mathbf{T}\colon \mathrm{grad}\dot{\mathbf{x}} + \mathbf{S}\cdot\mathrm{grad}\dot{\xi} + \rho g\dot{\xi} - \frac{1}{2}\rho\dot{k}\dot{\xi}^2 - \rho\dot{\Psi} - \eta\dot{\theta}. \tag{12}$$

The exploitation of the entropy inequality leads to thermodynamic consistent constitutive equations. Here, the approach of Coleman and Noll is used. By doing

this, we still follow the argumentation of Steeb and Diebels [17]. The entropy equality is given as

$$\frac{\mathrm{d}}{\mathrm{dt}}(\rho\eta) = -\mathrm{div}\boldsymbol{\varphi} + \rho s + \hat{\eta}, \tag{13}$$

where the entropy production $\hat{\eta}$ is introduced as well as the entropy flux $\boldsymbol{\varphi}$ and the entropy supply s. The entropy flux and the entropy supply will be defined as

$$\boldsymbol{\varphi} = \frac{\mathbf{q}}{\theta}, \tag{14}$$

$$s = \frac{r}{\theta}. \tag{15}$$

This definition may be questionable for microstructures. However, an evaluation of the entropy inequality in the sense of Müller-Liu, which might give a different definition of the entropy flux and supply, is left for future work. Introduction of the constitutive equations (14) into (15) and rearrangement leads to

$$\rho\dot{\eta}\theta + \mathrm{div}\mathbf{q} - \rho r = -\frac{\mathbf{q}}{\theta}\mathrm{grad}\theta + \hat{\eta}. \tag{16}$$

After a comparison of Eq. (12) with Eq. (16), while keeping in mind that the entropy production $\hat{\eta}$ is always positive, we obtain the Clausius-Duhem inequality

$$\mathbf{T}\colon \mathrm{grad}\dot{\mathbf{x}} + \mathbf{S}\cdot\mathrm{grad}\dot{\xi} + \rho g\dot{\xi} - \frac{1}{2}\rho\dot{k}\dot{\xi}^2 - \rho\dot{\Psi} - \eta\dot{\theta} + \frac{\mathbf{q}}{\theta}\mathrm{grad}\theta \geqslant 0. \tag{17}$$

The assumption of isothermal processes reduces the Clausius-Duhem inequality to the Clausius-Planck inequality, which as a consequence only contains mechanical quantities but no thermal ones,

$$\mathbf{T}\colon \mathrm{grad}\dot{\mathbf{x}} + \mathbf{S}\cdot\mathrm{grad}\dot{\xi} + \rho g\dot{\xi} - \frac{1}{2}\rho\dot{k}\dot{\xi}^2 - \rho\dot{\Psi} \geqslant 0. \tag{18}$$

To obtain pertinent constitutive equations, the Clausius-Planck inequality has to be evaluated. Suitable process variables are

$$\mathcal{S} = \mathcal{S}(\mathbf{E}, \xi, \mathrm{grad}\xi), \tag{19}$$

while the response functions are

$$\mathcal{R} = \mathcal{R}(\Psi, \mathbf{T}, \mathbf{S}, k). \tag{20}$$

Due to the concept of equipresence, it is assumed that every response function depends on all process variable. Hence, it is possible to expand the time derivatives $\dot{\Psi}$ and $\dot{k}$ by means of the chain rule into

$$\dot{\Psi} = \frac{\partial \Psi}{\partial \mathbf{E}} : \dot{\mathbf{E}} + \frac{\partial \Psi}{\partial \xi}\dot{\xi} + \frac{\partial \Psi}{\partial \mathrm{grad}\xi} \cdot \mathrm{grad}\dot{\xi}, \tag{21}$$

$$\dot{\mathrm{k}} = \frac{\partial \mathrm{k}}{\partial \mathbf{E}} : \dot{\mathbf{E}} + \frac{\partial \mathrm{k}}{\partial \xi}\dot{\xi} + \frac{\partial \mathrm{k}}{\partial \mathrm{grad}\xi} \cdot \mathrm{grad}\dot{\xi}. \tag{22}$$

Substitution of these expressions in Eq. 18 leads to

$$\begin{aligned}(\mathbf{T} - \rho\frac{\partial \Psi}{\partial \mathbf{E}} - \frac{1}{2}\rho\frac{\partial \mathrm{k}}{\partial \mathbf{E}}\dot{\xi}^2) : \dot{\mathbf{E}} + (\rho \mathrm{g} - \rho\frac{\partial \Psi}{\partial \xi} - \frac{1}{2}\rho\frac{\partial \mathrm{k}}{\partial \xi}\dot{\xi}^2)\dot{\xi} \\ + (\mathbf{S} - \rho\frac{\partial \Psi}{\partial \mathrm{grad}\xi} - \frac{1}{2}\rho\frac{\partial \mathrm{k}}{\partial \mathrm{grad}\xi}\dot{\xi}^2) \cdot \mathrm{grad}\dot{\xi} \geqslant 0.\end{aligned} \tag{23}$$

Out of this equation, the constitutive relations for the Cauchy stress $\mathbf{T}$, the order-parameter flux $\mathbf{S}$ and the order-parameter supply g are obtained as

$$\mathbf{T} = \rho\frac{\partial \Psi}{\partial \mathbf{E}} + \frac{1}{2}\rho\frac{\partial \mathrm{k}}{\partial \mathbf{E}}\dot{\xi}^2, \tag{24}$$

$$\mathbf{S} = \rho\frac{\partial \Psi}{\partial \mathrm{grad}\xi} + \frac{1}{2}\frac{\partial \mathrm{k}}{\partial \mathrm{grad}\xi}\dot{\xi}^2, \tag{25}$$

$$\rho \mathrm{g} = \rho\frac{\partial \Psi}{\partial \xi} + \frac{1}{2}\rho\frac{\partial \mathrm{k}}{\partial \xi}\dot{\xi}^2. \tag{26}$$

The constitutive equations used in this article are obtained through further assumptions. Small strain kinematic is assumed

$$\mathbf{E} = \frac{1}{2}(\mathrm{grad}\mathbf{u} + \mathrm{grad}^{\mathsf{T}}\mathbf{u}), \tag{27}$$

and the Helmholtz free energy is chosen as a quadratic function of its arguments

$$\rho\Psi = \frac{1}{2}\lambda(\mathbf{E} : \mathbf{I})^2 + \mu(\xi)\mathbf{E} : \mathbf{E} + \frac{1}{2}\beta(\xi - \xi_0)^2 + \frac{1}{2}\beta \mathrm{l}_{\mathrm{op}}^2(\mathrm{grad}\xi)^2, \tag{28}$$

which is closely linked to the respective energy in Steeb and Diebels [17]. The material parameter λ and the material function $\mu(\xi)$ represent the Lamé parameters, while β and l_{op} are parameters of the microstructure. There is a certain benefit in using the parameters β and l_{op} as is done here, which becomes clear in Eq. (35). Using assumptions (27)–(28) in the constitutive relations (24)–(26), the constitutive equations for the Cauchy stress, the order-parameter flux and the order-parameter supply are given as

$$\mathbf{T} = (3\lambda\overset{4}{\mathbf{I}}^{\mathrm{sph}} + 2\mu(\xi)\overset{4}{\mathbf{I}}) : \mathbf{E} + \frac{1}{2}\rho\frac{\partial \mathrm{k}}{\partial \mathbf{E}}\dot{\xi}^2, \tag{29}$$

$$\mathbf{S} = \beta l_{op}^2 \operatorname{grad}\xi + \frac{1}{2}\frac{\partial k}{\partial \operatorname{grad}\xi}\dot{\xi}^2, \tag{30}$$

$$\rho g = \beta(\xi - \xi_0) + \frac{\partial \mu(\xi)}{\partial \xi}\mathbf{E}\colon \mathbf{E} + \frac{1}{2}\rho\frac{\partial k}{\partial \xi}\dot{\xi}^2, \tag{31}$$

where the fourth-order tensors

$$\overset{4}{\mathbf{I}}^{\mathrm{sph}} = \tfrac{1}{3}\mathbf{I}\otimes\mathbf{I}, \tag{32}$$

$$\overset{4}{\mathbf{I}} = [\mathbf{I}\otimes\mathbf{I}]^{\overset{23}{\mathsf{T}}} \tag{33}$$

were introduced.

Finally, the model used in the article is reduced to the static case, vanishing macroscopic body forces, and small strain kinematics. The quadratic term $\mathbf{E}\colon\mathbf{E}$ in the equation of the order-parameter supply (31) is neglected due to the small strain assumption, the terms including $\dot{\xi}^2$ are neglected due to the static case assumption. In conclusion, the model becomes

$$\operatorname{div}\mathbf{T} = \mathbf{0}, \tag{34}$$

$$\operatorname{div}\operatorname{grad}\xi + \frac{1}{l_{op}^2}\xi = \frac{1}{l_{op}^2}\xi_0, \tag{35}$$

$$\mathbf{E} = \frac{1}{2}(\operatorname{grad}\mathbf{u} + \operatorname{grad}^{\mathsf{T}}\mathbf{u}), \tag{36}$$

$$\mathbf{T} = [3\lambda\overset{4}{\mathbf{I}}^{\mathrm{sph}} + 2\mu(\xi)\overset{4}{\mathbf{I}}]\colon\mathbf{E}. \tag{37}$$

For dimensional reasons in Eq. (35), it becomes obvious that l_{op} really represents an internal length. As can been seen in the equations, the coupling mechanism between macro- and microscale is formulated in the constitutive modeling only via the material function $\mu(\xi)$. Furthermore, the coupling is in one direction only. Both facts make this model appealing.

So far, nothing has been said about the material function $\mu(\xi)$ itself. The purpose of the function is to interpolate the shear modulus depending on the order-parameter ξ. For the sake of simplicity, we assume a linear interpolation between two extreme values of the shear modulus μ_1 and μ_2, i.e.

$$\mu(\xi) = (1-\xi)\mu_1 + \xi\mu_2. \tag{38}$$

Due to the construction of (35), we have requirements on the values of ξ_0, μ_1 and μ_2. Presuming that the boundary values for ξ are either 0 or 1, the values μ_1 and μ_2 reflect the shear moduli, if the influence of a free or a fixed boundary, respectively, dominates the shear modulus. Moreover, the value of μ at ξ_0 has to match the shear modulus in case the influence of the boundaries is negligible.

2.2 The Micro-Polar Model

Without derivation, the equations of the micro-polar model used in this article are given as

$$\mathrm{div}\mathbf{T} = \mathbf{0}, \tag{39}$$

$$\mathrm{div}\,\mathrm{grad}\boldsymbol{\varphi} + \frac{2}{l_c^2}\boldsymbol{\varphi} = \frac{1}{l_c^2}\overset{3}{\mathbf{E}}\colon \mathrm{grad}\mathbf{u}, \tag{40}$$

$$\mathbf{E} = \mathrm{grad}\mathbf{u} + \overset{3}{\mathbf{E}} \cdot \boldsymbol{\varphi}, \tag{41}$$

$$\mathbf{T} = [3\lambda\overset{4}{\mathbf{I}}^{\mathrm{sph}} + 2\mu\overset{4}{\mathbf{I}}^{\mathrm{sym}} + 2\mu_c\overset{4}{\mathbf{I}}^{\mathrm{skw}}]\colon \mathbf{E}. \tag{42}$$

Here, $\boldsymbol{\varphi}$ is the vector of microrotations, $\overset{3}{\mathbf{E}}$ is the third order permutation tensor, $\overset{4}{\mathbf{I}}^{\mathrm{sym}}$ is the fourth order tensor which projects a second order tensor on its symmetric part, $\overset{4}{\mathbf{I}}^{\mathrm{sym}} = \frac{1}{2}(\overset{4}{\mathbf{I}} + \overset{4}{\bar{\mathbf{I}}})$, $\overset{4}{\mathbf{I}}^{\mathrm{skw}}$ is the fourth order tensor which projects a second order tensor on its skew-symmetric part, $\overset{4}{\mathbf{I}}^{\mathrm{skw}} = \frac{1}{2}(\overset{4}{\mathbf{I}} - \overset{4}{\bar{\mathbf{I}}})$, and $\overset{4}{\bar{\mathbf{I}}}$ is the fourth order tensor which projects a second order tensor on its transpose, $\overset{4}{\bar{\mathbf{I}}} = [(\mathbf{I} \otimes \mathbf{I})^{23}{}^{\mathsf{T}}]^{24}{}^{\mathsf{T}}$.

2.3 Comparing the Models

There are some differences but also some similarities between the order-parameter model, Eqs. (34)–(37) and Eq. (38), and the micro-polar model, Eqs. (39)–(42). A first difference is in the underlying kinematics. While in the order-parameter model small strain kinematics is assumed, Eq. (36), in the micro-polar model the microrotations $\boldsymbol{\varphi}$ are introduced into the strain $\mathbf{E}$. Hence, the strain is no longer a symmetric tensor in the micro-polar model.

Due to the skew-symmetric parts of the strain, the Cauchy stress tensor in the micro-polar model has skew-symmetric parts too. This is a second difference. In fact, the constitutive equation for the Cauchy stress tensor is especially extended with the skew-symmetric part, Eq. (41). In the order-parameter model on the other hand, the constitutive equation for the Cauchy stress tensor still has no skew-symmetric parts, but is changed in the way, that the Lamé parameter μ is no longer a constant but a function of the order-parameter ξ,, Eq. (37).

The constitutive equation for the order-parameter model, Eq. (35), and the balance of moment of momentum in the micro-polar model, Eq. (41), show at least on the left-hand-side of the equations a structural similarity. Indeed, Capriz [5] showed that both models can be derived from the same general mathematical setting. However,

the crucial difference of both equations lies on the right-hand-side. Namely, the right-hand-side of Eq. (41) is the continuum rotation and, hence, the solution of the microrotations $\boldsymbol{\varphi}$ becomes the continuum rotation in areas where the influence from boundary effects vanish. This inherits two consequences. First, the physical interpretation of $\boldsymbol{\varphi}$ as a rotational vector is strengthened and second, the micro-polar model is fully coupled. In contrast, the order-parameter model is coupled in only one direction via the constitutive equation of the Cauchy stress tensor. Moreover, there is no reason to interpret the order-parameter ξ as a rotation, or, more generally, as a kinematic quantity at all.

2.4 Interpretation of the Order-Parameter

After the order-parameter has been identified to be *not* a kinematic quantity, the question arises, whether there is a physical interpretation for this additional field. The authors suggest having the explanation of the weakening size effect by Tekoğlu and Onck [20] in mind, that the order-parameter might be interpreted as a kind of measure related to the connectivity of the nodes in the microstructure. For a node on the fixed boundary, an arbitrary value of 6 is assumed representing the clamping condition.

A simple microstructure is shown on the left of Fig. 2. On the r.h.s. of the sketch, the structure is fixed and the beam tips cannot move at all. On the top, bottom and the l.h.s., there are free boundaries and the beam tips have only one kinematic restriction due to only one neighboring node. Counting the mean number of neighboring nodes for each node position in z-direction leads to a mean connectivity curve as is shown in Fig. 2 on the right. As an example, the second node position in Fig. 2 has 4 nodes with connectivity $p_{con} = 4$ and 2 bar tips, one at top and one at bottom, with connectivity $p_{con} = 1$. Hence, the mean value at this position is 3.

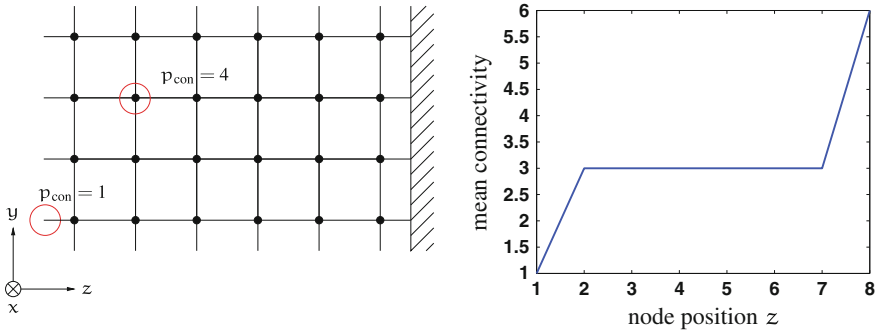

Fig. 2 Simple microstructure and its mean connectivity curve in z-direction

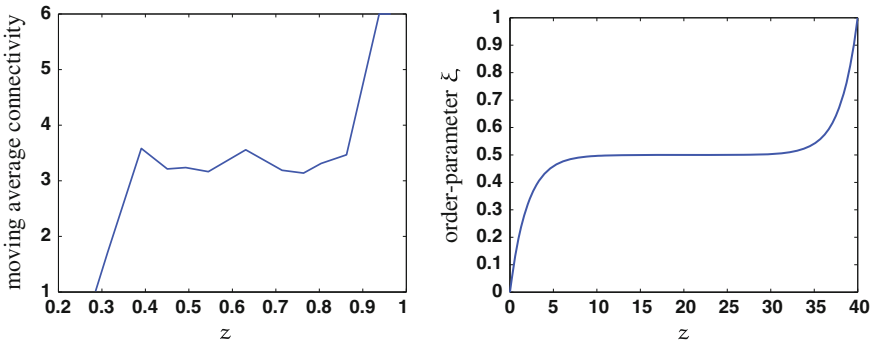

Fig. 3 Moving average of the connectivity of a real microstructure and the solution of the 1D order-parameter model for $l_{op} = 2\,\text{mm}$ and $\xi_0 = 0.5$

For real materials, a similar curve can be obtained by using a moving average along the z-direction. The result for one such a microstructure is shown on the left of Fig. 3. On the right of this figure, the result for the 1D order-parameter equation with $l_{op} = 2\,\text{mm}$ and $\xi_0 = 0.5$ is shown. Comparing both reveals striking similarities. Hence, the authors suggest to take the order-parameter in this model as a measure for the connectivity of the nodes in the microstructure, with $\xi = 0$ relates to free boundaries and $\xi = 1$ to fixed boundaries without any translational or rotational degree of freedom.

3 Simulation of the Order-Parameter Model

The order-parameter model is well suited for the Finite Element Method as solving tool. In the following, the pertinent FE formulation of the model is educed and, furthermore, a parameter study and a parameter identification is presented. The parameter study will provide insight into how the model parameter effects the results, the parameter identification will prove the usability of the model.

The simulations have been coded in the open-source C++ program library deal.ii [3, 4], the parameter identifications were performed with the MATLAB Global Optimization Toolbox [13]. However, if not stated different in the text, Table 1 gives the parameter values used in the simulations.

Table 1 Default parameter values in the simulations

λ [MPa]	μ_1 [MPa]	μ_2 [MPa]	l_{op} [mm]	ξ_0	$h:l$
28.71	5.5123	23.091	1.2915	0.62249	1:10

3.1 Finite Element Formulation

To obtain the FE formulation, the weak form of the problem has to be established first. For a domain Ω with boundary $\Gamma = \partial\Omega$, we have the primary variables $\mathbf{u} \in \mathbf{U}$ and $\xi \in \mathbf{P}$ with $\mathbf{U}, \mathbf{P}$ proper spaces. The boundary Γ can be split with respect to the primary variables into two independent Dirichlet and Neumann parts, such that $\Gamma_D^u \cup \Gamma_N^u = \Gamma = \Gamma_D^\xi \cup \Gamma_N^\xi$ and $\Gamma_D^u \cap \Gamma_N^u = \emptyset$, $\Gamma_D^\xi \cap \Gamma_N^\xi = \emptyset$ holds. The weak form pertinent to the Eqs. (34)–(37) and (38) reads

$$a_u(\mathbf{u}, \xi; \delta\mathbf{u}) = l_u(\delta\mathbf{u}) \quad \forall\, \delta\mathbf{u} \in \{\delta\mathbf{u} \in \mathbf{U} | \, \delta\mathbf{u} = 0 \text{ on } \Gamma_{\mathbf{D}}^u\}, \tag{43}$$

$$a_\xi(\xi; \delta\xi) = l_\xi(\delta\xi) \quad \forall \{\delta\xi \in \mathbf{P} | \, \delta\xi = 0 \text{ on } \Gamma_{\mathbf{D}}^\xi\}, \tag{44}$$

$$\mathbf{u} = \mathbf{g}_u \text{ on } \Gamma_{\mathbf{D}}^u, \tag{45}$$

$$\xi = g_\xi \text{ on } \Gamma_{\mathbf{D}}^\xi, \tag{46}$$

with

$$a_u(\mathbf{u}, \xi; \delta\mathbf{u}) = \int_\Omega \operatorname{grad}\delta\mathbf{u} : \mathbf{T}\, d\Omega, \tag{47}$$

$$a_\xi(\xi; \delta\xi) = \int_\Omega \left(\operatorname{grad}\delta\xi \cdot \operatorname{grad}\xi + \frac{1}{l_{op}^2}\delta\xi\,\xi \right) d\Omega, \tag{48}$$

$$l_u(\delta\mathbf{u}) = \int_{\Gamma_N^u} \delta\mathbf{u} \cdot \mathbf{t}\, d\Gamma, \tag{49}$$

$$l_\xi(\delta\xi) = \int_\Omega \frac{1}{l_{op}^2}\delta\xi\,\xi_0\, d\Omega + \int_{\Gamma_N^\xi} \delta\xi\, q\, d\Omega, \tag{50}$$

where the Cauchy assumption holds, i.e. $\mathbf{t} = \mathbf{T} \cdot \mathbf{n}$, with $\mathbf{n}$ as the normal at the boundary. Moreover, q is the flux of the order-parameter over the boundary, and

$$\mathbf{E} = \frac{1}{2}(\operatorname{grad}\mathbf{u} + \operatorname{grad}^T\mathbf{u}), \tag{51}$$

$$\mathbf{T} = [3\lambda \overset{4}{\mathbf{I}}^{sph} + 2\mu(\xi)\overset{4}{\mathbf{I}}] : \mathbf{E}, \tag{52}$$

$$\mu(\xi) = (1 - \xi)\mu_1 + \xi\mu_2. \tag{53}$$

A Newton-Raphson scheme has been utilized to solve Eqs. (43)–(46). Therefore, residuals $\mathbf{R}_u$ and R_ξ were introduced as

$$\mathbf{R}_u = a_u(\mathbf{u}, \xi; \delta\mathbf{u}) - l_u(\delta\mathbf{u}), \tag{54}$$

$$\mathbf{R}_z = a_\xi(\xi; \delta\xi) - l_\xi(\delta\xi). \tag{55}$$

The iteration scheme reads then

$$\begin{pmatrix} \mathbf{u} \\ \xi \end{pmatrix}_{k+1} = \begin{pmatrix} \mathbf{u} \\ \xi \end{pmatrix}_{k} + \begin{pmatrix} d\mathbf{u} \\ d\xi \end{pmatrix}, \tag{56}$$

$$\begin{pmatrix} d\mathbf{u} \\ d\xi \end{pmatrix} = \begin{pmatrix} \frac{\partial \mathbf{R}_u}{\partial \mathbf{u}} & \frac{\partial \mathbf{R}_u}{\partial \xi} \\ \frac{\partial \mathbf{R}_\xi}{\partial \mathbf{u}} & \frac{\partial \mathbf{R}_\xi}{\partial \xi} \end{pmatrix}^{-1}_{k} \cdot \begin{pmatrix} \mathbf{R}_u \\ \mathbf{R}_\xi \end{pmatrix}_{k}, \tag{57}$$

where k is the iteration index. To calculate the update, tangent forms with respect to the Cauchy stress are needed. These are

$$\frac{\partial \mathbf{T}}{\partial \mathbf{E}} = 3\lambda \overset{4}{\mathbf{I}}^{\text{sph}} + 2\mu(\xi) \overset{4}{\mathbf{I}}, \tag{58}$$

$$\frac{\partial \mathbf{T}}{\partial \xi} = 2(\mu_2 - \mu_1) \overset{4}{\mathbf{I}} : \mathbf{E}. \tag{59}$$

Finally, the FE formulation is obtained through the approximation of the displacement and order-parameter field as

$$\mathbf{u}(\mathbf{x}) = \sum_{l=1}^{\text{NVAR}_u} \mathbf{N}_l^{(u)}(\mathbf{x}) \bar{\mathbf{u}}_l, \tag{60}$$

$$\xi(\mathbf{x}) = \sum_{l=1}^{\text{NVAR}_\xi} \mathbf{N}_l^{(\xi)}(\mathbf{x}) \bar{\xi}_l, \tag{61}$$

where NVAR_u and NVAR_ξ represent the number of nodal variables of the respective field, $\mathbf{N}_l^{(u)}$ and $\mathbf{N}_l^{(\xi)}$ are basis functions associated with each nodal variable $\bar{\mathbf{u}}$ and $\bar{\xi}$. Utilizing the approximations in Eqs. (54)–(57) gives the FE formulation.

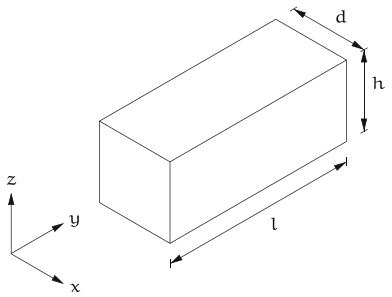

Fig. 4 Geometry of the specimen for the simulations

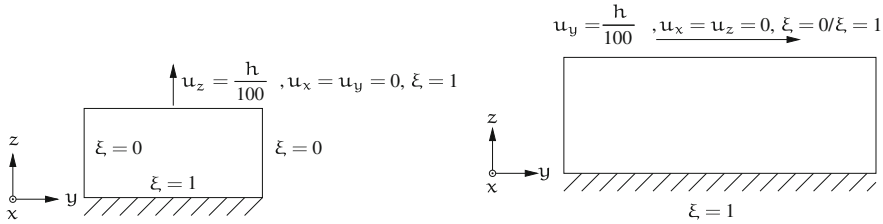

Fig. 5 Boundary values for the tension test (*left*) and the simple shear test (*right*)

3.2 Parameter Study

A simple shear test is utilized to show the effects of the different model parameters. The tests have been performed with rectangular prisms of different lengths l, heights h and depths d, cf. Fig. 4. Even though the height and the length are different for the different specimens, the depth was always equal to the height and the length to height ratio was kept constant. The pertinent boundary values were as given in Fig. 5, i.e. the placement is fixed and the order-parameter is set to $\xi = 1$ at the bottom. At the top, the displacement in x and z direction equals zero, while the displacement in y-direction is set to 1 % of the height, i.e. $u_y = \frac{h}{100}$. The order-parameter is set to $\xi = 0$ at the top of the specimens. Note that $\xi = 1$ at the bottom represents the fully clamped boundary with maximum local stiffness. But $\xi = 0$ at the top is inconsistent with the proposed interpretation of ξ. However, this inconsistency is used only in the parameter study to elucidate the influence of the parameters more clearly. In later parameter identification this value is set to $\xi = 1$ in accordance to the interpretation. No Dirichlet values were set on the 4 remaining sides. If not stated differently in the following paragraphs, the geometry and material parameters used were as is given in Table 1.

First, the size of the specimen has been varied to verify, whether the size effects are reproduced at all. In Fig. 6 on the left side, the results of simulations of specimens of height $h \in \{20, 80, 140, 200\,\text{mm}\}$ are shown. The height to length ratio 1 : 10 has

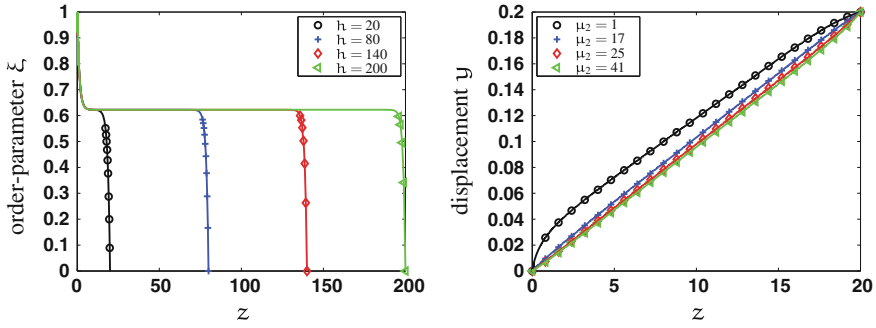

Fig. 6 *Left* order-parameter for specimens of different heights h in [mm]. *Right* displacement u for a specimen of height 20 mm and different μ_2 values in [MPa] ($\mu_1 = 21$ MPa)

been held constant. The remaining parameter were as in Table 1. As can be seen in the figure, the size and the shape of the solution ξ near the boundaries are the same for the different specimens, but the location of the top boundary shifts due to the different heights. Hence, the height of the specimen does not primarily influence the boundaries. Nevertheless, if the distance between two boundaries becomes too small, they will influence each other.

Next, the shear modulus μ_2 has been varied. While $\mu_1 = 21$ MPa has been held fixed, μ_2 takes the values $\mu_2 \in \{1, 13, 29, 41\,\text{MPa}\}$. The other parameters are as given in Table 1. As follows from Eq. 38, a change in μ_2 influences the whole material response due to a change in the material stiffness. The influence becomes larger as $\xi \to 1$. In this example, the bottom boundary ($z = 0$ mm) is affected by the value μ_2, while the top boundary ($z = 20$ mm) is affected by μ_1. This means, if $\mu_1 \leqslant \mu_2$ holds, then the bottom boundary layer responses stiffer than the bulk and the top boundary layer responds softer than the bulk. If $\mu_1 \geqslant \mu_2$, than the situation is vice versa. On the right side of Fig. 6, the displacement in shear direction over the height for different μ_2 values is shown. The solution of the order-parameter ξ does not depend on the value of the shear modulus.

The third parameter investigated is l_{op}. A look at the limits $\mathrm{l}_{\mathrm{op}} \to 0$ and $\mathrm{l}_{\mathrm{op}} \to \infty$, resp., in Eq. 35 reveals, that in the first case, i.e. $\mathrm{l}_{\mathrm{op}} \to 0$, follows $\xi = \xi_0$ in the interior. In the second case, $\mathrm{l}_{\mathrm{op}} \to \infty$, it follows that $\operatorname{div} \operatorname{grad} \xi = 0$. Since, in the general, the second derivatives in the coordinate directions are not linearly dependent, it follows further that $\operatorname{grad} \xi = \mathbf{const}$. This means, the solution of ξ at different values of the parameter l_{op} is situated between $\xi = \xi_0$ and $\operatorname{grad} \xi = \mathbf{const}$. The left picture in Fig. 7 visualizes this result. The figure shows, that the parameter l_{op} has influence on the shape and the size of the boundary effect.

Finally, the parameter ξ_0 has been considered. As the picture on the right of Fig. 7 shows, the parameter allows to control the values of ξ far away from the boundaries. In fact, $\xi = \xi_0$ holds where the boundary effects are negligible. Hence, the parameter ξ_0, together with the particular choice of the material function of the shear modulus (38), affects the stiffness of the bulk away from the boundaries. Additionally, the

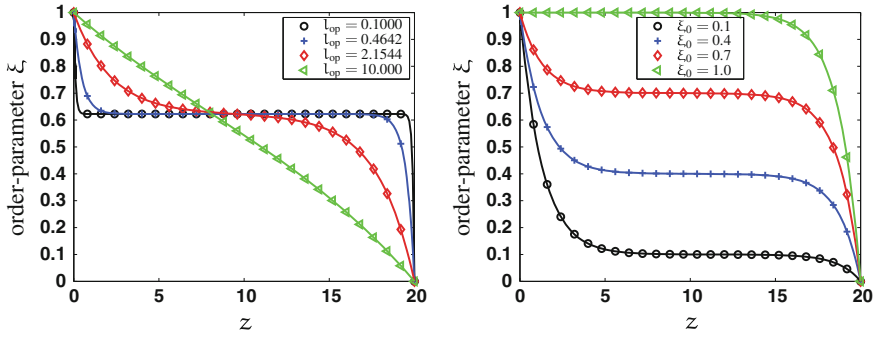

Fig. 7 Order-parameter ξ for a specimen of height 20 mm and different l_{op} values in [mm] (*left*) and different ξ_0 values (*right*)

actual choice of ξ_0 influences the size of the areas of influence of the boundary effects. Here, for values $\xi_0 \to 1$ the bottom boundary layer disappears, for values $\xi_0 \to 0$ the top boundary layer vanishes.

3.3 Parameter Identification

For the simple shear experiment introduced in the section above, a parameter study has been carried out for both, the order-parameter model and the micro-polar model. The pertinent reference data for the parameter identification has been taken from virtual experiments on a micro-structural model, which has been solved using the solver RADIOSS [15]. The micro-structural model is set up based on a stochastically disturbed Weaire-Phelan structure [22]. The parameter λ has been determined by a separate compression test without investigation of the size effect. This is done, because the parameter λ is not activated in simple shear. The other parameters have been identified with a genetic algorithm solver in MatLab [13]. The obtained material parameters are given in Tables 2 and 3.

Figure 8 shows the progress of μ_{eff} obtained from the identified parameters for specimen with heights between 20 and 160 mm. On the left of the figure, the curves for the order-parameter model (triangles) and the micro-polar model (+ sign) are given as well as the reference solutions of the micro-structural model (circles). Both models, micro-polar and order-parameter, capture the reference solutions well. This is verified on the right of the figure, where the relative error with respect to the reference solution is illustrated. The micro-polar model seems to fit the data slightly better than the order-parameter model. However, the relative error of both models is of the order 10^{-3}.

Besides the simple shear test, a parameter identification of the order-parameter model for a tension test has been performed. Here, the height of the specimen has been varied, $h \in \{40, 80, 160, 220, 320, 420\,\text{mm}\}$, while the height to length ratio has been held constant as 1:1. The parameters λ, α and l_{op} were taken from the simple shear test, μ_1 and μ_2 has been identified. Since the micro-polar model is not able to reproduce the weakening size effect, no parameter identification has been carried out

Table 2 Identified material parameters of the order-parameter model for the simple shear test

λ [MPa]	μ_1 [MPa]	μ_2 [MPa]	l_{op} [mm]	ξ_0
28.71	5.5123	23.091	3.2056	0.62249

Table 3 Identified material parameters of the micro-polar model for the simple shear test

λ [MPa]	μ [MPa]	μ_c [MPa]	l_c [mm]
28.71	16.53	12.257	4.323

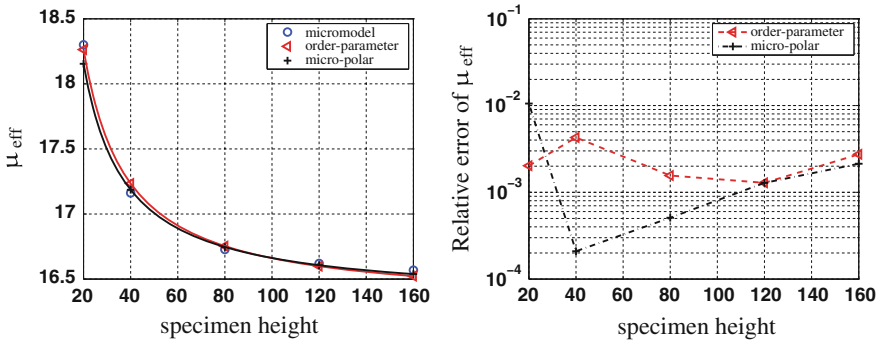

Fig. 8 Parameter identification on a simple shear test. *Left* solution of μ_{eff} w.r.t. the identified set of parameters for specimen heights between 20 mm and 160 mm and a constant height to length ratio. *Right* relative error of μ_{eff} with respect to the micro-structural solution

Table 4 Identified material parameters of the order-parameter model for the tension test

λ [MPa]	μ_1 [MPa]	μ_2 [MPa]	l_{op} [mm]	ξ_0
28.71	2.5	38.5	3.2056	0.62249

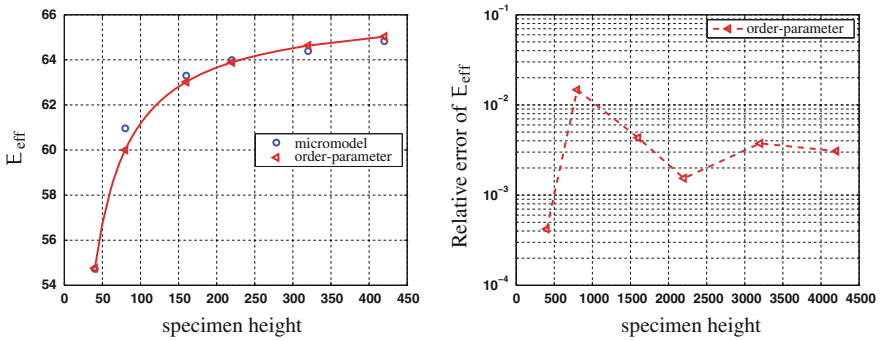

Fig. 9 Parameter identification on a tension test. *Left* solution of E_{eff} w.r.t. the identified set of parameters for specimen heights between 20 mm and 420 mm and a constant height to length ratio of 1:1. *Right* relative error of E_{eff} with respect to the micro-structural solution

for this model. The left picture in Fig. 9 shows the curve for the identified material parameters, which are given in Table 4. The relative error at the reference points is of the order 10^{-3}, cf. the right picture of Fig. 9. The example verifies, that the proposed order-parameter approach is able to model the weakening size effect.

4 Conclusions

In this contribution, a thermodynamically consistent order-parameter model for open-cell foams has been proposed which is primarily based on the work of Steeb and Diebels [17]. The order-parameter model is an extended continuum model. In more detail, it is a classical Boltzmann continuum extended by one additional scalar field. For the additional scalar field, the authors suggested to interpret it as a kind of measure for the connectivity of the nodes in the open-cell foam. A parameter study has been performed before a parameter identification has been carried out. The parameter study showed the flexibility of the proposed model with respect to weakening and stiffening size effects. In fact, the order-parameter model is able to render both types of size effect. This is of special interest, since micro-polar models, e.g., lack this feature. Even though micro-polar models can be extended to catch this phenomenon, it is exactly this what gives the proposed model its main strength. The order-parameter model shows a simplicity in its equations compared to other extended continuum models which makes it especially appealing.

References

1. Andrews, E., Sanders, W., Gibson, L.J.: Compressive and tensile behaviour of aluminum foams. Mat. Sci. Eng. A-Struct. **270**, 113–124 (1999)
2. Andrews, E.W., Gioux, G., Onck, P.R., Gibson, L.J.: Size effects in cellular solids. Part II: experimental results. Int. J. Mech. Sci. **43**, 701–713 (2001)
3. Bangerth, W., Hartmann, R., Kanschat, G.: deal.II—a general purpose object oriented finite element library. ACM Trans. Math. Softw. **33**, 24/1–24/27 (2007)
4. Bangerth, W., Heister, T., Kanschat, G.: deal.II Differential equations analysis library. Technical reference. http://www.dealii.org
5. Capriz, G.: Continua with Microstructure. Springer, Heidelberg (1989)
6. Cosserat, E., Cosserat, F., Brocato, M., Chatzis, K.: Théorie des corps déformables. A. Hermann, Paris (1909)
7. Diebels, S., Steeb, H.: The size effect in foams and its theoretical and numerical investigation. Proc. R. Soc. A **458**, 2869–2883 (2002)
8. Diebels, S., Johlitz, M., Steeb, H., Chatzouridou, A., Batal, J., Possart, W.: A continuum-based model capturing size effects in polymer bonds. J. Phys. **62**, 34–42 (2007)
9. Diebels, S., Geringer, A.: Modelling inhomogeneous mechanical properties in adhesive bonds. J. Adhes. **88**, 924–940 (2012)
10. Eringen, C.: Microcontinuum Field Theories: I. Foundations and Solids. Springer, Heidelberg (1999)
11. Hutter, K., Jöhnk, K.: Continuum Methods of Physical Modeling. Springer, Heidelberg (2004)
12. Lakes, R.S.: Size effects and micromechanics of a porous solid. J. Mater. Sci. **18**, 2572–2580 (1983)
13. MatLab. Version 7.14.0.739 (R2012a). The MathWorks Inc. Natick, Massachusetts (2012)
14. Onck, P.R., Andrews, E.W., Gibson, L.J.: Size effects in cellular solids. Part I: modeling. Int. J. Mech. Sci. **43**, 681–699 (2001)
15. Radioss. Version 11.0. Altair Engineering Inc. Troy, Michigan (2012)
16. Steeb, H., Diebels, S.: Modeling thin films applying an extended continuum theory based on a scalar-valued order parameter: Part I: isothermal case. Int. J. Solids Struct. **41**, 5071–5085 (2004)

17. Steeb, H., Diebels, S.: Continua with affine microstructure: theoretical aspects and applications. Proc. Appl. Math. Mech. **5**, 319–320 (2005)
18. Svendsen, B.: On the thermodynamics of thermoelastic materials with additional scalar degrees of freedom. Continuum Mech. Therm. **4**, 247–262 (1999)
19. Tekoğlu, C.: Size effects in cellular solids. Doctoral thesis, University of Groningen(2007)
20. Tekoğlu, C., Onck, P.R.: Size effects in the mechanical behavior of cellular materials. J. Mater. Sci. **41**, 5911–5917 (2005)
21. Tekoğlu, C., Onck, P.R.: Size effects in two-dimensional voronoi foams: a comparison between generalized continua and discrete models. J. Mech. Phys. Solids. **56**, 3541–3564 (2008)
22. Weaire, D., Phelan, R.: A counter-example to kelvin's conjecture on minimal surfaces. Phil. Mag. Lett. **69**, 107–110 (1994)

Measuring Material Coefficients of Higher Gradient Elasticity by Using AFM Techniques and Raman-Spectroscopy

Christian Liebold and Wolfgang H. Müller

Abstract Experiments on micro-specimens have shown that the deformation behavior of materials can be size dependent. The size dependence is, for example, reflected in a stiffer elastic response on the sub-microscale. A quantitative understanding of the size effect is important for the design of micro- and nanosize systems. In our paper higher-order theories of elasticity are used for the description of the bending behavior of micro-beams. These include additional material parameters in order to describe a size effect and they go beyond the limits of the classical Boltzmann continuum. In particular couple stress and strain gradient theory of linear elasticity are used in this work as special examples of higher gradient theories. Another objective of the paper is to determine the length scale parameters by measurements performed with extremely small cantilever beams. In particular, deflection measurements are performed and force data are recorded for submicron beams made of silicon and silicon nitride. The tests are performed by using a highly sensitive atomic force microscope. In addition Raman spectroscopy is used for the same purpose. The obtained data is fitted to the formulae of higher elasticity for the bending of slender beams and can be used for evaluation of higher gradient coefficients.

1 Introduction

Experiments have shown that the deformation behavior of materials can be size dependent at very small scales. An example of a size effect in sub-micron structures is their stiffer response to external forces. Clearly, knowing and quantifying such effects

C. Liebold · W. H. Müller (✉)
TU Berlin, Institut für Mechanik, Lehrstuhl für Kontinuumsmechanik und Materialtheorie,
Einsteinufer 5,10587 Berlin, Germany
e-mail: wolfgang.h.mueller@tu-berlin.de

C. Liebold
e-mail: christian.liebold@tu-berlin.de

H. Altenbach et al. (eds.), *Generalized Continua as Models for Materials*,
Advanced Structured Materials 22, DOI: 10.1007/978-3-642-36394-8_14,

is of great importance during the design phase of micro- and nanosize systems which includes modeling, e.g., with the finite element method. In order to achieve this, the material parameters characteristic of the size effect must be known, and these can only be obtained experimentally. The first observations of a different deformation behavior at the microscale were found during plastic deformation of some metals and polymers [14, 27, 29]. Fleck et al. observed an increase in torsional hardening of thin copper wires by a factor of three as the diameter of the wires decreased from 170 to 12 μm [13]. Ma et al. observed an increase of indentation hardness of monocrystalline silver by a factor of more than two as the penetration depth of the indenter decreased from 2.0 to 0.1 μm [22]. A few years ago Lam et al. observed an increase of bending rigidity, even in elastically reversible micro-beam bending tests on epoxy [21]. The bending rigidities were about 2.4 times larger than predicted by conventional theory as the beam thicknesses decreased from 50 to 12.5 μm. In 2004 and 2005 McFarland et al. measured similar deviations in stiffness of polypropylene micro-cantilevers bent in the range of linear elasticity [23] and [24].

Conventional mechanics on the basis of the Boltzmann (or Cauchy-) continuum fails to predict the size effect. Since the Cosserats introduced the idea of "point couples" [7] in 1909 the so-called micropolar continuum theories of Toupin [30], Mindlin and Tiersten [25], Koiter [18], Eringen [11] started to develop. A more detailed history of origin of micropolar theories is given in Altenbach et al. [1]. The main presumption in the present work is that every material point of a body can be interpreted as a *particle*, which is able to undertake a micro-rotation as well as a macro-translation. With this notion we uncouple the balance of angular momentum from linear momentum. Indeed, this had been anticipated in the very early days of mechanics by Euler, Bernoulli, or Lagrange in the middle of the 18th century [31]. The additional degree of freedom is reflected in an extension of the balance laws for angular momentum of conventional mechanics. It will form the starting point of this paper. To consider extended strain measures for rotations higher order derivatives of displacements will be introduced and interpreted as special parts of the strain gradient. Additional constitutive equations will be required in order to connect the higher order stress-strain measures. Up to now, different strain gradient theories have been developed to handle the size effect. Even so-called *methods of size effects* have been defined in terms of a better experimental access to these constitutive equations [20]. One of these methods will be used here and another one will be introduced: In addition to the determination of bending rigidities by means of force-deflection measurements on beams of decreasing thickness, Raman spectroscopy will be used as a tool that, in general, allows for a determination of bending rigidities by means of force-strain measurements. By taking the second derivatives of displacements into account these theories contradict the principle of local action and the restriction to simple bodies, since the finite neighborhood influences the deformation behavior of the material point.

In absence of strain gradients (e.g., in uniaxial tension tests) Lam et al. have shown that the elastic behavior of epoxy is independent of the thickness of the specimens, whereas the same specimens revealed a size effect in simple beam bending tests (and thus in presence of strain *gradients*) [21].

In this paper the size effect of single crystalline silicon and silicon nitride beams will be investigated experimentally. Simple beam bending tests for determining bending rigidities are performed following the corresponding experimental method of size effect. AFM bending experiments as well as Raman spectroscopy reveal strains and forces acting in and on such beams.

2 Theory

2.1 Balance Laws and Stored Energy Density of Couple Stress Theory

In this paper the couple stress theory is formulated as a special case of the Cosserat theory (cf., e.g., [17, 20]). An expression for the stored energy density will be derived from the extended balances of rational mechanics. In this approach it is assumed that a material point can be treated like a small rigid body, i.e., a local point but with an additional degree of freedom, namely rotation. This single point is situated in the center of mass of the so-called particle. The question if there is a measurable dilatation of the particle will not be examined here. By applying the principle of virtual work formulae for the deflection, the strain, and the flexural rigidity for a clamped beam on the basis of the Euler Bernoulli beam theory will be derived. The generalized strain measures for small deformations in a micropolar medium are defined by two independent fields: displacement u_i and micro rotation φ_i. By distinguishing macroscopic and intrinsic rotations the balance of angular momentum becomes an independent conserved quantity in terms of superposition of the moment of momentum, $\mathbf{x} \times \mathbf{v}$, and the spin, $\mathbf{s}$, [11, 31]. This becomes evident when examined in context with a general form of a balance equation without production terms [26]. Following the summation convention on repeated indices and applying Gauss' theorem to the surface integral the balance of *angular momentum* reads:

$$\begin{aligned} \frac{\mathrm{d}}{\mathrm{d}t} \overbrace{\int_M \left(\epsilon_{ijk} x_j v_k + s_i\right) \mathrm{d}m}^{\text{total angular momentum}} &= \overbrace{\oint_{\partial V} n_l \left(\epsilon_{ijk} x_j \sigma_{lk} + \mu_{li}\right) \mathrm{d}A}^{\text{flux}} \\ &\quad + \overbrace{\int_V \left(\rho \epsilon_{ijk} x_j f_k + \rho l_i\right) \mathrm{d}V}^{\text{supply}} \\ \epsilon_{ijk} x_j \underbrace{\left[\rho \dot{v}_k - \sigma_{lk,l} - \rho f_k\right]}_{\text{balance of momentum=0}} &= \underbrace{\left[-\rho \dot{s}_i + \mu_{li,l} + \rho l_i + \epsilon_{ikl} \sigma_{kl}\right]}_{\text{balance of spin=0}}, \end{aligned} \tag{1}$$

where σ_{kl} and μ_{li} represent the stress and the couple stress tensor, and f_i and l_i denote the body forces and the body couples, respectively. The expression $\frac{1}{2}\epsilon_{ikl}\sigma_{kl} = e_i$

represents the axial vector of the stress tensor and involves the non-symmetric part of σ_{kl}. This term contributes to the balance of spin as a production of spin. Yang et al. investigated the static case when the *moment of couples* vanishes [15]:

$$\frac{\mathrm{d}}{\mathrm{d}t}\int_M \epsilon_{ijk}x_j s_k \mathrm{d}m = \overbrace{\oint_{\partial V}\epsilon_{ijk}x_j n_l \mu_{lk}\mathrm{d}A}^{\text{flux}} + \overbrace{\int_V \rho\epsilon_{ijk}x_j l_k \mathrm{d}V}^{\text{supply}} + \overbrace{\int_V \epsilon_{ijk}x_j \epsilon_{klm}\sigma_{lm}\mathrm{d}V}^{\text{production}} = 0,$$
$$\epsilon_{ijk}x_j \underbrace{\left[\mu_{lk,l} + \rho l_k + \epsilon_{klm}\sigma_{lm}\right]}_{\text{balance of spin=0}} + \epsilon_{ilk}\mu_{lk} = 0\,. \tag{2}$$

This leads to the symmetry of the couple stress tensor. The *total kinetic energy* for the particles, which are considered as rigid bodies, reads in a local formulation:

$$\frac{\rho}{2}v_i v_i = \frac{\rho}{2}v_i^{\mathrm{c}} v_i^{\mathrm{c}} + \frac{\rho}{2}\dot{\varphi}_l \theta_{li}\dot{\varphi}_i\,, \tag{3}$$

where v^{c} is the velocity of the center of mass of the particle, and θ_{li} is the (constant) specific moment of inertia of the particle. The spin of the particle is represented by the term: $\dot{\varphi}_l\theta_{li} = s_i$. We make use of the symmetric part of the gradient of displacements for *small deformations*, $\epsilon_{ij} = \frac{1}{2}\left(u_{i,j} + u_{j,i}\right)$, and introduce the symmetric gradient of rotation by:

$$\chi_{ij} = \frac{1}{2}\left(\varphi_{i,j} + \varphi_{j,i}\right) \quad , \quad \chi_{ij} = -\frac{1}{4}\left(\epsilon_{ilk}u_{l,kj} + \epsilon_{jlk}u_{l,ki}\right) \tag{4}$$

with

$$\varphi_l = -\frac{1}{2}\epsilon_{lij}u_{i,j}\,,$$

where φ_l is the rotation vector resulting from a rotation of the gradient of displacements. The non-local character of this higher order strain measure can be realized by interpreting the second order derivatives of displacements in Eq. (4) as parts of a Taylor expansion in space which apparently incorporates the behavior of neighboring particles. By expanding all indices it is straightforward to realize that the trace of χ_{ij} is always zero, i.e., $\chi_{mm} \equiv 0$. This is an important result when dealing with the corresponding stress measure and new material parameters. The balance of *total kinetic*- and the *internal energy*, u, of the body without radiation reads [12]:

$$\frac{\mathrm{d}}{\mathrm{d}t}\int_M \left(\frac{\upsilon_k^{\mathrm{c}}\upsilon_k^{\mathrm{c}}}{2}+\frac{s_k\dot{\varphi}_k}{2}+u\right)\mathrm{d}m = \overbrace{\oint_{\partial V} n_l\left(\sigma_{lk}\upsilon_k^{\mathrm{c}}+\mu_{kl}\dot{\varphi}_k\right)\mathrm{d}A}^{\text{flux}} + \overbrace{\int_V \rho\left(f_k\upsilon_k^{\mathrm{c}}+l_k\dot{\varphi}_k\right)\mathrm{d}V}^{\text{supply}}$$

$$\rho\dot{u} = \upsilon_k^{\mathrm{c}}\underbrace{\left[-\rho\dot{\upsilon}_k^{\mathrm{c}}+\sigma_{lk,l}+\rho f_k\right]}_{\text{bal. of lin. momemtum=0}} + \sigma_{lk}\upsilon_{k,l}^{\mathrm{c}} + \dot{\varphi}_k\underbrace{\left[-\rho\dot{s}_k+\mu_{lk,l}+\rho l_k\right]}_{\text{balance of spin}=-\epsilon_{klm}\sigma_{lm}} + \mu_{lk}\dot{\varphi}_{k,l}\ . \tag{5}$$

The material time derivative $\left(\frac{1}{2}s_i\dot{\varphi}_i\right)^{\bullet} = \dot{s}_i\dot{\varphi}_i$ results if a constant specific moment of inertia for the particle is assumed. Furthermore, by using the vector of rotation of Eq. (4) it can be shown that only the symmetric part of the stress tensor, σ_{ij}^{S}, where $\sigma_{ij}^{\mathrm{S}} = \frac{1}{2}\left(\sigma_{ij}+\sigma_{ji}\right)$, contributes to the stored energy density. This is due to the direct coupling of the rotation of the displacement gradients to the field of rotations. The terms $\upsilon_{k,l}^{\mathrm{c}}$ and $\dot{\varphi}_{k,l}$ are approximately transformed into $\dot{\epsilon}_{kl}$, the strain rate, and into $\dot{\chi}_{kl}$, the rate of the rotation gradient, respectively. By assuming a *linear relationship* in both stress-strain measures and isothermal conditions the stored energy density, $\bar{u} = \rho u$, equals the internal energy density and is given by integration of Eq. (5):

$$\bar{u} = \frac{1}{2}\sigma_{lk}^{\mathrm{S}}\epsilon_{lk} + \frac{1}{2}\mu_{lk}\chi_{lk}\ , \tag{6}$$

For isotropic materials there are two independent material parameters, one for the spherical and one for the deviatoric part of the symmetric linear strain tensor (e.g., expressed in terms of the Lamé coefficients λ and $\mu \equiv G$, the latter being the shear modulus of engineering science). By observing the symmetry of the couple stress tensor shown in Eq. (2) and the deviatoric character of χ_{ij}, only one additional material parameter, l, is used for connecting the couple stress tensor to the rotation gradient: $\mu_{kl} = 2Gl^2\chi_{kl}$.

2.2 Euler-Bernoulli Beams Within Couple Stress Theory

2.2.1 Differential Equation of the Deflection Curve

The derivation of the deflection and the strain formulae for a bent beam in terms of the Euler-Bernoulli beam theory is straightforward: For the stress-strain relationship Hooke's law is observed. By using the coordinate system shown in Fig. 1 and by

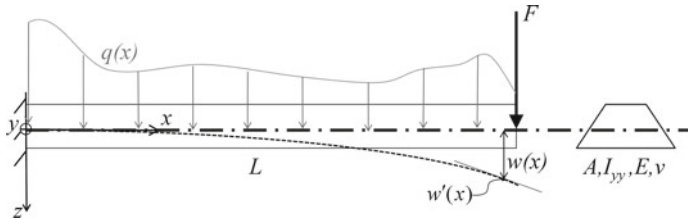

Fig. 1 Illustration of the quantities and the coordinate system used for simple beam bending

means of the following ansatz for the displacement field according to Euler and Bernoulli without a pre-deflection w_0:

$$u_x = -zw'(x) \ , \ u_y = 0 \ , \ u_z = w(x) \ , \tag{7}$$

in which a dash denotes a derivative with respect to x, the only non-vanishing components of the strain tensor, the stress tensor, the rotation gradient tensor, and the couple stress tensor read:

$$\begin{aligned} \epsilon_{xx} &= -zw''(x) \ , \ \sigma^{\mathrm{S}}_{xx} = -Ezw''(x) \ , \\ \chi_{xy} &= -\frac{1}{2}w''(x) \ , \ \mu_{xy} = -Gl^2 w''(x) \ . \end{aligned} \tag{8}$$

This describes a plane strain condition in which the Poisson ratio ν is assumed as zero. Remarkably, due to the connection of the angle of the plane cross-sections of the beam to the deflection line by assuming $\varphi(x) = w'(x)$, no additional field of rotations has to be proposed in Euler-Bernoulli beam theory (in contrast, e.g., in Timoshenko beam theory as outlined in [16]). The principle of virtual work for static deformations demands that the virtual work done by the external forces and moments equals the variation of the stored energy. By integrating Eq. (6) and by using the expressions of Eq. (8) the stored energy in variational formulation reads:

$$\delta U = Z \int_0^L w^{\mathrm{IV}} \, \delta w \mathrm{d}x - Z w''' \, \delta w \, \Big|_0^L + Z w'' \, \delta w' \Big|_0^L \ , \tag{9}$$

where Z is an abbreviation for constants of geometry and material data, more precisely: $Z = EI + \frac{1}{2}GAl^2$. If the so-called material length scale parameter l is equal to zero, Z turns into the conventional expression EI of Euler-Bernoulli beam theory. By comparing Eq. (9) to the virtual work done by the external forces and moments:

$$\delta W = \int_0^L q(x) \, \delta w \mathrm{d}x + V \, \delta w \, \Big|_0^L + M \, \delta w' \Big|_0^L \ , \tag{10}$$

the constitutive differential equation for beam bending in couple stress theory within the framework of the Euler-Bernoulli assumptions reads [19]:

$$\delta U = \delta W \quad \Rightarrow \quad \left[EI + \frac{1}{2} GAl^2 \right] w^{\mathrm{IV}}(x) = q(x) \quad , \forall x \in (0, L) \, . \tag{11}$$

The boundary conditions for forces and moments at the positions $\tilde{x} = 0$ or $\tilde{x} = L$ are $Zw'''(\tilde{x}) = -V|_{\tilde{x}}$ and $Zw''(\tilde{x}) = M|_{\tilde{x}}$, respectively.

2.2.2 Solution for a Clamped Beam

Without distributed forces $q(x)$ the ansatz with four constants:

$$Zw(x) = \frac{1}{6} C_1 x^3 + \frac{1}{2} C_2 x^2 + C_3 x + C_4 \tag{12}$$

allows us to solve the ODE in Eq. (11) of rank four. The constants $C_1, \ldots, C_4$ are determined with the following boundary conditions for a clamped beam with a single load $F = V|_L$ at its free end:

$$\begin{aligned} Zw'''(L) = -F = C_1 \quad &, \; Zw(0) = 0 = C_1 \, , \\ Zw'(0) = 0 = C_3 \quad &, \; Zw''(L) = 0 = C_1 L + C_2 \; \Rightarrow C_2 = FL \, , \end{aligned} \tag{13}$$

so that the solution for the bending curve, w^{CS}, and the strain in x-direction from Eq. (8), $\epsilon_{xx}^{\mathrm{CS}}$, derived with Couple Stress (CS) theory in context with the Euler-Bernoulli assumptions take the form:

$$\begin{aligned} w^{\mathrm{CS}}(x) &= -\frac{F}{\left(EI + \frac{1}{2} GAl^2 \right)} \left[\frac{x^3}{6} - \frac{Lx^2}{2} \right] \, , \\ \epsilon_{xx}^{\mathrm{CS}} &= z \frac{F}{\left(EI + \frac{1}{2} GAl^2 \right)} \left[x - L \right] \, . \end{aligned} \tag{14}$$

The bending rigidity D_h, which is a more or less standard measure of size effect, is obtained from the relationship between the acting force and the deflection of the point at where the force acts:

$$D_0 \left\{ 1 + \frac{3g}{(1+\nu)} \left(\frac{l^2}{t^2} \right) \right\} \frac{3 w^{\mathrm{CS}}(L)}{L^3} = F \quad , \quad \frac{D_h}{D_0} = \left\{ 1 + \frac{3g}{(1+\nu)} \left(\frac{l^2}{t^2} \right) \right\} \, . \tag{15}$$

The second moment of inertia, I, the area of the cross-sections, A, the Lamé constant, $\mu \equiv G = E/(2 + 2\nu)$, and the flexural rigidity, $D_0 = EI$, enter the equation as well as a correction factor, $g = A/(12I)$, for a potential trapezoidal

cross-section of the beam. For trapezoidal cross-sections the second moment of inertia and the area of the cross-section read:

$$I_{\mathrm{tr}} = \frac{t^3}{36}\frac{w_1^2 + 4w_1w_2 + w_2^2}{w_1 + w_2}\ ,\ A_{\mathrm{tr}} = \frac{w_1 + w_2}{2}t\ \ ,\ g = \frac{3}{2}\frac{(w_1 + w_2)^2}{w_1^2 + 4w_1w_2 + w_2^2}\ , \tag{16}$$

with w_1 and w_2 being the minor and major width. All micro-beams made of single crystalline silicon showed a trapezoidal cross-section with known minor and major width. The correction factor g varied between 1.005 and 1.035 and has negligible influence. A similar result for D_h, Eq. (15), which can be considered as a non-standard measure of size effect, results from the relationship between the acting force and the maximum strain at the fixture $\left(\epsilon_{xx}^{\mathrm{CS}}(x = 0, z = -g\frac{t}{2})\right)$. The deflection measurements have been performed using AFM techniques and the strain data has been obtained by Raman spectroscopy. It should be pointed out again that if the material length scale parameter l vanishes, the solutions of couple stress theory reduce to the conventional expressions. Evidently, the normalized bending rigidity in couple stress theory, D_h/D_0, is a function of the inverse of the square of the thickness of the micro-beam and not a constant as in conventional mechanics. Thus couple stress theory is capable of predicting a size effect in microstructures.

3 Experimental Apparatus

3.1 Atomic Force Microscopy for Deflection Measurement

Micro-beam bending tests have been performed on a laser-reflective AFM Multiview-1000 stage from Nanonics®. The deflection of the fixed AFM glass probe was observed by a Photo Sensitive Diode (PSD) system by means of a laser beam reflected from the top of the probe (cp., Fig. 2, top). The lift of the specimen, z, was realized by a calibrated screw thread driven by piezo-elements. This construction shows a resolution of about 1.0 nm in z. The deflection of the tip, $w_{\mathrm{tip}} = z - w_{\mathrm{beam}}$, was superimposed by the deflection of the micro-beam and by the lift of the specimen, z.

The calibration of the PSD data for measuring displacements and forces was performed in two steps. First, by lifting a rigid surface against the tip which connected the PSD data to the displacements of the tip in a nonlinear manner (see the discussion below) and, second, by comparing the spring constant of the AFM glass probe to a well calibrated silicon normal, tested at the Physikalisch Technische Bundesanstalt (PTB) by lifting the silicon normally to the tip. With a known spring constant, k, the force $F = kw_{\mathrm{tip}}$ could be calculated from the displacement data. The (small) nonlinearity could be fully attributed to the way of data conversion stemming from the four diode surfaces of the PSD from real intensities of the incoming laser light to a single electrical signal, U, in mV. When collecting the incoming laser light over the whole

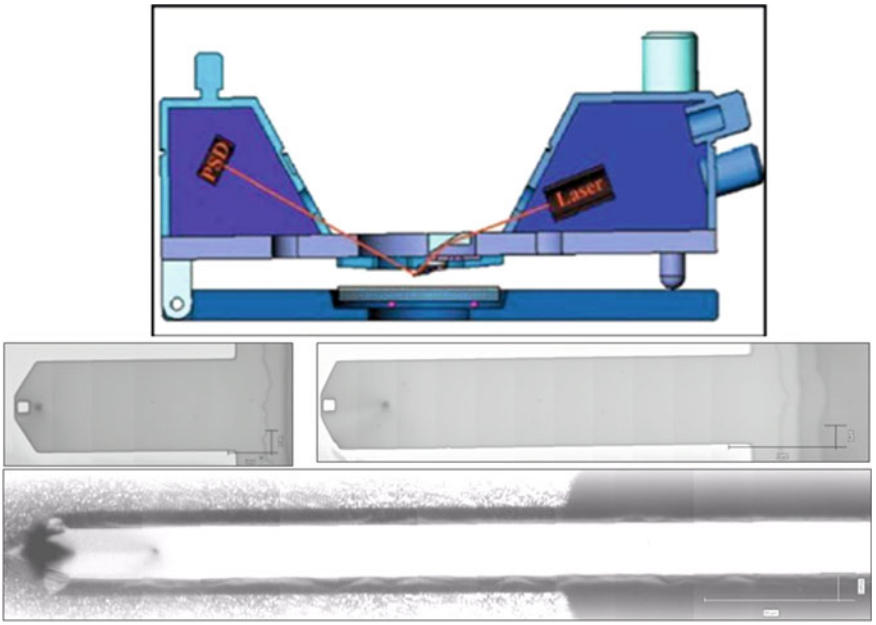

Fig. 2 Schematic of the AFM (*top*). Pictures through the optical microscope from the above of some Si- and SiN micro beams (*bottom*). The dark grey circular spots show the points of application of the force by the AFM glass probe

range of the possible tip deflections (about 35 μm) the movement of the laser beam exceeds the geometric limits of the four diode surfaces. The resulting "edge effect" vanishes only for small tip deflections. Compensation and, consequently, minimization of uncertainties became possible by assuming a quadratic target function of the form:

$$U(z) = (az + n)z \ , \ w_{\text{beam}} = z + \frac{n_{\text{rig}}}{2a_{\text{rig}}} - \sqrt{\frac{n_{\text{rig}}^2}{4a_{\text{rig}}^2} + \frac{U(z)}{a_{\text{rig}}}} \tag{17}$$

for fitting the PSD data for conversion of voltage U to displacement z. The values for a, n, a_{rig} and n_{rig} were taken from the linear regression lines of the different slopes of the bending behavior (cp., Fig. 3, right), where the subscript "rig" stands for values taken from the experiments with the tip on a rigid surface.

Measurements Made with an AFM

Experiments have been performed using 17 micro-beams as listed in Table 1. The deflection behavior $w_{\text{beam}} = w_{\text{beam}}(F)$ as a function of the force data has been evaluated analytically. The span of the beams was assigned during the experiments

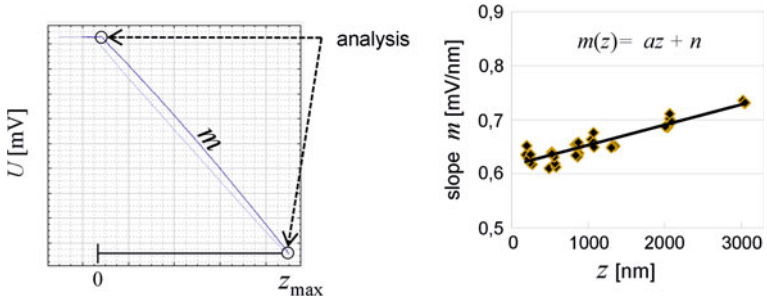

Fig. 3 Left: Illustration of the points of analysis for determination of the slope of the bending behavior in a single bending experiment; right: plot of the linear change in these slopes for increasing z lift

Table 1 List of the tested micro-beams dimensions and measured Young's moduli in comparison to literature values

Beam number	Material	t [μm]	E_{exp} [GPa]	E_{lit} [GPa]
1	silicon	6.90	166	
2	silicon	6.60	165	
3	silicon	2.97	173	
4	silicon	2.95	170	169
5	silicon	1.05	170	
6	silicon	1.05	173	
7	silicon	1.06	174	
8	silicon	1.03	171	
9	silicon nitride	0.8	375	
10	silicon nitride	0.8	383	
11	silicon nitride	0.8	300	
12	silicon nitride	0.8	243	
13	silicon nitride	0.6	260	255[a]
14	silicon nitride	0.6	208	
15	silicon nitride	0.6	308	
16	silicon nitride	0.6	249	
17	silicon nitride	0.2	294	

[a] Edwards et al. [10]

by controlling the point of the application of the force (see the dark grey spot in Fig. 2, bottom). All beams showed a thickness to length ratio of less than 1/20. The values for Young's modulus of each beam had been calculated from the Euler-Bernoulli formula of conventional continuum theory. They are plotted in Fig. 4 over the beam thickness. Some exemplary curves of bending rigidities of the couple stress theory for selected material length scale parameters are inserted into the diagram. The dimensions of beams number 1 through 8 were the result of measurements done by scanning electron microscopy and 3D laser microscopy, whereas the dimensions of the beams number 9 to 17 were determined by the manufacturer. Each load range

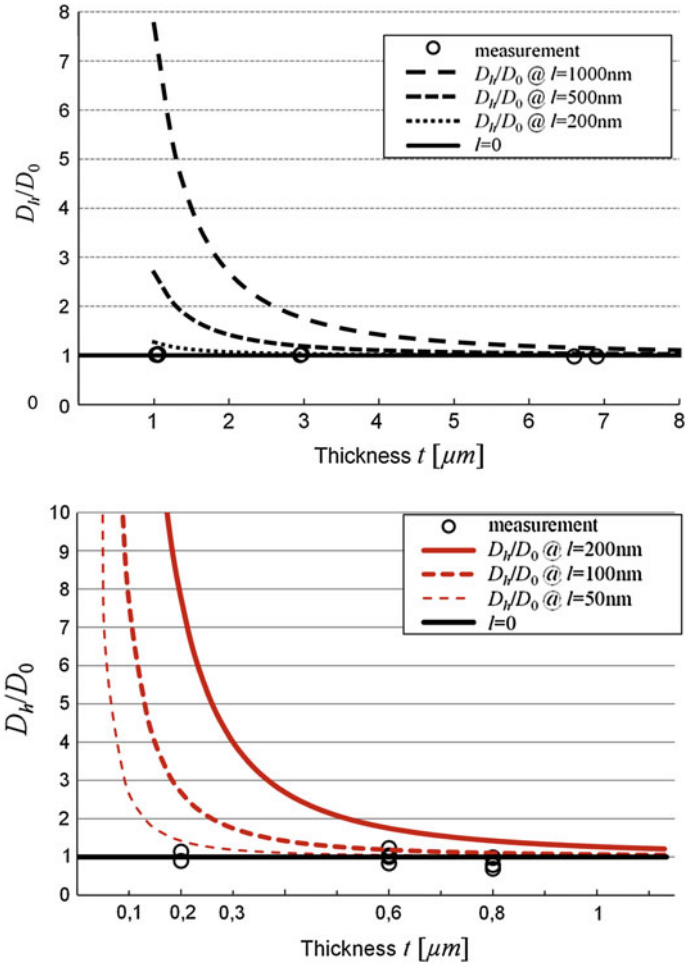

Fig. 4 Exemplary curves of bending rigidities of the couple stress theory for different values of l in combination with measurements on silicon (*top*) and silicon nitride (*bottom*)

was chosen to be in the elastic region of the material and in the region of small deflections. The latter was limited by defining the maximum bending angle as [6]:

$$\alpha = \frac{FL^2}{2EI}\frac{180^\circ}{\pi} \leqslant 5^\circ \tag{18}$$

For each of the six groups of thicknesses one deflection-force diagram is presented in Fig. 5. The error bars stem from the difference between each measurement and the linear regression line for each of the corresponding micro-beams (Fig. 3, right).

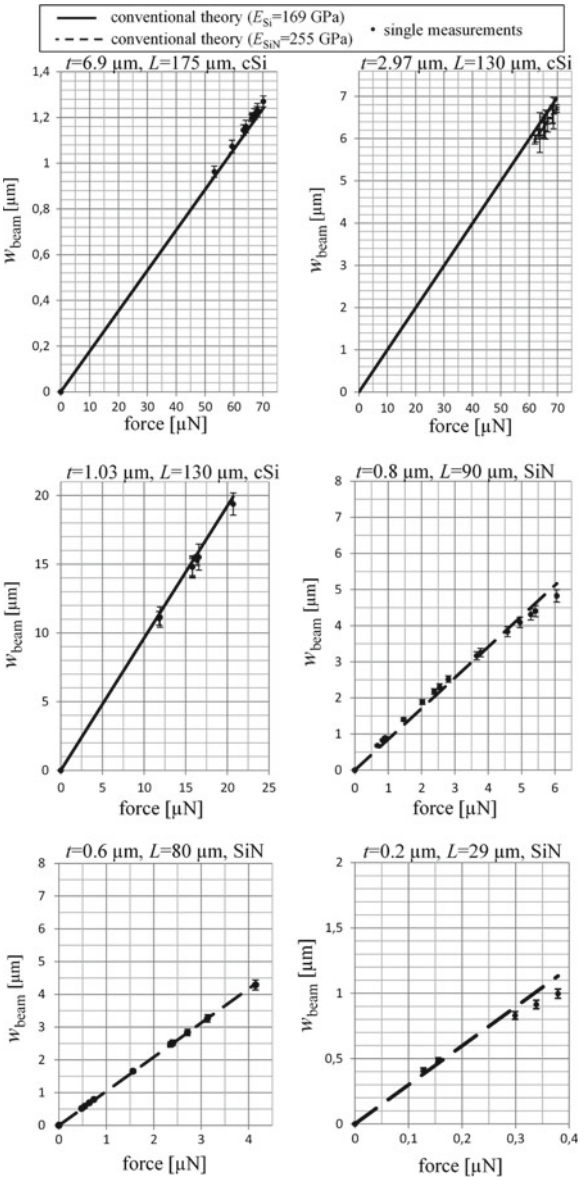

Fig. 5 Measurements of beam deflections versus load of silicon and silicon nitride micro-beams no.s 1, 4, 8, 12, 13, and 17

In fact these regression lines were the only regression made for the data in the AFM experiments.

3.2 Micro-Raman Spectroscopy for Strain Measurement

Today's laser technology offers the possibility to make use of the Raman effect and allows us to determine local strains with a lateral resolution of about one micrometer. The Raman effect is based on inelastic scattering of incoming mono-chromatic light. The location of the spectrum of the Raman scattered light, its "frequency," depends on the state of strain on and immediately below the surface of the specimen. In this process the laser light polarizes the molecules of the specimen. The lattice vibrations (phonons) modulate the frequency of the induced polarization. This, in general, is known as the Raman effect, which is observable in a highly sensitive spectrometer (Fig. 6).

The occurrence of the Raman effect is limited to opaque materials. The shift of the Raman peak $\Delta\omega$ under presence of strain ϵ_{kl} depends on the structure and the values of the PDP tensor (Phonon Deformation Potentials P_{ijkl}) and can be obtained from a solution of the following tensorial eigenvalue problem [5]:

$$\det\left(P_{ijkl}\epsilon_{kl} - \lambda\,\delta_{ij}\right) = 0 \;\;, \text{ with } \lambda = \left(\omega^2 - \omega_0^2\right) \approx 2\omega_0\Delta\omega \;, \tag{19}$$

where ω_0 describes the spectral position of the Raman peak from the unloaded material. By using so-called Raman selection rules, which describe a relationship between the crystal orientation of the specimen and the direction of the polarization of the laser light, the number of unknown eigenvalues of the tensor Eq. (19) can be reduced [9]. For known phonon deformation potentials p, q, and r for single crystalline silicon [2], in a constricted polarization configuration, and for a given uni-directional state of stress the following strain-shift equation holds:

$$\epsilon_{x,\text{Raman}} = 1.4001\,\frac{\Delta\omega}{\omega_0} \;. \tag{20}$$

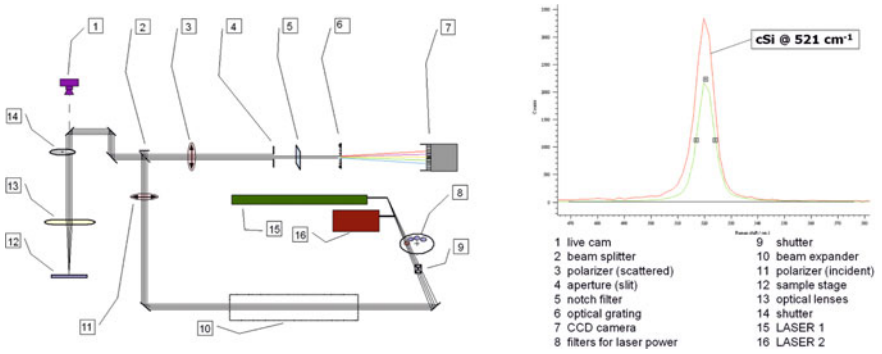

Fig. 6 The labeled optical path of the Raman laser (*left*) and an exemplary Raman peak of silicon with its Gauss' approximation (*right*)

Several Raman spectra were taken in a back scattering configuration, in which the Raman laser beam while intruding in z-direction scanned the upper surface in the x-y-plane of the micro-beam. The scattered Raman peaks related to the loaded and unloaded micro-beam fixture made of silicon were evaluated numerically by a Gauss/Lorentz fit with respect to the spectral position and its Full Width at Half Maximum (FWHM). After this had been done the local strain in x-direction was calculated by Eq. (20). Although silicon nitride exhibits a very similar strain-shift behavior for a selected SiN peak at $\omega_0 = 862\,\mathrm{cm}^{-1}$ [28], no single peaks were observed for SiN because of a 20–50 nm metal coating on the bottom of the specimens, whose spectral lines dramatically overlapped with the Raman effect of SiN.

As a result of the procedure described in Sect. 3.2, a pronounced decrease in the measured strain values for decreasing beam thicknesses was observed if the penetration depth of the laser light was not taken into account. In a first approximation the penetration depth is given by [8]:

$$d_p = \frac{2.3}{2\alpha}\,, \tag{21}$$

where α is an absorption coefficient depending upon the material and the wavelength of the laser in use. For silicon and a wavelength of the Raman laser of about $\lambda_{\mathrm{Laser}} = 532\,\mathrm{nm}$ the absorption coefficient given in [4] is $\alpha = 0.00096\,\mathrm{nm}^{-1}$, and the corresponding penetration depth of the laser light amounts to $d_p = 1200\,\mathrm{nm}$. In a second approximation the mean Raman shift is assumed to be collected at half of the penetration depth, what gives rise to a correction factor f, which is a function of the thickness t of the form:

$$\epsilon_{x,\mathrm{corr}} = f(t)\epsilon_{x,\mathrm{Raman}} \quad , \; f(t) = \frac{t}{|t - d_p|}\,. \tag{22}$$

Calculated correction factors for different beam thicknesses of several tested silicon beams are listed in Table 2 including a comparison to measured correction factors matching the maximum strain values of conventional Euler Bernoulli beam theory: $\epsilon_x(x = 0) = -zFL(EI)^{-1}$.

Table 2 Evaluation of calculated and measured values for the strain correction function of the tested micro-beams and their percental aberration

Beam number	Material	$t\,[\mu m]$	f from Eq. 22	f from experiments	%
1	silicon	6.90	1.21	1.20	0.83
3	silicon	2.97	1.68	1.71	1.78
4	silicon	2.95	1.69	1.78	5.3
5	silicon	1.05	7	6.3	10
8	silicon	1.03	6.06	4.2	30.7

4 Discussion and Outlook

Fixed micro-beams made of single crystalline silicon and silicon nitride with thicknesses of about 7, 3, 1, 0.8, 0.6 and 0.2 μm and a thickness to length ratio of less than 1/20 have been loaded at their free ends by forces of about 0.1–200 μN. Beam deflections of about 0.05–35 μm have been recorded using an AFM system and have been corrected by a nonlinear regression analysis. The resulting values for Young's modulus were in good agreement with the ones from the literature, what speaks in the favor of the accuracy of the experimental apparatus. For silicon nitride beams with thicknesses below 1 μm it was not possible to confirm the accurate thickness by scanning electron microscopy or 3D laser microscopy. However, note that a comparatively small deviation in the thickness will have a great influence on the calculation of Young's modulus. For these beams the thicknesses given by the manufacturer have been used leading to good agreement with the measured bending behavior. The impact of a distributed in contrast to a pointwise (theoretical) applied force as well as the ratio of the thickness to the width was not investigated in detail. The results suggest the material length scale parameter l of the couple stress theory to be below 200 nm for silicon and below 50 nm for silicon nitride. *Some of the single measurements revealed a stiffer elastic bending behavior* (e.g., beams no. 7, 9, and 15), which speaks in favor of an extended theory. The lower limit of detecting l had been shown to be $l > 50$ nm. The problem of detecting material length scale parameters below 50 nm will be more influenced by the problem of measuring the exact thickness of even thinner micro-beams (or nano-beams) than measuring their bending behavior with the present AFM technique.

In a second type of experiment Raman spectra of several loaded and unloaded silicon micro-beams have been taken in the vicinity of the fixture to evaluate the spectral shift of the Raman peak and hence to calculate strain values using Eq. (20). A correction function to incorporate the penetration depth of the laser light has been developed. This function corrects measured strain values out of the conventional Raman theory in comprehension to the lowering effect due to the penetration depth. The correction factors strongly increase for beams with a thickness close to the penetration depth, because for this beams the mean Raman shift related to regions close to the neutral axis inside the bent beam. Table 2 also points to the fact that the spread of the calculated correction factors for small changes in the underlying thicknesses strongly increases for beam thicknesses close to the penetration depth. Together with the standard uncertainty of about 3–6 % of the Raman spectroscope itself the strain values for silicon micro-beams are too inaccurate for an evaluation within the present higher order theory. This results in a high percental aberration of the measured to the calculated correction factors in Table 2 of about 30 % maximum.

The reason for not detecting a size effect for Si and SiN could be attributed to the simplicity of the micro- or atomic structure, as well as to the tested range of dimensions of the specimens. It is conceivable that the covalent bonding between the single atoms of silicon and the undersized dilatation of a silicon or a silicon

nitride molecule might provide an explanation for treating the inner structure of these materials as point masses as it is done in conventional theory.

Experiments with micro-beams made of polymethylmethacrylat (PMMA) and polycrystalline silicon are currently underway. The microstructure of polymers is more complex and the single molecules show a distinct size and even a shape. In polycrystalline silicon the grain size is supposed to be the medium for transmitting the couple stresses.

Acknowledgments The present work is supported by DFG MU 1752/33-1.

References

1. Altenbach, J., Altenbach, H., Eremeyev, V.A.: On generalized Cosserat-type theories of plates and shells: a short review and bibliography. Arch. Appl. Mech. **80**, 73–92 (2010)
2. Anastassakis, E., Pinczuk, A., Burstein, E.: Effect of static uniaxial stress on the Raman spectrum of silicon. Solid State Commun. **8**, 133–138 (1970)
3. Ascione, F., Mancusi, G.: FRP adhesive lap-joints: a micro-scale mechanical approach. Mech. Res. Commun. **37**(2), 169–172 (2010)
4. Aspnes, D.E., Studna, A.A.: Dielectric functions and optical parameters of Si, Ge, GaP, GaAs, GaSb, InP, InAs, and InSb from 1.5 to 6.0 eV. Am. Phys. Soc. **27**(2), 985–1009 (1983)
5. Becker, M.: Lokale Messung von Kornorientierungen und inneren mechanischen Spannungen in polykristallinem Solarsilizium mittels Mikro-Ramanspektroskopie. Promotion TU Erlangen-Nürnberg (2006)
6. Brüller, O., Neff, T.: Elastostatik für Ingenieure. Herbert Utz Verlag, München (2000)
7. Cosserat, E., Cosserat, F.: Theorie des corps deformables. Hermann et Fils, Paris (1909)
8. De Wolf, I.: Micro-Raman spectroscopy to study local mechanical stress in silicon integrated circuits. Semicond. Sci. Technol. **11**, 139–154 (1996)
9. De Wolf, I.: Mechanical stress measurements using micro-Raman spectroscopy. Microsyst. Technol. **5**, 13–17 (1998)
10. Edwards, R.L., Coles, G., Sharpe Jr, W.N.: Comparison of tensile and bulge tests for thin-film silicon nitride. Soc. Exp. Mech. **44**(1), 49–54 (2004)
11. Eringen, A.C.: Polar and nonlocal field theories. In: Continuum Physics, vol. IV. Academic Press, INC., New York (1976)
12. Eringen, A.C.: Microcontinuum field theories. I Foundations and solids. Springer, New York (1999)
13. Fleck, N.A., Müller, G.M., Ashby, M.F., Hutchinson, J.W.: Strain gradient plasticity: theory and experiment. Acta metall. mater. **42**(2), 475–487 (1994)
14. Guo, X.H., Fang, D.N., Li, X.D.: Measurement of deformation of pure Ni foils by speckle pattern interferometry. Mech. Eng. **27**(2), 21–25 (2005)
15. Yang, F., Chong, A.C.M., Lam, D.C.C., Tong, P.: Couple stress based strain gradient theory for elasticity. Int. J. Solids Struct. **39**(10), 2731–2743 (2002)
16. Kahrobaiyan, M.H., Asghari, M., Rahaeifard, M., Ahmadian, M.T.: Investigation of the size effect on the flexural characteristic of Timoshenko beams based on the couple stress theory. Int. J. Eng. Sci. **48**(12), 1985–1994 (2010)
17. Kaßbohm, S.: Fourierreihen zur Berechnung repräsentativer Volumenelemente mit Mikrostruktur. Dissertation, Fak. V, TU Berlin (2006)
18. Koiter, W.T.: Couple-stresses in the theory of elasticity. Pt. I-II. Proc. Koninkl. Nederland Akad. Wetensh. **67**, 17–44 (1964)
19. Kong, S., Zhou, S., Nie, Z., Wang, K.: Static and dynamic analysis of micro beams based on strain gradient elasticity theory. Int. J. Eng. Sci. **47**, 487–498 (2009)

20. Lakes, R.: Experimental methods for study of Cosserat elastic solids and other generalized elastic continua. In: Mühlhaus, H. Ch. 1, pp. 1–22. Wiley, N.Y. (1995)
21. Lam, D.C.C., Yang, F., Chong, A.C.M., Wang, J., Tong, P.: Experiments and theory in strain gradient elasticity. J. Mech. Phys. Sol. **51**(8), 1477–1508 (2003)
22. Ma, Q., Clarke, D.R.: Size dependent hardness of silver single crystals. J. Mater. Res. **10**(4), 853–863 (1995)
23. McFarland, A.W.: Production and analysis of polymer microcantilever parts. Ph.D, Georgia Institute of Technology, Atlanta (2004)
24. McFarland, A.W., Colton, J.S.: Role of material microstructure in plate stiffness with relevance to microcantilever sensors. J. Micromech. Microeng. **15**(5), 1060–1067 (2005)
25. Mindlin, R.D., Tiersten, H.F.: Effects of couple-stresses in linear elasticity. ARMA **11**, 415–448 (1962)
26. Müller, I.: Thermodynamik. Bertelsmann Universitätsverlag, Düsseldorf (1972)
27. Poole, W.J., Ashby, M.F., Fleck, N.A.: Micro-hardness of annealed and work-hardened copper polycrystals. Scripta Mater. **34**(4), 559–564 (1996)
28. Sergo, V., Pezzotti, G., Katagiri, G., Muraki, N., Nishida, T.: Stress dependence of the Raman spectrum of β-silicon nitride. J. Am. Ceram. Soc. **79**(3), 781–784 (1996)
29. Stelmashenko, N.A., Walls, M.G., Brown, L.M., Milman, Y.V.: Microindentations on W and Mo oriented single crystals: an STM study. Acta Metall. Mater. **41**(10), 2855–2865 (1993)
30. Toupin, R.A.: Elastic materials with couple-stresses. ARMA **11**, 385–414 (1962)
31. Truesdell, C.: Die Entwicklung des Drallsatzes. ZAMM **44**(4/5), 149–158 (1964)

On the Electrostatic Fields in Dielectric Continua with Self-Similar Properties

Thomas M. Michelitsch and Gérard A. Maugin

Abstract In this note we study the interaction of electromagnetic fields and matter for hypothetical dielectric materials of linear self-similar (scale free) constitutive properties. The physical sources of this constitutive behavior are harmonic and *scale free* (self-similar) interparticle interactions as introduced recently [10]. We analyze the continuum field equations and self-similar *electrostatic fields*. The assumption of self-similarity leads inevitably to a non-local self-similar (elliptic) Laplacian operator and, as a consequence, to constitutive relations in the forms of non-local convolutions with self-similar (in the continuum limit power law) kernels. The present approach is applicable in different physical contexts such as in mechanics of materials [8], gravitation (potential) theory, statistical physics [7, 9, 11] and it seems to have potential to model certain aspects in fluids mechanics (synthetic turbulence).

1 Introduction

In recent years there is an increasing interest in fractal aspects of material properties. Due to the lack of generally accepted approaches accounting for "fractality", phenomenological models are highly desirable which take into account the self-similarity of the constitutive behavior. There is a big deal of literature to model non-local and fractal aspects by employing fractional calculus by utilizing ad hoc certain fractional operators, and indeed it has been shown that fractional calculus is a powerful tool to model for instance non-local elasticity (see e.g. [2, 3, 12] among many others).

T. M. Michelitsch (✉) · G. A. Maugin
Institut Jean le Rond d'Alembert, CNRS UMR 7190, Université Pierre et Marie Curie (Paris 6), 4 Place Jussieu,75252 Paris cedex 05, France
e-mail: michel@lmm.jussieu.fr

G. A. Maugin
e-mail: gerard.maugin@upmc.fr

H. Altenbach et al. (eds.), *Generalized Continua as Models for Materials*, Advanced Structured Materials 22, DOI: 10.1007/978-3-642-36394-8_15,

However, in many fractional models the choice of the fractional operators appears somewhat arbitrary or only little physically motivated. It is often not clear or obvious whether or not the results of such models are physically meaningful and consistent. Therefore it is more than ever desirable to have models with a solid physical basis and which are deduced so to say from first principles without "too many" arbitrary assumptions on the fractional operators used. If we say "first principles" we mean that the starting point for such an approach should be a "Laplacian operator" that is uniquely determined by a variational principle such as Hamilton's principle from a potential energy or Lagragian (functional).

In the approach employed in this note which we introduced recently [8–11] (and its extension to dimensions $\mathfrak{n} = 1, 2, 3$ of the physical space [7]), the only (constitutive) assumption is a *self-similar*[1] potential energy (functional) from which the equations of motion (the Laplacian operator) are determined in *rigorous* manner by application of Hamilton's principle. It turns out that the "self-similar Laplacian" obtained in this way is a fractional operator. The advantage of this procedure is that the fractional (Laplacian) operator used in the model is physically properly motivated and physical consistency of the results is ensured in this way. The goal of the present note is to develop the laws of electrostatics in a dielectric material system with self-similar interparticle interactions.

The electromagnetic fields on (mass-) fractals, i.e. of the fractal distributions of matter which is *not subject of the present paper* has been developed by Tarasov [13]. In our approach the self-similarity and hence non-locality of the interparticle interactions determines the constitutive relations and the Laplacian operator and makes them to non-local fractional operators. In contrast, in the Tarasov approach interparticle interactions are local. We can say in a sense: the Tarasov approach refers to "kinematic fractals" and describes phenomena of fractal physical objects with "conventional" non-fractal local interparticle interactions. In contrast, our approach refers to "kinetic self-similarity" and "kinetic fractals" describing phenomena of geometrically non-fractal objects with fractal, self-similar interparticle interactions. The fractality in our approach can occur for instance in the potential energy, in the wave number space such as in terms of a fractal dispersion relation in the form of a Weierstrass-Mandelbrot function [10]. We emphasize that both approaches do not compete, but complement each other: the approach of Tarasov and our approach refer simply to different fractal aspects.

For the application of our (mechanically motivated) generalized model [7, 9] to problems of electrodynamics, we use the following formal correspondence between mechanical and electrical quantities: dielectric displacement $\mathbf{D} \leftrightarrow$ stress, electric field $\mathbf{E} \leftrightarrow$ (total) strain, electric potential $\Phi \leftrightarrow$ displacement field, free electric charge $\rho_f \leftrightarrow$ volume forces. That means a mechanical elastic energy which is expressed in terms of mechanical displacement fields will be translated by replacing displacements by electric potentials.

[1] The notion of self-similarity used corresponds to the notion of "self-similarity at a point", see details in [9].

The Laplacian of our model (below relations (5), (6)) is uniquely determined by a self-similar (electric) potential energy density $\frac{1}{2}\mathcal{V}$ where we *assume* (the only assumption in our model) the form

$$\mathcal{V}(\mathbf{x}) = \frac{\hbar^{\delta-n+1}}{4\zeta} \int \frac{(\Phi(\mathbf{x}+\mathbf{r}) - \Phi(\mathbf{x}))^2 + (\Phi(\mathbf{x}-\mathbf{r}) - \Phi(\mathbf{x}))^2}{r^{\delta+1}} \, d^n\mathbf{r} \qquad (1)$$

Φ denotes the *scalar electric potential*. We note that (1) has spatial isotropic symmetry. Expression (1) converges in the range $0 < \delta - (n-1) < 2$ where $n = 1, 2, 3$ denotes the dimension of the physical space [7]. The exponent δ measures the strengths $\sim r^{-\delta}$ of the harmonic interparticle springs acting between particles with distance r [10]. The exponent $r^{-\delta-1}$ in (1) is due to the fact that in the continuum limit the number of springs connecting a particle with particles of distance r located within the volume element $d^n\mathbf{r}$ scales as $\sim r^{-1} d^n\mathbf{r}$. The expression (1) is the spatially isotropic generalization of the continuum limit of the elastic energy density of a quasi-continuous linear chain with self-similar harmonic interparticle springs as introduced in [10] where Φ denotes in the general model a generalized displacement field (in the electromagnetic context the electric potential). The potential energy stored is the volume integral of the density (1) which is a non-local bi-linear functional of the electric potential Φ

$$V[\Phi, \Phi] = \frac{1}{2} \int \mathcal{V}(\mathbf{x}) \, d^n\mathbf{x} = \frac{1}{2} \int \rho_f(\mathbf{x}) \Phi(\mathbf{x}) \, d^n\mathbf{x} \qquad (2)$$

where $\rho_f(\mathbf{r})$ is the density of free electric charges at space point $\mathbf{r}$. Application of Hamilton's principle leads to a self-similar Laplacian defined by the functional derivative of the potential energy functional, namely

$$\Delta_{(n,\delta)}\Phi(\mathbf{x}) := -\frac{\delta V}{\delta \Phi(\mathbf{x})} = -\rho_f(\mathbf{x}) \qquad (3)$$

where we introduced the variation $\delta\Phi(\mathbf{r})$. At the same time (3) defines the Poisson equation of the self-similar (dielectric) medium. We can determine the self-similar Laplacian defined by (3) explicitly by using the chain rule for the functional derivative with respect to the field $\Phi(\mathbf{x})$ (see also the Appendix)

$$\frac{\delta \Phi(\mathbf{x})}{\delta \Phi(\mathbf{x}')} = \delta^n(\mathbf{x} - \mathbf{x}') \qquad (4)$$

which is the continuous analogue to the relation $\frac{\partial x_i}{\partial x_j} = \delta_{ij}$. This self-similar Laplacian has then the representations [7]

$$\Delta_{(n,\delta)}\Phi(\mathbf{x}) = \frac{h^{\delta-n+1}}{2\zeta}\int \frac{\{\Phi(\mathbf{x}+\mathbf{r})+\Phi(\mathbf{x}-\mathbf{r})-2\Phi(\mathbf{x})\}}{r^{\delta+1}} d^n\mathbf{r},\ 0<\delta-(n-1)<2 \tag{5}$$

or equivalently

$$\Delta_{(n,\delta)}\Phi(\mathbf{x}) = \frac{h^{\delta-n+1}}{\zeta}\int \frac{\{\Phi(\mathbf{r})-\Phi(\mathbf{x})\}}{|\mathbf{r}-\mathbf{x}|^{\delta+1}} d^n\mathbf{r}, \quad 0<\delta-(n-1)<2 \tag{6}$$

where $n = 1, 2, 3$ denotes the dimension of physical space. The linear non-local operator (6) exists in the same range $0 < \delta - (n-1) < 2$ as the elastic energy density (1) and merits to be called Laplacian by its following properties which we have proved in our recent paper [7]: positive-semidefiniteness (ellipticity), translational invariance, spatial isotropy and self-adjointness. The spatial isotropy is due to the choice of the potential energy functional as spatially isotropic.

In this note we confine ourselves on the dimension $n = 3$ of the physical space. We evoke the macroscopic Maxwell equations (Maxwell equations in matter). For an extensive treatment of general aspects of electrodynamics in matter we refer to standard textbooks such as [4–6]. We use the following notations: ρ_f denote the volume density of *free* electric charges, **D** the dielectric displacement field, and **E** the electric field, respectively. The Maxwell equations *in matter* have the well known form (in SI units), e.g. [4–6]

$$\nabla\cdot\mathbf{D} = \rho_f \tag{7}$$

$$\nabla\cdot\mathbf{B} = 0 \tag{8}$$

$$\nabla\times\mathbf{E} = -\frac{\partial\mathbf{B}}{\partial t} \tag{9}$$

$$\nabla\times\mathbf{H} = \mathbf{J}_f + \frac{\partial\mathbf{D}}{\partial t} \tag{10}$$

where $\nabla = (\frac{\partial}{\partial x_i})$ denotes the Gradient (Nabla-) operator. In the following section we elaborate some basic relations of *Electrostatics* in dielectric material with self-similar (fractal) interparticle interactions with the approach introduced above.

2 Self-Similar Electrostatics

The results of this section can be fully generalized to other scalar potential-field theories such as for instance gravitational theory. Let us begin with the general relations of *Electrostatics*. We note that these relations are determined by the above Maxwell equations when we put $\frac{\partial(\cdot)}{\partial t} = 0$. The Maxwell equations of statics then reduce to

$$\nabla \cdot \mathbf{D} = \rho_f \tag{11}$$

and

$$\nabla \times \mathbf{E} = 0 \tag{12}$$

We consider a material with a constitutive law which is such that the relation between the electric potential Φ and the free electric charge density ρ_f are connected by a *Poisson equation* with the non-local form of the Laplacian (6)

$$\Delta_{(n=3,\delta)}\Phi(\mathbf{x}) = -\rho_f(\mathbf{x}) \tag{13}$$

where we consider here only the case of $n = 3$ dimensions of the physical space. An important observation on the *physical consistency of this model* is the following: Since the Laplacian $\Delta_{(n,\delta)}$ is defined by *Hamilton's variational principle* (and not simply somewhat assumed), the Poisson equation (13) is consistent with the right hand side of (2).

The Laplacian (6) takes in 3D the form

$$\Delta_{(n=3,\delta)}\Phi(\mathbf{x}) = \frac{h^{\delta-2}}{\zeta}\int \frac{\{\Phi(\mathbf{r}) - \Phi(\mathbf{x})\}}{|\mathbf{r}-\mathbf{x}|^{\delta+1}} d^3\mathbf{r}, \qquad 0 < \delta - 2 < 2 \tag{14}$$

where the exponent δ is for $n = 3$ restricted within $2 < \delta < 4$ in order this integral to exist. We can assume that the constitutive relation between electric field and dielectric displacement consists in a linear functional relationship

$$\mathbf{D}[\mathbf{E}] = \underline{\epsilon} * \mathbf{E} \tag{15}$$

where "$*$" means here the convolution operation. The dielectric operator $\underline{\epsilon}$ is to be determined from the self-similar Laplacian (14) and Gauss law (11) together with the Poisson equation (13). We use the relation between the electric potential Φ and the electric field to be purely kinematic (analogue to the relation between total strain and displacement field), i.e.

$$\mathbf{E} = -\nabla\Phi \tag{16}$$

where $(\nabla)_i = \dfrac{\partial}{\partial x_i}$ denotes the gradient operator. Relation (16) is a consequence of the static Faraday's law (12). We note that constant electric potentials $\Phi = \mathrm{const}$ correspond to a zero electric fields $\mathbf{E}$ and to zero free charges $\rho_f = 0$ according to the vanishing of (14). To determine the constitutive relation connecting $\mathbf{D}$ and $\mathbf{E}$ (15), we use that the Gauss law (11) has to be fulfilled. Thus we can write for (14)

$$\Delta_{(n=3,\delta)}\Phi(\mathbf{x}) = -\nabla\cdot\mathbf{D} = \frac{h^{\delta-2}}{(\delta-2)\zeta}\int \frac{(\mathbf{x}-\mathbf{r})\cdot\mathbf{E}(\mathbf{r})}{|\mathbf{x}-\mathbf{r}|^{\delta+1}} d^3\mathbf{r}, \qquad 2 < \delta < 4 \tag{17}$$

which is useful to determine the dielectric displacement field $\mathbf{D}$ where $\mathbf{E}$ is defined by (16). Relation (17) is obtained by applying Gauss theorem [7]. We obtain then for the dielectric displacement field (up to an unimportant rotational field)

$$\mathbf{D}(\mathbf{x}) = \frac{\mathrm{h}^{\delta-2}}{(\delta-1)(\delta-2)\zeta}\int |\mathbf{x}-\mathbf{r}|^{1-\delta}\mathbf{E}(\mathbf{r})\,\mathrm{d}^3\mathbf{r}, \qquad 2<\delta<4 \tag{18}$$

This relation is the *constitutive law* connecting the dielectric displacement $\mathbf{D}$ with the electric field $\mathbf{E}$ in terms of a nonlocal linear functional having the nonlocal form

$$\mathbf{D}(\mathbf{x}) = \int \underline{\epsilon}(\mathbf{x}-\mathbf{r})\mathbf{E}(\mathbf{r})\,\mathrm{d}^3\mathbf{r} \tag{19}$$

with the *dielectric permittivity material function kernel*

$$\underline{\epsilon}(\mathrm{R}) = \mathbf{1}\epsilon(\mathrm{R}), \quad \epsilon(\mathrm{R}) = \frac{\mathrm{h}^{\delta-2}}{(\delta-1)(\delta-2)\zeta}\mathrm{R}^{1-\delta} > 0, \quad \mathrm{R}\neq 0, \quad 2<\delta<4 \tag{20}$$

which is a self-similar and isotropic diagonal tensor function where $\mathbf{1}$ denotes the 3×3 unity tensor. In the following we refer to as a *self-similar dielectricum*, a dielectric medium governed by a material law (20). We observe that (20) is within the admissible range of δ a positive (diagonal) self-similar tensor where its exponent δ is restricted in the range $-3<1-\delta<-1$.

2.1 Self-Similar Coulomb Potential

In this subsection we deduce the Coulomb potential generated by a point charge q and the Coulomb force between two point charges q and Q of distance r in a self-similar dielectricum.

The Coulomb potential can be represented as a convolution of the electric potential of a unit point charge g (located in the origin) having the charge density $\rho_{\mathrm{f}}(\mathbf{r}) = \mathrm{q}\delta^3(\mathbf{r})$ with $\mathrm{q}=1$. This fundamental potential g which is also called the Green's function of electrostatics and is defined by the Poisson equation

$$\Delta_{(\mathrm{n}=3,\delta)}\mathrm{g}(\mathbf{r}) = -\delta^3(\mathbf{r}) \tag{21}$$

where $\delta^3(\mathbf{x})$ denotes the three dimensional Dirac's δ-function and $\Delta_{(\mathrm{n}=3,\delta)}$ the self-similar Laplacian (5) for $\mathrm{n}=3$. Due to the spatial isotropy of the Laplacian (5), we can conclude that $\mathrm{g}=\mathrm{g}(\mathrm{r})$ depends only on $\mathrm{r}=|\mathbf{r}|$. The Green's function g defined by (21) is the self-similar analogue to the Newtonian $1/\mathrm{r}$-potential (classical Coulomb potential). Its physical interpretation is the following: $\mathrm{g}(\mathrm{r})$ represents the

scalar electric potential caused by a unit point charge $q = 1$ located in the origin $\mathbf{r} = 0$. The electric potential due to an arbitrary spatial density of free electric charges ρ_f has then the form

$$\Phi(\mathbf{r}) = \int g(\mathbf{r} - \mathbf{r}')\rho_f(\mathbf{r}')\, d^{3\mathbf{r}'} \tag{22}$$

To determine the Green's function g it is convenient to apply Fourier transformation. Taking into account that plane waves are eigenfunctions of the Laplacian with

$$\Delta_{(n,\delta)} e^{i\mathbf{k}\cdot\mathbf{r}} = -\omega^2(k) e^{i\mathbf{k}\cdot\mathbf{r}} \tag{23}$$

with the dispersion relation determined by

$$\omega^2(k) = \frac{h^{\delta-2}}{\zeta} \int \frac{1 - \cos \mathbf{k}\cdot\mathbf{r}}{r^{\delta+1}}\, d^3\mathbf{r} \tag{24}$$

which has the scaling property [7]

$$\omega^2(k) = Ak^{\alpha}, \qquad 0 < \alpha = \delta - 2 < 2 \tag{25}$$

The constant $A = \omega^2(k = 1)$ is strictly positive in the admissible range of $0 < \alpha = \delta - 2 < 2$ and has explicitly been obtained for $n = 1, 3$ [7]. In 3D the constant A is obtained as

$$A = \frac{2\pi^2 h^{\delta-2}}{\zeta(\alpha+1)! \sin\frac{\alpha\pi}{2}} > 0, \qquad 0 < \alpha = \delta - 2 < 2 \tag{26}$$

In (26) we introduced the faculty function (Γ-function) defined as [1]

$$z! = \Gamma(z+1) = \int_0^{\infty} e^{-\tau}\tau^z\, d\tau, \qquad \mathrm{Re}(z) > -1 \tag{27}$$

The Green's function is hence determined by ($n = 3$)

$$g(r) = \frac{1}{(2\pi)^3} \int \frac{e^{i\mathbf{k}\cdot\mathbf{r}}}{\omega^2(k)} d^3\mathbf{k} \tag{28}$$

We obtain finally the electrostatic Green's function (self-similar electric potential due to a unit-point charge) as

$$g(r) = g_\alpha r^{\alpha-3}, \qquad 0 < \alpha = \delta - 2 < 2 \tag{29}$$

and the electric potential is $\Phi(r) = qg(r)$ where $q = \pm 1$ with an exponent varying within $-3 < \alpha - 3 < -1$, i.e having a stronger decay at infinity than the classical $1/r$-Coulomb potential. The positive constant g_α is obtained in 3D as

$$g_\alpha = \frac{\Gamma(2-\alpha)\sin\left(\frac{\alpha\pi}{2}\right)}{2\pi^2 A} \tag{30}$$

or

$$g_\alpha = \frac{\zeta}{4\pi^4 h^{\delta-2}}\Gamma(2+\alpha)\Gamma(2-\alpha)\sin^2\left(\frac{\alpha\pi}{2}\right) > 0, \qquad 0 < \alpha = \delta - 2 < 2 \tag{31}$$

The electric potential of an arbitrary charge distribution ρ_f is then determined by the convolution (22) with the kernel of Coulomb potential (28). The electric field of an arbitrary charge distribution ρ_f in the self-similar dielelctricum is then given by

$$\mathbf{E}(\mathbf{r}) = (3-\alpha)g_\alpha \int \frac{(\mathbf{r}-\mathbf{r}')}{|\mathbf{r}-\mathbf{r}'|^{5-\alpha}}\rho_f(\mathbf{r}')\,d^3\mathbf{r} \tag{32}$$

2.2 *Electric Field of a Unit-Point Charge—Self-Similar Coulomb Law*

The electric field of the point charge q located in the origin $r = 0$ is then

$$\mathbf{E} = -q\nabla_{\mathbf{r}} g(r) = q(3-\alpha)g_\alpha r^{\alpha-5}\mathbf{r} \sim r^{\alpha-4}, \qquad -4 < \alpha - 4 < -2 \tag{33}$$

where $(3-\alpha)g_\alpha > 0$ as $0 < \alpha = \delta - 2 < 2$ and $g_\alpha > 0$ is given in (31).

Let us consider now the Coulomb force $\mathbf{F}_c$ on a point charge Q located at $\mathbf{r}$ in the field of a point charge q located in the origin

$$\mathbf{F}_c(\mathbf{r}) = Q\mathbf{E}(\mathbf{r}) = Qq(3-\alpha)g_\alpha r^{\alpha-5}\mathbf{r} = -\nabla_{\mathbf{r}} V_c(r) \tag{34}$$

with the Coulomb potential (energy) of two unit charges q and Q seperated by distance r

$$V_c(r) = qQg(r) = qQg_\alpha r^{\alpha-3}, \qquad -3 < \alpha - 3 < -1 \tag{35}$$

It follows that $\mathbf{F}_c$ is repulsive (parallel to $\mathbf{r}$) if $qQ > 0$ and attractive if $qQ < 0$ just as in traditional electrostatics. The Coulomb force (34) scales however as $r^{\alpha-4}$ with an exponent in the range $-4 < \alpha - 4 < -2$.

3 Conclusions

In this note we have deduced the basic electrostatic fields in the framework of a self-similar dielectric setting. We used our recently developed continuum approach of material systems with self-similar interparticle interactions [8, 9, 11] which is a generally applicable field approach for material systems with intrinsic self-similar

material symmetry. It follows that the self-similarity symmetry of interparticle interactions gives rise to new physical phenomena which are due to the criteria of existence of the self-similar Laplacian, especially the laws of electrostatics are modified by the range of existence (convergence) $2 < \delta < 4$ of the self-similar potential energy density $\frac{1}{2}\mathcal{V}(\mathbf{x})$ of Eq. (1) and the self-similar Laplacian (17) in 3D. Further relations of electrostatics in this self-similar setting can be deduced in a straight-forward manner. Of special interest would be in this context for instance Eshelby's inclusion problem and related subjects. A wide field opens to extend the present approach to electrodynamics. An electromagnetic theory including aspects of dynamics of self-similar continua is currently under development.

Appendix

Functional derivative. The Laplacian (5) is defined as the functional derivative of the potential energy (1) with respect to the field Φ. In order to calculate this functional derivative we make use of the following property of the functional derivative, so we have for instance by using the chain rule (4)

$$\frac{\delta}{\delta\phi(\tau)}\int_{-\infty}^{\infty}\int_{-\infty}^{\infty} d\tau_1 d\tau_2 f(\phi(\tau_1),\phi(\tau_1+\tau_2))$$

$$= \int_{-\infty}^{\infty}\int_{-\infty}^{\infty} d\tau_1 d\tau_2 \left(\frac{\partial f}{\partial\phi(\tau_1)}\delta(\tau_1-\tau)+\frac{\partial f}{\partial\phi(\tau_1+\tau_2)}\delta(\tau_1+\tau_2-\tau)\right)$$

$$= \int_{-\infty}^{\infty} ds \left(\frac{\partial}{\partial\phi(\tau)}f(\phi(\tau),\phi(\tau+s))+\frac{\partial}{\partial\phi(\tau)}f(\phi(\tau-s),\phi(\tau))\right).$$

References

1. Abramowitz, M., Stegun, I. (eds.): Handbook of Mathematical Functions, National Bureau of Standards, Applied Mathematics Series 55 (1972). http://people.maths.ox.ac.uk/macdonald/aands/index.html
2. Carpinteri, A., Mainardi, F. (eds.): Fractals and Fractional Calculus, CISM Courses and Lectures No. 378, CISM Udine. Springer, Wien, New York (1997). ISBN 3-211-82913-X
3. Carpinteri, A., Cornetti, P., Sapora, A.: A fractional calculus approach to nonlocal elasticity. Eur. Phys. J. Special Topics **193**, 193–204 (2011)
4. Eringen, A.C., Maugin, G.A.: Electrodynamics of Continua, vol. 2. Springer, New York (1990)
5. Jackson, J.D.: Classical Electrodynamics, 3rd edn, Wiley (1999). ISBN 0-471-30932-X
6. Maugin, G.A.: Continuum mechanics of electromagnetic solids. Appl. Math. Mech. 33 (1988)
7. Michelitsch, T.M., Maugin, G.A., Nicolleau, F.C.G.A., Nowakowski, A.F., Rahman, M.: A simple model for scale free anomalous diffusion in the n-dimensional space (submitted)

8. Michelitsch, T.M., Maugin, G.A., Rahman, M., Derogar, S., Nowakowski A.F., Nicolleau, F.C.G.A. An approach to generalized one-dimensional self-similar elasticity. Int. J. Eng. Sci. **61**, 103—111 (2012)
9. Michelitsch, T.M., Maugin, G.A., Rahman, M., Derogar, S., Nowakowski, A.F., Nicolleau, F.C.G.A.: A continuum theory for one-dimensional self-similar elasticity and applications to wave propagation and diffusion. Eur. J. Appl. Math. CJO (2012). doi:10.1017/S095679251200023X
10. Michelitsch, T.M., Maugin, G.A., Nicolleau, F.C.G.A., Nowakowski, A.F., Derogar, S.: Dispersion relations and wave operators in self-similar quasicontinuous linear chains. Phys. Rev. E **80**, 011135 (2009)
11. Michelitsch, T.M.: The self-similar field and its application to a diffusion problem. J. Phys. A: Math. Theor. **44**, 465206 (2011). doi:10.1088/1751-8113/44/46/465206
12. Sapora, A., Cornetti, P., Carpinteri, A.: Wave propagation in nonlocal elastic continua modelled by a fractional calculus approach. Commun. Nonlinear Sci. Numer. Simul. **18**(1), 63–74 (2013)
13. Tarasov, V.E.: Electromagnetic fields on Fractals. Mod. Phys. Lett. A **21**, 1587–1600 (2006)

Nonlinear Generalizations of the Born-Huang Model and Their Continuum Limits

Alexey V. Porubov, Eron L. Aero and Boris R. Andrievsky

Abstract One previously developed essentially nonlinear continuum model for a bi-atomic lattice is examined by comparing with the continuum limit of generalized Born-Huang model. It is found that these models do not correspond to each other, while the coefficients of the last model may be evaluated for real bi-atomic crystals. Some new features of the strain waves in the lattice are revealed on the basis of exact traveling wave solutions of the generalized Born-Huang model.

1 Introduction

Deep variations in the structure of a crystalline lattice, allows description of the cardinal, qualitative variations of the cell properties, lowering of potential barriers, switching of interatomic connections, arising from singular defects and other damages, phase transitions. Recently an essentially proper structural nonlinear model has been developed in [1, 2] that treats a continuum approach and a crystal translational symmetry of the bi-atomic lattice without making a continuum limit of its discrete model. According to [1, 2], the following variables are introduced in the 1D case:

$$U = \frac{m_1 U_1 + m_2 U_2}{m_1 + m_2}, \quad u = \frac{U_1 - U_2}{a}$$

A. V. Porubov · E. L. Aero · B. R. Andrievsky
Institute of Problems in Mechanical Engineering Bolshoy, av. 61, V.O., 199178
Saint-Petersburg, Russia
e-mail: alexey.porubov@gmail.com

E. L. Aero
e-mail: 16aero@mail.ru

B. R. Andrievsky
e-mail: bandri@yandex.ru

H. Altenbach et al. (eds.), *Generalized Continua as Models for Materials*,
Advanced Structured Materials 22, DOI: 10.1007/978-3-642-36394-8_16,

where a is a period of the lattice, U is a macro-displacement and u is a relative micro-displacement for the pair of atoms with masses m_1, m_2. Then the density of kinetic energy is introduced,

$$K = \frac{\rho U_t^2}{2} + \frac{\mu u_t^2}{2} \tag{1}$$

where ρ and μ are an average density of the mass of the atoms and a so-called density of the reduced masses of the pair of the atoms respectively. The internal density energy Π is suggested in [1, 2] as

$$\Pi = \frac{E\,U_x^2 + \kappa\,u_x^2}{2} + (p - SU_x)(1 - \cos(u)) \tag{2}$$

where E and κ are the second order macro-and micro-elastic constants, p is an energy of activation of interatomic connections in the elementary cell, S is the coefficient of nonlinear striction (re-arrangement of the microstructure under the action of macroscopic strains). The term $(1-\cos(u))$ was chosen to take into account a translational symmetry of the crystalline lattice. It accounts for a strong or essential nonlinearity allowing transition of atoms in neighboring cells to realize the micro-mechanism of the cardinal re-arrangement of the structure. The weakly nonlinear models give rise to only the description of small variations in the position of the atoms around undisturbed state.

The governing equations are obtained using the variation Hamilton-Ostrogradsky principle, and the coupled equations for U and u are obtained in the form

$$\rho U_{tt} - E\,U_{xx} = S(\cos(u) - 1)_x, \tag{3}$$

$$\mu u_{tt} - \kappa u_{xx} = (SU_x - p)\sin(u) \tag{4}$$

The model eqs. (3), (4) possess interesting localized wave solutions describing variations in the amplitude of the localized defect u as well as simultaneous propagation of the bell-shaped and kink-shaped defects u due to an influence of an external loading U_x, see [3–5]. However, the model (3), (4) is based on some suggestions, mentioned above. These suggestions are given on the basis of physical reasons, but they are not justified enough. Also the constants E, S, μ, κ and p are not defined for real bi-atomic materials, and application of the solutions to Eqs. (3), (4) is questionable. To overcome this difficulty, a comparison may be done with a continuum limit of the discrete equations accounting for the bi-atomic lattice. A natural candidate is the familiar Born-Huang model for bi-atomic lattices [6, 7]. However, this model is linear, and its extension by the nonlinear case is needed. It will be done further in this paper. It seems that possible correspondence may help to check the suggestions about the expressions for the energies (1), (2) and to estimate the values of the constants of the model (3), (4).

2 Generalization of the Born-Huang Lattice Model

The Born-Huang model accounts for a lattice that is a chain of the atoms of two kinds interacting with each other. The interaction is modeled by elastic springs with equal stiffness, see Fig. 1. Consider an elementary cell (marked in Fig. 1) with displacement u_l for the mass m_1 and displacement v_l for the mass m_2. Two possible elementary cells are marked in Fig. 1, the choice depends on the mass that is placed ahead, heavier or lighter. First the Born-Huang model is generalized up to a weakly nonlinear level. The discrete equations of motion for the elementary cell are written as

$$m_1\, u_{l,tt} = C[(v_{l+1} - u_l) - (u_l - v_{l-1})] + P[(v_{l+1} - u_l)^2 - (u_l - v_{l-1})^2],$$
$$m_2\, v_{l,tt} = C[(u_{l+1} - v_l) - (v_l - u_{l-1})] + P[(u_{l+1} - v_l)^2 - (v_l - u_{l-1})^2],$$

where C and P are the coefficients of the linear and nonlinear stiffness respectively. The continuum long-wave limit of these equations up to the terms of order $O(a^3)$ is

$$m_1\, u_{tt} = 2C\,(v - u) + 4a\,P(v - u)v_x + C\,a^2 v_{xx}, \tag{5}$$
$$m_2\, v_{tt} = 2C\,(u - v) + 4a\,P(u - v)u_x + C\,a^2 u_{xx}. \tag{6}$$

A comparison with the model (3), (4) requires transition to the variables,

$$U = \frac{m_1 u + m_2 v}{m_1 + m_2},\ V = \frac{u - v}{a}.$$

that have the same meaning as for the model (3), (4). Then the continuum eqs. (5), (6) are transformed to the coupled equations for the new variables,

$$(m_1 + m_2)U_{tt} - 2a^2\,CU_{xx} - 4a^3\,PVV_x + \frac{a^3\,C(m_1 - m_2)}{m_1 + m_2}\,V_{xx} = 0, \tag{7}$$

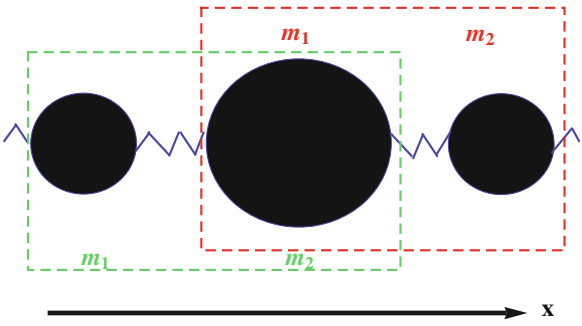

Fig. 1 Two kinds of establishing elementary cells in bi–atomic Born–Huang lattice. Two choices of an elementary cell are marked by dashed lines

$$\frac{m_1 m_2 a^2}{m_1+m_2} V_{tt} + \frac{a^4\, C m_1 m_2}{(m_1+m_2)^2}\, V_{xx} + 2a^2(C + 2a\, P U_x)V + \frac{a^3\, C(m_1-m_2)}{m_1+m_2}\, U_{xx} = 0. \tag{8}$$

A comparison will be done first between the linearized versions of Eqs. (3), (4) and (7), (8). Then Eqs. (7), (8) will be compared with the weakly nonlinear limit of Eqs. (3), (4) resulting from application of the power series expansions of the trigonometric functions. Finally, an essentially nonlinear extension of Eqs. (7), (8) will be suggested to compare with Eqs. (3), (4).

3 Comparison of the Models

The linearized equations (3), (4),

$$\rho U_{tt} - E\, U_{xx} = 0, \tag{9}$$

$$\mu u_{tt} - \kappa u_{xx} = 0. \tag{10}$$

demonstrate no coupling and no acoustical and optical branches in the dispersion relation. On the contrary, the Born-Huang model (linearized Eqs. (7), (8)),

$$(m_1+m_2)U_{tt} - 2a^2\, C U_{xx} + \frac{a^3\, C(m_1-m_2)}{m_1+m_2}\, V_{xx} = 0, \tag{11}$$

$$\frac{m_1 m_2 a^2}{m_1+m_2} V_{tt} + \frac{a^4\, C m_1 m_2}{(m_1+m_2)^2}\, V_{xx} + \frac{a^3\, C(m_1-m_2)}{m_1+m_2}\, U_{xx} = 0, \tag{12}$$

possesses both branches [6]. Also, one can note that the coefficients in Eqs. (9), (10) are independent, while they depend on each other in Eqs. (11), (12).

The weakly nonlinear limit of Eqs. (3), (4) is obtained by expanding the trigonometric functions and retaining only the first terms in the expansions,

$$\rho U_{tt} - E\, U_{xx} = -S\, u u_x, \tag{13}$$

$$\mu u_{tt} - \kappa u_{xx} = (S U_x - p)\, u. \tag{14}$$

A comparison with Eqs. (7), (8) may be done using exact traveling wave solutions depending only on the phase variable $\theta = x - c\, t$. Two kinds of decoupling are possible for Eqs. (13), (14). The Eq. (13) may be resolved for U_θ,

$$U_\theta = \frac{S\, u^2 - 2\sigma}{2(E - \rho\, c^2)}, \tag{15}$$

and Eq. (14) becomes an equation for finding the function u after substitution of Eq. (15). Alternatively, Eq. (13) gives rise to the relationship for u,

$$u = \frac{\sqrt{2((E - \rho c^2)U_\theta - \sigma)}}{S}, \tag{16}$$

while the function U is defined from Eq. (14) after substitution of Eq. (18). In both cases σ is a constant of integration.

Only the first kind of decoupling is realized for solving Eqs. (7), (8). Thus, Eqs. (7) yields

$$U_\theta = \frac{2a^3PV^2 + \sigma}{c^2(m_1 + m_2) - 2Ca^2} + \frac{(m_2 - m_1)C\, a^3 V_\theta}{(m_1 + m_2)(c^2(m_1 + m_2) - 2Ca^2)} \tag{17}$$

that is used for derivation of the governing equation for V from Eq. (8). One can note that the second term in Eq. (17) depends on the difference of the masses m_i.

Despite the relationships for U_θ for both models are different due to the last term in Eq. (17), the resulting ordinary differential equations (ODE) for the functions u and V are similar. Thus, Eq. (14) transforms to the ODE reduction of the modified Korteweg - de Vries (mKdV) equation,

$$(u_\theta)^2 = b_1 u^4 + b_2 u^2 + b_3,$$

$$b_1 = \frac{S^2}{4\left(\kappa - c^2\mu\right)\left(E - c^2\rho\right)}, b_2 = -\frac{\left(p(E - c^2\rho) + S\sigma\right)}{\left(\kappa - c^2\mu\right)\left(E - c^2\rho\right)}, b_3 - \text{const.}$$

while for the generalized Born- Huang model substitution of Eq. (17) into Eq. (8) results in the same ODE for the function V,

$$(V_\theta)^2 = q_1 V^4 + q_2 V^2 + q_3,$$

but with different coefficients,

$$q_1 = \frac{2a^4P^2}{C^2a^4 - m_1 m_2 c^4}, q_2 = \frac{2(2aP\sigma C(m_1 + m_2)c^2 - 2C^2a^2)}{C^2a^4 - m_1 m_2 c^4}, q_3 - \text{const.}$$

The known solitary wave solution of the mKdV equation is be written for u,

$$u = \frac{2\sqrt{p\left(c^2\rho - E\right) - S\sigma}}{S} \operatorname{sech}\left(\frac{\sqrt{p\left(E - c^2\rho\right) + S\sigma}}{\sqrt{\left(\kappa - c^2\mu\right)\left(E - c^2\rho\right)}}(\theta - \theta_0)\right) \tag{18}$$

while the same solution for V is

$$V = \frac{\sqrt{2C^2a^2 - c^2C(m_1 + m_2) - 2aP\sigma}}{\sqrt{2}a^2P}$$

$$\operatorname{sech}\left(\frac{\sqrt{2}\sqrt{2C^2a^2 - c^2C(m_1 + m_2) - 2aP\sigma}}{\sqrt{-C^2a^4 + c^4m_1m_2}}(\theta - \theta_0)\right). \tag{19}$$

However, the reality of the parameters of the solutions depend on the coefficients of the equation. The coefficients are independent for the model (13), (14), then the solution (18) exists, in particular, for $\sigma = 0$. It follows from Eq. (15) that U_θ vanishes at $\theta \to \pm\infty$, and the solitary wave of the moving defect u is accompanied by the solitary wave of an external loading, or a macro-strain, U_θ. However, the coefficients of Eqs. (7), (8) do not allow the value of the velocity c at $\sigma = 0$ for the solution (19). It means that the macro-strain wave U_θ (17) cannot vanish at infinities, and a constant external loading is needed to support the localized wave of defects V in this case. Typical shapes of the wave (17) are shown in Fig. 2 in the form of a localized wave but with constant negative shift that has a meaning of an external longitudinal compression. The shape of the wave is not symmetric with respect to its peak contrary to the symmetric shape of the solution (15). Also a trough appears ahead or behind the wave depending on the ratio of the masses, m_i.

Similarly the essentially nonlinear case may be considered. However, the weakly nonlinear Eqs. (7), (8) should be extended up to the essential level in the same manner as Eqs. (3), (4) are reduced up to the weakly nonlinear level, (13), (14). Now we assume that the nonlinear terms in Eqs. (7), (8) are the "traces" of the expansions of the trigonometric functions. Then the essentially nonlinear generalization of the continuum limit of the Born-Huang model is suggested in the form

$$(m_1+m_2)U_{tt} - 2a^2CU_{xx} - 4a^3P(1-\cos V)_x + \frac{a^3C(m_1 - m_2)}{m_1 + m_2}V_{xx} = 0 \tag{20}$$

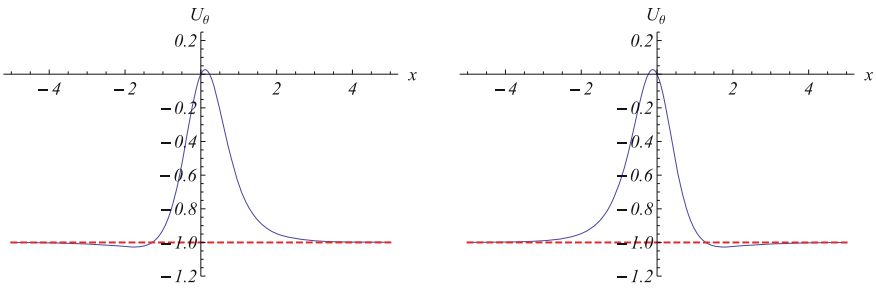

Fig. 2 Solitary wave with a constant shift (shown by dashed line), $m_1 < m_2$ (left), $m_1 > m_2$ (right)

$$\frac{m_1 m_2 a^2}{m_1+m_2} V_{tt} + \frac{a^4\, C m_1 m_2}{(m_1+m_2)^2}\, V_{xx} + 2a^2(C + 2a\, P U_x)\sin V + \frac{a^3\, C(m_1-m_2)}{m_1+m_2}\, U_{xx} = 0. \tag{21}$$

Again a comparison is done using exact traveling wave solutions to Eqs. (3), (4) and Eqs. (20), (21). Two kinds of decoupling are possible for Eqs. (3), (4):

$$U_\theta = \frac{S\,(1-\cos u) - \sigma}{2(E - \rho\, c^2)}$$

or

$$u = \arccos\left(\frac{(\rho\, c^2 - E)U_\theta - \sigma}{S} + 1\right).$$

Only the first kind is realized for the generalized essentially nonlinear Born-Huang model, (20), (21),

$$U_\theta = \frac{a^3 P(1-\cos V) + \sigma}{c^2(m_1+m_2) - 2Ca^2} + \frac{(m_2-m_1)C\, a^3 V_\theta}{(m_1+m_2)(c^2(m_1+m_2) - 2Ca^2)} \tag{22}$$

The equations both for the functions u and V have the form of the ODE reduction of the Double Sine-Gordon equation. In particular, substitution of Eq. (22) into Eq. (21) of the generalized essentially nonlinear Born-Huang model results in

$$\left(\frac{m_1 m_2 a^2(c^2 + C\, a^2)}{m_1+m_2} - \frac{(m_1-m_2)^2 C^2\, a^6}{(m_1+m_2)^2((m_1+m_2)c^2 - 2C\, a^2)}\right) V_{\theta\theta} + 2a^2\left(C + \frac{2AP(4a^3P+\sigma)}{(m_1+m_2)c^2 - 2C\, a^2}\right)\sin V - \frac{4a^4 P}{(m_1+m_2)c^2 - 2C\, a^2}\sin(2V) = 0. \tag{23}$$

The substitution of variable $V = 2\arctan W(\theta)$ allows us to convert Eq. (23) to the form of the mKdV equation for the function W. Then a comparison is done using already noted solitary wave solution. It turns out that the main deviations in the solutions are the same as in the weakly nonlinear case. Again the generalized essentially nonlinear Born-Huang model does not possess the bell-shaped solution for U_θ without constant shift, σ, while the shape of the wave U_θ is similar to that shown in Fig. 2.

4 Conclusions

The essentially nonlinear continuum model (3), (4) and the continuum limit of the discrete Born-Huang model do not correspond to each other at the linearized, weakly nonlinear and essentially nonlinear levels. The distinct features of the last model are the dependence of the profile of the solution on the ratio between the masses m_i of the atoms of the lattice and the need in a shift σ for the existence of the solution for the macro-strain U_θ needed for propagation of localized defects V. Therefore, both models similarly describe propagation of localized defects but under different loading, U_θ (with or without constant part or a pedestal). The coefficients in the continuum equations of the generalized Born- Huang model depends on the interaction forces of the lattice that makes possible their evaluation for real bi-atomic materials.

However, the essentially nonlinear continuum model (3), (4) corresponds well to the structural essentially nonlinear model after G. Pouget, G.A. Maugin and M.K. Sayadi [8, 9] for a one-dimensional atomic chain equipped with rotatory molecular groups. Therefore, all the solutions obtained in Refs. [3–5] may be successfully applied in this problem.

Acknowledgments The work has been supported by the Russian Foundation for Basic Researches, grants No 12-01-00521-a and 10-01-00243-a.

References

1. Aero, E.L.: Micromechanics of a double continuum in a model of a medium with variable periodic structure. J. Eng. Math. **55**, 81–95 (2002)
2. Aero, E.L., Bulygin, A.N.: Strongly nonlinear theory of nanostructure formation owing to elastic and nonelastic strains in crystalline solids. Mech. Solids. **42**, 807–822 (2007)
3. Porubov, A.V., Andrievsky, B.R.: Influence of coupling on nonlinear waves localization. Commun. Nonlinear Sci. Numer. Simulat. **16**, 3964–3970 (2011)
4. Porubov, A.V., Maugin, G.A., Andrievsky, B.R.: Solitary wave interactions and reshaping in coupled systems. Wave Motion. **48**, 773–781 (2011)
5. Porubov, A.V., Andrievsky, B.R.: Kink and solitary waves may propagate together. Phys. Rev. E. **85**, 046604 (2012)
6. Born, M., Huang, K.: Dynamic theory of crystal lattices. Clarendon Press, Oxford (1954)
7. Pnevmatikos St., Flytzanis N., and Remoissenet M.: Soliton dynamics of nonlinear diatomic lattices. Phys. Rev. B. **33**, 2308–2311 (1986)
8. Sayadi, M.K., Pouget, J.: Soliton dynamics in a microstructured lattice model. J. Phys. A: Math. Gen. **24**, 2151–2172 (1991)
9. Maugin, G.A., Pouget, J., Drouot, R., Collet, B.: Nonlinear electromechanical couplings. Wiley, Manchester (1992)

Buckling of Inhomogeneous Circular Plate of Micropolar Material

Denis N. Sheydakov

Abstract The present research is dedicated to the stability analysis of nonlinearly elastic highly porous plates. The mechanical properties and behavior of these plates are described using the model of an inhomogeneous micropolar (Cosserat) medium. Such approach allows for a more precise modeling and detailed analysis of the buckling process for constructional elements made of highly porous materials. In the framework of a general stability theory for three-dimensional bodies, we have studied the stability of a circular micropolar plate subject to radial compression. It is assumed that elastic properties of the plate vary through the thickness. Using the linearization method in a vicinity of a basic state, the neutral equilibrium equations are derived, which describe the perturbed state of a plate. For a special case of axisymmetric buckling modes this linearized equilibrium equations are reduced to the system of three ordinary differential equations. It is also shown that if elastic properties of a plate are symmetric through the thickness then the stability analysis is reduced to solving two independent linear homogeneous boundary-value problems for the half-plate.

1 Introduction

With the increasing number of new structural materials, the problem of stability analysis for bodies with a microstructure becomes important. One example of such materials is a porous material. Engineering structures made of porous materials, especially metal and polymer foams, have different applications in the last decades [2–4, 6, 9]. The foams are cellular structures consisting of a solid metal (for example aluminium, steel, copper, etc.), or polymer (polyurethane, polyisocyanurate,

D. N. Sheydakov (✉)
South Scientific Center of Russian Academy of Sciences, Chekhova Ave. 41,
344006 Rostov-on-Don, Russia
e-mail: sheidakov@mail.ru

H. Altenbach et al. (eds.), *Generalized Continua as Models for Materials*,
Advanced Structured Materials 22, DOI: 10.1007/978-3-642-36394-8_17,

polystyrene, etc.) and containing a large volume fraction of gas-filled pores. There are two types of foams. One is the closed-cell foam, while the second one is the open-cell foam. The defining characteristic of metal and polymer foams are the very high porosity: typically, well over 80 %, 90 % and even 98 % of the volume consists of void spaces.

Constructions made of porous materials are widely used in modern industries with airspace or automotive applications among others. The reason for this is the advantages of such materials: better density-stiffness ratios in comparison with classical structural materials, the possibility to absorb energy, etc. As a rule, these constructions have a functionally graded structure. For example, the porous core is quite often covered by hard and stiff shell, which can be necessary for corrosion or thermal protection, and optimization of mechanical properties in the process of loading.

2 Initial Strain State of Inhomogeneous Plate

We consider the circular plate of radius r_1 and thickness H, and made of functionally graded material. The behavior of the plate is described by the model of micropolar elastic body [1, 5, 8, 10, 13, 19]. For the radial compression (extension) of the plate, the position of a particle in the strained state is given by the radius vector $\mathbf{R}$ [12, 20]:

$$\begin{aligned} R &= \alpha r, \quad && 0 \leqslant r \leqslant r_1, \\ \Phi &= \varphi, && 0 \leqslant \varphi \leqslant 2\pi, \\ Z &= f(z), && |z| \leqslant H/2, \end{aligned} \tag{1}$$

$$\mathbf{R} = \alpha r \mathbf{e}_R + f(z)\,\mathbf{e}_Z. \tag{2}$$

Here r, φ, z are cylindrical coordinates in the reference configuration (Lagrangian coordinates), R, Φ, Z are Eulerian cylindrical coordinates, $\{\mathbf{e}_r, \mathbf{e}_\varphi, \mathbf{e}_z\}$ and $\{\mathbf{e}_R, \mathbf{e}_\Phi, \mathbf{e}_Z\}$ are orthonormal vector bases of Lagrangian and Eulerian coordinates, respectively, α is the radial compression ratio, $f(z)$ is some unknown function, which describe the strain in the thickness direction of the inhomogeneous plate.

In addition, a proper orthogonal tensor of microrotation $\mathbf{H}$ is given, which characterizes the rotation of the micropolar medium particle and for the considered strain has the form

$$\mathbf{H} = \mathbf{e}_r \otimes \mathbf{e}_R + \mathbf{e}_\varphi \otimes \mathbf{e}_\Phi + \mathbf{e}_z \otimes \mathbf{e}_Z. \tag{3}$$

According to expressions (1) and (2), the deformation gradient $\mathbf{C}$ is (hereinafter $'$ denotes the derivative with respect to z):

$$\mathbf{C} = \operatorname{grad} \mathbf{R} = \alpha\,(\mathbf{e}_r \otimes \mathbf{e}_R + \mathbf{e}_\varphi \otimes \mathbf{e}_\Phi) + f'\mathbf{e}_z \otimes \mathbf{e}_Z, \tag{4}$$

where grad is the gradient in Lagrangian coordinates. It follows from relations (3) and (4) that the wryness tensor $\mathbf{L}$ is equal to zero [14, 15]

$$\mathbf{L} \times \mathbf{E} = -(\operatorname{grad} \mathbf{H}) \cdot \mathbf{H}^{\mathrm{T}} = 0$$

and the stretch tensor $\mathbf{Y}$ is expressed as follows

$$\mathbf{Y} = \mathbf{C} \cdot \mathbf{H}^{\mathrm{T}} = \alpha (\mathbf{e}_r \otimes \mathbf{e}_r + \mathbf{e}_\varphi \otimes \mathbf{e}_\varphi) + f' \mathbf{e}_z \otimes \mathbf{e}_z. \tag{5}$$

We assume that the elastic properties of the plate vary through the thickness, and they are described by the model of physically linear micropolar material, whose specific strain energy is a quadratic form of the tensors $\mathbf{Y} - \mathbf{E}$ and $\mathbf{L}$ [7, 11]:

$$\begin{aligned} W(\mathbf{Y}, \mathbf{L}) = {} & \frac{1}{2}\lambda(z)\mathrm{tr}^2(\mathbf{Y} - \mathbf{E}) + \frac{1}{2}(\mu(z) + \kappa(z))\,\mathrm{tr}\left((\mathbf{Y} - \mathbf{E}) \cdot (\mathbf{Y} - \mathbf{E})^{\mathrm{T}}\right) \\ & + \frac{1}{2}\mu(z)\mathrm{tr}(\mathbf{Y} - \mathbf{E})^2 + \frac{1}{2}\gamma_1(z)\mathrm{tr}^2\mathbf{L} + \frac{1}{2}\gamma_2(z)\mathrm{tr}\left(\mathbf{L} \cdot \mathbf{L}^{\mathrm{T}}\right) + \frac{1}{2}\gamma_3(z)\mathrm{tr}\,\mathbf{L}^2. \end{aligned} \tag{6}$$

Here $\lambda(z)$, $\mu(z)$ are functions describing the change in the Lamé parameters, $\kappa(z)$, $\gamma_1(z)$, $\gamma_2(z)$, $\gamma_3(z)$ are micropolar elastic parameters changing with the thickness coordinate, $\mathbf{E}$ is the unit tensor.

It follows from expressions (3), (5) and (6) that the Piola-type couple stress tensor $\mathbf{G}$ is equal to zero for the deformation of radial compression (1)–(3) of the circular plate

$$\mathbf{G} = \frac{\partial W}{\partial \mathbf{L}} \cdot \mathbf{H} = \left(\gamma_1 (\mathrm{tr}\,\mathbf{L})\,\mathbf{E} + \gamma_2 \mathbf{L} + \gamma_3 \mathbf{L}^{\mathrm{T}}\right) \cdot \mathbf{H} = 0$$

and Piola-type stress tensor $\mathbf{D}$ is

$$\begin{aligned} \mathbf{D} = \frac{\partial W}{\partial \mathbf{Y}} \cdot \mathbf{H} &= \left(\lambda \mathrm{tr}(\mathbf{Y} - \mathbf{E})\,\mathbf{E} + \mu\left(\mathbf{Y}^{\mathrm{T}} - \mathbf{E}\right) + (\mu + \kappa)(\mathbf{Y} - \mathbf{E})\right) \cdot \mathbf{H} \\ &= (\lambda s + \chi(\alpha - 1))(\mathbf{e}_r \otimes \mathbf{e}_R + \mathbf{e}_\varphi \otimes \mathbf{e}_\Phi) + \left(\lambda s + \chi\left(f' - 1\right)\right)\mathbf{e}_z \otimes \mathbf{e}_Z, \end{aligned} \tag{7}$$

$$s = 2\alpha + f' - 3, \qquad \chi = 2\mu + \kappa.$$

The equilibrium equations of nonlinear micropolar elasticity in absence of mass forces and moments are written as follows [7, 20]

$$\mathrm{div}\mathbf{D} = 0, \qquad \mathrm{div}\mathbf{G} + \left(\mathbf{C}^{\mathrm{T}} \cdot \mathbf{D}\right)_\times = 0, \tag{8}$$

where div is the divergence in the Lagrangian coordinates. The symbol $_\times$ represents the vector invariant of a second-order tensor:

$$\mathbf{K}_\times = (K_{mn}\mathbf{e}_m \otimes \mathbf{e}_n)_\times = K_{mn}\mathbf{e}_m \times \mathbf{e}_n$$

We assume that there are no external loads on the faces of the plate ($z = \pm H/2$), and there is no vertical displacement on the middle surface $z = 0$:

$$\mathbf{e}_z \cdot \mathbf{D}|_{z=\pm\frac{H}{2}} = 0, \qquad f(0) = 0 \tag{9}$$

By solving the boundary problem (8), (9) while taking into account the relations (7) we found the unknown function $f(z)$:

$$f(z) = \int_0^z \frac{2(1-\alpha)\lambda(x)}{\lambda(x) + 2\mu(x) + \kappa(x)} dx + z$$

In the special case, when the pattern of variation for elastic parameters λ, μ, κ is the same

$$\lambda(z) = \lambda_0 \xi(z), \qquad \mu(z) = \mu_0 \xi(z), \qquad \kappa(z) = \kappa_0 \xi(z)$$

the expression for the function $f(z)$ is quite simple:

$$f(z) = \alpha_3 z, \qquad \alpha_3 = 1 + \frac{2\lambda_0(1-\alpha)}{\lambda_0 + 2\mu_0 + \kappa_0}$$

3 Equilibrium Bifurcation for Inhomogeneous Plate

We assume that in addition to the above-described state of equilibrium for the inhomogeneous plate, there is an infinitely close equilibrium state under the same external loads, which is determined by the radius vector $\mathbf{R} + \eta\mathbf{v}$ and microrotation tensor $\mathbf{H} - \eta\mathbf{H} \times \omega$. Here η is a small parameter, $\mathbf{v}$ is the vector of additional displacements, ω is a linear incremental rotation vector, which characterizes the small rotation of the micropolar medium particles, measured from the initial strain state.

The perturbed state of equilibrium for the micropolar medium is described by the equations [7]:

$$\mathrm{div}\mathbf{D}^\bullet = 0, \qquad \mathrm{div}\mathbf{G}^\bullet + \left[\mathrm{grad}\mathbf{v}^{\mathrm{T}} \cdot \mathbf{D} + \mathbf{C}^{\mathrm{T}} \cdot \mathbf{D}^\bullet\right]_\times = 0, \tag{10}$$

where $\mathbf{D}^\bullet$ and $\mathbf{G}^\bullet$ are the linearized Piola-type stress and couple stress tensors. In the case of physically linear micropolar material (6), the following relations are valid for these tensors [17, 18]:

$$\mathbf{D}^\bullet = \left(\frac{\partial W}{\partial \mathbf{Y}}\right)^\bullet \cdot \mathbf{H} + \frac{\partial W}{\partial \mathbf{Y}} \cdot \mathbf{H}^\bullet = \left(\lambda(\mathrm{tr}\,\mathbf{Y}^\bullet)\mathbf{E} + (\mu+\kappa)\mathbf{Y}^\bullet + \mu\mathbf{Y}^{\bullet\mathrm{T}}\right) \cdot \mathbf{H}$$
$$- \left(\lambda \mathrm{tr}(\mathbf{Y}-\mathbf{E})\mathbf{E} + \mu\left(\mathbf{Y}^{\mathrm{T}} - \mathbf{E}\right) + (\mu+\kappa)(\mathbf{Y}-\mathbf{E})\right) \cdot \mathbf{H} \times \omega, \tag{11}$$

$$\begin{aligned}\mathbf{G}^{\bullet} &= \left(\frac{\partial W}{\partial \mathbf{L}}\right)^{\bullet} \cdot \mathbf{H} + \frac{\partial W}{\partial \mathbf{L}} \cdot \mathbf{H}^{\bullet} \\ &= \left(\gamma_1 (\operatorname{tr} \mathbf{L}^{\bullet})\, \mathbf{E} + \gamma_2 \mathbf{L}^{\bullet} + \gamma_3 \mathbf{L}^{\bullet \mathrm{T}}\right) \cdot \mathbf{H} - \left(\gamma_1 (\operatorname{tr} \mathbf{L})\, \mathbf{E} + \gamma_2 \mathbf{L} + \gamma_3 \mathbf{L}^{\mathrm{T}}\right) \cdot \mathbf{H} \times \omega, \\ \mathbf{Y}^{\bullet} &= (\operatorname{grad} \mathbf{v} + \mathbf{C} \times \omega) \cdot \mathbf{H}^{\mathrm{T}}, \qquad \mathbf{L}^{\bullet} = \operatorname{grad} \omega \cdot \mathbf{H}^{\mathrm{T}}.\end{aligned} \tag{12}$$

Here $\mathbf{Y}^{\bullet}$ is the linearized stretch tensor, $\mathbf{L}^{\bullet}$ is the linearized wryness tensor. Linearized boundary conditions on the faces of the plate $(z = \pm H/2)$ are written as follows:

$$\mathbf{e}_z \cdot \mathbf{D}^{\bullet}|_{z=\pm\frac{H}{2}} = 0, \qquad \mathbf{e}_z \cdot \mathbf{G}^{\bullet}|_{z=\pm\frac{H}{2}} = 0. \tag{13}$$

We assume that there is no friction at the edge of the plate $(r = r_1)$, and constant normal displacement is given. This leads to the following linearized boundary conditions:

$$\begin{aligned}\mathbf{e}_r \cdot \mathbf{D}^{\bullet} \cdot \mathbf{e}_{\Phi}|_{r=r_1} = \mathbf{e}_r \cdot \mathbf{D}^{\bullet} \cdot \mathbf{e}_Z|_{r=r_1} = \mathbf{e}_r \cdot \mathbf{v}|_{r=r_1} = 0, \\ \mathbf{e}_r \cdot \mathbf{G}^{\bullet} \cdot \mathbf{e}_R|_{r=r_1} = \mathbf{e}_{\varphi} \cdot \omega|_{r=r_1} = \mathbf{e}_z \cdot \omega|_{r=r_1} = 0.\end{aligned} \tag{14}$$

We write the vector of additional displacements $\mathbf{v}$ and vector of incremental rotation ω in the basis of Eulerian cylindrical coordinates:

$$\mathbf{v} = v_R \mathbf{e}_R + v_{\Phi} \mathbf{e}_{\Phi} + v_Z \mathbf{e}_Z, \qquad \omega = \omega_R \mathbf{e}_R + \omega_{\Phi} \mathbf{e}_{\Phi} + \omega_Z \mathbf{e}_Z. \tag{15}$$

With respect to representation (15), the expressions for the linearized stretch tensor $\mathbf{Y}^{\bullet}$ and wryness tensor $\mathbf{L}^{\bullet}$ have the form:

$$\begin{aligned}\mathbf{Y}^{\bullet} = &\left(\frac{\partial v_{\Phi}}{\partial r} - \alpha \omega_Z\right) \mathbf{e}_r \otimes \mathbf{e}_{\varphi} + \frac{1}{r}\left(\frac{\partial v_R}{\partial \varphi} - v_{\Phi} + \alpha r \omega_Z\right) \mathbf{e}_{\varphi} \otimes \mathbf{e}_r \\ &+ \left(\frac{\partial v_Z}{\partial r} + \alpha \omega_{\Phi}\right) \mathbf{e}_r \otimes \mathbf{e}_z + \left(\frac{\partial v_R}{\partial z} - f' \omega_{\Phi}\right) \mathbf{e}_z \otimes \mathbf{e}_r \\ &+ \frac{1}{r}\left(\frac{\partial v_Z}{\partial \varphi} - \alpha r \omega_R\right) \mathbf{e}_{\varphi} \otimes \mathbf{e}_z + \left(\frac{\partial v_{\Phi}}{\partial z} + f' \omega_R\right) \mathbf{e}_z \otimes \mathbf{e}_{\varphi} \\ &+ \frac{\partial v_R}{\partial r} \mathbf{e}_r \otimes \mathbf{e}_r + \frac{1}{r}\left(\frac{\partial v_{\Phi}}{\partial \varphi} + v_R\right) \mathbf{e}_{\varphi} \otimes \mathbf{e}_{\varphi} + \frac{\partial v_Z}{\partial z} \mathbf{e}_z \otimes \mathbf{e}_z,\end{aligned} \tag{16}$$

$$\begin{aligned}\mathbf{L}^{\bullet} = &\frac{\partial \omega_R}{\partial r} \mathbf{e}_r \otimes \mathbf{e}_r + \frac{1}{r}\left(\frac{\partial \omega_{\Phi}}{\partial \varphi} + \omega_R\right) \mathbf{e}_{\varphi} \otimes \mathbf{e}_{\varphi} + \frac{\partial \omega_Z}{\partial z} \mathbf{e}_z \otimes \mathbf{e}_z \\ &+ \frac{\partial \omega_{\Phi}}{\partial r} \mathbf{e}_r \otimes \mathbf{e}_{\varphi} + \frac{1}{r}\left(\frac{\partial \omega_R}{\partial \varphi} - \omega_{\Phi}\right) \mathbf{e}_{\varphi} \otimes \mathbf{e}_r + \frac{\partial \omega_Z}{\partial r} \mathbf{e}_r \otimes \mathbf{e}_z \\ &+ \frac{\partial \omega_R}{\partial z} \mathbf{e}_z \otimes \mathbf{e}_r + \frac{1}{r}\frac{\partial \omega_Z}{\partial \varphi} \mathbf{e}_{\varphi} \otimes \mathbf{e}_z + \frac{\partial \omega_{\Phi}}{\partial z} \mathbf{e}_z \otimes \mathbf{e}_{\varphi}.\end{aligned} \tag{17}$$

According to relations (3)–(5), (11), (12), (15)–(17), the components of the linearized Piola-type stress tensor $\mathbf{D}^\bullet$ and couple stress tensor $\mathbf{G}^\bullet$ are written as follows:

$$
\begin{aligned}
&\mathbf{e}_r \cdot \mathbf{D}^\bullet \cdot \mathbf{e}_R = (\lambda+\chi)\frac{\partial v_R}{\partial r} + \frac{\lambda}{r}\left(\frac{\partial v_\Phi}{\partial \varphi} + v_R\right) + \lambda\frac{\partial v_Z}{\partial z},\\
&\mathbf{e}_r \cdot \mathbf{D}^\bullet \cdot \mathbf{e}_\Phi = (\mu+\kappa)\frac{\partial v_\Phi}{\partial r} + \frac{\mu}{r}\left(\frac{\partial v_R}{\partial \varphi} - v_\Phi\right) + (\lambda s + 2\mu\alpha - \chi)\,\omega_Z,\\
&\mathbf{e}_r \cdot \mathbf{D}^\bullet \cdot \mathbf{e}_Z = (\mu+\kappa)\frac{\partial v_Z}{\partial r} + \mu\frac{\partial v_R}{\partial z} - \left(\lambda s + \mu\left(f' + \alpha\right) - \chi\right)\omega_\Phi,\\
&\mathbf{e}_\varphi \cdot \mathbf{D}^\bullet \cdot \mathbf{e}_R = \frac{\mu+\kappa}{r}\left(\frac{\partial v_R}{\partial \varphi} - v_\Phi\right) + \mu\frac{\partial v_\Phi}{\partial r} - (\lambda s + 2\mu\alpha - \chi)\,\omega_Z,\\
&\mathbf{e}_\varphi \cdot \mathbf{D}^\bullet \cdot \mathbf{e}_\Phi = \lambda\frac{\partial v_R}{\partial r} + \frac{\lambda+\chi}{r}\left(\frac{\partial v_\Phi}{\partial \varphi} + v_R\right) + \lambda\frac{\partial v_Z}{\partial z},\\
&\mathbf{e}_\varphi \cdot \mathbf{D}^\bullet \cdot \mathbf{e}_Z = \frac{\mu+\kappa}{r}\frac{\partial v_Z}{\partial \varphi} + \mu\frac{\partial v_\Phi}{\partial z} + \left(\lambda s + \mu\left(f' + \alpha\right) - \chi\right)\omega_R z,\\
&\mathbf{e}_z \cdot \mathbf{D}^\bullet \cdot \mathbf{e}_R = (\mu+\kappa)\frac{\partial v_R}{\partial z} + \mu\frac{\partial v_Z}{\partial r} + \left(\lambda s + \mu\left(f' + \alpha\right) - \chi\right)\omega_P i,\\
&\mathbf{e}_z \cdot \mathbf{D}^\bullet \cdot \mathbf{e}_\Phi = (\mu+\kappa)\frac{\partial v_\Phi}{\partial z} + \frac{\mu}{r}\frac{\partial v_Z}{\partial \varphi} - \left(\lambda s + \mu\left(f' + \alpha\right) - \chi\right)\omega_R,\\
&\mathbf{e}_z \cdot \mathbf{D}^\bullet \cdot \mathbf{e}_Z = \lambda\frac{\partial v_R}{\partial r} + \frac{\lambda}{r}\left(\frac{\partial v_\Phi}{\partial \varphi} + v_R\right) + (\lambda+\chi)\frac{\partial v_Z}{\partial z},\\
&\mathbf{e}_r \cdot \mathbf{G}^\bullet \cdot \mathbf{e}_R = (\gamma_1+\gamma_2+\gamma_3)\frac{\partial \omega_R}{\partial r} + \frac{\gamma_1}{r}\left(\frac{\partial \omega_\Phi}{\partial \varphi} + \omega_R\right) + \gamma_1\frac{\partial \omega_Z}{\partial z},\\
&\mathbf{e}_r \cdot \mathbf{G}^\bullet \cdot \mathbf{e}_\Phi = \gamma_2\frac{\partial \omega_\Phi}{\partial r} + \frac{\gamma_3}{r}\left(\frac{\partial \omega_R}{\partial \varphi} - \omega_\Phi\right),\\
&\mathbf{e}_\varphi \cdot \mathbf{G}^\bullet \cdot \mathbf{e}_R = \frac{\gamma_2}{r}\left(\frac{\partial \omega_R}{\partial \varphi} - \omega_\Phi\right) + \gamma_3\frac{\partial \omega_\Phi}{\partial r},\\
&\mathbf{e}_r \cdot \mathbf{G}^\bullet \cdot \mathbf{e}_Z = \gamma_2\frac{\partial \omega_Z}{\partial r} + \gamma_3\frac{\partial \omega_R}{\partial z},\\
&\mathbf{e}_z \cdot \mathbf{G}^\bullet \cdot \mathbf{e}_R = \gamma_2\frac{\partial \omega_R}{\partial z} + \gamma_3\frac{\partial \omega_Z}{\partial r},\\
&\mathbf{e}_\varphi \cdot \mathbf{G}^\bullet \cdot \mathbf{e}_\Phi = \gamma_1\frac{\partial \omega_R}{\partial r} + \frac{\gamma_1+\gamma_2+\gamma_3}{r}\left(\frac{\partial \omega_\Phi}{\partial \varphi} + \omega_R\right) + \gamma_1\frac{\partial \omega_Z}{\partial z},\\
&\mathbf{e}_\varphi \cdot \mathbf{G}^\bullet \cdot \mathbf{e}_Z = \frac{\gamma_2}{r}\frac{\partial \omega_Z}{\partial \varphi} + \gamma_3\frac{\partial \omega_\Phi}{\partial z},\\
&\mathbf{e}_z \cdot \mathbf{G}^\bullet \cdot \mathbf{e}_\Phi = \gamma_2\frac{\partial \omega_\Phi}{\partial z} + \frac{\gamma_3}{r}\frac{\partial \omega_Z}{\partial \varphi},\\
&\mathbf{e}_z \cdot \mathbf{G}^\bullet \cdot \mathbf{e}_Z = \gamma_1\frac{\partial \omega_R}{\partial r} + \frac{\gamma_1}{r}\left(\frac{\partial \omega_\Phi}{\partial \varphi} + \omega_R\right) + (\gamma_1+\gamma_2+\gamma_3)\frac{\partial \omega_Z}{\partial z}.
\end{aligned}
\tag{18}
$$

Using expressions (4), (5), (7) and (15), (18), we write the equations of the neutral equilibrium (10) for the inhomogeneous plate in scalar form:

$$(\mu+\kappa)\left(\frac{1}{r^2}\frac{\partial^2 v_R}{\partial\varphi^2}+\frac{\partial^2 v_R}{\partial z^2}-\frac{1}{r^2}\frac{\partial v_\Phi}{\partial\varphi}\right)+(\lambda+\mu)\left(\frac{1}{r}\frac{\partial^2 v_\Phi}{\partial r\partial\varphi}+\frac{\partial^2 v_Z}{\partial r\partial z}\right)$$
$$+(\lambda+\chi)\left(\frac{\partial^2 v_R}{\partial r^2}+\frac{1}{r}\frac{\partial v_R}{\partial r}-\frac{1}{r^2}v_R-\frac{1}{r^2}\frac{\partial v_\Phi}{\partial\varphi}\right)+\left(\mu'+\kappa'\right)\frac{\partial v_R}{\partial z}+\mu'\frac{\partial v_Z}{\partial r}$$
$$+\xi\frac{\partial\omega_\Phi}{\partial z}+\xi'\omega_\Phi-\frac{1}{r}\left(\lambda s+2\mu\alpha-\chi\right)\frac{\partial\omega_Z}{\partial\varphi}=0,$$

$$\frac{\lambda+\chi}{r^2}\left(\frac{\partial^2 v_\Phi}{\partial\varphi^2}+\frac{\partial v_R}{\partial\varphi}\right)+\frac{\lambda+\mu}{r}\left(\frac{\partial^2 v_R}{\partial r\partial\varphi}+\frac{\partial^2 v_Z}{\partial\varphi\partial z}\right)+\left(\mu'+\kappa'\right)\frac{\partial v_\Phi}{\partial z}$$
$$+(\mu+\kappa)\left(\frac{\partial^2 v_\Phi}{\partial r^2}+\frac{1}{r}\frac{\partial v_\Phi}{\partial r}-\frac{1}{r^2}v_\Phi+\frac{1}{r^2}\frac{\partial v_R}{\partial\varphi}+\frac{\partial^2 v_\Phi}{\partial z^2}\right)+\frac{\mu'}{r}\frac{\partial v_Z}{\partial\varphi}$$
$$-\xi\frac{\partial\omega_R}{\partial z}-\xi'\omega_R+\left(\lambda s+2\mu\alpha-\chi\right)\frac{\partial\omega_Z}{\partial r}=0,$$

$$(\lambda+\chi)\frac{\partial^2 v_Z}{\partial z^2}+(\mu+\kappa)\left(\frac{\partial^2 v_Z}{\partial r^2}+\frac{1}{r}\frac{\partial v_Z}{\partial r}+\frac{1}{r^2}\frac{\partial^2 v_Z}{\partial\varphi^2}\right)$$
$$+(\lambda+\mu)\left(\frac{\partial^2 v_R}{\partial r\partial z}+\frac{1}{r}\frac{\partial v_R}{\partial z}+\frac{1}{r}\frac{\partial^2 v_\Phi}{\partial\varphi\partial z}\right)+\lambda'\frac{\partial v_R}{\partial r}+\frac{\lambda'}{r}\left(\frac{\partial v_\Phi}{\partial\varphi}+v_R\right)$$
$$+\left(\lambda'+\chi'\right)\frac{\partial v_Z}{\partial z}+\xi\left(\frac{1}{r}\frac{\partial\omega_R}{\partial\varphi}-\frac{\partial\omega_\Phi}{\partial r}-\frac{1}{r}\omega_\Phi\right)=0,$$

$$(\gamma_1+\gamma_2+\gamma_3)\left(\frac{\partial^2\omega_R}{\partial r^2}+\frac{1}{r}\frac{\partial\omega_R}{\partial r}-\frac{1}{r^2}\frac{\partial\omega_\Phi}{\partial\varphi}-\frac{1}{r^2}\omega_R\right)$$
$$+(\gamma_1+\gamma_3)\left(\frac{1}{r}\frac{\partial^2\omega_\Phi}{\partial r\partial\varphi}+\frac{\partial^2\omega_Z}{\partial r\partial z}\right)+\gamma_2\left(\frac{1}{r^2}\frac{\partial^2\omega_R}{\partial\varphi^2}+\frac{\partial^2\omega_R}{\partial z^2}-\frac{1}{r^2}\frac{\partial\omega_\Phi}{\partial\varphi}\right) \quad (19)$$
$$+\gamma_2'\frac{\partial\omega_R}{\partial z}+\gamma_3'\frac{\partial\omega_Z}{\partial r}+\xi\left(\frac{\partial v_\Phi}{\partial z}-\frac{1}{r}\frac{\partial v_Z}{\partial\varphi}+\left(\alpha+f'\right)\omega_R\right)=0,$$

$$\frac{\gamma_1+\gamma_2+\gamma_3}{r^2}\left(\frac{\partial^2\omega_\Phi}{\partial\varphi^2}+\frac{\partial\omega_R}{\partial\varphi}\right)+\frac{\gamma_1+\gamma_3}{r}\left(\frac{\partial^2\omega_R}{\partial r\partial\varphi}+\frac{\partial^2\omega_Z}{\partial\varphi\partial z}\right)+\gamma_2'\frac{\partial\omega_\Phi}{\partial z}$$
$$+\gamma_2\left(\frac{1}{r^2}\frac{\partial\omega_R}{\partial\varphi}+\frac{\partial^2\omega_\Phi}{\partial r^2}+\frac{1}{r}\frac{\partial\omega_\Phi}{\partial r}+\frac{\partial^2\omega_\Phi}{\partial z^2}-\frac{1}{r^2}\omega_\Phi\right)+\frac{\gamma_3'}{r}\frac{\partial\omega_Z}{\partial\varphi}$$
$$+\xi\left(\frac{\partial\nu_Z}{\partial r}-\frac{\partial\nu_R}{\partial z}+(\alpha+f')\,\omega_\Phi\right)=0$$

$$(\gamma_1+\gamma_3)\left(\frac{\partial^2\omega_R}{\partial r\partial z}+\frac{1}{r}\frac{\partial\omega_R}{\partial z}+\frac{1}{r}\frac{\partial^2\omega_\Phi}{\partial\varphi\partial z}\right)+\gamma_2\left(\frac{\partial^2\omega_Z}{\partial r^2}+\frac{1}{r}\frac{\partial\omega_Z}{\partial r}+\frac{1}{r^2}\frac{\partial^2\omega_Z}{\partial\varphi^2}\right)$$
$$+(\gamma_1+\gamma_2+\gamma_3)\frac{\partial^2\omega_Z}{\partial z^2}+\gamma_1'\frac{\partial\omega_R}{\partial r}+\frac{\gamma_1'}{r}\frac{\partial\omega_\Phi}{\partial\varphi}+\frac{\gamma_1'}{r}\omega_R+(\gamma_1'+\gamma_2'+\gamma'3)\frac{\partial\omega_Z}{\partial z}$$
$$+(\lambda s+2\mu\alpha-\chi)\left(\frac{1}{r}\frac{\partial\nu_R}{\partial\varphi}-\frac{1}{r}\nu_\Phi-\frac{\partial\nu_\Phi}{\partial r}+2\alpha\omega_Z\right)=0.$$

Substitution

$$\nu_R=V_R(r,z)\cos n\varphi,\quad \nu_\Phi=V_\Phi(r,z)\sin n\varphi,\quad \nu_Z=V_Z(r,z)\cos n\varphi,$$
$$\omega_R=\Omega_R(r,z)\sin n\varphi,\quad \omega_\Phi=\Omega_\Phi(r,z)\cos n\varphi,\quad \omega_Z=\Omega_Z(r,z)\sin n\varphi,$$

$$n=0,\ 1,\ 2,\ldots$$

allows us to separate the variable φ in these equations, reducing the stability analysis to the solution of homogeneous boundary problem (13), (14) and (19) for a system of six partial differential equations in the six unknown functions of two variables $r,\ z$.

4 Axisymmetric Buckling Modes

In the special case of axisymmetric perturbations $(n=0)$ the use of substitution

$$\begin{array}{lll}\nu_R=V_R(z)\,J_1(\beta r), & \nu_\Phi=0, & \nu_Z=V_Z(z)\,J_0(\beta r),\\ \omega_R=0, & \omega_\Phi=\Omega_\Phi(z)\,J_1(\beta r), & \omega_Z=0,\end{array}\qquad(20)$$

$$\beta=\zeta_m/r_1,\qquad J_1(\zeta_m)=0,\qquad m=1,2,\ldots$$

leads to the separation of variable r in the equations of neutral equilibrium and allows to satisfy the linearized boundary conditions (14) at the edge of the plate.

By taking into account the relations (20), the linearized equilibrium equations (19) are written as follows:

$$\begin{aligned}(\mu+\kappa)\,V_R''+\left(\mu'+\kappa'\right)V_R'-(\lambda+\chi)\,\beta^2V_R-(\lambda+\mu)\,\beta V_Z'-\\-\beta\mu' V_Z+\theta\Omega_\Phi'+\theta'\Omega_\Phi=0,\end{aligned}$$

$$\begin{aligned}(\lambda+\chi)\,V_Z''+\left(\lambda'+\chi'\right)V_Z'-(\mu+\kappa)\beta^2V_Z+(\lambda+\mu)\,\beta V_R'+\\+\beta\lambda' V_R-\theta\beta\Omega_\Phi=0,\end{aligned}\qquad(21)$$

$$\gamma_2\Omega_\Phi''+\gamma_2'\Omega_\Phi'+\left[\left(\alpha+f'\right)\theta-\gamma_2\beta^2\right]\Omega_\Phi-\theta V_R'-\beta\theta V_Z=0.$$

Here we use the following notation

$$\theta=\lambda s+\mu\left(\alpha+f'\right)-\chi.$$

The linearized boundary conditions on the faces of the plate (13) take the form:

$$(\mu+\kappa)\,V_R'-\mu\beta V_Z+\theta\Omega_\Phi=0,\quad \beta\lambda V_R+(\lambda+\chi)\,V_Z'=0,\quad \Omega_\Phi'=0.\qquad(22)$$

Thus, in the case of axisymmetric perturbations, the stability analysis of the inhomogeneous circular plate is reduced to solving a linear homogeneous boundary-value problem (21) and (22) for a system of three ordinary differential equations.

5 Symmetric Plate

It is easy to show that if the functions describing the change in the elastic parameters of the plate through the thickness are even, i.e. $\lambda(z)=\lambda(-z)$, $\mu(z)=\mu(-z)$, $\kappa(z)=\kappa(-z)$, $\gamma_1(z)=\gamma_1(-z)$, $\gamma_2(z)=\gamma_2(-z)$, $\gamma_3(z)=\gamma_3(-z)$, then the boundary-value problem (21), (22) has two independent sets of solutions [16], [18].

The **First set** is formed by solutions for which the deflection of a plate is an odd function of z (symmetric buckling):

$$V_R(z)=V_R(-z),\qquad V_Z(z)=-V_Z(-z),\qquad \Omega_\Phi(z)=-\Omega_\Phi(-z).$$

For the **Second set** of solutions, on the contrary, the deflection is an even function of z (bending buckling):

$$V_R(z)=-V_R(-z),\qquad V_Z(z)=V_Z(-z),\qquad \Omega_\Phi(z)=\Omega_\Phi(-z).$$

Due to this property of boundary-value problem (21) and (22), for the study of stability it is sufficient to consider only the upper half of the inhomogeneous plate $(0 \leqslant z \leqslant H/2)$. The boundary conditions at $z = 0$ follows from the evenness and oddness of the unknown functions V_R, V_Z, Ω_Φ:

(a) for the **First set** of solutions:

$$V_R'(0) = V_Z(0) = \Omega_\Phi(0) = 0, \tag{23}$$

(b) for the **Second set** of solutions:

$$V_R(0) = V_Z'(0) = \Omega_\Phi'(0) = 0. \tag{24}$$

Thus, in the case of symmetric inhomogeneous plate, the stability analysis is reduced to solving two linear homogeneous boundary-value problems—(21), (22), (23) and (21), (22), (24)—for a system of three ordinary differential equations.

6 Conclusion

In the framework of bifurcation approach, the stability of an inhomogeneous circular plate subjected to radial compression and composed of a micropolar material is studied. For the physically linear micropolar material, a system of linearized equilibrium equations (19) is derived, which describes the behavior of the inhomogeneous plate in a perturbed state. Using special substitution (20) this equations are simplified and the linearized boundary-value problem is formulated for the case of an axisymmetric perturbations. Namely, the stability analysis is reduced to solving a linear homogeneous boundary problem (21) and (22) for a system of three ordinary differential equations.

It was also shown that, if the inhomogeneous plate is symmetric with respect to the middle surface $z = 0$, then the stability analysis is reduced to solving two independent linear homogeneous boundary-value problems for the half-plate—(21), (22), (23) and (21), (22), (24).

For specific micropolar materials all formulated boundary-value problems can be solved numerically using the same method as in [17] and [18].

Acknowledgments This work was supported by the Russian Foundation for Basic Research (grant 12-01-91262-RFG-z and 11-08-01152-a) and German Academic Exchange Service (DAAD) (program “Forschungsaufenthalte für Hochschullehrer und Wissenschaftler”).

References

1. Altenbach, J., Altenbach, H., Eremeyev, V.A.: On generalized Cosserat-type theories of plates and shells: a short review and bibliography. Arch. Appl. Mech. **80**, 73–92 (2010)
2. Ashby, M.F., Evans, A.G., Fleck, N.A., Gibson, L.J., Hutchinson, J.W., Wadley, H.N.G.: Metal Foams: A Design Guide. Butterworth-Heinemann, Boston (2000)
3. Banhart, J.: Manufacturing routes for metallic foams. J. Miner. **52**(12), 22–27 (2000)
4. Banhart, M.F.A.J., Fleck, N.A. (eds.): Metal Foams and Porous Metal Structures. MIT Publishing, Bremen (1999)
5. Cosserat, E., Cosserat, F.: Théorie des Corps Déformables. Hermann et Fils, Paris (1909)
6. Degischer, H.P., Kriszt, B. (eds.): Handbook of Cellular Metals. Production, Processing, Applications. Wiley, Weinheim (2002)
7. Eremeyev, V.A., Zubov, L.M.: On stability of elastic bodies with couple-stresses. Mech. Solids **29**(3), 172–181 (1994)
8. Eringen, A.C.: Microcontinuum Field Theory. I. Foundations and Solids, Springer, New York (1999)
9. Gibson, L.J., Ashby, M.F.: Cellular Solids: Structure and Properties. 2nd edn. Cambridge Solid State Science Series, Cambridge University Press, Cambridge (1997)
10. Kafadar, C.B., Eringen, A.C.: Micropolar media - I. The classical theory. Int. J. Eng. Sci. **9**, 271–305 (1971)
11. Lakes, R.: Experimental methods for study of Cosserat elastic solids and other generalized elastic continua. In: Muhlhaus, H., Wiley, J. (eds.) Continuum Models for Materials with Micro-Structure, pp. 1–22. New York (1995)
12. Lurie, A.I.: Non-linear Theory of Elasticity. North-Holland, Amsterdam (1990)
13. Maugin, G.A.: On the structure of the theory of polar elasticity. Philos. Trans. Roy. Soc. London A **356**, 1367–1395 (1998)
14. Nikitin, E., Zubov, L.M.: Conservation laws and conjugate solutions in the elasticity of simple materials and materials with couple stress. J. Elast. **51**, 1–22 (1998)
15. Pietraszkiewicz, W., Eremeyev, V.A.: On natural strain measures of the non-linear micropolar continuum. Int. J. Solids Struct. **46**, 774–787 (2009)
16. Sheydakov, D.N.: Stability of a rectangular plate under biaxial tension. J. Appl. Mech. Tech. Phys. **48**(4), 547–555 (2007)
17. Sheydakov, D.N.: Buckling of elastic composite rod of micropolar material subject to combined loads. In: Altenbach, H., Erofeev, V.I., Maugin, G.A. (eds.) Mechanics of Generalized Continua—From Micromechanical Basics to Engineering Applications, Advanced Structured Materials, vol. 7, pp. 255–271. Springer, Berlin (2011a)
18. Sheydakov, D.N.: On stability of elastic rectangular sandwich plate subject to biaxial compression. In: Altenbach, H., Eremeyev, V.A. (eds.) Shell-like Structures—Non-classical Theories and Applications, Advanced Structured Materials, vol. 15, pp. 203–216, Springer, Berlin (2011b)
19. Toupin, R.A.: Theories of elasticity with couple-stress. Arch. Ration. Mechan. Anal. **17**, 85–112 (1964)
20. Zubov, L.M.: Nonlinear Theory of Dislocations and Disclinations in Elastic Bodies. Springer, Berlin (1997)

A Theory of Disclination and Dislocation Fields for Grain Boundary Plasticity

V. Taupin, L. Capolungo, C. Fressengeas, A. Das and M. Upadhyay

Abstract A continuum mechanics model is introduced for a core and structure sensitive modeling of grain boundary mediated plasticity. It accounts for long range elastic strain and curvature incompatibilities due to the presence of dislocation and disclination densities. The coupled spatio-temporal evolution of the crystal defects is also accounted for by transport equations. Based on atomistic structures, copper tilt boundaries are modeled with periodic sequences of wedge disclination dipoles. Their self-relaxation by transport leads to grain boundary configurations with lower elastic energies, which are compared to molecular statics values. The characteristic internal length inherent to strain gradient elasticity, which relates the elastic energy weight of couple-stresses to that of stresses, is chosen to retrieve the elastic energy obtained by atomistic simulations. This length is found to be lower than interatomic distances. In agreement with atomistic modeling, couple-stress elasticity is thought to be relevant for the modeling of highly heterogeneous defect microstructures at atomic resolution scales only.

V. Taupin (✉) · C. Fressengeas · A. Das
Laboratoire d'Etude des Microstructures et de Mécanique des Matériaux, Université de Lorraine/CNRS, Ile du Saulcy, 57045 Metz Cedex, France
e-mail: vincent.taupin@univ-lorraine.fr

L. Capolungo · M. Upadhyay
G.W. Woodruff School of Mechanical Engineering, Georgia Institute of Technology/CNRS, 57070 Metz Cedex, France

L. Capolungo
e-mail: laurent.capolungo@me.gatech.edu

C. Fressengeas
e-mail: claude.fressengeas@univ-lorraine.fr

A. Das
e-mail: amitdas.cmu@gmail.com

M. Upadhyay
e-mail: manasvupadhyay@gmail.com

H. Altenbach et al. (eds.), *Generalized Continua as Models for Materials*, Advanced Structured Materials 22, DOI: 10.1007/978-3-642-36394-8_18,

1 Introduction

When decreasing the grain size of polycrystals down to the nanometer range, the considerable gain in yield stress becomes usually counterbalanced by a loss of ductility, due to restricted dislocation glide inside grains [1]. The mechanisms producing plastic deformation are indeed different from the usual ones in coarse polycrystals. They mostly involve grain boundaries (GBs), which become the predominant source of plasticity. Well known examples of these new mechanisms are the shear coupled boundary migration [2–4], or the emission and glide of dislocations from grain boundaries [5–8]. Modeling efforts for the description of GBs include atomistic simulations [2, 5–9], dislocation/disclination-based models [2, 10–14] and mechanical approaches [15–19]. As shown from atomistic simulations, the grain boundary behavior is core and structure sensitive. Examples are the coupling factors in shear coupled boundary migration [2], or the free volume of grain boundaries, which is closely related to the dislocation emission mechanism [20].

Here we propose an original continuum mechanics model of crystal defects, for a core and structure sensitive description of GBs. By core description, we mean a continuous description, possibly below interatomic distances, of crystal defects and their associated elastic energy in the grain boundary area. By structure sensitive modeling, we mean that the crystal defect distributions which will be used to model grain boundaries must be based on real atomic structures. In addition to dislocations, which are the well known source of plastic deformation, we introduce disclinations. These rotation defects were shown to be more appropriate than dislocations for the modeling of high angle tilt grain boundaries [12]. The disclination structural unit model (DSUM) of grain boundaries, a structure sensitive model [14], is used in this work. In this model, atomic structural units, which, as revealed by molecular statics, compose the grain boundary [9], are modeled by equivalent wedge disclination dipoles. The great advantage of this model lies in the fact that it uses real atomic structures to define grain boundaries, but does not need to model atoms. Thus, it provides a time scale transition from atomistic simulations, because it does not need to solve for atomic vibrations and allows then using much larger and realistic simulation times. However this model is static. In addition, the DSUM uses discrete defects and is then singular in the interface plane. Therefore, we propose to set up the DSUM model into a continuous and dynamic framework. It is to note that even if it is often assumed that a wedge disclination dipole can be replaced by an equivalent edge dislocation, because the stress field of wedge disclination dipole with a small arm length is equivalent to that of an edge dislocation, the two kinds of defects are not equivalent. First, they are different in nature. The disclination is a rotational defect while a dislocation is a translational defect. Further, as discussed in the paper, disclination dipoles introduce incompatible elastic curvatures which contribute to the elastic energy of grain boundaries. Dislocations introduce compatible curvatures which are negligible in this respect. Then, the motion of disclinations leads to the nucleation of dislocations [21]. When modeling grain boundaries as disclination dipoles, we believe that this dislocation source mechanism will be at the origin of dislocation emission and absorption at grain boundaries. Such mechanisms have been proposed [22].

Use is made of a recent elasto-plastic theory of dislocation and disclination fields [21, 23]. In the latter, a continuous rendition of dislocations and disclinations, as well as their associated elastic energy is chosen, and plasticity mechanisms can be described by the coupled transport of dislocation and disclination densities. This theory is first applied to the self-relaxation of <001> tilt boundaries in copper [24]. Initial grain boundaries will be set up by using wedge disclination dipoles, based on the DSUM model. The reader is referred to [24] for a detailed description of initial conditions. Then, the continuous disclination dipoles will be allowed to relax in their self stress and couple-stress fields, until self-organized structures of lower energy emerge. The structure of relaxed grain boundaries will be analyzed, by comparison with atomistic simulations. Particularly, the importance of using a dynamic and continuous rendition of crystal defects to obtain elastic energies similar to those of molecular statics will be discussed.

The paper is organized as follows. In Sect. 2 notations are settled. In Sect. 3 the elasto-plastic theory of dislocation and disclination fields is briefly recalled, with special reference to the elasto-static theory developed by deWit [25]. In Sect. 4 a plane edge-wedge model is set up for tilt boundaries. The self-relaxation of <001> copper tilt boundaries is analyzed in Sect. 5 by comparison with molecular statics data. Conclusions follow.

2 Notations

A bold symbol denotes a tensor. The symmetric part of tensor $\mathbf{A}$ is denoted $\mathbf{A}^{\mathbf{sym}}$. Its skew-symmetric part is $\mathbf{A}^{\mathbf{skew}}$. The tensor $\mathbf{A}.\mathbf{B}$, with rectangular Cartesian components $A_{ik}B_{kj}$, results from the dot product of tensors $\mathbf{A}$ and $\mathbf{B}$, and $\mathbf{A} \otimes \mathbf{B}$ is their tensorial product, with components $A_{ij}B_{kl}$. A : represents the trace inner product of the two second order tensors $\mathbf{A} : \mathbf{B} = A_{ij}B_{ij}$, in rectangular Cartesian components, or the product of a higher order tensor with a second order tensor, e.g., $\mathbf{A} : \mathbf{B} = A_{ijkl}B_{kl}$. The cross product of a second-order tensor $\mathbf{A}$ and a vector $\mathbf{V}$, the **div** and **curl** operations for second-order tensors are defined row by row, in analogy with the vectorial case. For any base vector $\mathbf{e}_i$ of the reference frame:

$$(\mathbf{A} \times \mathbf{V})^t.\mathbf{e}_i = (\mathbf{A}^t.\mathbf{e}_i) \times \mathbf{V} \tag{1}$$

$$(\mathbf{div}\,\mathbf{A})^t.\mathbf{e}_i = \mathbf{div}(\mathbf{A}^t.\mathbf{e}_i) \tag{2}$$

$$(\mathbf{curl}\,\mathbf{A})^t.\mathbf{e}_i = \mathbf{curl}(\mathbf{A}^t.\mathbf{e}_i). \tag{3}$$

In rectangular Cartesian components:

$$(\mathbf{A} \times \mathbf{V})_{ij} = e_{jkl}A_{ik}V_l \tag{4}$$

$$(\mathbf{div}\,\mathbf{A})_i = A_{ij,j} \tag{5}$$

$$(\mathbf{curl}\,\mathbf{A})_{ij} = e_{jkl}A_{il,k}. \tag{6}$$

where e_{jkl} is a component of the third-order alternating Levi-Civita tensor $\mathbf{X}$. A vector $\mathbf{A}$ is associated with tensor $\mathbf{A}$ by using its trace inner product with tensor $\mathbf{X}$:

$$(\mathbf{A})_k = -\frac{1}{2}(\mathbf{A} : \mathbf{X})_k = -\frac{1}{2} e_{ijk} A_{ij}. \tag{7}$$

In the component representation, the spatial derivative with respect to a Cartesian coordinate is indicated by a comma followed by the component index. A superposed dot represents a material time derivative.

3 Review of the Elasto-Plastic Theory of Dislocation and Disclination Fields

In the present framework, it is assumed that the displacement vector $\mathbf{u}$ can be defined continuously at any point of a simply-connected body undergoing elasto-plastic deformation. Hence, it is required that the displacement field represents a consistent shape change, possibly defined between atoms, below interatomic distance. Therefore, the total distortion tensor is defined as the gradient of the displacement $\mathbf{U} = \mathbf{grad}\ \mathbf{u}$. As such, it is curl-free:

$$\mathbf{curl}\ \mathbf{U} = 0. \tag{8}$$

This equation is a necessary condition for the integrability of the displacement $\mathbf{u}$.

Conversely, this equation is sufficient to assure the existence of a single-valued continuous solution $\mathbf{u}$ to the equation $\mathbf{U} = \mathbf{grad}\ \mathbf{u}$, up to a constant translation. Equation (8) is referred to as the compatibility condition for the distortion $\mathbf{U}$. Defining the strain tensor $\boldsymbol{\epsilon}$ as the symmetric part of the distortion $\mathbf{U}$, the rotation tensor $\boldsymbol{\mathcal{W}}$ as its skew-symmetric part and the associated rotation vector $\boldsymbol{\omega}$ as:

$$\boldsymbol{\omega} = -\frac{1}{2}\boldsymbol{\mathcal{W}} : \mathbf{X} = \frac{1}{2}\mathbf{curl}\ \mathbf{u}, \tag{9}$$

Eq. (8) becomes:

$$\mathbf{curl}\ \boldsymbol{\epsilon} + div(\boldsymbol{\omega})\mathbf{I} - \mathbf{grad}^{\mathbf{t}}\boldsymbol{\omega} = 0, \tag{10}$$

where $\mathbf{I}$ is the identity tensor. Transposing, then taking the **curl** of Eq. (10) leads to:

$$\mathbf{curl}\ \mathbf{curl}^{\mathbf{t}}\ \boldsymbol{\epsilon} = 0. \tag{11}$$

This relation is the classical Saint-Venant compatibility condition for the strain $\boldsymbol{\epsilon}$. It is a necessary condition for the integrability of the displacement $\mathbf{u}$. The trace of Eq. (10) similarly yields a compatibility condition for the rotation vector in the form:

$$div(\boldsymbol{\omega}) = 0. \tag{12}$$

At this point, we define the elastic, $\boldsymbol{\kappa}_e$, plastic, $\boldsymbol{\kappa}_p$, and total, $\boldsymbol{\kappa}$, curvature tensors as:

$$\boldsymbol{\kappa}_e = \mathbf{grad}\ \boldsymbol{\omega}_e \tag{13}$$

$$\boldsymbol{\kappa}_p = \mathbf{grad}\ \boldsymbol{\omega}_p \tag{14}$$

$$\boldsymbol{\kappa} = \mathbf{grad}\ \boldsymbol{\omega} = \boldsymbol{\kappa}_e + \boldsymbol{\kappa}_p \tag{15}$$

In the above, the elastic and plastic curvatures $(\boldsymbol{\kappa}_e, \boldsymbol{\kappa}_p)$ are curl-free and integrable quantities. In the present theory however, $(\boldsymbol{\kappa}_e, \boldsymbol{\kappa}_p)$ are not supposed to be curl-free anymore, i.e., the possibility of a rotational incompatibility is acknowledged. Then the rotation vectors $(\boldsymbol{\omega}_e, \boldsymbol{\omega}_p)$ do not exist, and a non-zero tensor $\boldsymbol{\theta}$ such that

$$\boldsymbol{\theta} = -\mathbf{curl}\ \boldsymbol{\kappa}_p = \mathbf{curl}\ \boldsymbol{\kappa}_e \tag{16}$$

can be defined. $\boldsymbol{\theta}$ is the disclination density tensor, and Eq. (16) is part of the theory of crystal defects. On the one hand, Eq. (16) means that an incompatible plastic curvature, $\boldsymbol{\kappa}_p^{\perp}$, is associated with the presence of the disclination density $\boldsymbol{\theta}$ and, on the other hand, that the incompatible elastic curvature, $\boldsymbol{\kappa}_e^{\perp}$ is needed to ensure the continuity of matter in the presence of this density. To ensure that the incompatible parts $(\boldsymbol{\kappa}_e^{\perp}, \boldsymbol{\kappa}_p^{\perp})$ vanish identically throughout the body when $\boldsymbol{\theta} = 0$, Eq. (16) must be replaced with:

$$\boldsymbol{\theta} = -\mathbf{curl}\ \boldsymbol{\kappa}_p{}^{\perp} = \mathbf{curl}\ \boldsymbol{\kappa}_e{}^{\perp}, \tag{17}$$

augmented with the side conditions $\mathbf{div}\boldsymbol{\kappa}_e^{\perp} = \mathbf{div}\boldsymbol{\kappa}_p^{\perp} = 0$ and $\boldsymbol{\kappa}_e^{\perp}.\mathbf{n} = \boldsymbol{\kappa}_p^{\perp}.\mathbf{n} = \mathbf{0}$ on the boundary with unit normal $\mathbf{n}$. These conditions ensure uniqueness of the solution. The disclination density defined in Eq. (17) is an areal and tensorial rendition of the rotational incompatibility. The associated point-wise measure of incompatibility is the Frank vector, i.e. the rotational closure defect of a circuit C, obtained by integrating the incompatible elastic curvatures along the circuit:

$$\boldsymbol{\Omega} = \int_C \boldsymbol{\kappa}_e^{\perp}.\mathbf{dr} \tag{18}$$

This rotation discontinuity is related to the disclination density by applying Stokes theorem to the surface S of normal $\mathbf{n}$ delimited by the circuit C.

$$\boldsymbol{\Omega} = \int_S \boldsymbol{\theta}.\mathbf{n}\mathrm{d}S \tag{19}$$

The continuity condition for disclinations:

$$\mathbf{div}\ \boldsymbol{\theta} = 0 \tag{20}$$

follows directly from Eqs. (16), (17). Since the rotation vectors $(\boldsymbol{\omega}_e, \boldsymbol{\omega}_p)$ do not exist in the present theory, the corresponding elastic and plastic distortion tensors $\mathbf{U}_e$ and

$\mathbf{U}_\mathrm{p}$ are also undefined. Substituting the elastic and plastic curvatures $(\boldsymbol{\kappa}_e, \boldsymbol{\kappa}_\mathrm{p})$, which now include an incompatible part, for $(\mathbf{grad}\ \boldsymbol{\omega}_e, \mathbf{grad}\ \boldsymbol{\omega}_\mathrm{p})$ and using the above curl-trace procedure, allows splitting Eq. (10) into elastic and plastic components

$$\mathbf{curl}\ \boldsymbol{\epsilon}_e = +\boldsymbol{\alpha} + \boldsymbol{\kappa}_e^\mathrm{t} - \mathrm{tr}(\boldsymbol{\kappa}_e)\mathbf{I} \tag{21}$$

$$\mathbf{curl}\ \boldsymbol{\epsilon}_\mathrm{p} = -\boldsymbol{\alpha} + \boldsymbol{\kappa}_\mathrm{p}^\mathrm{t} - \mathrm{tr}(\boldsymbol{\kappa}_\mathrm{p})\mathbf{I}. \tag{22}$$

Equation (22) defines the incompatible plastic strain associated with the Nye's dislocation density tensor $\boldsymbol{\alpha}$ in the concurrent presence of plastic curvature, while Eq. (21) specifies the incompatible elastic strain needed to ensure the continuity of matter in the presence of dislocations and disclinations. Eqs. (21) and (22) are modified forms of the incompatibility equations $\mathbf{curl}\ \mathbf{U_e} = -\mathbf{curl}\ \mathbf{U_p} = \boldsymbol{\alpha}$ of the theory of dislocations [26]. A point-wise measure of the translational incompatibility due to the presence of dislocations is the Burgers vector. The latter contains a possible contribution from disclinations and reads

$$\mathbf{b} = \int_\mathrm{C} (\boldsymbol{\epsilon}_e - (\boldsymbol{\kappa}_e^\mathrm{t} \times \mathbf{r})^\mathrm{t}).\mathbf{dr} = \int_\mathrm{S} (\boldsymbol{\alpha} - (\boldsymbol{\theta} \times \mathbf{r})^\mathrm{t}).\mathbf{n}\mathrm{d}S \tag{23}$$

Note that Eqs. (16) and (21) may be utilized to estimate the disclination and Nye's dislocation density tensors from EBSD experiments, respectively [27]. The continuity condition $\mathbf{div}\ \boldsymbol{\alpha} = 0$ for dislocations is also modified when disclinations are present. Taking the divergence of Eq. (21) and defining the twist-disclination vector $\boldsymbol{\Theta}$ as:

$$\boldsymbol{\Theta} = -\frac{1}{2}\boldsymbol{\theta} : \mathbf{X}, \tag{24}$$

it is found that:

$$\mathbf{div}\ \boldsymbol{\alpha} + 2\boldsymbol{\Theta} = 0. \tag{25}$$

This continuity equation implies the existence of geometric interactions between twist-disclinations $(\mathrm{i} \neq \mathrm{j})$ and dislocations. As such, it is particularly relevant to modeling twist boundaries.

In the absence of body forces, the rate form of the momentum and moment of momentum equations is:

$$\mathbf{div}\,\dot{\mathbf{T}} = 0 \tag{26}$$

$$\mathbf{div}\,\dot{\mathbf{M}} + 2\dot{\mathbf{T}} = 0. \tag{27}$$

In these relations, the stress tensor $\mathbf{T}$ is generally non-symmetric. The skew-symmetric stress vector, $\mathbf{t}$, defined as $\mathbf{t} = -1/2\mathbf{T} : \mathbf{X}$, allows balancing the moment of momentum in the presence of the couple-stress tensor $\mathbf{M}$. A specific free energy density function is now introduced as follows:

$$\psi = \psi(\boldsymbol{\epsilon}_e, \boldsymbol{\kappa}_e). \tag{28}$$

In addition to elastic strains, ψ contains contributions from the elastic curvatures when disclinations are present, i.e., when incompatible elastic curvatures exist. Thus, the body is seen as a continuum containing capable of transmitting stresses and couple-stresses at nanometer scale. Differentiating Eq. (28), we obtain the following identification of the stress and couple-stress tensors with the partial derivatives of the free energy:

$$\dot{\psi} = \frac{\partial \psi}{\partial \boldsymbol{\epsilon}_e} : \dot{\boldsymbol{\epsilon}}_e + \frac{\partial \psi}{\partial \boldsymbol{\kappa}_e} : \dot{\boldsymbol{\kappa}}_e = \mathbf{T} : \dot{\boldsymbol{\epsilon}}_e + \mathbf{M} : \dot{\boldsymbol{\kappa}}_e. \tag{29}$$

Owing to the symmetry of the elastic strain rate tensor, only the symmetric part $\mathbf{T}^{\mathbf{sym}}$ of the stress tensor is contributing to the free energy. The elastic constitutive relations for $\mathbf{T}^{\mathbf{sym}}$ and $\mathbf{M}$ are consistently chosen in the form suggested in [25]:

$$\mathbf{T}^{\mathbf{sym}} = \mathbf{C} : \boldsymbol{\epsilon}_e + \mathbf{D} : \boldsymbol{\kappa}_e \tag{30}$$

$$\mathbf{M} = \mathbf{A} : \boldsymbol{\kappa}_e + \mathbf{B} : \boldsymbol{\epsilon}_e. \tag{31}$$

The skew-symmetric part $\mathbf{T}^{\mathbf{skew}}$ of the stress tensor is not involved in Eqs. (29) and (30) and is not constitutively specified. $\mathbf{A}$, $\mathbf{B}$, $\mathbf{C}$ and $\mathbf{D}$ are tensors of elastic constants. While the C_{ijkl} and A_{ijkl} constants have dimension of a stress and a stress times a squared length respectively, B_{ijkl} and D_{ijkl} have dimension of a stress multiplied by a length. Hence, the relations (30), (31) involve characteristic lengths and have nonlocal character. Indeed, the tensor $\mathbf{D}$ induces stresses due to the inhomogeneity in rotation over some (short) length scale, while the tensor $\mathbf{B}$ gives rise to couple stresses from inhomogeneity in strain over some other (short) length scale. In the presence of crystal defects, a general form of the tensors $\mathbf{A}$, $\mathbf{B}$, $\mathbf{C}$ and $\mathbf{D}$ is derived in [28], in the case of isotropic elasticity.

In terms of the plastic strain and curvature rates $\dot{\boldsymbol{\epsilon}}_p$ and $\dot{\boldsymbol{\kappa}}_p$, the stress rate and couple stress rate are:

$$\dot{\mathbf{T}}^{sym} = \mathbf{C} : (\{\mathbf{grad}\,\dot{\mathbf{u}}\} - \dot{\boldsymbol{\epsilon}}_p) + \mathbf{D} : (\mathbf{grad}\,\dot{\boldsymbol{\omega}} - \dot{\boldsymbol{\kappa}}_p) \tag{32}$$

$$\dot{\mathbf{M}} = \mathbf{A} : (\mathbf{grad}\,\dot{\boldsymbol{\omega}} - \dot{\boldsymbol{\kappa}}_p) + \mathbf{B} : (\{\mathbf{grad}\,\dot{\mathbf{u}}\} - \dot{\boldsymbol{\epsilon}}_p). \tag{33}$$

Solving the rate of equilibrium equations (26), (27) involves finding the total strain rate and curvature rate tensors. As is well-known, the strain tensor is the symmetric part of the displacement gradient. Similarly, because it is the gradient of the rotation vector, the curvature tensor also derives from the displacement (see Eqs. (9) and (15)). Thus the only independent kinematic variable in Eqs. (26) and (27) is the material velocity vector. Following Mindlin and Tiersten [29], the three additional independent scalar variables necessary for closure (see e.g. [30]) are the components of the skew-symmetric part $\mathbf{T}^{\mathbf{skew}}$ of the stress tensor. The latter is produced by the presence of unbalanced couple stresses and ensures the balance of moment of momentum [29, 31]. Taking the curl of Eq. (27) and eliminating $\mathbf{T}^{\mathbf{skew}}$ in Eq. (26), the latter can be rewritten as a single higher order partial differential equation for the

total velocity field:

$$\mathbf{div}\,\dot{\mathbf{T}} = \mathbf{div}\,\dot{\mathbf{T}}^{sym} + \mathbf{div}\,\dot{\mathbf{T}}^{skew} = \mathbf{div}\,\dot{\mathbf{T}}^{sym} + \frac{1}{2}\mathbf{curl}\,\mathbf{div}\,\dot{\mathbf{M}} = 0. \tag{34}$$

In terms of the elastic strains and curvatures, Eq. (34) reads:

$$\mathbf{div}\,(\mathbf{C} : \dot{\boldsymbol{\epsilon}}_e + \mathbf{D} : \dot{\boldsymbol{\kappa}}_e) + \frac{1}{2}\mathbf{curl}\,\mathbf{div}\,(\mathbf{A} : \dot{\boldsymbol{\kappa}}_e + \mathbf{B} : \dot{\boldsymbol{\epsilon}}_e) = 0. \tag{35}$$

Substituting the total and plastic strain and curvature rates to their elastic counterparts in Eq. (35), we obtain:

$$\mathbf{div}\,(\mathbf{C} : (\dot{\boldsymbol{\epsilon}} - \dot{\boldsymbol{\epsilon}}_p) + \mathbf{D} : (\dot{\boldsymbol{\kappa}} - \dot{\boldsymbol{\kappa}}_p)) + \frac{1}{2}\mathbf{curl}\,\mathbf{div}\,(\mathbf{A} : (\dot{\boldsymbol{\kappa}} - \dot{\boldsymbol{\kappa}}_p) + \mathbf{B} : (\dot{\boldsymbol{\epsilon}} - \dot{\boldsymbol{\epsilon}}_p)) = 0. \tag{36}$$

In the presence of stress and couple-stress fields, the dislocation and disclination densities may be transported (set into motion) with respective velocities $\mathbf{V}_\alpha$ and $\mathbf{V}_\theta$. The driving Peach-Köhler-type forces $\mathbf{F}_\alpha$ and $\mathbf{F}_\theta$ acting on these defects are defined thermodynamically such that the power dissipation due to defect mobility is not negative [21]. In the simplest possible setting, linear viscosity is assumed and the dislocation and disclination velocities are taken as:

$$\mathbf{V}_\alpha = \frac{\mathbf{F}_\alpha}{B_\alpha} = \frac{1}{B_\alpha}\mathbf{T}^{\mathbf{sym}}.\boldsymbol{\alpha} : \mathbf{X}; \quad V_l^\alpha = \frac{1}{B_\alpha} e_{jkl}\frac{T_{ij} + T_{ji}}{2}\alpha_{ik} \tag{37}$$

$$\mathbf{V}_\theta = \frac{\mathbf{F}_\theta}{B_\theta} = \frac{1}{B_\theta}\mathbf{M}^t.\boldsymbol{\theta} : \mathbf{X}; \quad V_l^\theta = \frac{1}{B_\theta} e_{jkl} M_{ij}\theta_{ik}. \tag{38}$$

Here, B_α and B_θ are positive drag coefficients. Eqs. (37) and (38) may be applicable at relatively high loading rate, but they need modification to account for thermally-activated motion of defects typical at low loading rates. This issue will be discussed further in Sect. 6. Note that the dislocations are driven by the symmetric part of the stress tensor, while the disclinations are set into motion by the couple-stress field. The mobility of disclinations and dislocations produces the plastic curvature and strain rates:

$$\dot{\boldsymbol{\kappa}}_p = \boldsymbol{\theta} \times \mathbf{V}_\theta \tag{39}$$

$$\dot{\boldsymbol{\epsilon}}_p = \frac{1}{2}(\boldsymbol{\alpha} \times \mathbf{V}_\alpha + (\boldsymbol{\alpha} \times \mathbf{V}_\alpha)^t). \tag{40}$$

In turn, $\dot{\boldsymbol{\kappa}}_p$ and $\dot{\boldsymbol{\epsilon}}_p$ feed the evolution of the disclination and dislocation densities through the transport equations

$$\dot{\boldsymbol{\theta}} = -\mathbf{curl}\,\dot{\boldsymbol{\kappa}}_p \tag{41}$$

$$\dot{\boldsymbol{\alpha}} = -\mathbf{curl}\,\dot{\boldsymbol{\epsilon}}_p + \dot{\boldsymbol{\kappa}}_p^t - \mathrm{tr}(\dot{\boldsymbol{\kappa}}_p)\mathbf{I} = -\mathbf{curl}\,\dot{\boldsymbol{\epsilon}}_p + \mathbf{s}_\theta. \tag{42}$$

Disclinations nucleate from the incompatibility of the plastic curvature rates in Eq. (41), but an outstanding consequence of Eq. (42) is that dislocations are nucleated not only because the plastic strain rate has an incompatible part, $\dot{\boldsymbol{\epsilon}}_{\mathrm{p}}^{\perp}$, but also because a source term, $\mathbf{s}_{\theta} = \dot{\boldsymbol{\kappa}}_{\mathrm{p}}^{\mathrm{t}} - \mathrm{tr}(\dot{\boldsymbol{\kappa}}_{\mathrm{p}})\mathbf{I}$, involving the mobility of the disclinations is existing. Thus, a wake of dislocations (nucleated or absorbed) is accompanying the motion of disclinations. Such an important mechanism was postulated in [25]. In contrast with the dislocations arising from lattice translational incompatibility (the curl term in Eq. (42)), this wake of dislocations may be seen as systematically contributing to the relaxation of internal stresses in the neighborhood of disclinations [22, 32].

The rate form of the elasto-plastic theory of crystal defects is then defined by the set of Eqs. (37)–(42), (36). The unknown fields are the material velocity, dislocation and disclination density fields.

4 A Plane Edge-Wedge Model

The plane edge-wedge model presented in this section was introduced in [21]. It is recalled briefly here for completeness. Let us consider a distribution of pure wedge disclinations. In an orthonormal reference frame $(\mathbf{e_1}, \mathbf{e_2}, \mathbf{e_3})$, let the disclination tensor be: $\boldsymbol{\theta} = \theta_{33}\mathbf{e_3} \otimes \mathbf{e_3}$, all other components being zero. In this simple setting, the continuity condition (20) implies: $\theta_{33,3} = 0$. Thus, the wedge disclination density θ_{33} only depends on the coordinates (x_1, x_2): $\theta = \theta(x_1, x_2)$. In component form, the rotational incompatibility equation (16) reads: $\theta_{ij} = -e_{jkl}\kappa^{\mathrm{p}}_{il,k} = e_{jkl}\kappa^{\mathrm{e}}_{il,k}$. In the present case, Eq. (16) reduces to:

$$\theta_{33} = \kappa^{\mathrm{p}}_{31,2} - \kappa^{\mathrm{p}}_{32,1} = \kappa^{\mathrm{e}}_{32,1} - \kappa^{\mathrm{e}}_{31,2}. \tag{43}$$

Hence the only relevant elastic and plastic curvatures are: $(\kappa^{\mathrm{e}}_{31}, \kappa^{\mathrm{e}}_{32})$ and $(\kappa^{\mathrm{p}}_{31}, \kappa^{\mathrm{p}}_{32})$. Additionally, we note that: $\mathrm{tr}(\boldsymbol{\kappa}_{\mathrm{p}}) = 0$. Thus, the disclination transport equation (41) is:

$$\dot{\theta}_{33} = \dot{\kappa}^{\mathrm{p}}_{31,2} - \dot{\kappa}^{\mathrm{p}}_{32,1}. \tag{44}$$

The plastic curvature rate (39) reads, in component form: $\dot{\kappa}^{\mathrm{p}}_{ij} = e_{jkl}\theta_{ik}V^{\theta}_{l}$. Hence, we find:

$$\dot{\kappa}^{\mathrm{p}}_{31} = -\theta_{33}V^{\theta}_{2} \tag{45}$$

$$\dot{\kappa}^{\mathrm{p}}_{32} = +\theta_{33}V^{\theta}_{1}. \tag{46}$$

Using the constitutive relation (38) for the disclination velocities provides their relationship with the couple-stresses:

$$V^{\theta}_{1} = +\frac{1}{B_{\theta}}M_{32}\theta_{33} \tag{47}$$

$$V_2^{\theta} = -\frac{1}{B_{\theta}} M_{31}\theta_{33}. \tag{48}$$

Since the trace of the plastic curvature rate tensor is zero, the source term $\mathbf{s}_{\theta}$ in the dislocation transport equation (42) feeds only the edge dislocations densities $(\alpha_{13}, \alpha_{23})$. Using Eq. (40), it is seen that the motion of these dislocations produces the plastic strain rate components $(\dot{\epsilon}^p_{11}, \dot{\epsilon}^p_{12}, \dot{\epsilon}^p_{21}, \dot{\epsilon}^p_{22})$:

$$\dot{\epsilon}^p_{11} = -\alpha_{13} V_2^{\alpha} \tag{49}$$

$$\dot{\epsilon}^p_{12} = \dot{\epsilon}^p_{21} = \frac{1}{2}(\alpha_{13} V_1^{\alpha} - \alpha_{23} V_2^{\alpha}) \tag{50}$$

$$\dot{\epsilon}^p_{22} = +\alpha_{23} V_1^{\alpha}. \tag{51}$$

The above relations suggest that out-of-plane motion of the edge dislocations $(\alpha_{13}, \alpha_{23})$ is involved in the extension rates $(\dot{\epsilon}^p_{11}, \dot{\epsilon}^p_{22})$, whereas their glide is responsible for $\dot{\epsilon}^p_{12}$. Consistently, the dislocation transport equation (42) reduces to:

$$\dot{\alpha}_{13} = \dot{\epsilon}^p_{11,2} - \dot{\epsilon}^p_{12,1} + \dot{\kappa}^p_{31} \tag{52}$$

$$\dot{\alpha}_{23} = \dot{\epsilon}^p_{21,2} - \dot{\epsilon}^p_{22,1} + \dot{\kappa}^p_{32}. \tag{53}$$

Thus, if all other dislocation densities are initially absent, the dislocation distribution involves only α_{13} and α_{23} edge densities. The continuity equation (25) then implies that this distribution be a plane state: $\alpha_{13} = \alpha_{13}(x_1, x_2), \alpha_{23} = \alpha_{23}(x_1, x_2)$. The symmetric "Peach-Köhler" constitutive relation (37) provides the dislocation velocities in terms of the stress tensor, for both the out-of-plane motion of dislocations:

$$V_1^{\alpha} = +\frac{1}{B_{\alpha}} T_{22}\alpha_{23} \tag{54}$$

$$V_2^{\alpha} = -\frac{1}{B_{\alpha}} T_{11}\alpha_{13}, \tag{55}$$

and their glide:

$$V_1^{\alpha} = +\frac{1}{2B_{\alpha}}(T_{12} + T_{21})\alpha_{13} \tag{56}$$

$$V_2^{\alpha} = -\frac{1}{2B_{\alpha}}(T_{12} + T_{21})\alpha_{23}. \tag{57}$$

The stress and couple-stress components relevant to the present problem are $(T_{11}, T_{12}, T_{21}, T_{22})$ and (M_{31}, M_{32}) respectively. Hence the Cosserat rate of momentum equations (26), (27) reduce to:

$$\dot{T}_{11,1} + \dot{T}_{12,2} = 0 \tag{58}$$

$$\dot{T}_{21,1} + \dot{T}_{22,2} = 0 \tag{59}$$

$$\dot{M}_{31,1} + \dot{M}_{32,2} + \dot{T}_{21} - \dot{T}_{12} = 0, \tag{60}$$

and the higher order rate of equilibrium equation (34) becomes:

$$\dot{T}^{sym}_{11,1} + \dot{T}^{sym}_{12,2} + \dot{T}^{skew}_{12,2} = \dot{T}^{sym}_{11,1} + \dot{T}^{sym}_{12,2} + \frac{1}{2}(\dot{M}_{31,1} + \dot{M}_{32,2})_{,2} = 0 \tag{61}$$

$$\dot{T}^{sym}_{21,1} + \dot{T}^{skew}_{21,1} + \dot{T}^{sym}_{22,2} = \dot{T}^{sym}_{21,1} + \dot{T}^{sym}_{22,2} - \frac{1}{2}(\dot{M}_{31,1} + \dot{M}_{32,2})_{,1} = 0. \tag{62}$$

As shown in [21], the elastic tensor $\mathbf{B}$ is zero in a plane strain formulation. Thus, the symmetric stress components write:

$$T^{sym}_{11} = C_{1111}\epsilon^e_{11} + C_{1122}\epsilon^e_{22} \tag{63}$$

$$T^{sym}_{12} = C_{1212}\epsilon^e_{12} + C_{1221}\epsilon^e_{21} \tag{64}$$

$$T^{sym}_{21} = C_{2112}\epsilon^e_{12} + C_{2121}\epsilon^e_{21} \tag{65}$$

$$T^{sym}_{22} = C_{2211}\epsilon^e_{11} + C_{2222}\epsilon^e_{22} \tag{66}$$

with $C_{1212} = C_{1221} = C_{2112} = C_{2121}$, $C_{1111} = C_{2222}$ and $C_{1122} = C_{2211}$ in cubic symmetry. The elasticity tensor $\mathbf{C}$ is expressed in the global reference frame because most of elastic strains are localized in the grain boundary area where the elastic rotation is null. It is to note that using cubic elasticity in this area is a rather loose approximation because the crystalline structure is modified. However, as shown in the next section, good predictions of the elastic energy of grain boundaries can still be obtained. For convenience, a simplified form of tensor $\mathbf{A}$ will be used:

$$M_{31} = A_{3131}\kappa^e_{31} \tag{67}$$

$$M_{32} = A_{3232}\kappa^e_{32}. \tag{68}$$

The coefficients C_{ijkl} may be determined from experiments or by atomistic simulations. In the forthcoming simulations, we shall use values for copper, as determined by molecular dynamics simulations [33]. In addition, we assume $A_{3131} = A_{3232} = \mu l^2$. The length l, which weights the contribution of couple-stresses to elastic energy, as compared to that of stresses, is a characteristic internal length, which enters the balance of momentum Eq. (36). The value of l should be the order of the smallest microstructure characteristic size and respect the small strain hypothesis in terms of curvatures $|\kappa_{ij}| < 1/l$ [31]. In the present paper, this value will be calibrated to fit the elastic energy of grain boundaries obtained by atomistic simulations. Further, we assume equal viscous drag coefficients $B_\theta = B_\alpha = B$. The mobility of the disclinations might be overestimated by doing so, but this value conveniently allows showing the features of disclination dynamics in the following. A more accurate value of B_θ will be derived from grain boundary migration data in future work. Parameter values for copper are presented in Table 1.

Table 1 Numerical constants used in the model

b	C_{1212}	C_{1111}	C_{1122}	b^2B	l
0.25 nm	27 GPa	175 GPa	125 GPa	0.4×10^{-4} Pa.s	0.15 nm

Substituting Eq. (63)–(68) and $(\dot{e}_{ij} - \dot{e}^{p}_{ij}, \dot{\kappa}_{ij} - \dot{\kappa}^{p}_{ij})$ for the elastic strain and curvature rates in the equilibrium equations (61), (62), one obtains two partial differential equations for the material velocity field (v_1, v_2). The plastic strains and curvatures and the disclination and dislocation densities are updated by using the plastic strain and curvature rates (45), (46), (49)–(51), and the transport equations (44), (52), (53) respectively. The boundary conditions for the equilibrium problem comprise the prescription of tractions and traction-moments, or/and displacements and rotations on the surface of the body. The equilibrium equations are solved by using a Galerkin finite element method, with 16-nodes complete cubic elements for the interpolation of the material velocity field, and 16 Gauss points for the integration. The transport equations are solved by using a least-squares finite element scheme [34] with bilinear elements for the interpolation of dislocation and disclination densities, and four Gauss points for the integration. Note that a cubic element contains nine bilinear elements such that the material velocity, the dislocation and disclination densities are discretized at the same nodes in the finite element mesh. Finally, the disclination and dislocation densities need to be specified on inflow boundaries, but no condition is required on outflow boundaries.

5 Self-Relaxation of Tilt Boundaries

In all forthcoming simulations, the relaxation of initial configurations will be stopped when the driving forces for the motion of disclinations and dislocations reach a limiting value. The common threshold value of $5\,\mathrm{MPa}/b = 2.10^{19}\,\mathrm{Pa/m}$ was used for both disclinations (in plane and out-of-plane motions) and dislocations. If the relaxation process was not interrupted, the disclination densities would finally vanish from the simulation box after annihilation and spreading over a sufficiently long computation time. This feature originates in the linear viscous drag velocity laws (37), (38) currently assumed in the model for the mobility of dislocations and disclinations. The value of the drag coefficient was checked to have an effect solely on the time needed for relaxation, but does not affect the relaxed structure and energy of grain boundaries. As already mentioned, a thermally activated law featuring a threshold stress/couple stress would also alleviate indefinite relaxation in time.

The relaxed structure of a $\Sigma 29(520)$ <001> boundary is shown in Figs. 1–3. We remind that this grain boundary is made of alternating B and C atomic structural units. The reader is referred to [24] for details about initial constructions of this boundary with disclination dipoles. A wealth of features emerges from the simulations. A significant mobility of the disclinations is seen during the relaxation. Their spatial rearrangement leads to spreading disclination densities and to decreasing values of

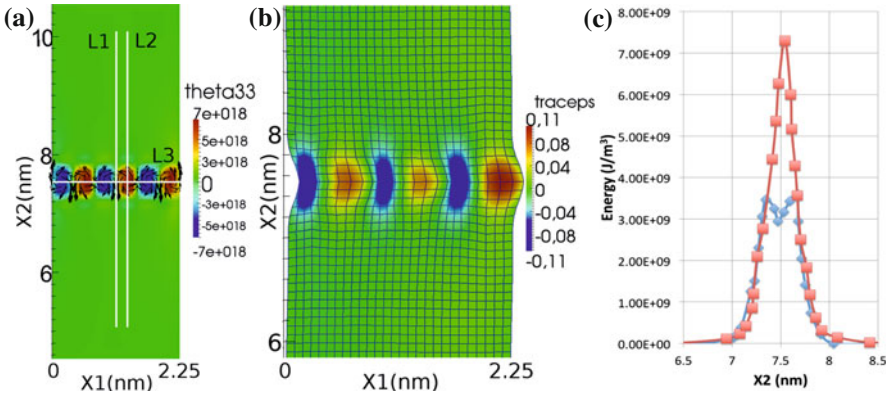

Fig. 1 Relaxed $< 001 >$ $\Sigma 29(520)$ tilt boundary of misorientation 46.40°. The simulation box is a 2.25 nm × 15 nm plane containing 9 × 60 cubic elements for the Galerkin finite element scheme for equilibrium, and 27 × 180 bilinear elements for the Least-Squares transport scheme. Close-up in vertical direction for figures a and b. **a** Color-coded is the disclination density θ_{33} in $\mathrm{rad.m}^{-2}$ units. Arrows show the orientation and the magnitude of the net Burgers vector due to edge dislocations. The maximum length of the Burgers vector corresponds to a density of $9.10^8 \mathrm{m}^{-1}$. **b** Trace of total strain tensor in the deformed mesh (displacements are magnified by a factor 5). **c** Profiles of elastic energy density ($\mathrm{J.m}^{-3}$) along white lines L1 (*blue diamonds*) and L2 (*red squares*) plotted in Fig. 1a

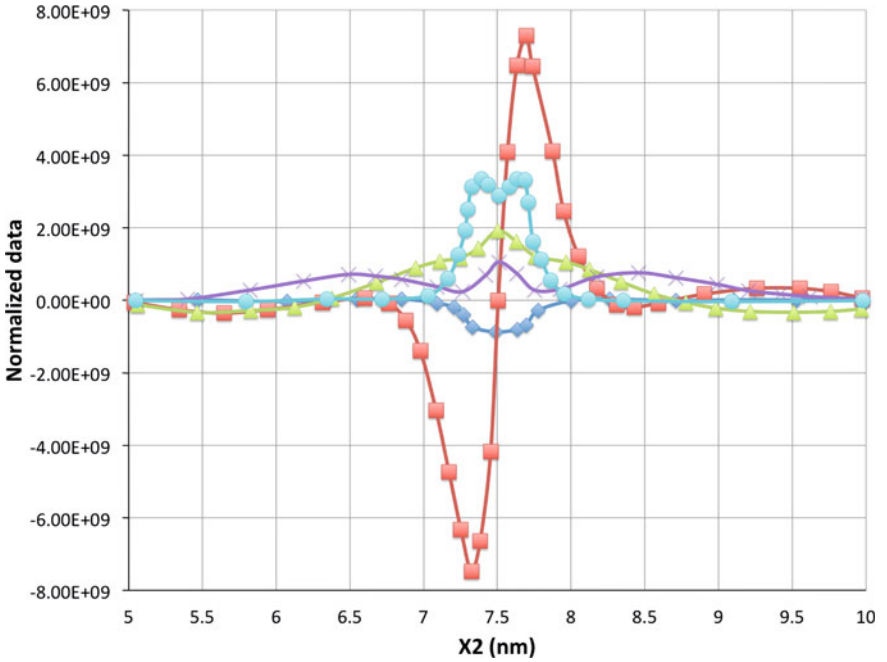

Fig. 2 Profiles across a disclination dipole (*white line* L1 in Fig. 1a) in the relaxed $< 001 >$ $\Sigma 29(520)$ tilt boundary of misorientation 46.40° shown in Fig. 1. Energy density ($\mathrm{J.m}^{-3}$) in *blue circle line*, stress $T_{11}^{sym}(\mathrm{Pa})$ in *green triangle line*, stress $T_{12}^{sym}(\mathrm{Pa})$ in *red square line*, stress $T_{22}^{sym}(\mathrm{Pa})$ in *purple cross line* and elastic curvature $\{\kappa_{32}^{e}\}(\mathrm{rad/m})$ in *blue diamond line*

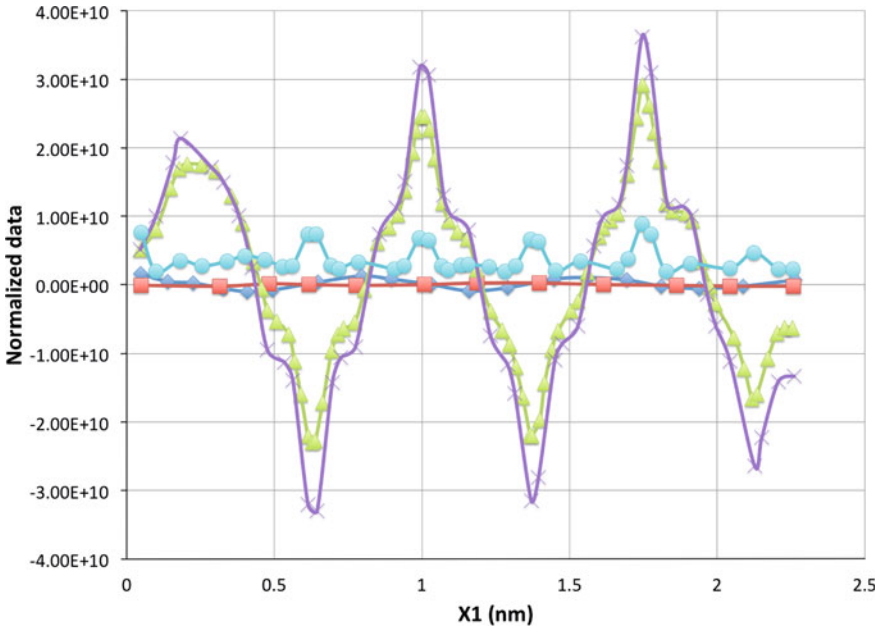

Fig. 3 Profiles along the grain boundary (*white line* L3 in Fig. 1a) in the relaxed $< 001 > \Sigma 29(520)$ tilt boundary of misorientation 46.40° shown in Fig. 1. Energy density ($\mathrm{J.m^{-3}}$) in *blue circle line*, stress $\mathrm{T_{11}^{sym}(Pa)}$ in *green triangle line*, stress $\mathrm{T_{12}^{sym}(Pa)}$ in *red square line*, stress $\mathrm{T_{22}^{sym}(Pa)}$ in *purple cross line* and elastic curvature $\{\kappa^{e}_{32}\}(\mathrm{rad/m})$ in *blue diamond line*

the Frank vectors, due to partial annihilation. As a result, the relaxed distribution of disclinations is extended. Further, edge dislocations α_{13} and α_{23} are also nucleated during the process. These dislocations relax the initial stress field through both in-plane glide and out-of-plane motion, possibly through climb or atom shuffling. The resulting Burgers vector field is shown in Fig. 1a. As suggested by a rotating pattern about the disclination dipoles, it is in close correlation with the disclination distribution. The net overall Burgers vector of the interface area is found to be zero, as could be expected from the absence of a discontinuity in the elastic strain and curvature tensors far away from the interface.[1] Shown in Fig. 1b, the trace of the total strain tensor in the deformed mesh reflects the structure of the grain boundary. Remarkably, a translational asymmetry of the positive and negative disclinations is observed along the boundary. The overall structure of the interface area exhibits geometrical patterns showing clear similarities with the structural units revealed by atomistic simulations. As shown in Figs. 2 and 3, the elastic strain field shows alternatively dilatation and contraction of the lattice along the boundary, in patches a few Å wide

[1] It is found from Frank's formula that the separation distance l between the edge dislocations in a dislocation-made tilt boundary of misorientation 46.40° is $\mathrm{l} = 0.34\,\mathrm{nm}$, a distance much too short to be realistic. Such a result supports the view that a consistent description of high-angle tilt boundaries should recourse to disclination dipole walls rather than edge dislocation walls.

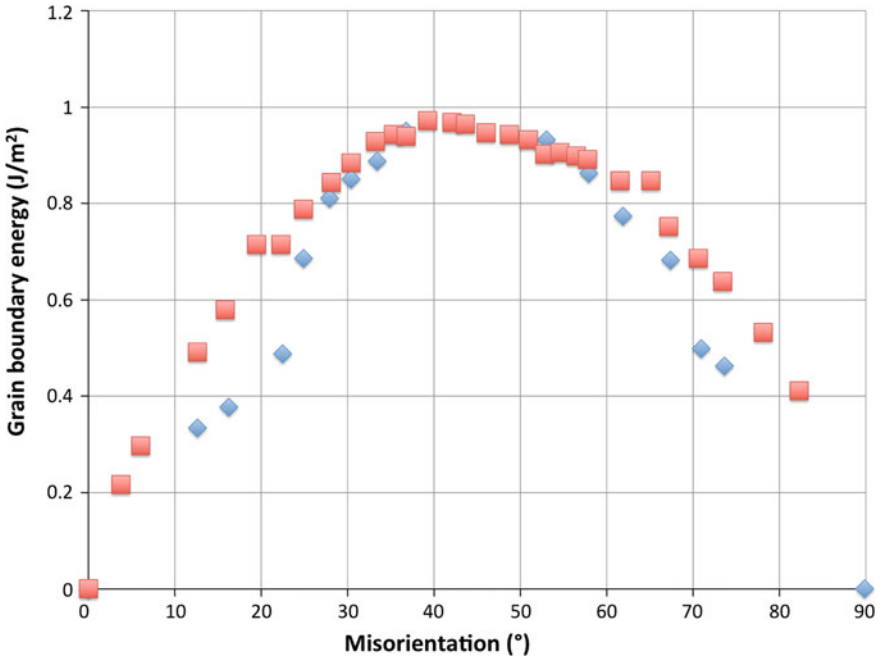

Fig. 4 Elastic energy density per unit length of grain boundary obtained by the present model (*blue diamonds*). Molecular statics data for copper (*red squares*) are shown for comparison (points were digitized from [35])

along the boundary also featuring the presence of negative and positive disclinations, respectively. This distribution is in good agreement with molecular statics predictions [9]. The tensile stress can reach values as high as 35 GPa, i.e., it is on the order of the shear modulus in copper. Such large values were also reported for the hydrostatic stress in structural units by atomistic simulations [9]. The tensile/compressive elastic energy is maximum at the interface, and it rapidly decreases within 5 Å, but remarkably, across the arm length of a disclination dipole, the energy is not at the highest at the interface but a few Å apart, due to the additional contribution of the shear stresses to that of curvatures. The shear stress correspondingly reaches 8 GPa. Between these patches, alternatively negative and positive curvature regions show up in the dipole interiors and between the dipoles respectively. These curvatures contribute significantly to the total energy of the grain boundary, as evidenced in Fig. 1c. Most of the elastic energy is localized in a 0.5 nm layer across the grain boundary. The energy density per unit length of boundary is $0.94\,\mathrm{J.m}^{-2}$, a value comparing rather well with that obtained from molecular statics calculations [35].

The tilt boundary energy is now plotted versus the tilt angle in Fig. 4, and compared with predictions of atomistic simulations [35]. The boundary energies predicted by the present model reach the levels obtained from molecular statics calculations and

display a similar distribution. Such a fit cannot be obtained with discrete disclination dipoles, because the contribution of defect cores to the energy is overlooked [36].

The only unknown parameter in our simulations is the internal characteristic length l, which weights the contribution of couple-stresses to the elastic energy in Eqs. (67) and (68). The measured constant value, which allowed to obtain a reasonable fit shown in Fig. 4, is $l = 0.15\,\mathrm{nm}$, lower than a Burgers vector. Such small lengths, or even smaller, are predicted by lattice-dynamics and molecular dynamics simulations, and are related to phonon dispersions [37]. In the case of bulk fcc crystals like copper or aluminum, strain gradient elasticity is then thought to be irrelevant, unless highly heterogeneous defect microstructures are modeled at a subnanometric resolution scale, which is the case in the present work.

6 Conclusions

Capitalizing on the powerful tools of differential geometry and the theory of partial differential equations, the modeling paradigm in this study is to account for lattice incompatibility in a continuous fashion, focusing on the fields of density of lattice defects rather than on the atoms themselves. Thus, the elasto-plastic theory of crystal defect fields [21] was used to model grain boundaries in a continuous manner. The theory accounts for the rotational and translational incompatibility of the lattice associated with the presence of disclinations and dislocations, and describes the latter by continuous densities. The material displacement, strain and curvature, are also defined continuously, even at a resolution length scale below interatomic distance. It is further assumed that, at this scale, the material is capable of transmitting stresses and couple-stresses. Dynamic tilt boundary modeling uses periodic arrangements of discrete wedge disclination dipoles as initial conditions. The latter relax by transport in their own couple-stress field into self-organized dislocation-disclination periodic patterns representing the atomistic structural units. Most of the elastic energy of the tilt boundary is also localized in this layer. The energy arises from a tension/compression state in disclination-rich areas, in good agreement with atomistic observations, and from curvature and shear in areas located within and between the disclination dipoles.

From the point of view of differential geometry, field modeling is fully appropriate at length scales below the elementary lattice parameters, and it is rather meaningful that the predictions on GB energy of a field theory of crystal defects show good agreement with results from atomistic modeling [35]. A more complete comparison with atomistic simulations involving field information and boundary structure will be provided in a forthcoming paper.

Finally, because it avoids resolving in time the atomic vibrations, the present approach allows using much larger time steps and smaller loading rates than molecular dynamics methods. Therefore, we believe that the present approach has an interesting potential for further modeling of grain boundaries and grain-boundary mediated plasticity.

Acknowledgments The authors benefited of financial support from the ANR (Agence Nationale de la Recherche) under grant ANR-11-JS09-007-01, NanoMec.

References

1. Wang, Y.M., Ma, E.: Strain hardening, strain rate sensitivity, and ductility of nanostructured metals. Mat. Sci. Eng. A **375–377**, 46 (2004)
2. Cahn, J.W., Mishin, Y., Suzuki, A.: Coupling grain boundary motion to shear deformation. Acta Mater. **54**, 4953–4975 (2006)
3. Gorkaya, T., Molodov, D.A., Gottstein, G.: Stress-driven migration of symmetrical <001> tilt grain boundaries in Al bicrystals. Acta Mater. **57**, 5396 (2009)
4. Mompiou, F., Caillard, D., Legros, M.: Grain boundary shear-migration coupling. I. In situ TEM straining experiments in Al polycrystals. Acta Mater. **57**, 2198 (2009)
5. Tschopp, M.A., Tucker, G.J., McDowell, D.L.: Atomistic simulations of tension-compression asymmetry in dislocation nucleation for copper grain boundaries. Comp. Mater. Science **44**, 351 (2008)
6. Tschopp, M.A., McDowell, D.L.: Grain boundary dislocation sources in nanocrystalline copper. Scripta Mater. **58**, 299 (2008)
7. Van Swygenhoven, H., Derlet, P.M., Froseth, A.G.: Nucleation and propagation of dislocations in nanocrystalline fcc metals. Acta Mater. **54**, 1975 (2006)
8. Van Swygenhoven, H.: Footprints of plastic deformation in nanocrystalline metals. Mat. Sci. Eng. A **483–484**, 33 (2008)
9. Sutton, A.P., Vitek, V.: On the structure of tilt grain boundaries in cubic metals. I. Symmetrical tilt boundaries. Philos. Trans. R. Soc. Lond. **A309**, 1 (1983)
10. Bilby, B.A.: Types of dislocation source. In: Bristol Conference Report on Defects in Crystalline Solids, p. 124. The Physical Society, London (1955)
11. Frank, F.C.: The resultant content of dislocations in an arbitrary intercrystalline boundary. In: Symposium on The Plastic Deformation of Crystalline Solids, p. 150. Mellon Institute, Pittsburgh, (NAVEXOS-P-834) (1950)
12. Li, J.C.M.: Disclination model of high angle grain boundaries. Surf. Sci. **31**, 12 (1972)
13. Shih, K.K., Li, J.C.M.: Energy of grain boundaries between cusp misorientations. Surf. Sci. **50**, 109 (1975)
14. Gertsman, VYu., Nazarov, A.A., Romanov, A.E., Valiev, R.Z., Vladimirov, V.I.: Disclination-structural unit model of grain boundaries. Philos. Mag. A 59, 1113 (1989)
15. Gurtin, M.E., Anand, L.: Nanocrystalline grain boundaries that slip and separate: a gradient theory that accounts for grain-boundary stress and conditions at a triple junction. J. Mech. Phys. Solids **56**, 184 (2008)
16. Warner, D.H., Sansoz, F., Molinari, J.F.: Atomistic based continuum investigation of plastic deformation in nanocrystalline copper. Int. J. Plast. **22**, 754–774 (2006)
17. Wei, Y.J., Anand, L.: Grain-boundary sliding and separation in polycrystalline metals: application to nanocrystalline fcc metals. J. Mech. Phys. Solids **52**, 2587 (2004)
18. Wei, Y., Gao, H., Bower, A.F.: Numerical simulations of crack deflection at a twist-misoriented grain boundary between two ideally brittle crystals. J. Mech. Phys. Solids **57**, 1865 (2009)
19. Zbib, H.M., Overman, C.T., Akasheh, F., Bahr, D.: Analysis of plastic deformation in nanoscale metallic multilayers with coherent and incoherent interfaces. Int. J. Plast. **27**, 1618–1639 (2011)
20. Tucker, G.J., Tschopp, M.A., McDowell, D.L.: Evolution of structure and free volume in symmetric tilt grain boundaries during dislocation nucleation. Acta Mater. **58**, 6464 (2010)
21. Fressengeas, C., Taupin, V., Capolungo, L.: An elasto-plastic theory of dislocation and disclination fields. Int. J. Solids Struct. **48**, 3499–3509 (2011)
22. Romanov, A.E., Vladimirov, V.I.: Disclinations in crystalline solids. In: Nabarro, F.R.N. (ed.) Dislocations in Solids, vol. 9, p. 191. Elsevier, Amsterdam (1992)

23. Fressengeas, C., Taupin, V., Capolungo, L., Upadhyay, M.: Tangential continuity of elastic/plastic curvature and strain at interfaces. Int. J. Solids Struct. **49**, 2660–2667 (2012)
24. Taupin, V., Capolungo, L., Fressengeas, C., Das, A., Upadhyay, M.: Grain boundary modeling using a theory of disclination and dislocation fields. J. Mech. Phys. Solids. **61**, 370 (2013)
25. deWit, R.: Linear theory of static disclinations. In: Simmons, J.A., deWit, R., Bullough, R. (eds.) Fundamental aspects of dislocation theory, (Nat. Bur. Stand.) vol. I, pp. 651–673. Special Publications 317, US (1970)
26. Acharya, A.: A model of crystal plasticity based on the theory of continuously distributed dislocations. J. Mech. Phys. Solids **49**, 761 (2001)
27. Beausir, B., Fressengeas, C.: Disclination densities from EBSD orientation mapping. Int. J. Solids Struct. **50**, 137 (2013)
28. Upadhyay, M., Capolungo, L., Taupin, V., Fressengeas, C.: Elastic constitutive laws for incompatible crystalline media: the contributions of dislocations, disclinations and G-disclinations. Philos. Mag. (2012). http://dx.doi.org/10.1080/14786435.2012.733829
29. Mindlin, R.D., Tiersten, H.F.: Effects of couple-stresses in linear elasticity. Arch. Rat. Mech. Anal. **11**, 415 (1962)
30. Shu, J.Y., King, W.E., Fleck, N.A.: Finite elements for materials with strain gradient effects. Int. J. Numer. Meth. Engng. **44**, 373 (1999)
31. Hadjesfandiari, A.R., Dargush, G.F.: Couple stress theory for solids. Int. J. Solids. Struc. **48**, 2496–2510 (2011)
32. Kleman, M., Friedel, J.: Disclinations, dislocations, and continuous defects: a reappraisal. Rev. Modern Phys. **80**, 61 (2008)
33. Spearot, D.: Atomistic calculations of nanoscale interface behavior in FCC metals. Ph.D. thesis, Georgia Institute of Technology (2005)
34. Varadhan, S., Beaudoin, A.J., Acharya, A., Fressengeas, C.: Dislocation transport using an explicit Galerkin/least-squares formulation. Modell. Simul. Mater. Sci. Eng. **14**, 1 (2006)
35. Bachurin, D.V., Murzaev, R.T., Nazarov, A.A.: Atomistic computer and disclination simulation of [001] tilt boundaries in nickel and copper. Phys. Met. Metall. **96**, 555 (2003)
36. Upadhyay, M., Capolungo, L., Taupin, V., Fressengeas, C.: Grain boundary and triple junction energies in crystalline media: a disclination based approach. Int. J. Solids. Struc. **48**, 3176–3193 (2011)
37. Marangantia, R., Sharma, P.: A novel atomistic approach to determine strain gradient elasticity constants: tabulation and comparison for various metals, semiconductors, silica, polymers and the (Ir) relevance for nanotechnologies. J. Mech. Phys. Solids **55**, 1823 (2007)

Material Strain Tensor

Pavel A. Zhilin, Holm Altenbach, Elena A. Ivanova and Anton Krivtsov

Abstract The problem of description of large inelastic deformations of solids is considered. On a simple discrete model it is shown that the classical concept of deformations used in continuum mechanics can exhibit serious difficulties due to reorganizations of the internal structure of materials. The way of construction of constitutive equations in continuum mechanics aimed to avoid these problems is proposed. A method of introduction of material strain tensor for the inelastic continuum is suggested. The paper is based on the report: *P. A. Zhilin, A. Krivtsov: Point mass simulation of inelastic extension process.* It was prepared for the ICIAM 95 (Third International Congress on Industrial and Applied Mathematics, Hamburg, Germany, July 3–7, 1995), but not accepted for publication.

1 Introductory Remarks

The conventional continuum mechanics contains [1–3]:

a) the theory of stresses and balance equations,
b) the geometrical theory of deformations and the introduction of strain tensors, and
c) the establishment of constitutive equations (sometimes added by evolution equations).

P. A. Zhilin–deceased. The original text by P. A. Zhilin (1942–2005) is presented in Sects. 1, 3 and 4 with some explanatory addenda.

H. Altenbach
Faculty of Mechanical Engineering, Otto-von-Guericke University, 39106 Magdeburg, Germany
e-mail: holm.altenbach@ovgu.de

E. A. Ivanova · A. Krivtsov (✉)
Saint Petersburg State Polytechnical University, Institute for Problems in Mechanical Engineering, Russian Academy of Sciences, Bolshoy pr. V. O., 61, 199178 St. Petersburg, Russia
e-mail: akrivtsov@bk.ru

H. Altenbach et al. (eds.), *Generalized Continua as Models for Materials*,
Advanced Structured Materials 22, DOI: 10.1007/978-3-642-36394-8_19,

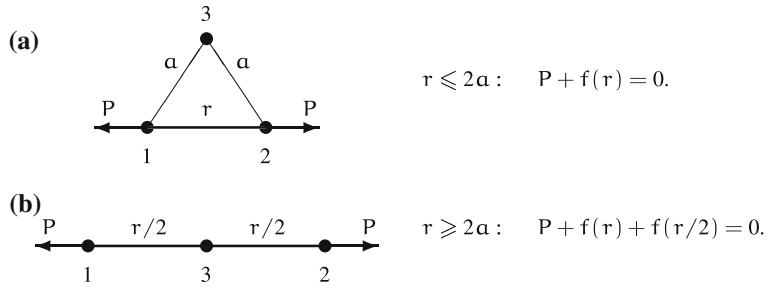

Fig. 1 Tension of the system of three interacting particles

Such approach was found by L. Euler (for one-dimensional continua) and by A. Cauchy (for three-dimensional continuum) in order to describe mechanics of elastic materials. It is often assumed that the Euler-Cauchy approach can be used for inelastic materials too. There are many theories of such kind. However, none of them is able to describe a lot of well established experimental results. By this reason many experimenters suppose that the Euler-Cauchy approach cannot be used in mechanics of inelastic materials.[1]

In this chapter a simple discrete model is used to illustrate these problems arising for the large inelastic deformations. Then a method of introduction of a material strain tensor suitable for solution of these problems is presented.

2 Simple Discrete Model of Inelastic Deformation

One of the main problems for the usage of the traditional stress tensors is that for an inelastic deformation an essential structure reorganization occurs in materials. In particular the idea of material line can loose its sense because a material particle can locate itself between the nearest neighboring particles. For illustration[2] let us consider the deformation of the simplest discrete system containing three interacting particles—see Fig. 1.

Let us describe the interaction between particles using the Morse potential [4]

$$\Pi(r) = D\left(e^{-2\alpha(r-a)} - 2e^{-\alpha(r-a)}\right), \tag{1}$$

where r is the distance between particles, D is the bond energy, a is the bond length, α is the interaction parameter. The Morse potential is one of the simplest interaction

[1] Among such theories probably the best results in explanation of experimental phenomena are given by the so-called "deformation theory" of H. Hencky, sometimes much better than the rate theory can do [13]. As it can be seen from below, there are serious reasons for that.

[2] This model was proposed by P. A. Zhilin and analyzed by A. Krivtsov.

potentials used for the qualitative description of the interaction between atoms. The corresponding interaction force $f(r)$ can be calculated as

$$f(r) = -\Pi'(r) = 2\alpha D\left(e^{-2\alpha(r-a)} - e^{-\alpha(r-a)}\right). \tag{2}$$

For $r < a$ the value of $f(r)$ is positive, which corresponds to repulsion, for $r > a$ the value of $f(r)$ is negative, which corresponds to attraction, for $r = a$ the force became zero. Let us introduce the bond strength

$$f_* = \alpha D/2, \tag{3}$$

which is the maximum of the absolute value of the attraction force.

For the system of three particles without external loading there exists the unique stable equilibrium configuration, that is an equilateral triangle with side length a. Let us set the loading of the system by quasistatic extension of the triangle along one of its sides—see Fig. 1a. The corresponding tension forces are shown in the picture, the absolute value of the forces is denoted by P. While the length r of the side being extended is less than $2a$, the system forms an isosceles triangle, where the length of the equal sides is a permanently. In fact in this case particle 3 is not interacting with other two particles—the forces between it and others is equal to zero, while the force P is determined by interaction between particles 1 and 2 only. The situation changes drastically, when r exceeds $2a$—see Fig. 1b. In this case particle 3 "put itself" between particles 1 and 2. In this case the interaction became more complex, since the distance between particle 3 and other two particles exceeds an equilibrium one, therefore an attraction between them appears, increasing the force P. The corresponding equations of equilibrium are given in Fig. 1a, b. The stress-strain diagram, obtained from these equations for $\alpha a = 3$ is shown in Fig. 2.

The obtained relation $P(r)$ has three extrema. For the soft loading (when the loading force is set, but not the deformation) the decreasing parts of the diagram are unstable (the dashed line). In the extrema the dynamic transitions with structure reorganization are possible (the arrows). Thus, even for such simple model with purely potential interaction it is quite possible to observe the main features inherent to stress-strain relation of real materials: yielding, residual deformation, hardening, loop of hysteresis and so on. The analysis of more complex discrete systems in [5], which was performed analytically and numerically, shows similar results. The more degrees of freedom are taken into account the closer these results are to the results of the nature experiments with real materials.

The main conclusion that follows from this consideration is that due to the internal structure reorganization such concept as the *material line* can loose its sense, and consequently the geometrical definition of deformation looses the sense for the significant inelastic deformations.

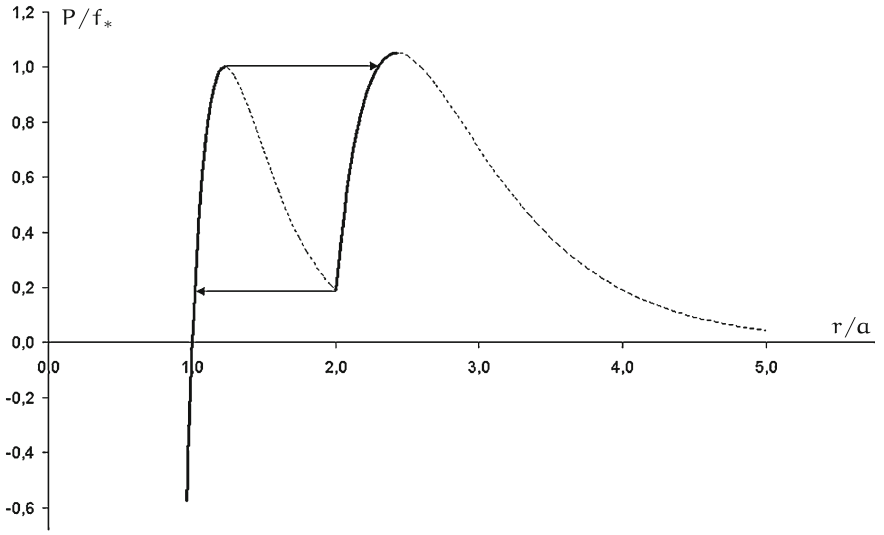

Fig. 2 Loading diagram for the system of three interacting particles

3 Continuum Description

From the previous section it follows that generally for significant inelastic deformations of materials the strain tensors defined from pure geometrical reasons are not suitable to be used in the theory of constitutive relations. It is necessary to look for another approach. Let us describe an idea of possible method of introduction of a strain tensor for inelastic continua. The starting point is the equation of energy balance

$$\rho\dot{\mathrm{U}} = \boldsymbol{\tau} \cdot\cdot\, \mathbf{D} + \rho s - \nabla\cdot\mathbf{h}, \qquad \mathbf{D} \equiv (\nabla\mathbf{v} + \nabla\mathbf{v}^{\mathrm{T}})/2, \tag{4}$$

where ρ is the material density; U is the specific internal energy (in terms of mass); $\boldsymbol{\tau}$ is the Cauchy stress tensor; $\mathbf{D}$ is the stretching tensor; s is the heat supply; $\mathbf{h}$ is the heating-flux vector; $\mathbf{v}$ is the velocity vector; ∇ is the vector differential operator in the actual configuration. The first term in the right side of Eq. (4) is called the power of stress. Note that here the direct tensor notation in the sense of [7, 8] is used. In addition, the gradient of a vector (for example, velocity) is introduced as in [7] that means as the transpose of the quantity defined in most other textbooks.

Let us accept the following definition:

Definition 19.1. The quantity $\boldsymbol{\mathcal{E}}$, on the variation of which the Cauchy stress tensor $\boldsymbol{\tau}$ is producing the work, is called material strain tensor.

From the definition it follows

$$\boldsymbol{\tau} \cdot\cdot\, \mathbf{D} = \boldsymbol{\tau} \cdot\cdot\, \dot{\boldsymbol{\mathcal{E}}} \quad \Rightarrow \quad \boldsymbol{\tau} \cdot\cdot\, (\dot{\boldsymbol{\mathcal{E}}} - \mathbf{D}) = 0, \qquad \forall\boldsymbol{\tau}:\ \boldsymbol{\tau} = \boldsymbol{\tau}^{\mathrm{T}}. \tag{5}$$

The symmetric tensor $\boldsymbol{\mathcal{E}}$ must be an objective one, i. e. under superposition of rigid motions we have to get

$$\boldsymbol{\mathcal{E}}_* = \mathbf{Q} \cdot \boldsymbol{\mathcal{E}} \cdot \mathbf{Q}^{\mathrm{T}}, \tag{6}$$

where $\boldsymbol{\mathcal{E}}_*$ is the tensor $\boldsymbol{\mathcal{E}}$ being transformed by the rigid rotation $\mathbf{Q}$ ($\mathbf{Q} \cdot \mathbf{Q}^{\mathrm{T}} = \mathbf{E}$ with $\mathbf{E}$ as the unit tensor), applied to the whole system. The tensors $\boldsymbol{\tau}$ and $\mathbf{D}$ are also objective ones:

$$\boldsymbol{\tau}_* = \mathbf{Q} \cdot \boldsymbol{\tau} \cdot \mathbf{Q}^{\mathrm{T}}, \qquad \mathbf{D}_* = \mathbf{Q} \cdot \mathbf{D} \cdot \mathbf{Q}^{\mathrm{T}} \quad \Rightarrow \quad \boldsymbol{\tau}_* \cdot\cdot \mathbf{D}_* = \boldsymbol{\tau} \cdot\cdot \mathbf{D}. \tag{7}$$

Let us accept that relation (5) remains after addition of the rigid motions

$$\boldsymbol{\tau}_* \cdot\cdot \mathbf{D}_* = \boldsymbol{\tau}_* \cdot\cdot \dot{\boldsymbol{\mathcal{E}}}_*. \tag{8}$$

Then according to Eqs. (7) and (8) we obtain the identity

$$\boldsymbol{\tau}_* \cdot\cdot \dot{\boldsymbol{\mathcal{E}}}_* = \boldsymbol{\tau} \cdot\cdot \dot{\boldsymbol{\mathcal{E}}} \tag{9}$$

The substitution of relations (6) and (7) for tensors $\boldsymbol{\tau}$ and $\boldsymbol{\mathcal{E}}$ in the identity (9) after some transformations[3] gives

$$\boldsymbol{\tau} \cdot \boldsymbol{\mathcal{E}} = \boldsymbol{\mathcal{E}} \cdot \boldsymbol{\tau}, \qquad \boldsymbol{\tau}_* \cdot \boldsymbol{\mathcal{E}}_* = \boldsymbol{\mathcal{E}}_* \cdot \boldsymbol{\tau}_*. \tag{10}$$

From Eq. (10) it is seen that the eigenvectors of tensors $\boldsymbol{\tau}$ and $\boldsymbol{\mathcal{E}}$ are the same. Thus for any material the tensor $\boldsymbol{\tau}$ is an isotropic function of $\boldsymbol{\mathcal{E}}$. It means that the tensor $\boldsymbol{\mathcal{E}}$ must depend on properties of the material and it cannot be found from pure geometrical considerations. This is clear at least from the fact that the equalities (10) should be valid also for an anisotropic material.[4]

Using Eq. (5) let us introduce the symmetric tensor $\mathbf{L}$ such as

$$\dot{\boldsymbol{\mathcal{E}}} + \mathbf{L} = \mathbf{D} \qquad (\boldsymbol{\tau} \cdot\cdot \mathbf{L} = 0, \quad \forall \boldsymbol{\tau} : \ \boldsymbol{\tau} = \boldsymbol{\tau}^{\mathrm{T}}), \tag{11}$$

where the symmetric tensor $\mathbf{L}$ is not a priori known. $\mathbf{L}$ depends on properties of the material. Let us point out only one possible form of the tensor $\mathbf{L}$

$$\mathbf{L} = \boldsymbol{\omega} \cdot \boldsymbol{\mathcal{E}} - \boldsymbol{\mathcal{E}} \cdot \boldsymbol{\omega}, \qquad \boldsymbol{\omega}^{\mathrm{T}} = -\boldsymbol{\omega}. \tag{12}$$

---

[3] Here it is used: $\dot{\mathbf{Q}} \cdot \mathbf{Q}^{\mathrm{T}}$—antisymmetric tensor, identity $\mathbf{A} \cdot\cdot \mathbf{B} \cdot \mathbf{C} = \mathbf{A} \cdot \mathbf{B} \cdot\cdot \mathbf{C}$ and statement: $\mathbf{A} \cdot\cdot \mathbf{B} = 0, \quad \forall \mathbf{A} : \ \mathbf{A}^{\mathrm{T}} = -\mathbf{A} \quad \Rightarrow \quad \mathbf{B}^{\mathrm{T}} = \mathbf{B}$.

[4] This statement becomes more evident if we consider the linear theory. Indeed, in the linear theory the elasticity relations have the form $\boldsymbol{\tau} = \mathbf{C} \cdot\cdot \boldsymbol{\varepsilon}$, where $\mathbf{C}$ is the stiffness tensor and $\boldsymbol{\varepsilon}$ is the linear strain tensor, which has pure geometrical definition. In the case of an anisotropic material the principal axis of the tensors $\boldsymbol{\varepsilon}$ and $\mathbf{C} \cdot\cdot \boldsymbol{\varepsilon}$ have different orientations. In our case we have to introduce an alternative strain tensor $\boldsymbol{\mathcal{E}}$ in such way, that it should be coaxial to the tensor $\mathbf{C} \cdot\cdot \boldsymbol{\mathcal{E}}$. It is clear, that such a strain tensor should by some means take into account the anisotropy of the material.

Using the objectivity of tensors $\boldsymbol{\mathcal{E}}$ and $\mathbf{D}$ and equality (11), e.g. taking into account that

$$\dot{\boldsymbol{\mathcal{E}}}_* + \mathbf{L}_* = \mathbf{D}_*, \qquad \mathbf{L}_* = \boldsymbol{\omega}_* \cdot \boldsymbol{\mathcal{E}}_* - \boldsymbol{\mathcal{E}}_* \cdot \boldsymbol{\omega}_*. \tag{13}$$

It can be shown that the tensor $\boldsymbol{\omega}$ under the superposition of rigid motions must satisfy the equation

$$\boldsymbol{\omega}_* = \mathbf{Q} \cdot \boldsymbol{\omega} \cdot \mathbf{Q}^{\mathsf{T}} - \dot{\mathbf{Q}} \cdot \mathbf{Q}^{\mathsf{T}}. \tag{14}$$

The substitution of the representation (12) for the tensor $\mathbf{L}$ in equality (11) gives the differential equation for the material strain tensor $\boldsymbol{\mathcal{E}}$

$$\dot{\boldsymbol{\mathcal{E}}} + \boldsymbol{\omega} \cdot \boldsymbol{\mathcal{E}} - \boldsymbol{\mathcal{E}} \cdot \boldsymbol{\omega} = \mathbf{D}. \tag{15}$$

Tensors $\boldsymbol{\mathcal{E}}$ and $\boldsymbol{\omega}$ in (15) are unknown. To find them we have to use additional (constitutive) equations.

4 Determination of the Material Strain Tensor in some Particular Cases

Let us find the trace of tensor $\boldsymbol{\mathcal{E}}$ by calculating the trace of Eq. (15). Using the identity $\boldsymbol{\omega} \cdot\cdot\, \boldsymbol{\mathcal{E}} = 0$ we can obtain

$$(\mathrm{tr}\, \boldsymbol{\mathcal{E}})^{\cdot} = \mathrm{tr}\mathbf{D} = \nabla \cdot \mathbf{v} = -\dot{\rho}/\rho. \tag{16}$$

Here the continuity equation is applied. The integration of relation (16) gives

$$\mathrm{tr}\, \boldsymbol{\mathcal{E}} = \ln(\rho_0/\rho) = \ln(1 + \Delta), \tag{17}$$

where ρ_0 is the density of the undeformed material, Δ is the cubic dilatation. Equality (16) is correct for all materials. However, the deviator of $\boldsymbol{\mathcal{E}}$ essentially depends on the material properties.

Let us neglect thermal effects. Then the energy balance (4) takes the form

$$\rho \dot{\mathsf{U}} = \boldsymbol{\tau} \cdot\cdot\, \dot{\boldsymbol{\mathcal{E}}}. \tag{18}$$

Assuming elastic material behavior the internal energy and the stress tensor depend on strains only, and they are not dependent on the strain rate. According to Eq. (18) the internal energy of an elastic material has the form $\mathsf{U} = \mathsf{U}(\boldsymbol{\mathcal{E}})$. The calculation of the time derivative from the internal energy gives

$$\rho \frac{\partial \mathsf{U}}{\partial \boldsymbol{\mathcal{E}}} \cdot\cdot\, \dot{\boldsymbol{\mathcal{E}}} = \boldsymbol{\tau} \cdot\cdot\, \dot{\boldsymbol{\mathcal{E}}} \quad \Rightarrow \quad \boldsymbol{\tau} = \rho \frac{\partial \mathsf{U}}{\partial \boldsymbol{\mathcal{E}}}. \tag{19}$$

To fulfil this relation tensor $\boldsymbol{\mathcal{E}}$ should be Hencky's tensor (logarithmic strain measure—the logarithm of the right kernel of the distortion tensor).

Proof. [5] Indeed, according to [6]

$$\boldsymbol{\tau} = 2\frac{\rho}{\rho_0}\,\mathbf{F}\cdot\frac{\partial W}{\partial \mathbf{F}}, \qquad \mathbf{F} = (\nabla \mathbf{r}\cdot\mathbf{r}\nabla)^{-1}, \tag{20}$$

where $\mathbf{r}$ is the reference position vector; $\mathbf{F}$ is Finger's strain tensor and $W = \rho_0 \mathrm{U}$ is the internal energy volume density in the reference configuration. For Hencky's tensor $\mathbf{H}$ we have [6]

$$\mathbf{H} = \ln \mathbf{V}, \qquad \mathbf{F} = \mathbf{V}^2. \tag{21}$$

Here $\mathbf{V}$ is the right kernel of the distortion tensor. The substitution of relation (21) in Eq. (20) for the Cauchy stress tensor one can obtain finally

$$\boldsymbol{\tau} = \rho\frac{\partial \mathrm{U}}{\partial \mathbf{H}} \quad \Rightarrow \quad \mathbf{H} = \boldsymbol{\mathcal{E}}. \tag{22}$$

So, *for elastic isotropic material the Cauchy stress tensor performs the work on Hencky's logarithmic strain measure.*[6] □

Therefore, according to the definition, which was introduced before, Hencky's measure and only it is the material strain tensor for the elastic isotropic material. It is known that Hencky's measure is frequently accepted by experimenters as the most convenient way for description of large deformations.

It can be shown,[7] that tensor $\boldsymbol{\omega}$ is uniquely determined for elastic isotropic materials and tensors $\boldsymbol{\mathcal{E}}$ and $\boldsymbol{\omega}$ also can be determined for materials with infinite short memory, which is good for the description of large plastic deformations.

5 Discussion and Concluding Remarks

Here the original text by P. A. Zhilin, which is used as a basis for this chapter, comes to an end. In private communications P. A. Zhilin has stated that this approach can form a basis for an essentially new theory of constitutive equations. In particular, he has noted that this approach allows to obtain the strain tensor, which for a periodical

[5] This proof is suggested by A. Krivtsov, the original proof by P.A. Zhilin unfortunately is lost.

[6] This result was obtained by P. A. Zhilin and it was explained in private communications to his pupils before 1995, however it was not officially published. In 1995 a short paper with this result was submitted to ICIAM 95 proceedings, however it was rejected. In 1997 a paper by other authors was published in Acta Mechanica [9], where the same result is presented as obtained for the first time.

[7] Proof of these statements by P. A. Zhilin unfortunately is not preserved.

twisting (with variable sign) of a rod gives an increase of deformation at each period, and this is convenient for describing such phenomena as fatigue.

Later the chapter [9] was published, which significantly correlates with the results, obtained by P. A. Zhilin. In this chapter the use of Hencky's logarithmic strain is analyzed and it is proved that this strain measure is the work-conjugate of the Cauchy stress tensor (the unpublished result by P. A. Zhilin, obtained earlier). Besides, in [9] it is proved, that $\mathbf{H}$ is the only strain measure, the objective corotational rate of which gives the stretching tensor $\mathbf{D}$. Let us remind that the corotational rate of a tensor $\mathbf{A}$ is defined as[8]

$$\mathbf{A}' = \dot{\mathbf{A}} + \boldsymbol{\Omega}\cdot\mathbf{A} - \mathbf{A}\cdot\boldsymbol{\Omega}, \tag{23}$$

where $\boldsymbol{\Omega}$ is the spin tensor, characterizing some rotations connected with the deformation process. The geometrical sense of the corotational rate is that it neglects changes of the tensor $\mathbf{A}$, connected with the rotation $\boldsymbol{\Omega}$. A variety of corotational rates is used in the literature. The rates differ by the choice of the tensor $\boldsymbol{\Omega}$. In particular, if $\boldsymbol{\Omega} = (\nabla\mathbf{v})^{A}$ (the vorticity tensor) then (20) gives the Jaumann rate [9, 10]. For many years there was no answer to the question: is the stretching tensor $\mathbf{D}$ an objective corotational rate of any strain tensor. In [9] for the first time it is shown that such tensor can be only the Hencky logarithmic strain. Moreover, in [9] the corresponding spin tensor is found $\boldsymbol{\Omega}^{\log}$, called by the authors logarithmic spin, for which it fulfils that[9]

$$\mathbf{H}'^{\log} = \dot{\mathbf{H}} + \boldsymbol{\Omega}^{\log}\cdot\mathbf{H} - \mathbf{H}\cdot\boldsymbol{\Omega}^{\log} = \mathbf{D}, \tag{24}$$

where $(\ldots)'^{\log}$ is logarithmic rate of $\mathbf{H}$, also introduced in [9]. If now one considers the equation obtained by P. A. Zhilin (15) for the material strain tensor, then the application of it to the Hencky logarithmic strain $\boldsymbol{\mathcal{E}} = \mathbf{H}$ will lead to the conclusion that the antisymmetric tensor used in (15) is the logarithmic spin: $\boldsymbol{\omega} = \boldsymbol{\Omega}^{\log}$.

Let us consider again Eq. (15)

$$\dot{\boldsymbol{\mathcal{E}}} + \boldsymbol{\omega}\cdot\boldsymbol{\mathcal{E}} - \boldsymbol{\mathcal{E}}\cdot\boldsymbol{\omega} = \mathbf{D}. \tag{25}$$

The problem of its solution can be now reformulated as the following: it is necessary to find such an objective tensor $\boldsymbol{\mathcal{E}}$, corotational rate of which is equal to the stretching tensor $\mathbf{D}$. In fact, this problem is solved in [9]—there it is proved that such tensor $\boldsymbol{\mathcal{E}}$ is Hencky's logarithmic strain $\mathbf{H}$, and tensor $\boldsymbol{\omega} = \boldsymbol{\Omega}^{\log}$ is found as some complex function[10] of tensors $\boldsymbol{\mathcal{E}}$ and $\mathbf{D}$ [9, 11].

---

[8] Frequently an alternative form of the corotational rate is used, where the difference is in the sign of $\boldsymbol{\Omega}$. This is because the definition of the gradient of a vector can be as in this chapter and [7] or in the transposed form. As a consequence the sign of the spin tensor can differ.

[9] This formula for logarithmic rate differs from the one in [9] by the sign of $\boldsymbol{\Omega}^{\log}$ (see the previous footnote).

[10] For some particular strain fields (e.g. when all the tensors $\mathbf{H}$ are coaxial) the tensor $\boldsymbol{\Omega}^{\log}$ is reduced to the vorticity tensor $(\nabla\mathbf{v})^{A}$ and logarithmic rate became Jaumann's rate. However in

Thus in [9] pure geometrical expressions are obtained for tensors $\boldsymbol{\mathcal{E}}$ and $\boldsymbol{\omega}$ being determined from Eq. (15). These results became very fruitful, as in the nonlinear theory of elasticity, as in the theory of elasto-plastic bodies [12–14]. In particular, later on it is shown [12] that the use of the logarithmic strain and logarithmic spin (connected by Eq. (15)) allows the correct formulation of the incremental elastic relations for hypoelastic materials. These incremental relations are widely used in numerical algorithms. Namely usage of these tensors makes these equations integrable, allowing transition from the incremental of the constitutive equations to the explicit one. This permits unique notions of hypoelastic and hyperelastic materials. Beyond the elasticity limit this approach allows to build the theory of elasto-plastic materials, where the decomposition of the strain tensor in elastic and plastic parts is not needed [13]. However, together with these successes there remained a lot of problems in description of inelastic behavior of materials.

The ideas of [9] partially coincides with the ideas of P. A. Zhilin. But this is only partial coincidence. The essence of P. A. Zhilin's idea is to introduce such a strain tensor that

1. the Cauchy stress tensor performs work on this strain tensor;
2. it should be materially objective;
3. *this tensor is not necessary a deformation in a classical sense.*

The latter means that this tensor is not necessary an isotropic function of the distortion (deformation gradient) tensor, in particular this strain tensor can depend on the space symmetry of the material. In the case of elastic isotropic material, according to [9], the problem of finding this tensor can be solved from purely geometrical means. In [9] it is stated that the unique solution of Eq. (15) is found. However, this solution is sought only on the set of classical strain tensors. For strain tensors in Zhilin's sense Eq. (15) probably has also another solutions. Let us show it on the example of an elastic anisotropic material. Tensors $\boldsymbol{\mathcal{E}}$, $\boldsymbol{\omega} = \boldsymbol{\Omega}^{\log}$ satisfy Eq. (15) for both isotropic and anisotropic materials. However, in the case of anisotropic material this solution contradict the condition of coaxiality of strain and stress tensors (10), which is the consequence from the material objectivity. In order to fulfill condition (10) tensor $\boldsymbol{\mathcal{E}}$ should have a structure, which depends on the material properties. Thus the idea of P. A. Zhilin of introduction of the material strain tensor, which should be determined using the energy balance equation and *properties of the considered material*, still is waiting for its development.

Remark 19.1. In his latest works in the area of inelastic media P. A. Zhilin was using the spatial representation instead of the material one. The results obtained for the material representation can not be transferred directly to the case of the spatial representation. From the mathematical point of view the problem became more complicated since in Eq. (15) the full time derivative is replaced by the material one. However, the statement of the problem of finding the strain tensor possessing the specified above properties is possible for the spatial representation as well. We

general case the representation for $\boldsymbol{\Omega}^{\log}$ is much more complex, which is connected with existence of two independent rotations—rotation of media and rotation of the main axis of the strain tensor.

believe that the application of the ideas of this work for the spatial representation could be the way for construction of inelastic constitutive equations.

Remark 19.2. In the current work an original approach, suggested by P. A. Zhilin, is presented. The approach is intended for obtaining constitutive equations for the solids subjected to large inelastic deformations in the case of the material representation, where the classical strain measures results in serious problems in description of the material subjected to reorganization of its to internal structure. Alternatively a space representation can be used, in principle allowing to obtain the constitutive equations in the considered case using classical strain measures. However, the strain representation can be used only in the case of 3D bodies. In the theories of shells and rods, where the differential operators are defined on a surface or on a curve in the 3D space only the material representation can be used. Therefore for the description of large inelastic deformations of rods and shells the approach by P. A. Zhilin is of particular interest.

Remark 19.3. [11] It is interesting to note that almost at the same time several groups had the same idea. The results of Bruhns and co-authors were first presented at the "International Symposium on Plasticity and Impact Mechanics" IMPLAST 96, held at New Delhi, India, 11–14 December 1996. The corresponding presentation was published in the conference book [15]. On this same symposium there was also a presentation by R.N. Dubey and W.D. Reinhardt, Waterloo, Canada, ([15], pp 79–99) who treated the same problem.

Remark 19.4. [12] With reference to the last paragraph of the contribution it should be mentioned that in a different paper [16] also non-corotational rates were taken into consideration by replacing the general spin tensor $\boldsymbol{\Omega}$ by a general asymmetric second order tensor $\boldsymbol{\Psi}$. This has led to more general solutions of the problem under consideration.

Acknowledgments Authors are deeply grateful to O.T. Bruhns for helpful discussions of the final version of the paper.

References

1. Truesdell, C.: First Course in Rational Continuum Mechanics: General Concepts (2nd edn.), vol. 1. Academic Press, San Diego (1991)
2. Palmov, V.A.: Vibrations of Elasto-Plastic Bodies. Springer, Berlin (1998)
3. Altenbach, H.: Kontinuumsmechanik - Eine elementare Einführung in die materialunabhängigen und materialabhängigen Gleichungen. Springer-Vieweg, Heidelberg (2012)
4. Morse, P.M.: Diatomic molecules according to the wave mechanics. II. Vibrational levels. Phys. Rev. **34**(1), 57–64 (1929)

[11] Personal communication by O.T. Bruhns

[12] Personal communication by O.T. Bruhns

5. Krivtsov, A.: Deformation and Fracture of Solids with Microstructure (in Russ.). Fizmatlit, Moscow (2007)
6. Lurie, A.I.: Nonlinear Theory of Elasticity. North-Holland, Amsterdam (1990)
7. Lurie, A.I.: Theory of Elasticity. Springer, Berlin (2005)
8. Lebedev, L.P., Cloud, M.J., Eremeyev, V.A.: Tensor Analysis with Applications to Mechanics. World Scientific, Singapore (2010)
9. Xiao, H., Bruhns, O.T., Meyers, A.: Logarithmic strain, logarithmic spin and logarithmic rate. Acta. Mech. **124**, 89–105 (1997)
10. Palmov, V.A.: Fundamental Laws of Nature in Nonlinear Thermomechanics of Deformoble Bodies (in Russ.). SPbSTU Publishing, St. Petersburg (2008)
11. Golovanov, A.I.: Kinematics of finite deformations 3D isoparametrical finite elements for shells (in Russ.). Probl. Strength. Plast. **70**, 109–122 (2008)
12. Xiao, H., Bruhns, O.T., Meyers, A.: Existence and uniqueness of the integrable-exactly hypoelastic equation $\boldsymbol{\tau}^{\circ *} = \lambda(\mathrm{tr}\mathbf{D})\mathbf{I} + 2\mu\mathbf{D}$ and its significance to finite inelasticity. Acta. Mech. **138**, 31–50 (1999)
13. Xiao, H., Bruhns, O.T., Meyers, A.: Elastoplasticity beyond small deformations. Acta.Mech. **182**, 31–111 (2006)
14. Korobeynikov, S.N.: Families of continuous spin tensors and applications in continuum mechanics. Acta. Mech. **216**, 301–332 (2011)
15. Xiao, H., Bruhns, O.T., Meyers, A.: A new aspect in the kinematics of large deformations. In: Gupta, N.K. (ed.) Plasticity and Impact Mechanics, pp. 100–109. New Age International Ltd Publishing, New Delhi (1997)
16. Bruhns, O.T., Meyers, A., Xiao, H.: On non-corotational rates of Oldroyd's type and relevant issues in rate constitutive formulations. Proc. Royal Soc. Lond. A. **460**, 909–928 (2004)